

# The application of network analysis in ethnopharmacology

**Edited by**

Ren-You Gan, Siew Bee Ng, Yibin Feng, Hua-Bin Li  
and Liang Zou

**Published in**

Frontiers in Pharmacology



## FRONTIERS EBOOK COPYRIGHT STATEMENT

The copyright in the text of individual articles in this ebook is the property of their respective authors or their respective institutions or funders. The copyright in graphics and images within each article may be subject to copyright of other parties. In both cases this is subject to a license granted to Frontiers.

The compilation of articles constituting this ebook is the property of Frontiers.

Each article within this ebook, and the ebook itself, are published under the most recent version of the Creative Commons CC-BY licence. The version current at the date of publication of this ebook is CC-BY 4.0. If the CC-BY licence is updated, the licence granted by Frontiers is automatically updated to the new version.

When exercising any right under the CC-BY licence, Frontiers must be attributed as the original publisher of the article or ebook, as applicable.

Authors have the responsibility of ensuring that any graphics or other materials which are the property of others may be included in the CC-BY licence, but this should be checked before relying on the CC-BY licence to reproduce those materials. Any copyright notices relating to those materials must be complied with.

Copyright and source acknowledgement notices may not be removed and must be displayed in any copy, derivative work or partial copy which includes the elements in question.

All copyright, and all rights therein, are protected by national and international copyright laws. The above represents a summary only. For further information please read Frontiers' Conditions for Website Use and Copyright Statement, and the applicable CC-BY licence.

ISSN 1664-8714  
ISBN 978-2-8325-2498-5  
DOI 10.3389/978-2-8325-2498-5

## About Frontiers

Frontiers is more than just an open access publisher of scholarly articles: it is a pioneering approach to the world of academia, radically improving the way scholarly research is managed. The grand vision of Frontiers is a world where all people have an equal opportunity to seek, share and generate knowledge. Frontiers provides immediate and permanent online open access to all its publications, but this alone is not enough to realize our grand goals.

## Frontiers journal series

The Frontiers journal series is a multi-tier and interdisciplinary set of open-access, online journals, promising a paradigm shift from the current review, selection and dissemination processes in academic publishing. All Frontiers journals are driven by researchers for researchers; therefore, they constitute a service to the scholarly community. At the same time, the *Frontiers journal series* operates on a revolutionary invention, the tiered publishing system, initially addressing specific communities of scholars, and gradually climbing up to broader public understanding, thus serving the interests of the lay society, too.

## Dedication to quality

Each Frontiers article is a landmark of the highest quality, thanks to genuinely collaborative interactions between authors and review editors, who include some of the world's best academicians. Research must be certified by peers before entering a stream of knowledge that may eventually reach the public - and shape society; therefore, Frontiers only applies the most rigorous and unbiased reviews. Frontiers revolutionizes research publishing by freely delivering the most outstanding research, evaluated with no bias from both the academic and social point of view. By applying the most advanced information technologies, Frontiers is catapulting scholarly publishing into a new generation.

## What are Frontiers Research Topics?

Frontiers Research Topics are very popular trademarks of the *Frontiers journals series*: they are collections of at least ten articles, all centered on a particular subject. With their unique mix of varied contributions from Original Research to Review Articles, Frontiers Research Topics unify the most influential researchers, the latest key findings and historical advances in a hot research area.

Find out more on how to host your own Frontiers Research Topic or contribute to one as an author by contacting the Frontiers editorial office: [frontiersin.org/about/contact](https://frontiersin.org/about/contact)



# The application of network analysis in ethnopharmacology

## Topic editors

Ren-You Gan — Singapore Institute of Food and Biotechnology Innovation, Agency for Science, Technology and Research, Singapore

Siew Bee Ng — Singapore Institute of Food and Biotechnology Innovation, Agency for Science, Technology and Research, Singapore

Yibin Feng — The University of Hong Kong, SAR China

Hua-Bin Li — Sun Yat-sen University, China

Liang Zou — Chengdu University, China

## Topic coordinator

Michael Heinrich — University College London, United Kingdom

## Citation

Gan, R.-Y., Ng, S. B., Feng, Y., Li, H.-B., Zou, L., eds. (2023). *The application of network analysis in ethnopharmacology*. Lausanne: Frontiers Media SA.  
doi: 10.3389/978-2-8325-2498-5

## Table of contents

- 05 **Network analysis combined with pharmacological evaluation strategy to reveal the mechanism of Tibetan medicine Wuwei Shexiang pills in treating rheumatoid arthritis**  
Qingxiu He, Xiaoyan Tan, Sang Geng, Qinyun Du, Zhaoqing Pei, Yingrui Zhang, Shaohui Wang and Yi Zhang
- 20 **Umbelliferone and scopoletin target tyrosine kinases on fibroblast-like synoviocytes to block NF- $\kappa$ B signaling to combat rheumatoid arthritis**  
Qilei Chen, Wenmin Zhou, Yueming Huang, Yuanyang Tian, Sum Yi Wong, Wing Ki Lam, Ka Yee Ying, Jianye Zhang and Hubiao Chen
- 36 **Wenshenyang recipe treats infertility through hormonal regulation and inflammatory responses revealed by transcriptome analysis and network pharmacology**  
Lan Xie, Shuai Zhao, Xiaoling Zhang, Wenting Huang, Liansheng Qiao, Delin Zhan, Chengmei Ma, Wei Gong, Honglei Dang and Hua Lu
- 56 **Evaluating the therapeutic role of selected active compounds in *Plumula Nelumbinis* on pulmonary hypertension via network pharmacology and experimental analysis**  
Xinghua Xiao, Fangmei Luo, Minyi Fu, Yueping Jiang, Shao Liu and Bin Liu
- 73 **The comparative effects of oral Chinese patent medicines combined with western medicine in stable angina: A systematic review and network meta-analysis of 179 trials**  
Peiying Huang, Zhishang Li, Li Chen, Jing Zeng, Shuai Zhao, Yong Tang, Bixuan Huang, Hansu Guan, Yan Chen, Yuchao Feng, Sisi Lei, Qihua Wu, Haobo Zhang, Xiaoyan Huang, Linsheng Zeng, Yuxiang Liu, Zhongyi Zeng and Bojun Chen
- 85 **Mailuoshutong pill for varicocele-associated male infertility—Phytochemical characterisation and multitarget mechanism**  
Dongfang Lv, Yun Ji, Qian Zhang, Zhuozhuo Shi, Tengfei Chen, Chao Zhang, Xiangyun Wang, Taotao Ren, Zhaowang Gao and Chongfu Zhong
- 102 **Triptolide in the treatment of systemic lupus erythematosus - regulatory effects on miR-146a in B cell TLR7 signaling pathway in mice**  
Yi Zhang, FengQi Zhang, YiNi Gao, MeiJiao Wang, Yan Gao, HaiChang Li, Jing Sun, ChengPing Wen and ZhiJun Xie
- 112 **The exploration of the potential mechanism of oxymatrine-mediated antipruritic effect based on network pharmacology and weighted gene co-expression network analysis**  
Zhenhui Luo, Tingting Zhao, Mengqin Yi, Tingting Wang, Zhenglang Zhang, Wenbin Li, Na Lin, Shangdong Liang, Alexei Verkhatsky and Hong Nie

- 130 **Network analysis and experimental pharmacology study explore the protective effects of Isoliquiritigenin on 5-fluorouracil-Induced intestinal mucositis**  
Yi-fan Liao, Feng-lin Luo, Shan-shan Tang, Jing-wei Huang, Ying Yang, Shuang Wang, Tang-yu Jiang, Qiong Man, Sha Liu and Yi-ying Wu
- 144 **Effects of dehydroabiatic acid on nontarget lipidomics and proteomics of HepG2**  
Zhikai Xiahou and Jun Han
- 161 **Uncovering the pharmacological mechanisms of Zizhu ointment against diabetic ulcer by integrating network analysis and experimental evaluation *in vivo* and *in vitro***  
Jie Wang, Yu Wang, Renyan Huang, Wenhui Li, Weijing Fan, Xiaoming Hu, Xiao Yang, Qiang Han, Hongfei Wang and Guobin Liu
- 179 **Comparative clinical-related outcomes of Chinese patent medicines for cardiac hypertrophy: A systematic review and network meta-analysis of randomized clinical trials**  
Tianqi Zhang, Haoyang Xu, Dong Zhen, Danni Fu, Ming Zhao, Chengxi Wei and Xue Bai
- 199 **Protective effects and mechanisms of the Erzhi formula on glucocorticoid induced primary cortical neuron injury**  
Rui Han, Guoying Han, Yiqi Yan, Lifeng Han, Lin Li and Han Zhang



## OPEN ACCESS

## EDITED BY

Ren-You Gan,  
Institute of Urban Agriculture (CAAS),  
China

## REVIEWED BY

Zhenfeng Wu,  
Jiangxi University of Traditional Chinese  
Medicine, China  
Li Shuran,  
Institute of Chinese Materia Medica,  
China Academy of Chinese Medical  
Sciences, China

## \*CORRESPONDENCE

Yi Zhang,  
zhangyi@cdutcm.edu.cn  
Shaohui Wang,  
winter9091@163.com

<sup>†</sup>These authors have contributed equally  
to this work

## SPECIALTY SECTION

This article was submitted to  
Ethnopharmacology,  
a section of the journal  
Frontiers in Pharmacology

RECEIVED 11 May 2022

ACCEPTED 01 July 2022

PUBLISHED 18 July 2022

## CITATION

He Q, Tan X, Geng S, Du Q, Pei Z,  
Zhang Y, Wang S and Zhang Y (2022),  
Network analysis combined with  
pharmacological evaluation strategy to  
reveal the mechanism of Tibetan  
medicine Wuwei Shexiang pills in  
treating rheumatoid arthritis.  
*Front. Pharmacol.* 13:941013.  
doi: 10.3389/fphar.2022.941013

## COPYRIGHT

© 2022 He, Tan, Geng, Du, Pei, Zhang,  
Wang and Zhang. This is an open-  
access article distributed under the  
terms of the [Creative Commons  
Attribution License \(CC BY\)](#). The use,  
distribution or reproduction in other  
forums is permitted, provided the  
original author(s) and the copyright  
owner(s) are credited and that the  
original publication in this journal is  
cited, in accordance with accepted  
academic practice. No use, distribution  
or reproduction is permitted which does  
not comply with these terms.

# Network analysis combined with pharmacological evaluation strategy to reveal the mechanism of Tibetan medicine Wuwei Shexiang pills in treating rheumatoid arthritis

Qingxiu He<sup>1†</sup>, Xiaoyan Tan<sup>2†</sup>, Sang Geng<sup>3†</sup>, Qinyun Du<sup>2</sup>,  
Zhaoqing Pei<sup>4</sup>, Yingrui Zhang<sup>1</sup>, Shaohui Wang<sup>1\*</sup> and Yi Zhang<sup>1\*</sup>

<sup>1</sup>State Key Laboratory of Southwestern Chinese Medicine Resources, School of Ethnic Medicine, Chengdu University of Traditional Chinese Medicine, Chengdu, China, <sup>2</sup>State Key Laboratory of Southwestern Chinese Medicine Resources, School of Pharmacy, Chengdu University of Traditional Chinese Medicine, Chengdu, China, <sup>3</sup>Affiliated Hospital of University of Tibetan Medicine, University of Tibetan Medicine, Lasa, China, <sup>4</sup>State Key Laboratory of Southwestern Chinese Medicine Resources, Innovative Institute of Chinese Medicine and Pharmacy, Chengdu University of Traditional Chinese Medicine, Chengdu, China

Tibetan medicine is an important part of traditional Chinese medicine and a significant representative of ethnic medicine in China. Tibetan medicine is gradually recognized by the world for its unique curative effects. Wuwei Shexiang pills (WPW) has been widely used to treat “Zhenbu” disease (Also known as rheumatoid arthritis) in Tibetan medicine, however, its potential bioactive ingredients and mechanism for RA treatment remain unclear. In this study, we used a combination of gas chromatography-mass spectrometry (GC-MS), ultra-performance liquid chromatography coupled with quadrupole time-of-flight mass spectrometry (UPLC-Q-TOF/MS), network analysis and experimental validation to elucidate the potential pharmacodynamic substances and mechanisms of WPW in the treatment of rheumatoid arthritis (RA). The results showed that songoramine, cheilanthifoline, saussureanine C, acoric acid, arjunolic acid, peraksine, ellagic acid, arjunenine and other 11 components may be the main activities of WPW in the treatment of RA. PI3KCA, AKT, MAPK, IL-6, TNF, MMP1, MMP3, and CDK1 are considered as core targets. PI3K-AKT, MAPK, apoptosis, cell cycle, and other signaling pathways may be the key pathways for WPW to play a role in the treatment of RA. Furthermore, we validated the underlying molecular mechanism of WPW predicted by network analysis and demonstrated its possible mechanism through *in vivo* animal experiments. It was found that WPW could significantly improve the degree of paw swelling, and reduce ankle joint diameter and arthritis index. Further histomorphological analysis showed that WPW could reduce the degree of synovial tissue inflammation and ankle joint cartilage damage. Meanwhile, WPW could down-regulate the levels of IL-6, IL-1 $\beta$ , and IL-17, and increase the levels of IL-10 and IL-4 in the serum of AA rats. TUNEL staining confirmed that WPW could significantly promote the

apoptosis of synovial cells. Moreover, the immunohistochemical results showed that WPW decreased the expression of PI3K, AKT, MAPK, MMP1, MMP3, CDK1, and Bcl-2, as well as increased the expression of Bax protein. In conclusion, we successfully combined GC-MS, UPLC-Q-TOF/MS, network analysis, and experimental validation strategies to elucidate the inhibition of inflammation by WPW in AA model rats via PI3K/AKT, MAPK, cell cycle and apoptotic pathways process. This not only provides new evidence for the study of potential pharmacodynamic substances and the mechanism of WPW in the treatment of RA, but also provides ideas for the study of other Tibetan medicine compound preparations.

#### KEYWORDS

Tibetan medicine, Wuwei Shexiang pills, rheumatoid arthritis, network analysis, GC-MS, UPLC-Q-TOF/MS

## 1 Introduction

Tibetan medicine originated in the Qinghai-Tibet Plateau of China. It is a complete theoretical system, unique therapeutic methods, and a medical system with strong ethnic characteristics formed by the Tibetan people through long-term practice (Wang et al., 2022b). Tibetan medicine has a long history and there are still a large number of classic works with far-reaching influence, such as “The Four Medical Tantras” and “Jingzhu Materia Medica” (Fu et al., 2020). Rheumatoid arthritis (RA) is a major and difficult disease characterized by progressive joint damage caused by chronic synovitis (Scott et al., 2010). The incidence of RA is high, currently, RA affects about 0.5%–1.0% of the global population, in particular, the risk of developing RA is 2–3 times higher in women than in men (Huang et al., 2021; Jin et al., 2017). Tibetan medicine has unique advantages in treating rheumatism, RA and gout (Wang S. et al., 2021). RA is called “Zhenbu (འཇུ་ཤེན་བུ་)” in Tibetan medicine. According to Tibetan medicine, “Zhenbu” was caused by “Huangshui” disease, the pathological mechanism of which was the imbalance of the three gastric fires and the passage of the dross into the liver, which further affected the function of “Chiba” (ཤིཁ་པ་ལྷོ་ལྷོ་) and caused incomplete separated blood to enter the gallbladder, resulting in “Huangshui” (ཆུ་ཤེན་བུ་) all over the body and accumulation in the joints, inducing “Zhenbu” disease (Su et al., 2021).

Wuwei Shexiang pills, also known as Wupeng pills (WPW, Tibetan name: འཇུ་ཤེན་བུ་པོ་), is included in the first part of the 2020 edition of the Chinese Pharmacopoeia and the Classic Tibetan medicine book “The Four Medical Tantras”. The formula is composed of *Terminalia chebula* Retz (Combretaceae; Chebulae fructus, 300 g), *Aucklandia lappa* Decne (Asteraceae; Aucklandiae radix, 100 g), *Moschus berezovskii* Flerov (Moschidae; Moschus, 10 g), *Aconitum pendulum* Busch (Ranunculaceae; Radixaconiti, 300 g), *Acorus calamus* L (Acoraceae; Acori calami rhizome, 60 g). And it has anti-inflammatory, analgesic and wind-dispelling effects (Gongbu et al., 2013). It is clinically used in Tibetan medicine

to treat “Zhenbu” disease and has a good effect (Ge and Nima, 2021). However, the potential pharmacodynamic substances and mechanisms of WPW against RA have not been elucidated. The pharmacodynamic substance of the compound is the key to the modernization of TCM/Tibetan medicine, which is the basis of safety, effectiveness and quality control of compound preparation of TCM/Tibetan medicine (Wang X. et al., 2021; Xu et al., 2021). Zhu et al. used HPLC to determine the content of Aconitum alkaloids in Wuwei Shexiang pills, and the results showed that the concentrations of aconitine in the range of 3.28–82.0  $\mu\text{g ml}^{-1}$  ( $r = 0.9998$ ), hypoaconitine in the range of 3.2–80.0  $\mu\text{g ml}^{-1}$  ( $r = 0.9998$ ) and mesaconitin in the range of 3.2–80.0  $\mu\text{g ml}^{-1}$  ( $r = 0.9998$ ) showed a good linear relationship (Zhu et al., 2012). Lu et al. used HPLC to analyze the content of costunolide and dehydrocostuslactone in Wuwei Shexiang pills, and it was found that their concentrations were 0.92 mg/g and 1.67 mg/g respectively (Lu and Feng, 2011). Fan et al. used TLC and HPLC methods to identify and determine the content of muscone in this formula, and the results showed that muscone has a good linear relationship in the range of 0.08–1.28  $\mu\text{g}$  (Fan et al., 2007). All in all, the current studies on the pharmacodynamic substances of this prescription mainly focus on the content determination of a certain component or the whole single component, which cannot fully explain the real pharmacodynamic value of WPW. With the development of modern science and technology, some studies on pharmacodynamic substances of traditional Chinese medicine/ethnic medicine have achieved a lot in practice (Zhang F. X. et al., 2021; Jiao et al., 2021; Shan et al., 2021), especially the emergence of artificial intelligence technologies such as network pharmacology (Gao et al., 2021) and systems biology (Joshi et al., 2021), which provide technical support for revealing the complex pharmacodynamic substances and mechanism of traditional Chinese medicine.

In this study, Wuwei Shexiang pills, a classic prescription of Tibetan medicine, was used as the research object. The strategy combining gas chromatography-mass spectrometry (GC-MS), ultra-performance liquid chromatography coupled with



quadrupole time-of-flight mass spectrometry (UPLC-Q-TOF/MS), network analysis, and experimental verification was used to explore the potential pharmacodynamic substances of WPW and clarify their possible mechanism of action, which is conducive to guiding the in-depth development and clinical application of WPW. In addition, it also provides ideas for revealing the effective substances of other Tibetan medicine compounds to treat diseases and realizing the quality control of higher-level compound preparations.

## 2 Materials and methods

### 2.1 Materials and chemicals

Chemical reference standards of cholic acid (DSTDD004201), chebulagic acid (DST200927-064), chebulic acid (DST200610-244), corilagin (DST210311-012), ethyl gallate (DSTDM006301), benzoic acid (DSTDB012001), linoleic acid (DST200611-211), betulin (DSTDB002701), aconitine (HR1001S4), benzoylmesaconine (DSTDB005601), benzoylaconitine (DSTDB005501), benzoylhypaconine (DSTDB005701), hypaconitine (DSTDC005801), mesaconitine (DSTDX002502), methyl caffeate (DST210427-054) and costunolide (DSTDM003001) were acquired from Chengdu Desite Biotechnology Co., (Chengdu, China), and the purity of all standards were above 98%. Ellagic acid (111959-201903, purity: HPLC  $\geq 98\%$ ) was purchased from China National Institute for Standard Products and Drug Control (Beijing, China). Deoxyaconitine was bought from Chenguang Biotechnology Company (Chengdu, China). Agilent 7890A-5975C Gas chromatography-mass spectrometry and Agilent GC-MSD workstation were purchased from Agilent Technologies (Santa Clara, USA). ACQUITY UPLC I-Class Ultra High-Performance Liquid Chromatography system, Xevo G2-XS QTOF High-resolution time of flight mass spectrometer, MassLynxV 4.2 Data acquisition and analysis workstation were obtained from Waters Corporation (Milford, MA, United States).

### 2.2 Sample extraction and preparation of GC-MS and UPLC-Q-TOF/MS

Wuwei Shexiang pills (Specifications: 0.3 g per 10 pills.) were purchased from Tibetan Xiongbalaqu Shenshui Tibetan Medicine Co., LTD (Tibet, China). For the extraction and preparation of GC-MS samples, the Chinese patent medicine WPW sample (15 g) was finely ground and passed through the second sieve. Further, the pills were put into a 250 ml triangular bottle, and 150 ml of n-hexane was added for 45 min of ultrasound. The solution was filtered out by filter paper, and the remaining medicinal materials were washed with n-hexane.

The obtained oil-like extract was dehydrated by adding anhydrous sodium sulfate, centrifuged for 1 min at  $12,000 \text{ r min}^{-1}$ , dissolved in 1 ml chromatographic hexane, diluted 60 times, and filtered by a microporous filter membrane ( $0.22 \mu\text{m}$ ), and the test solution was obtained.

For the extraction and preparation of UPLC-Q-TOF/MS samples, the WPW sample (5 g) was accurately weighed and placed in a 100 ml conical flask, then the ultrasonic extraction was performed twice with 6 times the amount of 70% ethanol, and the concentrated extract was dissolved in acetonitrile and placed in a 5 ml flask, then 1 ml constant volume into 10 ml measuring bottle, and the solution was then filtered through a  $0.22 \mu\text{m}$  microporous membrane. The standard stock solutions were prepared by dissolving appropriate amounts of the reference standards in acetonitrile.

### 2.3 GC-MS analysis

The determination was performed on an Agilent HP-5MS capillary mass spectrometry column with 5% Phenyl Methyl Silox ( $30 \text{ m} \times 250 \mu\text{m} \times 0.25 \mu\text{m}$ ). The carrier gas is helium (He), carrier gas velocity:  $1 \text{ ml min}^{-1}$ ; The heating procedure is as follows: the initial column temperature is  $50^\circ\text{C}$  and kept for 0.5 min; In the first stage, the temperature was increased to  $150^\circ\text{C}$  at  $5^\circ\text{C min}^{-1}$  for 0 min. In the second stage, the temperature was kept at  $6^\circ\text{C min}^{-1}$  L  $240^\circ\text{C}$  for 2 min. In the third stage, the temperature increased to  $250^\circ\text{C}$  at  $7^\circ\text{C min}^{-1}$ . Split injection, split ratio of 4:1, Injection volume:  $1 \mu\text{l}$ . The conditions of mass spectrometry were as follows: the ion source was EI, the electron energy was 70 eV, the ion source temperature was  $230^\circ\text{C}$ , the four-stage rod temperature was  $150^\circ\text{C}$ , the solvent delay was 4 min, and the data were collected in full scan mode, and the mass scan range was  $m/z$  12–550.

### 2.4 UPLC-Q-TOF/MS analysis

The chemical constituents of WPW were identified by UPLC-Q-TOF/MS. The chromatographic separation was performed on a Waters Acquity BEH-C18 column ( $2.1 \text{ mm} \times 100 \text{ mm}$ ,  $1.7 \mu\text{m}$ ). Mobile phase A: 0.1% formic acid aqueous solution, mobile phase B: acetonitrile; Flow rate,  $0.3 \text{ ml min}^{-1}$ ; Gradient elution (0–2 min, 2%–6%B; 2–10 min, 6%–15%B; 10–25 min, 15%–28%B; 25–35 min, 28%–40%B; 35–45 min, 40%–50%B; 45–50 min, 50%–60%B; 50–53 min, 60–70%; 53–55 min, 70–74%; 55–60 min, 74–80%; 60–70 min, 80–85%; 70–73 min, 85–95%; 73–74 min, 95–95%; 74–75 min, 95–2%; 75–77 min, 2–2%); Column temperature,  $35^\circ\text{C}$ ; The detection wavelength, 235 nm; Injection volume,  $2 \mu\text{l}$ . Xevo G2-XS QTOF with Electrospray ionization ion (ESI) source was used for mass spectrometry analysis, and the mass spectrometry data were collected under negative and positive ionization modes. The

source parameters were set as follows: Capillary voltage: 3 kV, Taper hole voltage: 40 V, Ion source temperature: 150°C, Desolvation temperature: 450°C, Desolvent flow velocity: 800 L Hr<sup>-1</sup>, Scanning range: *m/z* 50–1,200, Scan mode: MSE.

## 2.5 Network analysis

### 2.5.1 WPW active ingredient screening and potential targets prediction

Using the chemical components of *Terminalia chebula* Retz (Combretaceae; Chebulae fructus), *Aucklandia lappa* Decne (Asteraceae; Aucklandiae radix), *Moschus berezovskii* Flerov (Moschidae; Moschus), *Aconitum pendulum* Busch (Ranunculaceae; Radixaconiti), *Acorus calamus* L (Acoraceae; Acori calami rhizome) retrieved from CNKI (<https://www.cnki.net/>) and PubMed (<https://pubmed.ncbi.nlm.nih.gov/>) databases as a supplement to the chemical composition of WPW. Then SwissADME (<http://www.swissadme.ch/index.php>) and SwissTargetPrediction (<http://www.swisstargetprediction.ch/>) databases were used to screen the active ingredients and predict the potential targets with the threshold conditions were GI absorption = high, Druglikeness ≥ 2 Yes and Probability ≥ 0.1, respectively. Finally, the drugs-active components-potential targets network of WPW was constructed by Cytoscape software (Version 3.7.1).

### 2.5.2 Target acquisition of WPW for RA treatment

GeneCards (<https://www.genecards.org/>) database was performed to obtain targets of RA, and the overlap targets of RA and potential targets of active components of WPW obtained by R software (R package: mainly ggplot2 [version 3.3.3]) are the potential targets of WPW for RA treatment.

### 2.5.3 PPI interaction network construction and analysis

The potential targets of WPW for RA treatment were imported into the STRING (<https://cn.string-db.org/>) database for Protein-protein interaction (PPI) network analysis, and the interaction score was medium confidence. Then the results obtained from the STRING database are put into Cytoscape software to make a PPI network map. At the same time, Cytoscape plug-ins Cytohubba and MCODE were used to analyze the PPI interaction network.

### 2.5.4 GO and KEGG enrichment analysis

R software (R package: UpSetR [version 1.4.0]) was used to obtain the overlapping targets of Cytohubba and MCODE plug-in analysis results, namely the key targets of WPW for RA treatment, and then R software was utilized for GO and KEGG enrichment analysis (R package: org.Hs.eg.db [version 3.10.0], ggplot2 [version 3.3.3], clusterProfiler [version 3.14.3]),

with the species source limited to *Homo sapiens*, and filter condition was *p*. adj < 0.05 and *q* value < 0.2. Furthermore, the key “target-pathway” network map was visualized by Cytoscape software.

## 2.6 In Vivo pharmacological validation

### 2.6.1 Animals and ethics statement

SPF healthy male SD rats (weight 180–220 g) were provided by Chengdu EnsiWeier Biotechnology Co., Ltd (Chengdu, China, approval number: SCXK (Xiang)2019–0004). All animals were kept in a controlled environment with a temperature of 23 ± 2°C and humidity of 50 ± 5%. Also, keep the indoor light and dark cycles alternating for 12 h/12 h. All animals get free food and water. All procedures for animal experiments were approved by the Experimental Animal Ethics Committee of Chengdu University of Traditional Chinese Medicine and implemented in accordance with the Guidelines for the Care and Use of Laboratory Animals published by the US National Institutes of Health (revised 1996) (Ethical approval number: 2018-15).

### 2.6.2 AA rat model preparation and animal administration

36 Male SD rats were fed adaptively for 1 week and then randomly divided into six groups with six rats in each group: normal control group (Control), model control group (Model), MTX (1.05 mg/kg) group and WPW high (WPW-H, 18.9 mg/kg), medium (WPW-M, 9.45 mg/kg) and low (WPW-L, 4.725 mg/kg) dose treatment group. It should be noted that the high, medium and low doses of WPW were obtained by the conversion of the clinical dose of WPW. All drugs were dissolved in distilled water and intra-gastric administration (Gavage is given once a day, and each rat was given 1 ml/100 g at a time). The AA model establishment and treatment dose regimen are shown in Figure 4A. In brief, Rats were injected intradermally with a single dose of 0.1 ml complete Freund's adjuvant (CFA) into the posterior toe area of the hind paw to establish an adjuvant arthritis rat model, and the control group was given the same amount of normal saline. AA induction day was taken as day 0. After 10 days of modeling, except for the MTX group was given twice a week, the other rats were given drugs for 30 consecutive days. Then the rats were sacrificed on the 40th day, and the visceral organs, blood samples, and ankle joints were collected for subsequent analysis.

### 2.6.3 Arthritis assessment

Bodyweight, left paw swelling, ankle diameter and arthritis index of rats in each group were measured at the planned time (day 0, 5, 10, 15, 20, 25, 30, 35, and 40), respectively. The arthritis index scoring criteria were as follows: 0, no visible signs of arthritis (swelling or erythema); 1, swollen toes or

erythema; 2, red and swollen paws; 3, severe swelling and redness of the ankle; 4, severe swelling of the whole leg and all toes, and no bearing capacity (Bao et al., 2019). A total of 16 points was given by adding up the scores for all four paws.

#### 2.6.4 ELISA assay

After the experiment, abdominal aorta blood was taken and serum samples were centrifuged at 4°C, 3,500 r min<sup>-1</sup> for 15 min. Then, the levels of TNF-α, IL-6, IL-1β, IL-17, IL-4, and IL-10 in the serum of rats were detected in strict accordance with the instructions of the ELISA kit.

#### 2.6.5 Histological examination

The ankle joint after decalcification was taken out and dehydrated with gradient alcohol in turn. After that, paraffin embedding was carried out. The paraffin slicer was used to slice the embedded tissue wax blocks with a thickness of 3 μm. Then hematoxylin-eosin (H&E), safranin-fixed green, and toluidine Blue O, staining was performed, respectively. The slices are then placed for conventional transparency and sealed with neutral gum. The pathological features of the ankle joint and the morphology of articular cartilage were observed under a microscope.

#### 2.6.6 Immunohistochemistry

Paraffin sections of the ankle joint were dewaxed and washed with distilled water, then placed in citric acid antigen repair buffer for antigen repair. Next, the samples were further placed in a 3% hydrogen peroxide solution and sealed with serum. Subsequently, a primary antibody-containing PI3K, AKT, MAPK, MMP1, MMP3, CDK1, CDK3, BAX, and BCL-2 were added and incubated overnight at 4°C. On the second day, the primary antibody was washed and the secondary antibody was added and incubated for 50 min at room temperature. Finally, the images were observed under a microscope after staining with DAB and hematoxylin.

#### 2.6.7 TUNEL staining

Apoptosis of synovial cells in the synovial region of the ankle joint was achieved by TUNEL staining according to the instructions of the TUNEL staining kit and the previously reported method (Wang et al., 2022a). And then photographed by Olympus IX-83 inverted fluorescence microscope (Tokyo, Japan).

### 2.7 Data statistics and analysis

All data were statistically analyzed using Graphpad Prism 9 software, and the data were expressed as mean ± standard error of the mean (SEM). After the homogeneity of variance test, a *t*-test was used for comparison between the two groups. Comparison between multiple groups After one-way ANOVA,

the LSD test was used for pairwise comparison of the mean between each group. *p* < 0.05 were considered as statistically significant differences. \**p* < 0.05, \*\**p* < 0.01, \*\*\**p* < 0.001 vs. the Control group; \**p* < 0.05, \*\**p* < 0.01, \*\*\**p* < 0.001 vs. the Model group.

## 3 Results

### 3.1 Identification of chemical constituents of WPW

GC-MS combined with UPLC-Q-TOF/MS was used to comprehensively analyze and identify the chemical components of WPW. A total of 165 compounds were identified, including 49 sesquiterpenoids, 4 phenylpropanoids, 28 other volatile oils, 67 alkaloids, 10 triterpenoids, and 7 other compounds. The data obtained by GC-MS were searched and matched with the database of the National Institute of Standards and Technology (NIST2014), and a total of 49 volatile oil components were identified. The relative contents of dehydrocostus lactone, β-asarone, and muscone were found to be relatively high by using the peak area normalization method (Figure 1A, Supplementary Table S1). A total of 67 alkaloids, 3 triterpenoids, 51 volatile components, and 7 other compounds were identified in positive ion mode. And a total of 12 chemical constituents including triterpenoids and volatile oils were identified under anion mode by using UPLC-Q-TOF/MS, literature review, and chemical composition database of WPW (Figures 1B–C, Supplementary Tables S1–S5).

### 3.2 Potential target screening and PPI interaction network construction and analysis of WPW and RA

To identify the potential active components and targets of resveratrol in RA treatment, we further carried out a literature search through CNKI and Pubmed databases and combined with GC-MS and UPLC-Q-TOF/MS technology to obtain the chemical components of WPW. After deleting the repeated chemical components, a library of WPW chemical constituents was constructed. Then 83 active components were obtained by SwissADME screening. Potential targets of 83 active ingredients were further predicted by the SwissTargetPrediction database. Compounds with no target and those with target Probability < 0.1 were removed. Finally, 50 active ingredients were included in the subsequent analysis. Among them, there are 6 chemical components from *Acorus calamus* L, and 13 chemical components from *Aucklandia lappa* Decne, 10 chemical components from *Terminalia chebula* Retz, 11 chemical components from *Moschus berezovskii* Flerov, 10 chemical components from *Aconitum pendulum* Busch,

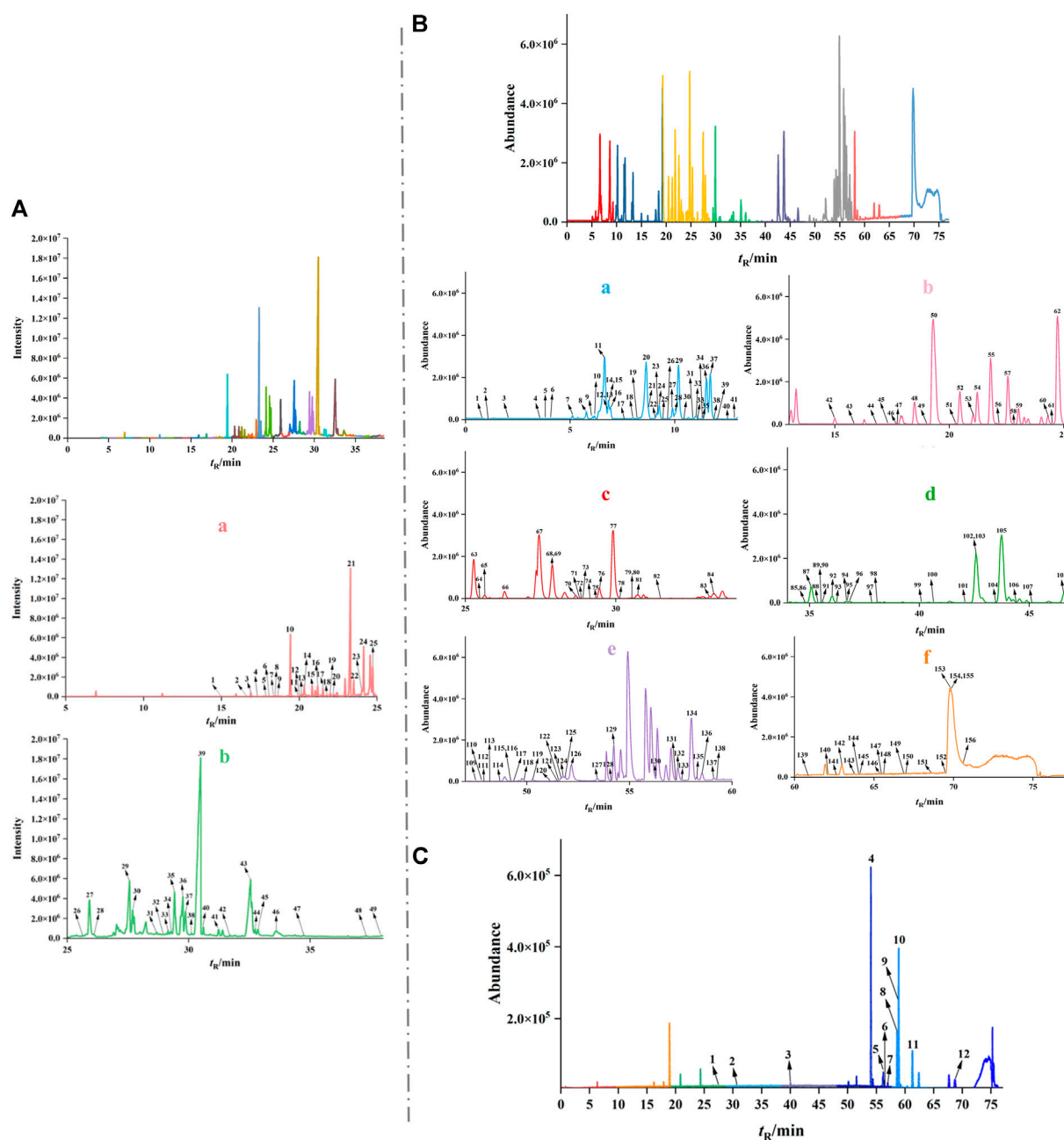


FIGURE 1

The total ion chromatograms (TICs) of WPW by GS-MS and UPLC-Q-TOF/MS. (A) TIC of WPW by GS-MS (a. 5–25 min GC-MS total ion flow diagram b. 25–38 min). (B) TIC of WPW in positive ion mode (a. 0–13 min total ion flow diagram, b. 13–25 min, c. 25–34 min, d. 34–47 min, e. 47–60 min, f. 60–77 min). (C) TIC of WPW in negative ion mode.

and their corresponding targets are 111, 245, 528, 176, 261 respectively. A total of 523 potential targets of WPW were obtained by combining and removing repeated targets. Finally, a drug-active component-potential target network of WPW was constructed using Cytoscape3.7.1 (Supplementary Figure S1A). Further analysis of the network found that there

were 11 with Degree  $\geq 50$ . Including songoramine, cheilanthifoline, quinidine, saussureanine C, linolic acid, acoric acid, songorine, arjunolic acid, peraksine, ellagic acid, and arjungenin. A total of 5017 potential targets of RA were obtained through GeneCards database screening, and further intersection with potential targets of WPW was conducted to



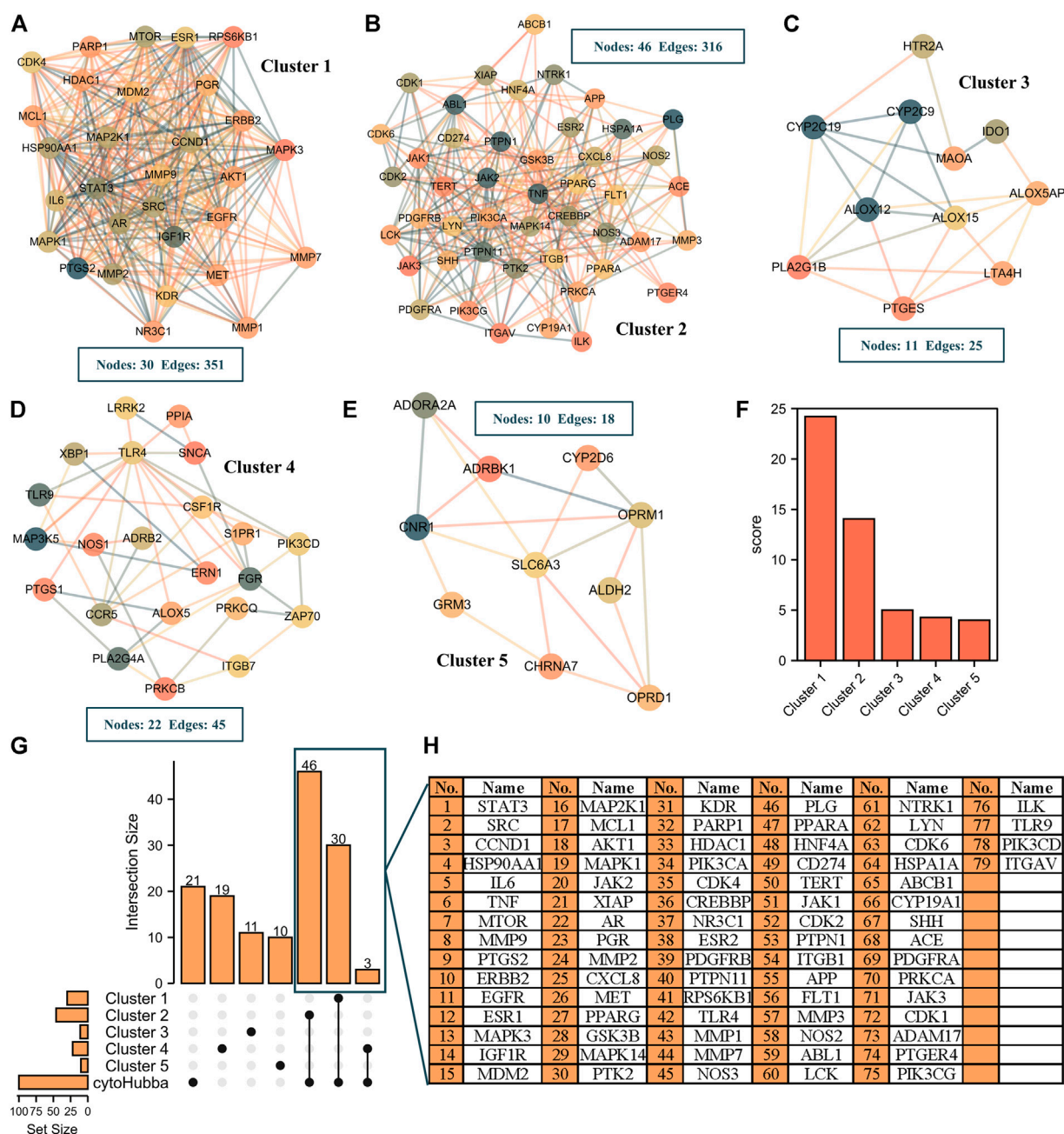


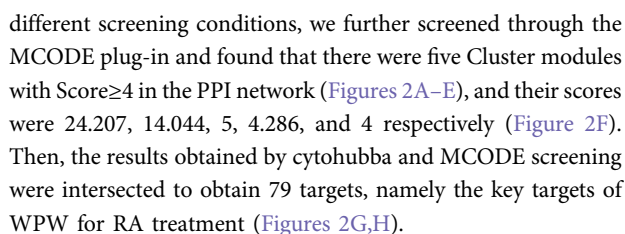
FIGURE 2

Screening of key targets in the treatment of RA with WPW. (A–E) The cluster module with a Score  $\geq 4$  in the PPI network was obtained by MCODE plug-in Cytoscape. (F) The score for the five cluster modules. (G) The upset plot was screened by MCODE and Cytoscape. (H) A list of 79 key targets in the upset plot.

obtain 307 intersection targets of WPW and RA, namely potential targets of WPW for RA treatment (Supplementary Figure S1B). The 307 intersection targets were imported into the STRING database to obtain PPI network information, and then the PPI network was visualized by Cytoscape software. The results showed that the PPI network consisted of 307 nodes and

4086 edges, with an average degree value of 26.6 and PPI enriched  $p$ -value  $< 1.0 \times 10^{-16}$  (Supplementary Figure S1C). Then, the Maximal Clique Centrality (MCC) algorithm of Cytoscape plug-in Cytoscape was used as the screening method to screen TOP100 nodes from the PPI network (Supplementary Figure S1D). Considering that there may be some differences among





In order to clarify the potential pathway of WPW in RA treatment, we then conducted an enrichment analysis of GO and

KEGG pathways for 79 key targets. And the results showed that 2048 biological processes (BP), 61 cell components (CC), 111 molecular functions (MF), and 148 KEGG enrichment pathways met the condition that  $p\text{-adj} < 0.05$  and  $q\text{-value} < 0.2$ . BP analysis showed that these 79 key targets were mainly enriched in regulation of MAP kinase activity, regulation of inflammatory response, regulation of apoptotic signaling pathways, regulation of phosphatidylinositol 3-kinase signaling, positive regulation of cell cycle, etc. (Figure 3A). CC analysis showed that it was mainly enriched in membrane rafts, membrane microdomain, cell-cell junction, and phosphatidylinositol 3-kinase complex (Figure 3B). MF analysis results showed that it was mainly enriched in cell adhesion molecule binding, cytokine receptor binding, MAP

kinase activity, cyclin binding, phosphatidylinositol 3-kinase binding, etc. (Figure 3C). KEGG pathway enrichment results showed that it was mainly concentrated in the PI3K-AKT signaling pathway, MAPK signaling pathway, apoptosis, cell cycle, rheumatoid arthritis, and other signaling pathways (Figure 3D). Further, 20 KEGG pathways and their mapping targets were constructed. Through the analysis of this network, it was found that PIK3CA, AKT1, MAPK1, IL-6, TNF, MMP1, MMP3, CDK1, and other targets were closely related to these 20 pathways, and this suggested that these targets might be the potential core targets for WPW to play a role in the treatment of RA (Figure 3E).

### 3.4 Effects of WPW on the arthritis index, paw swelling, ankle diameter, body weight, and histopathological changes in AA rats

To investigate the therapeutic effect of WPW on RA, we established AA model rats and administered them. In addition, the body weight, paw swelling, arthritis index, and ankle joint diameter of rats in different treatment groups were also detected (Figure 4A). We found that compared with the model group, the bodyweight of the rats treated with MTX and WPW was significantly improved (Figure 4B). By observing the paw swelling degree of the rats, we found that compared with the control group, the AA model group had red, swollen, ulcerated feet, stiff and deformed joints, and could not bend normally, which indicated that the modeling was relatively successful. Compared with the model group, after 10 days of MTX administration, the degree of foot swelling showed a trend of relief, and at the late stage of administration, the degree of foot swelling was significantly improved without redness, ulceration, and other symptoms. After treatment with different doses of WPW, the degree of redness and swelling of the feet of rats in each group was also significantly improved and showed a significant downward trend (Figures 4C–F). Interestingly, the ankle diameter and arthritis index showed similar trends in all treatment groups (Figures 4D,E). To further observe the pathological changes in ankle joints of AA model rats, hematoxylin-eosin staining (HE) was used for the ankle joints of rats. Compared with the control group, the surface of articular cartilage in the AA model group was slightly less smooth (black arrow), and the edge of articular cartilage was attached by a hyperplastic synovial membrane (red arrow), which showed a large number of fibrocytes and capillary hyperplasia (blue arrow), accompanied by a large number of lymphocyte infiltration (yellow arrow). Compared with the model group, dense connective tissue was observed in the subsynovial layer of rats in the MTX group, but no obvious inflammatory response was observed. There were some differences in sections of different WPW dose groups: in the WPW-M group, some synovial

hyperplasia could be observed invading the edge of articular cartilage (black arrow), and dense connective tissue could be seen in the subsynovial layer without an obvious inflammatory response. In the WPW-H group, synovial structure tended to be normal and only a few lymphocytes were observed (black arrow). In the WPW-L group, there is a local proliferation of synovial lining cells (black arrows) and a more diffuse infiltration of lymphocytes (red arrows). In conclusion, after treatment with WPW, all treatment groups showed different degrees of improvement compared with the model group (Figure 4G). In order to further demonstrate that WPW can control inflammation and reduce cartilage destruction, the changes of cartilage in the ankle joints of rats were detected by safranin-O staining and toluidine blue staining. The results showed that, compared with the model group, the degree of cartilage damage in AA rats was effectively reversed after drug administration. Especially in WPW-M and WPW-H groups, the positive staining area of safranin-O and toluidine blue staining were larger and closer to the normal control group (Figure 4H). These results fully indicated that WPW could effectively alleviate synovial inflammation and reduce cartilage destruction in AA model rats.

### 3.5 Effect of WPW on inflammatory factors in the serum of AA model rats

To clarify the anti-RA effect of WPW, we further detected the levels of pro-inflammatory cytokines IL-6, IL-17, TNF- $\alpha$ , IL-1 $\beta$ , and anti-inflammatory cytokines IL-10 and IL-4 in serum of rats in each group by ELISA. The results showed that compared with the control group, the levels of pro-inflammatory factors (TNF- $\alpha$ , IL-6, IL-1 $\beta$ , IL-17) in the serum of rats after modeling were significantly increased, and the levels of anti-inflammatory factors (IL-10, IL-4) were significantly decreased. After treatment with WPW, the levels of IL-6, IL-17, and IL-1 $\beta$  in the serum of WPW treatment groups were significantly lower than those of rats after modeling, the levels of IL-10 and IL-4 were significantly increased, while TNF- $\alpha$  level decreased, but there was no significant difference (Figures 5A–F). In a word, these results suggested that WPW could exert its anti-RA effect by reducing the secretion of inflammatory cytokines.

### 3.6 Effects of WPW on the PI3K-AKT, MAPK, apoptosis, cell cycle, and other pathway-related proteins

The results of network analysis suggested that PI3K-AKT, MAPK, apoptosis, cell cycle, and other signaling pathways might be the potential pathway of WPW in the treatment of RA. Therefore, we further detected the expression of PI3K, AKT, MAPK, MMP1, MMP3, CDK1, CDK3, and other core target proteins in the synovial region of the ankle joint by

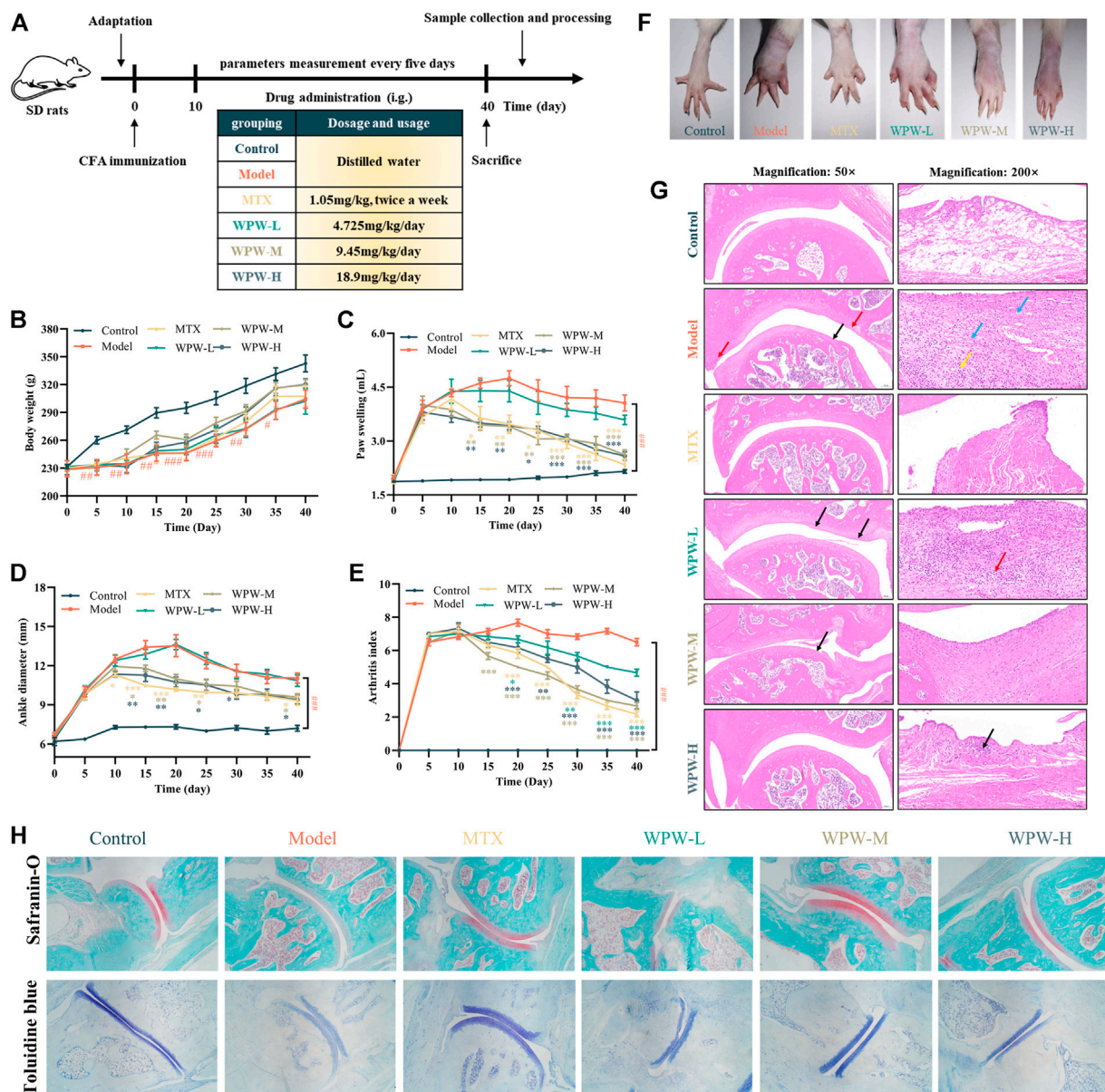


FIGURE 4

Effect of WPW on the pathological process of RA in AA model rats. (A) Experimental schedule of WPW on AA model rats. The arthritis index (B), paw swelling (C), ankle diameter (D), and body weight (E) in AA rats ( $n = 6$ ). (F) Representative images of the hind limbs of the different treatment groups at the end of the experiment. (G) Histopathological evaluation of the ankle joints of rats in different treatment groups was conducted by H&E staining ( $n = 3$ ; Magnification:  $\times 50$  and  $\times 200$ ; Scale bar: 200 and 50  $\mu\text{m}$ ). (H) Safranin-O and toluidine blue staining ( $n = 3$ ; Magnification:  $\times 40$ ).

immunohistochemical method (Figure 6A). The results showed that compared with the control group, the positive areas of PI3K, AKT, MAPK, MMP1, MMP3, CDK1, and Bcl-2 increased in the model group. Compared with the model group, the positive expression of MTX and WPW group decreased and tended to a normal level ( $p < 0.05$ ) (Figures 6B–I). Interestingly, Bax positive expression was elevated in the MTX and WPW group compared with the model group

(Figure 6J). Thus, we hypothesized that WPW could induce the apoptosis of synovial cells in the ankle joint. As a result, the TUNEL assay was used to detect cell apoptosis in the synovial region of the ankle joint. We found that the fluorescence signal in the synovial region of the ankle joint of AA rats was significantly enhanced after treatment with WPW, indicating that the morphological changes of apoptosis were obvious (Figure 6K). In conclusion, these results further



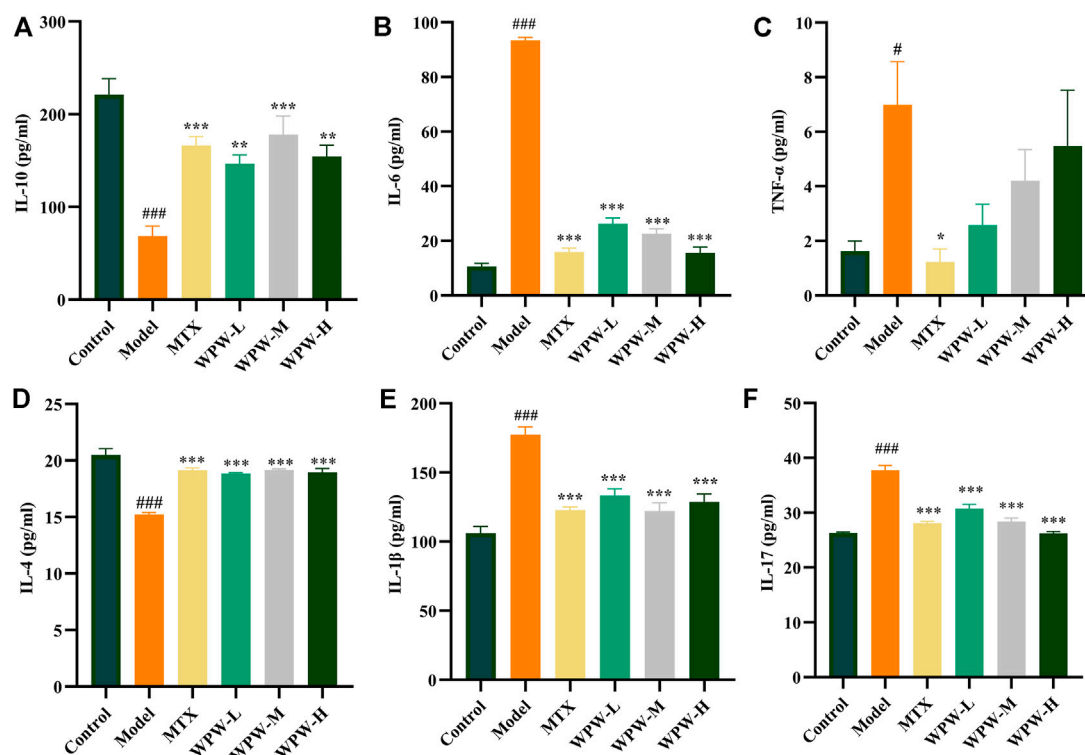


FIGURE 5

Effect of WPW on inflammatory factors (A) IL-10 (B) IL-6 (C) TNF-α (D) IL-4 (E) IL-1β (F) IL-17 in serum of AA model rats (n = 6).

validate the screening results of network analysis and suggest that the therapeutic effect of WPW on RA may be realized by regulating PI3K/AKT, MAPK, cell cycle, and apoptosis signaling pathways.

## 4 Discussion

The pathological manifestations of RA mainly include synovial lining cell proliferation, interstitial inflammatory cell infiltration, microvascular regeneration, pannus formation, cartilage and bone tissue destruction, etc. (Derksen et al., 2017; Rana et al., 2018). Although the exact etiology of RA is still unclear, it is certain that the onset of RA may be related to genetics, infection, sex hormones, and so on (van der Woude and van der Helm-van Mil, 2018; Wang S. et al., 2021). If RA patients cannot be treated in time, progressive joint stiffness, destruction, deformity, and disability may occur in patients, and even complications such as infection, gastrointestinal bleeding, heart, lung, or renal changes may occur in the later stage, which seriously threaten the life and health of patients (Tiniakou et al., 2018; Izuka et al., 2021). Traditional Chinese medicine and ethnic medicine are the precious wealth of the Chinese nation and have unique advantages in the prevention and treatment of some difficult diseases such as RA (Wang Y. et al., 2021; Li et al., 2022).

Network pharmacology aims to understand the network biological basis of complex diseases, syndromes, and drug therapy, and has made great progress in predicting targets, understanding the biological basis of diseases and syndromes, network regulation mechanism of compound preparations, and identification of disease biomarkers based on biological network (Ou et al., 2020; Zhang C. et al., 2021; Wang X. et al., 2021; Hou et al., 2021).

As a classic prescription of Tibetan medicine, the efficacy of WPW against RA urgently needs to be revealed. We first identified the volatile components in WPW by GC-MS, and the results showed that the volatile components in WPW mainly included terpenoids, phenylpropanoids, fatty acids, macrolides, and other compounds. Among them, the compounds with high content were dehydrocostus lactone, β-asarone, muscone, and so on. UPLC-Q-TOF/MS technology has been widely used in the separation and analysis of complex systems due to its high sensitivity and analysis efficiency, which has greatly promoted the modernization of Traditional Chinese medicine/ethnic medicine (Duan et al., 2019; Zhou et al., 2021). Therefore, we further analyzed 140 chemical components from WPW using this technique, among which 67 alkaloids were the most. Then, we further supplemented the chemical components of each drug in WPW and screened potential active ingredients and targets through a literature review. Finally, we obtained 50 potential active ingredients and 523 potential targets in the whole WPW prescription. Further

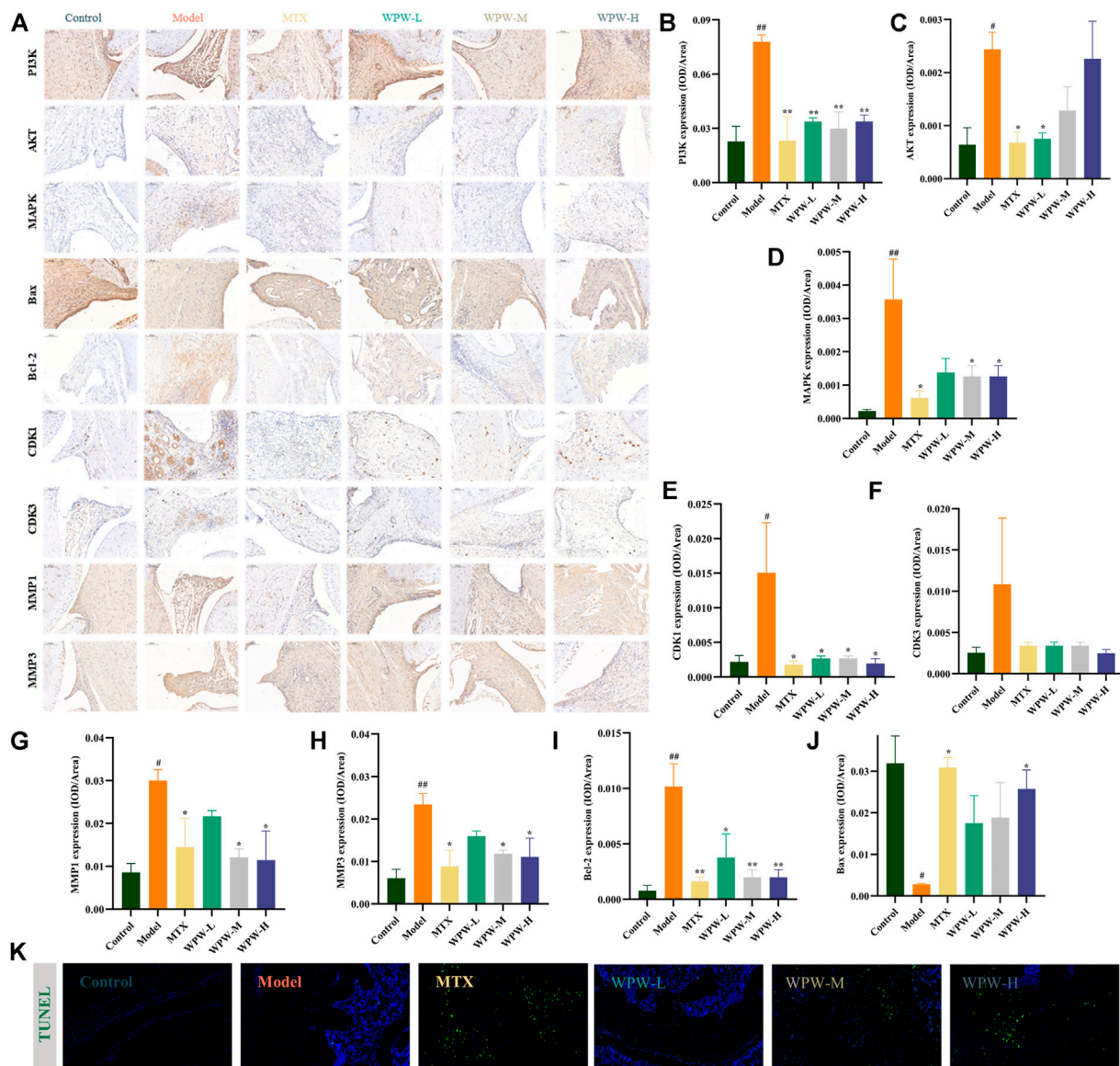


FIGURE 6

Effect of WPW on protein expression in the synovial region of the ankle joint in AA rats. (A) The expression levels of PI3K, AKT, MAPK, Bax, Bcl-2, CDK1, CDK3, MMP1, and MMP3 in arthritic joints were detected by the immunohistochemical method (n = 3; Magnification: x200; Scale bar: 100  $\mu$ m). (B–J) Quantitative analysis of PI3K, AKT, MAPK, Bax, Bcl-2, CDK1, CDK3, MMP1, and MMP3. (K) TUNEL fluorescence staining of ankle joints of rats in different groups (Magnification: x200; Scale bar: 50  $\mu$ m).

analysis found that there were 11 chemical components with a degree value  $\geq 50$ , including songoramine, cheilanthifoline, quinidine, saussureanine C, linolic acid, acoric acid, songorine, arjunolic acid, perakine, ellagic acid, and arjungenin. Four components were also identified by GC-MS and UPLC-Q-TOF/MS, which were linoleic acid, songorine, arjunolic acid, and arjungenin. Some scholars confirmed that linoleic acid can be used to prevent RA by a Mendelian randomized study (Zhao and Schooling, 2019; Lee, 2020). In addition, other studies have demonstrated that dietary conjugated linoleic acid (CLA) may be an effective means of

preventing and alleviating RA, which includes a variety of benefits, including inhibiting endosteal bone absorption, enhancing calcium absorption, affecting inflammatory cytokines, increasing cortical bone formation, and regulating the role and expression of cyclooxygenase (COX) (Butz et al., 2007; Hur and Park, 2007). Songorine is a typical active C20-diterpenoid alkaloid derived from the lateral roots of *Aconitum carmichaelii* Debeaux. (Li et al., 2021). The studies of Nesterova et al. and Zhang et al. confirmed that it had good anti-inflammatory and anti-rheumatic activities (Nesterova et al., 2014; Zhang L. et al., 2021). Arjunolic acid is a saponin component with



antioxidant, antibacterial, and anti-inflammatory activities (Hemalatha et al., 2010; Ghosh and Sil, 2013). Arjunolic acid is also an effective antioxidant that plays an important role in protecting cells and tissues from the harmful effects of reactive oxygen species (Hemalatha et al., 2010). Arjungenin has certain free radical scavenging activity and also shows a stronger inhibitory effect on hypochlorous acid produced by human neutrophils (Pawar and Bhutani, 2005). In conclusion, we have sufficient evidence to prove that these components may be the important components of WPW to exert an anti-RA effect.

Cytoscape is a plug-in for Cytoscape software to identify hub nodes, while the MCODE plug-in can be used to discover the dense region which interacts in the PPI network (Chin et al., 2014; Liu et al., 2019). So, we further analyzed the 307 targets using these two plug-ins in Cytoscape software, and finally obtained 79 important targets for WPW treatment of RA. Through enrichment analysis of GO and KEGG pathways, it was found that these 79 targets were mainly enriched in PI3K/AKT, MAPK, apoptosis, and cell cycle signaling pathways.

To further verify these predictions, we constructed an AA model to study the therapeutic effect of WPW on RA. As a chronic autoimmune disease, the inflammation of RA cannot subside spontaneously. Therefore, inflammatory homeostasis, which inhibits the development of inflammation and promotes its remission, maybe a new strategy for the treatment of RA (Chen et al., 2019). We found that WPW can exert its therapeutic effect on RA by inhibiting the expression of pro-inflammatory cytokines IL-6, IL-17, IL-1 $\beta$  and promoting the expression of anti-inflammatory cytokines IL-4 and IL-10. This bidirectional regulation may be an advantage of WPW for RA treatment. Recent studies have shown that the PI3K/AKT signaling pathway, as one of the main intracellular signal transduction pathways, widely exists in the synovial membrane and plays an important role in the growth, proliferation, survival, apoptosis, adhesion and migration of fibroblast-like synoviocytes (FLSs) (Li and Wang, 2020; Wang et al., 2022a). Mitogen-activated protein kinase (MAPK) is a serine/threonine-protein kinase family, which has been confirmed to be involved in the RA process by many studies (Liu et al., 2018; Yang et al., 2018; Du et al., 2019; Behl et al., 2021). In addition, in recent years, many molecules that regulate apoptosis and the cell cycle have been suggested to play a role in RA (Perlman et al., 2001; Taranto and Leech, 2006; Collison, 2017). We verified the prediction of network pharmacology by *in vivo* animal experiments and found that WPW decreased the expression of PI3K, AKT, and MAPK in the synovial region of the ankle joint. Moreover, it also decreased the expression of cell cycle-related protein CDK1 and apoptosis-related protein Bcl-2, and increased the expression of Bax. MMP-1 is produced primarily by synovial cells lining joints (Burrage et al., 2006). Other MMPs, such as MMP-3, are also elevated in arthritis, and these enzymes degrade non-collagenous matrix components of joints (Burrage et al., 2006; Di Spigna et al., 2021). We found that WPW significantly inhibited the expression of MMP-1 and MMP-3. These results suggest that WPW can regulate

PI3K/Akt, MAPK, apoptosis, and cell cycle pathways to exert its anti-RA effects under inflammatory conditions.

Although at present our preliminary research has been clear about the potential of WPW active ingredients, but these components are based on the analysis of the network. In the future we can further analyze WPW changes in the body, in addition, these ingredients are to work alone or collaborative work, it needs to be further validated through experiments *in vivo* and *in vitro*. It is worth noting that in the network predicted pathway, we found that the anti-RA effect WPW may also be related to osteoclast differentiation, which also provides direction for us to further reveal the mechanism.

## 5 Conclusion

All in all, we used GC-MS, UPLC-Q-TOF/MS technology, network analysis, and animal experimental validation to reveal the potential substance basis and mechanism of Action of Tibetan drug WPW in RA treatment. We found that linoleic acid, songorine, arjunolic acid, arjungenin and other components might be the main chemical components of WPW against RA. PI3K/AKT, MAPK, apoptosis and cell cycle signaling pathways may be the main anti-RA pathways of WPW. The above fully proved that WPW achieves its anti-RA effect through multiple components, multiple targets and multiple signaling pathways, which provides a solid scientific basis for the clinical application of WPW.

## Data availability statement

The original contributions presented in the study are included in the article/Supplementary Material, further inquiries can be directed to the corresponding authors.

## Ethics statement

The animal study was reviewed and approved by the Experimental Animal Ethics Committee of Chengdu University of Traditional Chinese Medicine.

## Author contributions

QH: Investigation, Methodology, Data curation, Writing-original draft. XT: Investigation, Methodology. SG: Investigation, Supervision, Validation. QD: Investigation, Formal analysis. ZP: Investigation, Formal analysis. YZ: Investigation, Formal analysis. SW: Methodology, Data curation, Project administration, Writing-original draft, Supervision, Writing-review and editing. YZ: Resources, Project administration, Supervision, Validation, Writing-review and editing.

## Funding

This study was supported by the National Natural Science Foundation of China (No. 82130113); the National Key R&D Program of China (2017YFC1703904); the Scientific Research Project of Construction of Doctoral Program of TCM in University of Tibetan Medicine (BSDJS-20-01).

## Conflict of interest

The authors declare that the research was conducted in the absence of any commercial or financial relationships that could be construed as a potential conflict of interest.

## References

- Bao, Y., Sun, Y. W., Ji, J., Gan, L., Zhang, C. F., Wang, C. Z., et al. (2019). Genkwanin ameliorates adjuvant-induced arthritis in rats through inhibiting JAK/STAT and NF- $\kappa$ B signaling pathways. *Phytomedicine* 63, 153036. doi:10.1016/j.phymed.2019.153036
- Behl, T., Upadhyay, T., Singh, S., Chigurupati, S., Alsabayel, A. M., Mani, V., et al. (2021). Polyphenols targeting MAPK mediated oxidative stress and inflammation in rheumatoid arthritis. *Molecules* 26, 6570. doi:10.3390/molecules26216570
- Burrage, P. S., Mix, K. S., and Brinckerhoff, C. E. (2006). Matrix metalloproteinases: role in arthritis. *Front. Biosci.* 11, 529–543. doi:10.2741/1817
- Butz, D. E., Li, G., Huebner, S. M., and Cook, M. E. (2007). A mechanistic approach to understanding conjugated linoleic acid's role in inflammation using murine models of rheumatoid arthritis. *Am. J. Physiol. Regul. Integr. Comp. Physiol.* 293, R669–R676. doi:10.1152/ajpregu.00005.2007
- Chen, Z., Bozec, A., Ramming, A., and Schett, G. (2019). Anti-inflammatory and immune-regulatory cytokines in rheumatoid arthritis. *Nat. Rev. Rheumatol.* 15, 9–17. doi:10.1038/s41584-018-0109-2
- Chin, C. H., Chen, S. H., Wu, H. H., Ho, C. W., Ko, M. T., Lin, C. Y., et al. (2014). cytoHubba: identifying hub objects and sub-networks from complex interactome. *BMC Syst. Biol.* 8 (Suppl. 4), S11. doi:10.1186/1752-0509-8-s4-s11
- Collison, J. (2017). Rheumatoid arthritis: cell cycle stalling linked to arthritis. *Nat. Rev. Rheumatol.* 13, 572. doi:10.1038/nrrheum.2017.148
- Derksen, V., Huizinga, T. W. J., and Van Der Woude, D. (2017). The role of autoantibodies in the pathophysiology of rheumatoid arthritis. *Semin. Immunopathol.* 39, 437–446. doi:10.1007/s00281-017-0627-z
- Di Spigna, G., Rossi, F. W., Mormile, I., Ladogana, P., Buonavolontà, L., Covelli, B., et al. (2021). Serum Metalloprotease 3 (MMP-3) biomarker of therapeutic efficacy during treatment of rheumatoid arthritis. *J. Biol. Regul. Homeost. Agents* 35, 1041–1045. doi:10.23812/21-86-1
- Du, H., Zhang, X., Zeng, Y., Huang, X., Chen, H., Wang, S., et al. (2019). A novel phytochemical, DIM, inhibits proliferation, migration, invasion and TNF- $\alpha$  induced inflammatory cytokine production of synovial fibroblasts from rheumatoid arthritis patients by targeting MAPK and AKT/mTOR signal pathway. *Front. Immunol.* 10, 1620. doi:10.3389/fimmu.2019.01620
- Duan, X., Pan, L., Bao, Q., and Peng, D. (2019). UPLC-Q-TOF-MS study of the mechanism of THSWD for breast cancer treatment. *Front. Pharmacol.* 10, 1625. doi:10.3389/fphar.2019.01625
- Fan, W. Q., Yu, Y. G., and Liao, Y. (2007). *Quality standard of musk in Tibetan medicine wuweisixiang pill*. China Pharm, 952–954. [https://oversea.cnki.net/KCMS/detail/detail.aspx?dbcode=CJFD&dbname=CJFD2007&filename=ZGYA200712035&uniplatform=OVERSEAS\\_EN&v=JcGdgqEH9fjgbyqHFBIuMDIjBRLcAivLU26P66oibJIUIGmquE686w5BEEOB](https://oversea.cnki.net/KCMS/detail/detail.aspx?dbcode=CJFD&dbname=CJFD2007&filename=ZGYA200712035&uniplatform=OVERSEAS_EN&v=JcGdgqEH9fjgbyqHFBIuMDIjBRLcAivLU26P66oibJIUIGmquE686w5BEEOB).
- Fu, K., Xu, M., Zhou, Y., Li, X., Wang, Z., Liu, X., et al. (2020). The Status quo and way forwards on the development of Tibetan medicine and the pharmacological research of Tibetan materia Medica. *Pharmacol. Res.* 155, 104688. doi:10.1016/j.phrs.2020.104688
- Gao, L., Cao, M., Li, J. Q., Qin, X. M., and Fang, J. (2021). Traditional Chinese medicine network pharmacology in cardiovascular precision medicine. *Curr. Pharm. Des.* 27, 2925–2933. doi:10.2174/1381612826666201112142408
- Ge, Z., and Nima, C. (2021). Research status of Tibetan medicine in the treatment of "zhenbu disease"(rheumatoid arthritis). *Guiding J. Tradit. Chin. Med. Pharm.* 28, 152–156. doi:10.13862/j.cn43-1446/r.2022.03.030
- Ghosh, J., and Sil, P. C. (2013). Arjunolic acid: a new multifunctional therapeutic promise of alternative medicine. *Biochimie* 95, 1098–1109. doi:10.1016/j.biochi.2013.01.016
- Gongbu, D. Z., Zhao, A., He, Q., Ren, Y., Ma, J., and Wu, G. T. (2013). Experimental study on the pharmacodynamics of Tibetan drug "WuWei SheXiang pill". *West J. Tradit. Chin. Med.* 26, 55–57.
- Hemalatha, T., Pulavendran, S., Balachandran, C., Manohar, B. M., and Puvanakrishnan, R. (2010). Arjunolic acid: a novel phytomedicine with multifunctional therapeutic applications. *Indian J. Exp. Biol.* 48, 238–247.
- Hou, Y., Wang, X., Zhang, Y., Wang, S., and Meng, X. (2021). Highland mate: Edible and functional foods in traditional medicine for the prevention and treatment of hypoxia-related symptoms. *Curr. Opin. Pharmacol.* 60, 306–314. doi:10.1016/j.coph.2021.07.018
- Huang, J., Fu, X., Chen, X., Li, Z., Huang, Y., Liang, C., et al. (2021). Promising therapeutic targets for treatment of rheumatoid arthritis. *Front. Immunol.* 12, 686155. doi:10.3389/fimmu.2021.686155
- Hur, S. J., and Park, Y. (2007). Effect of conjugated linoleic acid on bone formation and rheumatoid arthritis. *Eur. J. Pharmacol.* 568, 16–24. doi:10.1016/j.ejphar.2007.04.056
- Izuka, S., Yamashita, H., Iba, A., Takahashi, Y., and Kaneko, H. (2021). Acute exacerbation of rheumatoid arthritis-associated interstitial lung disease: clinical features and prognosis. *Rheumatology* 60, 2348–2354. doi:10.1093/rheumatology/keaa608
- Jiao, X., Jin, X., Ma, Y., Yang, Y., Li, J., Liang, L., et al. (2021). A comprehensive application: Molecular docking and network pharmacology for the prediction of bioactive constituents and elucidation of mechanisms of action in component-based Chinese medicine. *Comput. Biol. Chem.* 90, 107402. doi:10.1016/j.compbiolchem.2020.107402
- Jin, S., Li, M., Fang, Y., Li, Q., Liu, J., Duan, X., et al. (2017). Chinese registry of rheumatoid arthritis (CREDIT): II. Prevalence and risk factors of major comorbidities in Chinese patients with rheumatoid arthritis. *Arthritis Res. Ther.* 19, 251. doi:10.1186/s13075-017-1457-z
- Joshi, A., Rienks, M., Theofilatos, K., and Mayr, M. (2021). Systems biology in cardiovascular disease: a multiomics approach. *Nat. Rev. Cardiol.* 18, 313–330. doi:10.1038/s41569-020-00477-1
- Lee, Y. H. (2020). Role of linoleic acid in autoimmune disorders: a mendelian randomisation study. *Ann. Rheum. Dis.* 79, e28. doi:10.1136/annrheumdis-2018-214810
- Li, X., and Wang, Y. (2020). Cinnamaldehyde attenuates the progression of rheumatoid arthritis through down-regulation of PI3K/AKT signaling pathway. *Inflammation* 43, 1729–1741. doi:10.1007/s10753-020-01246-5
- Li, Y., Feng, Y. F., Liu, X. T., Li, Y. C., Zhu, H. M., Sun, M. R., et al. (2021). Songorine promotes cardiac mitochondrial biogenesis via Nrf2 induction during sepsis. *Redox Biol.* 38, 101771. doi:10.1016/j.redox.2020.101771

## Publisher's note

All claims expressed in this article are solely those of the authors and do not necessarily represent those of their affiliated organizations, or those of the publisher, the editors and the reviewers. Any product that may be evaluated in this article, or claim that may be made by its manufacturer, is not guaranteed or endorsed by the publisher.

## Supplementary material

The Supplementary Material for this article can be found online at: <https://www.frontiersin.org/articles/10.3389/fphar.2022.941013/full#supplementary-material>

- Li, Z., Nie, L., Li, Y., Yang, L., Jin, L., Du, B., et al. (2022). Traditional Tibetan medicine twenty-five wei'er tea pills ameliorate rheumatoid arthritis based on chemical crosstalk between gut microbiota and the host. *Front. Pharmacol.* 13, 828920. doi:10.3389/fphar.2022.828920
- Liu, F., Feng, X. X., Zhu, S. L., Huang, H. Y., Chen, Y. D., Pan, Y. F., et al. (2018). Sonic hedgehog signaling pathway mediates proliferation and migration of fibroblast-like synoviocytes in rheumatoid arthritis via MAPK/ERK signaling pathway. *Front. Immunol.* 9, 2847. doi:10.3389/fimmu.2018.02847
- Liu, J., Zhou, S., Li, S., Jiang, Y., Wan, Y., Ma, X., et al. (2019). Eleven genes associated with progression and prognosis of endometrial cancer (EC) identified by comprehensive bioinformatics analysis. *Cancer Cell Int.* 19, 136. doi:10.1186/s12935-019-0859-1
- Lu, X. G., and Feng, X. (2011). Determination of costunolide and dehydrocostuslactone in Wuwei Shexiang pills by HPLC. *China Pharm.* 14, 807–809.
- Nesterova, Y. V., Povetieva, T. N., Suslov, N. I., Zyuz'kov, G. N., Aksinenko, S. G., Pushkarskii, S. V., et al. (2014). Anti-inflammatory activity of diterpene alkaloids from *Aconitum baikalense*. *Bull. Exp. Biol. Med.* 156, 665–668. doi:10.1007/s10517-014-2421-4
- Ou, C., Geng, T., Wang, J., Gao, X., Chen, X., Luo, X., et al. (2020). Systematically investigating the pharmacological mechanism of Dazhu Hongjingtian in the prevention and treatment of acute mountain sickness by integrating UPLC/Q-TOF-MS/MS analysis and network pharmacology. *J. Pharm. Biomed. Anal.* 179, 113028. doi:10.1016/j.jpba.2019.113028
- Pawar, R. S., and Bhutani, K. K. (2005). Effect of oleanane triterpenoids from *Terminalia arjuna*-a cardioprotective drug on the process of respiratory oxyburst. *Phytomedicine* 12, 391–393. doi:10.1016/j.phymed.2003.11.007
- Pelzman, H., Pagliari, L. J., and Volin, M. V. (2001). Regulation of apoptosis and cell cycle activity in rheumatoid arthritis. *Curr. Mol. Med.* 1, 597–608. doi:10.2174/1566524013363429
- Rana, A. K., Li, Y., Dang, Q., and Yang, F. (2018). Monocytes in rheumatoid arthritis: Circulating precursors of macrophages and osteoclasts and, their heterogeneity and plasticity role in RA pathogenesis. *Int. Immunopharmacol.* 65, 348–359. doi:10.1016/j.intimp.2018.10.016
- Scott, D. L., Wolfe, F., and Huizinga, T. W. (2010). Rheumatoid arthritis. *Lancet* 376, 1094–1108. doi:10.1016/s0140-6736(10)60826-4
- Shan, Y., Wang, F., Wei, Z., and Lu, Y. (2021). Synthetic lethality theory approaches to effective substance discovery and functional mechanisms elucidation of anti-cancer phytomedicine. *Phytomedicine* 91, 153718. doi:10.1016/j.phymed.2021.153718
- Su, J., Li, Q., Liu, J., Wang, H., Li, X., Wünntrang, D., et al. (2021). Ethyl acetate extract of Tibetan medicine *Rhamnella gilgitica* ameliorated type II collagen-induced arthritis in rats via regulating JAK-STAT signaling pathway. *J. Ethnopharmacol.* 267, 113514. doi:10.1016/j.jep.2020.113514
- Taranto, E., and Leech, M. (2006). Expression and function of cell cycle proteins in rheumatoid arthritis synovial tissue. *Histol. Histopathol.* 21, 205–211. doi:10.14670/hh-21.205
- Tiniakou, E., Kontzialis, M., and Petri, M. (2018). Rheumatoid pachymeningitis: a rare complication of rheumatoid arthritis. *J. Rheumatol.* 45, 1325–1326. doi:10.3899/jrheum.171074
- Van Der Woude, D., and Van Der Helm-Van Mil, A. H. M. (2018). Update on the epidemiology, risk factors, and disease outcomes of rheumatoid arthritis. *Best. Pract. Res. Clin. Rheumatol.* 32, 174–187. doi:10.1016/j.berh.2018.10.005
- Wang, S., Hou, Y., Li, X., Meng, X., Zhang, Y., Wang, X., et al. (2021a). Practical implementation of artificial intelligence-based deep learning and cloud computing on the application of traditional medicine and western medicine in the diagnosis and treatment of rheumatoid arthritis. *Front. Pharmacol.* 12, 765435. doi:10.3389/fphar.2021.765435
- Wang, X., Wang, Z. Y., Zheng, J. H., and Li, S. (2021b). TCM network pharmacology: a new trend towards combining computational, experimental and clinical approaches. *Chin. J. Nat. Med.* 19, 1–11. doi:10.1016/s1875-5364(21)60001-8
- Wang, Y., Chen, S., Du, K., Liang, C., Wang, S., Owusu Boadi, E., et al. (2021c). Traditional herbal medicine: therapeutic potential in rheumatoid arthritis. *J. Ethnopharmacol.* 279, 114368. doi:10.1016/j.jep.2021.114368
- Wang, S., Du, Q., Sun, J., Geng, S., and Zhang, Y. (2022a). Investigation of the mechanism of Isobavachalcone in treating rheumatoid arthritis through a combination strategy of network pharmacology and experimental verification. *J. Ethnopharmacol.* 294, 115342. doi:10.1016/j.jep.2022.115342
- Wang, S., Qin, J., Meng, X., and Zhang, Y. (2022b). Research hotspots and trends in Chinese minority traditional medicine during 2021: a visual bibliometrics analysis. *Tradit. Med. Res.* 7, 29. doi:10.53388/TMR20220317271
- Xu, H., Zhang, Y., Wang, P., Zhang, J., Chen, H., Zhang, L., et al. (2021). A comprehensive review of integrative pharmacology-based investigation: A paradigm shift in traditional Chinese medicine. *Acta Pharm. Sin. B* 11, 1379–1399. doi:10.1016/j.apsb.2021.03.024
- Yang, G., Chang, C. C., Yang, Y., Yuan, L., Xu, L., Ho, C. T., et al. (2018). Resveratrol alleviates rheumatoid arthritis via reducing ROS and inflammation, inhibiting MAPK signaling pathways, and suppressing angiogenesis. *J. Agric. Food Chem.* 66, 12953–12960. doi:10.1021/acs.jafc.8b05047
- Zhang, C., Liu, C., Qu, Y., Cao, Y., Liu, R., Sun, Y., et al. (2021a). LC-MS-Based qualitative analysis and pharmacokinetic integration network pharmacology strategy reveals the mechanism of phlomis brevidentata H.W.Li treatment of pneumonia. *ACS Omega* 6, 4495–4505. doi:10.1021/acsomega.0c06201
- Zhang, F. X., Li, Z. T., Yang, X., Xie, Z. N., Chen, M. H., Yao, Z. H., et al. (2021b). Discovery of anti-flu substances and mechanism of Shuang-Huang-Lian water extract based on serum pharmaco-chemistry and network pharmacology. *J. Ethnopharmacol.* 268, 113660. doi:10.1016/j.jep.2020.113660
- Zhang, L., Siyiti, M., Zhang, J., Yao, M., and Zhao, F. (2021c). Anti-inflammatory and anti-rheumatic activities *in vitro* of alkaloids separated from *Aconitum soongoricum* Stapf. *Exp. Ther. Med.* 21, 493. doi:10.3892/etm.2021.9924
- Zhao, J. V., and Schooling, C. M. (2019). Role of linoleic acid in autoimmune disorders: a mendelian randomisation study. *Ann. Rheum. Dis.* 78, 711–713. doi:10.1136/annrheumdis-2018-214519
- Zhou, M., Huo, J., Wang, C., and Wang, W. (2021). UPLC/Q-TOF MS screening and identification of antibacterial compounds in *forsythia suspensa* (thunb.) vahl leaves. *Front. Pharmacol.* 12, 704260. doi:10.3389/fphar.2021.704260
- Zhu, Q. J., Wang, B. H., Chen, P. P., Zhang, W. H., and Zhang, X. F. (2012). Simultaneous determining on the content of three aconitine-type Alkaloids in Wuwei shenxiang pills by HPLC. *Chin. Arch. Tradit. Chin. Med.* 30, 1673–1675. doi:10.13193/j.archtcm.2012.07.235.zhuqj.069



## OPEN ACCESS

## EDITED BY

Alessandra Durazzo,  
Council for Agricultural Research and  
Economics, Italy

## REVIEWED BY

Yang Zhang,  
Capital Medical University, China  
Linghao Qin,  
Guangdong Pharmaceutical University,  
China

## \*CORRESPONDENCE

Hubiao Chen,  
hbchen@hkbu.edu.hk  
Jianye Zhang,  
jianyez@163.com

<sup>†</sup>These authors have contributed equally  
to this work

## SPECIALTY SECTION

This article was submitted to  
Ethnopharmacology,  
a section of the journal  
Frontiers in Pharmacology

RECEIVED 17 May 2022

ACCEPTED 29 June 2022

PUBLISHED 25 July 2022

## CITATION

Chen Q, Zhou W, Huang Y, Tian Y,  
Wong SY, Lam WK, Ying KY, Zhang J and  
Chen H (2022), Umbelliferone and  
scopoletin target tyrosine kinases on  
fibroblast-like synoviocytes to block  
NF- $\kappa$ B signaling to combat  
rheumatoid arthritis.  
*Front. Pharmacol.* 13:946210.  
doi: 10.3389/fphar.2022.946210

## COPYRIGHT

© 2022 Chen, Zhou, Huang, Tian, Wong,  
Lam, Ying, Zhang and Chen. This is an  
open-access article distributed under  
the terms of the [Creative Commons  
Attribution License \(CC BY\)](https://creativecommons.org/licenses/by/4.0/). The use,  
distribution or reproduction in other  
forums is permitted, provided the  
original author(s) and the copyright  
owner(s) are credited and that the  
original publication in this journal is  
cited, in accordance with accepted  
academic practice. No use, distribution  
or reproduction is permitted which does  
not comply with these terms.

# Umbelliferone and scopoletin target tyrosine kinases on fibroblast-like synoviocytes to block NF- $\kappa$ B signaling to combat rheumatoid arthritis

Qilei Chen<sup>1†</sup>, Wenmin Zhou<sup>2†</sup>, Yueming Huang<sup>1</sup>, Yuanyang Tian<sup>1</sup>,  
Sum Yi Wong<sup>1</sup>, Wing Ki Lam<sup>1</sup>, Ka Yee Ying<sup>1</sup>, Jianye Zhang<sup>2\*</sup> and  
Hubiao Chen<sup>1\*</sup>

<sup>1</sup>School of Chinese Medicine, Hong Kong Baptist University, Hong Kong Special Administrative Region, Kowloon, Hong Kong SAR, China, <sup>2</sup>Guangzhou Municipal and Guangdong Provincial Key Laboratory of Molecular Target and Clinical Pharmacology, the NMPA and State Key Laboratory of Respiratory Disease, School of Pharmaceutical Sciences and the Fifth Affiliated Hospital, Guangzhou Medical University, Guangzhou, China

Rheumatoid arthritis (RA) is a complex autoimmune condition primarily affecting synovial joints, which targeted synthetic drugs have damaging safety issues. *Saussurea laniceps*, a reputed anti-rheumatic medicinal herb, is an excellent place to start looking for natural products as safe, effective, targeted therapeutics for RA. Via biomimetic ultrafiltration, umbelliferone and scopoletin were screened as two anti-rheumatic candidates with the highest specific affinities towards the membrane proteomes of rheumatic fibroblast-like synoviocytes (FLS), the pivotal effector cells in RA. *In vitro* assays confirmed that the two compounds, to varying extents, inhibited RA-FLS proliferation, migration, invasion, and NF- $\kappa$ B signaling. Network pharmacology analysis and molecular docking analysis jointly revealed that umbelliferone and scopoletin act on multiple targets, mostly tyrosine kinases, in combating RA. Taken together, our present study identified umbelliferone and scopoletin as two major anti-rheumatic components from SL that may bind and inhibit tyrosine kinases and subsequently inactivate NF- $\kappa$ B in RA-FLSs. Our integrated drug discovery strategy could be valuable in finding other multi-target bioactive compounds from complex matrices for treating multifactorial diseases.

## KEYWORDS

rheumatoid arthritis, *Saussurea laniceps*, ultrafiltration, network pharmacology, ErbB network, drug discovery



## Introduction

Rheumatoid arthritis (RA) is a chronic inflammatory joint disease that causes progressive articular destruction and deformity, and affects approximately 1% of the global population (Almutairi et al., 2021). Despite advances in RA management, the disease is still not well controlled in up to 30% of patients due to the individualized pathogenic network (McInnes and Schett, 2017). Current first-line RA medications include non-steroidal inflammatory drugs (NSAIDs) and disease-modifying anti-rheumatic drugs (DMARDs). These drugs can only relieve symptoms but fail to control disease progression (McInnes and Schett, 2011). Recently, highly targeted small-molecule agents, such as tyrosine kinase inhibitors (TKI), open a new avenue for RA therapy with improved clinical responses (Koenders and Van DenBerg, 2015). However, such synthetic molecules bring inevitable safety issues. For example, tofacitinib and baricitinib, two TKIs, have black box warnings from the US Food and Drug Administration (FDA) for severe infections and malignancies (Petronelli, 2021). The adverse events may not be correlated to specific protein inhibition but the synthetic structures (Schwartz et al., 2019). Therefore, novel scaffolds with safe, effective, targeted biomarker inhibition are desired for precision medicine in RA.

Natural products from herbal medicines have long been valuable sources for drug discovery due to their enormous scaffold diversity and structural complexity (Wang et al., 2021). The therapeutic rationale of herbal medicines is a paradigm of the emerging drug discovery concept of “polypharmacology”, *i.e.*, multiple components hitting multiple targets (Shen, 2015). Multi-targeted chemicals provide a better balance of efficacy and safety than single-targeted drugs in multifactorial diseases (Fang et al., 2019). “Snow lotus” has been reputed as an effective anti-rheumatic herbal medicine in Asia for centuries (Committee of Chinese Pharmacopoeia, 1995). We previously discovered that, among official “snow lotus” species (Chik et al., 2015; Fan et al., 2015; Chen et al., 2016), *Saussurea laniceps* Hand.-Mazz (SL) exerts the most outstanding chemical composition (Chen et al., 2017) and most potent anti-rheumatic efficacies (Yi et al., 2010, 2012), and SL significantly ameliorates RA symptoms by targeted inhibition of multiple therapeutic biomarkers while maintaining good safety profiles (Chen et al., 2021). Therefore, it is believed that SL is a promising source of safe, effective, targeted anti-rheumatic agents. However, therapeutic components in SL and corresponding action mechanisms have not been thoroughly investigated.

Isolation and activity screening of active compounds from herbal medicines, which are structurally diverse and sometimes in trace amounts, has long been challenging with existing conventional methods (Cannell, 1998). An advanced approach, bio-affinity ultrafiltration, based on receptor-ligand interaction, is a powerful tool for compound (ligand) fishing in complicated matrices due to its excellent high-throughput online screening ability, sensitivity, and selectivity (Chen et al., 2018). Generally, bio-affinity ultrafiltration uses one or a few

recombinant cytosolic proteins as receptors (Wang et al., 2018). As one step further, a “biomimetic ultrafiltration” approach can be designed by employing natural disease-specific proteomes as receptors, which is more reasonable for screening active agents from complex matrices to treat multifactorial diseases, where most of the therapeutic targets remain highly underexplored (Fang et al., 2019).

Fibroblast-like synoviocytes (FLS) are the most common cell type at the pannus–cartilage junction and are critical effector cells in RA (Bustamante et al., 2017). A significant hallmark of FLS activation attributes to increased expression of surface proteins under inflammatory conditions (Wu Z et al., 2021). Therapies that target FLS, especially against their surface markers, are emerging as promising therapeutic tools for RA (Nygaard and Firestein, 2020). Therefore, proteins extracted from FLS of RA patients (HFLS-RA), including membrane and cytosolic proteomes, can be used as receptors in a tailored biomimetic ultrafiltration, to discover anti-rheumatic compounds from SL. The screened compounds are expected to hit multiple and even possibly unknown targets with minimized unspecific bindings. Such parallel study of compounds targeting natural proteomes from membrane and cytosol has not been reported.

In the present study, biomimetic ultrafiltration with FLS proteome fractions was conducted, followed by ultra-performance liquid chromatography coupled to a quadrupole/time-of-flight-mass spectrometer (UPLC-QTOF-MS) analysis, to fish out anti-rheumatic candidate compounds from SL. *In vitro* pharmacological performances of the screened compounds were verified, in terms of inhibiting RA-FLS proliferation, migration, invasion, and NF- $\kappa$ B activation. Protein targets and action pathways of the screened compounds were identified by network pharmacology analysis. Interaction modes between the compounds and key protein targets were investigated by molecular docking analysis. Our work provides valuable insights into the pharmacodynamic material basis of SL. It also serves as a case study to develop new drugs from natural resources for RA and other complex diseases.

## Materials and methods

### Chemicals and reagents

The standard compounds of umbelliferone, scopoletin, and celecoxib were purchased from Biomart Biotechnology Ltd. (Beijing, China). Acetonitrile (ACN) and methanol of chromatography grade were purchased from Lab-scan (Bangkok, Thailand). All aqueous solutions were prepared using ultra-pure water with a Milli-Q water purification system from Millipore (MA, United States). All chemicals not otherwise mentioned were purchased from Sigma-Aldrich (MO, United States) and were used without further purification.



## Plant material and extract preparation

SL was collected from Lhasa, Tibet, in 2008. The plant was authenticated by Prof. Hubiao Chen. Voucher specimens were deposited in the Hong Kong Baptist University. The aerial parts of the plant were powdered with a Fargo RT-04 grinder (Century Equipment Ltd., Kowloon, HK) and passed through a 20 mesh (0.9 mm) sieve. The dried and powdered sample (0.5 g) was reflux extracted with 25 ml water at 100°C for 1 h, twice. Total extracts were combined into a 100-ml volumetric flask and added up to the calibration mark with water. The extract was centrifuged at 14,000 g for 10 min before passed through a 0.2-μm syringe membrane (Alltech, IL, United States of America).

## Cell culture

Normal HFLS (HFLS-N) and HFLS-RA were purchased from Otwo Biotech Co., Ltd (Shenzhen, China) and Guandao Biological Engineering Co., Ltd (Shanghai, China), respectively. The cells were separately cultured in Dulbecco's Modified Eagle's medium (DMEM; Gibco, MD, United States) containing 10% (v/v) heat-inactivated fetal bovine serum (Gibco), 100 U/mL penicillin and 100 mg/ml streptomycin (Gibco). Cells were grown in a humidified atmosphere with 5% CO<sub>2</sub> at 37°C.

## Biomimetic ultrafiltration coupled with UPLC-QTOF-MS analysis

HFLS-N and HFLS-RA cells were collected and washed three times with PBS (pH 7.4) with 1 mM phenylmethylsulfonyl fluoride (PMSF). The isolation of cell membrane and cytosol proteins was conducted using the Membrane and Cytosol Protein Extraction Kit (Beyotime, Shanghai, China) following the manufacturer's instructions. Protein contents were determined by the Bradford method.

The screening procedure was conducted based on previous reports with modifications (Chen et al., 2018). Extracted proteins (2 mg/ml) and SL extract (5 mg/ml) were mixed in PBS buffer (pH 7.4) and rotated under 4°C for 30 min. To intercept the ligand-protein complexes, the mixtures were ultracentrifuged through filters (Molecular weight cut-off: 3 kDa; Amicon, Darmstadt, Germany) at 14,000 g under 4°C for 10 min, then washed with PBS four times. To release ligands, the obtained complexes were incubated with 500 μl MeOH for 10 min, then ultracentrifuged at room temperature for 15 min thrice. The combined filtrates were collected for chemical analysis. Heat-inactivated proteins were used as negative controls.

A UPLC-QTOF-MS system (Agilent Technologies, United States) was used for chemical analyses of SL extract and the ligand filtrates. The chromatographic and spectrometric parameters were set as previously published

(Chen et al., 2017, 2021), with minor modifications regarding the elution gradient (solvent A: 0.1% formic acid in water; solvent B: 0.1% formic acid in ACN): 0–2 min with 2% B; 2–10 min with 2–10% B; 16–20 min with 18–25% B; 20–25 min with 25–55% B.

Affinity degree (AD) of a ligand towards an extracted proteome =  $(A_1 - A_2)/A_0 \times 100\%$ , where  $A_1$ ,  $A_2$ , and  $A_0$  represented the peak areas of selected compounds obtained from the incubations of the SL extract with active, inactive, and without respective proteins, respectively.

RA- and membrane-specificity index =  $(AD_{RM}/AD_{NM})/(AD_{RC}/AD_{NC})$ , where  $AD_{RM}$ ,  $AD_{NM}$ ,  $AD_{RC}$ , and  $AD_{NC}$  represented the AD towards proteome from HFLS-RA membrane, HFLS-N membrane, HFLS-RA cytosol, and HFLS-N cytosol, respectively.

## MTT assay

Proliferation rate of HFLS-RA cells was monitored by an MTT assay as previously described (Chen et al., 2021). Briefly, cells ( $3 \times 10^4$ /well) in 100 μl complete culture medium were seeded in 96-well microtiter plates for 24 h. They were then exposed to varying doses of celecoxib (positive control), umbelliferone, and scopoletin in serum-free medium. After incubation for 24 and 48 h, MTT (5 mg/ml, 10 μl) was added to each well, and the plates were incubated for 2 h. Formazan crystals were dissolved with 100 μl DMSO, and absorbance at 570 nm was measured by a Benchmark microplate reader (Bio-Rad, Hercules, CA, United States) with 630 nm as reference filter.

## Wound healing assay

Collective migration of HFLS-RA cells was assessed by a scratch wound healing assay as reported (Li et al., 2019). Cells ( $3 \times 10^5$ /well) in 2 ml complete culture medium were seeded in 12-well microtiter plates for 24 h to reach 80% confluence. A linear wound was made in the cellular monolayer with a sterile 200 μl pipette tip. After removing the cell debris, the cells were incubated with 20 μM celecoxib, umbelliferone, and scopoletin in serum-free medium. Wound closures were observed and photographed at 0, 24, and 48 h under a light microscope (Leica DMI3000B, Wetzlar, Germany). The wound area was determined using ImageJ software.

## Transwell migration and invasion assay

24-well Transwell chambers (8 μm pore size; Corning, NY, United States) were used as published (Huang H et al., 2021). For single-cell migration assessment, HFLS-RA cells ( $4 \times 10^4$ /well) in 200 μl serum-free medium were seeded in the upper chambers and treated with 20 μM celecoxib, umbelliferone, and scopoletin, respectively. 600 μl

complete culture medium was added in the lower chambers. After incubation at 37°C for 24 h, non-migrating cells on the upper surface of the Transwell membrane were removed; cells migrated to the lower surface of the membrane were fixed with methanol, stained with 0.5% crystal violet, photographed under the microscope, and counted. The invasion assay was performed similarly, except that the membranes were pre-coated with Matrigel.

## Western blot analysis

HFLS-RA cells treated with 20  $\mu$ M celecoxib, umbelliferone, and scopoletin, respectively, for 24 h, were collected and lysed using RIPA buffer (containing phosphatase inhibitor and PMSF) to obtain protein samples. An equal amount of protein was separated by 10% SDS-PAGE and transferred to PVDF membranes (Millipore). The membranes were blocked with 5% non-fat milk for 1 h at room temperature, and then incubated overnight at 4°C with the following primary antibodies: anti-NF- $\kappa$ B p65 (#8242; CST, MA, United States), phospho-NF- $\kappa$ B p65 (#3033; CST), I $\kappa$ B $\alpha$  (#4814; CST), phospho-I $\kappa$ B $\alpha$  (#2859; CST), and anti-GAPDH (#AF7021; Affinity, OH, United States). Then, the membranes were washed with 3  $\times$  TBST and incubated with corresponding HRP-conjugated secondary antibodies for 1 h at room temperature. The blots were developed using the enhanced chemiluminescence solution and imaged by ChemiDoc™ XRS + system.

## Network pharmacology analysis

To predict protein targets of umbelliferone and scopoletin, the two compounds were input in the form of Simplified Molecular Input Line System (SMILES) into SwissTargetPrediction database (<http://www.swisstargetprediction.ch>) and Search Tool for Interactions of Chemical (STITCH; <http://stitch.embl.de>); targets with literature support after checking at Uniprot (<https://www.uniprot.org>) were retained for subsequent analysis. RA-related genes were collected using GeneCards database (<https://www.genecards.org>) and Therapeutic Target Database (TTD, <http://db.idrblab.net/ttd>). Candidate targets related to both umbelliferone/scopoletin and RA were selected using a Venn diagram.

To conduct gene ontology (GO) and Kyoto Encyclopedia of Genes and Genomes (KEGG) pathway enrichment analysis, the selected targets were imported into the Database for Annotation, Visualization and Integrated Discovery (DAVID; <https://david.ncicrf.gov>). The annotations with adjusted  $p < 0.05$  were considered significantly enriched.

For each compound, compound–target–pathway (C-T-P) networks were constructed using Cytoscape (<https://cytoscape.org>) to examine the relationships between the compound, corresponding protein targets, and related pathways; protein–protein interaction (PPI) networks were generated using STRING (<https://string-db.org>) and visualized by Cytoscape to present the relationships between major protein targets of the compound.

## Molecular docking

Discovery Studio Biovia 2019 (Dassault Systèmes, OH, United States), AutoDock Vina (The Scripps Research Institute, CA, United States), and PyMol (DeLano Scientific LLC, CA, United States) were employed for receptor/ligand structure modification, docking, 3D visualization, respectively. The crystal structures of the receptors were obtained from the Protein Data Bank (PDB; <https://www.rcsb.org>). All water molecules were removed, hydrogen polarities were assigned, and Gasteiger charges were computed. For each receptor, a grid was created to ensure the binding site covers the active pocket.

## Statistical analysis

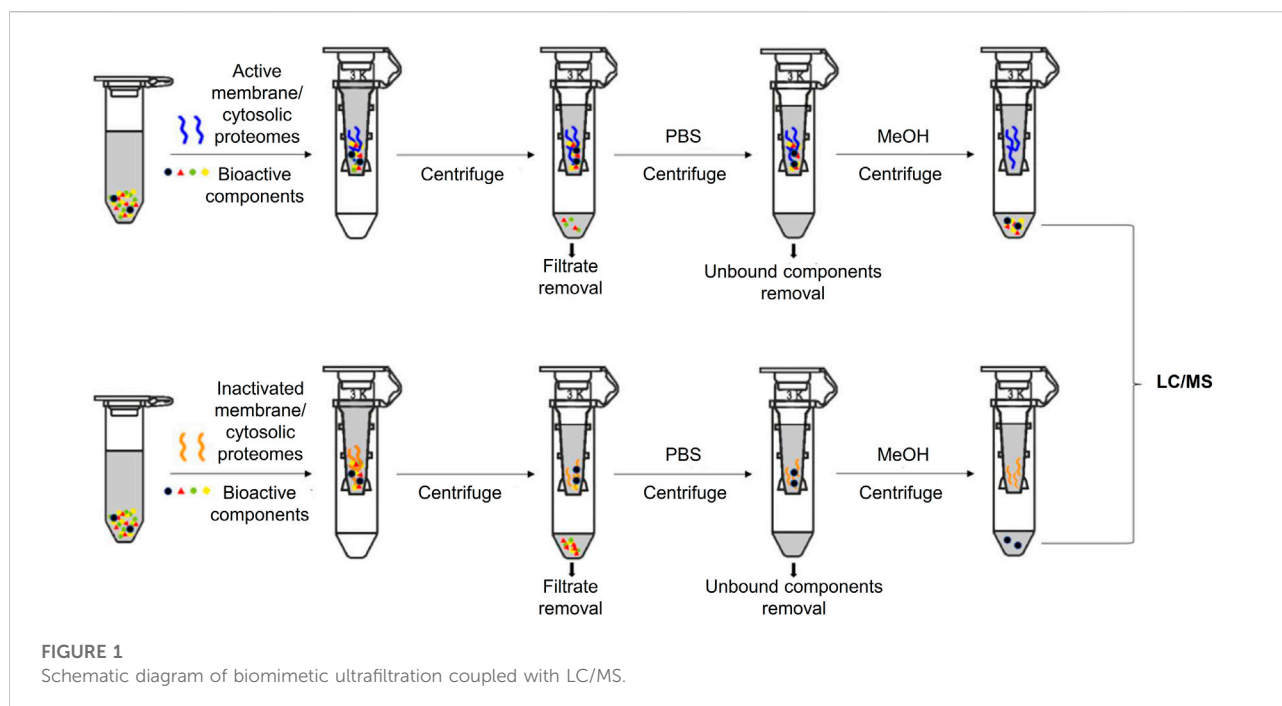
Data are presented as the mean  $\pm$  SD. Comparisons were performed using ANOVA tests unless specified.  $p < 0.05$  was considered significant.

## Results

### Umbelliferone and scopoletin are ligands of RA-FLS membrane proteome

Ligand fishing from the anti-rheumatic SL extract was based on biomimetic ultrafiltration coupled with UPLC-QTOF-MS analysis. Membrane and cytosolic protein fractions were employed as receptors in the ultrafiltration. To eliminate false-positive ligand fishing results, inactivated HFLS-RA-derived proteins were used as activity-negative control, and HFLS-N derived proteins as disease-negative control (Figure 1).

Based on our previous chemical profiling of SL, ten major components were detected from the herbal extract (Figure 2) (Chen et al., 2017). Among the extract components, three compounds showed a AD towards rheumatic membrane (RM) proteins than that towards normal membrane (NM) proteins, namely, umbelliferone (peak 6; AD<sub>RM</sub> = 25.82%; AD<sub>NM</sub> = 10.27%), scopoletin (peak 7; AD<sub>RM</sub> = 1.55%; AD<sub>NM</sub> = 1.42%), and involucratolactone- $\beta$ -D-glucoside (peak 10; AD<sub>RM</sub> = 1.08%; AD<sub>NM</sub> = 1.05%) (Table 1). Four compounds exerted higher AD



**FIGURE 1**  
Schematic diagram of biomimetic ultrafiltration coupled with LC/MS.

towards rheumatic cytosol (RC) than normal cytosol (NC) fraction, namely, skimmin (peak 1;  $AD_{RC} = 3.40\%$ ;  $AD_{NC} = 1.88\%$ ), chlorogenic acid (peak 2;  $AD_{RC} = 0.10\%$ ;  $AD_{NC} = 0\%$ ), piceol (peak 5;  $AD_{RC} = 2.76\%$ ;  $AD_{NC} = 0.88\%$ ), and 3,5-dicaffeoylquinic acid (peak 8;  $AD_{RC} = 0.63\%$ ;  $AD_{NC} = 0\%$ ).

Cell surface proteins play crucial physiological roles *in vivo* and are currently the most successful class of drug targets for pharmaceuticals (Huang Y et al., 2021). In this regard, specific RA- and membrane-targeting compounds will be selected as high potential anti-rheumatic agents. Two coumarins from SL extract exhibited outstanding RA- and membrane-specificity index, *i.e.* umbelliferone (peak 6; index = 4.27) and scopoletin (peak 7; index = 3.57) (Table 1). Therefore, umbelliferone and scopoletin were screened from SL extract as key ligands of RA-FLS membrane proteome for subsequent analyses.

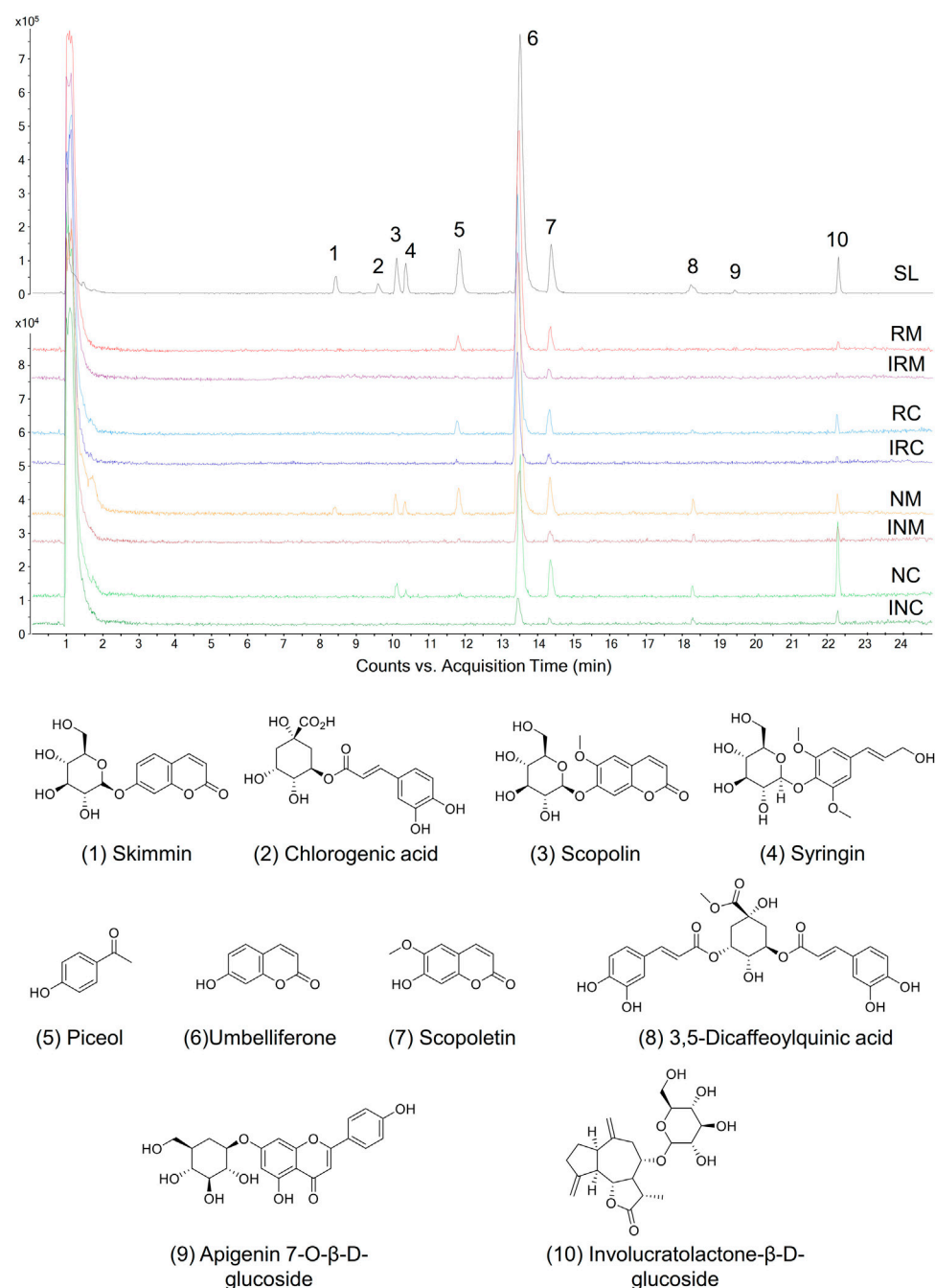
## Umbelliferone and scopoletin differentially inhibited RA-FLS activities

Inhibitory effects of the two compounds on RA-FLS activities were assessed regarding proliferation, migration, and invasion. An MTT study showed that umbelliferone and scopoletin shared similar inhibitory profiles on HFLS-RA proliferation with celecoxib, a first-line RA drug yet associated with increased cardiovascular risks (Figure 3A) (Fidahic et al., 2017). Specifically, scopoletin significantly inhibited HFLS-RA proliferation at 30  $\mu\text{M}$  and

onwards. In our previous research, umbelliferone and scopoletin were proved with evidently lower cardiomyocyte toxicity and less cardiac remodeling in rats than celecoxib did (Chen et al., 2021). Our previous and current findings collectively indicate that the two screened natural compounds are safer for the cardiovascular system yet match competitiveness in inhibiting RA-FLS proliferation compared to celecoxib.

For inhibition of HFLS-RA migration, umbelliferone showed similarly potent efficacies with celecoxib and was more effective than scopoletin. At 20  $\mu\text{M}$ , where the dosage was proved with no significant impact on cell proliferation, umbelliferone and celecoxib significantly reduced both single-cell and collective migration of HFLS-RA cells with 24 and 48 h incubation ( $p < 0.0026$ ) (Figures 3B,C). Scopoletin exhibited significant reduction of single-cell migration ( $p < 0.0001$ ) but only slight inhibition of collective migration ( $p \leq 0.8919$ ) (Figures 3B,C). Since cell-extracellular matrix (ECM) adhesion and cell-cell adhesion are central mechanisms in the process of collective migration (Pijuan et al., 2019), our results indicated that umbelliferone is more potent in inhibiting such adhesions than scopoletin.

The compounds' inhibitory effects on HFLS-RA invasion were also evaluated (Figure 3D). Umbelliferone exerted significant (71.82% inhibition;  $p < 0.0001$ ) and even more evident reduction of invasive cells than celecoxib (69.42% inhibition;  $p < 0.0001$ ). Scopoletin also reduced the number of invasive cells, yet the inhibitory rate was approximately half that of umbelliferone. The inhibitory pattern of invasion being similar to that of collective migration can be explained that the

**FIGURE 2**

Proteome ligands separated from SL extract by biomimetic ultrafiltration coupled to UPLC-QTOF-MS. RM, RC: membrane and cytosolic proteomes of HFLS-RA, respectively. NM, NC: membrane and cytosolic proteomes of HFLS-N, respectively. IRM, IRC, INM, INC: inactivated corresponding proteomes, respectively.

two processes share similar cell behaviors: they both involve cells with mesenchymal characteristics to degrade the ECM for directed cell movements (Friedl and Gilmour, 2009; Yang et al., 2019).

The transcription factor NF-κB is a pivotal mediator of inflammatory responses. NF-κB activation is associated with RA-HFLS hyperproliferation, migration, and invasiveness, leading to hyperplasia in the rheumatic synovium (Nejabatkhsh Samimi

TABLE 1 UPLC-QTOF-MS data and proteome affinity degrees of SL extract components.

Peak	t <sub>R</sub> (min)	Compound	Formula	Major fragment		AD <sub>RM</sub> (%) <sup>a</sup>	AD <sub>NM</sub> (%)	AD <sub>RC</sub> (%)	AD <sub>NC</sub> (%)	RA- and membrane- specific index
				m/z	Adduct ion					
1	8.43	Skimmin	C <sub>15</sub> H <sub>16</sub> O <sub>8</sub>	369.0893	[M + HCOO] <sup>-</sup>	0.31 ± 0.62	0.43 ± 0.58	3.40 ± 1.46	1.88 ± 0.13	0.40
2	9.59	Chlorogenic acid	C <sub>16</sub> H <sub>18</sub> O <sub>9</sub>	399.1004	[M-H] <sup>-</sup>	0.15 ± 0.01	0.26 ± 0.25	0.10 ± 0.13	0	/ <sup>b</sup>
3	10.11	Scopolin	C <sub>16</sub> H <sub>18</sub> O <sub>9</sub>	399.0933	[M + HCOO] <sup>-</sup>	0.04 ± 0.06	0.51 ± 0.24	2.13 ± 1.33	2.78 ± 1.57	0.10
4	10.35	Syringin	C <sub>17</sub> H <sub>24</sub> O <sub>9</sub>	417.1402	[M + HCOO] <sup>-</sup>	0.34 ± 0.28	0.60 ± 0.32	1.99 ± 1.21	2.83 ± 0.21	0.81
5	11.84	Piceol	C <sub>8</sub> H <sub>8</sub> O <sub>2</sub>	135.0481	[M-H] <sup>-</sup>	1.03 ± 1.51	1.06 ± 0.93	2.76 ± 1.54	0.88 ± 0.13	0.31
6	13.56	Umbelliferone	C <sub>9</sub> H <sub>6</sub> O <sub>3</sub>	161.0244	[M-H] <sup>-</sup>	25.82 ± 12.03	10.27 ± 9.45	10.64 ± 6.17	18.09 ± 2.33	4.27
7	14.38	Scopoletin	C <sub>10</sub> H <sub>8</sub> O <sub>4</sub>	191.0372	[M-H] <sup>-</sup>	1.55 ± 1.99	1.42 ± 1.13	2.00 ± 2.08	6.54 ± 1.02	3.57
8	18.22	3,5-Dicaffeoylquinic acid	C <sub>25</sub> H <sub>24</sub> O <sub>12</sub>	515.1195	[M-H] <sup>-</sup>	0.38 ± 0.46	0.98 ± 0.60	0.63 ± 0.62	0	/ <sup>b</sup>
9	18.73	Apigenin 7-O-β-D-glucoside	C <sub>21</sub> H <sub>20</sub> O <sub>10</sub>	577.1550	[M-H] <sup>-</sup>	1.60 ± 0.27	3.60 ± 2.43	8.03 ± 4.28	10.72 ± 2.77	0.59
10	22.31	Involucratolactone-β-D-glucoside	C <sub>21</sub> H <sub>30</sub> O <sub>8</sub>	455.2004	[M + HCOO] <sup>-</sup>	1.08 ± 1.10	1.05 ± 2.04	0	16.66 ± 2.12	/ <sup>b</sup>

Data as mean ± SD (n = 3).

<sup>a</sup>AD<sub>RM</sub>, AD<sub>NM</sub>, AD<sub>RC</sub>, and AD<sub>NC</sub>, represented affinity degrees (AD) towards proteome from HFLS-RA, membrane; HFLS-N, membrane; HFLS-RA, cytosol, and HFLS-N, cytosol, respectively.

<sup>b</sup>Not applicable.

et al., 2020). We hereby investigated whether the tested compounds inhibit the NF-κB signaling pathway. The western blot results indicated that the compounds decreased the phosphorylation of NF-κB p65 and IκB-α, paralleling their inhibitory levels (Figure 3E). Such suppressed NF-κB canonical signaling can decrease the expression of inflammatory cytokines, adhesion molecules, and other promoters in the inflammatory cascade (Liu et al., 2017). The conclusion of the two compounds suppressing NF-κB signaling can be supported by other studies showing that umbelliferone (Ouyang et al., 2019; Wu G et al., 2021) and scopoletin (Li et al., 2009; Chen et al., 2021) can effectively suppress phosphorylation of specific NF-κB subunits (e.g. p65 and IκBα) and expression of downstream genes (e.g. IL-1β, TNF-α, MMP-3, MMP-9, COX-2, Bcl-2) in RA synovial tissues and FLSs. Since both umbelliferone and scopoletin had high binding affinities towards RA-FLS membrane proteins (Table 1) and inhibited RA-FLS activities (Figure 3), it is believed that NF-κB is a primary node of the two compounds in treating RA.

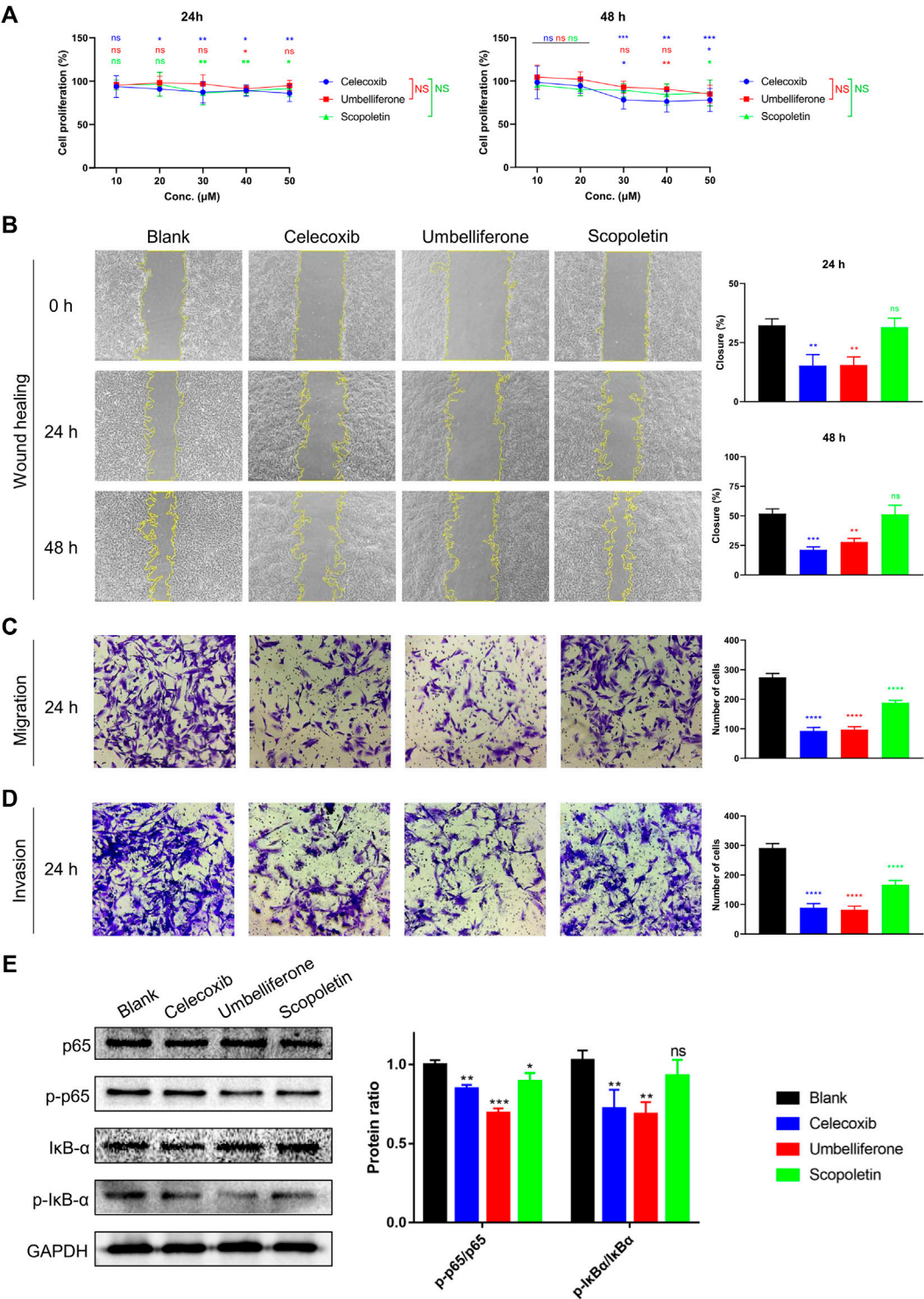
## Umbelliferone and scopoletin target key pathways and proteins against RA

A network pharmacology analysis was conducted to identify direct biological targets of umbelliferone and scopoletin in treating RA. From various databases, 5104 RA-related proteins, 116 umbelliferone protein targets, and 110 scopoletin protein

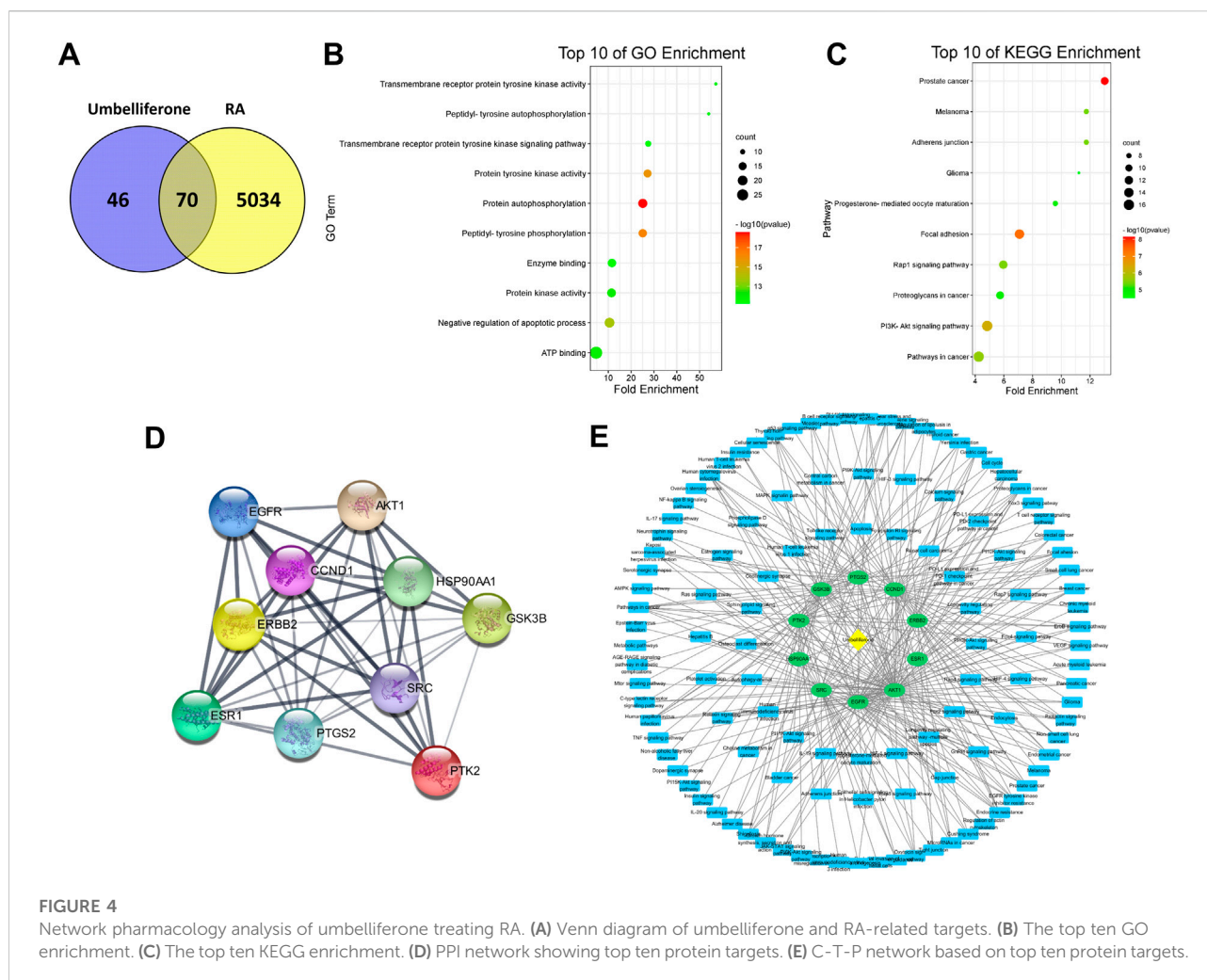
targets were collected with literature support. It is worth noticing that over half of the protein targets of the two screened compounds are linked with RA (Figure 4A and Figure 5A), i.e., 70 (60.34%) proteins and 62 (56.36%) proteins for umbelliferone and scopoletin, respectively, corresponding to their abovementioned promising anti-rheumatic efficacy. The overlapping proteins were recognized as candidate anti-rheumatic targets of the two respective compounds (Supplementary Tables S1, S2).

C-T-P networks were constructed for the two compounds. The C-T-P network of umbelliferone consisted of 70 targets and 117 pathways, and that of scopoletin included 62 targets and 109 pathways (Supplementary Figures S1, S2). On such basis, Gene Ontology (GO) and KEGG pathway enrichment analysis were employed to characterize the functional annotations of the proteins (Supplementary Figures S3, S4). Interestingly, umbelliferone and scopoletin shared highly similar GO and KEGG profiles. According to the GO enrichment results, the two compounds are both heavily involved with transmembrane receptor tyrosine kinases (RTKs), especially with their activities (GO: 0004714, 0004173, 0004672), phosphorylation (GO: 0038083, 0046777, 0018108), and signaling pathways (GO: 0007169) (Figure 4B and Figure 5B). As for the KEGG results, adherens junction (KEGG: hsa04520), focal adhesion (KEGG: hsa04510), and Rap1 signaling pathway (KEGG: hsa04015) are among the ten most significant pathways for both compounds (Figure 4C and Figure 5C). Apart from the shared KEGG enrichments, umbelliferone is particularly enriched in phosphatidylinositol 3-





**FIGURE 3**  
Umbelliferone and scopoletin differentially inhibited RA-FLS activities. (A) Proliferation, (B) wound healing, (C) Transwell migration, (D) Transwell invasion, and (E) western blot assays on HFLS-RA. Data are means  $\pm$  SD of independent experiments performed in triplicate. ns, not significant at  $p > 0.05$ ,  $*p < 0.05$ ,  $***p < 0.001$ , and  $****p < 0.0001$  vs blank control group; ns, not significant vs celecoxib group.



kinase (PI3K)-protein kinase B (Akt) signaling pathway (KEGG: hsa04151), while scopoletin particularly in signaling pathways of ErbB (ErbB; KEGG: hsa04012) and chemokines (KEGG: hsa04062). Therefore, it is predicted that both umbelliferone and scopoletin can act on TKs to regulate biological processes, including cell adhesion, cell-cell junction formation, and cell polarization, which are all critical during RA progression (Weyand and Goronzy, 2021).

PPI networks for umbelliferone and scopoletin were also analyzed (Supplementary Figures S5, S6). There were seven common proteins among the top ten targets of the two compounds, namely, epidermal growth factor receptor (EGFR/ ErbB1), proto-oncogene tyrosine-protein kinase Src (Src), Akt serine/threonine kinase 1 (Akt1), receptor tyrosine-protein kinase ErbB-2 (ErbB2/HER2), protein tyrosine kinase 2 (PTK2/FAK), prostaglandin-endoperoxide synthase 2 (PTGS2/COX-2), and estrogen receptor 1 (ESR1/ERα) (Figure 4D and Figure 5D). Most of the listed proteins can be located on cell membrane; many of them can be categorized as RTKs (e.g., EGFR and ErbB2), non-receptor TKs (e.g. Src and FAK), or proteins closely crosstalking with TKs (e.g.

Akt1 and ERα). Simplified C-T-P networks were constructed based on umbelliferone and scopoletin's top ten protein targets, respectively (Figure 4E and Figure 5E). Specifically, the present network pharmacology analysis results correspond with our previous study in which the two compounds exerted significant and selective COX-2 inhibition in rheumatic rat synovium tissues (Chen et al., 2021).

Molecular docking analyses of umbelliferone and scopoletin against the abovementioned seven common top protein targets were performed to investigate the ligand-receptor interactions (Figures 6, 7). The docking studies were all validated by redocking the co-crystallized ligand for each protein, where the root mean square deviation (RMSD) value below 2 Å was considered good solutions (Supplementary Figure S7) (Ramírez and Caballero, 2018). Generally, the analyzed proteins all showed satisfactory affinities towards the two compounds (Supplementary Table S3). Among the analyzed TKs, HER2 is the protein exhibiting the lowest binding energies towards umbelliferone (-6.9 kcal/mol) and scopoletin (-7.2 kcal/mol), respectively. All interacting residues of



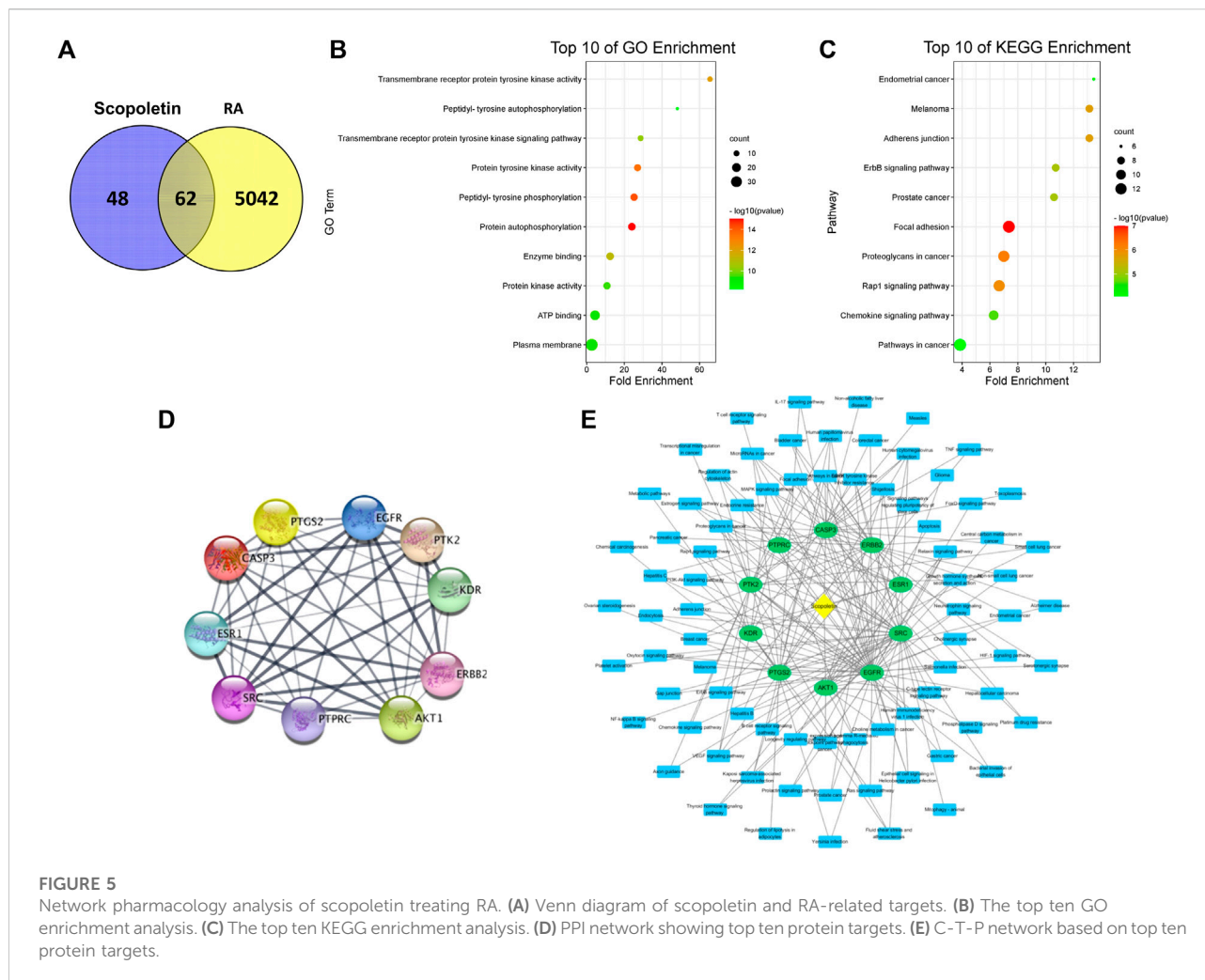


FIGURE 5

Network pharmacology analysis of scopoletin treating RA. (A) Venn diagram of scopoletin and RA-related targets. (B) The top ten GO enrichment analysis. (C) The top ten KEGG enrichment analysis. (D) PPI network showing top ten protein targets. (E) C-T-P network based on top ten protein targets.

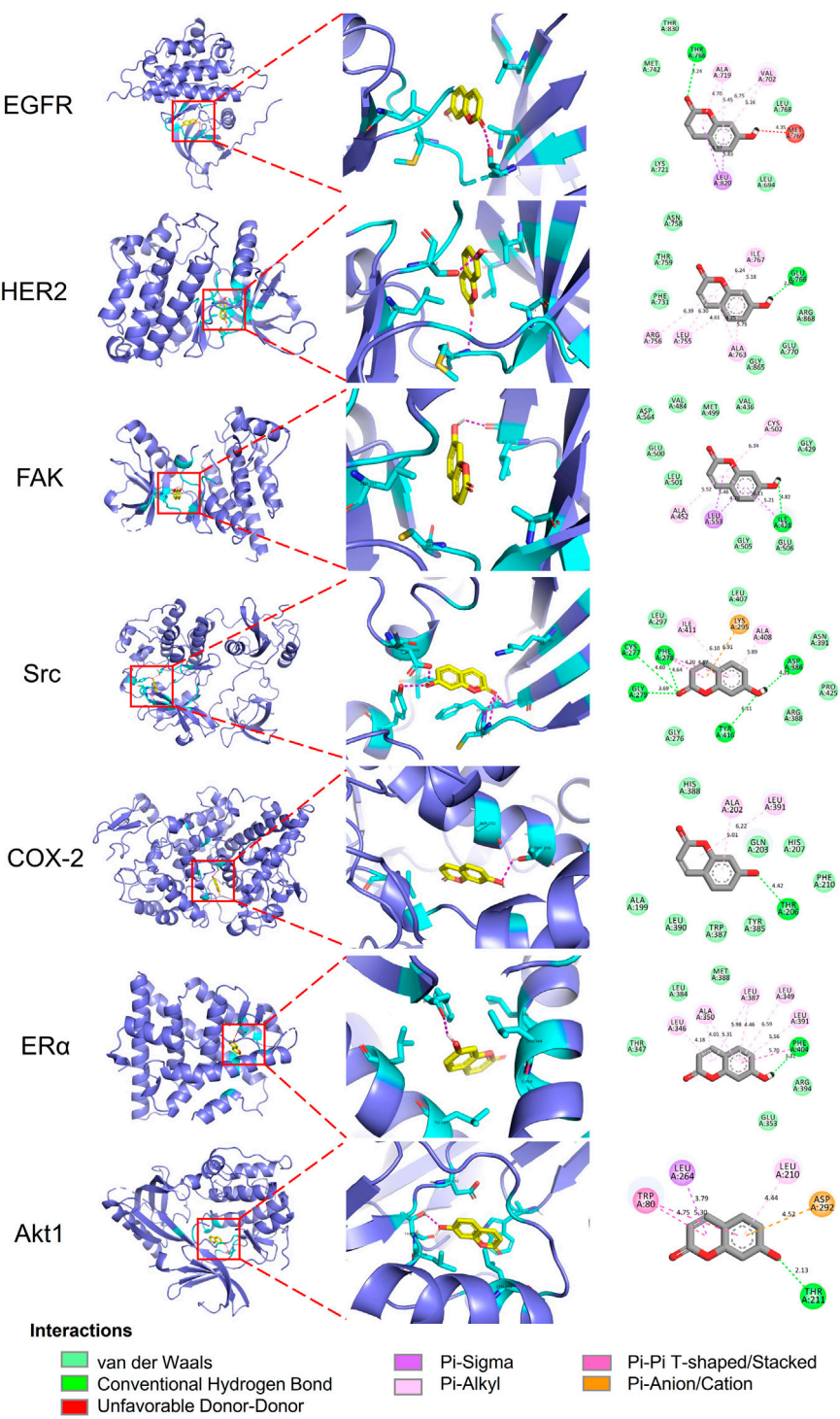
HER2 with both compounds lie in the active pocket. The interactions are mainly via conventional H-bonds (umbelliferone: Met<sub>801</sub>, Thr<sub>862</sub>; scopoletin: Asn<sub>520</sub>, Thr<sub>862</sub>),  $\pi$ -alkyl bonds (umbelliferone: Leu<sub>726</sub>, Val<sub>734</sub>, Ala<sub>751</sub>, Leu<sub>852</sub>; scopoletin: same except without Leu<sub>726</sub>), and  $\pi$ - $\sigma$  bonds (umbelliferone: Val<sub>734</sub>, Leu<sub>852</sub>; scopoletin: Val<sub>734</sub>). Collectively, the molecular docking results indicate favorable interactions and binding mechanisms between the two compounds and their top target proteins.

## Discussion

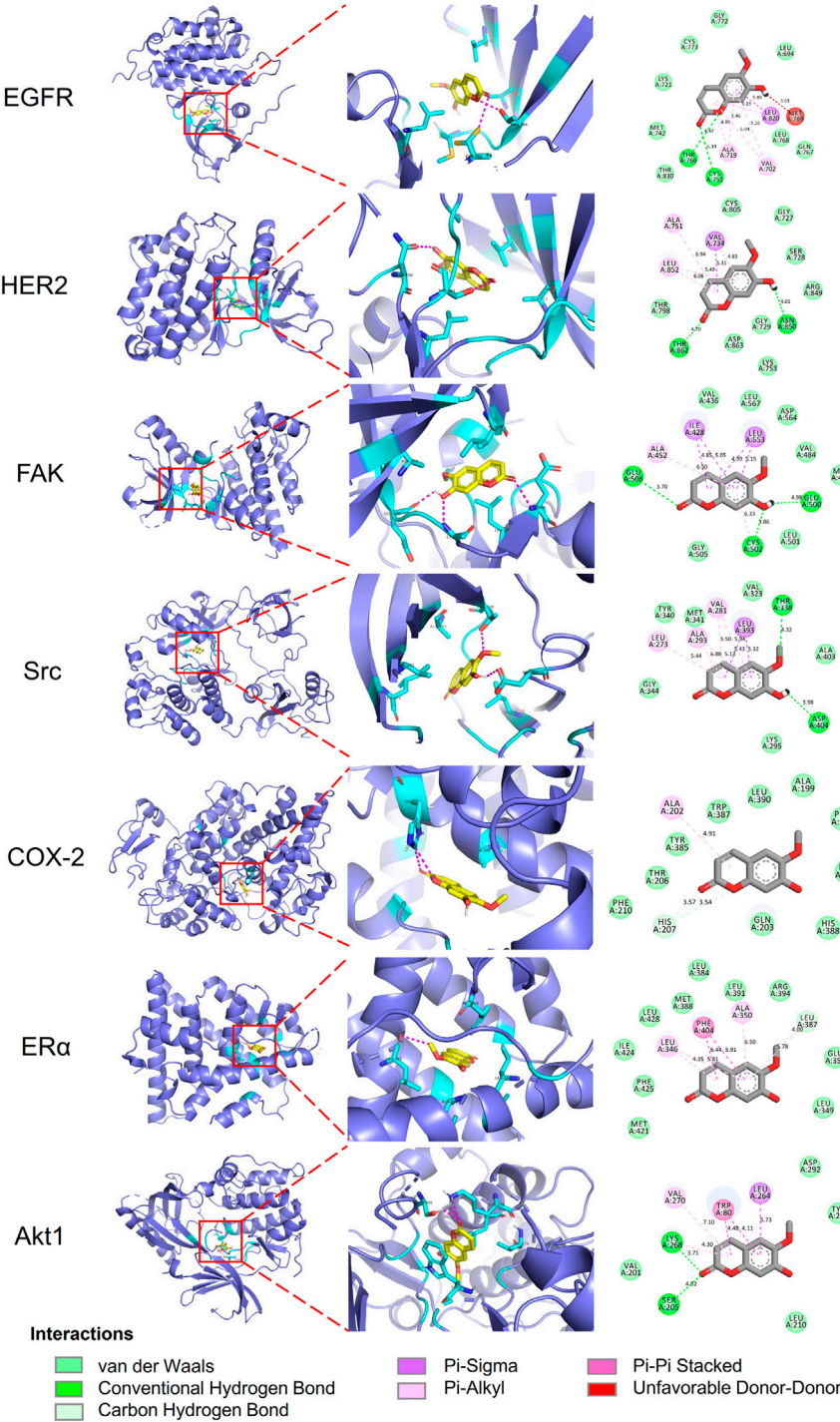
### Umbelliferone and scopoletin act on FLSs by targeting TKs and blocking NF- $\kappa$ B signaling

According to our present study, in treating RA, umbelliferone and scopoletin 1) exert high binding affinities

towards membrane proteins of RA-FLSs, 2) directly target TKs (mostly membrane-bound) and proteins with close interaction with TKs, 3) inhibit NF- $\kappa$ B signaling in RA-FLSs, and 4) attenuate RA-FLS activities (Figures 2–5). A schematic overview of the signaling network regarding the two compounds inhibiting FLS activation is drawn, featuring main protein targets shared by the two compounds, such as EGFR, ErbB2, Src, FAK, ER $\alpha$ , and Akt (Figure 8). In the ErbB signaling network, ErbB family members, including EGFR, ErbB2, and their heterodimers, signal through Src and FAK to activate a myriad of downstream signaling pathways (Yarden and Pines, 2012). Src-induced tyrosine phosphorylation of FAK is a central mediator of focal adhesion turnover and cell migration (Wu et al., 2015). ErbB RTKs, Src, and FAK activate the PI3K/Akt cascade to affect diverse cellular functions, including chemokine signaling and endocrine resistance. Akt also regulates NF- $\kappa$ B signaling to induce target gene expression (Liu et al., 2020). In the estrogen signaling network, stimulated ER $\alpha$  not only forms a complex with Src and PI3K, leading to Akt activation, but also

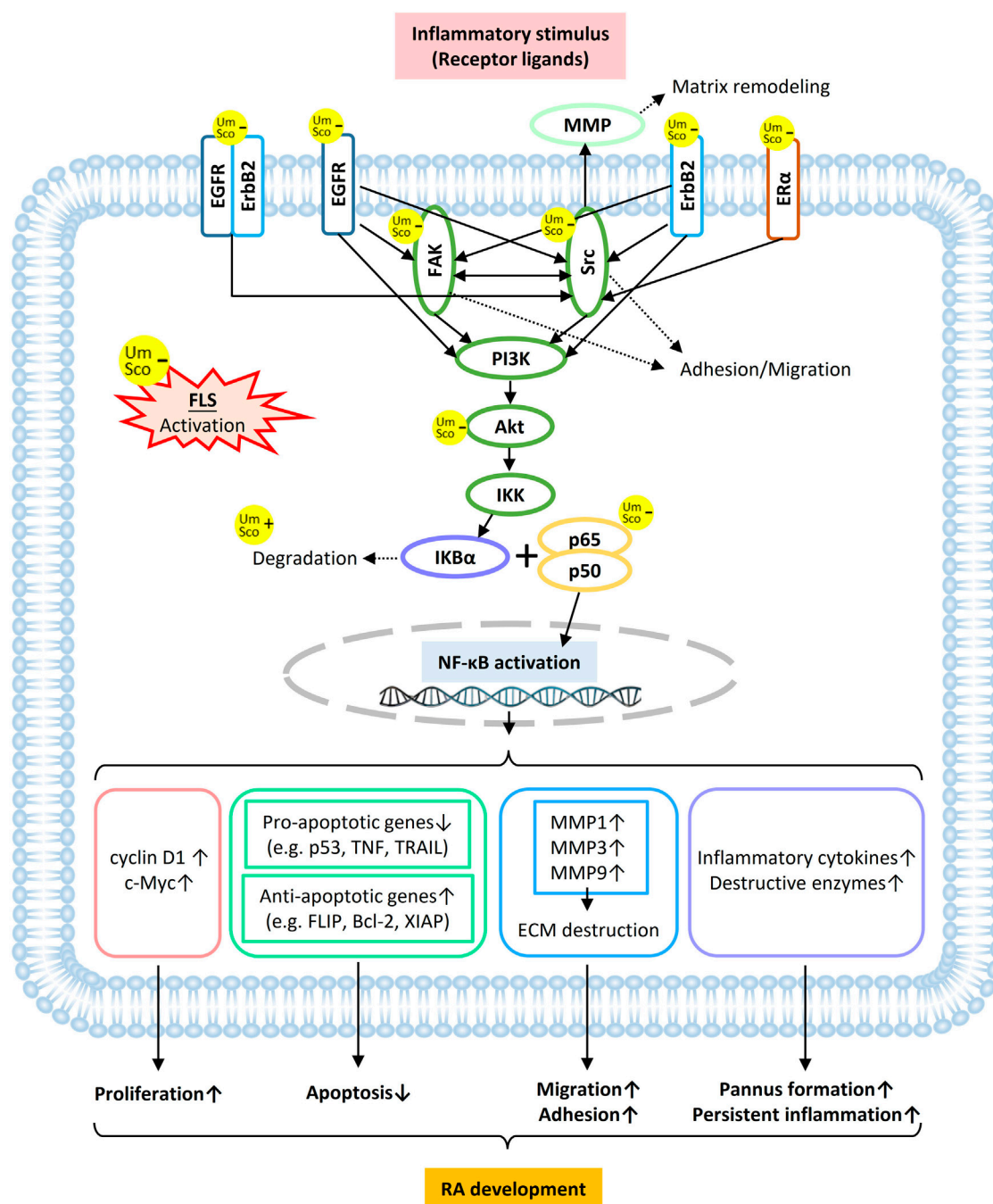


**FIGURE 6**  
Docking patterns of umbelliferone with selected top target proteins. 3D residues in cyan indicate representative ligand–receptor interactions. Numbers indicate bond distance (Å).



**FIGURE 7**  
Docking patterns of scopoletin with selected top target proteins. 3D residues in cyan indicate representative ligand–enzyme interactions. Numbers indicate bond distance (Å).



**FIGURE 8**

Schematic overview of umbelliferone and scopoletin targeting membrane and cytosolic proteins in RA-FLS in attenuating RA development via NF-κB blockade.

activates Src, which in turn enhances matrix metalloproteinase (MMP) expression to facilitate ECM destruction (Pan et al., 2020). In summary, umbelliferone and scopoletin inhibit NF-κB activation in RA FLSs mainly via the ErbB/PI3K/Akt signaling axis.

NF-κB activation in RA-FLSs can lead to a series of cancerous and inflammatory features of the synoviocytes (Figure 8). The activation of NF-κB induces the expression of cyclin D1 and c-Myc, which are cell growth promoters, subsequently boosting cell proliferation. Various anti-apoptotic signals are delivered,



including inhibition of pro-apoptotic genes (e.g., p53 activity loss due to p65 Ser536 phosphorylation) and increased expression of anti-apoptotic genes (e.g. FLIP in the Fas/FasL pathway). Since gene promoters of most MMPs have canonical sites for NF- $\kappa$ B, activated RA-FLSs secrete elevated levels of MMPs, resulting in increased invasiveness and cartilage erosion. I $\kappa$ B kinase (IKK) can be stimulated by inflammatory cytokines (e.g. IL-2 and TNF- $\alpha$ ) and further mediate the inflammatory signaling cascade (Ghosh and Karin, 2002; Liu et al., 2017). In addition, FLS-induced RA pathogenesis switches on inflammatory responses from various immune cells in the RA synovium, such as dendritic cells, lymphocytes, and monocytes, which further maintain FLS activation and perpetuate the disease progression (Nejabatkhsh Samimi et al., 2020). Therefore, it is believed that the anti-rheumatic effects of umbelliferone and scopoletin can be at least partly attributed to the blockage of NF- $\kappa$ B signaling via targeting TKs on activated FLSs.

## Umbelliferone and scopoletin targeting RA-FLS membrane raises hope to combat RA

Membrane proteins perform a myriad of biological functions, including cell communication, substance transportation, and catalytic reactions. Such proteins on the cell surface account for over 60% of the targets of all FDA-approved small-molecule drugs (Huang Y et al., 2021). As FLS are the critical effector cells in RA, FLS membrane proteins, such as transmembrane TKs, play pivotal roles in RA progression through orchestrating cellular signaling among different cell types (Kovács et al., 2014). However, despite the significance, drug discovery against membrane proteins is notoriously challenging, mainly because 1) membrane proteins are difficult to be isolated with maintained structure and functions, and 2) this category of proteins is still largely under-investigated. Our present study demonstrates an integrated drug discovery strategy, using SL herb as an example, featuring biomimetic ultrafiltration to screen compounds targeting RA-specific membrane proteins. As a result, our strategy enables the discovery of safe, effective compounds hitting intact, multiple membrane targets with minimized unspecific bindings to combat RA. Therapeutic agents discovered by this strategy are promising advantages compared with current first-line drugs for RA, e.g. NSAIDs and DMARDs, that lack clinical responses because 1) selectively inhibiting multiple and possibly novel targets, e.g., TKs, helps to control RA as a heterogeneous disease, 2) minimizing unspecific bindings can prevent adverse events of some current synthetic targeted drugs (Koenders and Van DenBerg, 2015).

There have been reports on anti-rheumatic performances of umbelliferone and scopoletin. On a rat model with Freund's

complete adjuvant (FCA)-induced arthritis, umbelliferone was found to reduce pro-inflammatory cytokines, such as TNF- $\alpha$  and IL-1 $\beta$  (Ouyang et al., 2019; Wu G et al., 2021), and osteoclastogenesis biomarkers, such as MMP-3 and MMP-9 (Wu G et al., 2021); according to the authors, such reduced gene expressions were due to suppressed NF- $\kappa$ B signaling upon umbelliferone administration. On the same rat model, scopoletin significantly alleviated clinical symptoms, immune responses, and joint pathological conditions (Chen et al., 2021); scopoletin was also proved to induce RA FLS apoptosis by inhibiting NF- $\kappa$ B activation (Li et al., 2009). Despite such findings, neither umbelliferone nor scopoletin has reached routine clinical therapy for RA. One possible reason might be a lack of confirmation on their direct target proteins and subsequent pivotal signaling axis. Our current study fills this gap by elucidating that membrane proteins on FLSs, especially TKs, are among the direct targets of umbelliferone and scopoletin; the two compounds may function via the RTK/PI3K/Akt axis to reach inhibition of NF- $\kappa$ B and downstream cascades.

## Drug discovery for natural resource preservation

Drug discovery and development from herbal medicines that are derived from rare herbal species can significantly preserve natural resources. There is little cultivation of SL; almost all SL material in commerce has been collected from the wild. In the Himalayan region, due to the reputed anti-rheumatic potency of SL, the population vitality and survival of the species are threatened by heavy and illegal harvesting of the plant (Chen et al., 2016). Since umbelliferone and scopoletin are the two most abundant and therapeutically potent components in SL, precise elucidation of action mechanisms of the two compounds enables the development of synthetic analog drugs, which can, in turn, effectively save the endangered situation of SL.

## Conclusion

Taken together, our present study demonstrates three main steps in elucidating therapeutic components and corresponding action mechanisms in the anti-rheumatic herb SL. Firstly, umbelliferone and scopoletin were screened from SL as two compounds with the highest specific binding affinities towards RA-FLS membrane proteins. Secondly, reduced activities of RA-FLSs and decreased NF- $\kappa$ B activation were confirmed under the administration of either umbelliferone or scopoletin. Thirdly, the two compounds are identified with crucial target proteins (including TKs) and pathways (including RTK/PI3K/Akt/NF- $\kappa$ B) against RA. Therefore, we can conclude that umbelliferone and scopoletin, as major active ingredients from SL, can target tyrosine kinases on FLSs to block NF- $\kappa$ B signaling in attenuating progression of RA. Our

study not only contributes to elucidating the multi-component and multi-target anti-rheumatic mechanisms of the endangered species of SL but also helps develop safe, effective anti-rheumatic drugs based on chemical scaffolds of umbelliferone and scopoletin.

## Data availability statement

The original contributions presented in the study are included in the article/Supplementary Materials, further inquiries can be directed to the corresponding authors.

## Author contributions

Conceptualization, HC and JZ; Funding acquisition, HC and JZ; Investigation, QC, WZ, SW, WL, and KY; methodology, QC, WZ, YH; Supervision, HC and JZ; writing—original draft, QC, SW; writing—review and editing, WZ, QC, YT. All authors have read and agreed to the published version of the manuscript.

## Funding

This work was supported by the National Natural Science Foundation of China (82074123, U1903126), the Health and Medical Research Fund in Hong Kong (16170251), and the

Innovation and Technology Fund in Hong Kong (PRP/036/20FX; MHP/023/20).

## Conflict of interest

The authors declare that the research was conducted in the absence of any commercial or financial relationships that could be construed as a potential conflict of interest.

## Publisher's note

All claims expressed in this article are solely those of the authors and do not necessarily represent those of their affiliated organizations, or those of the publisher, the editors and the reviewers. Any product that may be evaluated in this article, or claim that may be made by its manufacturer, is not guaranteed or endorsed by the publisher.

## Supplementary material

The Supplementary Material for this article can be found online at: <https://www.frontiersin.org/articles/10.3389/fphar.2022.946210/full#supplementary-material>

## References

- Almutairi, K., Nossent, J., Preen, D., Keen, H., and Inderjeeth, C. (2021). The global prevalence of rheumatoid arthritis: a meta-analysis based on a systematic review. *Rheumatol. Int.* 41, 863–877. doi:10.1007/s00296-020-04731-0
- Bustamante, M. F., Garcia-Carbonell, R., Whisenant, K. D., and Guma, M. (2017). Fibroblast-like synoviocyte metabolism in the pathogenesis of rheumatoid arthritis. *Arthritis Res. Ther.* 19, 110. doi:10.1186/s13075-017-1303-3
- Cannell, R. J. P. (1998). "How to approach the isolation of a natural product," in *Natural products isolation* (Germany: Springer), 1–51.
- Chen, G., Wu, J., Li, N., and Guo, M. (2018). Screening for anti-proliferative and anti-inflammatory components from *Rhamnus davurica* Pall. using bio-affinity ultrafiltration with multiple drug targets. *Anal. Bioanal. Chem.* 410, 3587–3595. doi:10.1007/s00216-018-0953-6
- Chen, Q. L., Chen, X. Y., Zhu, L., Chen, H. B., Ho, H. M., Yeung, W. P., et al. (2016). Review on *Saussurea laniceps*, a potent medicinal plant known as "snow lotus": botany, phytochemistry and bioactivities. *Phytochem. Rev.* 15, 537–565. doi:10.1007/s11101-015-9452-y
- Chen, Q. L., Zhu, L., Tang, Y. N., Kwan, H. Y., Zhao, Z. Z., Chen, H. B., et al. (2017). Comparative evaluation of chemical profiles of three representative "snow lotus" herbs by UPLC-DAD-QTOF-MS combined with principal component and hierarchical cluster analyses. *Drug Test. Anal.* 9, 1105–1115. doi:10.1002/dta.2123
- Chen, Q., Zhu, L., Yip, K. M., Tang, Y., Liu, Y., Jiang, T., et al. (2021). A hybrid platform featuring nanomagnetic ligand fishing for discovering COX-2 selective inhibitors from aerial part of *Saussurea laniceps* Hand.-Mazz. *J. Ethnopharmacol.* 271, 113849. doi:10.1016/j.jep.2021.113849
- Chik, W. I., Zhu, L., Fan, L. L., Yi, T., Zhu, G. Y., Gou, X. J., et al. (2015). *Saussurea involucreata*: A review of the botany, phytochemistry and ethnopharmacology of a rare traditional herbal medicine. *J. Ethnopharmacol.* 172, 44–60. doi:10.1016/j.jep.2015.06.033
- Committee of Chinese Pharmacopoeia (1995). "Xuelianhua," in *Standards of Tibetan medicines issued by ministry of Health of the people's Republic of China* (Beijing: People's Medical Publishing House), 94.
- Fan, J. Y., Chen, H. B., Zhu, L., Chen, H. L., Zhao, Z. Z., Yi, T., et al. (2015). *Saussurea medusa*, source of the medicinal herb snow lotus: a review of its botany, phytochemistry, pharmacology and toxicology. *Phytochem. Rev.* 14, 353–366. doi:10.1007/s11101-015-9408-2
- Fang, G., Zhang, Q., Pang, Y., Thu, H. E., and Hussain, Z. (2019). Nanomedicines for improved targetability to inflamed synovium for treatment of rheumatoid arthritis: Multi-functionalization as an emerging strategy to optimize therapeutic efficacy. *J. Control. Release* 303, 181–208. doi:10.1016/j.jconrel.2019.04.027
- Fidahic, M., Jelicic Kadic, A., Radic, M., and Puljak, L. (2017). Celecoxib for rheumatoid arthritis. *Cochrane database Syst. Rev.* 6, CD012095. doi:10.1002/14651858.CD012095.pub2
- Friedl, P., and Gilmour, D. (2009). Collective cell migration in morphogenesis, regeneration and cancer. *Nat. Rev. Mol. Cell Biol.* 10, 445–457. doi:10.1038/nrm2720
- Ghosh, S., and Karin, M. (2002). Missing pieces in the NF-kappaB puzzle. *Cell* 109 (Suppl. 1), S81–S96. doi:10.1016/s0092-8674(02)00703-1
- Huang, H., Park, S., Zhang, H., Park, S., Kwon, W., Kim, E., et al. (2021). Targeting AKT with costunolide suppresses the growth of colorectal cancer cells and induces apoptosis *in vitro* and *in vivo*. *J. Exp. Clin. Cancer Res.* 40, 114. doi:10.1186/s13046-021-01895-w
- Huang, Y., Meng, L., Nie, Q., Zhou, Y., Chen, L., Yang, S., et al. (2021). Selection of DNA-encoded chemical libraries against endogenous membrane proteins on live cells. *Nat. Chem.* 13, 77–88. doi:10.1038/s41557-020-00605-x
- Koenders, M. I., and Van Den Berg, W. B. (2015). Novel therapeutic targets in rheumatoid arthritis. *Trends Pharmacol. Sci.* 36, 189–195. doi:10.1016/j.tips.2015.02.001

- Kovács, M., Németh, T., Jakus, Z., Sitaru, C., Simon, E., Futosi, K., et al. (2014). The Src family kinases Hck, Fgr, and Lyn are critical for the generation of the *in vivo* inflammatory environment without a direct role in leukocyte recruitment. *J. Exp. Med.* 211, 1993–2011. doi:10.1084/jem.20132496
- Li, Y., Dai, Y., Liu, M., Pan, R., Luo, Y., Xia, Y., et al. (2009). Scopoletin induces apoptosis of fibroblast-like synoviocytes from adjuvant arthritis rats by a mitochondrial-dependent pathway. *Drug Dev. Res.* 70, 378–385. doi:10.1002/ddr.20314
- Li, Y., Yang, L., Dong, L., Yang, Z., Zhang, J., Zhang, S., et al. (2019). Crosstalk between the Akt/mTORC1 and NF- $\kappa$ B signaling pathways promotes hypoxia-induced pulmonary hypertension by increasing DPP4 expression in PSMCs. *Acta Pharmacol. Sin.* 40, 1322–1333. doi:10.1038/s41401-019-0272-2
- Liu, R., Chen, Y., Liu, G., Li, C., Song, Y., Cao, Z., et al. (2020). PI3K/AKT pathway as a key link modulates the multidrug resistance of cancers. *Cell Death Dis.* 11, 797. doi:10.1038/s41419-020-02998-6
- Liu, T., Zhang, L., Joo, D., and Sun, S.-C. (2017). NF- $\kappa$ B signaling in inflammation. *Signal Transduct. Target. Ther.* 2, 17023. doi:10.1038/sigtrans.2017.23
- McInnes, I. B., and Schett, G. (2017). Pathogenetic insights from the treatment of rheumatoid arthritis. *Lancet* 389, 2328–2337. doi:10.1016/S0140-6736(17)31472-1
- McInnes, I. B., and Schett, G. (2011). The pathogenesis of rheumatoid arthritis. *N. Engl. J. Med.* 365, 2205–2219. doi:10.1056/NEJMra1004965
- Nejabatbakhsh Samimi, L., Farhadi, E., Tahmasebi, M. N., Jamshidi, A., Sharafat Vaziri, A., Mahmoudi, M., et al. (2020). NF- $\kappa$ B signaling in rheumatoid arthritis with focus on fibroblast-like synoviocytes. *Autoimmun. Highlights* 11, 11. doi:10.1186/s13317-020-00135-z
- Nygaard, G., and Firestein, G. S. (2020). Restoring synovial homeostasis in rheumatoid arthritis by targeting fibroblast-like synoviocytes. *Nat. Rev. Rheumatol.* 16, 316–333. doi:10.1038/s41584-020-0413-5
- Ouyang, L., Dan, Y., Shao, Z., Yang, S., Yang, C., Liu, G., et al. (2019). Effect of umbelliferone on adjuvant-induced arthritis in rats by MAPK/NF- $\kappa$ B pathway. *Drug Des. devel. Ther.* 13, 1163–1170. doi:10.2147/DDDT.S190155
- Pan, Y., Wang, X., Zhang, Y., Qiao, J., Sasano, H., McNamara, K., et al. (2020). Estradiol-induced MMP-9 expression via PELP1-mediated membrane-initiated signaling in era-positive breast cancer cells. *Horm. Cancer* 11, 87–96. doi:10.1007/s12672-020-00380-8
- Petronelli, M. (2021). FDA requiring black box warning for certain JAK inhibitors. *Dermatol. Times* 42, 42. <https://www.dermatologytimes.com/view/fda-requiring-black-box-warning-for-certain-jak-inhibitors>
- Pijuan, J., Barceló, C., Moreno, D. F., Maiques, O., Sisó, P., Martí, R. M., et al. (2019). *In vitro* cell migration, invasion, and adhesion assays: From cell imaging to data analysis. *Front. Cell Dev. Biol.* 7, 107. doi:10.3389/fcell.2019.00107
- Ramírez, D., and Caballero, J. (2018). Is it reliable to take the molecular docking top scoring position as the best solution without considering available structural data? *Molecules* 23, E1038. doi:10.3390/molecules23051038
- Schwartz, D. M., Kanno, Y., Villarino, A., Ward, M., Gadina, M., and O'Shea, J. J. (2019). Filgotinib, a JAK1 inhibitor, for treatment-resistant rheumatoid arthritis. *JAMA - J. Am. Med. Assoc.* 322, 309–311. doi:10.1001/jama.2019.9056
- Shen, B. (2015). A new golden age of natural products drug discovery. *Cell* 163, 1297–1300. doi:10.1016/j.cell.2015.11.031
- Wang, L., Liu, Y., Luo, Y., Huang, K., and Wu, Z. (2018). Quickly screening for potential  $\alpha$ -glucosidase inhibitors from Guava leaves tea by bioaffinity ultrafiltration coupled with HPLC-ESI-TOF/MS method. *J. Agric. Food Chem.* 66, 1576–1582. doi:10.1021/acs.jafc.7b05280
- Wang, Y., Chen, S., Du, K., Liang, C., Wang, S., Owusu Boadi, E., et al. (2021). Traditional herbal medicine: Therapeutic potential in rheumatoid arthritis. *J. Ethnopharmacol.* 279, 114368. doi:10.1016/j.jep.2021.114368
- Weyand, C. M., and Goronzy, J. J. (2021). The immunology of rheumatoid arthritis. *Nat. Immunol.* 22, 10–18. doi:10.1038/s41590-020-00816-x
- Wu, G., Nie, W., Wang, Q., Hao, Y., Gong, S., Zheng, Y., et al. (2021). Umbelliferone ameliorates Complete Freund Adjuvant-induced arthritis via reduction of NF- $\kappa$ B signaling pathway in osteoclast differentiation. *Inflammation* 44, 1315–1329. doi:10.1007/s10753-021-01418-x
- Wu, J.-C., Chen, Y.-C., Kuo, C.-T., Wenshin Yu, H., Chen, Y.-Q., Chiou, A., et al. (2015). Focal adhesion kinase-dependent focal adhesion recruitment of SH2 domains directs SRC into focal adhesions to regulate cell adhesion and migration. *Sci. Rep.* 5, 18476. doi:10.1038/srep18476
- Wu, Z., Ma, D., Yang, H., Gao, J., Zhang, G., Xu, K., et al. (2021). Fibroblast-like synoviocytes in rheumatoid arthritis: Surface markers and phenotypes. *Int. Immunopharmacol.* 93, 107392. doi:10.1016/j.intimp.2021.107392
- Yang, Y., Zheng, H., Zhan, Y., and Fan, S. (2019). An emerging tumor invasion mechanism about the collective cell migration. *Am. J. Transl. Res.* 11, 5301–5312. <https://www.ncbi.nlm.nih.gov/pmc/articles/PMC6789225/>
- Yarden, Y., and Pines, G. (2012). The ERBB network: at last, cancer therapy meets systems biology. *Nat. Rev. Cancer* 12, 553–563. doi:10.1038/nrc3309
- Yi, T., Lo, H. W., Zhao, Z. Z., Yu, Z. L., Yang, Z. J., Chen, H. B., et al. (2012). Comparison of the chemical composition and pharmacological effects of the aqueous and ethanolic extracts from a Tibetan “Snow Lotus” (*Saussurea laniceps*) herb. *Molecules* 17, 7183–7194. doi:10.3390/molecules17067183
- Yi, T., Zhao, Z., Yu, Z., and Chen, H. (2010). Comparison of the anti-inflammatory and anti-nociceptive effects of three medicinal plants known as “Snow Lotus” herb in traditional Uighur and Tibetan medicines. *J. Ethnopharmacol.* 128, 405–411. doi:10.1016/j.jep.2010.01.037



## OPEN ACCESS

## EDITED BY

Ren-You Gan,  
Chinese Academy of Agricultural  
Sciences, China

## REVIEWED BY

Jayaprakash N Kolla,  
Institute of Molecular Genetics (ASCR),  
Czechia  
Yongqiang Du,  
Anhui Medical University, China

## \*CORRESPONDENCE

Lan Xie,  
xielan@tsinghua.edu.cn

<sup>†</sup>These authors contributed equally to  
this work

## SPECIALTY SECTION

This article was submitted to  
Ethnopharmacology,  
a section of the journal  
Frontiers in Pharmacology

RECEIVED 11 April 2022

ACCEPTED 11 July 2022

PUBLISHED 08 August 2022

## CITATION

Xie L, Zhao S, Zhang X, Huang W, Qiao L,  
Zhan D, Ma C, Gong W, Dang H and Lu H  
(2022), Wenshenyang recipe treats  
infertility through hormonal regulation  
and inflammatory responses revealed by  
transcriptome analysis and  
network pharmacology.  
*Front. Pharmacol.* 13:917544.  
doi: 10.3389/fphar.2022.917544

## COPYRIGHT

© 2022 Xie, Zhao, Zhang, Huang, Qiao,  
Zhan, Ma, Gong, Dang and Lu. This is an  
open-access article distributed under  
the terms of the [Creative Commons  
Attribution License \(CC BY\)](#). The use,  
distribution or reproduction in other  
forums is permitted, provided the  
original author(s) and the copyright  
owner(s) are credited and that the  
original publication in this journal is  
cited, in accordance with accepted  
academic practice. No use, distribution  
or reproduction is permitted which does  
not comply with these terms.

# Wenshenyang recipe treats infertility through hormonal regulation and inflammatory responses revealed by transcriptome analysis and network pharmacology

Lan Xie<sup>1,2\*†</sup>, Shuai Zhao<sup>2†</sup>, Xiaoling Zhang<sup>2</sup>, Wenting Huang<sup>1,2</sup>,  
Liansheng Qiao<sup>1,2</sup>, Delin Zhan<sup>1</sup>, Chengmei Ma<sup>2</sup>, Wei Gong<sup>2</sup>,  
Honglei Dang<sup>2</sup> and Hua Lu<sup>3</sup>

<sup>1</sup>Medical Systems Biology Research Center, Tsinghua University School of Medicine, Beijing, China,  
<sup>2</sup>National Engineering Research Center for Beijing Biochip Technology, Beijing, China, <sup>3</sup>Chengdu  
University of Traditional Chinese Medicine, Chengdu, China

The Wenshenyang recipe (WSYR) has the effect of treating infertility, but the mechanisms underlying this activity have not been fully elucidated. In this study, network pharmacology and RNA sequencing were combined, with database-based “dry” experiments and transcriptome analysis-based “wet” experiments used conjointly to analyse the mechanism of WSYR in the treatment of infertility. In the dry analysis, 43 active compounds in WSYR and 44 therapeutic targets were obtained through a database search, 15 infertility pathways were significantly enriched, and key targets, such as ESR1, TP53, AKT1, IL-6, and IL-10 were identified. Then the wet experiments were performed to detect the expression changes of the 412 genes from 15 infertility pathways identified by dry analysis. HK-2 cells were treated with the three herbs of WSYR and subjected to targeted RNA sequencing. Based on the results, 92 of the 412 genes in 15 infertility pathways were identified as DEGs. Additionally, key targets, such as ESR2, STAT1, STAT3, and IL6, were also identified in the wet experiments. RT-qPCR experiments further verified that WSYR played an anti-inflammatory role by upregulating *IL-4* and *IL-10* and *Epimedium brevicornu* Maxim (Yinyanghuo) showed broader effect than *Drynaria fortunei* (Kunze) J. Sm (Gusuibu) and *Cistanche deserticola* Y.C.Ma (Roucongrong). By screening compounds of WSYR using molecular docking models of ESR1 and ESR2, it was further found that xanthogalenol in Gusuibu, arachidonate in Roucongrong, and anhydroicaritin in Yinyanghuo had good affinity for estrogen receptors. These findings provide evidence for an estrogen-regulating role of the three herbs in WSYR.

## KEYWORDS

wenshenyang recipe, infertility, network pharmacology, transcriptome analysis, GO enrichment analysis, pathway enrichment analysis, molecular docking



## Introduction

According to WHO analyses, 186 million individuals (including 48 million couples) worldwide suffer from infertility (Rutstein and Shah, 2004; Boivin et al., 2007; Mascarenhas et al., 2012). Studies have shown annual increases in the incidence of infertility in recent years (Petraglia et al., 2013), and it has become an important factor affecting human health and family stability. Factors affecting both male and female fertility include hyperprolactinism, hypogonadism, cystic fibrosis, systemic diseases, infections and lifestyle-related factors (Vander Borgh and Wyns, 2018). The causes of female infertility mainly include ovulation disorders, blocked fallopian tubes, and cervical factors (Vander Borgh and Wyns, 2018). The most common cause of female infertility is ovulation failure, which occurs in 30%–40% of infertile women (Nahid and Sirous, 2012). Specifically, it includes anovulation caused by pituitary secretion disorders and ovulation disorders caused by endocrine disorders. Causes of male infertility include abnormal sperm, blocked sperm delivery, and immune factors (Vander Borgh and Wyns, 2018). Sperm abnormalities lead to impaired spermatogenesis, impaired maturation, blocked sperm transport ducts, and abnormal gonads, which are major causes of male infertility (Wang et al., 2020). Additional causes of male infertility mainly include abnormal semen, blocked sperm delivery and immune factors.

Assisted reproductive technology (ART) has been used in the treatment of infertility. More than 5 million children worldwide have been born through *in vitro* fertilization and other ART interventions (Messerlian and Gaskins, 2017). However, ART is technologically sophisticated and expensive, such that it is unaffordable or even unavailable in many countries and regions, especially low- and middle-income areas.

As an important category of complementary and alternative medicine, traditional Chinese medicine (TCM) has been widely used in treating infertility in recent decades. Compared with ART, TCM has the advantages of greater accessibility, lower cost, fewer adverse reactions, and higher safety (Huang and Chen, 2008). A study reported that the Wenshenyang recipe can promote the proliferation and differentiation of shoot stem cells and promote the synthesis of cartilage and cartilage matrix during the early limb development of the embryo, which is closely related to the formation and development of the foetus (Xue et al., 2021). The Wenshenyang Recipe consists of three Chinese medicines: *Cistanche deserticola* Y.C.Ma (Roucongrong), *Epimedium brevicornu* Maxim (Yinyanghuo) and *Drynaria fortunei* (Kunze) J. Sm (Gusuibu). All three herbs have similar effects, *i.e.*, warming the kidney and strengthening yang.

Modern pharmacological studies have proven that Yinyanghuo has a wide range of hormone-like effects, regulates the function of the hypothalamus-pituitary-gonad axis, and has the effect of “stimulating yang” in animal models of yang deficiency (An et al., 2015). Yinyanghuo can improve sperm motility in rats and protect against the epididymal damage caused by chemotherapy (Cao et al., 2008). Yinyanghuo also plays a role in reducing the levels of proinflammatory mediators and cytokines (Saba et al., 2020). Roucongrong and its active ingredient echinacoside (ECH) can enhance the biosynthesis of testosterone by upregulating the expression of a variety of steroid-generating enzymes, improving poor sperm quality and reducing testicular toxicity in rats (Jiang et al., 2016). ECH can block hypothalamic androgen receptor (AR) activity and increase the secretion of luteinizing hormone and testosterone, thereby increasing sperm number, to treat oligospermia (Jiang et al., 2018). Gusuibu strengthens muscles and bones and has immunomodulatory activity (Jeong et al., 2005). However, due to the complex components of herbs and the complicated process of infertility development, the mechanism of WSYR for treating infertility is still unclear.

Network pharmacology is a discipline that predicts the active ingredients in TCM prescriptions and explains the potential mechanism of action of TCM prescriptions from a systematic perspective. The concept of holism and focus on systems conforms to the characteristics of TCM and is a more suitable method for studying the multicomponent, multitarget, and multipath mechanisms of traditional Chinese medicine (Li and Zhang, 2013). However, the results predicted by network pharmacology are only speculative results based on available data, not validated effects. Therefore, we aimed to combine network pharmacology with gene expression profiling of TCM-treated cells. Transcriptome analysis was performed by RASL-seq, which combines the RNA annealing, selection, ligation (RASL) strategy and next-generation sequencing (Li et al., 2012). This technology can simultaneously detect the expression of thousands of genes after drug treatment (Shao et al., 2019) and effectively verify the large-scale gene data set predicted by network pharmacology.

In this study, the potential anti-infertility targets of WSYR were obtained through network pharmacology analysis. Pathway enrichment analysis was performed to identify the key pathways of WSYR in the treatment of infertility, and a “TCMs-components-targets-pathways” network map was constructed. Afterwards, transcriptome analysis was utilized to examine the expression of genes in the predicted pathways after drug intervention. Altogether, the key targets of WSYR in the treatment of infertility were identified, and its mechanism of action was explored.

## Materials and methods

### Collection of active ingredients of TCMs and their potential targets

The TCM System Pharmacology Database (TCMSP, <https://tcmsp.w.com/tcmsp.php>) (Ru et al., 2014) was used to collect the chemical components of WSYR with the keywords “roucongrong”, “yinyanghuo” and “gusuibu” respectively. Compounds with oral bioavailability (OB)  $\geq$  30% and drug-like properties (DL)  $\geq$  0.18 were selected as active components.

The potential targets of each compound were obtained through the TCMSP database. The Entrez ID, and gene symbol of each target were collected.

### Gene ontology analysis and pathway enrichment analysis

ClueGO (Bindea et al., 2009) was used to analyse the GO biological processes and enriched Reactome pathways of different gene sets. The bubble diagram and bar chart were drawn by the Bioinformatics Online Visualization Tool (<http://www.bioinformatics.com.cn>).

### Cell culture

HK-2 cells were obtained from the National Experimental Cell Resource Sharing Platform (Wuhan, China). SK-OV-3 cells were obtained from Procell Life Science and Technology Co., Ltd (Wuhan, China). All cells were maintained in DMEM (Gibco, Grand Island, NY) containing 10% foetal bovine serum (Gemini, Woodland, CA) and 100 U/mL penicillin–streptomycin (Gibco, Grand Island, NY) at 37°C.

### Preparation of medicinal extracts

Roucongrong (origin: Neimenggu), Yinyanghuo (origin: Guangdong) and Gusuibu (origin: Jilin) were purchased from Anguo Changda Chinese Herbal Medicine Co., Ltd. All three TCMs were powdered and extracted by a Soxhlet extractor (Extraction Unit B-811, Buchi, Switzerland) with 90% ethanol. Then, the solvent was concentrated in an electrically heated blast drying oven (GZX-9070MBE, Boxun, China) at 45°C. Subsequently, the concentrate was lyophilized with a freeze dryer (ALPHA1-2Dplus, Christ, Germany), weighed and stored at -80°C for later use.

## Transcriptome sequencing

Transcriptome sequencing were performed as previously described (Shao et al., 2019). Briefly, HK-2 cells were cultured in a 384-well plate for 24 h and treated with the three herbal extracts for 24 h. Then, the cells were lysed, incubated at room temperature for 10 min, and stored at -80°C. A total of 412 genes were detected by RNA annealing, selection and ligation with a high-throughput pipetting platform. The ligated products were amplified by PCR and sequenced by a gene sequencer (HiSeq X Ten, Illumina, United States). The data discussed in this publication have been deposited in NCBI's Gene Expression Omnibus and are accessible through GEO Series accession number GSE202626 (<https://www.ncbi.nlm.nih.gov/geo/query/acc.cgi?acc=GSE202626>).

## Sequencing data processing

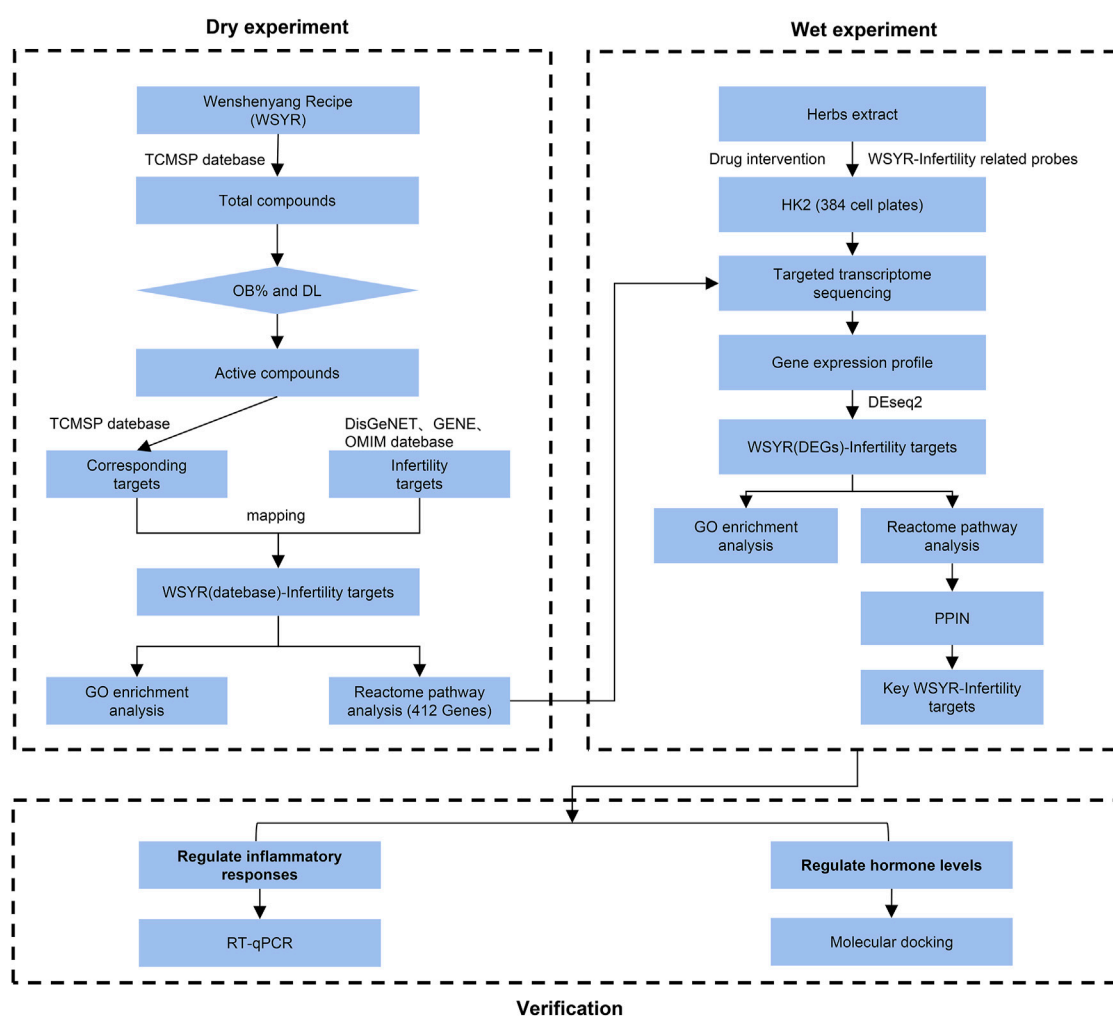
First, the high-throughput sequencing platform data files were converted into raw data for base identification analysis. Subsequently, the original data were filtered by more than 3 base sequence mismatches. Finally, the DESeq software package was used to identify differentially expressed genes (DEGs) with fold change (FC)  $> 1.5$  or  $< 0.67$  and  $p$  value  $< 0.05$ . The R package ggplot2 was used to construct a volcano plot of the DEGs (Anders and Huber, 2010).

## Construction of a protein-protein interaction network and screening of key targets

All DEGs were analysed by the STRING database to obtain protein–protein interactions. Protein–protein interaction networks were constructed by Cytoscape (Shannon et al., 2003). The cytoHubba plug-in included in Cytoscape was used for target topology analysis to obtain the main topological parameters of the PPI network. The sum of degree, betweenness and closeness after the standardization of deviation was used as the indicator to determine the key targets.

## RT-qPCR analysis

Total RNA was extracted with all in-one mini spin columns (Epoch Life Science, Fort Bend, TX). Reverse transcription into cDNA was performed using a high Capacity RNA-to-cDNA kit (Invitrogen) and qPCR was carried out using the SYBR FAST qPCR Kit (Kapa Biosystems, Wilmington, MA). Finally, the  $2^{-\Delta\Delta CT}$  method (Nolan et al., 2006) was used to calculate the data. The primer sequences are provided in [Supplementary Table S1](#).



**FIGURE 1**  
Experimental technical roadmap.

## Molecular docking of estrogen receptor $\alpha$ (ESR1) and estrogen receptor $\beta$ (ESR2)

The protein crystal structure of ESR1 and ESR2 were downloaded from the Protein Data Bank (PDB, <https://www.rcsb.org/>) for molecular docking. The protein crystal structure was imported into Discovery Studio, and the Prepare Protein module was used to remove water, add hydrogen atom and complement incomplete residues. Active pocket was defined based on the original ligand in the complex, and molecular docking was conducted by CDOCKER algorithm. The root-mean-square-deviation (RMSD) of the initial and re-docked conformations of the original ligand were calculated. RMSD <2 Å indicated that the conformation obtained by docking could reproduce the binding mode of the ligand and receptor, reflecting the reliability of the docking model. Finally,

potential antagonists were screened by the constructed docking model. Scoring function of -CDOCKER interaction energy was used to evaluate the binding ability of ligand and receptor.

## Results

### Potential targets of WSYR as an infertility treatment

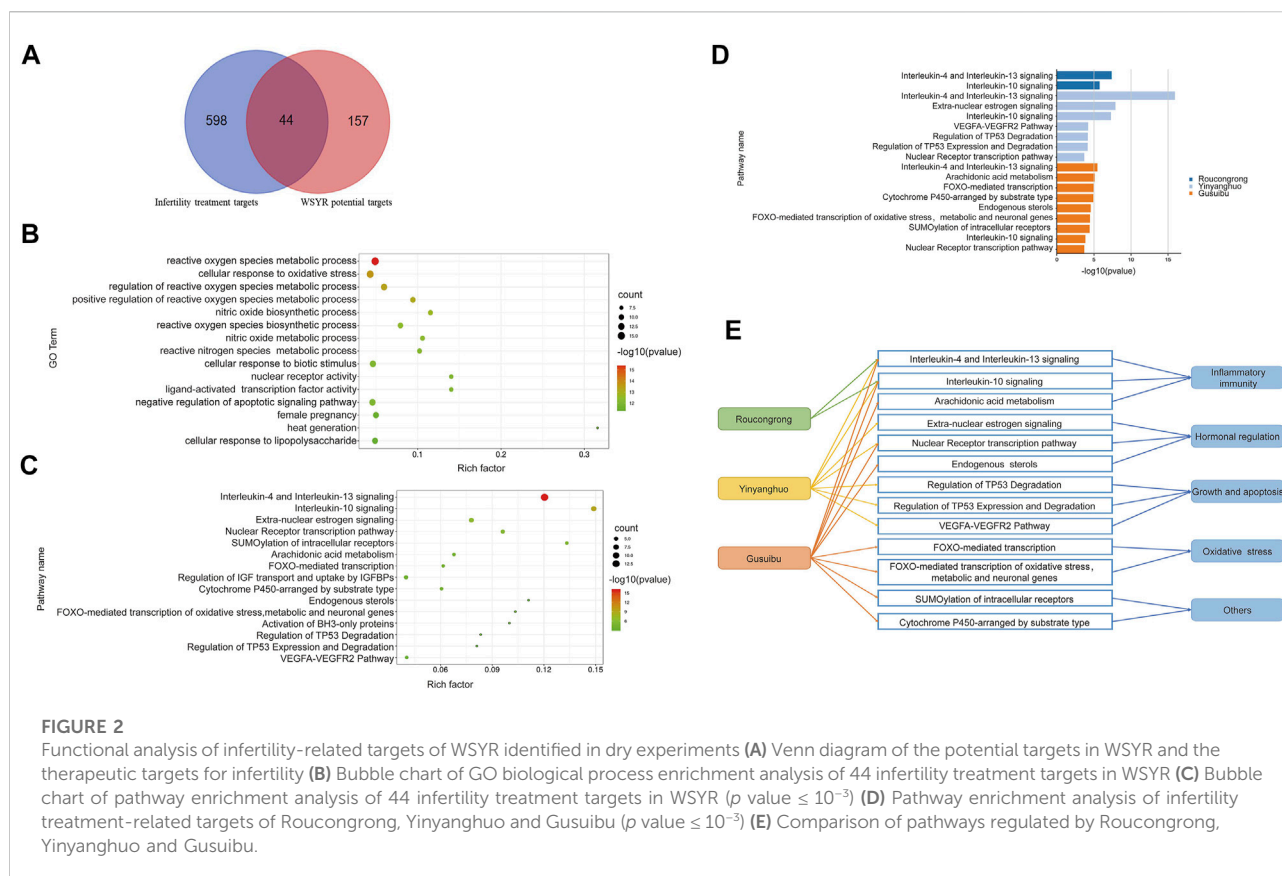
Figure 1 shows the technical roadmap of this study. This study combines a database-based dry experiment and a transcriptome analysis-based wet experiment to jointly analyse the mechanism of action of WSYR in the treatment of infertility.

A total of 75 chemical components for Roucongong, 130 for Yinyanghuo and 71 for Gusuibu were collected from TCMSP.

TABLE 1 Gusuibu, Roucongrong and Yinyanghuo compounds with oral bioavailability (OB)  $\geq 30\%$  and drug-likeness (DL)  $\geq 0.18$  from TCMSP.

NO.	Mol ID	Molecular name	OB(%)	DL	TCM	NO.	Mol ID	Molecular name	OB(%)	DL	TCM
1	MOL000449	Stigmasterol	43.83	0.76	GU_SUI_BU	23	MOL004382	Yinyanghuo A	56.96	0.77	YIN_YANG_HUO
2	MOL000492	(+)-catechin	54.83	0.24	GU_SUI_BU	24	MOL004396	CID 12468616	52.31	0.22	YIN_YANG_HUO
3	MOL000569	digallate	61.85	0.26	GU_SUI_BU	25	MOL004386	Yinyanghuo E	51.63	0.55	YIN_YANG_HUO
4	MOL001040	(2 R)-5,7-dihydroxy-2-(4-hydroxyphenyl) chroman-4-one	42.36	0.21	GU_SUI_BU	26	MOL004391	8-prenyl-flavone	48.54	0.25	YIN_YANG_HUO
5	MOL001978	Aureusidin	53.42	0.24	GU_SUI_BU	27	MOL004384	Yinyanghuo C	45.67	0.5	YIN_YANG_HUO
6	MOL002914	Eriodictiol (flavanone)	41.35	0.24	GU_SUI_BU	28	MOL004373	Anhydroicaritin	45.41	0.44	YIN_YANG_HUO
7	MOL004328	naringenin	59.29	0.21	GU_SUI_BU	29	MOL001645	Linoleyl acetate	42.1	0.2	YIN_YANG_HUO
8	MOL005190	eriodictyol	71.79	0.24	GU_SUI_BU	30	MOL004394	Anhydroicaritin-3-O-alpha-L-rhamnoside	41.58	0.61	YIN_YANG_HUO
9	MOL009061	22-Stigmasten-3-one	39.25	0.76	GU_SUI_BU	31	MOL004425	Icariin	41.58	0.61	YIN_YANG_HUO
10	MOL009063	Cyclolaudenol acetate	41.66	0.79	GU_SUI_BU	32	MOL004380	2,7-Dihydrohomoerysotrine	39.14	0.49	YIN_YANG_HUO
11	MOL009075	cycloartenone	40.57	0.79	GU_SUI_BU	33	MOL003542	8-Isopentenyl-kaempferol	38.04	0.39	YIN_YANG_HUO
12	MOL009076	cyclolaudenol	39.05	0.79	GU_SUI_BU	34	MOL001510	24-epicampesterol	37.58	0.71	YIN_YANG_HUO
13	MOL009078	davallioside A <sub>qt</sub>	62.65	0.51	GU_SUI_BU	35	MOL001771	poriferast-5-en-3beta-ol	36.91	0.75	YIN_YANG_HUO
14	MOL009087	marioside <sub>qt</sub>	70.79	0.19	GU_SUI_BU	36	MOL000359	sitosterol	36.91	0.75	YIN_YANG_HUO
15	MOL009091	xanthogalenol	41.08	0.32	GU_SUI_BU	37	MOL003044	Chryseriol	35.85	0.27	YIN_YANG_HUO
16	MOL005320	arachidonate	45.57	0.2	ROU_CONG_RONG	38	MOL001792	Liquiritigenin	32.76	0.18	YIN_YANG_HUO
17	MOL005384	suchilactone	57.52	0.56	ROU_CONG_RONG	39	MOL004427	Icariside A7	31.91	0.86	YIN_YANG_HUO
18	MOL008871	Marckine	37.05	0.69	ROU_CONG_RONG	40	MOL000006	luteolin	36.16	0.25	GU_SUI_BU; YIN_YANG_HUO
19	MOL007563	Yangambin	57.53	0.81	ROU_CONG_RONG	41	MOL000098	quercetin	46.43	0.28	ROU_CONG_RONG; YIN_YANG_HUO
20	MOL000622	Magnograndiolide	63.71	0.19	YIN_YANG_HUO	42	MOL000358	beta-sitosterol	36.91	0.75	GU_SUI_BU; ROU_CONG_RONG
21	MOL004367	olivil	62.23	0.41	YIN_YANG_HUO	43	MOL000422	kaempferol	41.88	0.24	GU_SUI_BU; YIN_YANG_HUO
22	MOL004388	CID 12115137	60.64	0.66	YIN_YANG_HUO						





With a screening criterion of  $OB \geq 30\%$  and  $DL \geq 0.18$ , 6 compounds were identified as active compounds for Roucongong, 23 for Yinyanghuo, 18 for Gusuibu, and 43 for all (Table 1). The 43 WSYR compounds predicted as active compounds for WSYR based on database were used for molecular docking, which were screened by  $OB \geq 30\%$  and  $DL \geq 0.18$  (as listed in Table 1). In addition, 4 compounds were shared by two herbs. For example, luteolin and kaempferol were shared by Yinyanghuo and Gusuibu,  $\beta$ -sitosterol was shared by Roucongong and Gusuibu, and quercetin was shared by Roucongong and Yinyanghuo.

Based on the TCMSP database, 201 potential targets were identified for WSYR, including 110 for Gusuibu, 90 for Roucongong and 111 for Yinyanghuo. Detailed information about these targets is listed in Supplementary Table S2.

Three databases, OMIM, NCBI-Gene and DisGeNET, were used to search for infertility-related genes. A total of 642 genes were identified, including 246 from OMIM, 448 from NCBI-Gene and 124 from DisGeNET (Supplementary Table S3).

Of those 642 genes, 22 genes were identified as potential target genes in treating infertility for Roucongong, 25 for Yinyanghuo and 25 for Gusuibu, 44 in total, as shown in Figure 2A and Table 2.

## Gene ontology and pathway enrichment analysis of infertility-related WSYR targets

There were 44 nonredundant infertility-related target genes in WSYR. To further explore the biological mechanisms of these 44 infertility targets of WSYR, GO biological process (BP) enrichment analysis was carried out. The targets were found to be involved in a variety of biological processes. The top 15 GO BPs are shown in Figure 2B and include the regulation of reactive oxygen species (ROS), the synthesis and metabolism of nitric oxide (NO), cellular response to oxidative stress, nuclear receptor activity, ligand-activated transcription factor activity, negative regulation of apoptosis signaling pathways, female pregnancy, heat generation, and cellular response to lipopolysaccharide.

At low concentrations, ROS participate in physiological regulation as a normal product of aerobic metabolism. However, excessive ROS can cause oxidative stress, which is regarded as related to oocyte maturation, embryonic development, and endometrial translocation (Wan and Qi, 2017). NO is an important free radical species that is important in embryonic development. The activity of NO and NOS is necessary for embryos to initiate the formation of

the vasculature, and inhibition of NOS can lead to developmental defects or death of the embryo (Wu et al., 2020; Hitchler and Domann, 2021). Nuclear receptors play a very important role in the regulation of the final stage of ovarian follicle growth. Under the influence of follicle stimulating hormone, nuclear receptors promote the proliferation and differentiation of granulosa cells and the synthesis of steroids (Hughes and Murphy, 2021). WSYR may promote oocyte maturation and embryo development through these biological processes.

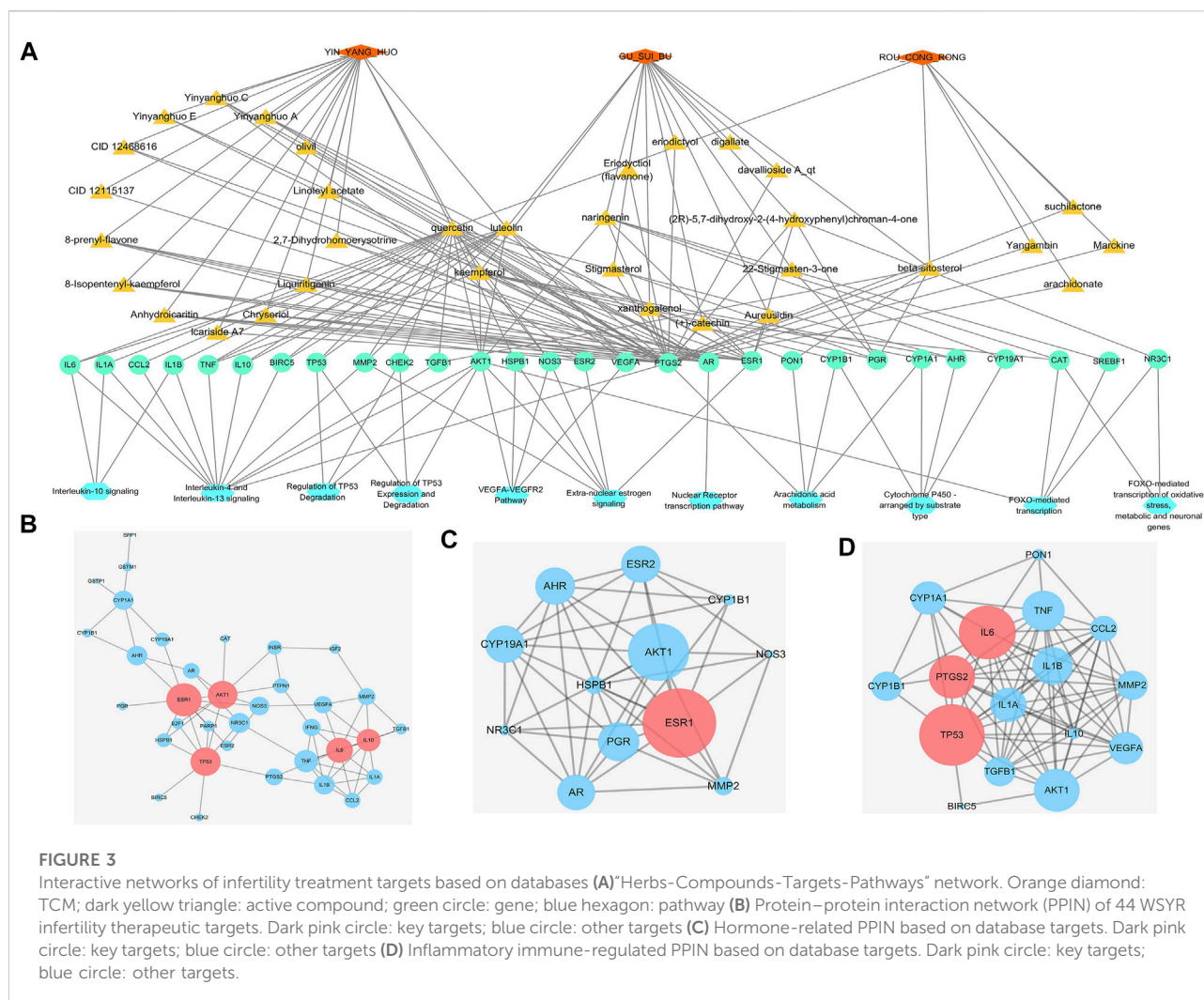
Pathway enrichment analysis was performed on the 44 infertility-related target genes of WSYR by ClueGO, and 15 pathways were enriched with a  $p$  value  $\leq 10^{-3}$ , as shown in Figure 2C. Among them, extra-nuclear estrogen signaling, the nuclear receptor transcription pathway, and endogenous sterols are all estrogen-related signaling pathways; regulation of TP53 degradation, regulation of TP53 expression and degradation, and the VEGFA-VEGFR2 pathway are all growth and apoptosis related pathways; interleukin-4 (IL-4) and interleukin-13 (IL-13) signaling, interleukin-10 (IL-10) signaling, and arachidonic

acid metabolism are inflammatory signaling pathways; FOXO-mediated transcription, FOXO-mediated transcription of oxidative stress, metabolic and neuronal genes are oxidative stress signaling pathways. Those pathways are closely related to infertility, and involve mechanisms such as sex hormone synthesis and secretion, growth and apoptosis, inflammatory responses, and oxidative stress.

Pathway enrichment analysis was also performed on 22 infertility-related target genes for Roucongrong, 25 for Yinyanghuo and 25 for Gusuibu. As shown in Figure 2D, 2 pathways were enriched for Roucongrong, 7 pathways for Yinyanghuo and 9 pathways for Gusuibu. Therefore, we concluded that WSYR acts on multiple signaling pathways to regulate infertility and that all three constitutive herbs have both common and unique pathways, as shown in Figure 2E. All three herbs regulate inflammatory pathways. Yinyanghuo and Gusuibu both act on hormone regulation pathways. Yinyanghuo acts specially on growth and apoptosis signaling. The unique pathways of Gusuibu include FOXO-mediated transcription, arachidonic acid metabolism and endogenous sterols.

TABLE 2 Database-based infertility treatment targets of Roucongrong, Yinyanghuo and Gusuibu.

NO.	Gene name	Entrez gene	TCM	NO.	UniProt ID	Gene name	TCM	NO.	Gene name	Entrez gene	TCM
1	ADRB1	153	Gusuibu	1	ADRB2	154	Roucongrong	1	ADRB2	154	Yinyanghuo
2	ADRB2	154	Gusuibu	2	AKT1	207	Roucongrong	2	AKT1	207	Yinyanghuo
3	AHR	196	Gusuibu	3	GSTM1	2944	Roucongrong	3	INSR	3643	Yinyanghuo
4	AKT1	207	Gusuibu	4	IL6	3569	Roucongrong	4	NFE2L2	4780	Yinyanghuo
5	APOB	338	Gusuibu	5	INSR	3643	Roucongrong	5	NOS3	4846	Yinyanghuo
6	CAT	847	Gusuibu	6	NFE2L2	4780	Roucongrong	6	PTGS2	5743	Yinyanghuo
7	CYP1A1	1543	Gusuibu	7	NOS3	4846	Roucongrong	7	TGFB1	7040	Yinyanghuo
8	CYP1B1	1545	Gusuibu	8	PGR	5241	Roucongrong	8	PARP1	142	Yinyanghuo
9	CYP19A1	1588	Gusuibu	9	PLAU	5328	Roucongrong	9	AR	367	Yinyanghuo
10	ESR1	2099	Gusuibu	10	PON1	5444	Roucongrong	10	IL10	3586	Yinyanghuo
11	NR3C1	2908	Gusuibu	11	PTGS2	5743	Roucongrong	11	CHEK2	11200	Yinyanghuo
12	GSTM1	2944	Gusuibu	12	TGFB1	7040	Roucongrong	12	AHR	196	Yinyanghuo
13	GSTP1	2950	Gusuibu	13	TNF	7124	Roucongrong	13	ESR1	2099	Yinyanghuo
14	IFNG	3458	Gusuibu	14	PARP1	142	Roucongrong	14	GSTP1	2950	Yinyanghuo
15	IL6	3569	Gusuibu	15	AR	367	Roucongrong	15	IFNG	3458	Yinyanghuo
16	INSR	3643	Gusuibu	16	E2F1	1869	Roucongrong	16	BIRC5	332	Yinyanghuo
17	NFE2L2	4780	Gusuibu	17	HSF1	3297	Roucongrong	17	ESR2	2100	Yinyanghuo
18	NOS3	4846	Gusuibu	18	IGF2	3481	Roucongrong	18	HSPB1	3315	Yinyanghuo
19	PGR	5241	Gusuibu	19	IL10	3586	Roucongrong	19	IL1A	3552	Yinyanghuo
20	PLAU	5328	Gusuibu	20	PTPN1	5770	Roucongrong	20	IL1B	3553	Yinyanghuo
21	PON1	5444	Gusuibu	21	SPP1	6696	Roucongrong	21	MMP2	4313	Yinyanghuo
22	PTGS2	5743	Gusuibu	22	CHEK2	11200	Roucongrong	22	PDE3A	5139	Yinyanghuo
23	SREBF1	6720	Gusuibu					23	CCL2	6347	Yinyanghuo
24	TGFB1	7040	Gusuibu					24	TP53	7157	Yinyanghuo
25	TNF	7124	Gusuibu					25	VEGFA	7422	Yinyanghuo



## Construction of a “Herbs-Compounds-Targets-Pathways” network for WSYR

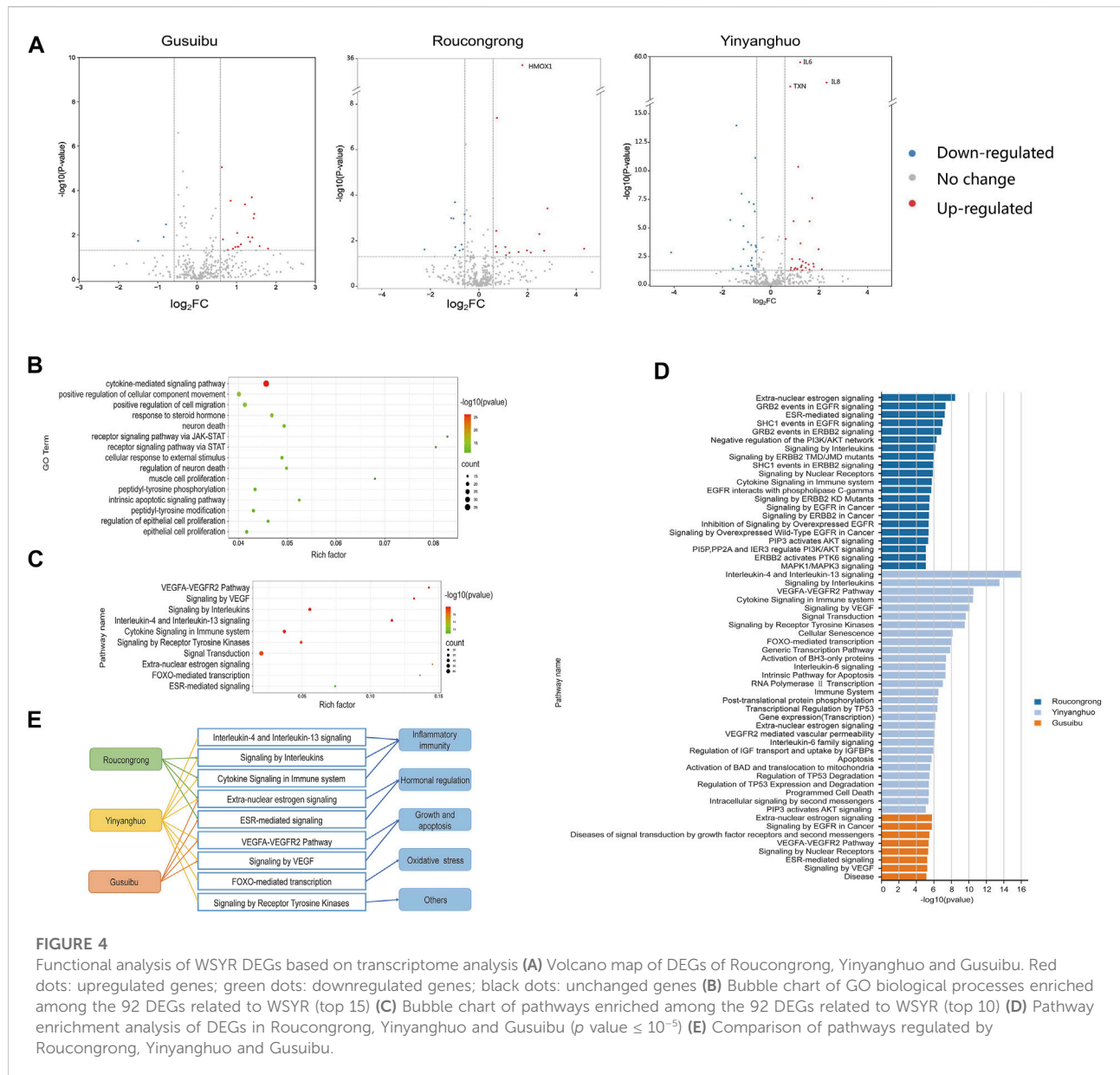
As shown in Figure 3A, a “Herbs-Compounds-Targets-Pathways” network was constructed to show the overall function of WSYR and its constitutive herbs.

Yinyanghuo A, Yinyanghuo B and Yinyanghuo C, representative compounds of Yinyanghuo, play immune inflammation regulatory and sex hormone regulatory roles in the treatment of infertility. The above three compounds all act on prostaglandin G/H synthase 2 (PTGS2) and androgen receptor (AR). Yinyanghuo A acts on ESR1, and Yinyanghuo B acts on ESR2. PTGS2 exerts inflammatory immune regulation by affecting IL-4 and IL-13 signaling, IL-10 signaling, and arachidonic acid metabolism. It has been reported that PTGS2 is closely associated with ovulation failure and implantation disorders in infertility (Szczyuko

et al., 2020). AR, ESR1 and ESR2 regulate the nuclear receptor transcription pathway, and ESR1 and ESR2 regulate extra-nuclear estrogen signaling to play a hormonal regulatory role.

As components of Gusuibu (+)-catechin and naringenin play a role in regulating oxidative stress in the treatment of infertility. Both (+)-catechin and naringenin can act on catalase (CAT). CAT is an enzyme involved in oxidative stress detoxification. It protects the human body from oxidative stress by regulating FOXO-mediated transcription and FOXO-mediated transcription of oxidative stress.

The Roucongong component quercetin plays a role in regulating inflammation immunity in infertility. Quercetin acts on IL-10, IL-1 $\alpha$ , IL-1 $\beta$ , IL-6, TNF, CCL2 and other inflammatory factors and chemokines and regulates IL-4 and IL-13 signaling and IL-10 signaling.



## Construction of protein-protein interaction networks of WSYR based on dry experiments

A total of 44 WSYR infertility therapeutic targets were used to construct a PPIN (confidence level  $>0.9$ ) and to calculate the degree, betweenness and closeness of each node in the network. The larger the three parameter values, the more critical are the targets in the network. The top 5 nodes with the highest sum of degree, betweenness and closeness were proposed as key targets of WSYR, including ESR1, TP53, AKT1, IL-6, and IL-10 (Figure 3B and Supplementary Table S4-A).

We constructed a hormone regulation-related PPIN (confidence level  $>0.4$ ) involving the three pathways of extra-nuclear estrogen signaling, nuclear receptor transcription pathway, and endogenous sterols and calculated the degree, betweenness and closeness of each node in the network. ESR1 was the most critical target (Figure 3C and Supplementary Table S4-B).

In addition, we constructed an immune inflammation-related PPIN (confidence level  $>0.4$ ) involving interleukin-4 and interleukin-13 signaling, interleukin-10 signaling, and arachidonic acid metabolism, and calculated the degree, betweenness and closeness of each node in the network. The



TABLE 3 92 DEGs of WSYR. Including 22 gusuibu DEGs, 26 RoucongrongDEGs and 54 yinyanghuo DEGs.

NO.	Gene symbol	Entrez gene	log2FC	p Value	Classification	NO.	Gene symbol	Entrez gene	log2FC	p Value	Classification	NO.	Gene symbol	Entrez gene	log2FC	p Value	Classification
1	EREG	2069	0.626	8.91E-06	Gusuibu	13	FOXO4	4303	1.087	1.88E-02	Roucongrong	21	NCK1	4690	−0.601	4.70E-04	Yinyanghuo
2	PTK2B	2185	1.386	2.03E-04	Gusuibu	14	CYBA	1535	−0.977	1.90E-02	Roucongrong	22	IGFBP7	3490	−1.128	7.29E-04	Yinyanghuo
3	VCAN	1462	0.849	2.91E-04	Gusuibu	15	GNG3	2785	4.330	2.25E-02	Roucongrong	23	CXCL1	2919	1.978	7.35E-04	Yinyanghuo
4	CAV2	858	1.214	4.29E-04	Gusuibu	16	TYK2	7297	−0.663	2.41E-02	Roucongrong	24	WASF1	8936	−0.623	1.15E-03	Yinyanghuo
5	PLCG1	5335	1.448	1.14E-03	Gusuibu	17	ESR2	2100	−2.243	2.45E-02	Roucongrong	25	RASA1	5921	−4.118	1.41E-03	Yinyanghuo
6	PIM1	5292	1.435	1.80E-03	Gusuibu	18	MMP7	4316	1.977	2.68E-02	Roucongrong	26	TP53	7157	−0.781	4.20E-03	Yinyanghuo
7	STAT3	6774	−0.792	3.42E-03	Gusuibu	19	BCL2L1	598	−0.797	2.69E-02	Roucongrong	27	NR1H2	7376	0.882	5.24E-03	Yinyanghuo
8	TXNIP	10628	1.017	8.30E-03	Gusuibu	20	IL1R1	3554	2.682	2.78E-02	Roucongrong	28	VCAM1	7412	1.191	5.48E-03	Yinyanghuo
9	GADD45 A	1647	−0.851	1.25E-02	Gusuibu	21	EGF	1950	1.629	3.13E-02	Roucongrong	29	CALM1	801	−0.814	7.22E-03	Yinyanghuo
10	CYP26C1	340665	1.296	1.27E-02	Gusuibu	22	HSPA8	3312	0.736	3.14E-02	Roucongrong	30	ARNT	405	1.323	8.66E-03	Yinyanghuo
11	KDR	3791	1.400	1.32E-02	Gusuibu	23	NR2C2	7182	2.133	3.32E-02	Roucongrong	31	PPARG	5468	1.447	1.14E-02	Yinyanghuo
12	GNAI1	2770	0.655	1.62E-02	Gusuibu	24	SIRT3	23410	1.250	3.41E-02	Roucongrong	32	NR4A2	4929	1.762	1.34E-02	Yinyanghuo
13	ARNT	405	−1.500	1.88E-02	Gusuibu	25	PIAS1	8554	−0.986	4.27E-02	Roucongrong	33	IL6R	3570	1.563	1.60E-02	Yinyanghuo
14	MARC1	64757	1.342	2.03E-02	Gusuibu	26	BCL6	604	1.112	4.30E-02	Roucongrong	34	SGK1	6446	−0.785	1.87E-02	Yinyanghuo
15	GNGT2	2793	1.110	2.70E-02	Gusuibu	1	IL6	3569	1.382	1.01E-55	Yinyanghuo	35	ATM	472	1.279	1.89E-02	Yinyanghuo
16	POMC	5443	1.586	3.24E-02	Gusuibu	2	IL8	3576	2.331	5.35E-27	Yinyanghuo	36	YWHAH	7533	−0.937	2.20E-02	Yinyanghuo
17	BMF	90427	1.028	3.42E-02	Gusuibu	3	TXN	7295	0.615	1.92E-24	Yinyanghuo	37	CYP4V2	285440	−1.242	2.32E-02	Yinyanghuo
18	KAT2B	8850	1.048	3.43E-02	Gusuibu	4	FN1	2335	−1.420	1.06E-14	Yinyanghuo	38	ROCK1	6093	1.777	2.42E-02	Yinyanghuo
19	F5	2153	0.969	3.53E-02	Gusuibu	5	HSP90B1	7184	−0.640	7.51E-12	Yinyanghuo	39	F5	2153	1.260	2.57E-02	Yinyanghuo
20	SHC2	25759	1.798		Gusuibu	6	HMOX1	3162	1.134		Yinyanghuo	40	IL23 A	51561	1.242		Yinyanghuo

(Continued on following page)

TABLE 3 (Continued) 92 DEGs of WSYR. Including 22 gusuibu DEGs, 26 RoucongrongDEGs and 54 yinyanghuo DEGs.

NO.	Gene symbol	Entrez gene	log2FC	p Value	Classification	NO.	Gene symbol	Entrez gene	log2FC	p Value	Classification	NO.	Gene symbol	Entrez gene	log2FC	p Value	Classification
				4.17E-02						4.38E-11						2.65E-02	
21	THRB	7068	0.909	4.24E-02	Gusuibu	7	STAT1	6772	-1.208	9.97E-09	Yinyanghuo	41	FOXO4	4303	1.443	3.10E-02	Yinyanghuo
22	PIK3R1	5295	0.778	4.81E-02	Gusuibu	8	CXCL2	2920	1.716	2.47E-08	Yinyanghuo	42	CYP2S1	29785	0.841	3.11E-02	Yinyanghuo
1	HMOX1	3162	1.873	2.87E-36	Roucongrong	9	CAV1	857	-0.899	5.29E-08	Yinyanghuo	43	ITGB2	3689	1.011	3.28E-02	Yinyanghuo
2	EREG	2069	0.795	4.12E-08	Roucongrong	10	CDKN2A	1029	-0.705	8.18E-08	Yinyanghuo	44	HDAC1	3065	-0.721	3.32E-02	Yinyanghuo
3	VCAN	1462	-0.990	2.03E-04	Roucongrong	11	SDC2	6383	-0.660	3.56E-07	Yinyanghuo	45	SOCS5	9655	1.091	3.64E-02	Yinyanghuo
4	TNFRSF1A	7132	2.819	3.81E-04	Roucongrong	12	VCAN	1462	-1.675	2.01E-06	Yinyanghuo	46	PAK3	5063	-1.565	3.65E-02	Yinyanghuo
5	EGFR	1956	-0.593	7.01E-04	Roucongrong	13	EREG	2069	0.942	2.60E-06	Yinyanghuo	47	LAMC1	3915	-0.622	3.72E-02	Yinyanghuo
6	CYP4V2	285440	-1.145	1.02E-03	Roucongrong	14	CDKN1A	1026	1.609	2.64E-06	Yinyanghuo	48	FOS	2353	2.111	4.13E-02	Yinyanghuo
7	SOD2	6648	-1.052	1.05E-03	Roucongrong	15	ITGAV	3685	-1.131	6.93E-06	Yinyanghuo	49	PPARGC1A	10891	1.096	4.16E-02	Yinyanghuo
8	MED1	5469	-0.609	1.68E-03	Roucongrong	16	IL18	3606	0.619	9.06E-05	Yinyanghuo	50	AKT2	208	0.975	4.24E-02	Yinyanghuo
9	SUMO2	6613	0.713	3.71E-03	Roucongrong	17	LCN2	3934	-0.940	1.70E-04	Yinyanghuo	51	MMP7	4316	1.605	4.53E-02	Yinyanghuo
10	HRAS	3265	2.482	5.12E-03	Roucongrong	18	BAD	572	1.229	2.24E-04	Yinyanghuo	52	JUNB	3726	0.822	4.71E-02	Yinyanghuo
11	THEM4	117145	-0.715	1.49E-02	Roucongrong	19	CTNND1	1500	-0.810	3.16E-04	Yinyanghuo	53	PTK2	5747	-0.704	4.77E-02	Yinyanghuo
12	PPP2CA	5515	0.691	1.77E-02	Roucongrong	20	TP53BP2	7159	-0.619	3.40E-04	Yinyanghuo	54	SFN	2810	1.300	4.94E-02	Yinyanghuo

key targets included TP53, IL-6, and PTGS2 (Figure 3D and Supplementary Table S4-C).

## Differentially expressed genes identified by transcriptome analysis in HK-2 cells

Due to the incomplete and unsystematic nature of network pharmacology, the predicted results may not fully reflect the actual mechanism of WSYR. The application of transcriptome analysis can identify differentially expressed genes in response to TCM treatment and complement the results from network pharmacology.

There is an old saying in Chinese medicine: the kidney stores the essence, which is the foundation of reproduction. Deficiency of kidney qi and inadequacy of Tiangui will result in insufficient production of fertilization-competent sperm, leading to infertility. Deficiency of kidney yang, inability to warm semen and warm uterus, can cause cold semen and cold uterus, thereby causing infertility. Based on this, transcriptome analysis was performed on HK-2 human renal epithelial cells to examine the transcriptional regulation of WSYR in infertility-related pathways.

According to the results above, 15 pathways with  $p$  values less than  $10^{-3}$  are the most important in the treatment of infertility by WSYR. Therefore, the 412 genes in these 15 pathways were subjected to transcriptome analysis in HK-2 cells treated with Roucongong, Yinyanghuo and Gusuibu.

As shown in the volcano map (Figure 4A), 26 DEGs were identified in Roucongong, including 15 upregulated genes and 11 downregulated genes; 54 DEGs were identified in Yinyanghuo, including 30 upregulated genes and 24 downregulated genes; and 22 DEGs were identified in Gusuibu, including 19 upregulated genes and 3 downregulated genes ( $FC > 1.5$  or  $< 0.67$  and  $p < 0.05$ ). In conclusion, a total of 92 DEGs (Table 3) were identified for WSYR based on transcriptome analysis.

## Gene ontology and pathway enrichment analysis of WSYR DEGs

To further explore the biological mechanism of these 92 DEGs in WSYR, GO BP enrichment analysis was carried out. As shown in Figure 4B, the DEGs were involved in a variety of biological processes, including regulation of cytokine-mediated signaling pathways, cell movement and migration, steroid hormone response, JAK-STAT receptor signaling pathways, neuronal death, intrinsic apoptosis signaling pathways, peptidyl-tyrosine phosphorylation modification, and proliferation of muscle and epithelial cells.

When inflammation occurs, cells such as leukocytes, fibroblasts, endothelial cells, and haematopoietic cells are

induced to produce chemokines by IL-1, TNF and other cytokines and are guided by chemokines to migrate to specific tissues (Borrelli et al., 2013). Studies have found that the chemokines CXCL1 and CXCL13 are abnormally expressed in female infertility patients with chronic endometritis (Kitaya and Yasuo, 2010). Sex steroid hormones are essential elements that affect reproduction. They affect follicle formation, endometrial development, ovulation, implantation and other developmental events (Reichman and Rosenwaks, 2017) that are critical for female pregnancy. In addition, members of the JAK-STAT pathway, TYK2, STAT1 and STAT4, have been shown to be active in human sperm, indicating that defects in the JAK-STAT pathway in sperm may be related to male infertility (D'Cruz et al., 2001).

Similarly, many pathways were enriched by the 92 DEGs of WSYR; the top 10 pathways are shown in Figure 4C. Among them, extra-nuclear estrogen signaling and ESR-mediated signaling are both estrogen-related signaling pathways; the VEGFA-VEGFR2 pathway and signaling by VEGF are both growth- and apoptosis-related pathways; Interleukin-4 and interleukin-13 signaling, signaling by interleukins and cytokine signaling in immune system are inflammatory immune signaling pathways; and FOXO-mediated transcription is an oxidative stress signaling pathway. These results are consistent with those of database-based network pharmacology.

Pathway enrichment analysis of the DEGs of the three herbs was also carried out. The total numbers of enriched pathways with  $p$  value  $\leq 10^{-5}$  were 21 for Roucongong, 29 for Yinyanghuo, and 8 for Gusuibu (Figure 4D). WSYR acts on a variety of signaling pathways to regulate infertility, and the three herbs have both common and unique pathways (Figure 4E). For example, Roucongong plays a role in inflammatory immune and hormone regulation, and Gusuibu plays a role in angiogenesis and hormone regulation. In addition to regulating inflammatory responses, angiogenesis and hormone levels, Yinyanghuo plays a unique role in the regulation of oxidative stress and receptor tyrosine kinases.

## Construction of a "herbs-degs-pathways" network for WSYR based on transcriptome analysis

Based on the results of transcriptome analysis, we drew a "Herbs-DEGs-Pathways" diagram to show the overall function of WSYR and its constituent herbs, as shown in Figure 5A.

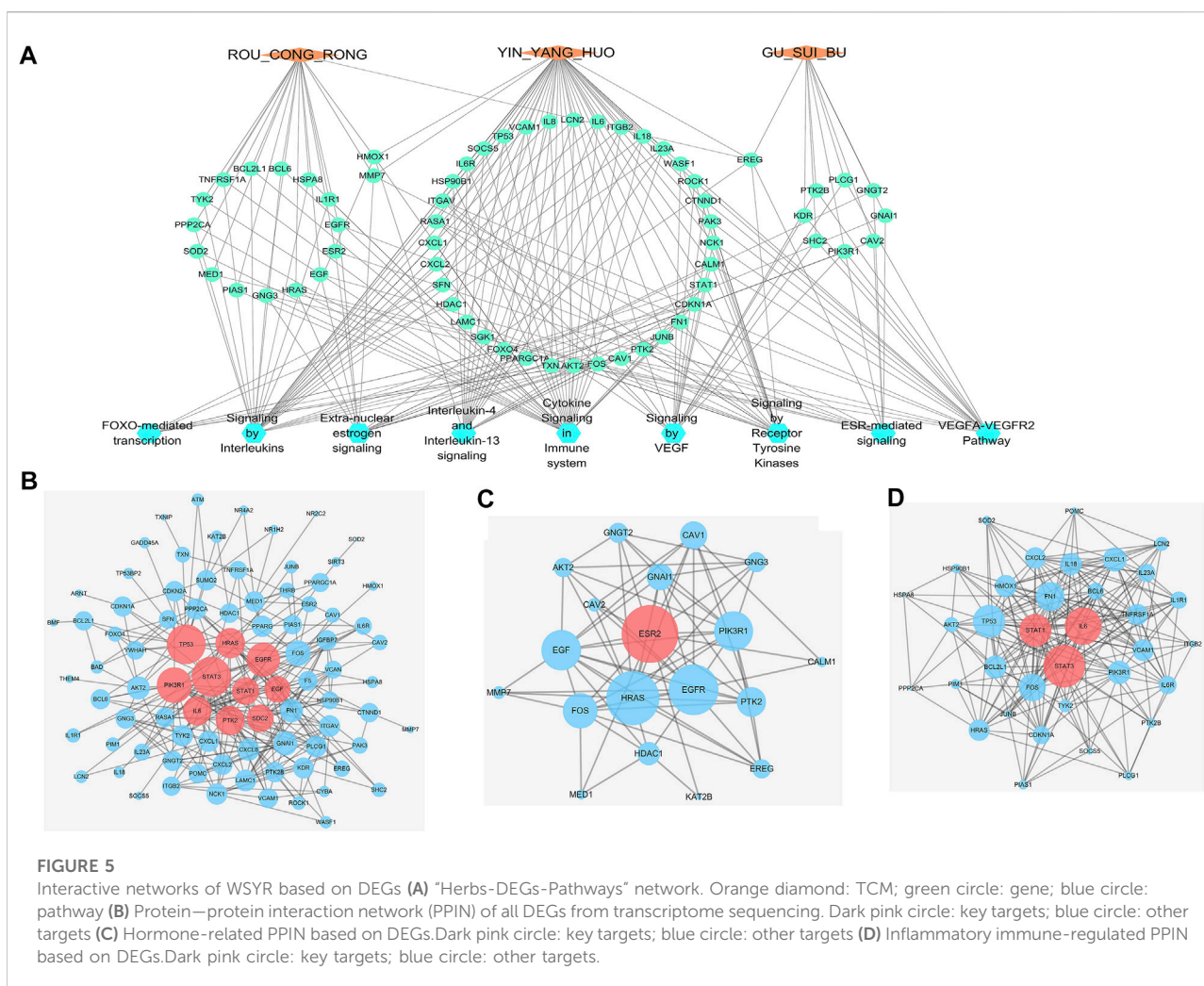
Proepiregulin (EREG) is coregulated by Roucongong, Yinyanghuo and Gusuibu and acts on three signaling pathways: extra-nuclear estrogen signaling, ESR-mediated signaling and signaling by receptor tyrosine kinases. EREG

is a member of the epidermal growth factor family, which can regulate angiogenesis and remodelling to promote tissue repair, wound healing and oocyte maturation (Riese and Cullum, 2014). Haem oxygenase 1 (HMOX1) is jointly regulated by Roucongrong and Yinyanghuo and acts on three signaling pathways: IL-4 and IL-13 signaling, signaling by interleukins and cytokine signaling in the immune system. HMOX1 catalyses the degradation of haem to produce carbon monoxide (CO), iron and biliverdin-IX $\alpha$ . The HMOX1/CO system has been found to exert cytoprotective effects on damaged organs and in animal models by regulating inflammation and apoptosis (Ryter, 2019). MMP7 is jointly regulated by Roucongrong and Yinyanghuo and acts on three signaling pathways: extranuclear estrogen signaling, ESR-mediated signaling and signal transduction. MMPs can degrade the extracellular matrix (ECM), affect the migration of germ cells, affect the spermatogenesis pathway, and play important roles in spermatogenesis and semen quality (Warinrak et al., 2015).

## Construction of PPINs of WSYR based on transcriptome analysis

To identify the key targets of WSYR, a PPIN was constructed based on the 92 DEGs obtained by transcriptome analysis (confidence level >0.9), and 86 nodes are illustrated in Figure 5B and Supplementary Table S5-A. The degree, betweenness and closeness of each node in the network were calculated. The results showed that the key targets included STAT3, TP53, PIK3R1, EGFR, HRAS, PTK2, IL6, STAT1, SDC2 and EGF.

To further identify the key targets of WSYR in hormones, 19 DEGs (confidence level >0.4) corresponding to the two hormone-related pathways of extra-nuclear estrogen signaling and ESR-mediated signaling in Figure 4E were selected to construct a PPIN. Nineteen nodes are shown in Figure 5C and Supplementary Table S5-B. Additionally, the degree, betweenness and closeness of each node in the network was calculated. The results showed that the most critical target of hormone regulation is ESR2.





To further identify the key targets of WSYR in immune inflammation, 35 DEGs (confidence level >0.4) corresponding to the three inflammatory immune-related pathways interleukin-4 and interleukin-13 signaling, signaling by interleukins, and cytokine signaling in the immune system, as shown in Figure 4E, were selected to construct a PPIN. Thirty-five nodes are shown in Figure 5D and Supplementary Table S5-C. The degree, betweenness and closeness of each node in the network are calculated. The results showed that the key targets of WSYR involved in inflammatory responses included STAT3, IL6 and STAT1.

Based on the dry experiments and wet experiments, we have found that WSYR mainly plays a role in hormone regulation and inflammatory responses. In the next step, we plan to use RT-qPCR to verify the regulatory effect of WSYR on key genes involved in inflammation and to perform molecular docking to further identify the active compounds present in WSYR and validate the interaction between compounds and potential targets of WSYR.

## RT-qPCR validation of WSYR in regulating inflammatory responses

To verify the anti-inflammatory effect of WSYR, we examined target genes in inflammatory responses by RT-qPCR. In this study,

IL-4 and IL-10 enriched by the inflammatory pathway were selected for RT-qPCR validation in SK-OV-3 cells. IL-4 and IL-10 are classic anti-inflammatory cytokines that limit excessive tissue destruction caused by inflammation.

The experimental results showed that WSYR could play an anti-inflammatory role by upregulating the expression of *IL-4* and *IL-10* (Figure 6A and Figure 6C). Specifically, Gusuibu and Roucongrong can upregulate the expression of *IL-4*, and Yinyanghuo can upregulate the expression of *IL-4* and *IL-10* to exert anti-inflammatory effects (Figure 6B and Figure 6D).

## Construction of ESR1 and ESR2 molecular docking models and drug screening

Studies have reported that estrogen receptors are important for maintaining follicle, oocyte growth and ovulation function (Tang et al., 2019). Our results suggested that WSYR treats infertility by regulating estrogen receptors, but the specific mechanism of action is still unclear. The molecular docking model of ESR1 and ESR2 was constructed, and the compounds of WSYR were evaluated by docking.

The protein crystal complex (pdb id: 5FQP) was selected as the docking target of ESR1. The original ligand ESR1 antagonist (Scott

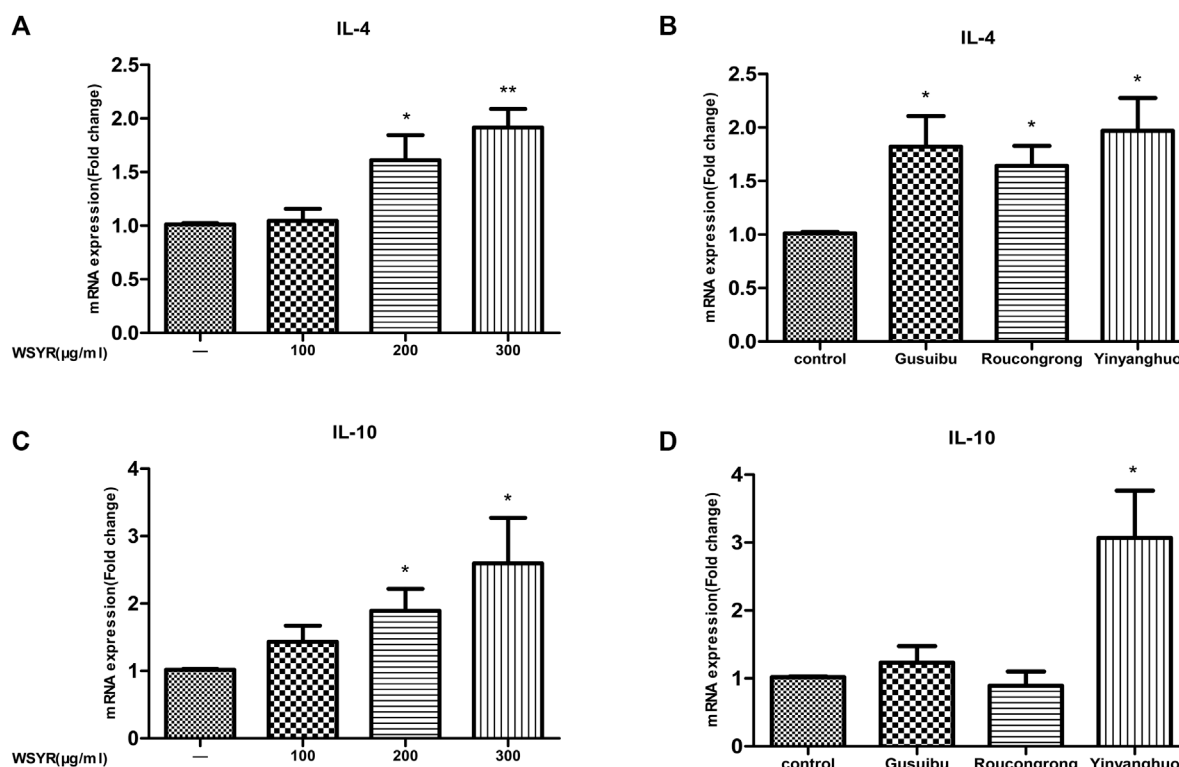


FIGURE 6

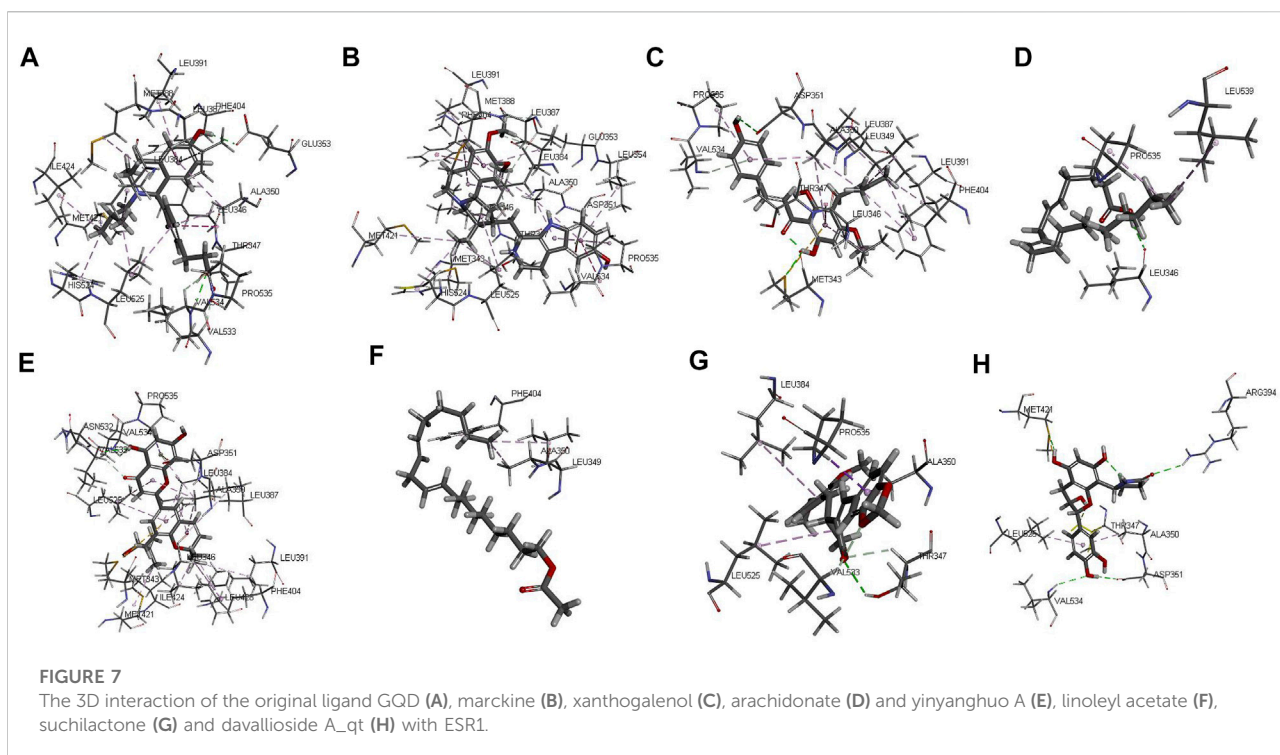
Action of WSYR and its herbs Gusuibu, Roucongrong, Yinyanghuo on SK-OV-3 cells. SK-OV-3 cells were treated with WSYR (100, 200, 300 µg/ml), Gusuibu (200 µg/ml), Roucongrong (200 µg/ml), Yinyanghuo (200 µg/ml) for 24 h. The mRNA expression of *IL-4* (A,B), *IL-10* (C,D) was analyzed by qPCR. \* $p < 0.05$  and \*\* $p < 0.01$  indicate statistical significance compared to control.

TABLE 4 ESR1 molecular docking results.

NO.	ID	-CDOCKER_INTERACTION_ENERGY	Molecular name	TCM
1	original ligand	65.414	GQD	—
2	MOL008871	54.530	Marckine	Roucongrong
3	MOL009091	53.776	Xanthogalenol	Gusuibu
4	MOL005320	51.688	Arachidonate	Roucongrong
5	MOL004382	51.053	Yinyanghuo A	Yinyanghuo
6	MOL001645	50.828	Linoleyl acetate	Yinyanghuo
7	MOL005384	50.592	Suchilactone	Roucongrong
8	MOL009078	49.776	davallioside A_qt	Gusuibu
9	MOL004367	47.811	Olivil	Yinyanghuo
10	MOL007563	47.178	Yangambin	Roucongrong
11	MOL004396	46.845	CID 12468616	Yinyanghuo
12	MOL003542	46.101	8-Isopentenyl-kaempferol	Yinyanghuo
13	MOL000569	45.932	Digallate	Gusuibu
14	MOL005190	44.156	Eriodictyol	Gusuibu
15	MOL000492	43.466	(+)-catechin	Gusuibu
16	MOL004373	43.293	Anhydroicaritin	Yinyanghuo
17	MOL001978	43.188	Aureusidin	Gusuibu
18	MOL004384	42.640	Yinyanghuo C	Yinyanghuo
19	MOL000098	42.464	Quercetin	Roucongrong, Yinyanghuo
20	MOL001040	42.130	(2 R)-5,7-dihydroxy-2-(4-hydroxyphenyl)chroman-4-one	Gusuibu
21	MOL004386	41.695	Yinyanghuo E	Yinyanghuo
22	MOL004391	40.476	8-prenyl-flavone	Yinyanghuo
23	MOL003044	39.899	Chryseriol	Yinyanghuo
24	MOL002914	39.767	Eriodictyol (flavanone)	Gusuibu
25	MOL001792	39.745	Liquiritigenin	Yinyanghuo
26	MOL009087	39.734	marioside_qt	Gusuibu
27	MOL000006	39.021	Luteolin	Gusuibu, Yinyanghuo
28	MOL004380	38.627	2,7-Dihydrohomoerysotrine	Yinyanghuo
29	MOL004328	38.601	Naringenin	Gusuibu
30	MOL000422	38.113	Kaempferol	Gusuibu, Yinyanghuo
31	MOL004427	36.341	Icariside A7	Yinyanghuo
32	MOL000622	33.682	Magnograndiolide	Yinyanghuo
33	MOL009061	30.159	22-Stigmasten-3-one	Gusuibu
34	MOL004388	25.106	CID 12115137	Yinyanghuo
35	MOL001771	17.943	poriferast-5-en-3beta-ol	Yinyanghuo
36	MOL009075	16.345	cycloartenone	Gusuibu
37	MOL001510	15.266	24-epicampesterol	Yinyanghuo
38	MOL000449	11.704	Stigmasterol	Gusuibu
39	MOL000359	8.864	sitosterol	Yinyanghuo
40	MOL009076	-0.891	cyclolaudenol	Gusuibu
41	MOL000358	-8.363	beta-sitosterol	Gusuibu, Roucongrong
42	MOL004394	No refined poses	Anhydroicaritin-3-O-alpha-L-rhamnoside	Yinyanghuo
43	MOL004425	No refined poses	Icariin	Yinyanghuo
44	MOL009063	No refined poses	Cyclolaudenol acetate	Gusuibu

et al., 2015) was used as the positive control. Its -cdocker interaction energy (-CIE) score is 65.414, RMSD is 0.3557, pocket radius is 8.522, and pocket site is (14.230, 22.133, 65.663). The positive drug score

(65.414) was set as the threshold, and the drug score value > threshold×75% as the standard for the drug to have a good affinity with ESR1. The molecular docking results of 43 WSYR



compounds with ESR1 are shown in Table 4. Finally, the following components have strong affinity with ESR1: marckine (54.5303), xanthogalenol (53.776), arachidonate (51.688), yinyanghuo A (51.0526), linoleyl acetate (50.8283), suchilactone (50.5918), and davallioside A<sub>qt</sub> (49.7764), and the result is shown in Figure 7.

The protein crystal complex 1L2J (Shiau et al., 2002) was selected as the docking target of ESR2. The original ligand ESR2 antagonist was used as the positive control. Its -cdocker interaction energy score is 52.8724, RMSD is 0.6922, pocket radius is 7.574, and pocket site is (32.212, 82.073, -11.407). The positive drug score (52.8724) was set as the threshold, and the drug score value > threshold×90% was set as the standard for the drug to have a good affinity with ESR2. The molecular docking results of 43 WSYR compounds with ESR2 are shown in Table 5. Finally, the following components have strong affinity with ESR2: anhydroicaritin (50.9932), 8-isopentenyl-kaempferol (50.8610), davalliosideA<sub>qt</sub> (50.4315), xanthogalenol (49.4134), and linoleyl acetate (49.0539) and the results are shown in Figure 8.

In summary, the results showed that xanthogalenol in Gusuibu, arachidonate in Roucongong, and anhydroicaritin in Yinyanghuo have good affinity for estrogen receptors. The proposed mechanism of WSYR in treating infertility was summarized in Supplementary Table S6, including the constituent herbs, compounds and corresponding functions.

## Discussion

By integrating the results of dry and wet experiments, it was found that the WSYR treats infertility by regulating hormone

levels and inflammatory responses. Estrogen, estrogen receptors and various enzymes are closely related to clinical polycystic ovary syndrome, endometriosis and other reproductive endocrine diseases (Tang et al., 2019). Estrogen receptor is a ligand-activated transcription factor, which has several functional domains such as DNA binding domain, protein binding domain and transcriptional regulatory domain (Kuiper et al., 1996). Estrogen functions through ESR1 and ESR2 in follicle formation and ovulation. During the growth of follicles, ESR1 is mainly expressed on the follicle theca to regulate the proliferative effect of estrogen; while ESR2 is mainly expressed in the granulosa cells of the growing follicles at various stages to promote cell differentiation and retard proliferation (Pelletier and El-Alfy, 2000).

Various drugs by targeting estrogen receptors have been developed. For example, Clomiphene citrate (CC) is a clinically used estrogen receptor antagonistic drug to treat female and male infertility for 50 years (Roth et al., 2013). CC is an artificially synthetic estrogen derivative that can bind with estrogen receptor. CC antagonizes the hypothalamus-pituitary ER, leading to inhibition of the negative feedback effect of estradiol in circulation and increasing the pulse frequency of hypothalamus gonadotropin-releasing hormone. This leads to an increase in luteinizing hormone and follicle-stimulating hormone generated by the pituitary. Eventually, follicle growth and sperm generation are promoted (Revelli et al., 2011; Scovell and Khera, 2018; Quaas and Legro, 2019).

In our study, crystal complexes of ESR1 and ESR2 and their antagonists were selected to construct a molecular

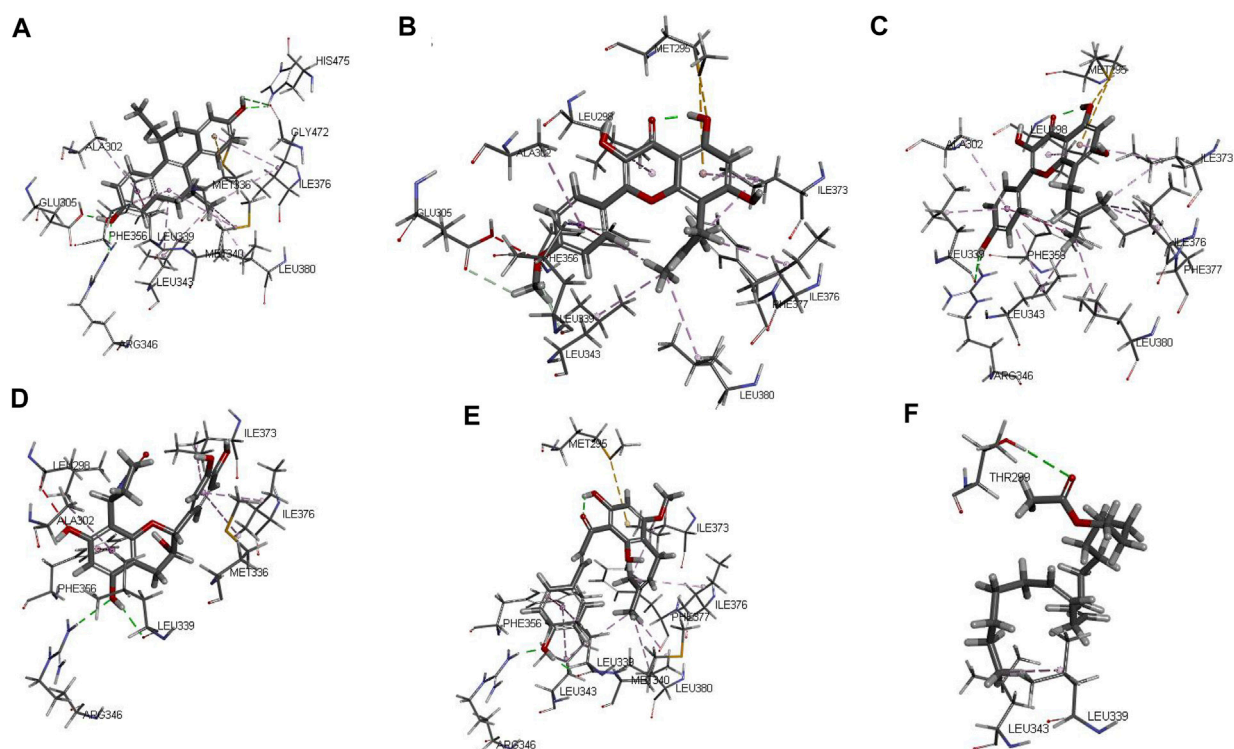
TABLE 5 ESR2 molecular docking results.

NO.	ID	-CDOCKER_INTERACTION_ENERGY	Molecular name	TCM
1	original ligand	52.872	THC	—
2	MOL004373	50.993	Anhydroicaritin	Yinyanghuo
3	MOL003542	50.861	8-Isopentenyl-kaempferol	Yinyanghuo
4	MOL009078	50.432	davallioside A_qt	Gusuibu
5	MOL009091	49.413	xanthogalenol	Gusuibu
6	MOL001645	49.054	Linoleyl acetate	Yinyanghuo
7	MOL004367	47.226	olivil	Yinyanghuo
8	MOL004380	44.539	2,7-Dihydrohomoerysotrine	Yinyanghuo
9	MOL000098	43.411	quercetin	Roucongong; Yinyanghuo
10	MOL001040	42.865	(2 R)-5,7-dihydroxy-2-(4-hydroxyphenyl)chroman-4-one	Gusuibu
11	MOL004396	42.624	CID 12468616	Yinyanghuo
12	MOL000422	42.237	kaempferol	Gusuibu; Yinyanghuo
13	MOL000569	41.823	digallate	Gusuibu
14	MOL003044	41.674	Chryseriol	Yinyanghuo
15	MOL005190	41.543	eriodictyol	Gusuibu
16	MOL002914	41.484	Eriodyctiol (flavanone)	Gusuibu
17	MOL009087	41.415	marioside_qt	Gusuibu
18	MOL000006	41.160	luteolin	Gusuibu; Yinyanghuo
19	MOL001978	40.544	Aureusidin	Gusuibu
20	MOL004382	40.506	Yinyanghuo A	Yinyanghuo
21	MOL005320	40.259	arachidonate	Roucongong
22	MOL007563	39.614	Yangambin	Roucongong
23	MOL005384	39.439	suchilactone	Roucongong
24	MOL000492	38.231	(+)-catechin	Gusuibu
25	MOL004328	36.992	naringenin	Gusuibu
26	MOL001792	36.862	Liquiritigenin	Yinyanghuo
27	MOL004427	36.796	Icariside A7	Yinyanghuo
28	MOL000622	36.103	Magnograndiolide	Yinyanghuo
29	MOL004388	34.448	CID 12115137	Yinyanghuo
30	MOL004391	34.278	8-prenyl-flavone	Yinyanghuo
31	MOL004386	28.124	Yinyanghuo E	Yinyanghuo
32	MOL004384	26.056	Yinyanghuo C	Yinyanghuo
33	MOL008871	24.876	Marckine	Roucongong
34	MOL001510	18.730	24-epicampestrol	Yinyanghuo
35	MOL009061	17.976	22-Stigmasten-3-one	Gusuibu
36	MOL009076	16.461	cyclolaudenol	Gusuibu
37	MOL009075	15.128	cycloartenone	Gusuibu
38	MOL009063	5.975	Cyclolaudenol acetate	Gusuibu
39	MOL000358	-1.136	beta-sitosterol	Gusuibu; Roucongong
40	MOL000359	-9.681	sitosterol	Yinyanghuo
41	MOL001771	-17.121	poriferast-5-en-3beta-ol	Yinyanghuo
42	MOL000449	-21.647	Stigmasterol	Gusuibu
43	MOL004394	No refined poses	Anhydroicaritin-3-O-alpha-L-rhamnoside	Yinyanghuo
44	MOL004425	No refined poses	Icariin	Yinyanghuo

docking model to screen potential estrogen receptor antagonists in WSYR. The results revealed several compounds with high affinity to ESR1 or ESR2 and some

of them have already been reported as related to estrogen regulation. For example, xanthogalenol in Gusuibu showed high affinity for both ESR1 and ESR2. Xanthogalenol may play





**FIGURE 8**  
The 3D interaction of the original ligand THC (**A**), anhydroicaritin (**B**), 8-isopentenyl-kaempferol (**C**), davallioside A<sub>qt</sub> (**D**), xanthogalenol (**E**) and linoleyl acetate (**F**) with ESR2.

a role in bone protection by activating the estrogen signaling pathway and promoting the differentiation and mineralization of osteoblasts *in vitro* (Wang et al., 2011). The arachidonate in Roucongong showed high affinity for ESR1. It has been reported that arachidonate has pervasive modulatory effects on estrogen receptors in central and peripheral tissues (Kato, 1989). Anhydroicaritin in Yinyanghuo, which is the aglycone of Yinyanghuo's indicator component icariin, showed high affinity to ESR2. As reported, anhydroicaritin has selective estrogen receptor regulatory activity (Tong et al., 2011). In addition, compounds such as marckine, yinyanghuo A, linoleyl acetate, suchilactone, davallioside A<sub>qt</sub>, and 8-isopentenylkaempferol were also predicted by molecular docking. They may have potential estrogen-regulating effects and need further study.

In addition, WSYR was found with an anti-inflammatory role by our study. IL-4 and IL-10 are multipotent anti-inflammatory cytokines that mainly inhibit the proinflammatory processes. IL-4 signaling plays a part in not only Th2 cell function but also the regulation of regulatory T cells, which is essential in successful pregnancies. IL-10 mainly exerts anti-inflammatory effects by inhibiting proinflammatory cytokines such as IL-1, IL-12 and

TNF. During normal pregnancy, IL-4 and IL-10 perform multiple functions, promoting placental formation and regulating trophoblast invasion and differentiation. Thus, the precise regulation of IL-4 and IL-10 is important for reducing maternal inflammation during different stages of pregnancy (Chatterjee et al., 2014). In this study, it was found that WSYR can exert an anti-inflammatory effect by upregulating the expression of *IL-4* and *IL-10*. Among them, Gusuibu, Roucongong and Yinyanhuo upregulate the expression of *IL-4*, while Yinyanghuo upregulates the expression of *IL-4* and *IL-10*. The role of the inflammatory markers was illustrated in [Supplementary Figure S1](#).

This study integrates the methodical nature of dry experiments and the authenticity of wet experiments, systematically analyses the mechanism of action of WSYR in the treatment of infertility, and provides theoretical support and evidence for the clinical application of WSYR. However, the interaction of active compounds in WSYR and therapeutic targets needs to be further validated by *in vitro* experiments. Besides, since infertility is a complex disease, animal experiments are necessary to verify the regulatory role of WSYR on hormonal regulation and inflammatory responses *in vivo*.

## Data availability statement

The datasets presented in this study can be found in online repositories. The names of the repository/repositories and accession number(s) can be found below: NCBI GEO, GSE202626.

## Author contributions

Conceptualization: LX and SZ. Transcriptome experiment: WH and LQ. Data analysis and visualization: XZ and SZ. Validation: CM and WG. Project administration: HD and HL. Writing original draft: LX, SZ and DZ.

## Funding

This work was supported by National Key Research and Development Plan (2018YFC1704300) and National Natural Science Foundation of China (61927819).

## References

- An, R., Li, B., You, L. S., and Wang, X. H. (2015). Improvement of kidney yang syndrome by icariin through regulating hypothalamus-pituitary-adrenal Axis. *Chin. J. Integr. Med.* 21 (10), 765–771. doi:10.1007/s11655-015-2063-z
- Anders, S., and Huber, W. (2010). Differential expression analysis for sequence count data. *Genome Biol.* 11 (10), R106. doi:10.1186/gb-2010-11-10-r106
- Bindea, G., Mlecnik, B., Hackl, H., Charoentong, P., Tosolini, M., Kirilovsky, A., et al. (2009). Cluego: A cytoscape plug-in to decipher functionally grouped gene ontology and pathway annotation networks. *Bioinformatics* 25 (8), 1091–1093. doi:10.1093/bioinformatics/btp101
- Boivin, J., Bunting, L., Collins, J. A., and Nygren, K. G. (2007). International estimates of infertility prevalence and treatment-seeking: Potential need and demand for infertility medical care. *Hum. Reprod. (Oxf)* 22 (6), 1506–1512. doi:10.1093/humrep/dem046
- Borrelli, G. M., Carvalho, K. I., Kallas, E. G., Mechtersner, S., Barakat, E. C., Abrão, M. S., et al. (2013). Chemokines in the pathogenesis of endometriosis and infertility. *J. Reprod. Immunol.* 98 (1–2), 1–9. doi:10.1016/j.jri.2013.03.003
- Cao, Y. Q., Ma, S. M., Fan, X. L., Lin, Y. X., Chen, M. X., Song, X. A., et al. (2008). Epimedium alleviates chemotherapy-induced damage to the ultrastructure and function of rat epididymides. *Natl. J. Androl.* 14 (2), 184–188. Chinese.
- Chatterjee, P., Chiasson, V. L., Bounds, K. R., and Mitchell, B. M. (2014). Regulation of the anti-inflammatory cytokines interleukin-4 and interleukin-10 during pregnancy. *Front. Immunol.* 5, 253. doi:10.3389/fimmu.2014.00253
- D'Cruz, O. J., Vassilev, A. O., and Uckun, F. M. (2001). Members of the janus kinase/signal transducers and activators of transcription (JAK/STAT) pathway are present and active in human sperm. *Fertil. Steril.* 76 (2), 258–266. doi:10.1016/s0015-0282(01)01896-9
- Hitchler, M. J., and Domann, F. E. (2021). The epigenetic and morphogenetic effects of molecular oxygen and its derived reactive species in development. *Free Radic. Biol. Med.* 170, 70–84. doi:10.1016/j.freeradbiomed.2021.01.008
- Huang, S. T., and Chen, A. P. (2008). Traditional Chinese medicine and infertility. *Curr. Opin. Obstet. Gynecol.* 20 (3), 211–215. doi:10.1097/GCO.0b013e3282f88e22
- Hughes, C., and Murphy, B. D. (2021). Nuclear receptors: Key regulators of somatic cell functions in the ovulatory process. *Mol. Asp. Med.* 78, 100937. doi:10.1016/j.mam.2020.100937
- Jeong, J. C., Lee, B. T., Yoon, C. H., Kim, H. M., and Kim, C. H. (2005). Effects of drynaria rhizoma on the proliferation of human bone cells and the

## Conflict of interest

The authors declare that the research was conducted in the absence of any commercial or financial relationships that could be construed as a potential conflict of interest.

## Publisher's note

All claims expressed in this article are solely those of the authors and do not necessarily represent those of their affiliated organizations, or those of the publisher, the editors and the reviewers. Any product that may be evaluated in this article, or claim that may be made by its manufacturer, is not guaranteed or endorsed by the publisher.

## Supplementary Material

The Supplementary Material for this article can be found online at: <https://www.frontiersin.org/articles/10.3389/fphar.2022.917544/full#supplementary-material>

- immunomodulatory activity. *Pharmacol. Res.* 51 (2), 125–136. doi:10.1016/j.phrs.2004.06.005
- Jiang, Z., Wang, J., Li, X., and Zhang, X. (2016). Echinacoside and Cistanche tubulosa (schenk) R. Wight ameliorate bisphenol A-induced testicular and sperm damage in rats through gonad Axis regulated steroidogenic enzymes. *J. Ethnopharmacol.* 193, 321–328. doi:10.1016/j.jep.2016.07.033
- Jiang, Z., Zhou, B., Li, X., Kirby, G. M., and Zhang, X. (2018). Echinacoside increases sperm quantity in rats by targeting the hypothalamic androgen receptor. *Sci. Rep.* 8 (1), 3839. doi:10.1038/s41598-018-22211-1
- Kato, J. (1989). Arachidonic acid as a possible modulator of estrogen, progesterone, androgen, and glucocorticoid receptors in the central and peripheral tissues. *J. Steroid Biochem.* 34 (1–6), 219–227. doi:10.1016/0022-4731(89)90085-x
- Kitaya, K., and Yasuo, T. (2010). Aberrant expression of selectin E, CXCL1, and CXCL13 in chronic endometritis. *Mod. Pathol.* 23 (8), 1136–1146. doi:10.1038/modpathol.2010.98
- Kuiper, G. G., Enmark, E., Peltö-Huikko, M., Nilsson, S., and Gustafsson, J. A. (1996). Cloning of a novel receptor expressed in rat prostate and ovary. *Proc. Natl. Acad. Sci. U. S. A.* 93 (12), 5925–5930. doi:10.1073/pnas.93.12.5925
- Li, H., Zhou, H., Wang, D., Qiu, J., Zhou, Y., Li, X., et al. (2012). Versatile pathway-centric approach based on high-throughput sequencing to anticancer drug Discovery. *Proc. Natl. Acad. Sci. U. S. A.* 109 (12), 4609–4614. doi:10.1073/pnas.1200305109
- Li, S., and Zhang, B. (2013). Traditional Chinese medicine network pharmacology: Theory, methodology and application. *Chin. J. Nat. Med.* 11 (2), 110–120. doi:10.1016/S1875-5364(13)60037-0
- Mascarenhas, M. N., Flaxman, S. R., Boerma, T., Vanderpoel, S., and Stevens, G. A. (2012). National, regional, and global trends in infertility prevalence since 1990: A systematic analysis of 277 health surveys. *PLoS Med.* 9 (12), e1001356. doi:10.1371/journal.pmed.1001356
- Messerlian, C., and Gaskins, A. J. (2017). Epidemiologic approaches for studying assisted reproductive technologies: Design, methods, analysis, and interpretation. *Curr. Epidemiol. Rep.* 4 (2), 124–132. doi:10.1007/s40471-017-0105-0
- Nahid, L., and Sirous, K. (2012). Comparison of the effects of letrozole and Clomiphene citrate for ovulation induction in infertile women with polycystic ovary syndrome. *Minerva Ginecol.* 64 (3), 253–258.
- Nolan, T., Hands, R. E., and Bustin, S. A. (2006). Quantification of mRNA using real-time RT-PCR. *Nat. Protoc.* 1 (3), 1559–1582. doi:10.1038/nprot.2006.236

- Pelletier, G., and El-Alfy, M. (2000). Immunocytochemical localization of estrogen receptors alpha and beta in the human reproductive organs. *J. Clin. Endocrinol. Metab.* 85 (12), 4835–4840. doi:10.1210/jcem.85.12.7029
- Petraglia, F., Serour, G. I., and Chapron, C. (2013). The changing prevalence of infertility. *Int. J. Gynaecol. Obstet.* 123, S4–S8. doi:10.1016/j.ijgo.2013.09.005
- Quaas, A. M., and Legro, R. S. (2019). Pharmacology of medications used for ovarian stimulation. *Best. Pract. Res. Clin. Endocrinol. Metab.* 33 (1), 21–33. doi:10.1016/j.beem.2018.10.002
- Reichman, D., and Rosenwaks, Z. (2017). The impact of genetic steroid disorders on human fertility. *J. Steroid Biochem. Mol. Biol.* 165, 131–136. doi:10.1016/j.jsbmb.2016.04.014
- Revelli, A., Casano, S., Salvagno, F., and Delle Piane, L. (2011). Milder is better? Advantages and disadvantages of "mild" ovarian stimulation for human *in vitro* fertilization. *Reprod. Biol. Endocrinol.* 9, 25. doi:10.1186/1477-7827-9-25
- Riese, D. J., and Cullum, R. L. (2014). Epipegulin: Roles in normal physiology and cancer. *Semin. Cell Dev. Biol.* 28, 49–56. doi:10.1016/j.semcdb.2014.03.005
- Roth, L. W., Ryan, A. R., and Meacham, R. B. (2013). Clomiphene citrate in the management of male infertility. *Semin. Reprod. Med.* 31 (4), 245–250. doi:10.1055/s-0033-1345271
- Ru, J., Li, P., Wang, J., Zhou, W., Li, B., Huang, C., et al. (2014). Tcmisp: A database of systems pharmacology for drug Discovery from herbal medicines. *J. Cheminform.* 6, 13. doi:10.1186/1758-2946-6-13
- Rutstein, S. O., and Shah, I. H. (2004). "Infecundity, infertility, and childlessness in developing countries," in *DHS comparative reports No. 9* (Calverton, Maryland, USA: ORC Macro and the World Health Organization).
- Ryter, S. W. (2019). Heme oxygenase-1/carbon monoxide as modulators of autophagy and inflammation. *Arch. Biochem. Biophys.* 678, 108186. doi:10.1016/j.abb.2019.108186
- Saba, E., Lee, Y. Y., Kim, M., Hyun, S. H., Park, C. K., Son, E., et al. (2020). A novel herbal formulation consisting of red ginseng extract and Epimedium koreanum nakai-attenuated dextran sulfate sodium-induced colitis in mice. *J. Ginseng Res.* 44 (6), 833–842. doi:10.1016/j.jgr.2020.02.003
- Scott, J. S., Bailey, A., Davies, R. D., Degorce, S. L., MacFaul, P. A., Gingell, H., et al. (2015). Tetrahydroisoquinoline phenols: Selective estrogen receptor downregulator antagonists with oral bioavailability in rat. *ACS Med. Chem. Lett.* 7 (1), 94–99. doi:10.1021/acsmedchemlett.5b00413
- Scovell, J. M., and Khera, M. (2018). Testosterone replacement therapy versus Clomiphene citrate in the young hypogonadal male. *Eur. Urol. Focus* 4 (3), 321–323. doi:10.1016/j.euf.2018.07.033
- Shannon, P., Markiel, A., Ozier, O., Baliga, N. S., Wang, J. T., Ramage, D., et al. (2003). Cytoscape: A software environment for integrated models of biomolecular interaction networks. *Genome Res.* 13 (11), 2498–2504. doi:10.1101/gr.1239303
- Shao, W., Li, S., Li, L., Lin, K., Liu, X., Wang, H., et al. (2019). Chemical genomics reveals inhibition of breast cancer lung metastasis by ponatinib via C-jun. *Protein Cell* 10 (3), 161–177. doi:10.1007/s13238-018-0533-8
- Shiau, A. K., Barstad, D., Radek, J. T., Meyers, M. J., Nettles, K. W., Katzenellenbogen, B. S., et al. (2002). Structural characterization of a subtype-selective ligand reveals a novel mode of estrogen receptor antagonism. *Nat. Struct. Biol.* 9 (5), 359–364. doi:10.1038/nsb787
- Szczuko, M., Kikut, J., Komorniak, N., Bilicki, J., Celewicz, Z., Ziętek, M., et al. (2020). The role of arachidonic and linoleic acid derivatives in pathological pregnancies and the human reproduction process. *Int. J. Mol. Sci.* 21 (24), 9628. doi:10.3390/ijms21249628
- Tang, Z. R., Zhang, R., Lian, Z. X., Deng, S. L., and Yu, K. (2019). Estrogen-receptor expression and function in female reproductive disease. *Cells* 8 (10), 1123. doi:10.3390/cells8101123
- Tong, J. S., Zhang, Q. H., Huang, X., Fu, X. Q., Qi, S. T., Wang, Y. P., et al. (2011). Icaritin causes sustained ERK1/2 activation and induces apoptosis in human endometrial cancer cells. *PloS one* 6 (3), e16781. doi:10.1371/journal.pone.0016781
- Vander Borgh, M., and Wyns, C. (2018). Fertility and infertility: Definition and epidemiology. *Clin. Biochem.* 62, 2–10. doi:10.1016/j.clinbiochem.2018.03.012
- Wan, Y., and Qi, C. (2017). The mechanism of oxidative stress in infertility and the research progress of Chinese and western medicine treatment. *Hebei J. Traditional Chin. Med.* 39 (5), 788–796. Chinese.
- Wang, X., Zhen, L., Zhang, G., Wong, M. S., Qin, L., Yao, X., et al. (2011). Osteogenic effects of flavonoid aglycones from an osteoprotective fraction of *Drynaria fortuneana* *in vitro* efficacy study. *Phytomedicine* 18 (10), 868–872. doi:10.1016/j.phymed.2011.01.022
- Wang, M., Wang, Q., Du, Y., Jiang, H., and Zhang, X. (2020). Vitamins combined with traditional Chinese medicine for male infertility: A systematic review and meta-analysis. *Andrology* 8 (5), 1038–1050. doi:10.1111/andr.12787
- Warinrak, C., Wu, J. T., Hsu, W. L., Liao, J. W., and Cheng, F. P. (2015). Expression of matrix metalloproteinases (MMP-2, MMP-9) and their inhibitors (TIMP-1, TIMP-2) in canine testis, epididymis and semen. *Reprod. Domest. Anim.* 50 (1), 48–57. doi:10.1111/rda.12448
- Wu, Z., Yao, H., Xu, H., Wang, Y., Hu, W., Lou, G., et al. (2020). Inhibition of enos by L-NAME resulting in rat hind limb developmental defects through PFKFB3 mediated angiogenic pathway. *Sci. Rep.* 10 (1), 16754. doi:10.1038/s41598-020-74011-1
- Xue, C., Wang, L., Li, X., Shi, Q., Wang, K., Wang, Y., et al. (2021). Wenshenyang recipe and its disassembled recipes promote the proliferation and differentiation of mouse limb bud stem cells through the TGF- $\beta$  signaling pathway. *Chin. J. Integr. Traditional Chin. West. Med.* 41 (9), 1–7. Chinese.



## OPEN ACCESS

## EDITED BY

Ren-You Gan,  
Institute of Urban Agriculture (CAAS),  
China

## REVIEWED BY

Xiansheng Liu,  
Huazhong University of Science and  
Technology, China  
Dharmani Devi Murugan,  
University of Malaya, Malaysia

## \*CORRESPONDENCE

Bin Liu,  
liubin@csu.edu.cn

<sup>†</sup>These authors have contributed equally  
to this work

## SPECIALTY SECTION

This article was submitted to  
Ethnopharmacology,  
a section of the journal  
Frontiers in Pharmacology

RECEIVED 25 June 2022

ACCEPTED 27 July 2022

PUBLISHED 17 August 2022

## CITATION

Xiao X, Luo F, Fu M, Jiang Y, Liu S and  
Liu B (2022), Evaluating the therapeutic  
role of selected active compounds in  
*Plumula Nelumbinis* on pulmonary  
hypertension via network  
pharmacology and  
experimental analysis.  
*Front. Pharmacol.* 13:977921.  
doi: 10.3389/fphar.2022.977921

## COPYRIGHT

© 2022 Xiao, Luo, Fu, Jiang, Liu and Liu.  
This is an open-access article  
distributed under the terms of the  
[Creative Commons Attribution License](https://creativecommons.org/licenses/by/4.0/)  
(CC BY). The use, distribution or  
reproduction in other forums is  
permitted, provided the original  
author(s) and the copyright owner(s) are  
credited and that the original  
publication in this journal is cited, in  
accordance with accepted academic  
practice. No use, distribution or  
reproduction is permitted which does  
not comply with these terms.

# Evaluating the therapeutic role of selected active compounds in *Plumula Nelumbinis* on pulmonary hypertension via network pharmacology and experimental analysis

Xinghua Xiao<sup>1,2,3†</sup>, Fangmei Luo<sup>4†</sup>, Minyi Fu<sup>1,2,3</sup>,  
Yueping Jiang<sup>1,2,3</sup>, Shao Liu<sup>1,2,3</sup> and Bin Liu<sup>1,2,3\*</sup>

<sup>1</sup>Department of Pharmacy, Xiangya Hospital, Central South University, Changsha, China, <sup>2</sup>Institute for Rational and Safe Medication Practices, National Clinical Research Center for Geriatric Disorders, Xiangya Hospital, Central South University, Changsha, China, <sup>3</sup>The Hunan Institute of Pharmacy Practice and Clinical Research, Xiangya Hospital, Central South University, Changsha, China, <sup>4</sup>Department of Pharmacy, Hunan Children's Hospital, Changsha, China

Excessive proliferation and migration of pulmonary artery smooth muscle cells (PASMCs) are critical factors leading to vascular remodeling in pulmonary hypertension (PH). This study aimed to explore the effect and potential mechanism of *Plumula Nelumbinis* on PH by using network pharmacology and experimental analysis. Network pharmacology and molecular docking results indicated that the potential active components of *Plumula Nelumbinis* against PH were mainly alkaloid compounds, including neferine, liensinine, and isoliensinine. Subsequently, by constructing a Su5416 plus hypoxia (SuHx)-induced PH rat model, we found that the total alkaloids of *Plumula Nelumbinis* (TAPN) can reduce the right ventricular systolic pressure, delay the process of pulmonary vascular and right ventricular remodeling, and improve the right heart function in PH rats. In addition, TAPN can effectively reverse the upregulation of collagen1, collagen3, MMP2, MMP9, PCNA, PIM1, and p-SRC protein expression in lung tissue of PH rats. Finally, by constructing a hypoxia-induced PASMCs proliferation and migration model, we further found that TAPN, neferine, liensinine, and isoliensinine could inhibit the proliferation and migration of PASMCs induced by hypoxia; reverse the upregulation of collagen1, collagen3, MMP2, MMP9, PCNA, PIM1 and p-SRC protein expression in PASMCs. Based on these observations, we conclude that the alkaloid compounds extracted from *Plumula Nelumbinis* (such as neferine, liensinine, and isoliensinine) can inhibit the abnormal proliferation and migration of PASMCs by regulating the expression of p-SRC and PIM1, thereby delaying the progression of PH.

## KEYWORDS

pulmonary hypertension, network pharmacology, *Plumula Nelumbinis*, alkaloids, PASMCs proliferation, PASMCs migration



## Introduction

Pulmonary hypertension (PH) is a malignant cardiopulmonary vascular disease characterized by persistently elevated pulmonary arterial pressure (Poch and Mandel, 2021; Walter, 2021). Pulmonary vascular remodeling is the most basic pathological feature of PH, involving processes such as the excessive proliferation and migration of pulmonary artery smooth muscle cells (PASMCs), endothelial dysfunction, and extracellular matrix deposition (Shimoda, 2020). Currently approved drugs for the treatment of PH mainly target three molecular pathways related to the pathogenesis of PH: prostacyclins and prostacyclin-receptor agonists (such as iloprost, selexipag, and treprostinil), endothelin receptor antagonists (such as ambrisentan, bosentan, and macitentan), and nitric oxide pathway agents (such as sildenafil and tadalafil) (Poch and Mandel, 2021). However, the above existing drug treatment usually only improves symptoms and cannot achieve the purpose of a radical cure. Therefore, finding more safe and effective drugs to prevent and treat PH is urgent.

Network pharmacology is a useful bioinformatics tool to reveal the complex biological network relationship between drugs, targets, and diseases by using high-throughput screening, network visualization, and analysis techniques (Nogales et al., 2021). In recent years, with the rise of network pharmacology, systematic research on the underlying mechanisms of traditional Chinese medicine (TCM) has been widely carried out, providing a foundation for the modernization of TCM (An et al., 2021). Accumulating evidence suggests that active ingredients derived from TCM, such as magnolol (Fu et al., 2021), magnesium lithospermate B (Li et al., 2019b), and resveratrol (Mirhadi et al., 2021), could delay the process of pulmonary vascular and right ventricular remodeling during PH, which brings a promising future for the prevention and treatment of PH.

*Plumula Nelumbinis*, a TCM derived from the dried young leaves and radicles of the mature seeds of the water lily plant *Nelumbo nucifera Gaertn.*, could be used for medicine and food. It has multiple pharmacological activities such as cardiovascular protection, anti-oxidation, anti-inflammatory, and anti-tumor (Chen et al., 2021). Recent studies have shown that alkaloids from *Plumula Nelumbinis* could attenuate vascular remodeling in spontaneously hypertensive rats (Li Q et al., 2019; Wicha et al., 2020). However, its effect on vascular remodeling in PH is still unclear.

In this study, we first screened out the main active components and targets of *Plumula Nelumbinis* against PH through a network pharmacology strategy and then performed GO function and KEGG pathway enrichment analysis. Next, the interaction between the core compounds and targets was simulated by molecular

docking. Finally, by establishing a Su5416 plus hypoxia (SuHx) induced PH rats model and a hypoxia-induced PASMCs proliferation model, the prediction results were experimentally verified from *in vivo* and *in vitro* levels. The overall design of this study is shown in Figure 1. The results of this study can further clarify the mechanism of *Plumula Nelumbinis* in treating PH and provide a basis for developing novel anti-PH drugs.

## Materials and methods

### Identification of the main active ingredient of *Plumula Nelumbinis*

The active ingredients of *Plumula Nelumbinis* were obtained from the TCMSP database (Traditional Chinese Medicine Systems Pharmacology and Analysis Platform, <https://old.tcmsp-e.com/tcmsp.php>) (Ru et al., 2014) and related literature (Jiang et al., 2018b; Chen et al., 2021) by using search terms such as “*Plumula Nelumbinis*” or “*Hindu Lotus Plumule*”. The chemical information (such as PubChem CID, 3D conformer, and canonical SMILES) and pharmacokinetic parameters of these active ingredients were collected from the PubChem (<https://pubchem.ncbi.nlm.nih.gov/>) and SwissADME (<http://www.swissadme.ch/>) database. The main active ingredients of *Plumula Nelumbinis* were screened according to the following conditions as described in the previous study (Daina et al., 2017): 1) The gastrointestinal absorption coefficient was set to High, which indicates that these compounds have good oral bioavailability and could be effectively absorbed; 2) The flexibility was evaluated by rotatable bonds: rotatable bonds  $\leq 10$ ; 3) The polarity was evaluated by topological polar surface area (TPSA):  $20 \text{ \AA}^2 \leq \text{TPSA} \leq 140 \text{ \AA}^2$ ; 4) The drug-likeness ability was evaluated by five different rule-based filters (Lipinski, Chose, Veber, Egan, and Muegge filter) and the bioavailability score: the bioavailability score  $\geq 10\%$ . The potential targets of the main active ingredients of *Plumula Nelumbinis* were predicted through the PharmMapper database (<http://www.lilab-ecust.cn/pharmmapper/submitfile.html>, Normalized Fit Score  $\geq 0.70$ ) (Wang et al., 2017). The potential targets were identified and normalized through the UniProt database (<https://www.uniprot.org/>).

### Identification of PH-Related targets

The PH-related targets were obtained from GeneCards (<https://www.genecards.org/>), Online Mendelian Inheritance in Man (OMIM, <https://omim.org/>) (Amberger et al., 2019), DisGeNET (<https://www.disgenet.org/>) (Pinero et al., 2021),



and Therapeutic Target Database (TTD, <http://db.idrblab.net/ttd/>) (Zhou et al., 2021) by using search terms such as “pulmonary hypertension” or “pulmonary arterial hypertension” (accessed on 21 October 2021). The above targets were summarized, de-duplicated, and then identified as PH-related targets.

## Construction of drug-target-disease and protein-protein interaction network

The intersection between the potential targets of *Plumula Nelumbinis* and the PH-related targets was obtained by the VENNY online tool (<https://bioinfo.gp.cnb.csic.es/tools/venny/index.html>). The overlapping targets were considered as the potential therapeutic targets of *Plumula Nelumbinis* against PH. The protein interaction relationships of the overlapped targets were acquired through the STRING database (<https://cn.string-db.org/>, Version 11.5) (Szklarczyk et al., 2017). In brief, the overlapped targets were uploaded to the STRING database, and the species was limited to “*Homo sapiens*”. Finally, the obtained PPI network information of the intersection targets was led to the Cytoscape software for visual analysis (<https://cytoscape.org/>, Version 3.8.2) (Shannon et al., 2003).

## GO and KEGG pathway enrichment analysis

The Metascape online tool (<https://metascape.org/>) was applied for GO and KEGG enrichment analysis (Zhou et al., 2019). Briefly, the potential therapeutic targets of *Plumula Nelumbinis* against PH were uploaded to the Metascape platform. The filter thresholds of GO function and KEGG pathway analysis were set as the following conditions: 1) the species was set as “*Homo sapiens*”; 2) the minimum overlap value was set to 3; 3) the *P* cutoff value was set to 0.01; 4) the minimum enrichment value was set to 1.5. The GO and KEGG enrichment analysis results were visualized through the ggplot2 package (Version 3.3.5) of the R language (Version 4.0.2) (Wickham et al., 2016).

## Construction of the drug-target-pathway network

The main component-target-pathway enrichment network was visualized using the Cytoscape software (Shannon et al., 2003). The supporting tool “Network Analyzer” of Cytoscape software was used to obtain the network topology parameters (such as degree, betweenness, and closeness) between the

effective ingredients and targets. The top-ranked compounds and targets based on degree, betweenness, and closeness were defined as the core compounds and targets. These core compounds and targets were subsequently prepared for molecular docking.

## Molecular docking

The binding situation of core compounds and targets was analyzed using AutoDock Vina software (<https://vina.scripps.edu/>, Version 1.1.2). Firstly, the three-dimensional crystal structures of the top 10 core target proteins were obtained from the Protein Data Bank (PDB, <https://www.pdbus.org/>) (Burley et al., 2021). The PDB ID of these target proteins are as follows: proto-oncogene tyrosine-protein kinase Src (SRC, PDB ID: 2SRC); serine/threonine-protein kinase PIM-1 (PIM1, PDBID:1XWS); transthyretin (TTR, PDB ID:1BZE); prothrombin (F2, PDB ID:2CN0); estrogen receptor- $\alpha$  (ESR1, PDB ID:5FQV); cyclophilin A (PPIA, PDB ID: 5LUD); mitogen-activated protein kinase 14 (MAPK14, PDB ID:2FST); phenylalanine-4-hydroxylase (PAH, PDB ID:5FII);  $\beta$ -secretase 1 (BACE1, PDB ID: 1TQF); endothelial nitric oxide synthase (NOS3, PDB ID:1M9M). Secondly, the 3D structures of the core compounds were obtained from the PubChem database (<https://pubchem.ncbi.nlm.nih.gov/>) and then were converted into PDB file format by using OPEN Babel software (<http://openbabel.org/>, Version 2.4.1) (O’Boyle et al., 2011). Finally, the molecular docking of core compounds and targets was performed using AutoDock Vina software (Trott and Olson, 2010). The binding energy volcano map was drawn through the pheatmap package (Version 1.0.12) of the R language. At the same time, the molecular docking results were visualized using the PyMol software (Version 2.2.0). The binding affinity value  $<0$  kcal/mol indicates that the compounds effectively bind to the targets.

## Chemicals and reagents

The separation, extraction, and identification of the total alkaloids from *Plumula Nelumbinis* (TAPN), neferine, liensinine, and isoliensinine were performed as described in our previous study (Liu et al., 2009; Jiang et al., 2018a; Chen et al., 2020). Dimethyl sulfoxide (DMSO) was purchased from Sigma-Aldrich (C6164, Darmstadt, Germany). High-glucose Dulbecco’s modified Eagle’s medium (DMEM) and fetal bovine serum (FBS) were purchased from Gibco (Thermo Fisher Scientific). Primary antibodies against collagen1, collagen3, MMP2, MMP9, PCNA, PIM1, p-SRC, and SRC were purchased from Beyotime (Shanghai, China).  $\alpha$ -Tubulin was purchased from Santa Cruz Biotechnology (CA, United States).

## Establishment of the SU5416/hypoxia-induced PH rat model

To validate the predicted results of network pharmacology and molecular docking, we further evaluated the therapeutic effect of TAPN on PH from the *in vivo* level. The initial doses of TAPN *in vivo* (5 mg/kg/d and 10 mg/kg/d) were determined based on previous studies (Li Q et al., 2019). SuHx-induced PH rat model was constructed as described in the previous study (Legchenko et al., 2018). SD rats (~160 g) were randomly divided into the following 4 groups (n = 12 per group): 1) the normoxia group, rats were given the same volume of vehicle (a mixture with 5% DMSO, 30% PEG300, 5% Tween-80, and 60% saline) and then placed in the normoxic environment for 4 weeks; 2) the SuHx group, rats were given a single subcutaneous injection of Su5416 (20 mg/kg, S832952, Macklin, Shanghai, China) and then placed immediately into a hypoxic chamber (10% O<sub>2</sub>) for 4 weeks; 3) the SuHx plus TAPN (L) group (low dose, 5 mg/kg/d); 4) and the SuHx plus TAPN (H) group (high dose, 10 mg/kg/d). After the injection of Su5416 plus hypoxia for 2 weeks, the rats were administered with TAPN at 5 or 10 mg/kg (i.g.) once a day for 2 weeks. After 4 weeks of SuHx treatment, the cardiac function of rats was detected by Doppler echocardiography. The right ventricular systolic pressure (RVSP) in rats was measured by the right heart catheterization. The Fulton index (RV/LV + IVS) and the ratio of RV weight to body weight were used to assess the degree of right ventricular remodeling. The lung tissue of rats was collected for subsequent molecular biology and morphological analysis.

## Morphological analysis for lung tissue

Hematoxylin-eosin (HE), Masson, and immunofluorescence staining were used to evaluate the morphological changes in lung tissues. The detailed procedures for morphological analysis were performed as described in our previous studies (Wang et al., 2019; Xiao et al., 2022). The proportion of vessel wall thickness (ratio of wall thickness to vessel diameter, WT%) and the proportion of vessel wall area (ratio of wall area to total vessel area, WA%) were used to measure the severity of pulmonary vascular remodeling. In addition,  $\alpha$ -SMA immunofluorescence staining was used to assess the degree of pulmonary vascular media thickening.

## Western blotting

The lung tissues or PSMCs were homogenized in RIPA lysis buffer (Beyotime, Shanghai, China) with a protease and phosphatase inhibitor cocktail (Beyotime, Shanghai, China). Samples containing 20–40  $\mu$ g of protein were separated by 10% SDS-PAGE gel and then transferred to polyvinylidene

fluoride (PVDF) membranes (G.E. Healthcare, Germany). After blocking with 5% skim milk or 5% BSA, the PVDF membranes were incubated overnight on a shaker at 4°C with the following primary antibodies: collagen1 (AF6524, 1:1,000, Beyotime), collagen3 (AF6531, 1:1,000, Beyotime), MMP2 (AF0234, 1:1,000, Beyotime), MMP9 (AF5234, 1:1,000, Beyotime), PCNA (AF0261, 1:1,000, Beyotime), SRC (AF1831, 1:1,000, Beyotime), p-SRC (AF5923, 1:1,000, Beyotime), PIM1 (AF1807, 1:1,000, Beyotime), eNOS (AF6792, 1:1,000, Beyotime), and  $\alpha$ -tubulin (sc-5286, 1:500, Santa Cruz). After incubation with horseradish peroxidase (HRP)-linked secondary antibody (Beyotime, Shanghai, China), the protein bands were imaged through Molecular Imager ChemiDoc XRS System (Bio-Rad, Philadelphia, USA). Densitometric quantification was performed by ImageJ (NIH, USA). The  $\alpha$ -tubulin served as a loading control.

## Cell experiments

To further clarify the underlying mechanism of TAPN against PH, we constructed a hypoxia-induced proliferation and migration model of PSMCs. The initial doses of TAPN, neferine, liensinine, and isoliensinine were determined based on previous studies (Jun et al., 2016). The isolation of PSMCs from pulmonary arteries of rats and the hypoxia-induced PSMCs proliferation model were performed as described in our previous study (Li et al., 2019a; Xiao et al., 2022). PSMCs at passages 3 to 6 were used for cell identification and the subsequent experiments. In order to evaluate the effect of the screened main active components of *Plumula Nelumbinis* on the proliferation of PSMCs induced by hypoxia, the cell experiments were grouped as follows: 1) the normoxia group, PSMCs were cultured in a normoxic incubator (21% O<sub>2</sub>) for 48 h; 2) the hypoxia group, PSMCs were cultured in a hypoxia incubator (3% O<sub>2</sub>) for 48 h; 3) the hypoxia plus drug intervention group, PSMCs were pretreated with different doses of drugs for 1 h and then treated with hypoxia for 48 h, the initial drug doses for neferine, liensinine, and isoliensinine were set at 1, 2.5, 5, 10, and 20  $\mu$ M, respectively, while the initial doses of TAPN were 5, 10, 25, 50 and 100  $\mu$ g/ml, respectively. 4) the hypoxia plus vehicle group, PSMCs were pretreated with an equal volume of vehicle (DMSO, volume  $\leq$  1/1,000 of the total medium) for 1 h and then treated with hypoxia for 48 h. At the end of the experiments, the PSMCs were collected for cell proliferation detection and molecular analysis.

## Cell proliferation assay

Cell proliferation was detected by CCK-8 Assay Kit (C6005M, Uelandy, Suzhou, China) and EdU Assay Kit (C6017L, Uelandy, Suzhou, China) according to the protocol provided by the manufacturer. For the CCK-8



assay, PSMCs were seeded at 96-well plates and then starved with a high-glucose DMEM culture medium containing 1% fetal bovine serum (FBS) for 24 h. After drug and hypoxia intervention, the CCK-8 solution (10  $\mu$ L) was added to each well and then incubated in the dark for 2 h in the 37°C cell incubator. The optical density (OD) value was detected at 450 nm with SpectraMax 190 (Molecular Devices, California, USA).

For the EdU array, PSMCs were inoculated into the 96-well plates and synchronized for 24 h when cell density reached 50%. After drug and hypoxia intervention, the EdU solution (50  $\mu$ M) was added to each well and then incubated for 2 h in the 37°C cell incubator. After fixation with 4% (w/v) paraformaldehyde and treatment with 0.5% Triton X-100 for 20 min, EdU working solution and Hoechst 33,342 were added for staining, respectively. The number of EdU positive cells was observed under a fluorescence microscope, and the positive cells in each group were counted and analyzed by ImageJ (Version 1.46).

## Cell migration assay

Cell migration ability was measured by Transwell assay as described in our previous studies (Wang et al., 2019; Xiao et al., 2022). In brief,  $1 \times 10^5$  PSMCs were seeded into the upper chamber of the 24-well Transwell plate (3,422, Corning, NY, USA). After serum starvation treatment for 12 h, the DMEM culture medium containing 20% FBS was added into the lower chamber, and then the cells were treated with hypoxia and drugs for 48 h. Cells attached to the upper surface were removed with a cotton swab, while the migrated cells on the lower surface were incubated in 4% paraformaldehyde and 0.1% crystal violet solution (C0121, Beyotime, Shanghai, China). The number of migrated cells was observed and counted under an optical microscope.

## Statistical analysis

All quantitative data were presented as the means  $\pm$  standard error of mean (S.E.M) and analyzed using SPSS 20.0 software (SPSS, Chicago, United States). One-way analysis of variance (ANOVA) was used to compare the means among different groups.  $p \leq 0.05$  was considered statistically significant.

## Results

### Screening of main active compounds from *Plumula Nelumbinis*

More than 100 compounds have been isolated and identified from the *Plumula Nelumbinis*, including alkaloids (such as

neferine, liensinine, and isoliensinine), flavonoids (such as quercetin, rutin, and kaempferol), volatile oil, and polysaccharides. A total of 92 possible active compounds were initially screened by matching with information from the PubChem database. Then the pharmacokinetic parameters of those compounds were obtained from the SwissADME database. Next, we conducted a secondary screening of those compounds based on the gastrointestinal absorption rate, flexibility, polarity, and drug-likeness. A total of 46 main active ingredients of *Plumula Nelumbinis* were finally obtained, including 30 alkaloids, 7 flavonoids, and 9 other compounds (volatile oil or polysaccharides). The above 46 compounds are numbered LZX1-LZX46; relevant information is shown in Table 1.

### Identification of potential targets of *Plumula Nelumbinis* against PH

The potential targets of the main active ingredients were obtained from the PharmMapper database. LZX46 (Propanethial S-oxide) was excluded because the predicted target of LZX46 was not available in the PharmMapper database. A total of 173 potential targets for the other 45 compounds were obtained after deduplication. The drug-target network is shown in Figure 2A.

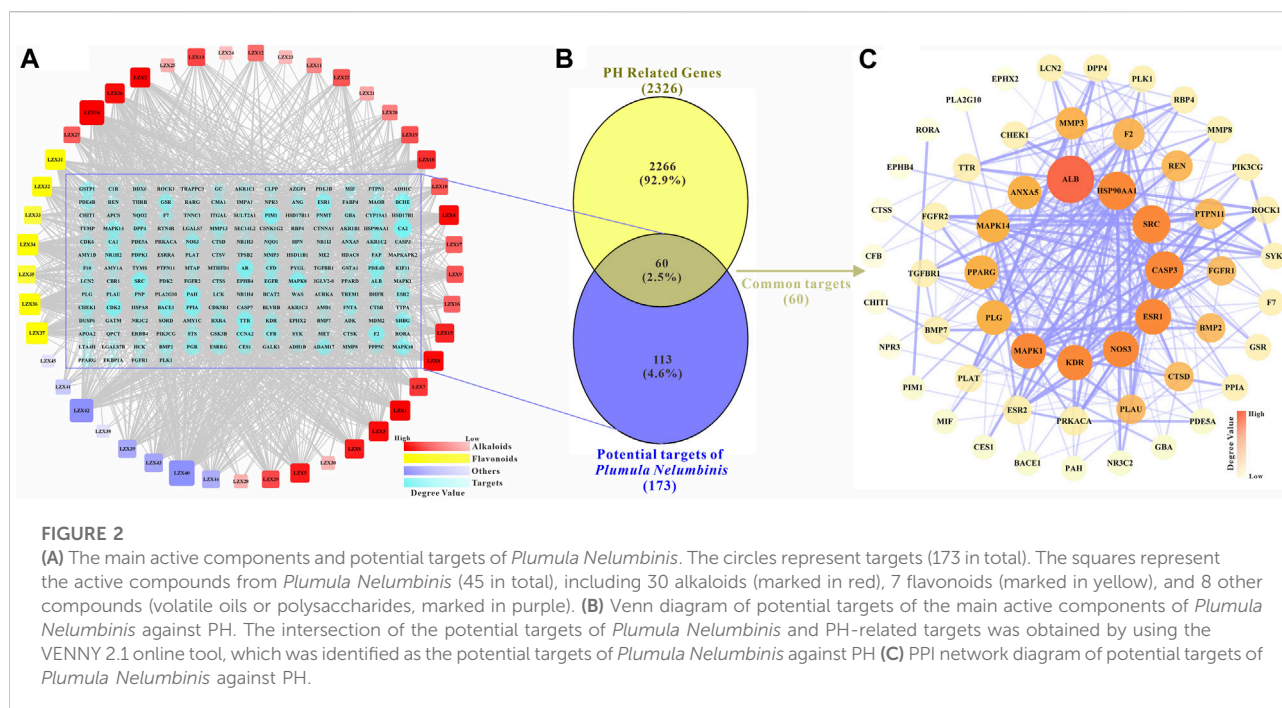
After summarizing and de-duplicating the targets, a total of 2326 PH-related targets were collected from GeneCards, OMIM, DisGeNET, and TTD databases. As shown in Figure 2B, 60 common targets were obtained after the intersection of *Plumula Nelumbinis*-related and PH-related targets. These common targets were identified as potential therapeutic targets of *Plumula Nelumbinis* against PH, and the interaction relationship between these targets is shown in Figure 2C.

### GO and KEGG enrichment analysis of common targets

GO enrichment analyses were conducted to confirm the intersection targets' function. GO function analysis results showed that the anti-PH effect of *Plumula Nelumbinis* might be closely related to a variety of biological processes (BP), including regulation of MAPK cascade (GO:0043408), wound healing (GO:0042060), reproductive structure development (GO:0048608), negative regulation of response to external stimulus (GO:0032102), cellular response to organic cyclic compound (GO:0071407), tube morphogenesis (GO:0035239), and protein phosphorylation (GO:0006468) (Figure 3A). GO cellular components (CC) analysis terms mainly include cytoplasmic vesicle lumen (GO:0060205), membrane raft (GO:0045121), collagen-containing extracellular matrix (GO:0062023), lytic vacuole (GO:0000323), and receptor complex (GO:0043235) (Figure 3B). GO molecular function (MF)

TABLE 1 The main active ingredients of *Plumula Nelumbinis*.

Number	Pubchem name	PubChem ID	Class
LZX1	Neferine	159654	Alkaloids
LZX2	Liensinine	160644	Alkaloids
LZX3	Isoliensinine	5274591	Alkaloids
LZX4	Higenamine	114840	Alkaloids
LZX5	(S)-isococlaurine	138319297	Alkaloids
LZX6	(+)-N-Methylisococlaurine	21817819	Alkaloids
LZX7	Coclaurine	160487	Alkaloids
LZX8	(R)-N-Methylcoclaurine	440595	Alkaloids
LZX9	Lotusine	5274587	Alkaloids
LZX10	N-Nornuciferine	12313579	Alkaloids
LZX11	Nuciferine	10146	Alkaloids
LZX12	O-Nornuciferine	197017	Alkaloids
LZX13	Nornuciferidine	183520	Alkaloids
LZX14	Nelumboferine	76046684	Alkaloids
LZX15	Dauricine	73400	Alkaloids
LZX16	Pronuciferine	200480	Alkaloids
LZX17	Berberine	2353	Alkaloids
LZX18	(-)-Armepavine	442169	Alkaloids
LZX19	Lysicamine	122691	Alkaloids
LZX20	Anonaine	160597	Alkaloids
LZX21	Roemerine	119204	Alkaloids
LZX22	Liriodenine	10144	Alkaloids
LZX23	Thalifoline	89048	Alkaloids
LZX24	N-Methylcorydaldine	303906	Alkaloids
LZX25	2-Methyl-1H-indole-3-carbaldehyde	73166	Alkaloids
LZX26	(R)-Norcoclaurine	440988	Alkaloids
LZX27	1alpha-(4-Methoxybenzyl)-2-methyl-6-methoxy-1,2,3,4-tetrahydroisoquinoline	132579667	Alkaloids
LZX28	N-Methylisosalsoline	40091	Alkaloids
LZX29	O-Methylarmepavine	821338	Alkaloids
LZX30	6,7-Dimethoxy-2-methyl-1,2,3,4-tetrahydroisoquinoline	27694	Alkaloids
LZX31	Quercetin	5280343	Flavonoids
LZX32	Isorhamnetin	5281654	Flavonoids
LZX33	Kaempferol	5280863	Flavonoids
LZX34	Diosmetin	5281612	Flavonoids
LZX35	Naringenin	932	Flavonoids
LZX36	Luteolin	5280445	Flavonoids
LZX37	Tricetin	5281701	Flavonoids
LZX38	5-Hydroxymethylfurfural	237332	Others
LZX39	Linalool	6549	Others
LZX40	(1,7,7-Trimethyl-2-bicyclo [2.2.1]heptanyl) 3-phenylprop-2-enoate	583021	Others
LZX41	Gallic acid	370	Others
LZX42	Dibutyl phthalate	3026	Others
LZX43	Gamabufotalin	259803	Others
LZX44	Loureirin A	5319081	Others
LZX45	Methyl 4-hydroxycinnamate	5319562	Others
LZX46	Propanethial S-oxide	441491	Others



analysis terms mainly include endopeptidase activity (GO: 0004175) and protein serine/threonine/tyrosine kinase activity (GO:0004712) (Figure 3C). KEGG pathway enrichment analysis indicated that the anti-PH effect of *Plumula Nelumbinis* might be achieved by regulating the following pathways: proteoglycans in cancer (hsa05205) and pathways in cancer (hsa05200) (Figure 3D).

## Identification of core compounds and targets of *Plumula Nelumbinis*

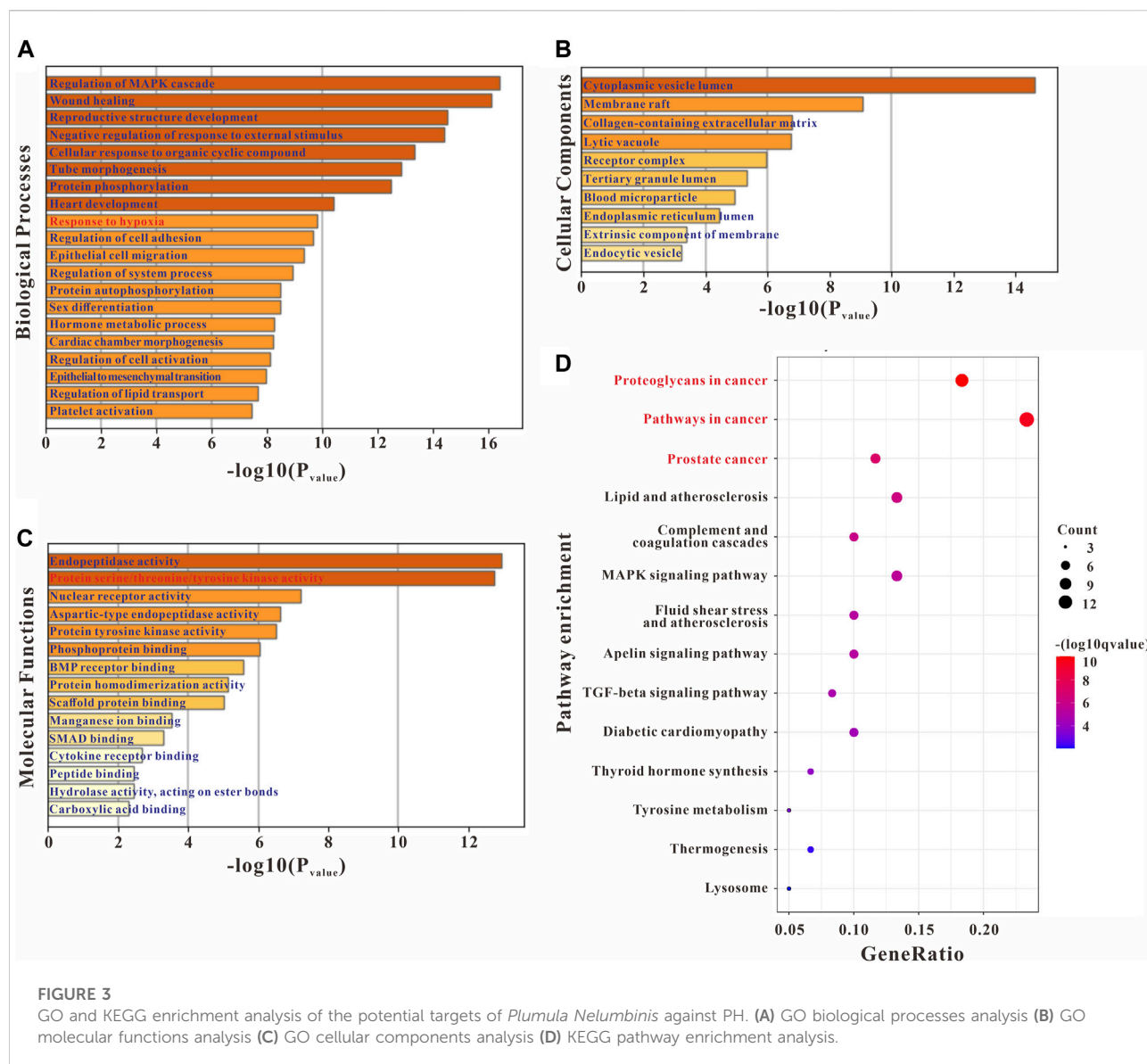
The compounds-targets-pathways network was constructed to clarify the core compounds and corresponding targets of *Plumula Nelumbinis* in PH treatment (Figure 4A). We first screened out nodes with degrees  $\geq 25$  in the compound-target-pathway network as core targets, namely SRC, PIM1, TTR, F2, ESR1, PPIA, MAPK14, PAH, BACE1, and NOS3, respectively. Then the top 7 candidate core compounds were screened out according to the network topological parameters with the core targets, namely LZX1 (Neferine), LZX2 (Liensinine), LZX3 (Isoliensinine), LZX6 (N-Methylisococlaurine), LZX8 (N-Methylcoclaurine), LZX14 (Nelumboferine), and LZX18 (Armeapavine).

In order to determine the possible binding interaction between core compounds and targets, molecular docking analysis was performed using AutoDock Vina. The molecular docking results showed that the average binding energy between the core compounds and targets is  $-7.03$  kcal/mol, indicating an effective

binding between the compounds and targets. As we all know, the lower the binding energy score, the stronger the compound's ability to bind to the targets. By setting the binding energy threshold to  $-8.00$  kcal/mol, we finally obtained three compounds (LZX1, LZX2, and LZX3) and three targets (SRC, PIM1, and NOS3) for subsequent experiments verification (Figure 4B). The molecular docking pattern between the core compounds and targets is shown in Figure 4C.

## Effects of TAPN on hemodynamics and right ventricular function in SuHx-induced PH rats

Based on the network pharmacology and molecular docking results, we further explored the effects of *Plumula Nelumbinis* on hemodynamics and right heart function of SuHx-induced PH rats. Since the core compounds (neferine, liensinine, and isoliensinine) belong to alkaloids, we firstly evaluated the therapeutic effect of TAPN on PH rats *in vivo*. The construction of the PH rat model and the TAPN dosing schedule are shown in Figure 5A. Compared with the control group, the RVSP and Fulton index of SuHx rats were significantly increased, accompanied by a marked increase in right heart dysfunction, manifested as a significant decrease in PAAT, PAAT/PAET, TAPSE, and CO; these phenomena were markedly reversed by TAPN (Figures 5B–J). Interestingly, our results showed that TAPN had no significant effect on PAET and heart rate in rats (Figures 5G,K).



## Effects of TAPN on pulmonary vascular remodeling in SuHx-induced PH rats

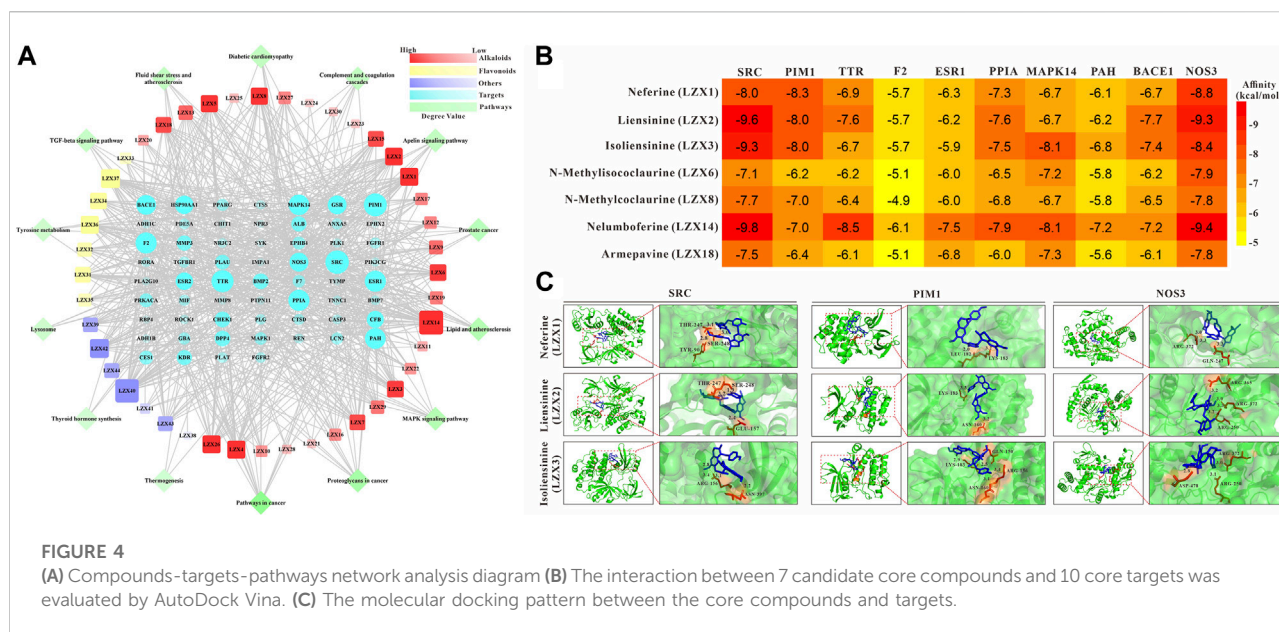
Subsequently, we further evaluated the effect and underlying mechanism of TAPN on SuHx-induced pulmonary vascular remodeling in PH rats. HE and Masson staining showed that the pulmonary vascular remodeling and collagen production was significantly increased in SuHx-induced PH rats, manifesting as a significant increase in the ratio of WT% and WA% (Figures 6A–D). Immunofluorescence results showed that the pulmonary vascular smooth muscle layer (marked by  $\alpha$ -SMA) was significantly thickened in SuHx rats (Figure 6E). In addition, western blot results showed that the protein expressions of collagen1, collagen3, MMP2, MMP9, and

PCNA in the lung tissue of the SuHx group were significantly increased, accompanied by a significant increase in the expressions of PIM1 and p-SRC; these phenomena were markedly attenuated by TAPN (Figures 6F,G).

## Effect of *Plumula Nelumbinis* on hypoxia-induced proliferation and migration of PSMCs

The primary PSMCs were cultured under hypoxia for 48 h to establish a cell proliferation and migration model. As shown in Figures 7A–D, under normoxic conditions, TAPN, neferine, liensinine, and isoliensinine did not affect the





viability of PSMCs, suggesting that TAPN (5–100  $\mu\text{g/ml}$ ) and the 3 alkaloid active components (1–20  $\mu\text{M}$ ) have no toxic effects on PSMCs. However, under hypoxic conditions, the abnormal proliferation of PSMCs was inhibited by TAPN, neferine, liensinine, and isoliensinine in a dose-dependent manner. The drug concentration (TAPN: 50  $\mu\text{g/ml}$ ; neferine: 5  $\mu\text{M}$ ; liensinine and isoliensinine: 10  $\mu\text{M}$ ) for subsequent experiments was determined based on the results of CCK-8. Further results showed that hypoxia could promote the proliferation and migration of PSMCs (Figures 7E–H), along with an increase in the protein expressions of collagen1, collagen3, MMP2, MMP9, and PCNA in PSMCs (Figures 7I,J), these phenomena were markedly attenuated in the treatment of TAPN, neferine, liensinine, and isoliensinine.

Finally, we evaluated the underlying mechanisms of *Plumula Nelumbinis* on hypoxia-induced hyperproliferation and migration of PSMCs. Compared to the control group, the protein expression of p-SRC and PIM1 in the hypoxia group was significantly upregulated; these increases were attenuated by TAPN, neferine, liensinine, and isoliensinine (Figures 7I,J).

## Discussion

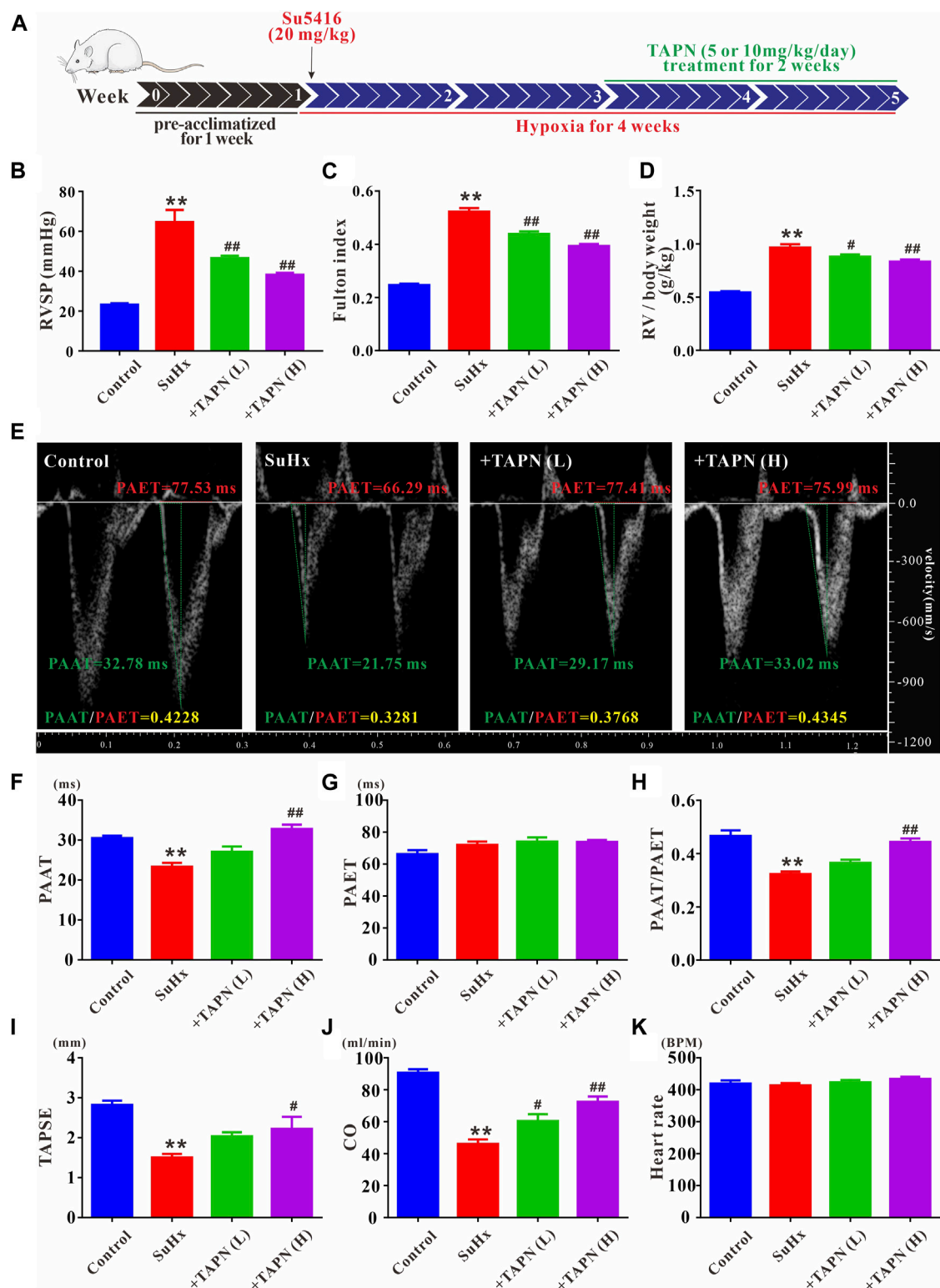
In this study, the anti-PH effect and potential mechanisms of the main active components of *Plumula Nelumbinis* were evaluated by network pharmacology, molecular docking, *in vivo*, and *in vitro* experimental verification. Firstly, we screened out the main active components of *Plumula Nelumbinis* against PH by using network pharmacology and molecular docking analysis. Then, by constructing a

SuHx-induced PH rat model and a hypoxia-induced PSMCs proliferation model, we further revealed that the anti-PH mechanism of *Plumula Nelumbinis* might be achieved by inhibiting the proliferation and migration of PSMCs, and its mechanism is related to the inactivation of SRC and PIM1.

PH is a malignant cardiopulmonary vascular disease characterized by pulmonary vascular remodeling. With the continuous improvement of diagnosis and treatment technology in recent years, the 5-year survival rate of patients with PH has reached 53.6% (Gall et al., 2017). Unfortunately, PH is still an intractable disease for the current therapies can only alleviate patients' symptoms and cannot effectively reverse the process of vascular remodeling. Therefore, it is an urgent clinical problem to seek more precise and effective interventions to prevent or treat PH. TCM has been used to treat PH through a multi-level and multi-target approach (Xue et al., 2021). The rise of network pharmacology, characterized by "multiple compounds-multiple targets-multiple signaling pathways", provides an effective way to systematically explore the internal mechanism of TCM in treating PH (Nogales et al., 2021).

*Plumula Nelumbinis* is composed of various active ingredients, of which alkaloids are one of the main active ingredients. Recent studies showed that TAPN has the protective effect of inhibiting vascular remodeling in spontaneously hypertensive rats (Li Q et al., 2019). In addition, Jun et al. demonstrated that TAPN could inhibit the proliferation and migration of vascular smooth muscle cells, thereby inhibiting the carotid artery restenosis induced by balloon injury (Jun et al., 2016). The above studies have shown that TAPN plays a cardiovascular protective effect by regulating the proliferation and migration of vascular smooth

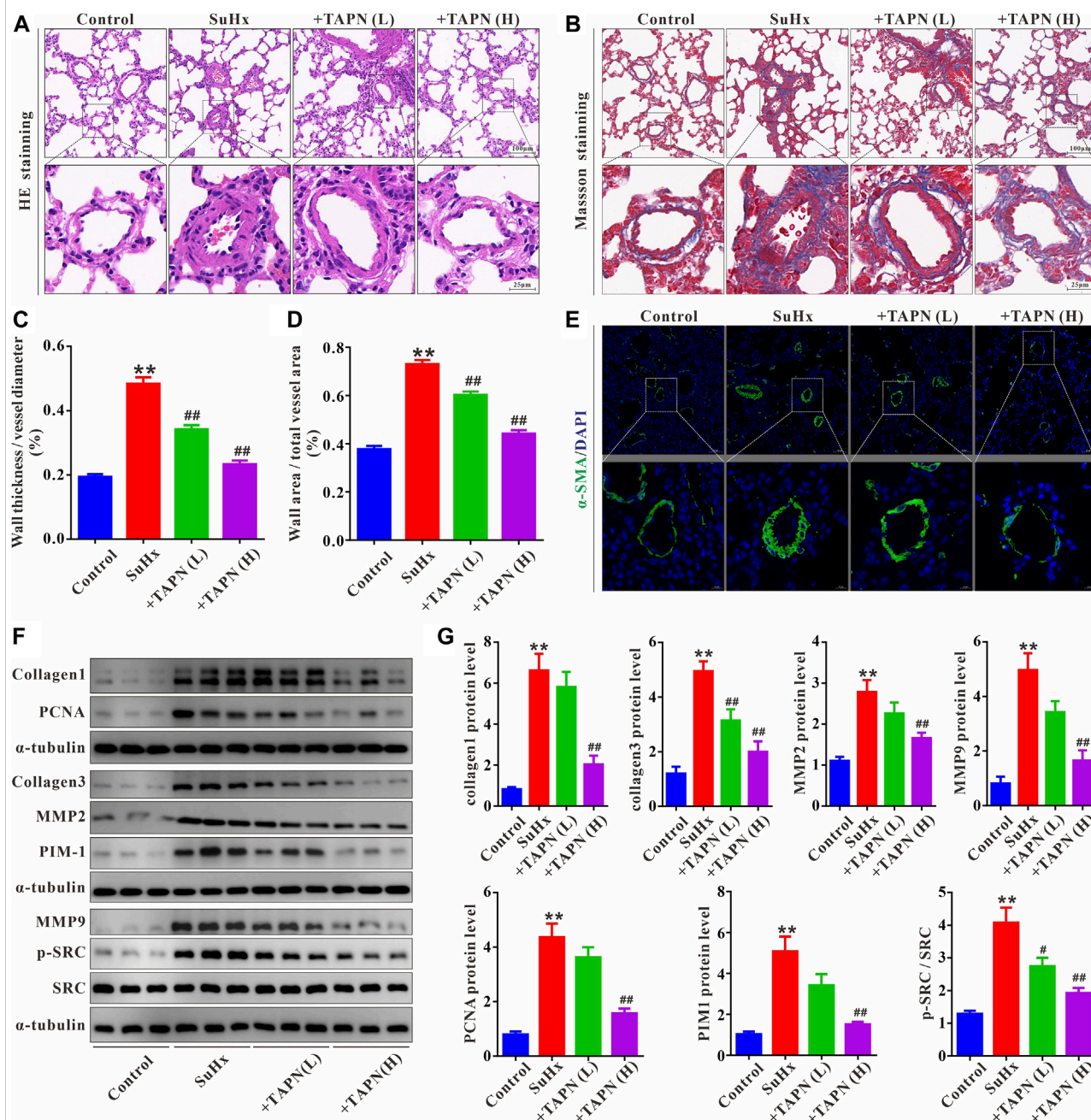




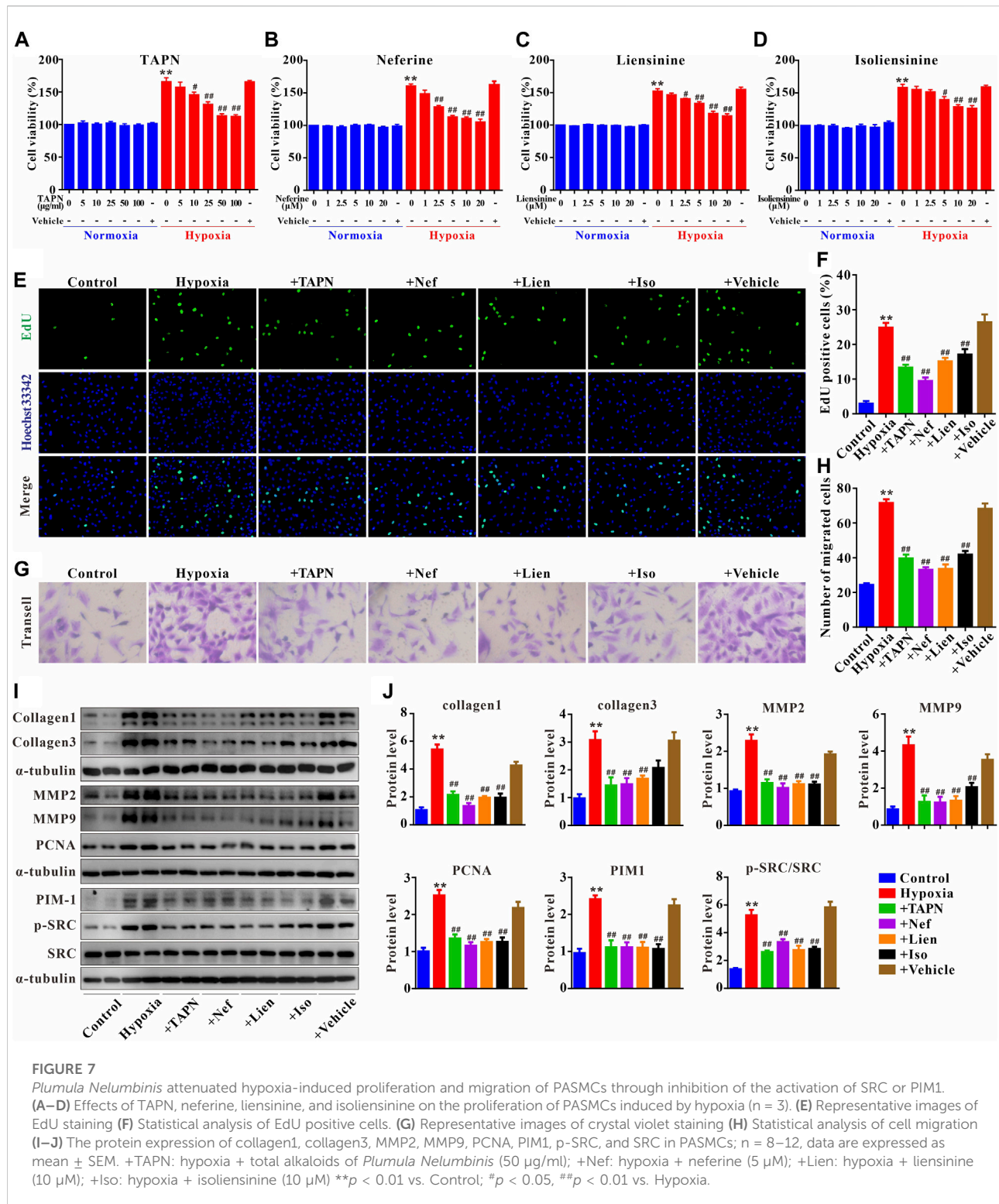
**FIGURE 5** TAPN inhibits right ventricular remodeling and right heart dysfunction in SuHx rats. **(A)** Design diagram of *in vivo* drug administration experiment in SD rats **(B)** RVSP in each group **(C)** Fulton index: RV/LV + IVS **(D)** The ratio of RV weight to body weight **(E)** Representative images of pulsed Doppler from pulmonary artery flow tract recorded in parasternal long axis, the pulmonary artery acceleration time (PAAT, green horizontal line), the pulmonary artery ejection time (PAET, red horizontal line) **(F)** The value of PAAT in each group **(G)** The value of PAET in each group **(H)** The ratio PAAT/PAET **(Continued)**

**FIGURE 5**

of PAAT to PAET **(I)** The value of tricuspid annular plane systolic excursion (TAPSE) **(J)** Cardiac output (CO) **(K)** Heart rate.  $n = 8-12$  per group, Data are expressed as mean  $\pm$  SEM. SuHx: the Su5416 + hypoxia group; +TAPN (L): SuHx + TAPN low dose group (5 mg/kg/d); +TAPN (H): SuHx + TAPN high dose group (10 mg/kg/d); \*\* $p < 0.01$  vs. Control; # $p < 0.05$ , ## $p < 0.01$  vs. SuHx.

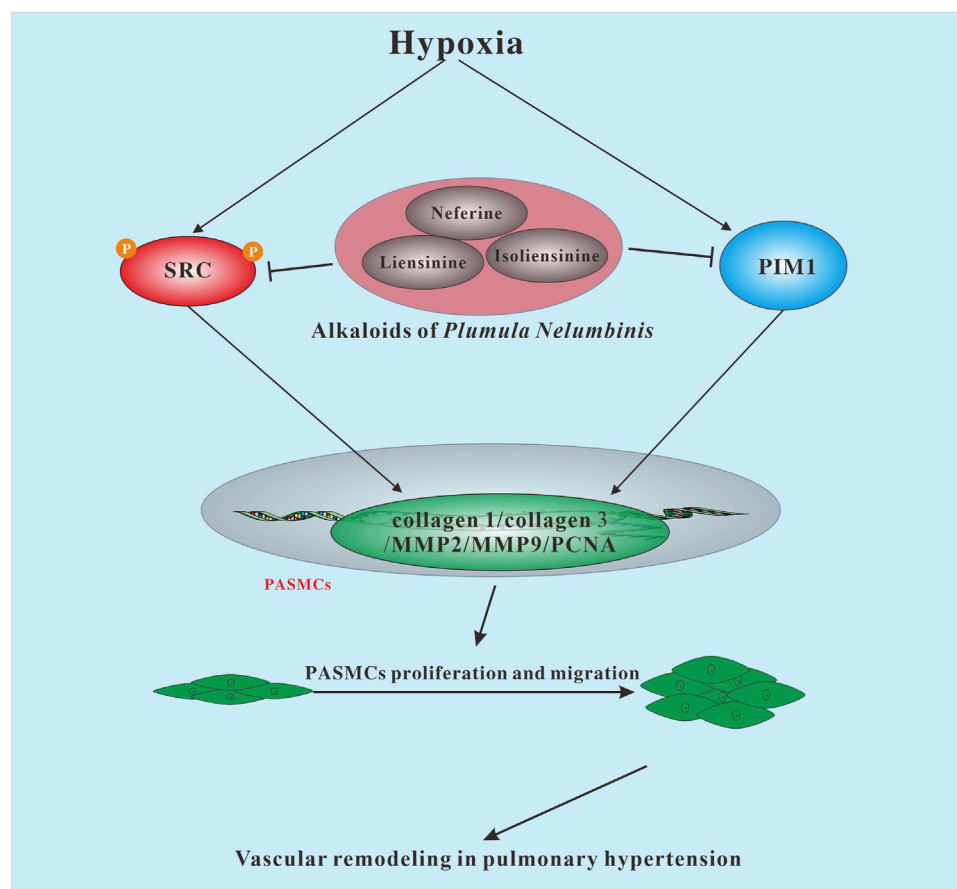
**FIGURE 6**

TAPN inhibits pulmonary vascular remodeling and collagen production in SuHx rats. **(A)** Representative images of HE staining **(B)** Representative images of Masson staining **(C)** The ratio of wall thickness to total vessel external diameter (WT%) **(D)** The ratio of wall area to total vessel area **(E)** Representative images of immunofluorescence staining (labeling of pulmonary vascular smooth muscle layer with  $\alpha$ -SMA) **(F-G)** The protein expression of collagen1, collagen3, MMP2, MMP9, PCNA, PIM1, p-SRC, and SRC in the lung tissue of rats.  $n = 9$ , Data are expressed as mean  $\pm$  SEM. SuHx: the Su5416 + hypoxia group; +TAPN (L): SuHx + TAPN low dose group (5 mg/kg/d); +TAPN (H): SuHx + TAPN high dose group (10 mg/kg/d); \*\* $p < 0.01$  vs. Control; # $p < 0.05$ , ## $p < 0.01$  vs. SuHx.



muscle cells. However, its effect on PH is still unclear. In this study, we first predict the potential therapeutic targets of *Plumula Nelumbinis* against PH by using network pharmacology combined with molecular docking. Our prediction results

indicated that the main active components of *Plumula Nelumbinis* in treating PH were alkaloids, including neferine, liensinine, and isoliensinine. Subsequently, we further prove that TAPN has a therapeutic effect on PH by using the SuHx-induced



**FIGURE 8**  
The possible mechanism of *Plumula Nelumbinis* against pulmonary hypertension.

rat model, manifested as a significant decrease in RVSP, along with a significant improvement in cardiovascular remodeling and right heart function.

PH is a complex disease involving multiple targets and pathways. GO enrichment analysis showed that the anti-PH effect of *Plumula Nelumbinis* might be related to multiple biological processes and molecular functions, including regulation of MAPK cascade, wound healing, endopeptidase activity, and protein serine/threonine/tyrosine kinase activity. KEGG enrichment analysis revealed that its anti-PH effect might involve regulating cancer signaling pathways (hsa05205: proteoglycans in cancer; hsa05200: pathways in cancer; hsa05215: prostate cancer). It is worth noting that, comparable to cancer, PH is also a proliferative disease with high mortality and is thus known as the “cancer” of the cardiopulmonary vascular system. However, unlike cancer, which is caused by the excessive proliferation of cancer cells, PH is mainly caused by the excessive proliferation of vascular cells, especially the PSMCs in the media layer. Previous

studies have demonstrated that neferine and isoliensinine have protective effects on angiotensin II (Ang II)-induced hyperproliferation of smooth muscle cells (Xiao et al., 2006; Li et al., 2010; Zheng et al., 2014). In the present study, we found that the alkaloid compounds in *Plumula Nelumbinis* (including TAPN, neferine, liensinine, and isoliensinine) have the ability to inhibit the abnormal proliferation and migration of PSMCs induced by hypoxia, suggesting that the therapeutic effect of *Plumula Nelumbinis* on PH vascular remodeling may be related to the inhibition of excessive proliferation and migration of PSMCs.

SRC, a proto-oncogene tyrosine-protein kinase, has been shown to mediate the occurrence and development of hypoxic PH by regulating vasoconstriction, cell proliferation, and apoptosis (Gao and Raj, 2020; Norton et al., 2020). Recently studies have proved that the effect of SRC in promoting hypoxic PH is closely related to the regulation of the activation of downstream proteins such as HIF-1 $\alpha$ , HIF-2 $\alpha$ , signal transducer and activator of transcription 3



(STAT3), and NADPH oxidase (Gao and Raj, 2020). In addition, inhibition of SRC activation by drug intervention could effectively reverse vascular remodeling in experimental PH (Pullamsetti et al., 2012), further clarifying the vital role of SRC in the promotion of PH. PIM1, a serine/threonine family kinase, has now been recognized as a novel biomarker and therapeutic target in the development of PH (Satoh et al., 2020). A large number of studies have demonstrated that PIM1 is overactivated in patients with PH, preclinical animal models, or cell models (Paulin et al., 2011; Ge et al., 2021), and inhibition of PIM1 expression by drug intervention could also effectively delay the progression of PH (Lampron et al., 2020). NOS3, also known as eNOS, is mainly expressed in endothelial cells and could play a protective role in PH vascular remodeling by regulating nitric oxide synthesis (Hua et al., 2018). The above studies show that SRC and PIM1 may participate in the development of PH by promoting the proliferation of PSMCs. On the contrary, NOS3 may alleviate the PH process by regulating the function of endothelial cells. In this study, we found that the protein expressions of p-SRC and PIM1 in lung tissues were significantly increased in SuHx-induced PH rats, and these increases were suppressed in the presence of TAPN. Expectedly, our *in vitro* experiment results further showed that the expression of PIM1 and p-SRC in PSMCs were significantly increased under hypoxic conditions; these phenomena were attenuated in the presence of TAPN, neferine, liensinine, and isoliensinine. These findings are consistent with our network pharmacology and molecular docking predictions, suggesting that the alkaloids of *Plumula Nelumbinis* may inhibit the proliferation and migration of PSMCs by targeting SRC and PIM1 thereby achieving the purpose of treating PH. It is worth noting that we also detected the expression of eNOS in PSMCs after hypoxia treatment. However, the results showed that the basal expression of eNOS in PSMCs was deficient and challenging to detect. Further studies are needed to confirm the role of *Plumula Nelumbinis* on eNOS activity in pulmonary artery endothelial cells.

## Conclusion

In summary, this study demonstrated for the first time that TAPN (such as neferine, liensinine, and isoliensinine) exerts a therapeutic effect on PH by inhibiting the excessive proliferation and migration of PSMCs, and its mechanism is related to promoting the inactivation of SRC and PIM1 (Figure 8). The above results can provide an experimental basis for the development of new drugs for PH.

## Data availability statement

The datasets presented in this study can be found in online repositories. The names of the repository/repositories and accession number(s) can be found in the article/supplementary material.

## Ethics statement

The animal study was reviewed and approved by the Central South University Veterinary Medicine Animal Care and Use Committee.

## Author contributions

XX participated in cell experiments, data collection, processing, and analysis; Funding acquisition; Writing—original draft. FL participated in animal experiments and wrote the first draft. MF participated in data collection. YJ, SL, and BL were accountable for project administration, funding acquisition, and manuscript preparation. All authors reviewed and approved the final version of the manuscript.

## Funding

This work was supported by the National Natural Science Foundation of China (No. 81703516 and No. 81703384), China Postdoctoral Science Foundation (No. 2021M693575), and the Natural Science Foundation of Hunan Province, China (No. 2019JJ50943, No. 2020JJ6100, No. 2021JJ80020, and No. 2022JJ80084).

## Conflict of interest

The authors declare that the research was conducted in the absence of any commercial or financial relationships that could be construed as a potential conflict of interest.

## Publisher's note

All claims expressed in this article are solely those of the authors and do not necessarily represent those of their affiliated organizations, or those of the publisher, the editors and the reviewers. Any product that may be evaluated in this article, or claim that may be made by its manufacturer, is not guaranteed or endorsed by the publisher.



## References

- Amberger, J. S., Bocchini, C. A., Scott, A. F., and Hamosh, A. (2019). OMIM.org: leveraging knowledge across phenotype-gene relationships. *Nucleic Acids Res.* 47 (D1), D1038–D1043. doi:10.1093/nar/gky1151
- An, W., Huang, Y., Chen, S., Teng, T., Shi, Y., Sun, Z., et al. (2021). Mechanisms of Rhizoma Coptidis against type 2 diabetes mellitus explored by network pharmacology combined with molecular docking and experimental validation. *Sci. Rep.* 11 (1), 20849. doi:10.1038/s41598-021-00293-8
- Burley, S. K., Bhikadiya, C., Bi, C., Bittrich, S., Chen, L., Crichlow, G. V., et al. (2021). RCSB protein Data Bank: Powerful new tools for exploring 3D structures of biological macromolecules for basic and applied research and education in fundamental biology, biomedicine, biotechnology, bioengineering and energy sciences. *Nucleic Acids Res.* 49 (D1), D437–D451. doi:10.1093/nar/gkaa1038
- Chen, J., Tang, M., Liu, M., Jiang, Y., Liu, B., and Liu, S. (2020). Neferine and lianzixin extracts have protective effects on undifferentiated caffeine-damaged PC12 cells. *BMC Complement. Med. Ther.* 20 (1), 76. doi:10.1186/s12906-020-2872-2
- Chen, S., Li, X., Wu, J., Li, J., Xiao, M., Yang, Y., et al. (2021). Plumula nelumbinis: A review of traditional uses, phytochemistry, pharmacology, pharmacokinetics and safety. *J. Ethnopharmacol.* 266, 113429. doi:10.1016/j.jep.2020.113429
- Daina, A., Michielin, O., and Zoete, V. (2017). SwissADME: a free web tool to evaluate pharmacokinetics, drug-likeness and medicinal chemistry friendliness of small molecules. *Sci. Rep.* 7, 42717. doi:10.1038/srep42717
- Fu, M., Luo, F., Wang, E., Jiang, Y., Liu, S., Peng, J., et al. (2021). Magnolol attenuates right ventricular hypertrophy and fibrosis in hypoxia-induced pulmonary arterial hypertensive rats through inhibition of the JAK2/STAT3 signaling pathway. *Front. Pharmacol.* 12, 755077. doi:10.3389/fphar.2021.755077
- Gall, H., Felix, J. F., Schneck, F. K., Milger, K., Sommer, N., Voswinkel, R., et al. (2017). The giessen pulmonary hypertension registry: Survival in pulmonary hypertension subgroups. *J. Heart Lung Transpl.* 36 (9), 957–967. doi:10.1016/j.healun.2017.02.016
- Gao, Y., and Raj, J. U. (2020). Src and epidermal growth factor receptor: Novel partners in mediating chronic hypoxia-induced pulmonary artery hypertension. *Am. J. Respir. Cell Mol. Biol.* 62 (1), 5–7. doi:10.1165/rcmb.2019-0230ED
- Ge, X., Zhang, W., Zhu, T., Huang, N., Yao, M., Liu, H., et al. (2021). Hypoxia-activated platelets stimulate proliferation and migration of pulmonary arterial smooth muscle cells by phosphatidylserine/LOX-1 signaling-impelled intercellular communication. *Cell. Signal.* 87, 110149. doi:10.1016/j.cellsig.2021.110149
- Hua, C., Zhao, J., Wang, H., Chen, F., Meng, H., Chen, L., et al. (2018). Apple polyphenol relieves hypoxia-induced pulmonary artery hypertension via pulmonary endothelium protection and smooth muscle relaxation: *In vivo* and *in vitro* studies. *Biomed. Pharmacother. = Biomedicine Pharmacother.* 107, 937–944. doi:10.1016/j.biopha.2018.08.080
- Jiang, Y., Liu, R., Liu, M., Yi, L., and Liu, S. (2018a). An integrated strategy to rapidly characterize non-targeted benzyloisoquinoline alkaloids from Plumula nelumbinis ethanol extract using UHPLC/Q-orbitrap HRMS. *Int. J. Mass Spectrom.* 432, 26–35. doi:10.1016/j.jms.2018.06.002
- Jiang, Y., Zi, W., Pei, Z., and Liu, S. (2018b). Characterization of polysaccharides and their antioxidant properties from Plumula nelumbinis. *Saudi Pharm. J.* 26 (5), 656–664. doi:10.1016/j.jsps.2018.02.026
- Jun, M. Y., Karki, R., Paudel, K. R., Sharma, B. R., Adhikari, D., and Kim, D.-W. (2016). Alkaloid rich fraction from *Nelumbo nucifera* targets VSMC proliferation and migration to suppress restenosis in balloon-injured rat carotid artery. *Atherosclerosis* 248, 179–189. doi:10.1016/j.atherosclerosis.2016.03.020
- Lampron, M.-C., Vitry, G., Nadeau, V., Grobs, Y., Paradis, R., Samson, N., et al. (2020). PIM1 (moloney murine leukemia provirus integration site) inhibition decreases the nonhomologous end-joining DNA damage repair signaling pathway in pulmonary hypertension. *Arterioscler. Thromb. Vasc. Biol.* 40 (3), 783–801. doi:10.1161/ATVBAHA.119.313763
- Legchenko, E., Chouvarine, P., Borchert, P., Fernandez-Gonzalez, A., Snay, E., Meier, M., et al. (2018). PPAR $\gamma$  agonist pioglitazone reverses pulmonary hypertension and prevents right heart failure via fatty acid oxidation. *Sci. Transl. Med.* 10 (438), eaa0303. doi:10.1126/scitranslmed.aao0303
- Li, Q., Wo, D., Huang, Y., Yu, N., Zeng, J., Chen, H., et al. (2019). Alkaloids from Nelumbinis Plumula (AFNP) ameliorate aortic remodeling via RhoA/ROCK pathway. *Biomed. Pharmacother. = Biomedicine Pharmacother.* 112, 108651. doi:10.1016/j.biopha.2019.108651
- Li, T., Luo, X. J., Wang, E. L., Li, N. S., Zhang, X. J., Song, F. L., et al. (2019a). Magnesium lithospermate B prevents phenotypic transformation of pulmonary arteries in rats with hypoxic pulmonary hypertension through suppression of NADPH oxidase. *Eur. J. Pharmacol.* 847, 32–41. doi:10.1016/j.ejphar.2019.01.020
- Li, T., Peng, J. J., Wang, E. L., Li, N. S., Song, F. L., Yang, J. F., et al. (2019b). Magnesium lithospermate B derived from salvia miltiorrhiza ameliorates right ventricle remodeling in pulmonary hypertensive rats via inhibition of NOX/VPO1 pathway. *Planta Med.* 85 (9–10), 708–718. doi:10.1055/a-0863-4741
- Li, X.-c., Tong, G.-x., Zhang, Y., Liu, S.-x., Jin, Q.-h., Chen, H.-h., et al. (2010). Neferine inhibits angiotensin II-stimulated proliferation in vascular smooth muscle cells through heme oxygenase-1. *Acta Pharmacol. Sin.* 31 (6), 679–686. doi:10.1038/aps.2010.57
- Liu, S., Wang, B., Li, X. Z., Qi, L. F., and Liang, Y. Z. (2009). Preparative separation and purification of liensinine, isoliensinine and neferine from seed embryo of *Nelumbo nucifera* GAERTN using high-speed counter-current chromatography. *J. Sep. Sci.* 32 (14), 2476–2481. doi:10.1002/jssc.200800766
- Mirhadi, E., Roufogalis, B. D., Banach, M., Barati, M., and Sahebkar, A. (2021). Resveratrol: Mechanistic and therapeutic perspectives in pulmonary arterial hypertension. *Pharmacol. Res.* 163, 105287. doi:10.1016/j.phrs.2020.105287
- Nogales, C., Mamdouh, Z. M., List, M., Kiel, C., Casas, A. I., and Schmidt, H. H. H. W. (2021). Network pharmacology: curing causal mechanisms instead of treating symptoms. *Trends Pharmacol. Sci.* 43, 136–150. doi:10.1016/j.tips.2021.11.004
- Norton, C. E., Sheak, J. R., Yan, S., Weise-Cross, L., Jernigan, N. L., Walker, B. R., et al. (2020). Augmented pulmonary vasoconstrictor reactivity after chronic hypoxia requires Src kinase and epidermal growth factor receptor signaling. *Am. J. Respir. Cell Mol. Biol.* 62 (1), 61–73. doi:10.1165/rcmb.2018-0106OC
- O'Boyle, N. M., Banck, M., James, C. A., Morley, C., Vandermeersch, T., and Hutchison, G. R. (2011). Open Babel: An open chemical toolbox. *J. Cheminform.* 3, 33. doi:10.1186/1758-2946-3-33
- Paulin, R., Courboulon, A., Meloche, J., Mainguy, V., Dumas de la Roque, E., Saksouk, N., et al. (2011). Signal transducers and activators of transcription-3/pim1 axis plays a critical role in the pathogenesis of human pulmonary arterial hypertension. *Circulation* 123 (11), 1205–1215. doi:10.1161/CIRCULATIONAHA.110.963314
- Pinero, J., Sauch, J., Sanz, F., and Furlong, L. I. (2021). The DisGeNET cytoscape app: Exploring and visualizing disease genomics data. *Comput. Struct. Biotechnol. J.* 19, 2960–2967. doi:10.1016/j.csbj.2021.05.015
- Poch, D., and Mandel, J. (2021). Pulmonary hypertension. *Ann. Intern. Med.* 174 (4), ITC49–ITC64. doi:10.7326/ATTC202104200
- Pullamsetti, S. S., Berghausen, E. M., Dabral, S., Tretyn, A., Butrous, E., Savai, R., et al. (2012). Role of Src tyrosine kinases in experimental pulmonary hypertension. *Arterioscler. Thromb. Vasc. Biol.* 32 (6), 1354–1365. doi:10.1161/ATVBAHA.112.248500
- Ru, J., Li, P., Wang, J., Zhou, W., Li, B., Huang, C., et al. (2014). TCMSP: a database of systems pharmacology for drug discovery from herbal medicines. *J. Cheminform.* 6, 13. doi:10.1186/1758-2946-6-13
- Satoh, K., Kikuchi, N., and Shimokawa, H. (2020). PIM1 (provirus integration site for moloney murine leukemia virus) as a novel biomarker and therapeutic target in pulmonary arterial hypertension: Another evidence for cancer theory. *Arterioscler. Thromb. Vasc. Biol.* 40 (3), 500–502. doi:10.1161/ATVBAHA.120.313975
- Shannon, P., Markiel, A., Ozier, O., Baliga, N. S., Wang, J. T., Ramage, D., et al. (2003). Cytoscape: a software environment for integrated models of biomolecular interaction networks. *Genome Res.* 13 (11), 2498–2504. doi:10.1101/gr.1239303
- Shimoda, L. A. (2020). Cellular pathways promoting pulmonary vascular remodeling by hypoxia. *Physiology* 35 (4), 222–233. doi:10.1152/physiol.00039.2019
- Szklarczyk, D., Morris, J. H., Cook, H., Kuhn, M., Wyder, S., Simonovic, M., et al. (2017). The STRING database in 2017: Quality-controlled protein-protein association networks, made broadly accessible. *Nucleic Acids Res.* 45 (D1), D362–D368. doi:10.1093/nar/gkw937
- Trott, O., and Olson, A. J. (2010). AutoDock Vina: improving the speed and accuracy of docking with a new scoring function, efficient optimization, and multithreading. *J. Comput. Chem.* 31 (2), 455–461. doi:10.1002/jcc.21334
- Walter, K. (2021). Pulmonary hypertension. *JAMA* 326 (11), 1116. doi:10.1001/jama.2021.11054
- Wang, E. L., Jia, M. M., Luo, F. M., Li, T., Peng, J. J., Luo, X. J., et al. (2019). Coordination between NADPH oxidase and vascular peroxidase 1 promotes dysfunctions of endothelial progenitor cells in hypoxia-induced pulmonary hypertensive rats. *Eur. J. Pharmacol.* 857, 172459. doi:10.1016/j.ejphar.2019.172459
- Wang, X., Shen, Y., Wang, S., Li, S., Zhang, W., Liu, X., et al. (2017). PharmMapper 2017 update: a web server for potential drug target identification

with a comprehensive target pharmacophore database. *Nucleic Acids Res.* 45 (W1), W356–W360. doi:10.1093/nar/gkx374

Wicha, P., Onsa-Ard, A., Chaichompoo, W., Suksamrarn, A., and Tocharus, C. (2020). Vasorelaxant and antihypertensive effects of neferine in rats: An *in vitro* and *in vivo* study. *Planta Med.* 86 (7), 496–504. doi:10.1055/a-1123-7852

Wickham, H., Chang, W., Henry, L., Pedersen, T. L., Takahashi, K., Wilke, C., et al. (2016). *ggplot2: Elegant graphics for data analysis*. New York: Springer-Verlag.

Xiao, J. H., Zhang, Y. L., Feng, X. L., Wang, J. L., and Qian, J. Q. (2006). Effects of isoliensinine on angiotensin II-induced proliferation of porcine coronary arterial smooth muscle cells. *J. Asian Nat. Prod. Res.* 8 (3), 209–216. doi:10.1080/1028602042000325609

Xiao, X. H., Luo, F. M., Wang, E. L., Fu, M. Y., Li, T., Jiang, Y. P., et al. (2022). Magnolol alleviates hypoxia-induced pulmonary vascular remodeling through inhibition of phenotypic transformation in pulmonary arterial smooth muscle cells. *Biomed. Pharmacother.* 150, 113060. doi:10.1016/j.biopha.2022.113060

Xue, Z., Li, Y., Zhou, M., Liu, Z., Fan, G., Wang, X., et al. (2021). Traditional herbal medicine discovery for the treatment and prevention of pulmonary arterial hypertension. *Front. Pharmacol.* 12, 720873. doi:10.3389/fphar.2021.720873

Zheng, L., Cao, Y., Liu, S., Peng, Z., and Zhang, S. (2014). Neferine inhibits angiotensin II-induced rat aortic smooth muscle cell proliferation predominantly by downregulating fractalkine gene expression. *Exp. Ther. Med.* 8 (5), 1545–1550. doi:10.3892/etm.2014.1952

Zhou, Y., Zhang, Y., Lian, X., Li, F., Wang, C., Zhu, F., et al. (2021). Therapeutic target database update 2022: facilitating drug discovery with enriched comparative data of targeted agents. *Nucleic Acids Res.* 50, D1398–D1407. doi:10.1093/nar/gkab953

Zhou, Y., Zhou, B., Pache, L., Chang, M., Khodabakhshi, A. H., Tanaseichuk, O., et al. (2019). Metascape provides a biologist-oriented resource for the analysis of systems-level datasets. *Nat. Commun.* 10 (1), 1523. doi:10.1038/s41467-019-09234-6



## OPEN ACCESS

## EDITED BY

Ren-You Gan,  
Institute of Urban Agriculture (CAAS),  
China

## REVIEWED BY

Qiaobo Ye,  
Chengdu University of Traditional  
Chinese Medicine, China  
Xin Li,  
Shanghai University of Traditional  
Chinese Medicine, China

## \*CORRESPONDENCE

Bojun Chen,  
719523476@qq.com

## SPECIALTY SECTION

This article was submitted to  
Ethnopharmacology,  
a section of the journal  
Frontiers in Pharmacology

RECEIVED 12 April 2022

ACCEPTED 15 July 2022

PUBLISHED 17 August 2022

## CITATION

Huang P, Li Z, Chen L, Zeng J, Zhao S,  
Tang Y, Huang B, Guan H, Chen Y,  
Feng Y, Lei S, Wu Q, Zhang H, Huang X,  
Zeng L, Liu Y, Zeng Z and Chen B (2022),  
The comparative effects of oral Chinese  
patent medicines combined with  
western medicine in stable angina: A  
systematic review and network meta-  
analysis of 179 trials.  
*Front. Pharmacol.* 13:918689.  
doi: 10.3389/fphar.2022.918689

## COPYRIGHT

© 2022 Huang, Li, Chen, Zeng, Zhao,  
Tang, Huang, Guan, Chen, Feng, Lei,  
Wu, Zhang, Huang, Zeng, Liu, Zeng and  
Chen. This is an open-access article  
distributed under the terms of the  
[Creative Commons Attribution License](#)  
(CC BY). The use, distribution or  
reproduction in other forums is  
permitted, provided the original  
author(s) and the copyright owner(s) are  
credited and that the original  
publication in this journal is cited, in  
accordance with accepted academic  
practice. No use, distribution or  
reproduction is permitted which does  
not comply with these terms.

# The comparative effects of oral Chinese patent medicines combined with western medicine in stable angina: A systematic review and network meta-analysis of 179 trials

Peiying Huang<sup>1</sup>, Zhishang Li<sup>2</sup>, Li Chen<sup>2</sup>, Jing Zeng<sup>2</sup>, Shuai Zhao<sup>2</sup>,  
Yong Tang<sup>3</sup>, Bixuan Huang<sup>4</sup>, Hansu Guan<sup>3</sup>, Yan Chen<sup>2</sup>,  
Yuchao Feng<sup>5</sup>, Sisi Lei<sup>1</sup>, Qihua Wu<sup>1</sup>, Haobo Zhang<sup>1</sup>,  
Xiaoyan Huang<sup>2</sup>, Linsheng Zeng<sup>6</sup>, Yuxiang Liu<sup>6</sup>, Zhongyi Zeng<sup>6</sup>  
and Bojun Chen<sup>1,2,5\*</sup>

<sup>1</sup>The Second Clinical Medical School of Guangzhou University of Chinese Medicine, Guangzhou, China, <sup>2</sup>Emergency Department of Guangdong Provincial Hospital of Traditional Chinese Medicine, Guangzhou, China, <sup>3</sup>The Third Affiliated Hospital of Guangzhou University of Chinese Medicine, Guangzhou, China, <sup>4</sup>Department of Nursing, Hubei University of Arts and Science, Xiangyang, China, <sup>5</sup>Guangdong Provincial Key Laboratory of Research on Emergency in Traditional Chinese Medicine, Clinical Research Team of Prevention and Treatment of Cardiac Emergencies with Traditional Chinese Medicine, Guangzhou, China, <sup>6</sup>Shenzhen Traditional Chinese Medicine Hospital, Shenzhen, China

**Background:** Stable angina is a common condition with high morbidity and mortality rates. It has been reported that combining oral Chinese patent medicines (OCPMs) and Western medicine (WM) could potentially achieve a better effect than WM alone. However, the optimal OCPMs for stable angina remain controversial and merit further empirical research.

**Methods:** PubMed, Embase, Web of Science, Cochrane Library, Ovid-Medline, Clinical [Trials.gov](#), China National Knowledge Infrastructure, Wanfang Database, Weipu Journal Database, and Chinese Biomedical Literature Database were all searched from inception to 13 March 2022. We employed Version 2 of the Cochrane risk-of-bias tool (ROB2) to assess the overall quality of the selected studies. We also used R 4.1.2 and STATA 14.0 software applications to perform network meta-analysis, followed by sensitivity and subgroup analysis.

**Results:** A total of 179 randomized controlled trials with 16,789 patients were included. The selected trials were all assessed as some concerns. OCPMs combined with WM had a better treatment effect than WM alone. In terms of the effective clinical rate, a significant increase was detected for Qishen Yiqi dripping pill (QSYQ)+WM as compared with Shensong Yangxin capsule (SSYX)+WM, Shexiang Baoxin pill (SXBX)+WM, Tongxinluo capsule (TXL)+WM, Xuefu Zhuyu capsule (XFZY)+WM, Qiliqiangxin capsule (QLQX)+WM, Naixintong capsule (NXT)+WM, Fufang Danshen dripping pill (FFDS)+WM, and Danlou tablet (DL)+WM. QSYQ + WM had the highest-ranking

probability (98.12%). Regarding the effective rate in ECG, QSYQ + WM was superior to SXBX + WM, TXL + WM, DL + WM, FFDS + WM, and NXT + WM. QSYQ + WM ranked first (94.21%). In terms of weekly frequency of angina, QLQX + WM obtained a better effect than FFDS + WM, Kuanxiong aerosol (KXQW)+WM, NXT + WM, QLQX + WM, SSYX + WM, SXBX + WM, and TXL + WM. QLQX + WM ranked first (100.00%). Regarding the duration of an angina attack, KXQW + WM was superior to SSYX + WM; KXQW + WM ranked first (95.71%). Adverting to weekly nitroglycerin usage, TXL + WM had the highest-ranking probability (82.12%). Referring to cardiovascular event rate, DL + WM had the highest effect (73.94%). Additionally, SSYX + WM had the lowest rate of adverse drug reactions (1.14%).

**Conclusion:** OCPMs combined with WM had a higher efficacy. QSYQ + WM, QLQX + WM, KXQW + WM, TXL + WM, DL + WM, SSYX + WM, and SXBX + WM merit further investigation. SXBX + WM is presumably the optimal treatment prescription for both clinically effective and cardiovascular event rates. Further high-quality empirical research is needed to confirm the current results.

**Systematic Review Registration:** URL = [https://www.crd.york.ac.uk/PROSPERO/display\\_record.php?RecordID=316534](https://www.crd.york.ac.uk/PROSPERO/display_record.php?RecordID=316534), CRD 42022316534

#### KEYWORDS

stable angina, oral chinese patent medicines, Western medicine, effect, network meta-analysis

## 1 Introduction

Coronary artery disease, the leading cause of death worldwide, has affected 423 million people on a global scale, causing an estimated 31% of deaths (17.8 million) per year (Roth et al., 2017; Mensah et al., 2019). As a common manifestation of coronary heart disease, stable angina is conventionally defined as episodic discomfort in the anterior chest area (chest pain or tightness), lasting less than 10 min, typically being provoked by physical exertion or mental stimulation, and being relieved by rest or with nitroglycerin (Ohman, 2016). This disease suggests a certain degree of stenosis in a patient's coronary arteries, resulting in a relative lack of blood supply to the heart when cardiac oxygen demand increases (Fihn et al., 2012; Montalescot et al., 2013; Joshi and De Lemos, 2021). Research suggests that stable angina might double the risk of major cardiovascular events (Jones et al., 2006; Bhatt et al., 2010).

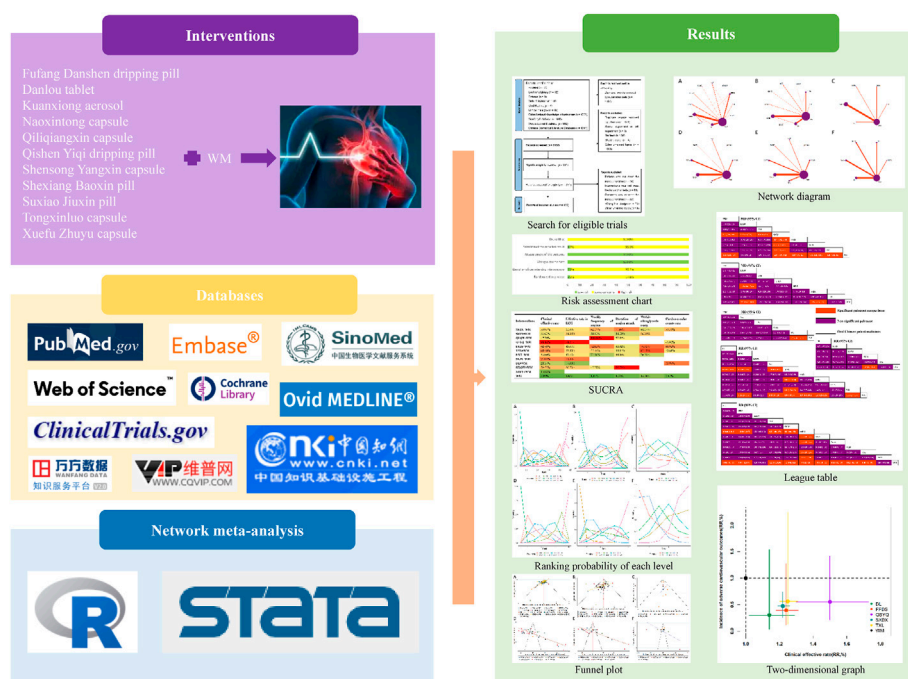
The treatment of patients with stable angina currently primarily focuses on education for patients (e.g., smoking cessation and moderate exercise) and oral administration of Western medicine (WM) to control symptoms of discomfort, reduce the probability of adverse cardiovascular events, and improve the overall quality of life (Joshi and De Lemos, 2021). Percutaneous coronary intervention is not routinely applied to stable angina, primarily due to the growing evidence showing that it is not associated with any reduction in myocardial infarction and mortality rates for most patients (Boden et al., 2007; Joshi and De Lemos, 2021).

Apart from the treatment methods mentioned previously, Chinese clinicians choose oral Chinese patent medicines (OCPMs) for stable angina based on WM implementation. Some studies showed that OCPMs relieved symptoms and improved prognoses in some target populations, such as the reduction in the duration of angina attack and a decrease in the probability of acute coronary syndrome (Mao et al., 2013; Mao et al., 2021). However, there is a great variety of OCPMs for the treatment of stable angina, and it remains controversial which OCPM has the optimal effect on stable angina.

As an extension of conventional pairwise meta-analysis, network meta-analysis enables the comparison between two or more interventions by integrating a direct comparison between various interventions, as well as an indirect comparison and further implementation ranking among the interventions (Caldwell et al., 2005; Li et al., 2011; Mills et al., 2012). In light of this, we used a network meta-analysis to compare the OCPMs recommended in a Chinese guideline for the treatment of stable angina (Mao et al., 2021) to determine the difference between them and provide some suggestions for clinical medication. The profile of the current study is summarized in Figure 1.

## 2 Methods

We followed the Preferred Reporting Items for Systematic Reviews and Meta-Analyses (PRISMA) Extension Statement to perform this network meta-analysis, with a PRISMA checklist detailed in Supplementary Material S1.



**FIGURE 1**  
Graphical abstract of the network meta-analysis. WM, Western medicine.

## 2.1 Search strategy

In this study, we searched nine academic databases for published research, including five English databases: PubMed, Embase, Web of Science, Cochrane Library, and Ovid-Medline; as well as four Chinese databases: China National Knowledge Infrastructure, Wanfang Database, Weipu Journal Database, and Chinese Biomedical Literature Database. Additionally, we also retrieved unpublished studies through Clinical [Trials.gov](#). The database retrieval time was set from inception to 13 March 2022. The search strategies employed are detailed in [Supplementary Material S2](#).

## 2.2 Inclusion and exclusion criteria

1) Patients with a definitive diagnosis of stable angina according to predefined guidelines were considered in this study (relying on angina symptoms and auxiliary examinations). It is worth noting that patients with other heart diseases such as arrhythmia or heart failure or with serious underlying diseases, for example, chronic obstructive pulmonary disease, advanced tumor, or shock, were beyond the scope of our study.

2) Patients in the experimental group were treated with one type of OCPM and WM without other traditional Chinese

medicine treatments, such as the implementation of traditional Chinese medicine injections, oral traditional Chinese medicine decoction, acupuncture, or massage. Notably, the OCPMs must be within the 12 OCPMs recommended by the Chinese guideline ([Mao et al., 2021](#)).

3) Patients in comparison were a control group treated with WM alone or another experimental group treated with another type of OCPM and WM. WM treatment mainly included secondary coronary heart disease prevention, namely, ABCDE protocol for coronary heart disease ([Dancy et al., 2018](#)).

4) Outcomes of the selected studies included one or more of the following:

Primary outcomes:

- 1) Clinical effective rate (percentage of patients whose conditions improved after treatment).
- 2) Cardiovascular events rate (acute coronary syndrome, heart failure, and cardiac death).

Secondary outcomes:

- 1) Effective rate in electrocardiograph (ECG) (Percentage of patients with improved myocardial ischemia according to ECG after treatment, e.g., ST segment improved from depression, or T wave changes from inversion to normal).
- 2) Weekly frequency of angina.



- 3) Duration of an angina attack.
- 4) Weekly nitroglycerin usage.
- 5) Adverse drug reactions (ADRs).

5) We searched for only randomized controlled trials (RCTs) for inclusion in this network meta-analysis. Randomized crossover trials were excluded if the first phase's results were unavailable.

## 2.3 Data collection

After software and manual removal of any duplicate studies, two investigators screened the remaining studies according to the pre-designed inclusion and exclusion criteria. They then extracted the following data from the final selected studies independently:

- 1) Trials information: trial title, study site, publication year, and author(s).
- 2) Population: sample size within each intervention group, sex ratio, age, and between-group comparison of patients' baseline characteristics primarily for gender, age, underlying disease, and length of illness.
- 3) Intervention: treatment modalities and treatment courses for each trial.
- 4) Outcomes: details of the seven aforementioned outcomes.
- 5) Study design: randomized approach, allocation concealment, and blinding.
- 6) Additional information: pharmaceutical company sponsorship.

## 2.4 Quality assessment

Two investigators independently assessed the risk of bias of the selected RCTs according to Version 2 of the Cochrane risk-of-bias tool for randomized trials (RoB 2) in five entries: randomization process, deviations from intended interventions, missing outcome data, measurement of the outcome, and selection of the reported results (Sterne et al., 2019). All entries were rated as "low risk", "high risk", or "some concerns", in which a trial was rated as "low risk" overall only if all the entries were assessed as "low risk". Any disagreements were resolved by discussion first or, if necessary, by arbitration by a third investigator to reach a final consensus.

## 2.5 Data analysis

Direct and indirect comparisons of all interventions were integrated via a random-effects network meta-analysis within a Bayesian framework based on 200,000 iterations and

10,000 annealings (Salanti, 2012). A contribution plot was generated to present the contribution of every direct comparison and indirect comparison to the mixed effect. Continuous variables were integrated as Mean Differences (MD) with a 95% confidence interval (CI), while categorical variables were as Risk Ratio (RR) with 95% CI. A league table was generated to summarize the comparison among interventions included in each corresponding outcome. According to the pooled effect size, each intervention obtained a probability of each level and, through a "sucra" code, summarized these probabilities to obtain a total ranking probability of surface under the cumulative ranking curve (SUCRA) (Dias et al., 2013). Furthermore, two different outcomes were integrated by 2D coordinates to assess their comparison among different interventions after integration.

A design-by-treatment approach was performed to detect the global inconsistency, while a node-splitting method was applied to assess the local inconsistency of the model (Higgins et al., 2012; van Valkenhoef et al., 2016). In addition, global  $I^2$ -statistic and predictive interval plots were employed to assess the extent of heterogeneity. A higher value of  $I^2$  suggests a greater degree of heterogeneity (Higgins and Thompson, 2002).

Sensitivity analysis of network meta-analysis was implemented by excluding studies published before 2010 to validate the robustness of the results. A subgroup network meta-analysis incorporated age group, sample size, and treatment course. Additionally, a comparison-adjusted funnel plot detected potential publication bias in the outcome with greater than or equal to 10 selected studies.

For data analysis, we applied R 4.1.2 (network meta-analysis, global heterogeneity, subgroup analysis, sensitivity analysis, probability rankings graph, and two-dimensional graph) and STATA 14.0 (network plot, inconsistency, predictive interval plot, contribution plot, and funnel plot).

## 3 Results

### 3.1 Literature retrieval and study characteristics

A total of 4,153 records were retrieved in this study. After removing 2,082 duplicates, the remaining 2,071 records were screened according to the pre-established criteria, from which 1,720 studies were deleted by abstract reading and 172 by full-text reading. Finally, 179 published RCTs with 16,789 patients (9,620 reported male patients; 57.30%) were included in the current analysis, involving 177 two-arm trials and two three-arm trials (see [Supplementary Material S3](#) for citations of the selected studies). A flow chart of the literature screening process is presented in [Supplementary Material S4](#). Overall, 11 OCPMs were included in our study, involving Fufang Danshen dripping pill (FFDS, 30 RCTs), Danlou tablet (DL, 5 RCTs), Kuanxiong

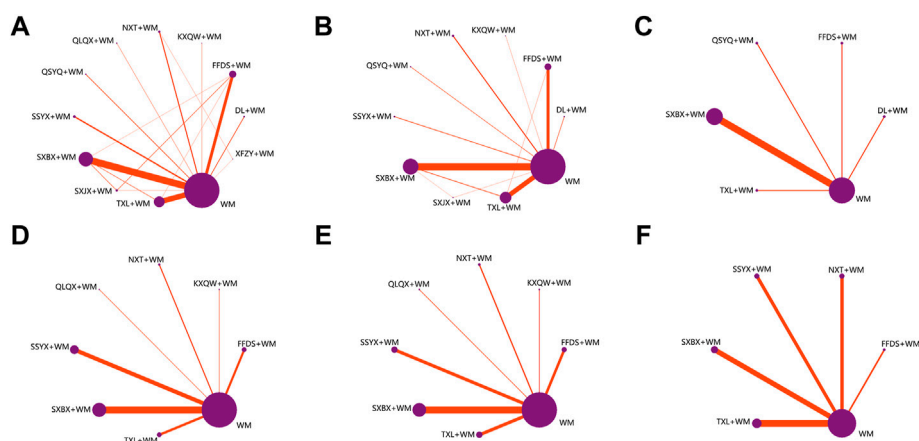


FIGURE 2

Network graph for different outcomes (A) Clinical effective rate; (B) Effective rate in ECG; (C) Cardiovascular events rate; (D) Weekly frequency of angina; (E) Duration of an angina attack; (F) Weekly nitroglycerin usage; WM, Western medicine; FFDS, Fufang Danshen dripping pill; DL, Danlou tablet; KXQW, Kuanxiong aerosol; NXT, Naoxintong capsule; QLQX, Qiliqiangxin capsule; QSYQ, Qishen Yiqi dripping pill; SSYX, Shensong Yangxin capsule; SXBX, Shexiang Baoxin pill; SXJX, Suxiao Jiuxin pill; TXL, Tongxinluo capsule; XFZY, Xuefu Zhuyu capsule.

aerosol (KXQW, 1 RCT), Naoxintong capsule (NXT, 10 RCTs), Qiliqiangxin capsule (QLQX, 3 RCTs), Qishen Yiqi dripping pill (QSYQ, 4 RCTs), Shensong Yangxin capsule (SSYX, 15 RCTs), Shexiang Baoxin pill (SXBX, 67 RCTs), Suxiao Jiuxin pill (SXJX, 6 RCTs), Tongxinluo capsule (TXL, 47 RCTs), and Xuefu Zhuyu capsule (XFZY, 2 RCTs) (see [Supplementary Material S5](#) for details of the included OCPMs). Among the 179 selected RCTs, 159 RCTs, 89 RCTs, 11 RCTs, 38 RCTs, 29 RCTs, 12 RCTs, and 90 RCTs contributed to the effective clinical rate, effective rate in ECG, weekly frequency of angina, duration of an angina attack, weekly nitroglycerin usage, cardiovascular events rate, and ADRs, respectively. Baseline data were balanced between groups in all the included studies, with the course of treatment ranging from two to 144 weeks. Characteristics of the included studies are summarized in [Supplementary Material S6](#). Meanwhile, a network graph visualized the relationship between different interventions in each outcome, in which the node sizes indicate the total sample sizes for treatment. Conversely, the width of the connecting line between each node represents the number of the included studies. The network graph is depicted in [Figure 2](#).

### 3.2 Risk-of-bias assessment

Of the selected RCTs, 53 trials reported specific randomization methods, including 48 trials using simple random number tables, three trials performing central randomization, one RCT implementing block randomization, and one RCT using stratified randomization. Four studies reported allocation concealment, which was rated “low risk”

in the “randomization process” (2.2%). Seven studies reported blinding, including two trials of single-blind methods and five trials of double-blind methods. In contrast, only five of them might use appropriate analytical methods for the results and be thus considered as “low risk” in “deviation from intended interventions” (2.8%). Although some trials had a minority of patients lost to follow-ups, all the included trials reported the number of participants in outcome assessment, causing a minor effect on outcomes assessment. Therefore, all the included trials were rated as “low risk” in “missing outcomes data” (100%). In addition, the selected studies were all rated as “low risk” in the “measurement of the outcome” primarily due to the objectivity of outcome measurement to investigators (100%). Three studies conducted experiments according to their pre-designed protocols and were considered “low risk” in the “selection of the reported result” (1.7%). Overall, the trials included in this network meta-analysis were rated as “some concerns”. [Supplementary Material S7](#) summarizes the quality of the assessment of the trials.

### 3.3 Network meta-analysis

The contribution plots of this network meta-analysis suggested that SXBX + WM vs. WM had the greatest contribution for effective clinical rate, effective rate in ECG, weekly frequency of angina, duration of an angina attack, and cardiovascular events rate, with 32.52%, 37.08%, 39.47%, 37.93%, and 63.64%, respectively. Additionally, TXL + WM vs. WM contributed the most to weekly nitroglycerin usage (33.33%). The contribution plots are provided in [Supplementary Material S8](#).

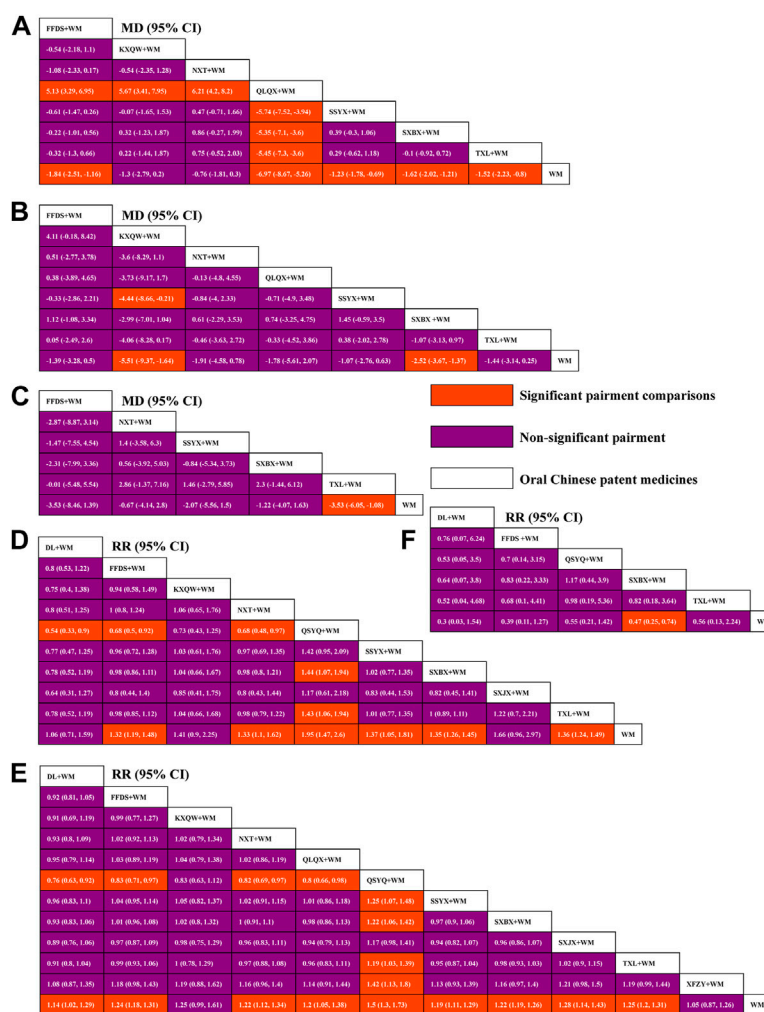


FIGURE 3

League tables for comparison between each intervention. (A) Weekly frequency of angina; (B) Duration of an angina attack; (C) Weekly nitroglycerin usage; (D) Effective rate in ECG; (E) Clinical effective rate; (F) Cardiovascular events rate; WM, Western medicine; FFDS, Fufang Danshen dripping pill; DL, Danlou tablet; KXQW, Kuanxiong aerosol; NXT, Naoxintong capsule; QLQX, Qiliqiangxin capsule; QSYQ, Qishen Yiqi dripping pill; SSYX, Shensong Yangxin capsule; SXBX, Shexiang Baoxin pill; SXJX, Suxiao Jiuxin pill; TXL, Tongxinluo capsule; XFZY, Xuefu Zhuyu capsule.

### 3.4 Primary outcomes

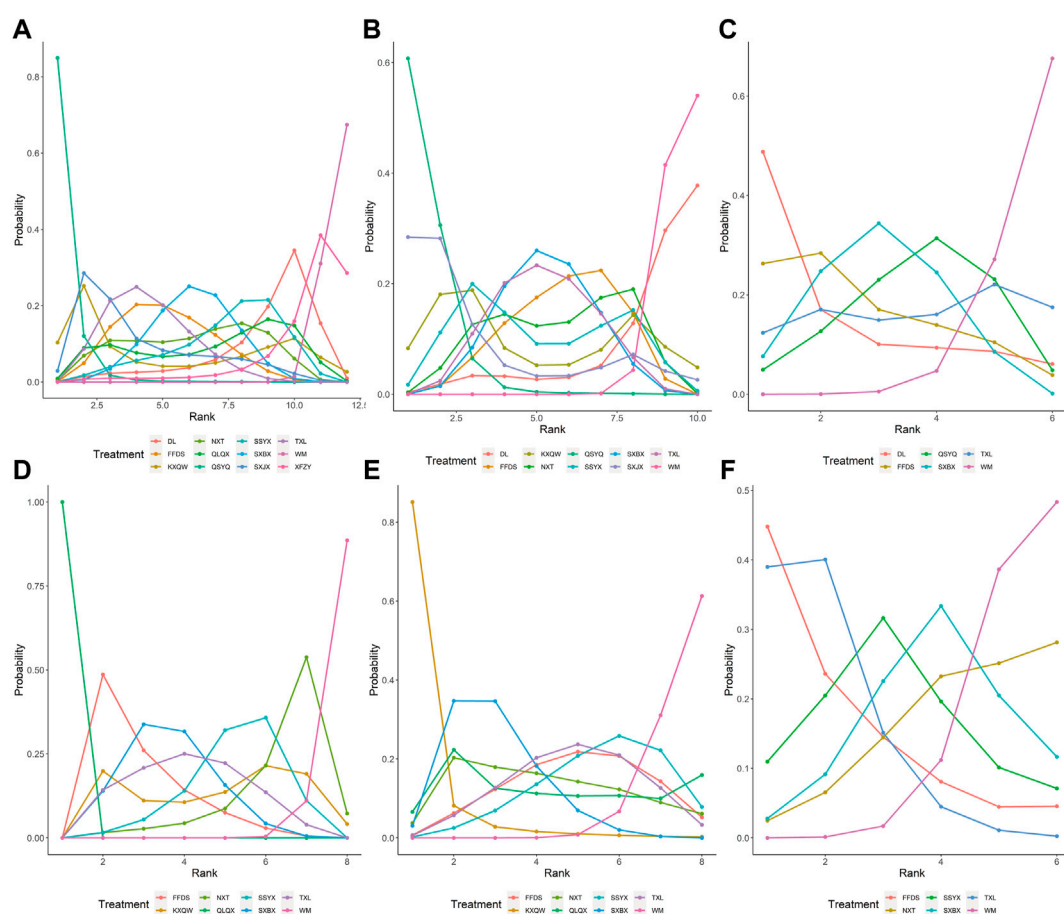
#### 3.4.1 Effective clinical rate

Twelve treatment nodes were compared in effective clinical rate, including DL + WM, FFDS + WM, KXQW + WM, NXT + WM, QLQX + WM, QSYQ + WM, SSYX + WM, SXBX + WM, SXJX + WM, TXL + WM, XFZY + WM, and WM. We found that all the included OCPMs plus WM, apart from KXQW + WM and XFZY + WM, had a higher clinical effectiveness rate than WM alone. Additionally, QSYQ + WM improved its clinical effectiveness rate compared with SSYX + WM, SXBX + WM, TXL + WM, XFZY + WM, QLQX + WM, NXT + WM, FFDS + WM, and DL + WM. The comparison between each intervention is depicted in Figure 3E. Based on the ranking probability of each

level and SUCRA, QSYQ + WM had the highest effective rate (98.12%), followed by SXJX + WM (71.04%) and TXL + WM (68.40%), whereas WM alone obtained the worst effect (3.09%). The ranking probability is presented in Figure 4A and Table 1.

#### 3.4.2 Cardiovascular event rate

Six interventions were involved in evaluating cardiovascular events rate, including DL + WM, FFDS + WM, QSYQ + WM, SXBX + WM, TXL + WM, and WM alone. The decrease in cardiovascular events rate was statistically significant for SXBX + WM as compared with WM alone, while no significant association was found within other interventions. The comparison between each intervention is revealed in Figure 3F. Based on the ranking probability of each level and



Note: Oral Chinese patent medicines are added on the basis of using Western medicine.

**FIGURE 4**

Ranking probability at each level for the included interventions. (A) Weekly frequency of angina; (B) Duration of an angina attack; (C) Weekly nitroglycerin usage; (D) Effective rate in ECG; (E) Clinical effective rate; (F) Cardiovascular events rate; WM, Western medicine; FFDS, Fufang Danshen dripping pill; DL, Danlou tablet; KXQW, Kuanxiong aerosol; NXT, Naioxintong capsule; QLQX, Qiliqiangxin capsule; QSYQ, Qishen Yiqi dripping pill; SSYX, Shensong Yangxin capsule; SXBX, Shexiang Baoxin pill; SXJX, Suxiao Jiuxin pill; TXL, Tongxinluo capsule; XFZY, Xuefu Zhuyu capsule.

SUCRA, DL + WM had the highest effect (73.94%), followed by FFDS + WM (66.92%) and SXBX + WM (59.59%), whereas WM alone obtained the worst effect (7.67%). The ranking probability is demonstrated in Figure 4C and Table 1.

### 3.5 Secondary outcome

#### 3.5.1 Effective rate in ECG

Ten treatment options were compared in this network geometry, including DL + WM, FFDS + WM, KXQW + WM, NXT + WM, QSYQ + WM, SSYX + WM, SXBX + WM, SXJX + WM, TXL + WM, and WM. Apart from DL + WM, KXQW + WM, and SXJX + WM, an improvement effect of effective rate in ECG was detected for all of the included OCPMs plus WM as compared with WM alone. QSYQ + WM obtained a better effect than SXBX + WM, TXL + WM, DL + WM, FFDS + WM, and

NXT + WM. The comparison between each intervention is depicted in Figure 3D. Based on the ranking probability of each level and SUCRA, QSYQ + WM had the highest effective rate (94.21%), followed by SXJX + WM (73.80%) and KXQW + WM (56.70%), whereas WM alone obtained the worst effect (5.63%). The ranking probability is presented in Figure 4B; Table 1.

#### 3.6 Weekly frequency of angina

Eight interventions were involved in the evaluation of the weekly frequency of angina, including FFDS + WM, KXQW + WM, NXT + WM, QLQX + WM, SSYX + WM, SXBX + WM, TXL + WM, and WM. Apart from KXQW + WM and NXT + WM, the remaining OCPMs plus WM earned a better effect of decreasing weekly angina frequency than WM alone. In addition,



TABLE 1 Ranking probabilities of surface under the cumulative ranking area curves (SUCRA) for the outcomes.

Interventions	Clinical effective rate (%)	Effective rate in ECG (%)	Weekly frequency of angina (%)	Duration of an angina attack (%)	Weekly nitroglycerin usage (%)	Cardiovascular event rate (%)
SXBX + WM	53.03	52.09	62.29	71.60	41.07	59.59
SSYX + WM	41.62	54.36	38.82	34.58	56.23	
QLQX + WM	47.29		100.00	50.19		
QSYQ + WM	98.12	94.21				46.07
FFDS + WM	62.41	45.47	72.62	42.82	76.50	66.92
TXL + WM	68.40	52.85	55.44	44.14	82.12	45.81
NXT + WM	53.00	47.40	23.36	44.10	30.73	
SXJX + WM	71.04	73.80				
DL + WM	28.57	17.49				73.94
KXQW + WM	59.55	56.70	45.79	95.71		
XFZY + WM	13.88					
WM	3.09	5.63	1.69	6.74	13.34	7.67

WM, Western medicine; FFDS, fufang danshen dripping pill; DL, danlou tablet; KXQW, kuanxiong aerosol; NXT, naoxintong capsule; QLQX, qiliqiangxin capsule; QSYQ, qishen yiqi dripping pill; SSYX, shensong yangxin capsule; SXBX, shexiang baoxin pill; SXJX, suxiao jiuxin pill; TXL, tongxinluo capsule; XFZY, Xuefu Zhuyu capsule.

QLQX + WM statistically reduced the weekly frequency of angina as compared with other included OCPMs plus WM. The comparison between each intervention is revealed in Figure 3A. According to the ranking probability of each level and SUCRA, QLQX + WM had the highest effective rate in reducing the weekly frequency of angina (100.00%), followed by FFDS + WM (72.62%) and SXBX + WM (62.29%). In contrast, WM alone obtained the worst effect (1.69%). The ranking probability is presented in Figure 4D; Table 1.

### 3.7 Duration of an angina attack

There were eight separate treatment nodes in the network geometry for the duration of the angina attack, including FFDS + WM, KXQW + WM, NXT + WM, QLQX + WM, SSYX + WM, SXBX + WM, TXL + WM, and WM. KXQW + WM and SXBX + WM revealed a higher effect in shortening angina attack duration than WM; meanwhile, KXQW + WM was superior to SSYX + WM. The between-intervention differences were demonstrated in Figure 3B. According to the ranking probability of each level and SUCRA, KXQW + WM ranked first (95.71%), followed by SXBX + WM (71.60%) and QLQX + WM (50.19%), whereas WM alone obtained the worst effect (6.74%). The ranking probability is demonstrated in Figure 4E; Table 1.

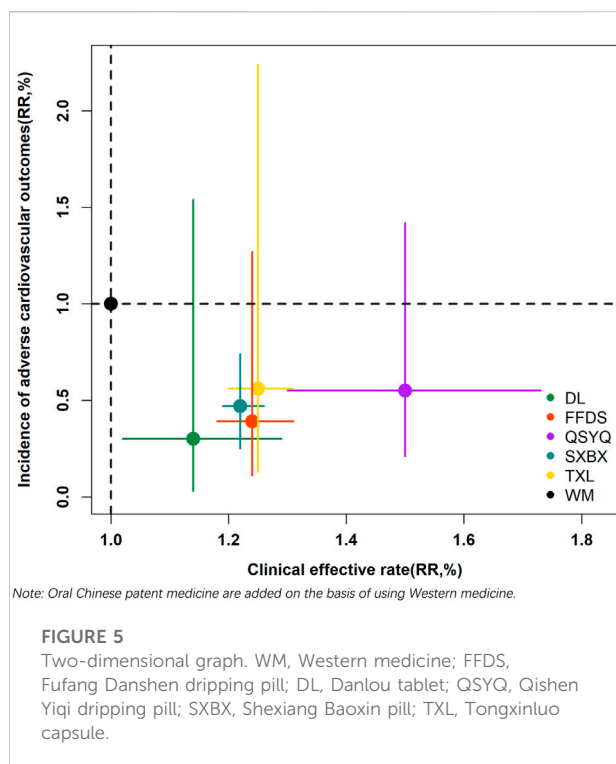
### 3.8 Weekly nitroglycerin usage

Eight interventions (FFDS + WM, NXT + WM, SSYX + WM, SXBX + WM, TXL + WM, and WM) were involved in the

evaluation of weekly nitroglycerin usage. TXL + WM was superior for WM alone in reducing weekly nitroglycerin usage. No significant association was found among other interventions. The comparison between each intervention is displayed in Figure 3C. According to the ranking probability of each level and SUCRA, TXL + WM had the highest SUCRA value (82.12%), followed by FFDS + WM (76.50%) and SSYX + WM (56.23%), whereas WM alone obtained the worst effect (13.34%). The ranking probability is demonstrated in Figure 4F; Table 1.

### 3.9 Adverse drug reactions

In the current study, network meta-analysis was impossible for ADRs as most studies reported negative results (0% in incidence). Of 4,514 patients observed, 250 occurred with ADRs (5.54%), involving 96 with mild abdominal discomfort, 91 with dizziness/headache, 11 with numbness of tongue and lips, 24 with rash, and 28 with mild chest discomfort, whereas had no serious ADRs. Among 1,951 SXBX + WM-treated patients, the incidences of mild abdominal discomfort, dizziness/headache, numbness of tongue and lips, rash, and mild chest discomfort, were 2.67%, 2.41%, 0.56%, 0.56%, and 0.67%, respectively, with the total adverse reaction rate of 6.87%. In 81 patients treated with SXJX + WM, the incidences of mild abdominal discomfort, dizziness/headache, rash, and mild chest discomfort, were 2.47%, 17.28%, 7.41%, and 8.64%, separately, with a total adverse reaction rate of 35.80%. The incidence of ADRs in FFDS + WM groups (616 patients) was



7.79%, in which 2.11% of mild abdominal discomfort, 3.25% of dizziness/headache, 1.14% of rash, and 1.30% of mild chest discomfort. DL + WM groups (54 patients) had an incidence of ADRs of 1.85%, in which only one patient occurred with mild abdominal discomfort. 188 patients treated with NXT + WM had an ADRs incidence of 1.60%, including 1.06% mild abdominal discomfort and 0.53% dizziness/headache. There was a 4.12% incidence of ADRs in 97 patients treated with QLQX + WM, including 3.09% mild abdominal discomfort and 1.03% dizziness/headache. Four of 350 patients treated with SSYX + WM reported mild abdominal discomfort, contributing to 1.14% of the incidence of ADRs. Among 832 TXL + WM-treated patients, the incidences of mild abdominal discomfort and dizziness/headache were 2.28% and 0.96%, individually, with a total adverse reaction rate of 3.25%. Additionally, no ADRs occurred in 55 patients treated with KXQW + WM and 190 patients treated with QSYQ + WM. The ADRs are detailed in [Supplementary Material S9](#).

### 3.10 Integrated outcome

OCPMs + WM shared in effective clinical rate, and cardiovascular events rate were integrated into a two-dimensional graph with WM as the comparison. As depicted in [Figure 5](#), the RR of each intervention was demonstrated as a center point while 95% CI was presented as the length of the horizontal

and vertical lines. In the current analysis, only SXBX + WM had no vertical and horizontal lines intersecting the futility line, indicating that it may be the best intervention for the combined outcome.

### 3.11 Inconsistency, heterogeneity, and publication bias

Inconsistency can only be detected within outcomes, with treatment nodes forming one or more loops; we detected an inconsistency in effective clinical rate and effective rate in ECG. The results of global inconsistency did not indicate any significant difference for each of the two outcomes ( $p = 0.077$  and  $p = 0.081$  for effective clinical rate and effective rate in ECG, respectively). The detection of the node-splitting model suggested that only three comparisons for effective clinical rate and two for effective rate in ECG presented significant differences between direct and indirect comparisons. The results of inconsistency detection are shown in [Supplementary Material S10](#). Global  $I^2$ -statistic were revealed as 0%, 0.4%, 98.15%, 99.67%, 99.51%, and 0% for effective clinical rate, effective rate in ECG, weekly frequency of angina, duration of an angina attack, weekly nitroglycerin usage, and cardiovascular events rate, individually. The results of predictive interval plots suggested that 10.61%, 17.78%, 14.29, 10.71%, 6.67%, and 6.67% of the comparisons of effective clinical rate, effective rate in ECG, weekly frequency of angina, duration of an angina attack, weekly nitroglycerin usage, and cardiovascular events rate, separately, were significantly affected by the estimated heterogeneity. The predictive interval plots are detailed in [Supplementary Material S11](#). As depicted in [Supplementary Material S12](#), all the fitted straight lines' slopes are close to the centerline, and the points on both sides of the centerline are relatively symmetric, indicating that there was no obvious publication bias for all the outcomes.

### 3.12 Sensitivity analyses and subgroup analyses

Sensitivity analyses, the network meta-analyses being performed among studies published in 2010 and beyond/ studies that do not include OCPMs with selected RCTs less than 3, i.e., KXQW + WM and XFZY + WM, confirmed the more-effective benefit of OCPMs plus WM in all the outcomes as compared with WM and further verified the best intervention for effective clinical rate, effective rate in ECG, weekly frequency of angina, and cardiovascular events rate as QSYQ + WM, QSYQ + WM, QLQX + WM, and DL + WM, respectively (see [Supplementary Material S13](#) for sensitivity analyses). Subgroup analyses suggested that the benefits of effective clinical rate, effective rate in ECG, duration of an angina attack, and cardiovascular events rate of OCPMs + WM vs. WM, individually, were more evident in patients with a trial

duration of fewer than three months, sample size less than 100, trial duration greater than or equal to three months, trial duration greater than or equal to three months/sample size greater than or equal to 100. The results of the subgroup analyses are provided in [Supplementary Material S14](#).

## 4 Discussion

The current network meta-analysis is the first study investigating OCPMs on stable angina pectoris. Although there have been several published network meta-analyses reporting the efficacy of Chinese patent medicine on stable angina pectoris, they all included traditional Chinese medicine injections or unlisted oral decoctions as the interventions and enrolled unstable angina patients as the target population, with a limited number of included studies (Ding, 2017; Ji et al., 2019; Wang Z. X. et al., 2021; Sun et al., 2021). Our study revealed that the addition of OCPMs based on WM could achieve a better clinical effect than WM alone for stable angina pectoris, which was consistent with the results of published pairwise meta-analyses (Lu et al., 2017; Pan et al., 2019; Xi et al., 2019; Zheng et al., 2021; Zhuan et al., 2021). Additionally, by comparing different interventions, this study also suggested that QSYQ + WM, QLQX + WM, KXQW + WM, TXL + WM, DL + WM, SSYX + WM, and SXBX + WM deserve more attention in treating stable angina.

Stable angina pectoris belongs to the category of “chest impediment with stabbing pain” based on the theoretical principles of traditional Chinese medicine (Wang and Chen, 2018). The theory expounds that this disease is caused by blood stasis, status as a result of qi deficiency or qi stagnation, thereby leading to the occlusion of the heart vessel (Wu, 2017). Based on the pathogenesis, therefore, traditional Chinese medicines that possess efficacy for invigorating qi, activating blood, regulating qi, and dredging collaterals, are used to treat stable angina pectoris (Wu, 2017). The selected OCPMs in this study all belong to this class of drugs.

Among the included OCPMs, QSYQ is a dripping pill made by *Astragalus mongholicus* Bunge [Fabaceae], *Salvia miltiorrhiza* Bunge [Lamiaceae], *Panax notoginseng* (Burkill) F.H.Chen [Araliaceae], and *Dalbergia odorifera* T.C.Chen [Fabaceae] by water-extraction and an alcohol-precipitation method, primarily containing salvianolic acid, protocatechuic aldehyde, and flavonoids (Fu et al., 2012). Some published research demonstrated that QSYQ could ameliorate ventricular remodeling, suppress arachidonic acid lipoxigenase pathway as well as elevation of nitric oxide, improve dyslipidemia mediated via fatty acid oxidation, and regulate the PI3K/Akt-mTOR pathway, all of which possessed positive effects on the heart and blood vessels in patients with stable angina (Wang et al., 2017; Lv et al., 2020). QLQX is prepared from 11 different botanical drugs, including *Astragalus mongholicus* Bunge [Fabaceae], *Panax ginseng* C.A.Mey [Araliaceae], and *Aconitum carmichaeli* Debeaux [Ranunculaceae], containing mainly

flavonoids, saponins, and triterpenoids (Lu et al., 2021). Based on a published study, the drug could potentially modulate metabolic proteins regionally to guide the border myocardium against hypoxia injuries and oxidize fatty acids to maximize energy utilization, thus protecting surviving cardiomyocytes (Cheng et al., 2020). KXQW are composed of *Borneolum Syntheticum*, volatile oils of *Asarum heterotropoides* F. Schmidt [Aristolochiaceae], *Santalum album* L [Santalaceae], *Alpinia officinarum* Hance [Zingiberaceae], and *Piper longum* L [Piperaceae], mainly containing 1, 8-cineole, borneol, methyleugenol, and satanol (Sun, 1985). The mechanism of action of KXQW includes dilating the coronary artery by activating the CaMK II/ERK signaling pathway and suppressing the influx and release of calcium, which might improve myocardial injury among stable angina patients (Lu et al., 2022). TXL is prepared from 12 different traditional Chinese medicines (e.g., *Panax ginseng* C.A.Mey [Araliaceae] and *Santalum album* L [Santalaceae]), comprising active ingredients such as resveratrol, arbutin, and palmitic acid (Mi, 2018; Sun, 2018). A basic experiment elaborated on the effects of TXL on suppressing atherosclerosis development and stabilizing plaque by regulating inflammation, lipid metabolism, cell physical function, hormone secretion, protein binding, and immune response process (Ma et al., 2019). DL comprises ten different types of botanical drugs such as *Trichosanthes rosthornii* Harms [Cucurbitaceae] and *Allium macrostemon* Bunge [Amaryllidaceae] with components primarily as artemisinolide (17.49%),  $\beta$ -Elemene (11.07%), and (-) Spartol (8.95%) (Zhang et al., 2016). Studies of mechanism indicated that DL could inhibit NF- $\kappa$ B signaling, trigger PPAR $\alpha$ /ABCA1 signaling pathway, and activate PI3K/Akt/mTOR-mediated autophagy of vascular adventitial fibroblasts, thus preventing atherosclerosis (Hao et al., 2019; Wang L. et al., 2021). SXBX is composed of seven traditional Chinese medicines such as *Panax ginseng* C.A.Mey [Araliaceae], *Cinnamomum verum* J. Presl [Lauraceae], and *Liquidambar orientalis* Mill [Altingiaceae]. A systematic review summarized the mechanism of SXBX for vessels and the heart, including promotion of angiogenesis, amelioration of inflammation, improvement of endothelium dysfunction, mitigation of dyslipidemia, proliferation/migration repression of vascular smooth muscle cells, and restraint of cardiac remodeling (Lu et al., 2018). SSYX contains 12 types of traditional Chinese medicines, including *Panax ginseng* C.A.Mey [Araliaceae], *Ophiopogon japonicus* (Thunb.) Ker Gawl [Asparagaceae], and *Cornus officinalis* Siebold and Zucc. [Cornaceae], etc. (Bai et al., 2018). Published studies confirmed that SSYX could reduce the incidence and severity of myocardial ischemic arrhythmias and decrease the area of myocardial necrosis caused by coronary insufficiency, which may be related to extending the action potential and alleviating Ca<sup>2+</sup> overload (Zhao et al., 2016).

In addition to the curative effect of OCPMs on stable angina, the ADRs caused by the drug should also be of great concern, although our study demonstrated that the selected OCPMs did not cause severe ADRs. To generate fewer ADRs when using OCPMs, a study suggests avoiding taking the selected OCPMs on

an empty stomach (Dai and Yu, 2002). Additionally, prescribing drugs according to patients' traditional Chinese syndromes may be another suggestion (Ye et al., 2021).

## 4.1 Limitations

First, all trials included were assessed as some concerns according to RoB2. Therefore, the results should be interpreted cautiously. Second, some interventions included a limited number of studies, such as one RCT for KXQW + WM, three RCTs for QLQX + WM, and four RCTs for QSYQ + WM, and two RCTs for XFZY + WM. Therefore, these results should be interpreted with caution. Finally, the studies selected in the current network meta-analysis were conducted in China, so the results may not be generalizable to other countries.

## 5 Conclusion

In treating stable angina, adding OCPMs besides WM may acquire a better curative effect. QSYQ + WM, QLQX + WM, KXQW + WM, TXL + WM, DL + WM, SSYX + WM, and SXBX + WM are worth taking into account in treating patients with stable angina, while SXBX + WM merits more attention. Further careful assessment of this conclusion is needed in future clinical studies which must be of higher quality.

## Data availability statement

The original contributions presented in the study are included in the article/Supplementary Material; further inquiries can be directed to the corresponding author.

## Author contributions

PH and BC conceived the study. YF and SL performed the literature search, screening, and extraction. QW and HZ implemented quality assessment. PH, ZL, LC, JZ, YT, YC, BH, XH, and LZ performed the network meta-analysis. PH wrote the

manuscript. BC, ZZ, YL, HG, and SZ coordinated the revision of the manuscript. All authors approved the final version of this manuscript.

## Funding

This study was funded by the National Natural Science Foundation of China (Grant Nos. 81273961 and 81303117), the Municipal School (college) Joint Funding Project of Guangzhou Municipal Science and Technology Foundation (Grant No. 202201020352), Science and Technology Foundation of Shenzhen City (Grant No. JSGG20220226085800001), Science and Technology Foundation of Shenzhen City (Grant No. JCYJ20190812164009243), and Guangdong Medical Research Foundation (Grant No. B2020135).

## Conflict of interest

The authors declare that the research was conducted in the absence of any commercial or financial relationships that could be construed as a potential conflict of interest.

## Publisher's note

All claims expressed in this article are solely those of the authors and do not necessarily represent those of their affiliated organizations, or those of the publisher, the editors, and the reviewers. Any product that may be evaluated in this article, or claim that may be made by its manufacturer, is not guaranteed or endorsed by the publisher.

## Supplementary material

The Supplementary Material for this article can be found online at: <https://www.frontiersin.org/articles/10.3389/fphar.2022.918689/full#supplementary-material>

## References

- Bai, Y. D., Qiao, Z., Xue, J. W., Liu, F. L., and Liu, W. Y. (2018). Simultaneous determination of different constituents in Shensong Yangxin capsules and method validation. *Chin. J. Pharm. Anal.* 38 (08), 1358–1368. doi:10.16155/j.0254-1793.2018.08.10
- Bhatt, D. L., Eagle, K. A., Ohman, E. M., Hirsch, A. T., Goto, S., Mahoney, E. M., et al. (2010). Comparative determinants of 4-year cardiovascular event rates in stable outpatients at risk of or with atherothrombosis. *J. Am. Med. Assoc.* 304 (12), 1350–1357. doi:10.1001/jama.2010.1322
- Boden, W. E., O'Rourke, R. A., Teo, K. K., Hartigan, P. M., Maron, D. J., Kostuk, W. J., et al. (2007). Optimal medical therapy with or without PCI for stable coronary disease. *N. Engl. J. Med.* 356 (15), 1503–1516. doi:10.1056/NEJMoa070829
- Caldwell, D. M., Ades, A. E., and Higgins, J. P. (2005). Simultaneous comparison of multiple treatments: combining direct and indirect evidence. *Bmj* 331 (7521), 897–900. doi:10.1136/bmj.331.7521.897
- Cheng, W., Wang, L., Yang, T., Wu, A., Wang, B., Li, T., et al. (2020). Qiliqiangxin capsules optimize cardiac metabolism flexibility in rats with heart failure after myocardial infarction. *Front. Physiol.* 11, 805. doi:10.3389/fphys.2020.00805
- Dai, L., and Yu, X. H. (2002). Rational use of proprietary Chinese medicines. *Strait Pharm. J.* 14 (04), 86–87. doi:10.3969/j.issn.1006-3765.2002.04.052
- Dancy, L., O'Gallagher, K., Milton, P., and Sado, D. (2018). New NICE guidelines for the management of stable angina. *Br. J. Gen. Pract.* 68 (669), 202–203. doi:10.3399/bjgp18X695693



- Dias, S., Sutton, A. J., Ades, A. E., and Welton, N. J. (2013). Evidence synthesis for decision making 2: a generalized linear modeling framework for pairwise and network meta-analysis of randomized controlled trials. *Med. Decis. Mak.* 33 (5), 607–617. doi:10.1177/0272989x12458724
- Ding, L. L. (2017). *Network Meta-analysis and summary evaluation of Chinese patent medicine adjuvant treatment of angina pectoris*. Kunming: Kunming Medical University. Master.
- Fihn, S. D., Gardin, J. M., Abrams, J., Berra, K., Blankenship, J. C., Dallas, A. P., et al. (2012). 2012 ACCF/AHA/ACP/AATS/PCNA/SCAI/STS guideline for the diagnosis and management of patients with stable ischemic heart disease: a report of the American college of cardiology foundation/American heart association task force on practice guidelines, and the American college of physicians, American association for thoracic surgery, preventive cardiovascular nurses association, society for cardiovascular angiography and interventions, and society of thoracic surgeons. *J. Am. Coll. Cardiol.* 60 (24), e44–e164. doi:10.1016/j.jacc.2012.07.013
- Fu, J. Z., Song, Y. S., Jiang, M., Peng, J. M., Wang, J., Huang, H., et al. (2012). Simultaneous determination of the contents of astragaloside, danshensu, protocatechualdehyde, ginsenosides Rg1 and Rb1 in qishenyiqi dropping pills by LC-MS. *Chin. Pharm. J.* 47 (01), 61–64.
- Hao, D., Danbin, W., Maojuan, G., Chun, S., Bin, L., Lin, Y., et al. (2019). Ethanol extracts of Danlou tablet attenuate atherosclerosis via inhibiting inflammation and promoting lipid effluent. *Pharmacol. Res.* 146, 104306. doi:10.1016/j.phrs.2019.104306
- Higgins, J. P., and Thompson, S. G. (2002). Quantifying heterogeneity in a meta-analysis. *Stat. Med.* 21 (11), 1539–1558. doi:10.1002/sim.1186
- Higgins, J. P., Jackson, D., Barrett, J. K., Lu, G., Ades, A. E., White, I. R., et al. (2012). Consistency and inconsistency in network meta-analysis: Concepts and models for multi-arm studies. *Res. Synth. Methods* 3 (2), 98–110. doi:10.1002/jrsm.1044
- Ji, Z. C., Yang, F. W., Zhang, L. S., Jin, X. Y., Wang, H. C., Pang, W. T., et al. (2019). Network Meta-analysis of Yiqi Huoxue Chinese patent medicine for coronary heart disease with angina pectoris. *China J. Chin. Materia Med.* 44 (09), 1927–1937. doi:10.19540/j.cnki.cjcmm.20190114.001
- Jones, M., Rait, G., Falconer, J., and Feder, G. (2006). Systematic review: prognosis of angina in primary care. *Fam. Pract.* 23 (5), 520–528. doi:10.1093/fampra/cml038
- Joshi, P. H., and De Lemos, J. A. (2021). Diagnosis and management of stable angina: A review. *J. Am. Med. Assoc.* 325 (17), 1765–1778. doi:10.1001/jama.2021.1527
- Li, T., Puhon, M. A., Vedula, S. S., Singh, S., and Dickersin, K. (2011). Network meta-analysis-highly attractive but more methodological research is needed. *BMC Med.* 9, 79. doi:10.1186/1741-7015-9-79
- Lu, J. J., Lei, X., and Shang, H. C. (2017). Systematic review of Danlou Tablets in the treatment of stable angina pectoris with mutual resistance of phlegm and blood stasis. *Chin. J. Integr. Med. Cardio/Cerebrovasc. Dis.* 15 (10), 1198–1202. doi:10.3969/j.issn.1672-1349.2017.10.014
- Lu, L., Sun, X., Chen, C., Qin, Y., and Guo, X. (2018). Shexiang Baoxin pill, derived from the traditional Chinese medicine, provides protective roles against cardiovascular diseases. *Front. Pharmacol.* 9, 1161. doi:10.3389/fphar.2018.01161
- Lu, S. L., Feng, Y., Gao, J., Jin, X. G., Wang, Y. X., and Chen, K. J. (2021). Recent advances in clinical application of Panax notoginseng saponins in cardiovascular diseases. *Chin. General Pract.* 24 (5), 539–545. doi:10.12114/j.issn.1007-9572.2020.00.623
- Lu, Y., Yang, M. L., Shen, A. L., Lin, S., Peng, M. Z., Wang, T. Y., et al. (2022). Pharmacodynamic mechanism of Kuanxiong aerosol for vasodilation and improvement of myocardial ischemia. *Chin. J. Integr. Med.* 28 (4), 319–329. doi:10.1007/s11655-021-2882-z
- Lv, S., Yuan, P., Dong, J., Lu, C., Li, M., Qu, F., et al. (2020). QiShenYiQi pill improves the reparative myocardial fibrosis by regulating autophagy. *J. Cell. Mol. Med.* 24 (19), 11283–11293. doi:10.1111/jcmm.15695
- Ma, J., Qiao, L., Meng, L., Ma, L., Zhao, Y., Liu, X., et al. (2019). Tongxinluo may stabilize atherosclerotic plaque via multiple mechanisms scanning by genechip. *Biomed. Pharmacother.* 113, 108767. doi:10.1016/j.biopha.2019.108767
- Mao, C., Chung, V. C., Yuan, J. Q., Yu, Y. Y., Yang, Z. Y., Wu, X. Y., et al. (2013). Evaluation of the add-on effect of Chinese patent medicine for patients with stable or unstable angina: a systematic review and meta-analysis. *Evid. Based. Complement. Altern. Med.* 2013, 673193. doi:10.1155/2013/673193
- Mao, J. Y., Wu, Y. J., and Shi, D. Z. (2021). Guidelines for clinical application of Chinese patent medicines in the treatment of coronary heart disease (2020). *Chin. J. Integr. Med. Cardio/Cerebrovasc. Dis.* 19 (09), 1409–1435. doi:10.12102/j.issn.1672-1349.2021.09.001
- Mensah, G. A., Roth, G. A., and Fuster, V. (2019). *The global burden of cardiovascular diseases and risk factors: 2020 and beyond*. Washington, DC: American College of Cardiology Foundation.
- Mi, H. Y. (2018). *Analysis of the medical records of Professor Wu Yiling in the treatment of coronary heart disease and angina pectoris based on data mining and network pharmacology research of Tongxinluo Capsules*. Hubei: Hebei Medical University. doctor.
- Mills, E. J., Ioannidis, J. P., Thorlund, K., Schünemann, H. J., Puhon, M. A., Guyatt, G. H., et al. (2012). How to use an article reporting a multiple treatment comparison meta-analysis. *J. Am. Med. Assoc.* 308 (12), 1246–1253. doi:10.1001/2012.jama.11228
- Montalescot, G., Sechtem, U., Achenbach, S., Andreotti, F., Arden, C., Budaj, A., et al. (2013). 2013 ESC guidelines on the management of stable coronary artery disease: the task force on the management of stable coronary artery disease of the European society of cardiology. *Eur. Heart J.* 34 (38), 2949–3003. doi:10.1093/eurheartj/ehz296
- Ohman, E. M. (2016). Chronic stable angina. *N. Engl. J. Med.* 374 (12), 293. doi:10.1056/NEJMc1605394
- Pan, F. Q., Xi, Y. T., Huang, T. F., Cao, Y. H., and Wu, W. (2019). Meta-analysis of Shexiang Baoxin Pill in the treatment of stable angina pectoris. *Shizhen Tradit. Chin. Med.* 30 (12), 3041–3045. CNKI:SUN:SZGY.0.2019-12-078.
- Roth, G. A., Johnson, C., Abajobir, A., Abd-Allah, F., Abera, S. F., Abyu, G., et al. (2017). Global, regional, and national burden of cardiovascular diseases for 10 causes, 1990 to 2015. *J. Am. Coll. Cardiol.* 70 (1), 1–25. doi:10.1016/j.jacc.2017.04.052
- Salanti, G. (2012). Indirect and mixed-treatment comparison, network, or multiple-treatments meta-analysis: many names, many benefits, many concerns for the next generation evidence synthesis tool. *Res. Synth. Methods* 3 (2), 80–97. doi:10.1002/jrsm.1037
- Sterne, J. A. C., Savović, J., Page, M. J., Elbers, R. G., Blencowe, N. S., Boutron, I., et al. (2019). RoB 2: a revised tool for assessing risk of bias in randomised trials. *Bmj* 366, 14898. doi:10.1136/bmj.14898
- Sun, Y. Z., Wang, Z. Y., Tang, Z. R., Huang, L. X., and Zhao, H. B. (2021). Network meta-analysis of Chinese patent medicines of regulating qi and activating blood circulation for angina pectoris. *World Chin. Med.* 16 (21), 3204–3212+3218. doi:10.3969/j.issn.1673-7202.2021.21.017
- Sun, E. T. (1985). Gas chromatographic determination of Chinese patent medicine Kuanxiong aerosol. *Chromatography* 2 (06), 342–345+354.
- Sun, M. S. (2018). *The therapeutic effect and mechanism of Tongxinluo through PI3K/Akt pathway on cerebral ischemia reperfusion injury in rats*. Jilin: Jilin University. doctor.
- van Valkenhoef, G., Dias, S., Ades, A. E., and Welton, N. J. (2016). Automated generation of node-splitting models for assessment of inconsistency in network meta-analysis. *Res. Synth. Methods* 7 (1), 80–93. doi:10.1002/jrsm.1167
- Wang, J., and Chen, G. (2018). Expert consensus on TCM diagnosis and treatment of stable angina pectoris with coronary heart disease. *J. Traditional Chin. Med.* 59 (05), 447–450. doi:10.13288/j.11-2166/r.2018.05.020
- Wang, Y., Lin, W., Li, C., Singhal, S., Jain, G., Zhu, L., et al. (2017). Multipronged therapeutic effects of Chinese herbal medicine qishenyiqi in the treatment of acute myocardial infarction. *Front. Pharmacol.* 8, 98. doi:10.3389/fphar.2017.00098
- Wang, L., Wu, T., Si, C., Wang, H., Yue, K., Shang, S., et al. (2021a). Danlou tablet activates autophagy of vascular adventitial fibroblasts through PI3K/Akt/mTOR to protect cells from damage caused by atherosclerosis. *Front. Pharmacol.* 12, 730525. doi:10.3389/fphar.2021.730525
- Wang, Z. X., Ban, J. F., Li, R. L., Wang, T. F., and Ke, R. (2021b). Network-meta analysis of 9 kinds of patent Chinese medicine for nourishing qi and activating blood in the treatment of angina pectoris of coronary heart disease. *J. Hainan Med. Univ.* 27 (11), 845–854. doi:10.13210/j.cnki.jhmu.20200924.001
- Wu, M. H. (2017). *Internal medicine of traditional Chinese medicine*. Beijing: China Traditional Chinese Medicine Press.
- Xi, Y. T., Yuan, L. Y., Zeng, Y. Y., Yan, M. L., Liang, X. R., Feng, A. T., et al. (2019). Shensong Yangxin Capsules in the adjuvant treatment of stable angina pectoris: a Meta-analysis and trial sequential analysis. *China J. Chin. Materia Med.* 44 (17), 3816–3824. doi:10.19540/j.cnki.cjcmm.20190624.503
- Ye, L., Xie, H., Yu, H. M., and Yuan, H. (2021). Analysis of the current situation of traditional Chinese medicine and rational drug use countermeasures. *J. Tradit. Chin. Med. Manag.* 29 (24), 86–88. doi:10.16690/j.cnki.1007-9203.2021.24.049
- Zhang, N., Li, L., Gao, S., Zhu, Y., Wang, J. M., Zhang, P., et al. (2016). HS-SPME-GC-MS analysis of the volatile components of Dan-lou tablets. *J. Tianjin Univ. Tradit. Chin. Med.* 35 (04), 258–261. doi:10.11656/j.issn.1673-9043.2016.04.10
- Zhao, Y., Gao, F., Zhang, Y., Wang, H., Zhu, J., Chang, L., et al. (2016). Shensong Yangxin capsules prevent ischemic arrhythmias by prolonging action potentials and alleviating Ca<sup>2+</sup> overload. *Mol. Med. Rep.* 13 (6), 5185–5192. doi:10.3892/mmr.2016.5203
- Zheng, Y. Y., Wang, X. L., and Wang, X. Y. (2021). Meta-analysis and pharmacoeconomic evaluation of compound danshen dropping pills and isosorbide nitrate tablets in the treatment of stable Angina pectoris. *China Pharm.* 30 (12), 87–91. doi:10.3969/j.issn.1006-4931.2021.12.023
- Zhuan, S. P., Zhu, Y. F., and Wei, J. R. (2021). A meta-analysis of the efficacy of compound Danshen dripping pills (CSDP) combined with nitrates in the treatment of stable angina pectoris of coronary heart disease. *Int. Med. Health Guid. News* 27 (04), 501–508. doi:10.3760/cma.j.issn.1007-1245.2021.04.007



## OPEN ACCESS

## EDITED BY

Ren-You Gan,  
Chinese Academy of Agricultural  
Sciences, China

## REVIEWED BY

Farah Farokhi,  
Urmia University, Iran  
Shengjing Liu,  
China Academy of Chinese Medical  
Sciences, China  
Li Yajing,  
Beijing University of Chinese Medicine,  
China

## \*CORRESPONDENCE

Chongfu Zhong,  
zhongcf212@163.com

<sup>†</sup>These authors have contributed equally  
to this work and share the first  
authorship.

## SPECIALTY SECTION

This article was submitted to  
Ethnopharmacology,  
a section of the journal  
Frontiers in Pharmacology

RECEIVED 03 June 2022

ACCEPTED 26 August 2022

PUBLISHED 09 September 2022

## CITATION

Lv D, Ji Y, Zhang Q, Shi Z, Chen T,  
Zhang C, Wang X, Ren T, Gao Z and  
Zhong C (2022), Mailuoshutong pill for  
varicocele-associated male  
infertility—Phytochemical  
characterisation and  
multitarget mechanism.  
*Front. Pharmacol.* 13:961011.  
doi: 10.3389/fphar.2022.961011

## COPYRIGHT

© 2022 Lv, Ji, Zhang, Shi, Chen, Zhang,  
Wang, Ren, Gao and Zhong. This is an  
open-access article distributed under  
the terms of the [Creative Commons  
Attribution License \(CC BY\)](#). The use,  
distribution or reproduction in other  
forums is permitted, provided the  
original author(s) and the copyright  
owner(s) are credited and that the  
original publication in this journal is  
cited, in accordance with accepted  
academic practice. No use, distribution  
or reproduction is permitted which does  
not comply with these terms.

# Mailuoshutong pill for varicocele-associated male infertility—Phytochemical characterisation and multitarget mechanism

Dongfang Lv<sup>1†</sup>, Yun Ji<sup>2†</sup>, Qian Zhang<sup>2</sup>, Zhuozhuo Shi<sup>2</sup>,  
Tengfei Chen<sup>2</sup>, Chao Zhang<sup>1</sup>, Xiangyun Wang<sup>1</sup>, Taotao Ren<sup>1</sup>,  
Zhaowang Gao<sup>2</sup> and Chongfu Zhong<sup>2\*</sup>

<sup>1</sup>College of First Clinical Medicine, Shandong University of Traditional Chinese Medicine, Jinan, China.,  
<sup>2</sup>Affiliated Hospital of Shandong University of Traditional Chinese Medicine, Jinan, China.

**Background:** Varicocele (VC) is a relatively common and treatable cause of male infertility. Mailuoshutong pill (MLST), a traditional Chinese patent medicine, is widely used for treating varicose vein disease, but the underlying mechanism of MLST on varicocele-associated male infertility is unclear.

**Objective:** To reveal the phytochemical characterisation and multitarget mechanism of MLST on varicocele-associated male infertility.

**Methods:** The components in MLST were determined using UHPLC-MS/MS. Through network analysis, we constructed the “Drug-Components-Targets-Disease” network and predicted the potential biological functions and signaling pathways of MLST. Finally, the therapeutic effects and potential mechanisms of MLST were discovered by pharmacological experiments.

**Results:** By network analysis, the “Drug-Components-Targets-Disease” network was constructed, 62 components such as apigenin, limonin, kaempferol, and obacunoic acid may be the main active components of MLST for varicocele-associated male infertility, 28 targets such as VEGFA, PIK3CA, AKT1, and MTOR are considered as hub targets, signaling pathways such as HIF-1, Estrogen, PI3K/Akt, and mTOR may be key pathways for MLST against varicocele-associated male infertility. Through pharmacological experiments, we found that MLST ameliorated VC-induced testicular atrophy. Further histomorphology showed that MLST reduced VC-induced damage to testicular spermatogonia and seminiferous tubule, while MLST reduced ROS and MDA levels and increased antioxidant enzymes (GSH, GSH-Px, SOD, and CAT) levels. TUNEL staining and immunofluorescence showed that MLST reduced VC-induced apoptosis in testicular tissue, decreased BAX, and increased BCL2. Western blot results showed that MLST decreased the phosphorylation of PI3K, AKT, and mTOR proteins, and decreased the expression of HIF1α.

**Conclusion:** The phytochemical characterisation and multitarget mechanism of MLST on varicocele-associated male infertility were discovered using network analysis and pharmacological experiments. We verified that MLST can inhibit the activation of the PI3K/Akt/mTOR signaling pathway, reduce the expression of HIF1 $\alpha$ , and further attenuate VC-induced oxidative stress and apoptosis in the testis. These findings provide evidence for the therapeutic role of MLST in varicocele-associated male infertility.

#### KEYWORDS

mailuoshutong pill, varicocele-associated male infertility, phytochemical characterisation, multitarget mechanism, network analysis, pharmacological experiments

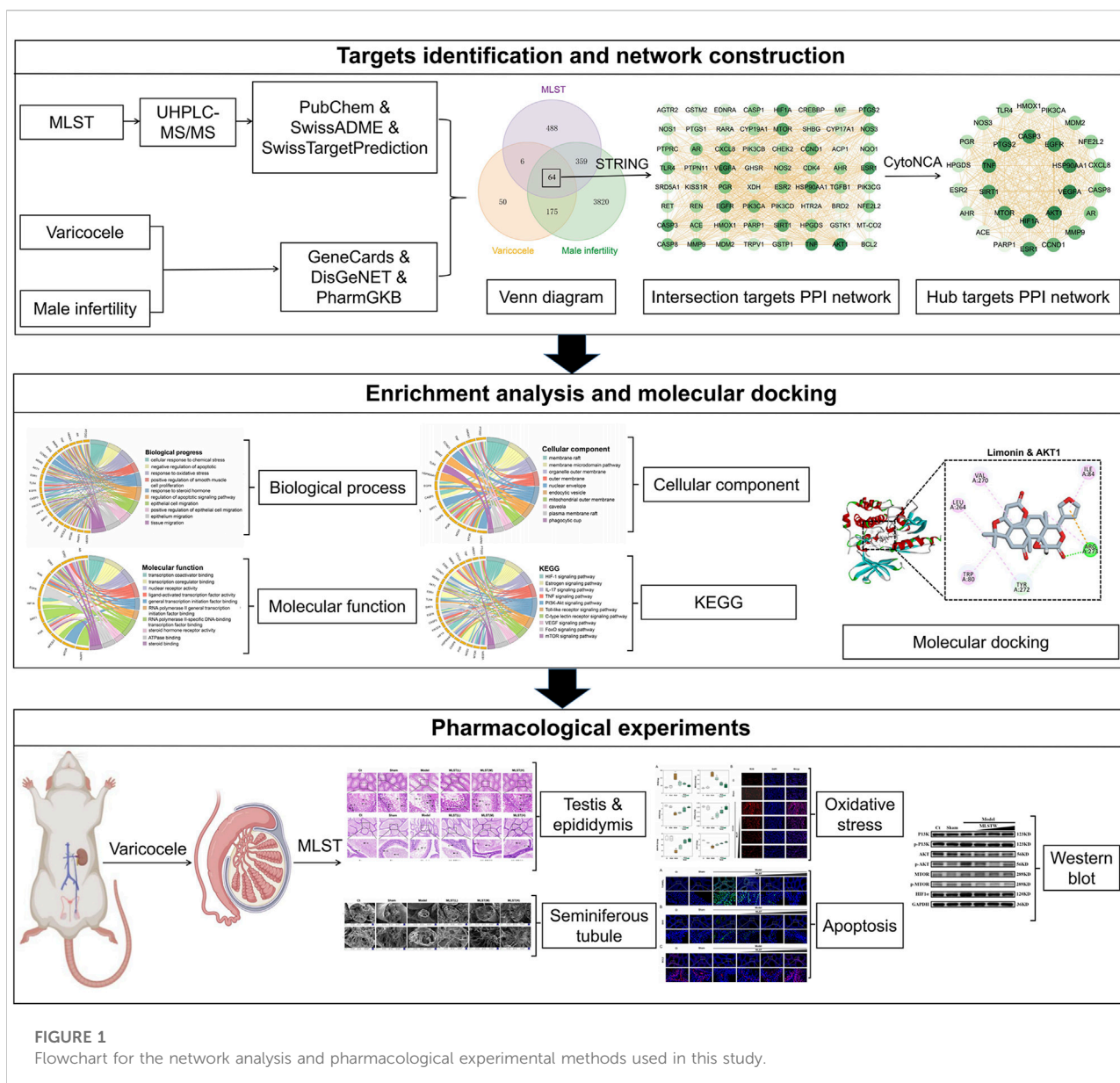
## Introduction

Varicocele (VC), one of the leading causes of male infertility, is characterized by abnormally enlarged veins within the pampiniform plexus (Jensen et al., 2017). Venous valve insufficiency and venous reflux disorder are currently recognized as the causes of VC (Silay et al., 2019). According to early reports, VC affects 15% of men, while 35%–40% of infertile men are affected (Agarwal et al., 2020; Gill et al., 2021). Studies have also shown that men with VC experience testicular atrophy and abnormal semen quality to varying degrees and that the negative effects of VC on spermatogenic function are progressive (Santana et al., 2020). Although the pathophysiological mechanisms of male infertility caused by VC have not been elucidated, current studies have focused on elevated local testicular temperature, oxidative stress, metabolite accumulation, and hormonal disorders (Razi et al., 2021). Varicolectomy, the primary treatment for varicocele-associated male infertility, can mitigate delayed testicular development and impaired semen quality, but studies have shown that some patients still do not return to baseline semen quality after surgery (Arab et al., 2021; Shomarufvov et al., 2022). There is an urgent need to find effective complementary alternative therapies. Since the etiology of VC-induced male infertility is complex and cannot be treated by single-target therapy, the multi-target treatment model of traditional Chinese medicine (TCM) is more suitable for the treatment of varicocele-associated male infertility. In recent years, the use of TCM has achieved better efficacy in the treatment of varicocele-associated male infertility, and some botanical preparations are gradually being applied against varicocele-associated male infertility (Dun et al., 2015; Nimrouzi and Zarshenas, 2016; Lu et al., 2020).

Mailuoshutong pill (MLST), a traditional Chinese herbal formula, each Gram of MLST is made from *Astragalus mongholicus* Bunge (Fabaceae, 0.833 g), *Lonicera japonica* Thunb (Caprifoliaceae, 0.833 g), *Phellodendron amurense* Rupr (Rutaceae, 0.417 g), *Atractylodes lancea* DC

(Asteraceae, 0.417 g), *Coix lacryma-jobi* L (Poaceae, 0.833 g), *Scrophularia ningpoensis* Hemsl (Scrophulariaceae, 0.833 g), *Angelica sinensis* Diels (Apiaceae, 0.417 g), *Paeonia lactiflora* Pall (Paeoniaceae, 0.417 g), *Glycyrrhiza glabra* L (Fabaceae, 0.138 g), *Hirudo* (Hirudinidae, 0.417 g), *Scolopendra* (Scolopendridae, 0.033 g), *Scorpio* (Buthidae, 0.138 g). Pharmacological studies of TCM have shown that the active components of these herbs have biological activities of antioxidant, anti-inflammatory, blood circulation promotion, hormone regulation, and immune enhancement (Chen et al., 2010; Chen et al., 2011; Zhang et al., 2011; Chen et al., 2021). Clinical study has shown that MLST is effective in improving VC local clinical symptoms and secondary spermatogenic dysfunction (Liu and Hou, 2020). The effect of MLST against varicocele-associated male infertility and its mechanism is worthy of being studied. However, the mechanism of MLST for treating varicocele-associated male infertility is unclear due to its complex components and therapeutic targets. Therefore, an effective method is needed to decipher the relationship between MLST and varicocele-associated male infertility.

In this study, we used a combination of ultra-high-pressure liquid chromatography-mass spectrometry/mass spectrometry (UHPLC-MS/MS), network analysis, and pharmacological experiments to discover the phytochemical characterisation and multitarget mechanism of MLST against varicocele-associated male infertility. UHPLC-MS/MS was used to identify the main active components of MLST, and network analysis was used to construct the “Drug-Components-Targets-Disease” network to predict the potential drug components, drug targets, and drug mechanisms of MLST. Finally, after the prediction of network analysis, we conducted an experimental pharmacological evaluation based on the pathogenesis of varicocele-related male infertility to elucidate its therapeutic effects and possible mechanisms of action, which can help guide the further development and clinical application of MLST. The flowchart of this study is shown in Figure 1.



## Materials and methods

### Chemicals and instruments

MLST was provided by Shandong Lunan Pharmaceutical Group (Linyi, China). Methanol and acetonitrile were supplied by Merck KGaA at LC-MS purity, and formic acid was supplied by Sia Reagents at LC-MS purity. Malondialdehyde (MDA) colorimetric assay kit (eLabscience, E-BC-K025-M), superoxide dismutase (SOD) activity assay kit (eLabscience, E-BC-K022-M), catalase (CAT) activity assay kit (eLabscience, E-BC-K031-M), glutathione peroxidase activity assay kit (eLabscience, E-BC-K096-M), reduced glutathione colorimetric

assay kit (eLabscience, E-BC-K030-M), reactive oxygen species (ROS) (Beijing Huaying Biotechnology Research Institute, HY-M0087), TUNEL test kit (Genepool, GPB 1829), BAX antibody (Bioss, bs-0127r), BCL2 antibody (Bioss, bs-33047 m), PI3K antibody (bioss, bs-10657r), p-PI3K antibody (bioss, bs-6417r), AKT antibody (bioss, bs-6951r), p-AKT antibody (bioss, bs-0876r), mTOR antibody (bioss, bs-1992r), p-mTOR antibody (bioss, bs-3495r), HIF1 $\alpha$  antibody (bioss, bs-0737r), ECL kit (SUKER, ED0015-B). Ultra-performance liquid chromatography (Thermo Fisher Scientific, Q-Exactive HF), high-resolution mass spectrum (Thermo Fisher Scientific, Q-Exactive HF), column (Agilent technologies, Zorbax Eclipse C18), inverted fluorescence microscope (Japan's Nikon, Nikon



Eclipse Ti-SR), panoramic scanner (3D HISTECH, Panoramic MIDI), scanning electron microscopy (SEM) (FEI Corporation of America, FEI Quanta250).

## MLST components identification

By using UHPLC-MS/MS to determine the components in MLST. Weigh 100 mg of MLST, add 1 ml of 70% methanol, shake and centrifuge, take the supernatant for dilution, 10  $\mu$ l 100  $\mu$ g/ml internal standard, pass through 0.22  $\mu$ m PTFE filter tip on the machine for analysis, using ultra-performance liquid chromatography and high-resolution mass spectrum, the column for separation, separation conditions are column temperature of 30°C; flow rate of 0.3 ml/min; mobile phase composition A: water +0.1% formic acid, B: pure acetonitrile, the injection volume was 2  $\mu$ l, and the autosampler temperature was 4°C. In this study, the identified components of MLST were further screened based on gastrointestinal absorption rate and drug similarity (ADME principles) using SwissADME online system (<http://www.swissadme.ch/>) (Daina et al., 2017). The components in MLST obtained from the screening were used for further studies.

## Network analysis, drug targets and disease targets screening

SwissTargetPrediction online platform (<http://www.swisstargetprediction.ch/>) (Daina et al., 2019) is a web server that accurately predicts chemical component targets based on known ligands combined with 2D and 3D similarity measures. SwissTargetPrediction was used to predict the targets of the study component, and the species was set to “Homo sapiens,” and the targets with “probability >0” were selected for the follow-up study. The predicted targets were imported into an Excel sheet to create a database of MLST targets.

GeneCards (<https://www.genecards.org/>) (Stelzer et al., 2016) is a comprehensive human genetic database that includes all known and predicted human genes in terms of genome, proteome, transcription, and genetics. DisGeNET (<https://www.disgenet.org/>) (Pinero et al., 2020) is a general-purpose platform for studying the molecular basis of human diseases and their complications, validating disease candidate genes, and evaluating the performance of text mining methods. Pharmacogenetics and Pharmacogenomics Knowledge Base (PharmGKB) (<https://www.pharmgkb.org/>) (Barbarino et al., 2018) is the most authoritative and complete pharmacogenomic database containing information on how human genetic variation affects drug response. We searched the GeneCards database, DisGeNET database, and PharmGKB database for the targets related to varicocele-associated male infertility by

using “varicocele” and “male infertility” as keywords, and recorded them in an Excel sheet.

## Protein-protein interaction network and drug-components-targets-disease network construction

Duplicate data of drug targets and disease targets were removed separately and imported into origin software (version 2021) to plot Venn diagrams, and the intersection targets were considered to be effective targets for MLST treatment of varicocele-associated male infertility. STRING (<https://cn.string-db.org/>) (Szklarczyk et al., 2019) can be used to identify interactions between target proteins. The intersection targets were imported into the STRING database, the species was set to “Homo sapiens,” and the interaction between the target proteins was constructed. The results of the PPI analysis were imported into Cytoscape software (Version 3.7.2), and topological analysis of the PPI network was performed using the CytoNCA plug-in to obtain comprehensive data of each node (Tang et al., 2015). According to the network analysis method (Liu et al., 2022), the hub targets of MLST for the treatment of varicocele-related male infertility were screened by setting the degree centrality greater than 2 times the median and the betweenness centrality and closeness centrality both greater than the median. The components-targets mapping relationships were imported into Cytoscape software to construct a “Drug-Components-Targets-Disease” network.

## Enrichment analysis of hub targets

Gene ontology (GO) and Kyoto Encyclopedia of Genes and Genomes (KEGG) enrichment analyses of hub targets were performed to reveal the role of identifying hub targets in varicocele-associated male infertility progression and treatment. Enrichment analysis of hub targets was performed using the clusterProfiler package (Wu et al., 2021) in R software. GO enrichment analysis annotates the hub targets' function in terms of cellular component, biological process, and molecular function, and KEGG enrichment analysis describes the pathways of action of the hub targets. When  $p < 0.05$ , these targets were found to be significantly enriched in GO terms or KEGG pathways. The GOplot package (Walter et al., 2015) of R software was used to visualize the results of the GO and KEGG analyses.

## In silico molecular docking

The structures of the ligands were obtained from the PubChem database (<https://pubchem.ncbi.nlm.nih.gov/>) (Kim

et al., 2016), and the structures of the receptors were obtained from the RCSB Protein Data Bank (<https://www.pdbus.org/>) (Burley et al., 2022). The protein crystal structures were imported into Discovery Studio (Version 2019) and water was removed, hydrogen atoms were added and incomplete residues were supplemented. Active pockets were defined based on the original ligands in the complex and molecular docking was performed by the CDocker algorithm to calculate the root mean square deviation (RMSD) of the co-crystallized ligands, where RMSD values below 2 Å were considered as good solutions reflecting the reliability of the docking model, and the scoring of the -CDocker interaction energy (-CIE) was used to evaluate the ligand and receptor binding ability, and the original ligand-CIE was used as a positive control (Ramirez and Caballero, 2018). Finally, the ligand-receptor affinity was assessed by docking the active ingredient with key potential targets and calculating the -CIE compared with the original ligand, using the positive control score as the threshold and a drug score value > threshold  $\times$  75% as the criteria for strong ligand-receptor affinity.

## In Vivo pharmacological experiments

### Preparation of animal models and interventions

36 SD rats, aged 8 weeks (body weight, 240–260 g), were purchased from Beijing Viton Lever Laboratory Animal Technology Co., (Beijing, China). The rats were placed in an animal room under  $22 \pm 1^\circ\text{C}$  and  $60\% \pm 2\%$  interior design conditions with a light/dark cycle for 12 h. All experimental procedures involving animals were approved by Institutional Animal Care and Use Committee of Shandong University of Traditional Chinese Medicine and Animal Ethics Committee of Affiliated Hospital of Shandong University of Traditional Chinese Medicine, Jinan, China (Approval Number: 2021-40). The animal care and use system and guidelines of Shandong University of Traditional Chinese Medicine were followed. Rats needed at least 1 week to adapt to the environment before doing the experiments.

In this study, the classical way of establishing a VC rat model through a narrow left renal vein created by Turner (Turner, 2001) was used. The rats were anesthetized intraperitoneally with 3% chloral hydrate (10 ml/kg), and after successful anesthesia, the rats were fixed, the skin was taken for positioning, dissected layer by layer, and the left abdominal contents were gently pushed to the right upper abdomen to fully reveal the left renal vein, and a 0.85 mm diameter metal probe was placed under the left renal vein, and after the 4–0 silk ligated the renal vein, the probe was withdrawn, resulting in local stenosis of the left renal vein. The left kidney was observed for approximately 2 min and it was confirmed that the organ was not significantly ischemic. In the sham-operated group, only the left renal vein was isolated and

not ligated. The experimental diagram of the rat spermatic varicocele model construction is shown in Figure 4A. The criteria for the success of the model: the left spermatic vein is significantly tortuous and dilated compared with the right, and the left kidney has no atrophy.

One week after modeling, 36 rats were randomly divided into the following six groups (6 rats in each group): a normal control group (Ct), a sham-operated group (Sham), a VC-induced model group (Model), a VC-induced group administrated with low-dose MLST, a VC-induced group administrated with medium-dose MLST, and a VC-induced group administrated with high-dose MLST. The dose of MLST intervention in rats was determined based on the human equivalent dose, which was calculated from the body surface area equivalent dose (Blanchard and Smoliga, 2015). The low-dose MLST group, medium-dose MLST group, and high-dose MLST group were gavaged with MLST 0.162 g/kg, 0.324 g/kg, and 0.648 g/kg respectively, and MLST was dissolved in 2 ml sodium carboxymethyl cellulose (CMC-Na) solution during gavage. The Ct group, Sham group, and model group were given 2 ml CMC-Na solution by gavage as control. After 30 days of intervention, the rats and left testes were weighed and the testis index was calculated, testis index (%) = (testis weight/body weight)  $\times$  1,000‰ (Wang et al., 2020). Take a piece of testicular tissue and epididymal tissue, and store them in formalin respectively for histological evaluation (HE) staining. Take a piece of testicular tissue and store it in glutaraldehyde at room temperature for SEM observation. Three pieces of testicular tissue were put into cryopreservation tubes and stored in liquid nitrogen for Western blot (WB) analysis, oxidative stress level detection, and apoptosis detection.

### Histological evaluation staining

HE staining was used to evaluate the degree of testicular and epididymal tissue damage and sperm quality in each group. The left testis and epididymis tissues of each group of rats were fixed with 4% paraformaldehyde, dehydrated in alcohol, transparently treated with xylene, embedded in paraffin, and serially sectioned on a microtome with a slice thickness of 4  $\mu\text{m}$ . The 4  $\mu\text{m}$  sections were dewaxed, dehydrated, stained with hematoxylin, and sealed with neutral gum. Images of testicular and epididymal tissue structures were observed and acquired under an inverted fluorescence microscope and panoramic scanner.

#### Observation of. Spermatogenic Tubule by SEM

Testicular tissues were taken and gently rinsed with PBS, fixed at room temperature for 2 h with electron microscopy fixative, fixed at room temperature for 2 h with 0.1 M phosphate buffer PB (PH 7.4) prepared with 1% osmium acid, and rinsed 3 times with 0.1 M phosphate buffer PB. The tissues were sequentially dehydrated with alcohol and isoamyl acetate. The samples were dried and placed tightly on the double-sided

adhesive of conductive carbon film on the sample stage of the ion jetting instrument for the 30 s. Finally, the structure of the spermatogenic tubule was observed by SEM.

## Measurement of oxidative stress biomarkers

The levels and activities of MDA, GSH, SOD, CAT, and GSH-Px were measured with kits according to the instructions. Determination of ROS content by DHE fluorescence staining. Fresh testicular tissue was rewarmed in frozen sections, and the tissue was incubated with DHE diluted in PBS for 30 min at 37°C under light-proof conditions, then the slides were washed in PBS (PH 7.4) on a decolorized shaking table, and the sections were shaken dry, and then the nuclei were stained with DAPI staining solution for 10 min at room temperature and light-proof. The slides were then placed in PBS and washed three times for 5 min each time on a decolorized shaking table with no light, and the sections were shaken dry and sealed with an anti-fluorescence quenching sealer. The slides were placed under an inverted fluorescence microscope and panoramic scanner, and images were collected to determine the amount and variation of ROS content in the cells according to the red fluorescence in the cells.

## TUNEL Staining

The testicular tissue was fixed with 4% paraformaldehyde, dehydrated, embedded, sectioned, dewaxed, added with fluorescence quenching agent for 5 min, washed with running water for 10 min, and the slides were treated according to the instructions of the TUNEL test kit (fluorescence method). After operating according to the instructions, wash with PBS (PH 7.4). After the slices are slightly dried, they are sealed with anti fluorescence quenching sealing agent (including DAPI). Slices were observed in the panoramic scanner and images were collected.

## Immunofluorescence

Testicular tissue was fixed in 4% paraformaldehyde, dehydrated, embedded, sliced, and washed with PBS (10X). The slices were placed in the repair box of EDTA (PH 8.0) antigen repair buffer, and the antigen was repaired in the steamer. The fluorescent quenching agent was added, washed with running water, and incubated with 5% BSA at room temperature. After discarding the serum, the primary antibody (1:100) was incubated overnight. After the slices were washed and dried with PBS, they were covered with a suitable kind of secondary antibody, dripped with DAPI dye, and sealed with anti fluorescence quenching sealant. Bax and BCL2 were selected for

the primary antibody. The staining of Bax and BCL2 in testicular tissue was observed by the panoramic scanner.

## Western blot analysis

Rat testicular tissue samples were ground into a powder with liquid nitrogen, lysed at 1 mg plus 10 µl of lysis solution for 30 min on ice, and the supernatant was collected by centrifugation at 4°C for 10 min after lysis. Protein (20 µg) was electrophoresed on 8%–12% SDS-PAGE gels, transferred to PVDF membranes, blocked with 5% BSA for 1 h at room temperature, and incubated with the following primary antibodies: PI3K, p-PI3K, AKT, p-AKT, mTOR, p-mTOR, HIF1α, diluted according to the antibody instructions. The primary antibody was incubated overnight at 4°C. The membrane was washed 5 times with TBST buffer for 5 min each time, and the goat anti-rabbit antibody was diluted with 5% BSA (1:5,000) according to the antibody instructions, mixed well, and the secondary antibody was incubated at room temperature for 1 h. The membrane was washed 5 times with 1 × TBST buffer for 5 min each time, and the ECL assay was performed using the ECL kit. Band intensity was analyzed by ImageJ software.

## Statistical analysis

All quantitative data were expressed as mean ± standard error of mean and statistically analyzed using GraphPad Prism 9 (GraphPad Software, San Diego, CA, United States), and one-way analysis of variance (ANOVA) was used for comparison between groups. A difference of  $p < 0.05$  was considered statistically significant.

## Results

### Potential components and targets of MLST on varicocele-associated male infertility

Through UHPLC-MS determined, a total ion flow spectrum of the components in MLST was obtained (Figure 2A), and a total of 346 components were determined by comparison with the secondary mass spectrometry data. Through SwissADME online system, setting the gastrointestinal absorption rate as “high” and drug similarity as “yes,” 62 components were screened for future study (Supplementary Table S1).

Prediction of the targets of the included components by SwissTargetPrediction yielded a total of 62 components acting on 917 targets. Targets for varicocele and male infertility were searched in the GeneCards database, DisGeNET database, and PharmGKB database, and a total of 4,418 male infertility targets and 295 varicocele targets were obtained after removing duplicate



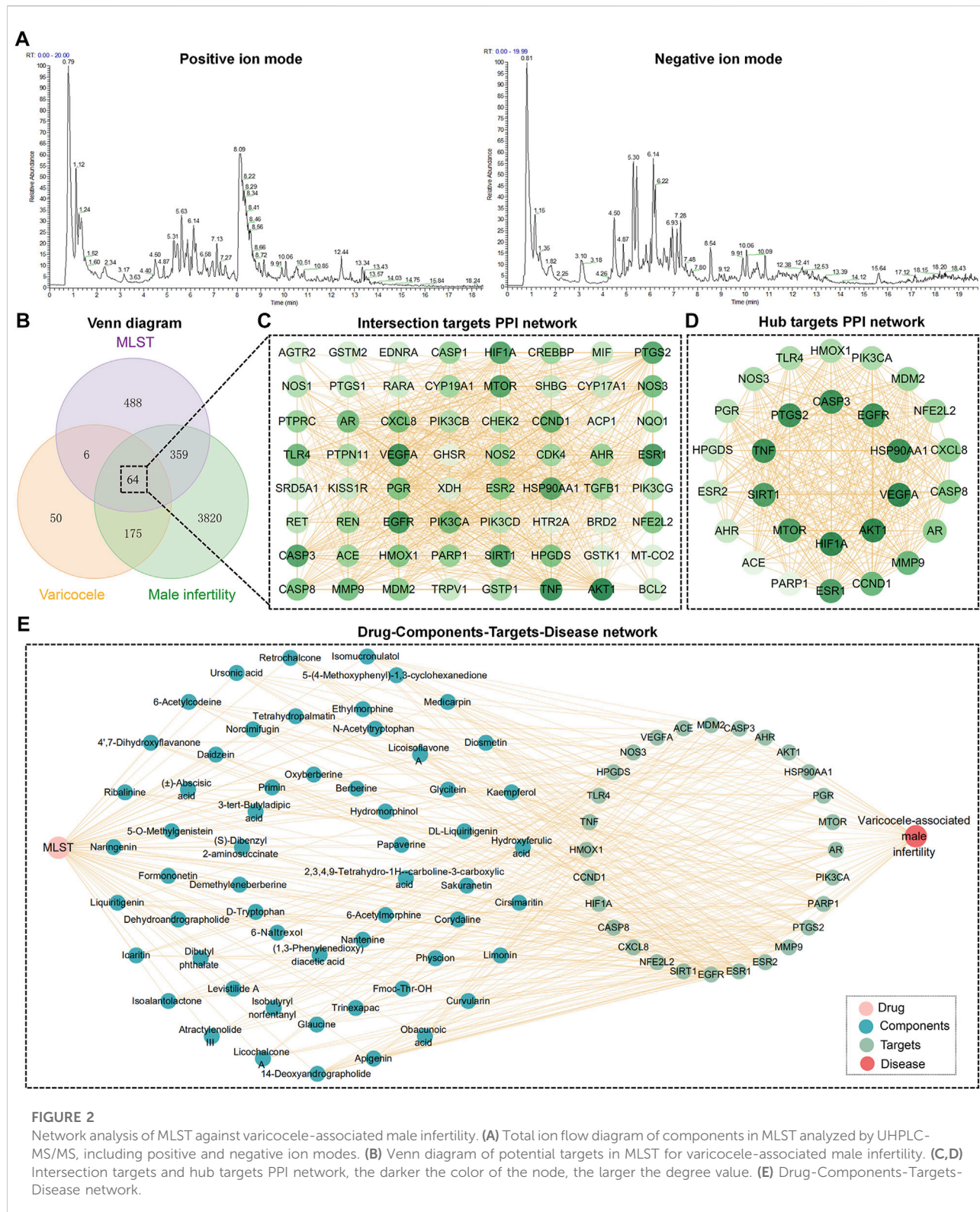


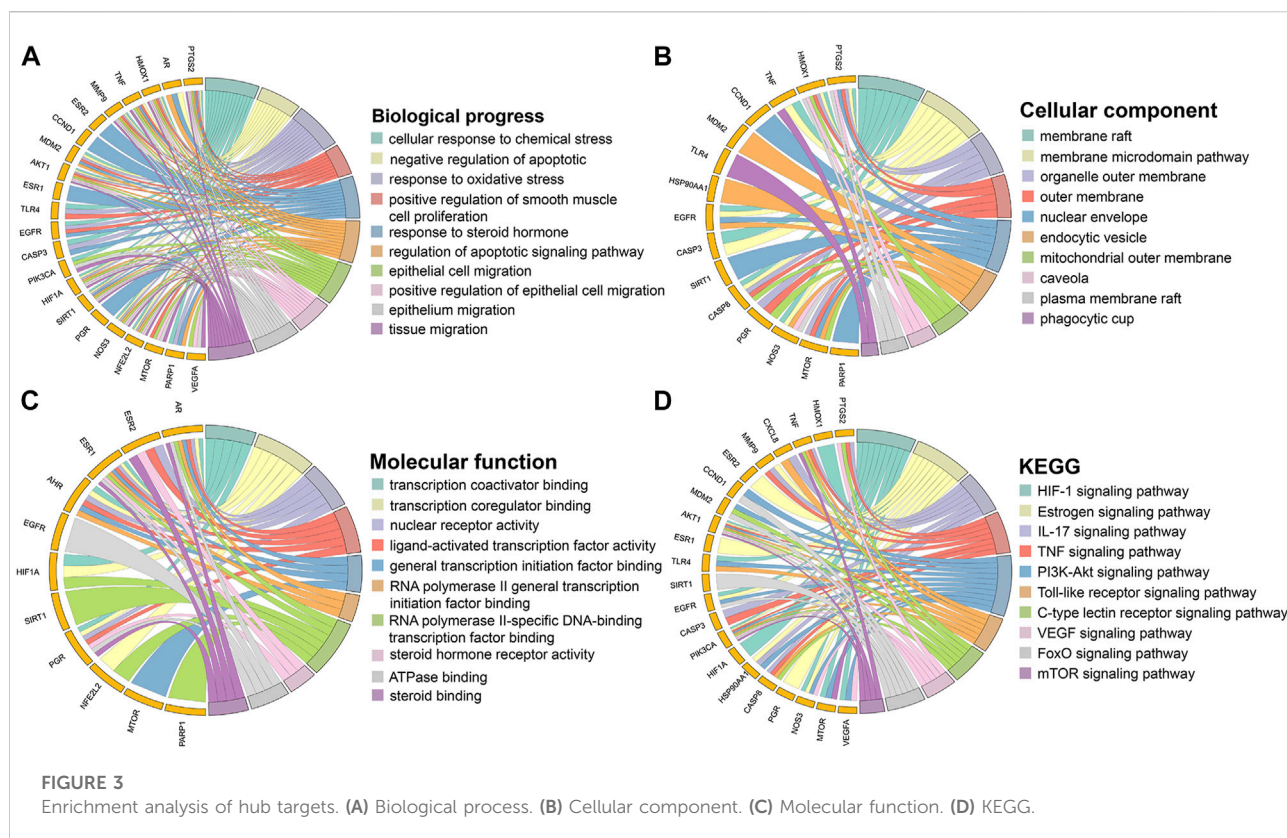
FIGURE 2

Network analysis of MLST against varicocele-associated male infertility. (A) Total ion flow diagram of components in MLST analyzed by UHPLC-MS/MS, including positive and negative ion modes. (B) Venn diagram of potential targets in MLST for varicocele-associated male infertility. (C, D) Intersection targets and hub targets PPI network, the darker the color of the node, the larger the degree value. (E) Drug-Components-Targets-Disease network.

entries. Finally, 64 intersecting targets were obtained by making a Venn diagram (Figure 2B). These 64 intersecting targets were imported into STRING for PPI analysis, and 665 pairs of

interactions were obtained and visualized using Cytoscape software (Figure 2C). The analysis was performed by Cytoscape software, and 28 hub targets were obtained by





filtering based on degree centrality, betweenness centrality, and closeness centrality. 28 hub targets were imported into STRING for PPI analysis and visualized using Cytoscape (Figure 2D).

The information of components and hub targets was imported into Cytoscape to construct the “Drug-Components-Targets-Disease” network, as shown in Figure 2E. The topological structure of the network was assessed with the network analyzer function of Cytoscape, and the node importance was expressed in terms of the degree. The top 10 components about degree were 14-Deoxyandrographolide, apigenin, cirsimaritin, kaempferol, obacunonic acid, curvularin, limonin, hydroxyferulic acid, medicarpin, and diosmetin.

## GO and kyoto encyclopedia of genes and genomes enrichment analysis of hub targets

GO enrichment analysis yielded 1,485 significant results, including 1,422 BPs, 17 CCs, and 46 MFs. In the BP category, the main biological processes in which the core targets are involved are cellular responses to chemical stress, responses to oxidative stress, and regulation of apoptotic signaling pathways. In the CC category, the core targets were mainly enriched in cellular components such as membrane rafts, membrane

microdomains, and organelle outer membranes. In the MF category, the core targets mainly play molecular functions such as transcriptional cofactor binding, transcriptional coregulator binding, and nuclear receptor activity. A total of 120 pathways were obtained by KEGG enrichment analysis. Signaling pathways for cancer and other diseases were excluded, and the top 10 pathways of high significance were selected based on their *p*-values. These signaling pathways included HIF-1 signaling pathways, IL-17 signaling pathways, TNF signaling pathways, PI3K/Akt signaling pathways, and mTOR signaling pathways. The top 10 entries in each category of biological process, cellular component, molecular function, and KEGG signaling pathways were screened based on *p*-value and plotted in a circle diagram in Figure 3.

## MLST relieves testicular and epididymal tissue damage

The VC rat model was successfully induced by narrowing the left renal vein, as shown in Figure 4B. The testis index of the rats in the model group decreased compared with the control group and the sham-operated group ( $p < 0.05$ ), while the testis index of the rats with MLST intervention was better than that in the model group ( $p < 0.05$ ) (Figures 4C,D).

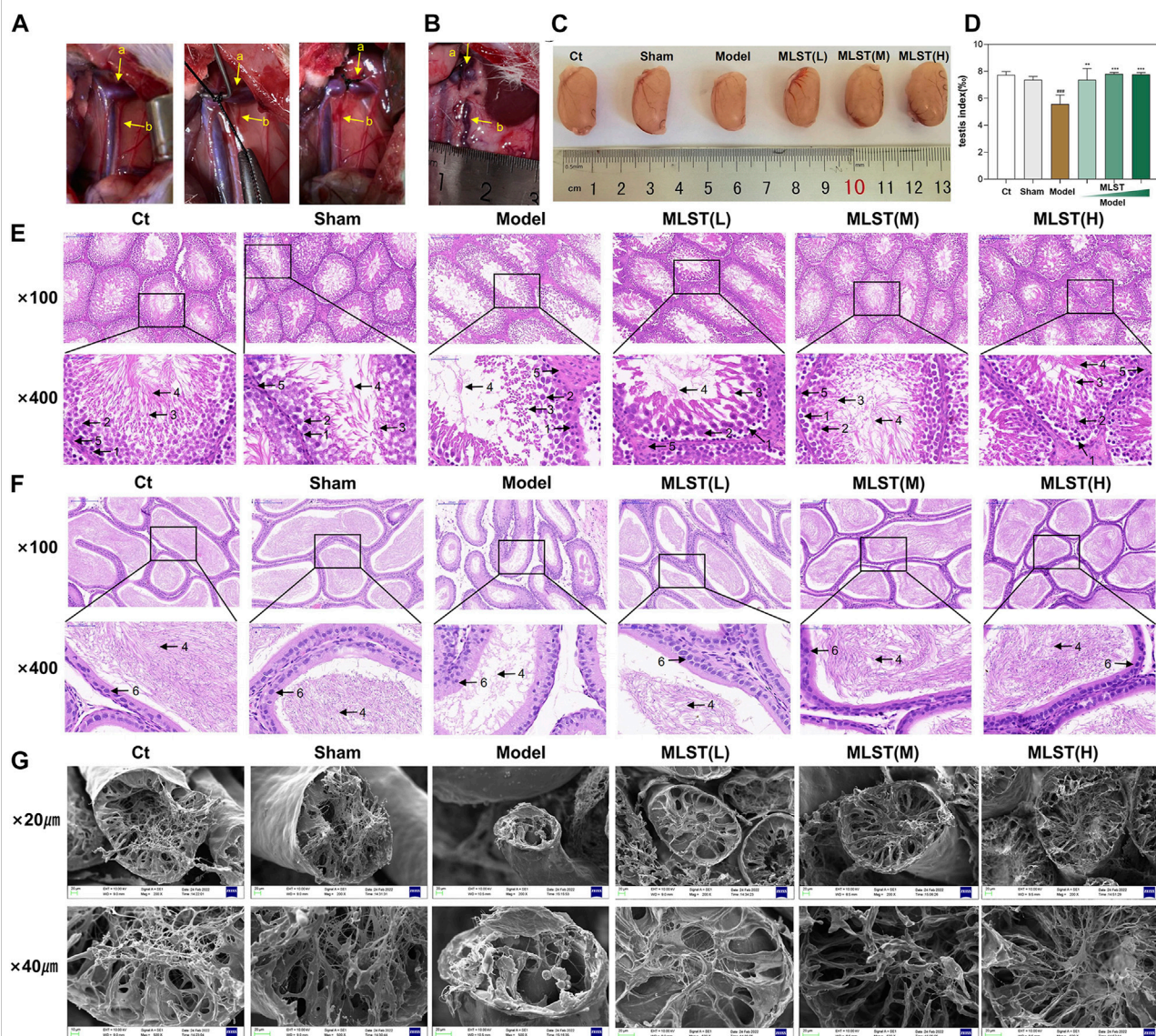


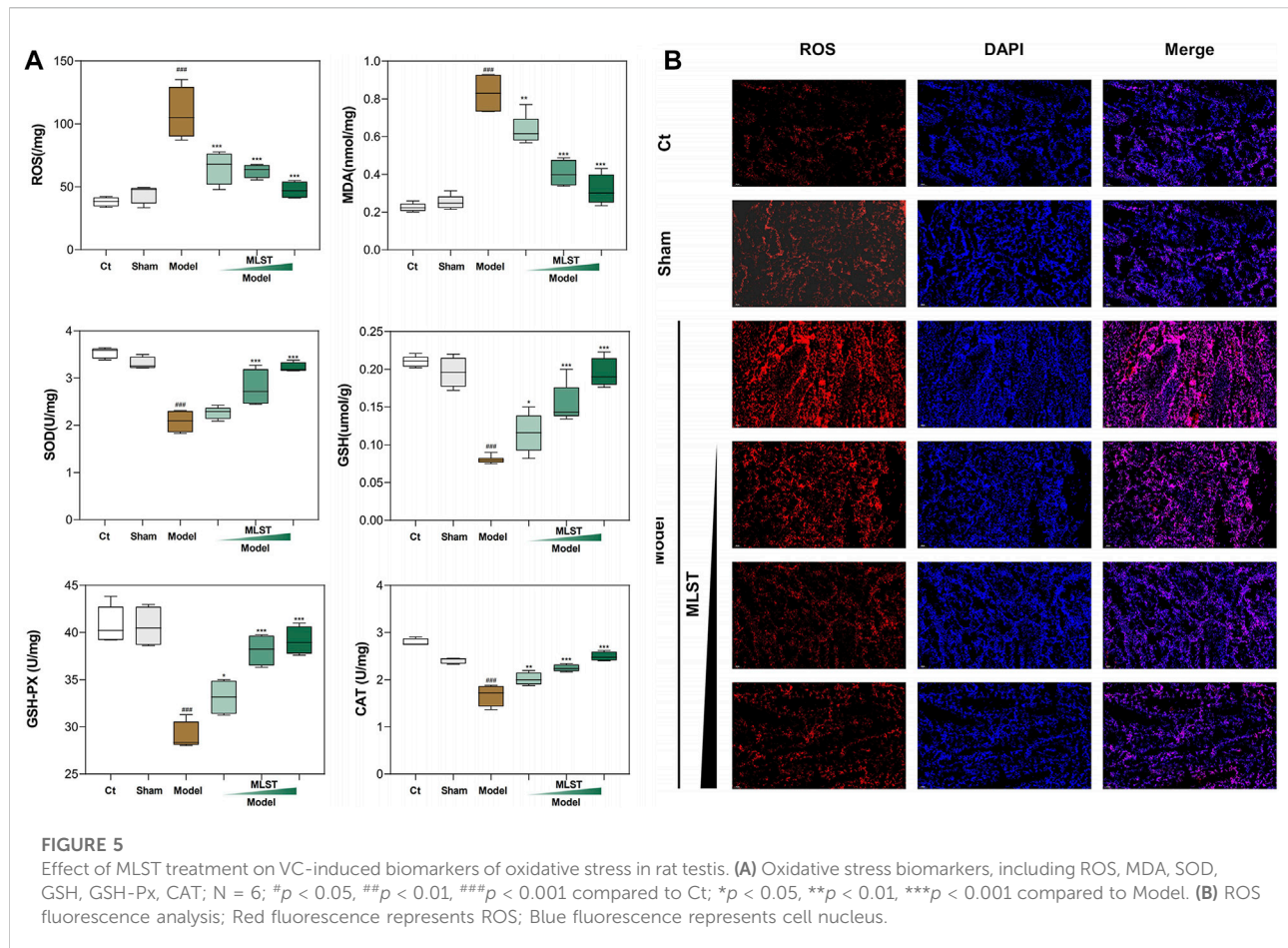
FIGURE 4

Preparation of VC rat model and histopathological changes of testicular tissue and epididymis. (A) The model of varicocele was made by narrowing the left renal vein and increasing the reflux pressure of the spermatic vein; a, left renal vein; b, spermatic vein. (B) The rat model of VC was successfully prepared by Turner's method, and obvious varicocele was seen. (C) Testis of different groups. (D) Changes in testicular mass in different groups;  $N = 6$ ;  $^{\#}p < 0.05$ ,  $^{\#\#}p < 0.01$ ,  $^{\#\#\#}p < 0.001$  compared to Ct;  $^{*}p < 0.05$ ,  $^{**}p < 0.01$ ,  $^{***}p < 0.001$  compared to Model. (E) HE staining of testicular tissue; 1, spermatogonia; 2, spermatocyte; 3, spermatid; 4, sperm; 5, leydig cell; (original magnification  $\times 100$ ,  $\times 400$ ). (F) HE staining of epididymal tissue; 4, sperm; 6, epithelial cell; (original magnification  $\times 100$ ,  $\times 400$ ). (G) Structural changes in the seminiferous tubules (scale bar  $\times 20 \mu\text{m}$ ,  $\times 40 \mu\text{m}$ ).

Histopathological changes in testes and epididymis were observed by HE staining. As shown in Figure 4E, the testicular tissues of the control group were relatively intact, the germinal ducts were structurally sound and consisted of composite epithelium, and the spermatogonia, spermatocyte, and sperm, and, and leydig cells were neatly arranged, and there were a large number of sperm. Compared with the control group, the testicular tissue structure and morphology

of the mice in the model group were changed, the spermatogonia, spermatocyte, and spermatid in the germinal ducts were disorganized and reduced in number, and the number of sperm was significantly reduced. Compared with the model group, the morphological structure of the testicular germinal ducts of rats in the low-dose MLST group was significantly improved, and the number of spermatogonia, spermatocyte, and spermatid was increased and arranged in a relatively





orderly manner, and the number of sperm in seminiferous tubule was increased. The testicular tissue morphology of the medium-dose MLST group and high-dose MLST was similar to that of the control group. As shown in Figure 4F, the epithelial cells of the epididymal duct lumen in the control and sham-operated groups were neatly arranged, which contained a large number of normal sperm. In the model group, the epididymal duct lumen was atrophied, the arrangement of the epithelial cells was disordered, and the density of sperm in the lumen of the epididymal duct was reduced. Compared with the model group, the morphological structure of the epididymal ducts in the low-dose MLST group was significantly improved, with epithelial cell arrangement and increased sperm density. The morphology, structure, and sperm density of the epididymal ducts in the medium-dose MLST group and high-dose MLST group were similar to those in the control group.

Furthermore, the damage of VC on the seminiferous tubule was further observed by scanning electron microscopy, and the protective effect of MLST on the seminiferous tubule was observed. As shown in Figure 4G, the structure of the seminiferous tubule in the control and sham-operated groups was normal. In the model group, the seminiferous

tubule of rats was narrowed and concentrated, the number of spermatozoa tails was significantly reduced, supporting irregular arrangement, only a small number of spermatozoa were visible, and the lumen of the tubules was reduced. In the low-dose MLST group, the structure of the seminiferous tubules was improved, and an increase in the number of tubule lumens and normal spermatozoa was visible. The morphological structure of the seminiferous tubule in the medium-dose MLST group and high-dose MLST group was similar to that of the normal group. These results suggest that MLST ameliorates VC-induced impairment of spermatogenic function.

## MLST relieves varicocele-induced oxidative stress

The results of ROS, MDA, and antioxidant enzymes (SOD, GSH, GSH-Px, and CAT) in testicular tissues are shown in Figure 5A. The levels of MDA and ROS in the model group were significantly higher than those in the control and sham-operated groups (*p* < 0.05). MLST reduced the levels of ROS and

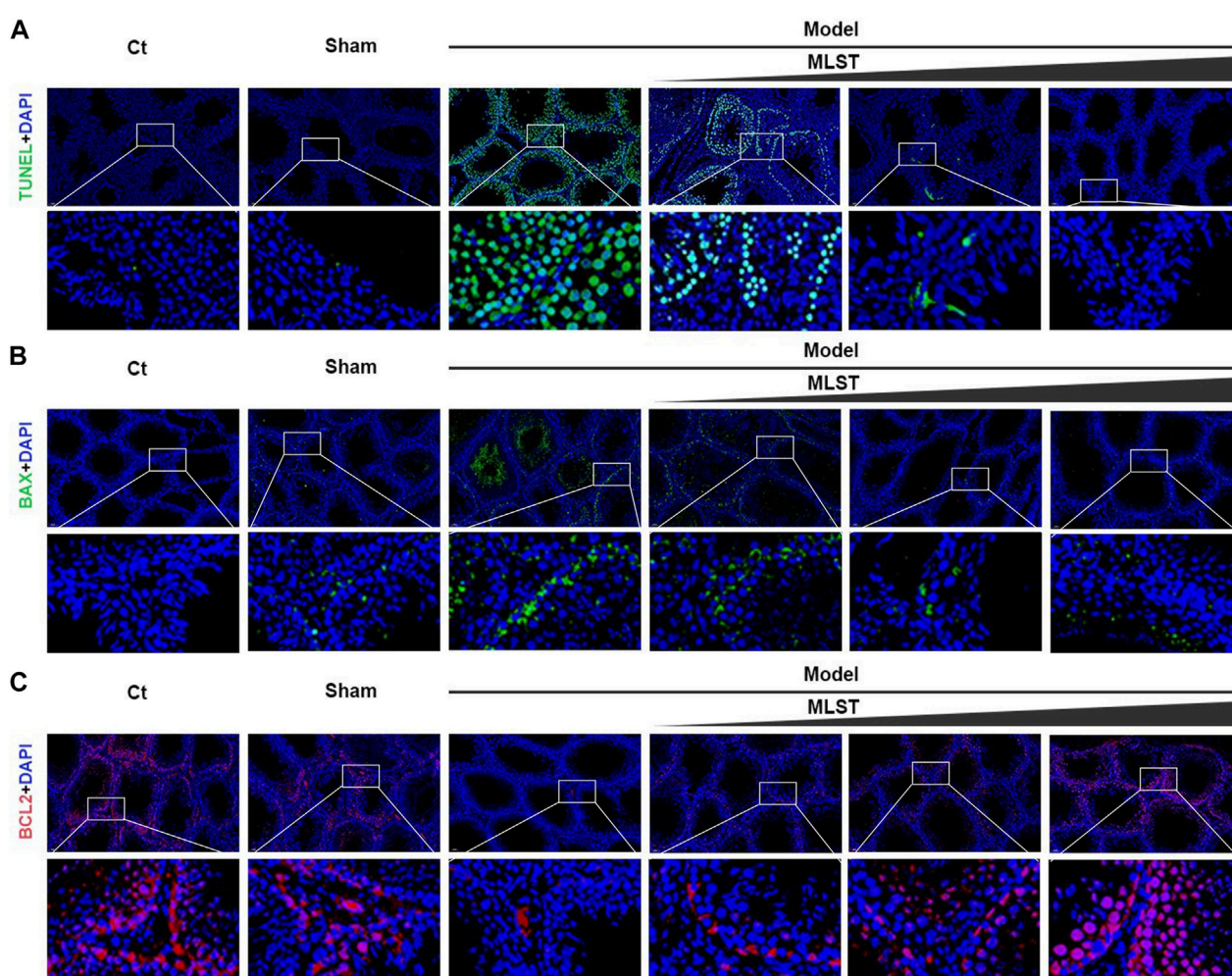


FIGURE 6

Effect of MLST on VC-induced apoptosis of rat testicular cells. (A) Green indicates TUNEL positive; Blue indicates cell nucleus stained by DAPI. (B) Green indicates DAPI staining of BAX; Blue indicates cell nucleus stained by DAPI. (C) Red indicates DAPI staining of BCL2; Blue indicates cell nucleus stained by DAPI.

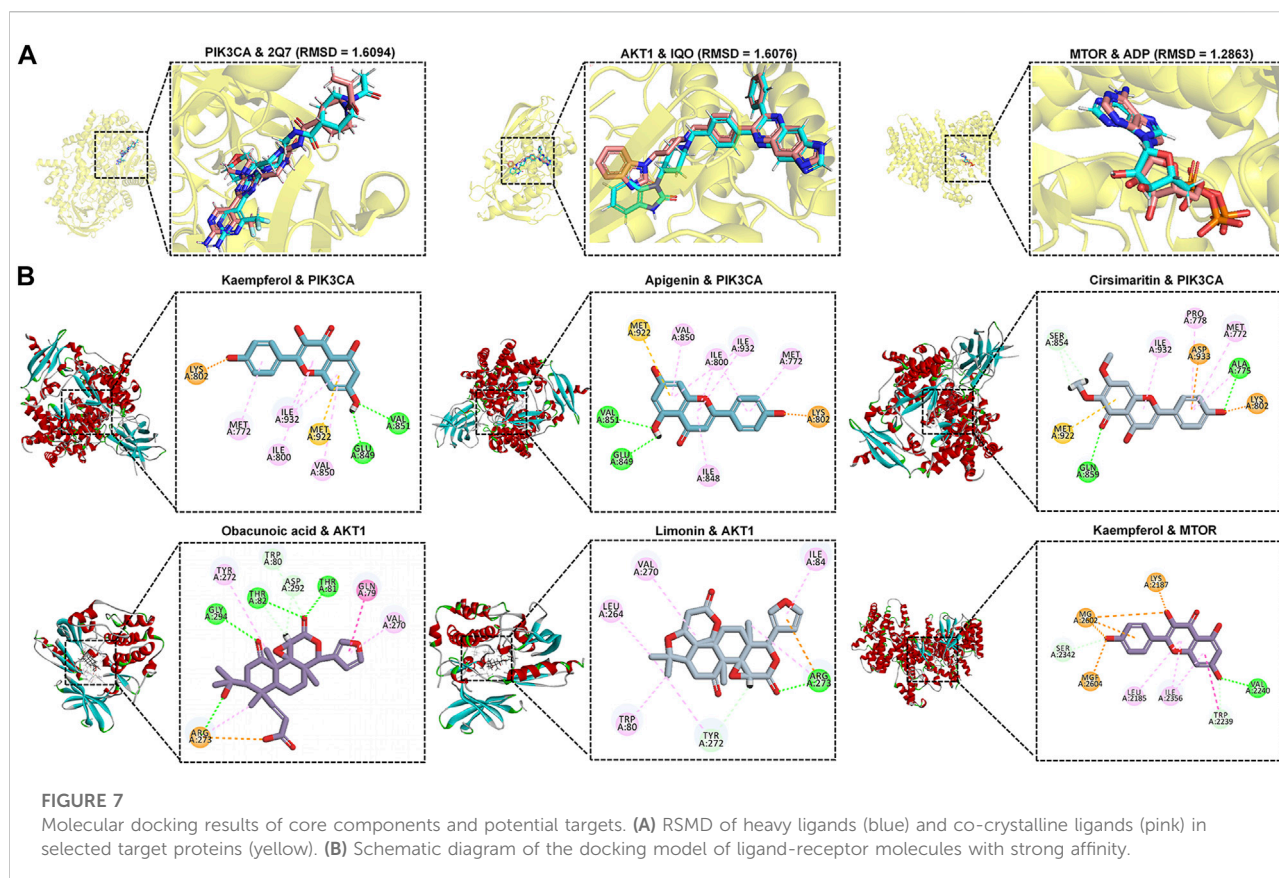
MDA in testicular tissues of rats with VC, and the higher the dose, the more significant the effect. The levels of testicular antioxidant enzymes (SOD, GSH, GSH-Px, and CAT) were significantly decreased in the model rats compared with the control and sham-operated rats ( $p < 0.05$ ). The levels of these enzymes were significantly increased in the rats with VC treated with MLST ( $p < 0.05$ ), and the effect was more pronounced with higher doses. In terms of SOD parameters, the low-dose group showed increased values compared with the model group, but the results were not significantly different ( $p > 0.05$ ).

In addition, ROS fluorescence analysis showed that the percentage of ROS expression in testis tissue was significantly higher in the model group than in the control and sham-operated groups, and MLST significantly reduced the ROS content in the testes of VC rats (Figure 5B). These results suggest that MLST can inhibit the VC-induced oxidative stress response.

## MLST relieves varicocele-induced apoptosis

TUNEL staining was used to detect apoptosis in testicular tissue. The number of TUNEL positive cells (green fluorescence) in the model group was significantly higher than that in the control group, while the number of TUNEL positive cells was significantly reduced by MLST intervention (Figure 6A). The expression of BAX and BCL2 in the testis was detected by immunofluorescence. For BAX (Figure 6B), the fluorescence intensity (green fluorescence) of the model group was significantly stronger than that of the control group, while the fluorescence intensity after MLST intervention was significantly lower than that of the control group. For BCL2 (Figure 6C), the fluorescence intensity (red fluorescence) of the model group was significantly lower than that of the control group, while the



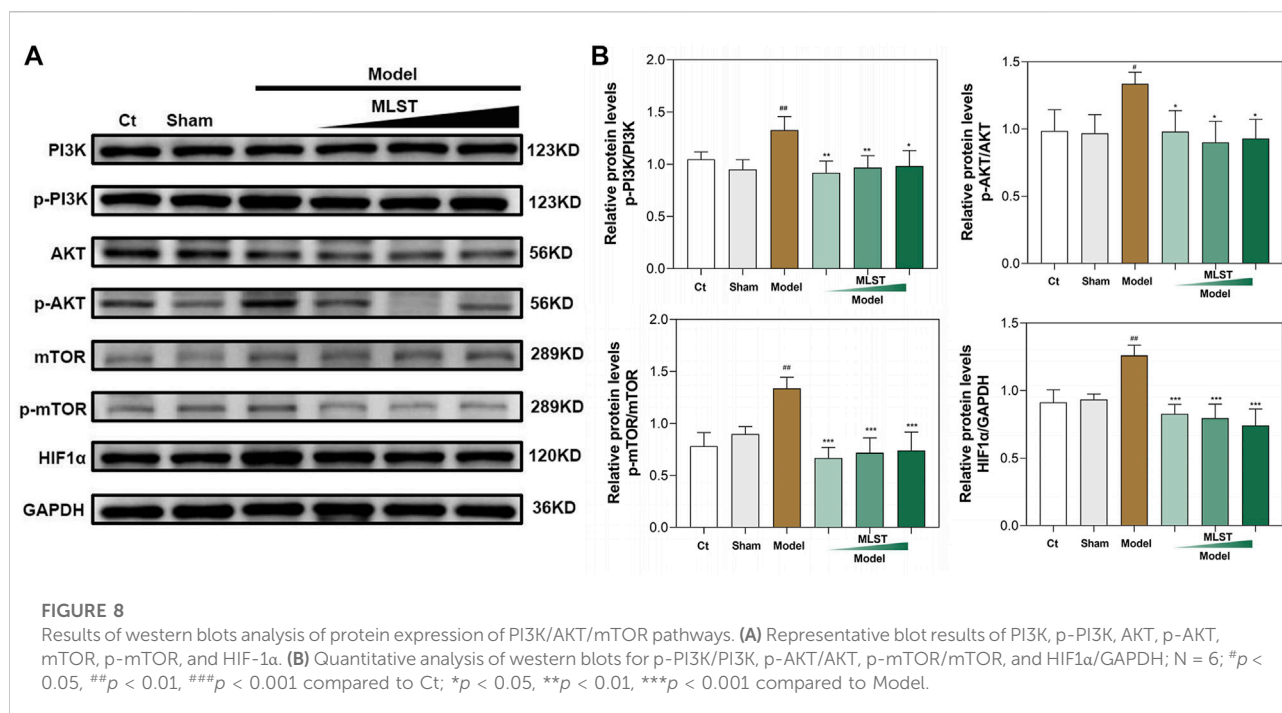


fluorescence intensity after MLST intervention was significantly higher than that of the control group. These findings suggest that MLST treatment can prevent VC-induced apoptosis in testicular tissue.

## Affinity of MLST core components to potential targets

Hypoxia-inducible factor-1 $\alpha$  (HIF1 $\alpha$ ) is crucial in varicocele-induced oxidative stress and apoptosis, and we found that PI3K/Akt, mTOR, and HIF-1 signaling pathways play an important role in HIF1 $\alpha$  expression by enrichment analysis and review of related literature (Babaei et al., 2021), and by constructing the hub targets PPI network, it was found that HIF1 $\alpha$  upstream related targets PIK3CA, AKT1, MTOR may be potential core targets for MLST in treating varicocele-associated male infertility. The protein crystal complexes (7R9V, 3O96, 3JBZ) were selected as docking targets for PIK3CA, AKT1, and MTOR, respectively, and the original ligands (2Q7, IQO, ADP) were used as positive controls, respectively (Wu et al., 2010; Lau et al., 2016; Borsari et al., 2022). The initial conformation and re-docking

results of the original ligands were shown in [Supplementary Table S2](#). The initial conformation and redocked conformation of the original ligands are shown in [Figure 7A](#), and their RMSD values were less than 2Å, which responded to the reliability of the docking model. The -CDOCKER interaction energy value of PIK3CA with 2Q7 was 67.076, AKT1 with IQO was 69.216, and MTOR with ADP was 94.204, as a positive control drug score. The positive control drug score was used as the threshold value, and the drug score value > threshold value  $\times$  75% was used as the criterion that the drug had a strong affinity with the ligand. The results of the drug score value for the molecular docking of the top 10 components mentioned above with PIK3CA, AKT1, and MTOR were shown in [Supplementary Table 3](#). Finally, kaempferol (56.668), apigenin (54.973), and cirsimaritin (51.116) had a strong affinity with PIK3CA, obacunoic acid (54.880), limonin (55.787) had a strong affinity with AKT1 and kaempferol (73.040) had a strong affinity with MTOR, and the interaction diagrams of the above drug components with the target proteins are shown in [Figure 7B](#). In summary, kaempferol, apigenin, cirsimaritin, obacunoic acid, and limonin in MLST have a strong affinity for the upstream target proteins of HIF1 $\alpha$  (PIK3CA, AKT1, MTOR).



## MLST relieves testicular damage by regulating the PI3K/Akt/mTOR signaling pathways

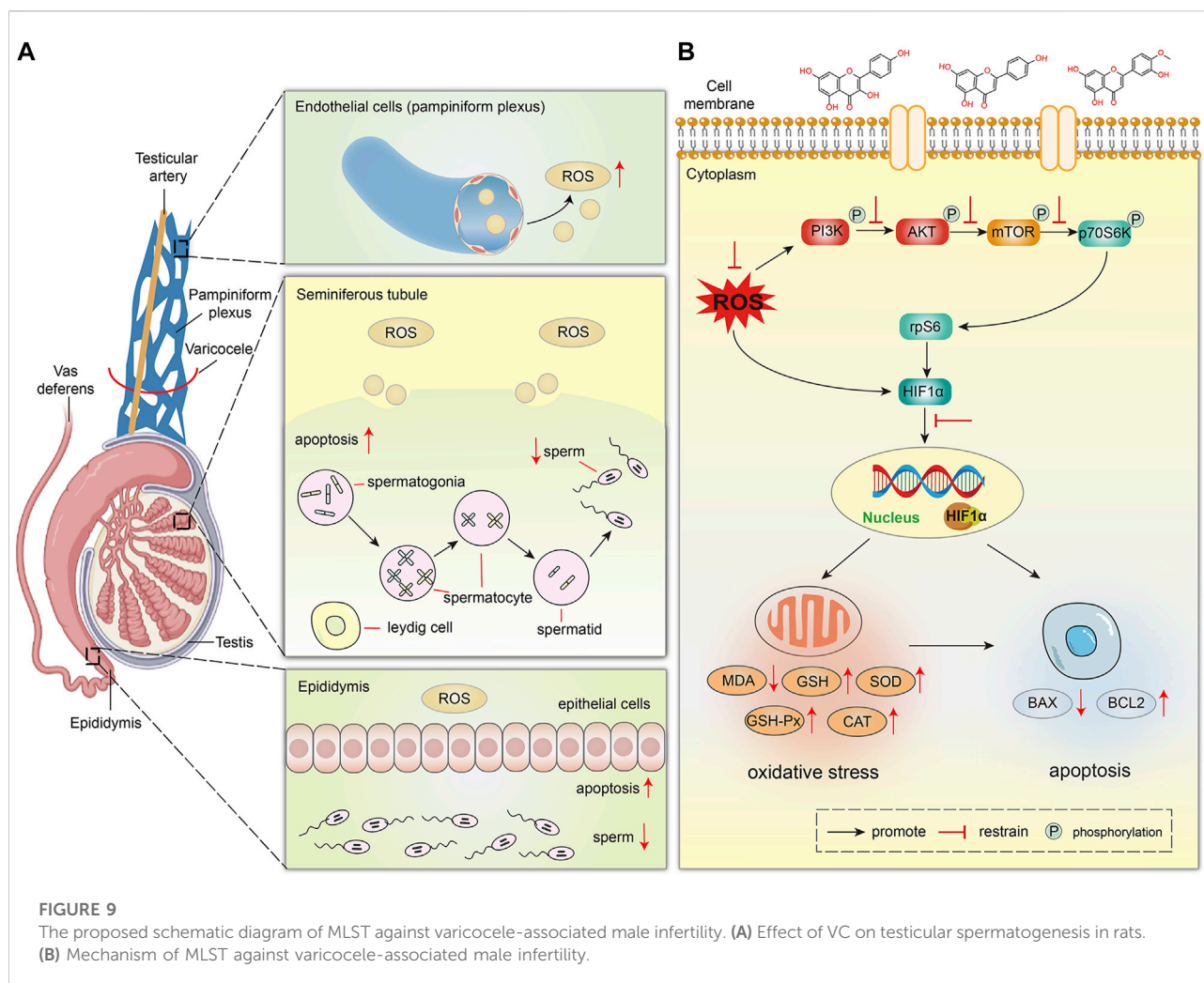
As shown in Figure 8, by western blots analysis, HIF1α was significantly expressed in VC-induced rat testis compared to control ( $p < 0.05$ ), and its upstream PI3K/Akt/mTOR signaling pathways-related protein (p-PI3K, p-AKT, p-mTOR) expression was increased ( $p < 0.05$ ), indicating that VC activates the PI3K/Akt/mTOR signaling pathways and induces the expression of HIF1α. In contrast, HIF1α protein expression was reduced in MLST-treated rats compared with the model group ( $p < 0.05$ ), and the expression of upstream PI3K/Akt/mTOR signaling pathways-related proteins (p-PI3K, p-AKT, p-mTOR) was reduced ( $p < 0.05$ ), indicating that MLST inhibited the activation of PI3K/Akt/mTOR signaling pathways and reduced the expression of HIF1α.

## Discussion

VC is the main known cause of male infertility, and among male infertility patients with VC, there are varying degrees of abnormalities in total sperm count, sperm motility, and sperm morphology (Ni et al., 2016). Currently, semen quality can be improved and fertility improved in some patients through varicocelectomy (Lira Neto et al., 2021). However, some patients whose semen quality fails to improve after surgery, and the treatment effect is not satisfactory with the use of a

single drug (Garg and Kumar, 2016; Yaris and Kilinc, 2022). The main reason for this is that the mechanism of male infertility caused by VC is complex and the use of a single drug, covering too few therapeutic targets, cannot play a better role. The multi-targeted therapeutic characteristics of TCM may be more applicable to the treatment of varicocele-associated male infertility (Qi et al., 2001). MLST is a Chinese patent medicine made by combining multiple Chinese medicines, and its “multicomponent, multitarget, multi-pathway” therapeutic characteristics have unique advantages over the use of other single drugs.

Firstly, we identified 62 components in MLST by UHPLC-MS/MS and ADME screening principles to provide component-based information on MLST. By constructing a “Components-Targets-Pathways” network and molecular docking, we screened the components with the strong binding ability to the pathway targets related to varicocele-associated male infertility: apigenin, kaempferol, limonin. Apigenin, as a biologically active flavonoid, has various biological properties (e.g., anti-inflammatory and antioxidant effects) and can reduce oxidative stress in the testis (Dang et al., 2017). Kaempferol is a natural flavonoid with a wide range of therapeutic properties such as antioxidant, anticancer and anti-inflammatory, and has been shown to promote spermatogenesis in VC-induced SD rats by modulating abnormal sex hormones, reducing oxidative stress, endoplasmic reticulum stress and apoptosis (Imran et al., 2019; Karna et al., 2019). Limonin is a natural tetracyclic triterpene compound with anti-inflammatory, analgesic, and antioxidant, and can reduce apoptosis by regulating the PI3K/



Akt signaling pathway (Fan et al., 2019; Qiu et al., 2022). Although some of the components have been reported for the treatment of varicocele and male infertility, there are still some ingredients that have not been tested pharmacologically and need further validation.

Furthermore, the PPI network analysis was used to screen 28 hub targets of MLST against varicocele-associated male infertility. Among them, HIF1α, a highly specific nuclear transcription factor, is usually overexpressed in hypoxic environments and is an important hub for regulating oxygen homeostasis, and overexpression of HIF1α can induce testicular tissue damage (Kilinc et al., 2004). Vascular endothelial growth factor A (VEGFA), the most important vascular endothelial growth factor, plays an important role in regulating angiogenesis and formation and is involved in VC-induced testicular development and spermatogenesis (Shiraishi and Naito, 2008; Wang et al., 2017). Mammalian rapamycin (mTOR) is an important regulator of cell growth and proliferation, and studies have shown a positive correlation

between mTOR expression and sperm DFI (Mahran et al., 2019). The results illustrated that MLST might regulate the above targets against varicocele-associated male infertility.

Furthermore, enrichment analysis of the hub targets revealed that MLST may regulate regulates oxidative stress and apoptosis to treat varicocele-associated male infertility. Oxidative stress is one of the main causes of testicular tissue damage induced by VC (Lai et al., 2022). Oxidative stress produces excessive ROS, which can not only lead to male infertility through lipid peroxidation or DNA damage but also lead to male infertility by inactivating enzymes and proteins in spermatogenesis (Wang et al., 2022). VC causes excessive ROS in testicular tissue, and can also cause testicular germ cell apoptosis, resulting in decreased spermatogenesis (Dolatkhah et al., 2020; Chakraborty and Roychoudhury, 2022).

Furthermore, we established a VC rat model to study the effect of VC on testicular spermatogenesis and the therapeutic effect of MLST on varicocele-associated male infertility. In this study, we found that VC can cause the decline of the testicular

index, previous studies have also confirmed this phenomenon (Sakamoto et al., 2008), and MLST treatment can improve the testicular index of the VC rat model, indicating that MLST can improve VC-induced testicular dysplasia. In addition, VC-induced rats showed atrophy of seminiferous tubules and epididymal tubules, causing the loss and disorder of spermatogonia, spermatocyte, spermatid, leydig cell, and epithelial cell, resulting in impaired sperm, similar results have been reported in previous experimental studies of VC (Soni et al., 2018; Karna et al., 2019), these phenomena were significantly improved in rats treated with MLST, indicating that MLST can prevent VC-induced spermatogenic function damage. In this study, higher levels of MDA and ROS were detected in the testicular tissues of VC rats, while the activities of antioxidant enzymes, including SOD, GSH, GSH-Px, and CAT, were relatively low. The testicular tissue test results were similar to those of VC patients in the clinic (Dogan et al., 2014). The right amount of ROS is necessary for the maintenance of normal sperm function, and it can regulate sperm capacitation, acrosome reaction, and fusion with egg cells through intracellular signal transduction (Ford, 2004). Excessive ROS mediates the formation of MDA, which not only causes changes in cell membrane fluidity, and changes in the membrane composition of the sperm head and somatic cells, but also reacts with sperm DNA, causing DNA damage and changes (Serafini and O'Flaherty, 2021). TUNEL test showed that VC could cause apoptosis of testicular germ cells, and testicular germ cells affected sperm production (Kopalli et al., 2022). BAX and BCL2 fluorescence analysis also showed this result. In VC-induced rats, BAX expression increased and BCL2 expression decreased. After MLST treatment, testicular germ cell apoptosis decreased, BAX expression decreased, and BCL2 expression increased. It showed that MLST could treat varicocele-associated male infertility by inhibiting oxidative stress and apoptosis in testicular tissue. The effect of VC on testicular spermatogenesis is shown in Figure 9A.

Finally, HIF1 $\alpha$  was overexpressed in VC-induced rat testes by western blot analysis, and excessive HIF1 $\alpha$  expression could lead to impairment of testicular spermatogenesis, which was similar to previous reports (Lee et al., 2006), and MLST could reduce the impairment of testicular spermatogenesis by inhibiting HIF1 $\alpha$  expression. Previous reports suggest that the expression of HIF1 $\alpha$  is mainly affected by ROS and regulated by PI3K/Akt/mTOR signaling pathways (Babaei et al., 2021). On the one hand, excessive ROS can directly induce the expression of HIF1 $\alpha$ , on the other hand, excessive ROS can activate the PI3K/Akt/mTOR signaling pathways, which can induce the expression of HIF1 $\alpha$ . This was also confirmed in the present study that VC can lead to increased ROS expression in testicular tissue and activate the PI3K/Akt/mTOR signaling pathways. In contrast, in rats treated with MLST, the ROS content in testicular tissue was reduced and the PI3K/Akt/mTOR signaling pathways were also inhibited. The

mechanism of MLST against varicocele-associated male infertility is shown in Figure 9B.

## Conclusion

The present study found that MLST was effective in alleviating VC-induced testicular tissue damage. The components in MLST were identified by UHPLC-MS/MS, which provided an important basis for the clarification of the material basis and subsequent network analysis. By predicting and elucidating the multi-component, multi-target, and multi-pathway therapeutic effects of MLST on varicocele-associated male infertility through network analysis, it was experimentally verified that MLST can inhibit the activation of the PI3K/Akt/mTOR signaling pathway, reduce the expression of HIF1 $\alpha$ , and further attenuate VC-induced oxidative stress and apoptosis in the testis. These findings provide evidence for the therapeutic role of MLST in varicocele-associated male infertility, as well as an idea for the study of other herbal compounding.

## Data availability statement

The original contributions presented in the study are included in the article/Supplementary Material, further inquiries can be directed to the corresponding author.

## Ethics statement

The animal study was reviewed and approved by Institutional Animal Care and Use Committee of Shandong University of Traditional Chinese Medicine and Animal Ethics Committee of Affiliated Hospital of Shandong University of Traditional Chinese Medicine.

## Author contributions

DL wrote the manuscript and analyzed the data. ZCF, QZ, and ZG designed the experiments. DL, ZS, TC, XW, CZ, and TR performed the experiments. YJ and CZ supervised and revised the manuscript.

## Funding

This study was supported by the Horizontal Project of The Affiliated Hospital of Shandong University of Traditional Chinese Medicine (H20210201-01).



## Conflict of interest

The authors declare that the research was conducted in the absence of any commercial or financial relationships that could be construed as a potential conflict of interest.

## Publisher's note

All claims expressed in this article are solely those of the authors and do not necessarily represent those of their affiliated

organizations, or those of the publisher, the editors and the reviewers. Any product that may be evaluated in this article, or claim that may be made by its manufacturer, is not guaranteed or endorsed by the publisher.

## Supplementary material

The Supplementary Material for this article can be found online at: <https://www.frontiersin.org/articles/10.3389/fphar.2022.961011/full#supplementary-material>

## References

- Agarwal, A., Majzoub, A., Parekh, N., and Henkel, R. (2020). A schematic overview of the current status of male infertility practice. *World J. Mens. Health* 38 (3), 308–322. doi:10.5534/wjmh.190068
- Arab, D., Doustmohammadi, H., and Ardestani Zadeh, A. (2021). Dietary supplements in the management of varicocele-induced infertility: A review of potential mechanisms. *Andrologia* 53 (1), e13879. doi:10.1111/and.13879
- Babaei, A., Moradi, S., Hoseinkhani, Z., Rezazadeh, D., Dokaneheifard, S., Asadpour, R., et al. (2021). Expression of hypoxia-inducible factor1-alpha in varicocele disease: A comprehensive systematic review. *Reprod. Sci.* doi:10.1007/s43032-021-00696-y
- Barbarino, J. M., Whirl-Carrillo, M., Altman, R. B., and Klein, T. E. (2018). PharmGKB: A worldwide resource for pharmacogenomic information. *Wiley Interdiscip. Rev. Syst. Biol. Med.* 10 (4), e1417. doi:10.1002/wsbm.1417
- Blanchard, O. L., and Smoliga, J. M. (2015). Translating dosages from animal models to human clinical trials--revisiting body surface area scaling. *FASEB J.* 29 (5), 1629–1634. doi:10.1096/fj.14-269043
- Borsari, C., Keles, E., McPhail, J. A., Schaefer, A., Sriramaratnam, R., Goch, W., et al. (2022). Covalent proximity scanning of a distal cysteine to target PI3Kα. *J. Am. Chem. Soc.* 144 (14), 6326–6342. doi:10.1021/jacs.1c13568
- Burley, S. K., Bhikadiya, C., Bi, C., Bittrich, S., Chen, L., Crichlow, G. V., et al. (2022). RCSB Protein Data Bank: Celebrating 50 years of the PDB with new tools for understanding and visualizing biological macromolecules in 3D. *Protein Sci.* 31 (1), 187–208. doi:10.1002/pro.4213
- Chakraborty, S., and Roychoudhury, S. (2022). Pathological roles of reactive oxygen species in male reproduction. *Adv. Exp. Med. Biol.* 1358, 41–62. doi:10.1007/978-3-030-89340-8\_3
- Chen, M. L., Xian, Y. F., Ip, S. P., Tsai, S. H., Yang, J. Y., and Che, C. T. (2010). Chemical and biological differentiation of cortex phellodendri chinensis and cortex phellodendri amurensis. *Planta Med.* 76 (14), 1530–1535. doi:10.1055/s-0030-1249774
- Chen, J., Liu, L., Hou, R., Shao, Z., Wu, Y., Chen, X., et al. (2011). Calycosin promotes proliferation of estrogen receptor-positive cells via estrogen receptors and ERK1/2 activation *in vitro* and *in vivo*. *Cancer Lett.* 308 (2), 144–151. doi:10.1016/j.canlet.2011.04.022
- Chen, L., Yang, J., Zhao, S. J., Li, T. S., Jiao, R. Q., and Kong, L. D. (2021). Atractylodis rhizoma water extract attenuates fructose-induced glomerular injury in rats through anti-oxidation to inhibit TRPC6/p-CaMK4 signaling. *Phytomedicine*. 91, 153643. doi:10.1016/j.phymed.2021.153643
- Daina, A., Michielin, O., and Zoete, V. (2017). SwissADME: A free web tool to evaluate pharmacokinetics, drug-likeness and medicinal chemistry friendliness of small molecules. *Sci. Rep.* 7, 42717. doi:10.1038/srep42717
- Daina, A., Michielin, O., and Zoete, V. (2019). SwissTargetPrediction: Updated data and new features for efficient prediction of protein targets of small molecules. *Nucleic Acids Res.* 47 (1), W357–W364. doi:10.1093/nar/gkz382
- Dang, Y., Li, Z., Luo, B., Pan, L., Wei, Q., and Zhang, Y. (2017). Protective effects of apigenin against acrylonitrile-induced subchronic sperm injury in rats. *Food Chem. Toxicol.* 109 (1), 517–525. doi:10.1016/j.fct.2017.09.025
- Dogan, F., Armagan, A., Oksay, T., Akman, T., Aylak, F., and Bas, E. (2014). Impact of micronised purified flavonoid fraction on increased malondialdehyde and decreased metalloproteinase-2 and metalloproteinase-9 levels in varicocele: Outcome of an experimentally induced varicocele. *Andrologia* 46 (4), 380–385. doi:10.1111/and.12091
- Dolatkhah, M. A., Shokoohi, M., Charvandeh, S., Tvrdá, E., Shoorei, H., Moghimian, M., et al. (2020). Fumaria parviflora regulates oxidative stress and apoptosis gene expression in the rat model of varicocele induction. *Andrologia* 52 (11), e13826. doi:10.1111/and.13826
- Dun, R. L., Yao, M., Yang, L., Cui, X. J., Mao, J. M., Peng, Y., et al. (2015). Traditional Chinese herb combined with surgery versus surgery for varicocele infertility: A systematic review and meta-analysis. *Evid. Based. Complement. Altern. Med.* 2015, 689056. doi:10.1155/2015/689056
- Fan, S., Zhang, C., Luo, T., Wang, J., Tang, Y., Chen, Z., et al. (2019). Limonin: A review of its Pharmacology, toxicity, and pharmacokinetics. *Molecules* 24 (20), E3679. doi:10.3390/molecules24203679
- Ford, W. C. (2004). Regulation of sperm function by reactive oxygen species. *Hum. Reprod. Update* 10 (5), 387–399. doi:10.1093/humupd/dmh034
- Garg, H., and Kumar, R. (2016). An update on the role of medical treatment including antioxidant therapy in varicocele. *Asian J. Androl.* 18 (2), 222–228. doi:10.4103/1008-682X.171657
- Gill, K., Kups, M., Harasny, P., Machalowski, T., Grabowska, M., Lukaszk, M., et al. (2021). The negative impact of varicocele on basic semen parameters, sperm nuclear DNA dispersion and oxidation-reduction potential in semen. *Int. J. Environ. Res. Public Health* 18 (11), 5977. doi:10.3390/ijerph18115977
- Imran, M., Rauf, A., Shah, Z. A., Saeed, F., Imran, A., Arshad, M. U., et al. (2019). Chemo-preventive and therapeutic effect of the dietary flavonoid kaempferol: A comprehensive review. *Phytother. Res.* 33 (2), 263–275. doi:10.1002/ptr.6227
- Jensen, C. F. S., Ostergren, P., Dupree, J. M., Ohl, D. A., Sonksen, J., and Fode, M. (2017). Varicocele and male infertility. *Nat. Rev. Urol.* 14 (9), 523–533. doi:10.1038/nrurol.2017.98
- Karna, K. K., Choi, B. R., You, J. H., Shin, Y. S., Cui, W. S., Lee, S. W., et al. (2019). The ameliorative effect of monotropein, astragaloside, and spiraeoside on oxidative stress, endoplasmic reticulum stress, and mitochondrial signaling pathway in varicocele rats. *BMC Complement. Altern. Med.* 19 (1), 333. doi:10.1186/s12906-019-2736-9
- Kilinc, F., Kayaselcuk, F., Aygun, C., Guvel, S., Egilmez, T., and Ozkardes, H. (2004). Experimental varicocele induces hypoxia inducible factor-1alpha, vascular endothelial growth factor expression and angiogenesis in the rat testis. *J. Urol.* 172 (3), 1188–1191. doi:10.1097/01.ju.0000135455.97627.15
- Kim, S., Thiessen, P. A., Bolton, E. E., Chen, J., Fu, G., Gindulyte, A., et al. (2016). PubChem substance and compound databases. *Nucleic Acids Res.* 44 (1), D1202–D1213. doi:10.1093/nar/gkv951
- Kopalli, S. R., Yoo, S. K., Kim, B., Kim, S. K., and Koppula, S. (2022). Apigenin isolated from carduus crispus protects against H2O2-induced oxidative damage and spermatogenic expression changes in GC-2spd sperm cells. *Molecules* 27 (6), 1777. doi:10.3390/molecules27061777
- Lai, T. C., Roychoudhury, S., and Cho, C. L. (2022). Oxidative stress and varicocele-associated male infertility. *Adv. Exp. Med. Biol.* 1358, 205–235. doi:10.1007/978-3-030-89340-8\_10
- Lau, W. C., Li, Y., Liu, Z., Gao, Y., Zhang, Q., and Huen, M. S. (2016). Structure of the human dimeric ATM kinase. *Cell Cycle* 15 (8), 1117–1124. doi:10.1080/15384101.2016.1158362
- Lee, J. D., Jeng, S. Y., and Lee, T. H. (2006). Increased expression of hypoxia-inducible factor-1alpha in the internal spermatic vein of patients with varicocele. *J. Urol.* 175, 1045–1048. discussion 1048. doi:10.1016/S0022-5347(05)00417-9

- Lira Neto, F. T., Roque, M., and Esteves, S. C. (2021). Effect of varicocelectomy on sperm deoxyribonucleic acid fragmentation rates in infertile men with clinical varicocele: A systematic review and meta-analysis. *Fertil. Steril.* 116 (3), 696–712. doi:10.1016/j.fertnstert.2021.04.003
- Liu, S., Zhao, F., Deng, Y., Zeng, Y., Yan, B., Guo, J., et al. (2022). Investigating the multi-target therapeutic mechanism of Guihuang formula on Chronic Prostatitis. *J. Ethnopharmacol.* 294, 115386. doi:10.1016/j.jep.2022.115386
- Liu, T., and Hou, S. (2020). Clinical efficacy and safety analysis on mailuo shutong pills in the treatment of varicocele. *World Chin. Med.* 15, 252–255. doi:10.3969/j.issn.1673-7202.2020.02.024
- Lu, X., Liu, J., Yin, H., Ding, C., Wang, Y., Zhang, F., et al. (2020). Effects of liver-regulating herb compounds on testicular morphological and ultrastructural changes in varicocele rats through SCF/C-KIT pathway. *Andrologia* 52 (9), e13658. doi:10.1111/and.13658
- Mahran, A. M., Mosad, E., Abdel-Raheem, M. A., Ahmed, E. H., Abdel Motaleb, A. A., and Hofny, E. R. (2019). The correlation between mammalian target of rapamycin (mTOR) gene expression and sperm DNA damage among infertile patients with and without varicocele. *Andrologia* 51 (9), e13341. doi:10.1111/and.13341
- Ni, K., Steger, K., Yang, H., Wang, H., Hu, K., Zhang, T., et al. (2016). A comprehensive investigation of sperm DNA damage and oxidative stress injury in infertile patients with subclinical, normozoospermic, and astheno/oligozoospermic clinical varicocele. *Andrology* 4 (5), 816–824. doi:10.1111/andr.12210
- Nimrouzi, M., and Zarshenas, M. M. (2016). Phytochemical and pharmacological aspects of *descurainia sophia* webb ex prantl: Modern and traditional applications. *Avicenna J. Phytomed.* 6 (3), 266–272.
- Pinero, J., Ramirez-Anguita, J. M., Sauch-Pitarch, J., Ronzano, F., Centeno, E., Sanz, F., et al. (2020). The DisGeNET knowledge platform for disease genomics: 2019 update. *Nucleic Acids Res.* 48 (D1), D845–D855. doi:10.1093/nar/gkz1021
- Qi, G. C., Lu, J. K., and Kan, Q. L. (2001). Comparative clinical study on treatment of varicocele caused infertility by tongling granule and surgical operation. *Zhongguo Zhong Xi Yi Jie He Za Zhi* 21 (6), 412–415.
- Qiu, Y., Yang, J., Ma, L., Song, M., and Liu, G. (2022). Limonin isolated from pomelo seed antagonizes aβ25-35-mediated neuron injury via PI3K/AKT signaling pathway by regulating cell apoptosis. *Front. Nutr.* 9, 879028. doi:10.3389/fnut.2022.879028
- Ramirez, D., and Caballero, J. (2018). Is it reliable to take the molecular docking top scoring position as the best solution without considering available structural data? *Molecules* 23 (5), E1038. doi:10.3390/molecules23051038
- Razi, M., Tavalae, M., Sarrafzadeh-Rezaei, F., Moazamian, A., Gharagozloo, P., Drevet, J. R., et al. (2021). Varicocele and oxidative stress: New perspectives from animal and human studies. *Andrology* 9 (2), 546–558. doi:10.1111/andr.12940
- Sakamoto, H., Ogawa, Y., and Yoshida, H. (2008). Relationship between testicular volume and varicocele in patients with infertility. *Urology* 71 (1), 104–109. doi:10.1016/j.urology.2007.08.019
- Santana, V. P., James, E. R., Miranda-Furtado, C. L., Souza, M. F., Pompeu, C. P., Esteves, S. C., et al. (2020). Differential DNA methylation pattern and sperm quality in men with varicocele. *Fertil. Steril.* 114 (4), 770–778. doi:10.1016/j.fertnstert.2020.04.045
- Serafini, S., and O'Flaherty, C. (2021). Redox regulation to modulate phosphorylation events in human spermatozoa. *Antioxid. Redox Signal.* doi:10.1089/ars.2021.0117
- Shiraishi, K., and Naito, K. (2008). Involvement of vascular endothelial growth factor on spermatogenesis in testis with varicocele. *Fertil. Steril.* 90 (4), 1313–1316. doi:10.1016/j.fertnstert.2007.08.030
- Shomarufov, A. B., Bozhedomov, V. A., Sorokin, N. I., Matyukhov, I. P., Fozilov, A. A., Abbosov, S. A., et al. (2022). Predictors of microsurgical varicocelectomy efficacy in male infertility treatment: Critical assessment and systematization. *Asian J. Androl.* 0, 0. doi:10.4103/aja2021125
- Silay, M. S., Hoen, L., Quadackaers, J., Undre, S., Bogaert, G., Dogan, H. S., et al. (2019). Treatment of varicocele in children and adolescents: A systematic review and meta-analysis from the European association of urology/European society for paediatric urology guidelines panel. *Eur. Urol.* 75 (3), 448–461. doi:10.1016/j.eururo.2018.09.042
- Soni, K. K., Zhang, L. T., Choi, B. R., Karna, K. K., You, J. H., Shin, Y. S., et al. (2018). Protective effect of MOTILIPERM in varicocele-induced oxidative injury in rat testis by activating phosphorylated inositol requiring kinase 1α (p-IRE1α) and phosphorylated c-Jun N-terminal kinase (p-JNK) pathways. *Pharm. Biol.* 56 (1), 94–103. doi:10.1080/13880209.2017.1421672
- Stelzer, G., Rosen, N., Plaschkes, I., Zimmerman, S., Twik, M., Fishilevich, S., et al. (2016). The GeneCards suite: From gene data mining to disease genome sequence analyses. *Curr. Protoc. Bioinforma.* 54, 1 30 31–31 30 33. doi:10.1002/cpbi.5
- Szklarczyk, D., Gable, A. L., Lyon, D., Junge, A., Wyder, S., Huerta-Cepas, J., et al. (2019). STRING v11: Protein-protein association networks with increased coverage, supporting functional discovery in genome-wide experimental datasets. *Nucleic Acids Res.* 47 (D1), D607–D613. doi:10.1093/nar/gky1131
- Tang, Y., Li, M., Wang, J., Pan, Y., and Wu, F. X. (2015). CytoNCA: A cytoscape plugin for centrality analysis and evaluation of protein interaction networks. *Biosystems.* 127, 67–72. doi:10.1016/j.biosystems.2014.11.005
- Turner, T. T. (2001). The study of varicocele through the use of animal models. *Hum. Reprod. Update* 7 (1), 78–84. doi:10.1093/humupd/7.1.78
- Walter, W., Sanchez-Cabo, F., and Ricote, M. (2015). GOpot: an R package for visually combining expression data with functional analysis. *Bioinformatics* 31 (17), 2912–2914. doi:10.1093/bioinformatics/btv300
- Wang, S. H., Yang, W. K., and Lee, J. D. (2017). Increased expression of the sonic hedgehog and vascular endothelial growth factor with co-localization in varicocele veins. *Phlebology* 32 (2), 115–119. doi:10.1177/0268355515627717
- Wang, A., Wang, L., Lu, X., Wang, Y., Chen, X., Shi, Z., et al. (2020). A Chinese herbal prescription Yiqi Jiedu decoction attenuates irradiation induced testis injury in mice. *Biomed. Pharmacother.* 123, 109804. doi:10.1016/j.biopha.2019.109804
- Wang, K., Gao, Y., Wang, C., Liang, M., Liao, Y., and Hu, K. (2022). Role of oxidative stress in varicocele. *Front. Genet.* 13, 850114. doi:10.3389/fgene.2022.850114
- Wu, W. I., Voegtli, W. C., Sturgis, H. L., Dizon, F. P., Vigers, G. P., and Brandhuber, B. J. (2010). Crystal structure of human AKT1 with an allosteric inhibitor reveals a new mode of kinase inhibition. *PLoS One* 5 (9), e12913. doi:10.1371/journal.pone.0012913
- Wu, T., Hu, E., Xu, S., Chen, M., Guo, P., Dai, Z., et al. (2021). clusterProfiler 4.0: A universal enrichment tool for interpreting omics data. *Innovation.* 2 (3), 100141. doi:10.1016/j.xinn.2021.100141
- Yaris, M., and Kilinc, R. (2022). Effect of varicocelectomy on detailed sperm morphology parameters: An observational retrospective clinical cohort study. *Med. Baltim.* 101 (17), e29193. doi:10.1097/MD.00000000000029193
- Zhang, L. J., Liu, H. K., Hsiao, P. C., Kuo, L. M., Lee, I. J., Wu, T. S., et al. (2011). New isoflavonoid glycosides and related constituents from *astragalus radix* ( *Astragalus membranaceus* ) and their inhibitory activity on nitric oxide production. *J. Agric. Food Chem.* 59 (4), 1131–1137. doi:10.1021/jf103610j



## OPEN ACCESS

## EDITED BY

Ren-You Gan,  
Agency for Science, Technology and  
Research, Singapore

## REVIEWED BY

S Ansar Ahmed,  
Virginia Tech, United States  
Jianjian Ji,  
Nanjing University of Chinese Medicine,  
China

## \*CORRESPONDENCE

ChengPing Wen,  
wengcp@163.com  
ZhiJun Xie,  
xzj575@163.com

<sup>†</sup>These authors have contributed equally  
to this work

## SPECIALTY SECTION

This article was submitted to  
Ethnopharmacology,  
a section of the journal  
Frontiers in Pharmacology

RECEIVED 25 May 2022

ACCEPTED 29 August 2022

PUBLISHED 23 September 2022

## CITATION

Zhang Y, Zhang F, Gao Y, Wang M,  
Gao Y, Li H, Sun J, Wen C and Xie Z  
(2022), Triptolide in the treatment of  
systemic lupus erythematosus -  
regulatory effects on miR-146a in B cell  
TLR7 signaling pathway in mice.  
*Front. Pharmacol.* 13:952775.  
doi: 10.3389/fphar.2022.952775

## COPYRIGHT

© 2022 Zhang, Zhang, Gao, Wang, Gao,  
Li, Sun, Wen and Xie. This is an open-  
access article distributed under the  
terms of the [Creative Commons  
Attribution License \(CC BY\)](#). The use,  
distribution or reproduction in other  
forums is permitted, provided the  
original author(s) and the copyright  
owner(s) are credited and that the  
original publication in this journal is  
cited, in accordance with accepted  
academic practice. No use, distribution  
or reproduction is permitted which does  
not comply with these terms.

# Triptolide in the treatment of systemic lupus erythematosus - regulatory effects on miR-146a in B cell TLR7 signaling pathway in mice

Yi Zhang<sup>1†</sup>, FengQi Zhang<sup>1†</sup>, YiNi Gao<sup>1</sup>, MeiJiao Wang<sup>1</sup>,  
Yan Gao<sup>1</sup>, HaiChang Li<sup>1</sup>, Jing Sun<sup>2</sup>, ChengPing Wen<sup>1\*</sup> and  
ZhiJun Xie<sup>1\*</sup>

<sup>1</sup>School of Basic Medical Science, Zhejiang Chinese Medical University, Hangzhou, China, <sup>2</sup>The Second School of Clinical Medicine, Zhejiang Chinese Medical University, Hangzhou, China

**Objective:** To clarify the mechanism of triptolide (TP) in alleviating the conditions underlying SLE.

**Methods:** Eight-week-old MRL/lpr mice were randomly divided into a model group ( $n = 5$ ), low-dose TP (TP-L) group ( $n = 5$ ), and high-dose TP (TP-H) group ( $n = 5$ ). Mice in these groups were gavaged with normal saline, low-dose TP solution, and high-dose TP solution for 8 weeks, respectively. The expression levels of anti-dsDNA, IgG, IgM, IgA, C3, C4, and CREA, BUN, ALT, AST, ALB, and ALP indexes in the serum of mice were detected. The proportion of CD19<sup>+</sup>CD138<sup>+</sup>B220<sup>+</sup> cells in the spleen and the pathological changes of kidney tissue in the mice were also evaluated. The possible signaling pathways and microRNA (miRNA) targets of TP in the treatment of SLE were analyzed using network pharmacology. The expressions of TLR7 mRNA and miR-146a in Raji cells (a B lymphocyte line) were detected using qPCR before and after intervention with a miR-146a inhibitor. The protein expression levels of TLR7, MyD88, p-IRAK1, and p-NF- $\kappa$ Bp65 were detected using western blot analysis.

**Results:** TP could significantly decrease the levels of ds-DNA and IgG, alleviate pathological injury in renal tissue, and upregulate miR-146a expression in the B cells of MRL/lpr mice without obvious liver and kidney toxicity. Network pharmacology analysis showed that TP could mainly regulate the Toll-like receptor signaling pathway, and NF- $\kappa$ B signaling pathway, among others. miRNA target prediction suggested that TP could regulate miRNAs such as miR-146a. *In vitro* cell experiments further confirmed that TP could significantly upregulate miR-146a expression and downregulate the expression of TLR7 mRNA and protein levels TLR7, MyD88, p-IRAK1, and p-NF- $\kappa$ Bp65. After intervention with a miR-146a inhibitor, TP had no obvious inhibitory effects on TLR7, MyD88, p-IRAK1, and p-NF- $\kappa$ Bp65 expression.

**Conclusion:** TP may exert therapeutic effects on SLE by regulating miR-146a expression, inhibiting the TLR7/NF- $\kappa$ B signaling pathway, and affecting B cell activation.

#### KEYWORDS

triptolide, systemic lupus erythematosus, B cell, miR-146a, toll-like receptor 7

## Introduction

Systemic lupus erythematosus (SLE) is characterized by the production of autoantibodies. It is a chronic autoimmune disease that seriously affects the quality of life of patients. B lymphocytes proliferate after being stimulated by antigens and produce specific antibodies. The current treatment paradigm in SLE revolves around effectively regulating B cell activation and reducing the production of autoantibodies (Liossis and Melissaropoulos, 2014). It is worth noting that Toll-like receptor 7 (TLR7) is crucial for the development of this B cell population (Rubtsov et al., 2011). TLR7 is an endosomal Toll-like receptor recognizing single-stranded RNA (ssRNA) (Diebold et al., 2004). Overexpression of the RNA-recognizing TLR7 has been linked to SLE in humans and mice (Weindel et al., 2015). On the one hand, the excessive activation of TLR7 is thought to be involved in the pathogenesis of SLE (Souyris et al., 2018). It has been shown that the overexpression of TLR7 induces systemic autoimmunity in a lupus-prone mouse strain (Walsh et al., 2012). On the other hand, the deletion of TLR7 reduces the development of lupus in strains that spontaneously develop the disease (Christensen et al., 2006). Moreover, over the past few years, significant advances have been made in understanding how TLR7 functions in B cells promote autoimmune disease (Satterthwaite, 2021). Thus, TLR7 signaling in B cells is important in disease progression. Recent studies have further highlighted that blocking TLR7 or MyD88 may be effective and therapeutic in human SLE (Brown et al., 2022). These results show that TLR7 plays an important role in the pathogenesis of SLE; hence, the role of TLR7 in B cells cannot be ignored.

Triptolide (TP) is the main active component isolated from *Tripterygium wilfordii* Hook F. *Tripterygium wilfordii* has excellent immunosuppressive and anti-inflammatory effects (Law et al., 2011; Ziaei and Halaby, 2016; Cheng et al., 2021; Cao et al., 2022), and it can be used for the treatment of SLE (Tao and Lipsky, 2000). TP has been reported to play a role in various diseases by inhibiting the NF- $\kappa$ B signaling pathway (Jiang et al., 2021; Liu et al., 2022). Moreover, it can inhibit the differentiation of B cells into CD138<sup>+</sup>CD27<sup>+</sup> plasma cells and inhibit the secretion of IgA, IgG, and IgM by plasma cells (Zhao et al., 2018). In previous studies, triptolide has been shown to alleviate proteinuria and reduce serum anti-dsDNA antibody and TNF- $\alpha$  levels in

MRL/lpr lupus mice (Huang et al., 2022). However, the specific mechanism of TP on SLE has not been fully investigated.

MicroRNAs (microRNA, miRNA) comprise a class of endogenous non-coding single-stranded RNA with a size of approximately 22 nucleotides, which mainly regulate gene expression at the post-transcriptional level. They can also participate in immune regulation (Dai and Ahmed, 2011). In addition, the activation of B cells and the expression of miRNAs may influence SLE. Studies have shown that TP can ameliorate lupus *via* the induction of miR-125a-5p-mediated Treg proliferation (Zhao et al., 2019). Therefore, studying the regulatory effect of TP on miRNA can further explore the therapeutic mechanism of TP on SLE.

Accordingly, this study aimed to investigate the therapeutic mechanism of TP on B cells in SLE based on the miR-146a/TLR7/NF- $\kappa$ B signaling pathway.

## Materials and methods

### Experimental animals

Fifteen SPF-grade female 8-week-old MRL/lpr mice were used in this study (production license number: SCXK (Shanghai) 2017-0005). MRL/lpr mice, a well-established representative animal model of lupus pathogenesis, can produce lupus symptoms similar to human disease. They were randomly divided into the model ( $n = 5$ ), low-dose TP (TP-L) ( $n = 5$ ), and high-dose TP (TP-H) groups ( $n = 5$ ). Based on the background of previous studies, the dose concentrations of TP administered were set at 30  $\mu$ g/ml and 60  $\mu$ g/ml. Mice in the TP-L group received 0.2 ml of a 30  $\mu$ g/mL TP solution *via* gavage once a day. Mice in the TP-H group received 0.2 ml of a 60  $\mu$ g/ml TP solution *via* gavage once a day. Mice in the model group received 0.2 ml of a normal saline solution *via* gavage once a day. Mice were dosed starting at the eighth week and continued for 8 weeks. The animal study was approved by the Laboratory Animal Management and Ethics Committee of the Zhejiang Chinese Medical University.

### Experimental cell and drugs

Raji cells, a B lymphocyte cell line, were cultured in RPMI 1640 medium supplemented with 10% fetal bovine serum. Triptolide was purchased from Shanghai Yuanye

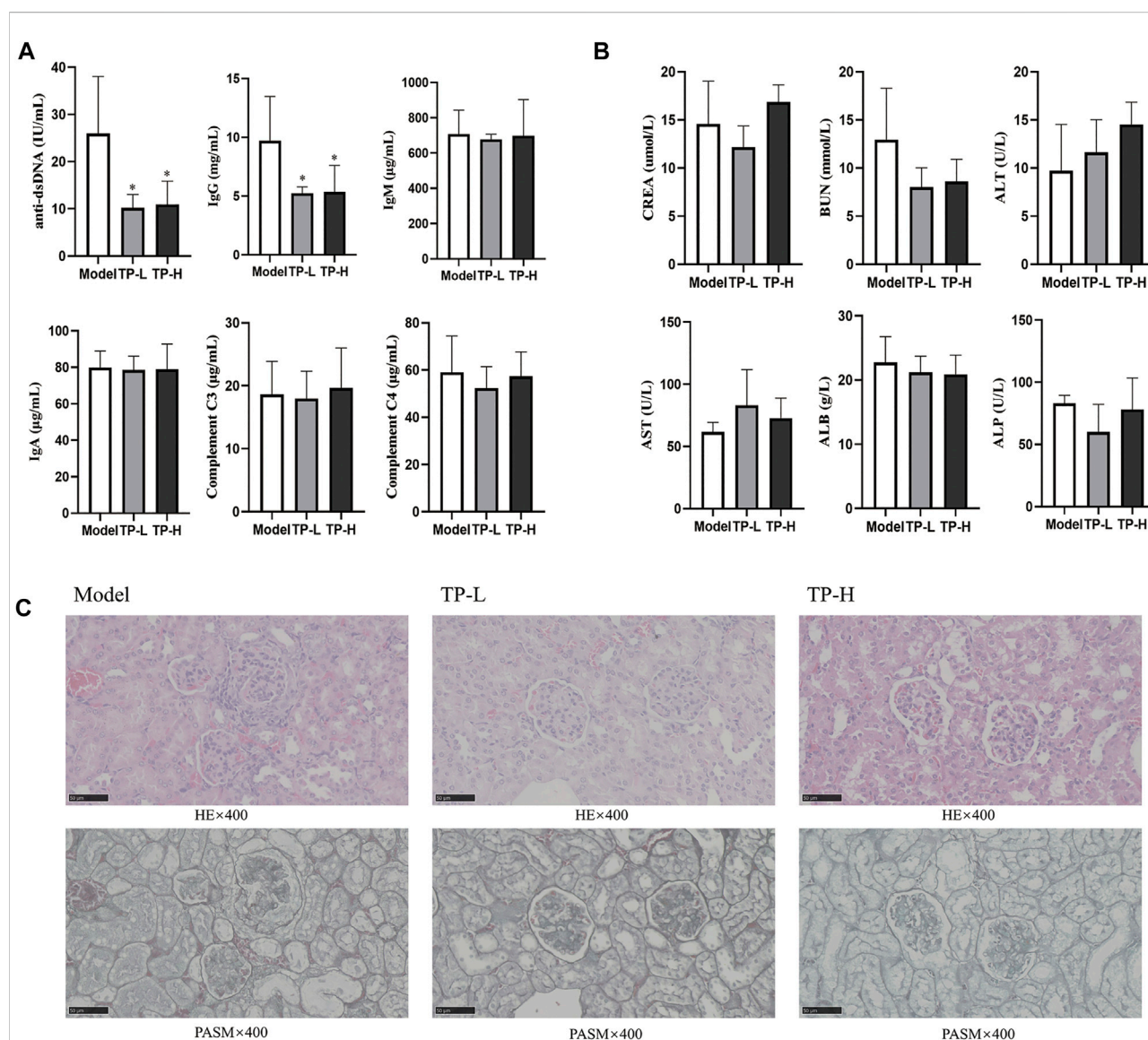


Biotechnology Co., Ltd. (product number: B20709-20mg). The has-miR-146a inhibitor and transfection reagent were purchased from Guangzhou Ribo Biotechnology Co., Ltd.

## Animal experiments and cell sorting

After 8 weeks of administration, the peripheral sera of mice were collected, and the levels of anti-dsDNA antibody, complement C3, complement C4, IgA, IgM, and IgG were detected using ELISA. Mouse Anti ds-DNA antibody elisa kit: MM-46291M1; Mouse Complement 3 elisa kit: MM-0354M1; Mouse Complement 4 elisa

kit: MM-0343M1; Mouse Immunoglobulin A elisa kit: MM-0055M1; Mouse Immunoglobulin M elisa kit: MM-0058M1. Mouse Immunoglobulin G elisa kit: MM-0057M1. Purchased from MEIMIAN kit mall. CREA, BUN, ALT, AST, ALB, and ALP levels were detected using a fully automatic biochemical analyzer (HITACHI Automatic Analyzer 3100). After sacrificing *via* cervical dislocation, the kidneys of the mice were collected and fixed in 4% PFA for pathological examination. The spleens were also collected, immediately placed in RPMI 1640 medium, and ground, and the resulting cell solution was used for red blood cell lysis to obtain a single-cell suspension. Approximately  $10^7$  cells were taken for flow antibody incubation, and the number of CD19<sup>+</sup>CD138<sup>+</sup>B220<sup>+</sup> plasma



**FIGURE 1**

TP alleviates the disease condition in MRL/lpr mice. **(A)** Immune-related indexes in MRL/lpr mice. **(B)** Liver and kidney function indexes in MRL/lpr mice. **(C)** HE and PASM staining of the kidneys from MRL/lpr mice (Magnification x400; Scale bar = 50 μm). ( $n = 5$ , \* $p < 0.05$ , \*\* $p < 0.01$ , \*\*\* $p < 0.001$ ).

cells was detected using a Beckman Cytoflex flowmeter. The remaining cells were sorted using CD43 (Ly-48) MicroBeads to obtain mouse spleen B cells. Reagent manufacturers and lot number: anti-mouse CD19: Biolegend, 115520; anti-mouse CD138: Biolegend, 142506; anti-mouse/human B220: Biolegend, 103247. CD43 (Ly-48) MicroBeads: Miltenyi, 130-049-801.

## Bioinformatic approach for predicting the targets and miRNAs of TP in treating SLE

“Triptolide” related targets were retrieved using the TCMSP database (<https://old.tcm-sp-e.com/tcm-sp.php>). The targets related to “systemic lupus erythematosus” were indexed using the GeneCards database (<https://www.genecards.org/>) and the Online Mendelian Genetics (OMIM) database (<http://omim.org/>). The targets of TP and SLE were intersected to obtain their overlapping targets. The overlapping targets were then analyzed in the STRING database, and the resulting PPI network was further visualized using Cytoscape 3.7.1 software. Gene Ontology (GO) and KEGG pathway enrichment analysis of overlapping targets were analyzed using R software (Yu et al., 2012). We used the R package clusterProfiler for analysis and defined  $p < 0.05$ .

The miRWalk and miRDB databases were used for the miRNA prediction of the overlapping targets. Briefly, the experimentally verified TP-related miRNAs were retrieved to determine their intersection, then the related miRNAs were obtained and visualized using Cytoscape 3.7.1 software.

## Detecting miR-146a expression using RT-qPCR

Total RNA from mouse spleen B cells was extracted, and reverse transcription-PCR (RT-PCR) was performed using a Bio-Rad Total RNA Kit. PCR amplification system: RNA Template 1 µg, miR-146a/U6 RT primer (5 µM) 1 µl, 5× Reverse Transcription Buffer 2 µl, RNase free H<sub>2</sub>O to make up to 10 µl. After mixing the above system, centrifuge briefly. The RT reaction program is as follows: 42°C for 60 min, 70°C for 10 min. The qPCR reaction system for miR-146a/U6 comprised 10 µl 2×SYBR Green Mix, 2 µl RT product, 0.8 µl each of the forward and reverse PrimermiR-146a/U6 primers (primer concentration: 5 µM), and 6.4 µl dd H<sub>2</sub>O.

## Raji cell culture and transfection with a miR-146a inhibitor

In addition, after stable culture of Raji cells, TP solution was administered, and the expression of miR-146a and TLR7 mRNA was detected using qPCR at 3, 6, 12, and 24 h after drug intervention. Simultaneously, western blotting was

used to detect the protein expressions of TLR7, MyD88, p-IRAK1, and p-NF-κBp65 following TP administration at the optimal intervention time. Moreover, after stable culture of Raji cells, Raji cells were transfected with 10, 20, 30, 50, 100 nM miR-146a inhibitor, respectively, and cultured at each concentration for 12, 24, 36, 48, and 72 h. The optimal inhibition time and concentration were determined using qPCR. TP solution was administered under the intervention of miR-146a inhibitor at the optimal concentration and time. The mRNA expressions of miR-146a and TLR7 were detected using qPCR, and the protein expressions of TLR7, MyD88, p-IRAK1, and p-NF-κBp65 were detected by western blot.

## Detecting the mRNA expression of related genes using RT-qPCR

Raji cells were collected after administration for total RNA extraction. Then, RT-qPCR was performed using a Bio-Rad Total RNA Kit. The sequences of the primers used were: TLR7, primer-F 5'-TCAGCGTCTAATATCACCAGAC-3' and primer-R 5'-CACTGTCTTTTGGCTAAGCTGT-3'; IRAK1, primer-F 5'-GAGAGTGACGAGAGCCTAGG-3' and primer-R 5'-CTCGATTCTCCTGCCGTGTC-3'; NF-κBp65, primer-F 5'-ACAGAAGCAGGCTGGAGGTAAGG-3' and primer-R 5'-GGACAATGCCAGTGCCATACAGG-3'; and GAPDH, primer-F 5'-GAACGGGAAGCTCACTGG-3' and primer-R 5'-GCCTGCTTACCACCTTCT-3'.

## Protein expression detection via western blot

Cells were lysed with RIPA lysis buffer to extract total protein. SDS-PAGE gels were prepared, followed by ECL chemiluminescence and exposure development. The primary antibodies (concentrations) used were anti-TLR7 (1:3000), anti-MyD88 (1:1000), anti-IRAK-1 (phospho-T209) (1:300), and phospho-NF-κBp65 antibodies (1:1000). Reagent manufacturers and lot number: PAGE Gel Rapid Preparation Kit: Yamei, PG112; anti-TLR7 antibody: abcam, ab124928; anti-MyD88 antibody: abcam, ab2064; anti-IRAK-1 (phospho-T209) antibody: abcam, ab218130; phospho-NF-κBp65 antibody (Ser536): CST, 3033S; Beta actin antibody: BLOK, BK7018.

## Statistical analysis

SPSS (Statistical Package for Social Sciences) 25.0 software, Flow Jo-V10 software, and GraphPad Prism 8 software were used to analyze and graph the experimental

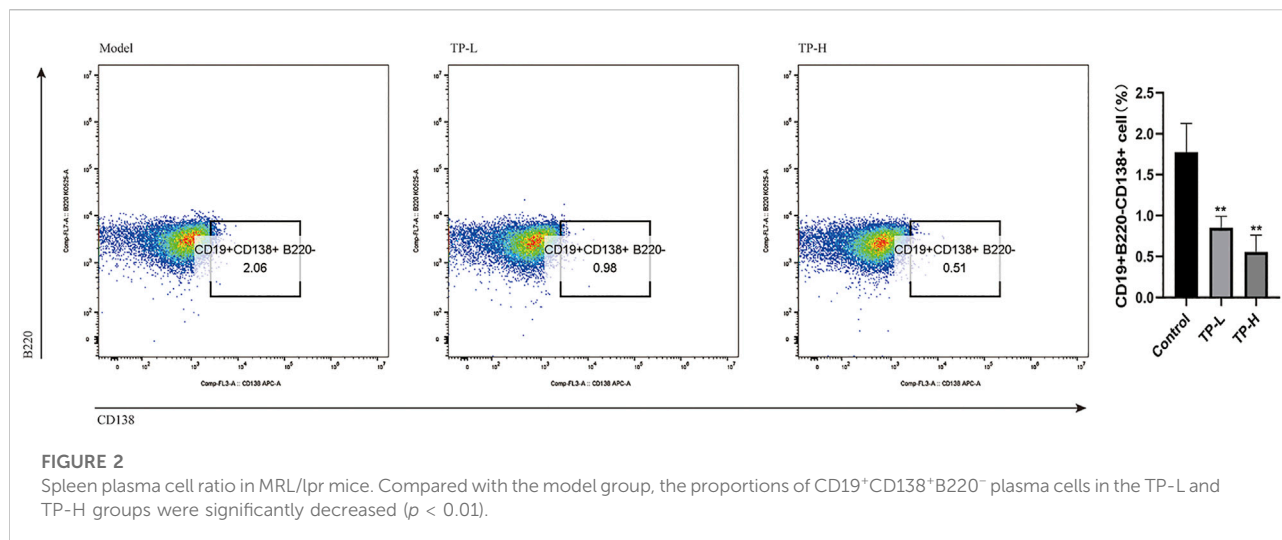


FIGURE 2

Spleen plasma cell ratio in MRL/lpr mice. Compared with the model group, the proportions of CD19<sup>+</sup>CD138<sup>+</sup>B220<sup>-</sup> plasma cells in the TP-L and TP-H groups were significantly decreased ( $p < 0.01$ ).

data. One-way ANOVA was used to compare multiple groups, and differences were considered statistically significant at  $p < 0.05$ .

## Results

### TP exerted therapeutic effects on MRL/lpr mice without obvious liver and kidney toxicity

Compared with the model group, the levels of serum anti-dsDNA and IgG were decreased in the TP-L and TP-H groups ( $p < 0.05$ ), while there were no significant differences in IgM, IgA, C3, and C4 levels (Figure 1A) and CREA, BUN, ALT, AST, ALB, and ALP levels between the model, TP-L, and TP-H groups (Figure 1B). Renal histopathological examination revealed inflammatory cell infiltration around the glomerulus and renal tubules, glomerular mesangial hyperplasia, capillary endothelial cell proliferation, and fibrocytic crescents in some glomeruli in the model group. In TP-L and TP-H mice, no fibrocytic crescents were found in the glomeruli, the infiltration of inflammatory cells around the glomerulus and renal tubules was significantly less than that of the model group, and the glomerular mesangial hyperplasia and proliferation of capillary endothelial cells were significantly better than that of the model group (Figure 1C). Compared with the model group, the proportions of CD19<sup>+</sup>CD138<sup>+</sup>B220<sup>-</sup> plasma cells in the TP-L and TP-H groups were decreased ( $p < 0.01$ ) (Figure 2).

### Bioinformatics prediction of the targets of TP in the treatment of SLE

Thirty-four TP-related targets were retrieved in the TCMSP database and 4,573 SLE-related targets were retrieved in the Genecards database. In total, 28 overlapping targets were obtained (Figure 3A), including TNF, C3, IFNG, TP53, TGFBI, IL4, IL2, VEGFA, CXCL8, STAT1, STAT3, CD40, CD274, CD80, CD86, PTGS2, CXCR4, IL23A, CCR7, BCL2, CDKN1A, CASP3, PLA2, FOS, REL, JUN, MAPK8, CD14. The interaction between the overlapping targets was analyzed in the STRING database, and a PPI network map was obtained. Cytoscape 3.7.1 software was used to visualize the network map (Figure 3B).

Next, we performed Gene Ontology (GO) analysis on the overlapping targets to further explore the mechanism of TP in the treatment of SLE. We found that the overlapping targets were mainly enriched in cytokine receptor binding, cytokine activity, ubiquitin-like protein ligase binding, ubiquitin protein ligase binding, core promoter sequence-specific DNA binding, receptor-ligand activity, signaling receptor activator activity, DNA-binding transcription factor binding, RNA polymerase II core promoter sequence-specific DNA binding, and repressing transcription factor binding (Figure 3C). We also performed a KEGG pathway enrichment analysis on the overlapping targets. We found that TP regulated SLE-related immune signaling pathways mainly involved in Toll-like receptor signaling, Th17 cell differentiation, and the IL-17 signaling pathway, among others (Figure 3D). Based on previous studies and our prediction of network pharmacological mechanisms, we selected the TLR-7 signaling pathway to verify the mechanism of TP in the treatment of SLE.

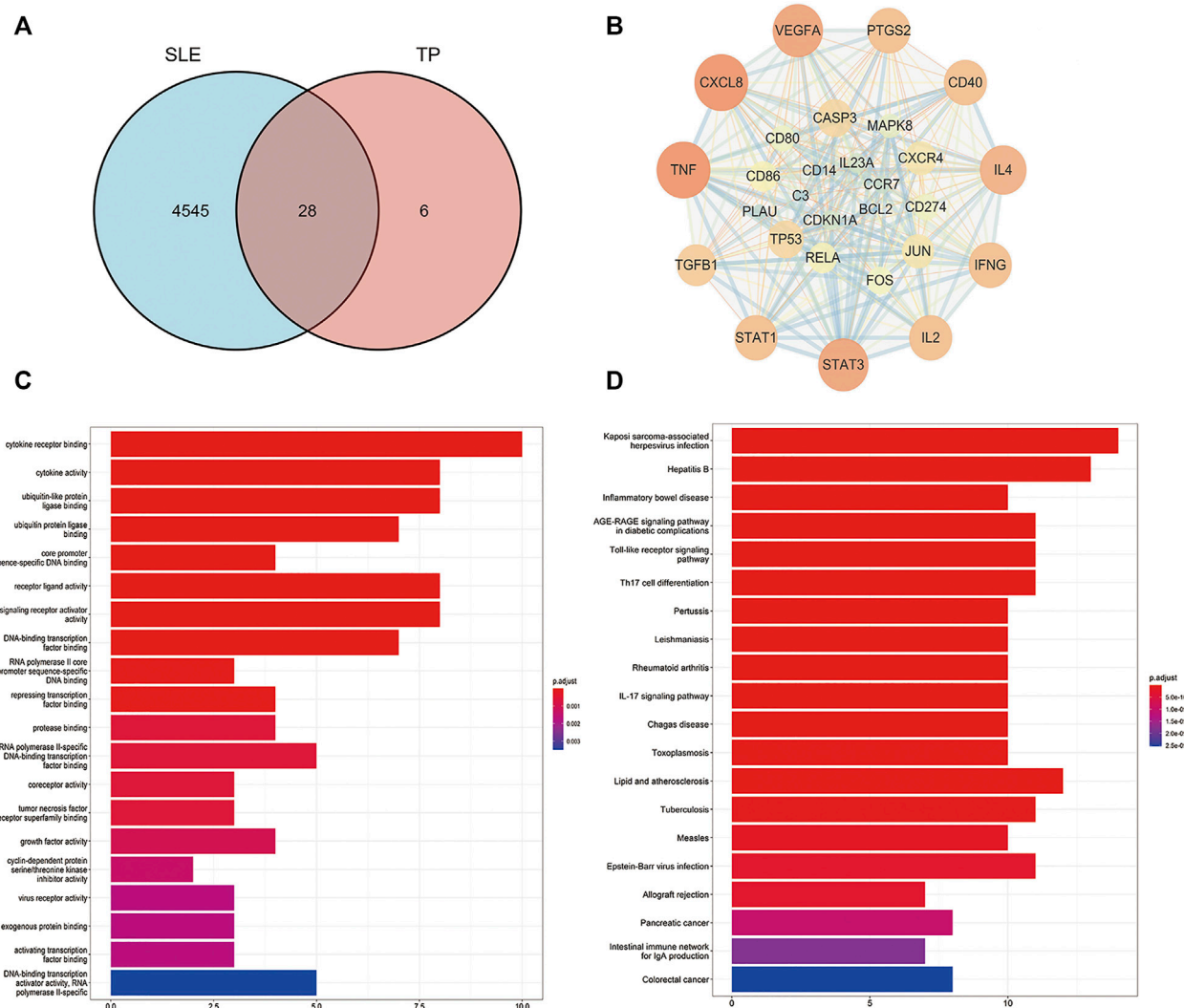


FIGURE 3

Network pharmacological analysis of the overlapping targets of TP and SLE. (A) Venn diagram of the compound targets of SLE and TP. (B) Visualization of the intersection targets of TP and SLE using Cytoscape 3.7.1 software. The dots represent the target of TP in the treatment of SLE and the edges represent the interactions between targets. (C) Gene ontology (GO) analysis of the overlapping targets of TP and SLE. (D) Kyoto Encyclopedia of Genes and Genomes (KEGG) analysis of the overlapping targets of TP and SLE.

## Predicted miRNAs associated with the overlapping targets between TP and SLE

Next, we predicted related miRNAs acting on the overlapping targets of TP and SLE according to the miRWalk and miRDB databases. A total of 261 related miRNAs were obtained (Figure 4A). The predicted miRNAs were intersected with the TP-related miRNAs validated in the literature, and 14 miRNAs were obtained: miR-146a, miR-204, miR-181b, miR-20b, miR-125a, miR-181a, miR-200a, miR-124, miR-193b, miR-26a, miR-21, miR-138, miR-155, and miR-106b (Figure 4B). The results were visualized using Cytoscape 3.7.1 software (Figure 4C).

## TP upregulated miR-146a expression to inhibit the TLR7/NF- $\kappa$ B signaling pathway

Compared with the model group, the expression of miR-146a was upregulated in splenic B cells of MRL/lpr mice treated with TP-L and TP-H. The expression of miR-146a in the TP-L group was significantly increased ( $p < 0.05$ ) (Figure 5A). Next, we carried out cell experiments using Raji cells and found that the expression of miR-146a was upregulated and the expression of TLR7 mRNA was downregulated after 12 h of TP administration (Figures 5B,C). Western blotting showed that TP could downregulate the protein expression levels of TLR7, MyD88, p-IRAK1, and p-NF- $\kappa$ Bp65 (Figure 5D).



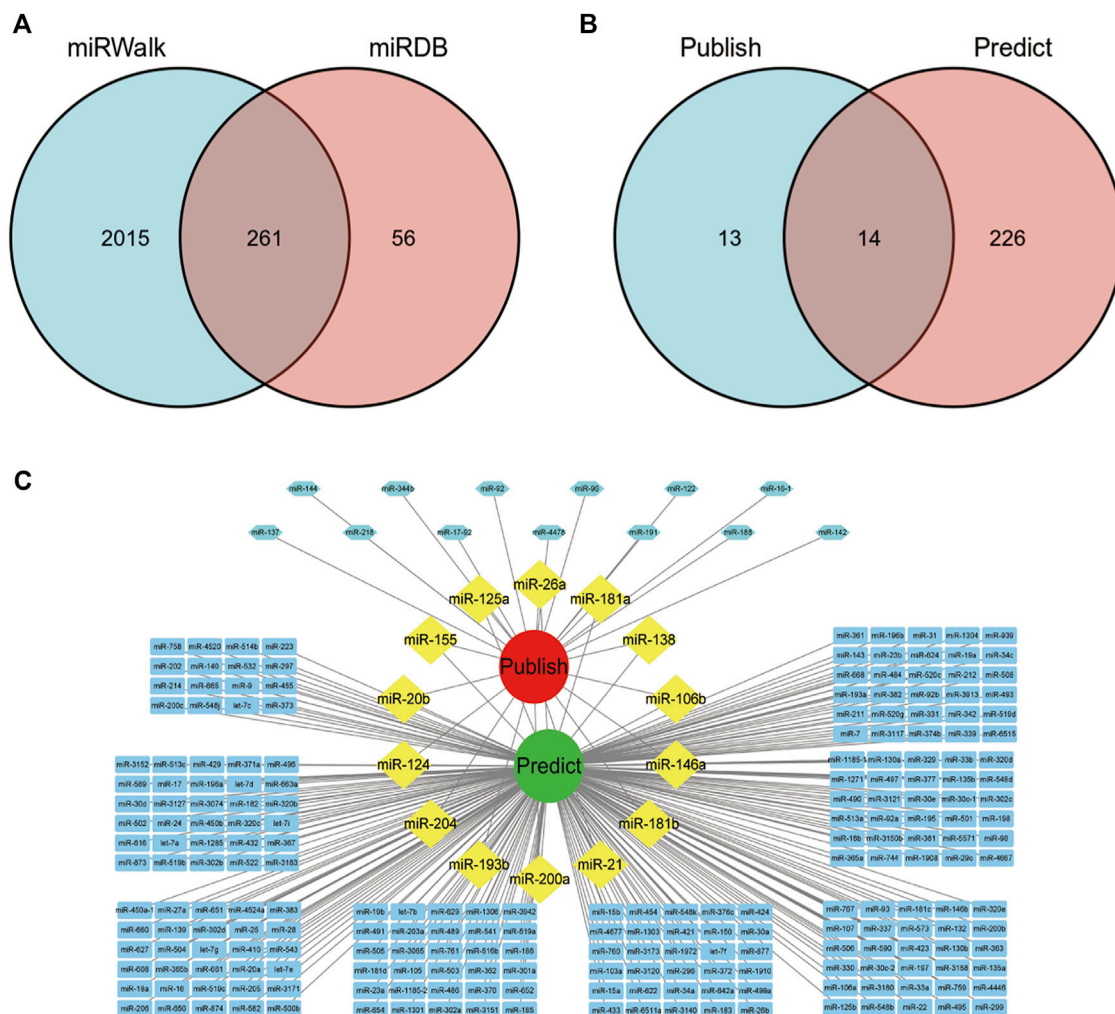


FIGURE 4

miRNAs acting on overlapping targets of SLE and TP. (A) Venn diagram of miRNAs predicted by the miRWalk and miRDB databases. (B) Venn diagram of TP-related miRNAs verified in literature and predicted in this paper. (C) Visualization of the network diagram of TP-related miRNAs verified in literature and predicted in this paper.

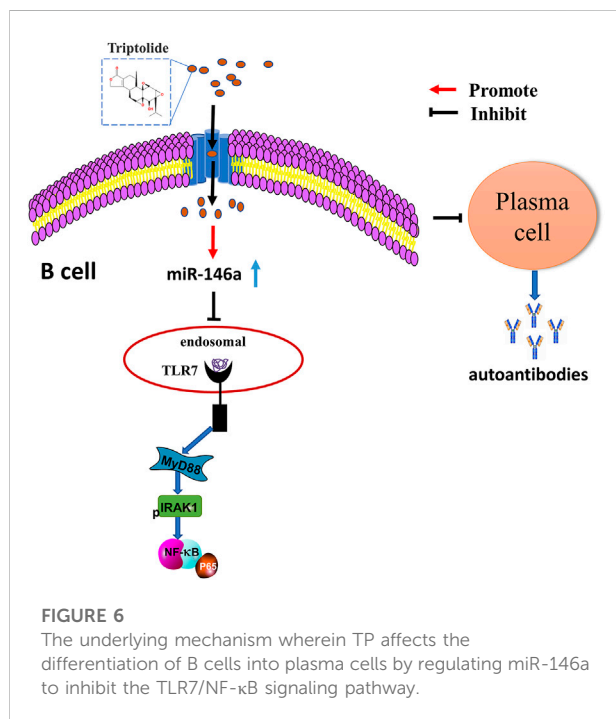
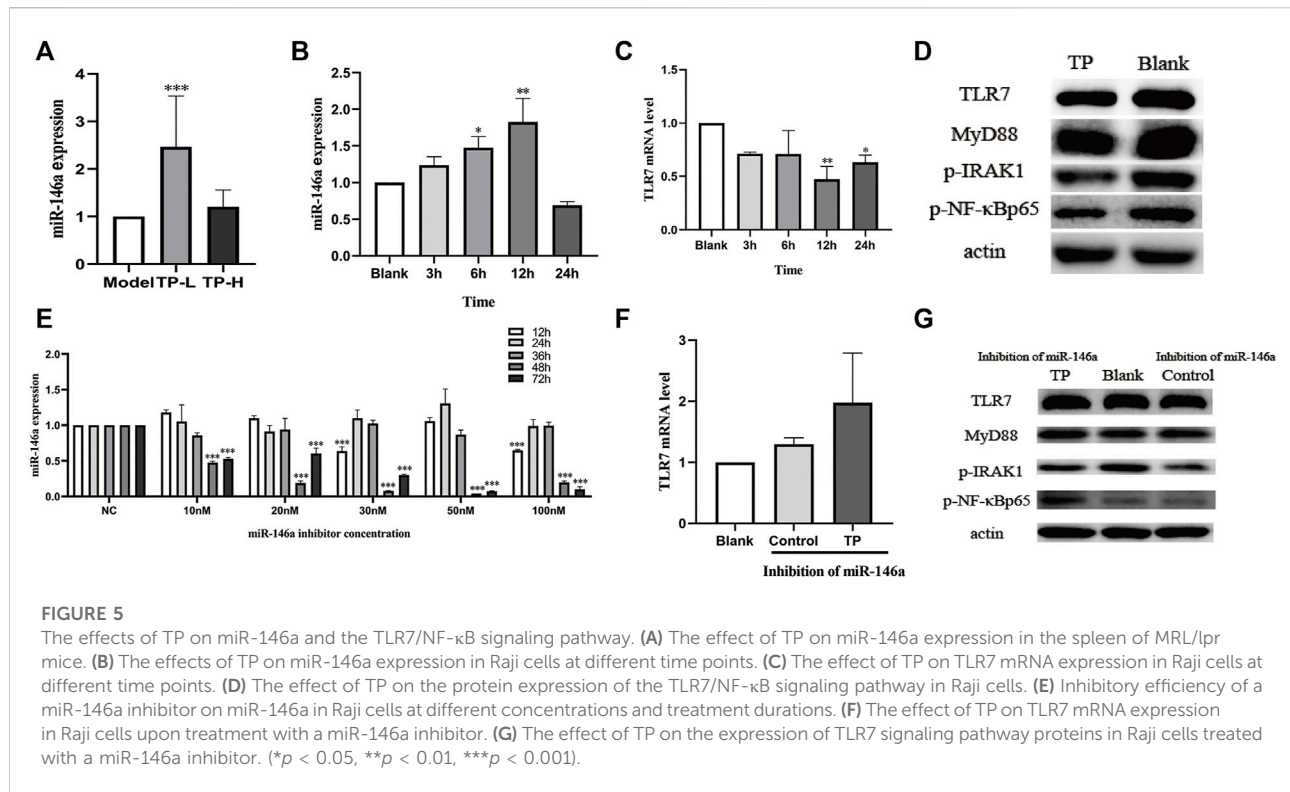
We then detected the inhibition efficiency of the miR-146a inhibitor in Raji cells and found that the optimal conditions were 50 nM concentration and 48 h of treatment (Figure 5E). Therefore, this condition was selected for subsequent experiments. In case of miR-146a inhibition in Raji cells, TLR7 mRNA was not downregulated in the TP groups (Figure 5F). Moreover, the protein expressions of TLR7, MyD88, p-IRAK1, and p-NF-κBp65 were also not downregulated (Figure 5G).

## Discussion

SLE is an autoimmune disease where B cell abnormalities are a key factor in its pathogenesis (Yap and Chan, 2019; Atisha-

Fregoso et al., 2021). Plasma cells are the terminal differentiation link of B cells, which produce pathogenic antibodies in SLE (Malkiel et al., 2018). Toll-like receptors (TLRs) play pivotal roles in B cell activation and contribute to the pathogenesis of SLE (Jackson et al., 2014). For example, enhanced TLR7 signaling drives the aberrant survival of B cell receptor (BCR)-activated B cells (Brown et al., 2022). Moreover, TLR7 drives B cell response and the germinal center reaction involved in autoantibody production (Fillatreau et al., 2021). Notably, microRNAs also play a role in germinal center B cell production and their differentiation into antibody-secreting plasma cells (Meininger et al., 2018).

*Tripterygium wilfordii* Hook F has significant anti-inflammatory and immunosuppressive properties and is widely used in treating autoimmune and inflammatory



diseases such as SLE (Song et al., 2020). TP is the main active ingredient in *Tripterygium wilfordii* Hook F. Previous studies have shown that TP can inhibit NF-κB transcription (Qiu and

Kao, 2003), inhibit NF-κB/GADD45B signaling and attenuate proteinuria and podocyte apoptosis (Wang et al., 2018), and exert anti-inflammatory effects by inhibiting NF-κB activation (Bai et al., 2016). In this study, we found that an appropriate dose of TP could reduce the expression of ds-DNA and IgG, alleviate kidney damage, and reduce the proportion of CD19<sup>+</sup>CD138<sup>+</sup>B220<sup>+</sup> plasma cells in MRL/lpr mice. Moreover, TP improved the disease condition of MRL/lpr mice without serious side effects. Accordingly, we further analyzed the mechanism of TP alleviating SLE.

We predicted *via* network pharmacology that the key pathways of the TP-and SLE-related overlapping targets include the Toll-like receptor signaling pathway. TLRs promote pathogen recognition by immune cells, producing pro-inflammatory cytokines and chemokines. TLRs are critical in the pathogenesis of SLE (Jackson et al., 2014). Specifically, the TLR7 in B cells plays an important role in regulating SLE, and regulating TLR7 expression can alleviate the symptoms of SLE (Fillatreau et al., 2021). TLRs are essential molecules that influence B cell activation signaling (Suthers and Sarantopoulos, 2017), as TLRs could decrease the activation threshold of B cells to some extent (Singh et al., 2016).

Accordingly, this study mainly focused on B cells and explored the effect of TP on the expression of TLR7 on B cells. We verified that TP could inhibit the expression of TLR7 mRNA and TLR7, MyD88, p-IRAK1, and p-NF-κB-p65 proteins in B cells. This evidence suggests that TP may

inhibit the TLR7 signaling pathway in B cells and affect the differentiation of B cells into plasma cells.

miRNAs can regulate gene expression (Chen et al., 2013) and have potential roles in autoimmune regulation (O'Connell et al., 2010). The miRNA-mRNA network shows that hsa-miR-146a plays a vital role in pulmonary arterial hypertension secondary to SLE (Yao et al., 2021). Research has reported that the SLE risk variant rs2431697 likely causes SLE by disrupting a regulatory element and modulating miR-146a expression (Hou et al., 2021). The role of miR-146a in regulating the inflammatory response in SLE has been elucidated (Zhou et al., 2019), and studies have shown that miR-146a through the NF- $\kappa$ B signaling pathway reduces SLE-induced kidney injury in MRL/lpr mice (Fu et al., 2019). In this study, we predicted 14 miRNAs related to the overlapping targets of TP and SLE, including miR-146a. miR-146a is a major negative regulator of MyD88-dependent NF- $\kappa$ B activation and affects TLR7 expression (Chan et al., 2013). A decreased expression of miR-146a can downregulate the expression of IRAK1 and induce the development of SLE (Tang et al., 2009). Taganov and others confirmed that IRAK1 is the target of miR-146a and a critical downstream molecule in the TLR signaling pathway (Taganov et al., 2006). miR-146a can inhibit the expression of TLR7 and MyD88 (Karrich et al., 2013); hence, we further explored the effect of TP administration on TLR7 and miR-146a expression.

We found that TP could upregulate miR-146a expression in the spleen B cells of MRL/lpr mice. Accordingly, we further explored the effect of TP on TLR7 and miR-146a. We found that TP no longer played a role in inhibiting the expression of TLR7 in B cells when the cells were treated with a miR-146a inhibitor. Thus, we concluded that TP could inhibit the TLR7-NF- $\kappa$ B signaling pathway by upregulating the expression of miR-146a in B cells (Figure 6).

Our results showed that TP alleviated SLE through the miR-146a-mediated downregulation of TLR7 expression. Herein, we propose a novel mechanism by which TP alleviates the disease conditions in MRL/lpr mice, which may provide support for the pharmacodynamic mechanisms underlying the application of TP in the treatment of SLE.

## Conclusion

In this paper, we confirmed that TP could alleviate SLE, and the mechanism of its efficacy may be elicited by affecting the differentiation of B cells into plasma cells by regulating miR-146a to inhibit the TLR7/NF- $\kappa$ B signaling pathway.

## Data availability statement

The original contributions presented in the study are included in the article/Supplementary Material, further inquiries can be directed to the corresponding authors.

## Ethics statement

The animal study was reviewed and approved by Laboratory Animal Management and Ethics Committee of Zhejiang Chinese Medical University.

## Author contributions

YZ and FZ contributed equally to this work. YZ and FZ were responsible for the research design, cell experiments, data analyses, figure preparation, and writing the manuscript. YG and MW contributed to the animal experiments. YG and HL contributed to the cell experiments. JS critically reviewed the manuscript. CW and ZX contributed to the research design, methodology, and reviewing, and editing of this paper. All authors read and approved the manuscript.

## Funding

This work was financially supported by the National Natural Science Foundation of China (81873266), (81973829) and the Zhejiang TCM Science and Technology Plan of China (2021ZA063).

## Conflict of interest

The authors declare that the research was conducted in the absence of any commercial or financial relationships that could be construed as a potential conflict of interest.

## Publisher's note

All claims expressed in this article are solely those of the authors and do not necessarily represent those of their affiliated organizations, or those of the publisher, the editors and the reviewers. Any product that may be evaluated in this article, or claim that may be made by its manufacturer, is not guaranteed or endorsed by the publisher.

## References

- Atisha-Fregoso, Y., Toz, B., and Diamond, B. (2021). Meant to B: B cells as a therapeutic target in systemic lupus erythematosus. *J. Clin. Invest.* 131 (12), 149095. doi:10.1172/jci149095
- Bai, S., Hu, Z., Yang, Y., Yin, Y., Li, W., Wu, L., et al. (2016). Anti-inflammatory and neuroprotective effects of triptolide via the NF- $\kappa$ B signaling pathway in a rat MCAO model. *Anat. Rec.* 299 (2), 256–266. doi:10.1002/ar.23293
- Brown, G. J., Cañete, P. F., Wang, H., Medhavy, A., Bones, J., Roco, J. A., et al. (2022). TLR7 gain-of-function genetic variation causes human lupus. *Nature* 605, 349–356. doi:10.1038/s41586-022-04642-z
- Cao, Z., Liu, B., Li, L., Lu, P., Yan, L., and Lu, C. (2022). Detoxification strategies of triptolide based on drug combinations and targeted delivery methods. *Toxicology* 469, 153134. doi:10.1016/j.tox.2022.153134
- Chan, E. K., Ceribelli, A., and Satoh, M. (2013). MicroRNA-146a in autoimmunity and innate immune responses. *Ann. Rheum. Dis.* 72 (2), i90–95. doi:10.1136/annrheumdis-2012-202203
- Chen, C. Z., Schaffert, S., Fragos, R., and Loh, C. (2013). Regulation of immune responses and tolerance: The microRNA perspective. *Immunol. Rev.* 253 (1), 112–128. doi:10.1111/imr.12060
- Cheng, Y., Zhao, Y., and Zheng, Y. (2021). Therapeutic potential of triptolide in autoimmune diseases and strategies to reduce its toxicity. *Chin. Med.* 16 (1), 114. doi:10.1186/s13020-021-00525-z
- Christensen, S. R., Shupe, J., Nickerson, K., Kashgarian, M., Flavell, R. A., and Shlomchik, M. J. (2006). Toll-like receptor 7 and TLR9 dictate autoantibody specificity and have opposing inflammatory and regulatory roles in a murine model of lupus. *Immunity* 25 (3), 417–428. doi:10.1016/j.immuni.2006.07.013
- Dai, R., and Ahmed, S. A. (2011). MicroRNA, a new paradigm for understanding immunoregulation, inflammation, and autoimmune diseases. *Transl. Res.* 157 (4), 163–179. doi:10.1016/j.trsl.2011.01.007
- Diebold, S. S., Kaisho, T., Hemmi, H., Akira, S., and Reis e Sousa, C. (2004). Innate antiviral responses by means of TLR7-mediated recognition of single-stranded RNA. *Science* 303 (5663), 1529–1531. doi:10.1126/science.1093616
- Fillatreau, S., Manfroi, B., and Dörner, T. (2021). Toll-like receptor signalling in B cells during systemic lupus erythematosus. *Nat. Rev. Rheumatol.* 17 (2), 98–108. doi:10.1038/s41584-020-00544-4
- Fu, H. X., Fan, X. P., Li, M., Liu, M. J., and Sun, Q. L. (2019). MiR-146a relieves kidney injury in mice with systemic lupus erythematosus through regulating NF- $\kappa$ B pathway. *Eur. Rev. Med. Pharmacol. Sci.* 23 (16), 7024–7032. doi:10.26355/eurrev\_201908\_18744
- Hou, G., Harley, I. T. W., Lu, X., Zhou, T., Xu, N., Yao, C., et al. (2021). SLE non-coding genetic risk variant determines the epigenetic dysfunction of an immune cell specific enhancer that controls disease-critical microRNA expression. *Nat. Commun.* 12 (1), 135. doi:10.1038/s41467-020-20460-1
- Huang, S., Chen, L. M., Zhu, Z. Y., Lin, L., Fan, Y. S., and Bao, J. (2022). Effects of triptolide on DNA methylation of CD4<sup>+</sup>T cells in MRL/lpr lupus mice. *China J. Traditional Chin. Med. Pharm.* 37 (05), 2495–2500.
- Jackson, S. W., Scharping, N. E., Kolhatkar, N. S., Khim, S., Schwartz, M. A., Li, Q. Z., et al. (2014). Opposing impact of B cell-intrinsic TLR7 and TLR9 signals on autoantibody repertoire and systemic inflammation. *J. Immunol.* 192 (10), 4525–4532. doi:10.4049/jimmunol.1400098
- Jiang, H. Y., Bao, Y. N., Lin, F. M., and Jin, Y. (2021). Triptolide regulates oxidative stress and inflammation leading to hepatotoxicity via inducing CYP2E1. *Hum. Exp. Toxicol.* 40 (12), S775–S787. doi:10.1177/09603271211056330
- Karrich, J. J., Jachimowski, L. C., Libouban, M., Iyer, A., Brandwijk, K., Taanman-Kueter, E. W., et al. (2013). MicroRNA-146a regulates survival and maturation of human plasmacytoid dendritic cells. *Blood* 122 (17), 3001–3009. doi:10.1182/blood-2012-12-475087
- Law, S. K., Simmons, M. P., Techen, N., Khan, I. A., He, M. F., Shaw, P. C., et al. (2011). Molecular analyses of the Chinese herb Leigongteng (Tripterygium wilfordii Hook.f.). *Phytochemistry* 72 (1), 21–26. doi:10.1016/j.phytochem.2010.10.015
- Liou, S. N., and Melissaropoulos, K. (2014). Molecular abnormalities of the B cell in systemic lupus erythematosus are candidates for functional inhibition treatments. *Expert Opin. Pharmacother.* 15 (6), 833–840. doi:10.1517/14656566.2014.894976
- Liu, G., Wang, L., Tuexunyming, M., Xu, J., Wu, Z., Wang, W., et al. (2022). Triptolide ameliorates osteoarthritis by regulating nuclear factor kappa B-mediated inflammatory response. *J. Pharm. Pharmacol.* 74, 360–366. doi:10.1093/jpp/rgab182
- Malkiel, S., Barlev, A. N., Atisha-Fregoso, Y., Suurmond, J., and Diamond, B. (2018). Plasma cell differentiation pathways in systemic lupus erythematosus. *Front. Immunol.* 9, 427. doi:10.3389/fimmu.2018.00427
- Meininger, J., Jäck, H. M., and Pracht, K. (2018). miRNA meets plasma cells "How tiny RNAs control antibody responses. *Clin. Immunol.* 186, 3–8. doi:10.1016/j.clim.2017.07.015
- O'Connell, R. M., Rao, D. S., Chaudhuri, A. A., and Baltimore, D. (2010). Physiological and pathological roles for microRNAs in the immune system. *Nat. Rev. Immunol.* 10 (2), 111–122. doi:10.1038/nri2708
- Qiu, D., and Kao, P. N. (2003). Immunosuppressive and anti-inflammatory mechanisms of triptolide, the principal active diterpenoid from the Chinese medicinal herb *Tripterygium wilfordii* Hook. f. *Drugs R. D.* 4 (1), 1–18. doi:10.2165/00126839-200304010-00001
- Rubtsov, A. V., Rubtsova, K., Fischer, A., Meehan, R. T., Gillis, J. Z., Kappler, J. W., et al. (2011). Toll-like receptor 7 (TLR7)-driven accumulation of a novel CD11c<sup>+</sup> B-cell population is important for the development of autoimmunity. *Blood* 118 (5), 1305–1315. doi:10.1182/blood-2011-01-331462
- Satterthwaite, A. B. (2021). TLR7 signaling in lupus B cells: New insights into synergizing factors and downstream signals. *Curr. Rheumatol. Rep.* 23 (11), 80. doi:10.1007/s11926-021-01047-1
- Singh, N., Kumar, B., Aluri, V., and Lenert, P. (2016). Interfering with baffled B cells at the lupus tollway: Promises, successes, and failed expectations. *J. Allergy Clin. Immunol.* 137 (5), 1325–1333. doi:10.1016/j.jaci.2015.12.1326
- Song, C. Y., Xu, Y. G., and Lu, Y. Q. (2020). Use of Tripterygium wilfordii Hook F for immune-mediated inflammatory diseases: Progress and future prospects. *J. Zhejiang Univ. Sci. B* 21 (4), 280–290. doi:10.1631/jzus.B1900607
- Souyris, M., Cenac, C., Azar, P., Daviaud, D., Canivet, A., Grunenwald, S., et al. (2018). TLR7 escapes X chromosome inactivation in immune cells. *Sci. Immunol.* 3 (19), eaap8855. doi:10.1126/sciimmunol.aap8855
- Suthers, A. N., and Sarantopoulos, S. (2017). TLR7/TLR9- and B Cell receptor-signaling crosstalk: Promotion of potentially dangerous B cells. *Front. Immunol.* 8, 775. doi:10.3389/fimmu.2017.00775
- Taganov, K. D., Boldin, M. P., Chang, K. J., and Baltimore, D. (2006). NF- $\kappa$ B-dependent induction of microRNA miR-146, an inhibitor targeted to signaling proteins of innate immune responses. *Proc. Natl. Acad. Sci. U. S. A.* 103 (33), 12481–12486. doi:10.1073/pnas.0605298103
- Tang, Y., Luo, X., Cui, H., Ni, X., Yuan, M., Guo, Y., et al. (2009). MicroRNA-146A contributes to abnormal activation of the type I interferon pathway in human lupus by targeting the key signaling proteins. *Arthritis Rheum.* 60 (4), 1065–1075. doi:10.1002/art.24436
- Tao, X., and Lipsky, P. E. (2000). The Chinese anti-inflammatory and immunosuppressive herbal remedy Tripterygium wilfordii Hook F. *Rheum. Dis. Clin. North Am.* 26 (1), 29–50. viii. doi:10.1016/s0889-857x(05)70118-6
- Walsh, E. R., Pisitkun, P., Voynova, E., Deane, J. A., Scott, B. L., Caspi, R. R., et al. (2012). Dual signaling by innate and adaptive immune receptors is required for TLR7-induced B-cell-mediated autoimmunity. *Proc. Natl. Acad. Sci. U. S. A.* 109 (40), 16276–16281. doi:10.1073/pnas.1209372109
- Wang, L., Zhang, L., Hou, Q., Zhu, X., Chen, Z., and Liu, Z. (2018). Triptolide attenuates proteinuria and podocyte apoptosis via inhibition of NF- $\kappa$ B/GADD45B. *Sci. Rep.* 8 (1), 10843. doi:10.1038/s41598-018-29203-1
- Weindel, C. G., Richey, L. J., Bolland, S., Mehta, A. J., Kearney, J. F., and Huber, B. T. (2015). B cell autophagy mediates TLR7-dependent autoimmunity and inflammation. *Autophagy* 11 (7), 1010–1024. doi:10.1080/15548627.2015.1052206
- Yao, M., Zhang, C., Gao, C., Wang, Q., Dai, M., Yue, R., et al. (2021). Exploration of the shared gene signatures and molecular mechanisms between systemic lupus erythematosus and pulmonary arterial hypertension: Evidence from transcriptome data. *Front. Immunol.* 12, 658341. doi:10.3389/fimmu.2021.658341
- Yap, D. Y. H., and Chan, T. M. (2019). B cell abnormalities in systemic lupus erythematosus and lupus nephritis-role in pathogenesis and effect of immunosuppressive treatments. *Int. J. Mol. Sci.* 20 (24), E6231. doi:10.3390/ijms20246231
- Yu, G., Wang, L. G., Han, Y., and He, Q. Y. (2012). clusterProfiler: an R package for comparing biological themes among gene clusters. *Omic* 16 (5), 284–287. doi:10.1089/omi.2011.0118
- Zhao, D., Li, S., Liao, T., Wei, Y., Liu, M., Han, F., et al. (2018). Triptolide inhibits donor-specific antibody production and attenuates mixed antibody-mediated renal allograft injury. *Am. J. Transpl.* 18 (5), 1083–1095. doi:10.1111/ajt.14602
- Zhao, X., Tang, X., Yan, Q., Song, H., Li, Z., Wang, D., et al. (2019). Triptolide ameliorates lupus via the induction of miR-125a-5p mediating Treg upregulation. *Int. Immunopharmacol.* 71, 14–21. doi:10.1016/j.intimp.2019.02.047
- Zhou, C., Zhao, L., Wang, K., Qi, Q., Wang, M., Yang, L., et al. (2019). MicroRNA-146a inhibits NF- $\kappa$ B activation and pro-inflammatory cytokine production by regulating IRAK1 expression in THP-1 cells. *Exp. Ther. Med.* 18 (4), 3078–3084. doi:10.3892/etm.2019.7881
- Ziaei, S., and Halaby, R. (2016). Immunosuppressive, anti-inflammatory and anti-cancer properties of triptolide: A mini review. *Avicenna J. Phytomed.* 6 (2), 149–164.





## OPEN ACCESS

## EDITED BY

Yibin Feng,  
The University of Hong Kong, Hong  
Kong SAR, China

## REVIEWED BY

Ke-Wu Zeng,  
Health Science Centre, Peking  
University, China  
Wuping Sun,  
Affiliated Nanshan Hospital of Shenzhen  
University Health Science Center, China

## \*CORRESPONDENCE

Hong Nie,  
hongnie1970@163.com

## SPECIALTY SECTION

This article was submitted to  
Ethnopharmacology,  
a section of the journal  
Frontiers in Pharmacology

RECEIVED 17 May 2022

ACCEPTED 01 August 2022

PUBLISHED 23 September 2022

## CITATION

Luo Z, Zhao T, Yi M, Wang T, Zhang Z,  
Li W, Lin N, Liang S, Verkhatsky A and  
Nie H (2022), The exploration of the  
potential mechanism of oxymatrine-  
mediated antipruritic effect based on  
network pharmacology and weighted  
gene co-expression network analysis.  
*Front. Pharmacol.* 13:946602.  
doi: 10.3389/fphar.2022.946602

## COPYRIGHT

© 2022 Luo, Zhao, Yi, Wang, Zhang, Li,  
Lin, Liang, Verkhatsky and Nie. This is an  
open-access article distributed under  
the terms of the [Creative Commons  
Attribution License \(CC BY\)](https://creativecommons.org/licenses/by/4.0/). The use,  
distribution or reproduction in other  
forums is permitted, provided the  
original author(s) and the copyright  
owner(s) are credited and that the  
original publication in this journal is  
cited, in accordance with accepted  
academic practice. No use, distribution  
or reproduction is permitted which does  
not comply with these terms.

# The exploration of the potential mechanism of oxymatrine-mediated antipruritic effect based on network pharmacology and weighted gene co-expression network analysis

Zhenhui Luo<sup>1,2</sup>, Tingting Zhao<sup>1,2</sup>, Mengqin Yi<sup>1,2</sup>,  
Tingting Wang<sup>1,2</sup>, Zhenglang Zhang<sup>1,2</sup>, Wenbin Li<sup>2</sup>, Na Lin<sup>3</sup>,  
Shangdong Liang<sup>4</sup>, Alexei Verkhatsky<sup>5</sup> and Hong Nie<sup>1,2\*</sup>

<sup>1</sup>Guangdong Province Key Laboratory of Pharmacodynamic Constituents of TCM and New Drugs Research, College of Pharmacy, Jinan University, Guangzhou, China, <sup>2</sup>International Cooperative Laboratory of Traditional Chinese Medicine Modernization and Innovative Drug Development of Chinese Ministry of Education (MOE), College of Pharmacy, Jinan University, Guangzhou, China, <sup>3</sup>Institute of Chinese Materia Medica, China Academy of Chinese Medical Sciences, Beijing, China, <sup>4</sup>Neuropharmacology Laboratory of Physiology Department, Basic Medical School, Nanchang University, Nanchang, China, <sup>5</sup>Faculty of Biology, Medicine and Health, the University of Manchester, Manchester, United Kingdom

The treatment of chronic itch is considered to be a challenge for its non-histamine dependence and the search for alternative medicine is still striving. The pathology of the chronic itch is closely related to immune system regulation and inflammatory response. Oxymatrine (OMT) is a traditional Chinese medicine ingredient extracted from the roots of *Sophora flavescens* Aiton with significant antitumor, analgesic, and anti-inflammatory effects. However, the underlying mechanism of OMT on chronic itch is obscure, which limits clinical application. Hence, this study is aimed to clarify the pruritus alleviation mechanism of OMT by combining network pharmacology analysis, weighted gene co-expression analysis (WGCNA), and molecular docking. We screened 125 common targets of OMT regulating inflammation and pruritus with pharmacology technology, the GO enrichment function analysis and KEGG signaling pathway analysis to demonstrate the close relation to the signaling pathways regulating inflammation such as MAPK signaling pathway and PI3K-AKT signaling pathway. We adopted the most relevant templates for pruritus diseases, combined with network pharmacology to preliminarily screen out 3 OMT functions and regulatory targets, exerting a good connection and correlation with the target at the screened disease targets. Further experiments were conducted to explore the potential mechanism of OMT using the LPS-induced RAW264.7 cell inflammation model. The results showed that pretreatment with different concentrations of OMT (25  $\mu$ M, 50  $\mu$ M, and 100  $\mu$ M) for 24 h, inhibited expression of IL-6, iNOS, TLR4 and TGFR-1 as well as apoptosis of

Raw264.7 cells induced by LPS. Moreover, OMT effectively inhibited LPS-induced MAPK pathway activation and the expression of related sites MAP2K1, MAPK8, MAP2K4, and MAPKAP-K2 in RAW 264.7 cells. The OMT also reduced the phosphorylation of p-38, associated with site in the activation of MAPK signaling pathway. These results could contribute to a better understanding of the mechanisms underlying how OMT alleviates inflammation to treat chronic pruritic diseases and provide a potential drug for the treatment of chronic itch.

#### KEYWORDS

oxymatrine, itching, inflammation, WGCNA, network pharmacology

## Introduction

Itching is a typical side effect of skin conditions, which was initially defined as a feeling that may inspire the desire to scratch by Samuel Hafenreffer in 1660 (Bernhard, 2005). Chronic itching has no effective treatment, which significantly influences patients' quality of life and physical and mental health (Pereira and Stander, 2019). About 280 million individuals worldwide (4% of global population) suffer from pruritus, with those suffering from severe pruritus accounting for 1% of the overall population (Matterne et al., 2013; Nutten, 2015). Many chronic diseases, including most skin diseases (allergic contact dermatitis, psoriasis, etc.), neurological diseases (multiple sclerosis, herpes zoster, etc.), cancers, and mental problems, are associated with long-term skin itching (Kiebert et al., 2002; Rishe et al., 2008; Reich et al., 2016).

Antihistamines, hormone medications, anticonvulsants, antidepressants, immunosuppressants, and other systemic therapy agents are commonly used to treat intractable pruritus in more severe cases. However, the majority of these medications have substantial side effects, such as sleepiness, gastrointestinal reactions, raised or lowered blood pressure, upper respiratory tract infection, mental problems, and so on (Stander et al., 2007). Patients taking these medications for a long period have been suffering from these side effects for years. As a result, society must understand the cause of intractable pruritus and create specific antipruritic medications that are safe, effective, and non-toxic.

*Sophora flavescens* (SF) is a typical traditional Chinese medicine (TCM) widely used in China to relieve itch through oral administration in tablet, capsule and decoction, or topical application (He et al., 2015). Previous pharmacological studies found that SF contains various components, mainly alkaloids, flavonoids, and polysaccharides, exerting various biological activities including antibacterial, anti-inflammatory, and immunomodulatory (Li et al., 2020; You et al., 2020). In addition, some vital compounds of SF, such as oxymatrine (OMT), have been reported to have antipruritic activity (Xiang et al., 2020). However, the potential mechanism of

action by which bioactive compounds in SF can treat histamine-independent pruritus has not been fully elucidated.

OMT, a weakly basic quinolizidine alkaloid produced from the roots of *Sophora flavescens* Aiton [Fabaceae], is a white or off-white crystalline powder with a bitter taste that is soluble in water, methanol, ethanol, chloroform, and benzene. It has the chemical formula  $C_{15}H_{24}N_2O_2$ , with a molecular weight of 264.36, and a molecular structure that is depicted in Figure 2. OMT possesses a range of biological effects, including antipruritic (Xu et al., 2018; Zhu et al., 2020), antiviral (Jiang et al., 2017), anticancer (Halim et al., 2019), and antifibrosis (Liu et al., 2020). In addition, OMT can improve ischemia-reperfusion injury and has cardioprotective, hypoglycemic, hypolipidemic and sedative, analgesic, anti-epileptic, and other central nervous system effects (Liu et al., 2012; Guo et al., 2014; Zhou et al., 2017; Wang et al., 2022). Moreover, OMT exhibits anti-pruritic and anti-inflammatory effects in ACD mice by regulating inflammatory mediators and restoring Th1/Th2 and Th17/Treg immunological balance, according to prior research (Xu et al., 2018). However, its effect on innate immune cells and on neutrophils and macrophages remain unknown, necessitating more investigation.

Therefore, this study utilized a multi-dimensional network and experimental verification to reveal the biological mechanism of OMT's antipruritic activity and to provide a scientific foundation for OMT clinical trial research and commercial development. The technical methods and experimental results for evaluating the effect and mechanism of OMT on chronic pruritus are shown in the flowchart in Figure 1.

## Materials and methods

### Network pharmacology analysis data preparation

The molecular structure file of OMT was downloaded from PubChem (<https://pubchem.ncbi.nlm.nih.gov/>) (Kim

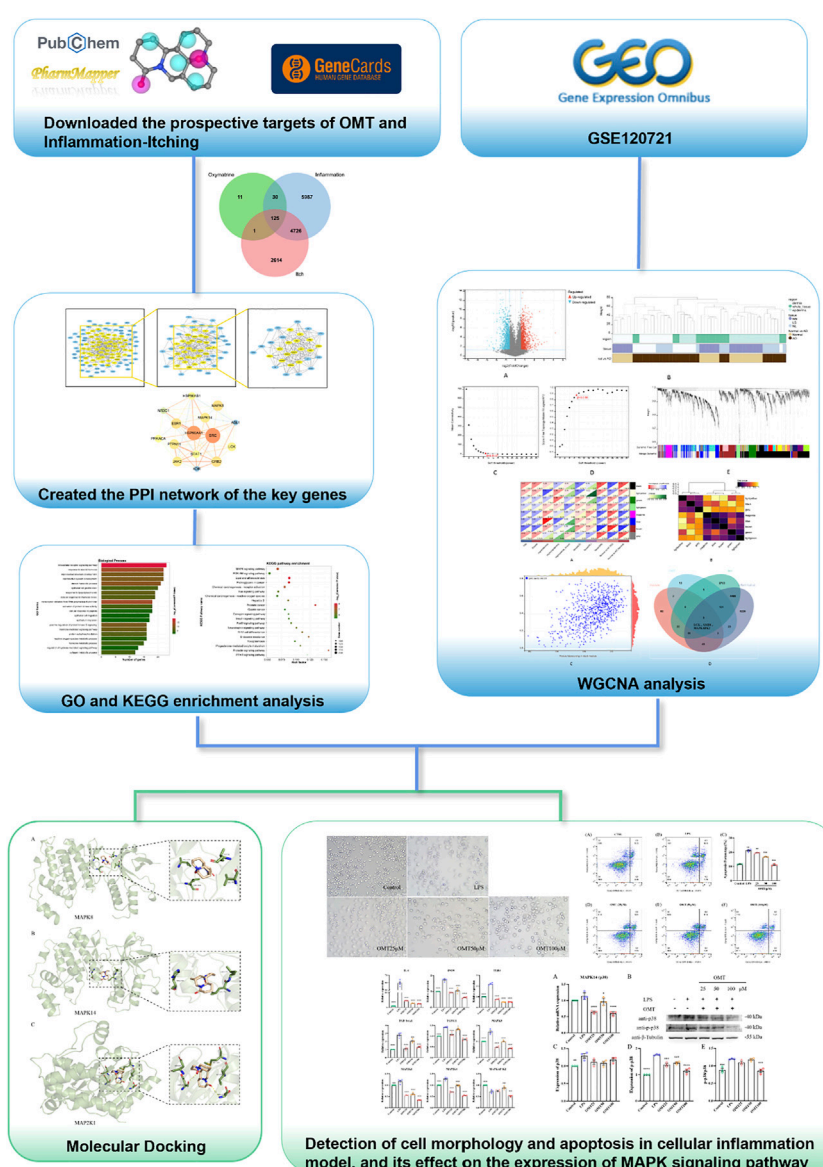


FIGURE 1

This flow chart of this study aims to investigate the potential mechanism of action of OMT in the treatment of pruritus.

et al., 2019) and uploaded to the PharmMapper (<http://www.lilab-ecust.cn/pharmmapper/>) (Liu et al., 2010) database's target prediction tool to screen for potential OMT interaction targets, and the gene name matching to the target protein was acquired using the Uniprot protein database (<https://www.uniprot.org/>) (UniProt, 2021). The reported inflammation and pruritus-related genes were searched using the keywords "inflammation," "pruritus," and "itch" in the GeneCards database (<https://www.genecards.org/>, ver.4.9.0) (Safran et al., 2010), and the Venn diagram was utilized to screen the common targets with the prospective targets of OMT.

## OMT-inflammation-itching target network construction and analysis

The reported inflammation and pruritus-related genes were searched using the keywords "inflammation," "pruritus," and "itch" in the GeneCards database, and the Venn diagram was utilized to screen the common targets with the prospective targets of OMT. The common targets were loaded into the String database, the species was confined to "*Homo sapiens*," the PPI network map was created, and the minimum needed interaction score was set to a high confidence level of 0.07, with the discrete targets concealed. The PPI network diagram was then fine-tuned

using the Cytoscape statistical tools (version 3.7.0) (Doncheva et al., 2019).

## Enrichment analysis

### GO analysis

We utilized the GO annotations of genes in the R package org for gene set functional enrichment analysis. Hs.eg.DB (version 3.1.0) as the background to mapping the genes to the background set using the R package cluster profile (version 3.14.3) to perform enrichment analysis to obtain gene set enrichment results. *p* values of 0.05 and an FDR of 0.25 were deemed statistically significant when the minimum gene set was 5 and the largest gene set was 5,000.

### KEGG analysis

We utilized the KEGG rest API (<https://www.kegg.jp/kegg/rest/keggapi.html>) to retrieve the most recent gene annotations from the KEGG Pathway as a backdrop for gene set functional enrichment analysis. To obtain the results of gene set enrichment in the background set, the enrichment analysis was performed using the R software package cluster profile (version 3.14.3). *p* values of 0.05 and an FDR of 0.25 were deemed statistically significant when the minimum gene set was 5 and the largest gene set was 5,000.

## Weighted gene co-expression network analysis of disease-related potential target genes

GSE120721 (GPL570) data were obtained from the GEO database. We deleted genes with a standard deviation of 0 in each sample, removed outlier genes and samples using the good samples genes method of the R software package WGCNA, built a scale-free co-expression network with WGCNA, and Pearson all paired genes were conducted. Correlation matrix and mean linkage method, then use the power function  $Amn = |Cmn|^\beta$  ( $Cmn$  = Pearson correlation) to construct a weighted adjacency matrix between Gene *m* and Gene *n* ( $Amn$  = the adjacency between Gene *m* and Gene *n*) (Zhang and Horvath, 2005; Langfelder and Horvath, 2008).  $\beta$  was a soft-thresholding parameter that emphasized high gene-gene correlations while penalizing weak correlations. The adjacency was turned into a topological overlap matrix (TOM), which could quantify a Gene's network connection defined as the sum of its adjacency with all other Genes for network generation, and the corresponding dissimilarity (1-TOM) was determined after choosing the power of 9. Average linkage hierarchical clustering was used to categorize Genes with comparable expression patterns into Gene modules using the TOM-based dissimilarity measure with a minimum size (Gene group) of 30 for the genes dendrogram and sensitivity set to 3. We estimated the dissimilarity of module

eigengenes, set a cut line for the module dendrogram, and merged certain modules to further investigate the modules.

## Molecular docking simulation

OMT was obtained and downloaded from PubChem and converted OMT files to PDBQT format using Open Babel 2.4.1. Then we obtained and download the target protein's crystal structure from the RCSB Protein Data Bank database (RCSB PDB, <https://www.rcsb.org/>) (Goodsell et al., 2020). The water and ligands were removed from the target protein with AutoDock Tools (Trott and Olson, 2010) and produced a new protein. It adds hydrogen atoms, calculates charge, exports the PDBQT format file, and determines the size and center of the docking box all at once. Vina was adopted to dock the active components with the target protein one by one and took the conformation with the highest docking score (Affinity). Finally, the results were analyzed with Pymol and created graphs.

## Cell culture and cell viability assay

RAW264.7 cells (Procell CL-0190, Wuhan Procell Life Technology Co., Ltd.) were grown in MEM-ALPHA culture medium (containing 10% FBS, 1% penicillin, and 1% streptomycin) at 37°C in a 5% CO<sub>2</sub> incubator. The cytotoxicity of OMT on RAW264.7 cells was measured by CellCountingKit-8 (CCK-8, Dojindo). The cells were incubated for 24 h in 96-well plates. The cells were then co-treated for 6 h with different concentrations of OMT (0, 1, 2, 4, and 8 mM) (OMT, Aladdin, concentration  $\geq 98\%$ ). 10  $\mu$ L CCK-8 was added to each well and cultured. The well's absorbance at 450 nm was monitored for another 1–4 h. The feasibility of the project was calculated. The following is how it was calculated: Cell viability =  $[(As-Ab)/(Ac-Ab)] \times 100\%$ . As: Absorbance of the experimental well (containing cells, culture medium, CCK8 solution, and drug solution), Ac: Absorbance of control wells (containing cells, culture medium, CCK8 solution), Ab: Absorbance of the blank well (containing medium, CCK8 solution).

## Quantitative real-time PCR

Total RNA was isolated from RAW264.7 cells using Trizol reagent, and the collected RNA was analyzed using a spectrophotometer for concentration and purity. RNA with an absorbance ratio of roughly 2.0 (OD260 nm/OD280 nm) was chosen for qPCR and transcribed into cDNA using RT Master Mix for qPCR II. Using a qPCR PreMix (SYBR Green) Kit, quantitative real-time PCR (qRT-PCR) was used to quantify the expression of the mRNA. Primers used in the test are shown in Table 1. The  $2^{-\Delta\Delta Ct}$  method was used to calculate the relative expressions of the relevant genes.



TABLE 1 Primer sequences for RT-qPCR.

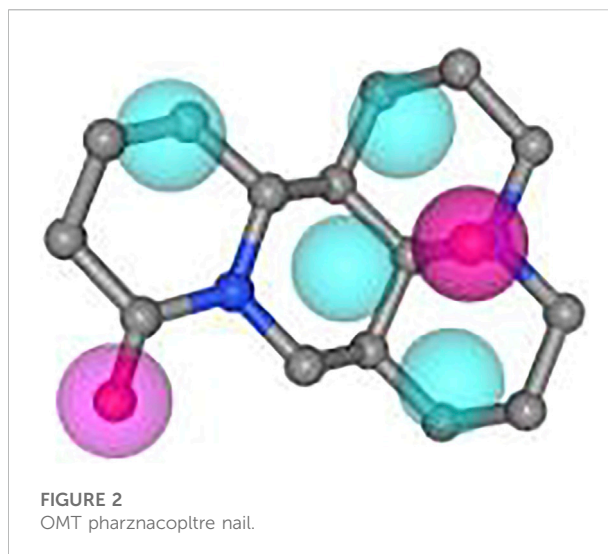
Name	Sequence (5'–3')
iNOS(Sense sequence)	CAGCTGGGCTGTACAAACCTT
iNOS (Antisense sequence)	CATTGGAAGTGAAGCGTTTCG
IL-6 (Sense sequence)	CTGCAAGAGACTTCCATCCAG
IL-6 (Antisense sequence)	AGTGGTATAGACAGGTCTGTTTCG
TLR4(Sense sequence)	GCATGGCTTACACCACCTCT
TLR4 (Antisense sequence)	GTCTCCACAGCCACCAGATT
Tgfb1 (Sense sequence)	CTCCCGTGGCTTCTAGTGC
Tgfb1 (Antisense sequence)	GCCTTAGTTTGGACAGGATCTG
Tgfb1 (Sense sequence)	TCTGCATTGCATTATGCTGA
Tgfb1 (Antisense sequence)	AAAGGGCGATCTAGTGATGGA
Mapk8(Sense sequence)	AGCAGAAGCAAACGTGACAAAC
Mapk8 (Antisense sequence)	GCTGCACACACTATTCCTTGAG
Mapkapk2(Sense sequence)	TTCCCCCAGTTCCACGTCA
Mapkapk2 (Antisense sequence)	GCAGCACCTTCCCCTTGAT
Map2k4(Sense sequence)	AATCGACAGCACGGTTTACTC
Map2k4 (Antisense sequence)	TGAAATCCCAGTGTGTTTCAGG
Map2k1(Sense sequence)	AAGGTGGGGAACGAAGGAT
Map2k1 (Antisense sequence)	CGGATTGCGGGTTTGATCTC
Mapk14(Sense sequence)	#333333
	TGACCCTTATGACCAGTCCTTT
Mapk14 (Antisense sequence)	GTCAGGCTCTTCCACTCATCTAT
GAPDH (Sense sequence)	GUAUGACAACAGCCUCAAGTT
GAPDH (Antisense sequence)	CUUGAGGCGUUGUCAUACTT

## Flow cytometry

The apoptosis of RAW264.7 cells induced by LPS induced by OMT was detected by flow cytometry. The cells in the six-well plate were pretreated with OMT and then LPS was added for co-culture for 24 h. After that, the cells in each group were harvested and subjected to two experiments. Wash with PBS, resuspended in 100  $\mu$ L 1 $\times$  Binding Buffer, add 2  $\mu$ L 0.5 mg/ml 7-AAD and 2  $\mu$ L L Annexin V-FITC solution, incubate for 15min at room temperature in the dark, add 300  $\mu$ L 1 $\times$  Binding Buffer, mix well, transfer to 96-well plate, 1 h Fluorescence detection was performed by flow cytometry. (Annexin V-FITC has a maximum excitation light of 488 nm and an emission light of 520 nm. 7-AAD has a maximum excitation light of 488 nm and an emission light of 647 nm).

## Western blot

The procession of protein extraction in this study can be referred to the article (Luo et al., 2021). 20  $\mu$ g per sample of proteins were separated by sodium dodecyl sulfate-polyacrylamide gel electrophoresis (SDS-PAGE) and deposited onto a polyvinylidene fluoride (PVDF)



membrane after the concentration of proteins was determined. The membranes were blocked with 5% milk for 2 h before incubation with the primary antibody at 4°C overnight, which is as follow, Anti-p-38 (Affinity Biosciences, OH, United States), Anti-p-p-38 (Affinity Biosciences, OH, United States),  $\beta$ -Tubulin (Affinity Biosciences, OH, United States). After response with the primary antibody, the blotted PVDF membrane was treated with horseradish peroxidase (HRP) conjugated secondary antibody (Boster Biological Technology Co. Ltd.). The ECL chemiluminescence western blot detection technique was performed with a gel imaging system and the band intensity were analyzed *via* ImageJ.

## Statistical analysis

All data are presented as mean  $\pm$  SEM of independent experiments. Statistical evaluation of the results was performed by one-way ANOVA and a *p*-value of 0.05 or less was considered statistically significant, GraphPad Prism 7 software was used for graphical analysis and visualization.

## Results

### Prediction of potential targets of OMT pharmacophore

OMT has a total of six pharmacophores, the structure of which is depicted in Figure 2. The molecule was uploaded to the PharmMapper database for target prediction and was combined with the Uniprot database to obtain the corresponding gene name of the target protein. Table 2 presents the probable

TABLE 2 Potential mutual targets of OMT.

Serial number	Pharma model	Num feature	Fit	Norm fit	Uniprot	Gene symbol
1	1reu_v	3	2.894	0.9646	BMP2_HUMAN	BMP2
2	1w8l_v	3	2.804	0.9347	P62937	PPIA
3	1p49_v	3	2.794	0.9315	STS_HUMAN	STS
4	1e7a_v	3	2.772	0.9239	ALBU_HUMAN	ALB
5	2o65_v	3	2.765	0.9218	PIM1_HUMAN	PIM1
6	1j96_v	3	2.762	0.9207	AK1C2_HUMAN	AKR1C2
7	1rs0_v	3	2.685	0.8951	CFAB_HUMAN	CFB
8	3gam_v	3	2.662	0.8874	P16083	NQO2
9	1pmv_v	3	2.62	0.8734	MK10_HUMAN	MAPK10
10	1uki_v	3	2.582	0.8607	MK08_HUMAN	MAPK8
11	1l6l_v	3	2.4	0.7999	APOA2_HUMAN	APOA2
12	1if4_v	3	2.277	0.7591	CAH2_HUMAN	CA2
13	2ao6_v	4	2.96	0.74	ANDR_HUMAN	AR
14	1bm6_v	3	2.202	0.7341	MMP3_HUMAN	MMP3
15	1shj_v	3	2.201	0.7337	CASP7_HUMAN	CASP7
16	2ipw_v	4	2.927	0.7319	ALDR_HUMAN	AKR1B1
17	2fky_v	4	2.913	0.7283	KIF11_HUMAN	KIF11
18	2zas_v	4	2.912	0.7279	P62508	ESRRG
19	2of0_v	4	2.891	0.7228	BACE1_HUMAN	BACE1
20	1mx1_v	4	2.865	0.7162	EST1_HUMAN	CES1

interaction targets with a score greater than 0.7, out of a total of 167 potential interaction targets found according to the pharmacophore.

### Collection of targets related to inflammatory and pruritic diseases

To understand the link between inflammation and itching, here we collected 10,868 “inflammation” related targets and found 7,466 reported pruritus-related genes inputting the keywords “pruritus” and “itch” and were used to screen OMT Co-acting targets of prospective targets through Venn diagrams as shown in Figure 3A. The estimated 156 OMT targets all lie within the targets of inflammation and pruritus, with 125 targets working together by the three, 30 of which were operating on OMT and inflammation alone. The target acting on OMT and pruritus alone is just one.

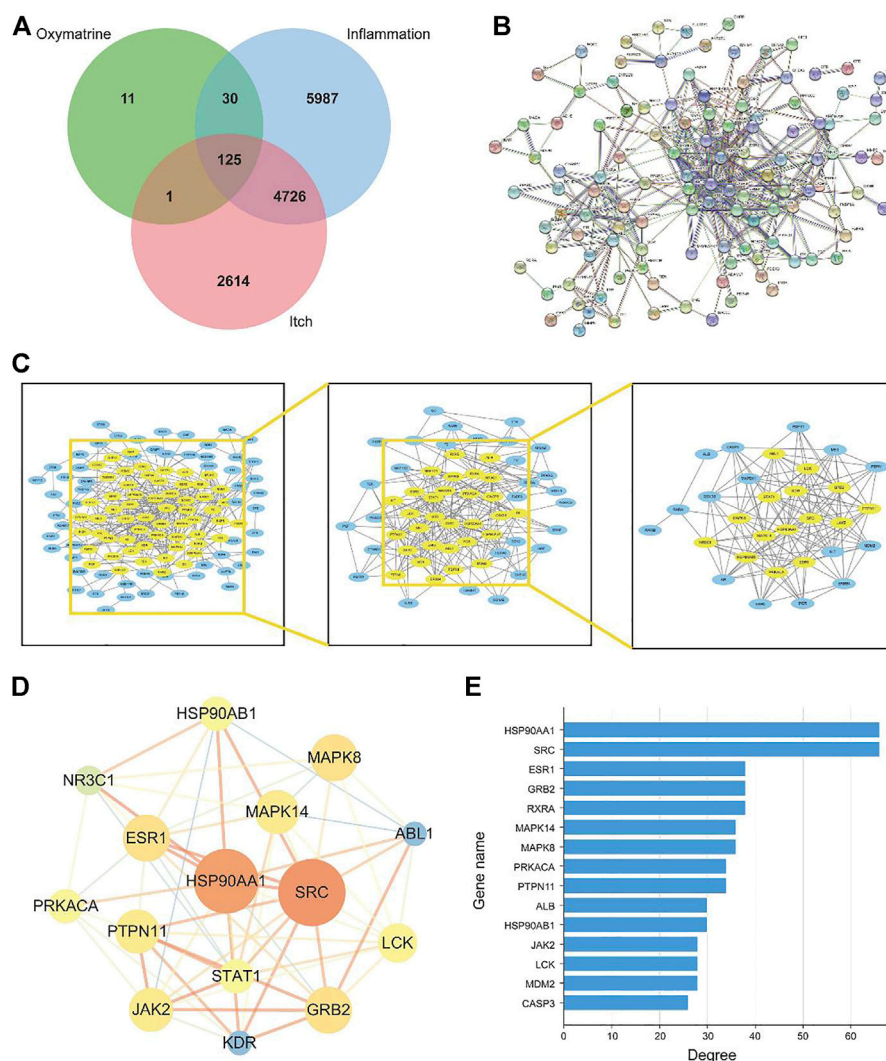
### OMT-inflammation-itching target network construction and analysis

The 125 target genes in Figure 3A implicated in OMT, inflammation, and itch was built into a PPI network diagram using the String database, as illustrated in Figure 3B. The network had 125 nodes, 385 edges, a node degree of 6.21 on average, and a

local clustering coefficient of 0.462 on average. The PPI results revealed a complex network of anti-inflammatory and antipruritic actions of OMT. The network diagram of the “OMT-inflammation-pruritus” target was constructed and shown by Cytoscape 3.7.1 software to describe the complicated network interaction of OMT anti-inflammatory and antipruritic more simply and intuitively, as shown in Figure 3C. Figure 3D showed the fraction of genes in the network, with HSP90AA1, SRC, ESR1, GRB2, and RXRA as the key genes. OMT interacts with several targets, as shown in the diagram in Figure 3E, reflecting the intricate network of multi-target interactions prevalent in traditional Chinese medicine.

### The GO and KEGG enrichment analysis of potential anti-inflammatory and antipruritic targets of OMT

To reveal the action of OMT on inflammation and itching, the biological process (BP), cellular component (CC), and molecular function (MF) were analyzed. The biological processes, components, and molecular activities of common targets are the primary focus of GO enrichment analysis. A total of 125 common targets were enriched in BP, CC, and MF, and the top 20 with the highest relevance ( $p < 0.05$ ) were selected listed in Figures 4A–C. The results showed that the main BP terms were the reaction to steroid hormones, the response to

**FIGURE 3**

The construction and analysis of the intersection targets of OMT, inflammation, and itch. **(A)** Venn diagram of OMT, itch, and inflammation **(B)** Protein-protein interaction (PPI) network of targets regulated by common targets of OMT, itch, and inflammation **(C)** Target network analysis diagram **(D)** Intersection target network diagram generated using Cytoscape. **(E)** Target degree value histogram of common targets of OMT, itch, and inflammation.

peptides, and the positive regulation of the MAPK cascade the biological processes that were most abundant; The CC mainly were enriched in the cytoplasmic cavity, cyst cavity, secretory granule cavity. The main MF terms were the endopeptidase activity, steroid hormone receptor activity, nuclear receptor activity, transcription factor activity, and direct control of ligand sequence-specific DNA binding. In the KEGG pathway enrichment, MAPK signaling pathway, PI3K-AKT signaling pathway, proteoglycan in cancer, Ras signaling pathway, hepatitis B, and other pathways mostly occupied the forefront, indicating that OMT may treat itching by suppressing inflammation-related signaling pathways. Therefore, this study focused primarily on the MAPK signaling pathway in OMT's

anti-inflammatory and antipruritic properties. MAPK10, MAPK8, MAPKAP2, HSPA8, MAPK14, MET, PGF, ERBB4, PRKACA, TGFR1, TGF2, FGFR1, KDR, BRAF, MAP2K1, CASP3, GRB2, TEK, KIT, INSR are among the targets shown in Figures 4D,E.

## WGCNA analysis of potential target genes related to atopic dermatitis

To accurately reflect the characteristics of itching, the atopic dermatitis clinical dataset GSE120721 from the GEO was adopted to show the differential gene analysis, and

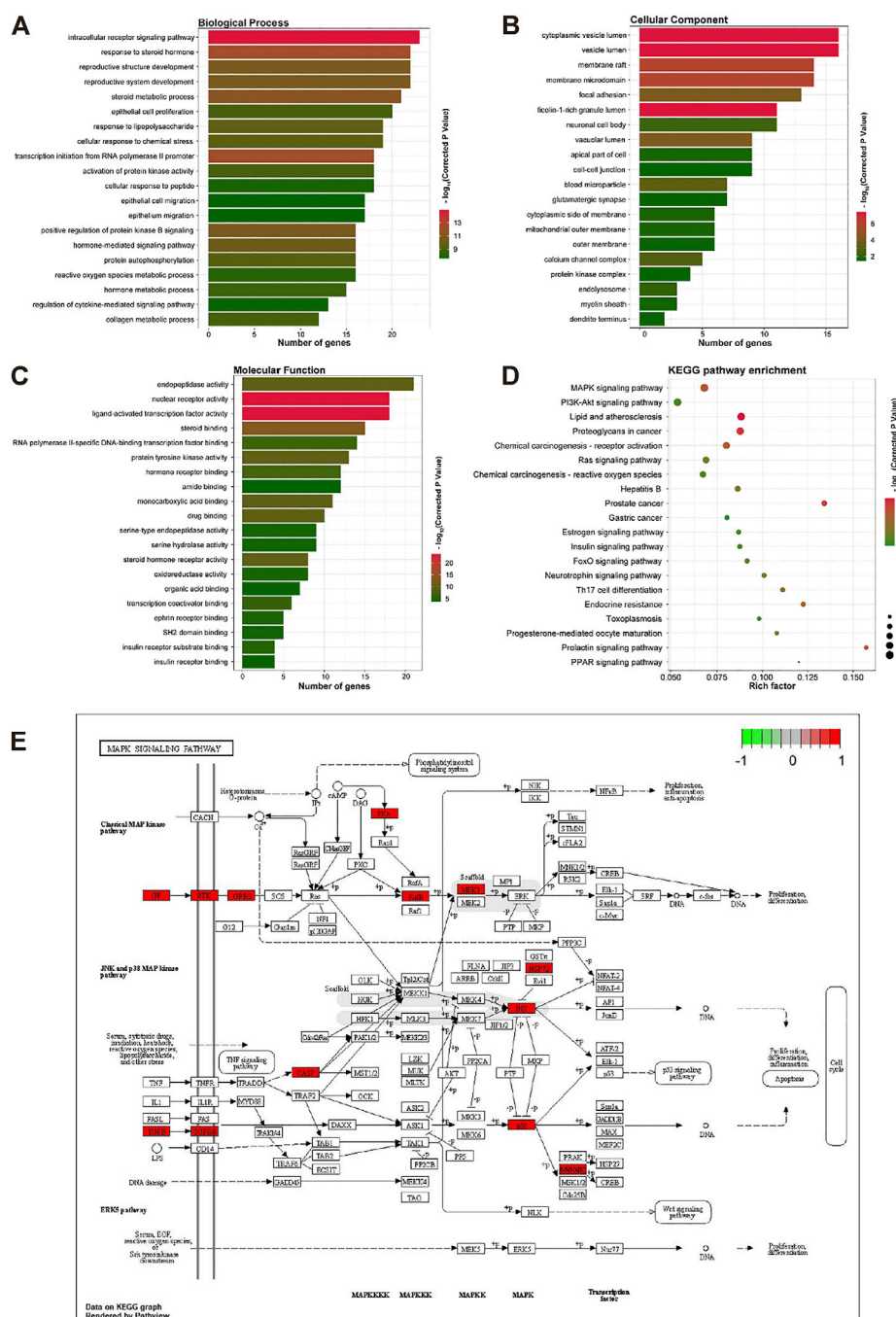


FIGURE 4

The GO and KEGG enrichment analysis of the common targets of OMT, inflammation, and itch. (A–C) GO enrichment analysis of the biological process, molecular function, and all components; X-axis for gene number and *p*-value for color. (D) KEGG enrichment analysis of the Common targets of OMT, inflammation, and itch. Y-axis for pathway, X-axis for gene number and *p*-value for color. (E) MAPK signaling pathway in the anti-inflammatory and antipruritic effect of OMT. Pathway analysis of the common targets of OMT, inflammation, and itch. The functional analysis of genes was enriched in the KEGG signaling pathway. The MAPK signaling pathways in the anti-inflammatory and antipruritic effect of OMT were highlighted in red.

2127 differential genes were obtained utilizing shown in Figure 5A. All samples were in the clusters and within the cut-off threshold value (height < 80), and three clinical

variables (disease status, tissue, and region) were adopted in the WGCNA as shown in Figure 5B. Furthermore, the soft threshold is set to 9 (Figure 5C) to make the created network



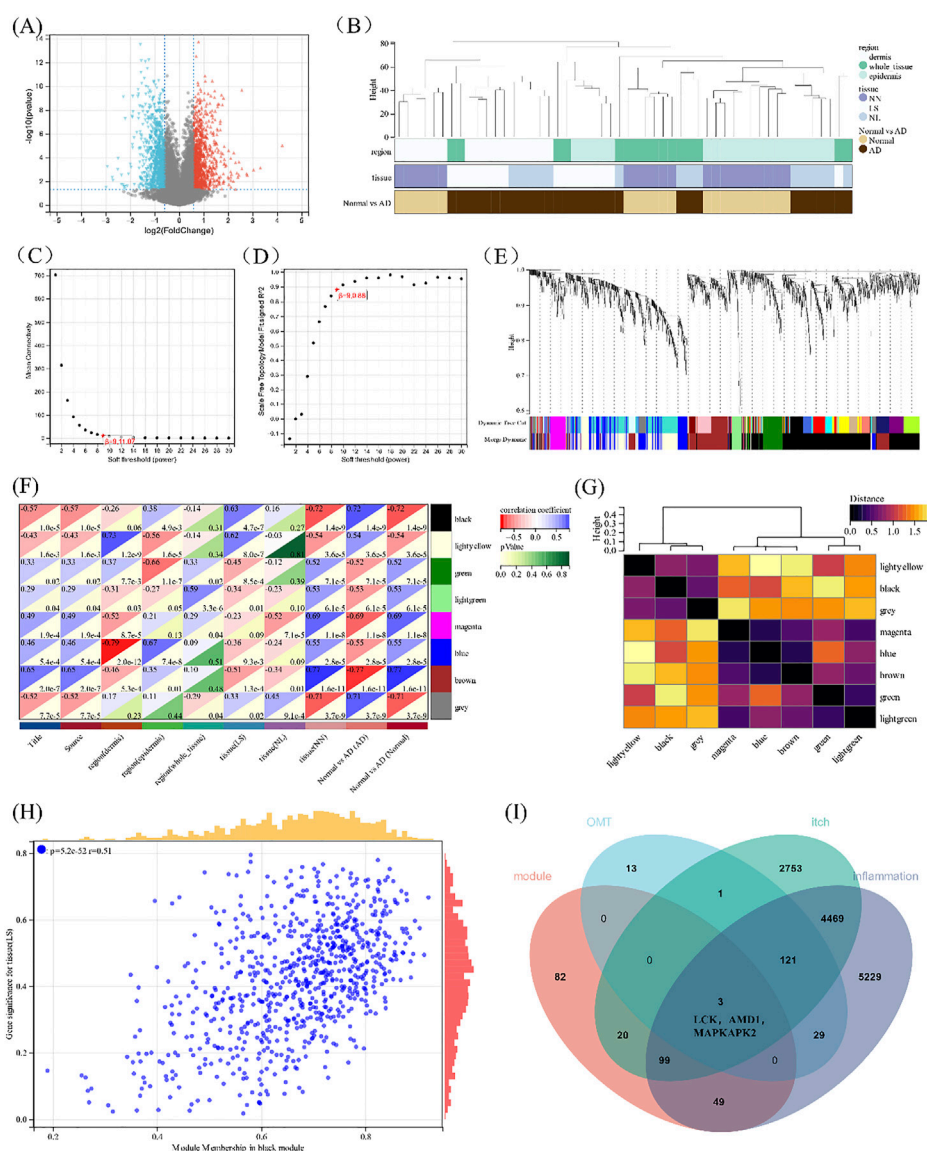


FIGURE 5

Construction of WGCNA. (A) The volcano plot of differentially expressed genes between atopic dermatitis and normal samples. (B) Clustering dendrogram of samples. (C, D) Analysis of the scale-free fitting indices for various soft-thresholding powers ( $\beta$ ) and mean connectivity analysis of various soft-thresholding powers. (E) Clustering dendrogram of genes based on the measurement of dissimilarity (1-TOM). (F) The heat map of correlation between the module eigengenes and atopic dermatitis. (G) Heat map of the module eigengenes. (H) Scatter plot of module tissue (LS) in the black module. (I) Venn diagram of the black and yellow module eigengenes, the target of OMT, itching, and inflammation.

more by the features of a scale-free network. To produce distinct gene modules, hierarchical clustering analysis was done using a weighted approach, and segmentation was performed using the specified soft threshold and the clustering findings of clinical indications (Figures 5D,E). Based on normalization with soft threshold = 9, the number of genes inside a module  $n = 30$ , and module cut, eight modules were determined. Normalization with soft threshold = 9, the number of genes inside a module  $n = 30$ , and module cut height 0.25 resulted in the identification of eight

modules. Figure 5F depicts the eight modules, as well as atopic illness, severity, and depth of skin lesions. In addition, the GS scatterplot of the disease progression in atopic dermatitis ( $p < 0.001$ ) MM in the black module was plotted in Figure 5H. The  $p$  values of the black and yellow panels are less than 0.001, indicating that they are highly correlated. Therefore, these two modules were selected for subsequent analysis.

When the 254 genes in these two modules were compared to drug-disease relevant genes, it was discovered that LCK, AMD1,

and MAPKAPK2 shared three genes in common (Figure 5I). KEGG is linked to the MAPK signaling pathway when combined with the above drug-disease targets. As a result, these three genes were chosen for further molecular docking and experimental research, for which were thought to be involved in the occurrence and progression of the disease, are related to the MAPK pathway upstream of MAPKAPK2 and may become potential targets of OMT in the treatment of pruritus.

## Molecular docking of OMT with related target proteins

Molecular docking was applied to validate the binding of OMT to 20 important target proteins which are shown in Table 3. The results showed that OMT is compatible with the structure of protein receptors, and it mostly binds to histidine, phenylalanine, leucine, tryptophan, and other amino acid residues in proteins *via* hydrogen bonds and  $\pi$ - $\pi$  bonds interactions. AR, the docking protein with the highest score, attaches to amino acids like ASN705, LEU707/873, MET742/787, and PHE764 through hydrogen bonds and  $\pi$ -bonds. MAPK8, MAPK14, and MAPK2K1, all of which are involved in the MAPK signaling pathway, had binding energies of  $-7.8$ ,  $-7.9$ , and  $-8.4$ , respectively, indicating excellent binding (Figures 6A–C). The results indicated that OMT could be bound to the active site of the above targets.

## The effect of OMT on the viability of RAW264.7 cells

The CCK-8 kit was utilized to assess the effect of OMT administration alone on the viability of RAW264.7 cells to determine the safe administration range of OMT to RAW264.7 cells. The results revealed that OMT in concentrations below 4 mM did not affect RAW264.7 cell viability, but at 8 mM, viability was reduced by around 50% as shown in Figure 7. As a result, the safe dosing range of OMT to RAW264.7 cells is thought to be 0–4 mM. The low, medium and high administration concentrations of OMT were determined to be 25, 50, and 100  $\mu$ M according to previous studies (Zhang et al., 2015).

## The effect of OMT on LPS-induced RAW264.7 cell in cell morphology

Next, LPS-induced RAW264.7 cell inflammation model was adopted to investigate the effects of OMT on inflammation. The OMT medium was discarded, washed twice with PBS, and RAW264.7 cells were grown with 1  $\mu$ g/ml LPS media for 24 h after being pre-protected with different doses of OMT for 1 h. As

shown in Figure 8 and Figure 9, the RAW264.7 cells in the control group were smaller, spherical, and prismatic, however, after 24 h of LPS 1  $\mu$ g/ml treatment, the morphology of the cells changed to a dendritic form, and the specific expression was the cell volume, after various amounts of OMT pre-protected, compared to the LPS group. The RAW264.7 cells in the control group were smaller, spherical, and prismatic, after 24 h of exposure to LPS 1  $\mu$ g/ml, the morphology of the cells changed to a dendritic form, and the specific expression was the cell volume. The cell morphology was improved to varying degrees after different doses of OMT pre-protected the cells, and the LPS-induced RAW264.7 cell morphology was suppressed. The result showed that OMT exhibits inflammatory protective effect with a certain concentration gradient of 25, 50, 100  $\mu$ M.

## The effect of OMT on LPS-induced RAW264.7 cell in apoptosis

To investigate the protective effect of OMT on LPS-induced RAW264.7 cells, flow cytometry was applied for evaluation. Figure 10 showed that the apoptosis in an LPS-induced RAW264.7 cell inflammation model, the control group had an apoptosis rate of 11.2 percent, however, the LPS group had an apoptosis rate of 20.29 percent, which was considerably greater than the control group, which is significantly different ( $p < 0.05$ ). RAW264.7 cells' apoptosis rate was decreased to varying degrees following pre-protection with different concentrations of 25, 50, and 100  $\mu$ M OMT as compared to the LPS group. The proportions were 19.73 percent, 16.91 percent, and 11.77 percent, respectively, indicating that there was a dosage dependency. These results showed that OMT exerted a protective effect on LPS-induced inflammation.

## The effect of OMT on the expression of MAPK signaling pathway in LPS-induced RAW264.7 cell

RT-qPCR was used to identify the amounts of inflammatory components to validate whether the inflammation model was effective. As shown in Figure 11, RT-qPCR analysis of expression indicated that when LPS was cultured at 1  $\mu$ g/ml for 24 h, the relative expressions of IL-6 and iNOS mRNA were dramatically raised, showing that the inflammatory model had been successfully generated. The pre-protective impact of different doses of OMT considerably prevented the rise in relative expression levels of IL-6 and iNOS mRNA induced by LPS as compared to the LPS group, indicating that OMT has a considerable anti-inflammatory effect. The relative expression of TLR4 mRNA was observed for LPS activates the TLR4 receptor. When cells were cultured with LPS 1  $\mu$ g/ml

TABLE 3 Affinities and amino acid sites of ligand-protein detected by molecular docking.

Protein	Ligand	Binding energy kcal/mol	Amino acid binding site
OMT	ABL1	-8.1	LEU248/370, TYR253, VAL256/299, LYS271
	ALB	-8.4	LEU398/529, LYS402, ALA406, VAL409, ASP549
	AR	-9.1	ASN705, LEU707/873, MET742/787, PHE764
	CASP3	-6	TRP206/214, ASN208, PHE250
	ESR1	-8.9	LEU346/384/387/391/525, ALA350, MET388, PHE404
	GRB2	-6.9	ILE85, PHE95, VAL110, TYR118, LEU120
	HSP90AA1	-7.8	MET98, LEU107, PHE138, TYR139
	HSP90AB1	-7.2	ASN51, ALA55, MET98, LEU107
	JAK2	-8.3	LEU855/983, VAL863, SER936
	LCK	-7.8	VAL259/301, ALA271/381, GLU288, MET292, THR316
	MAP2K1	-8.4	ASP190/208, SER212, ILE216, MET219
	MAPK14	-7.9	LEU74/75, HIS148
	MAPK8	-7.8	ILE32, VAL40/158, VAL158
	MDM2	-6	ILE57, MET58, TYR63, VAL71/89
	NR3C1	-8.2	GLY567, MET601/604/646, ALA605, LEU608, PHE623
	PRKACA	-7.8	LEU49/173, VAL57, ALA70, GLU127, PHE327
	PTPN11	-7.4	LYS358, GLU359, VAL360, HIS394, ASP395/431
	RXRA	-7.7	ILE268/310, ALA271/272, TRP305, LEU309/326, PHE313, CYS432
	SRC	-7.6	PHE278/307, GLU280/310, LYS295, LEU297, ILE336
	STAT1	-7.9	GLN275, GLU353, TYR1356, ASN1357

for 24 h, the relative expression of TLR4 mRNA increased. Different concentrations of OMT were used in comparison to the LPS group. The relative expression of TLR4 mRNA produced by LPS was considerably decreased after the pre-protective impact of OMT, suggesting that OMT may suppress the action of LPS on TLR4 receptors. Furthermore, the relative mRNA expression levels of MAPK signaling pathway-related genes were found to be suppressed. Except for the MAPKAPK-2 gene, the other administration groups were able to considerably reduce the abnormally high production of gene mRNA produced by LPS, including TGF-beta1, TGFR-1, MAPK8, MAP2K1, and MAP2K4, suggesting that OMT may be involved. Through the MAPK signaling pathway, it has anti-inflammatory action.

Effects of OMT on the mRNA, protein, and phosphorylation levels of p38 gene in LPS-induced RAW264.7 cell

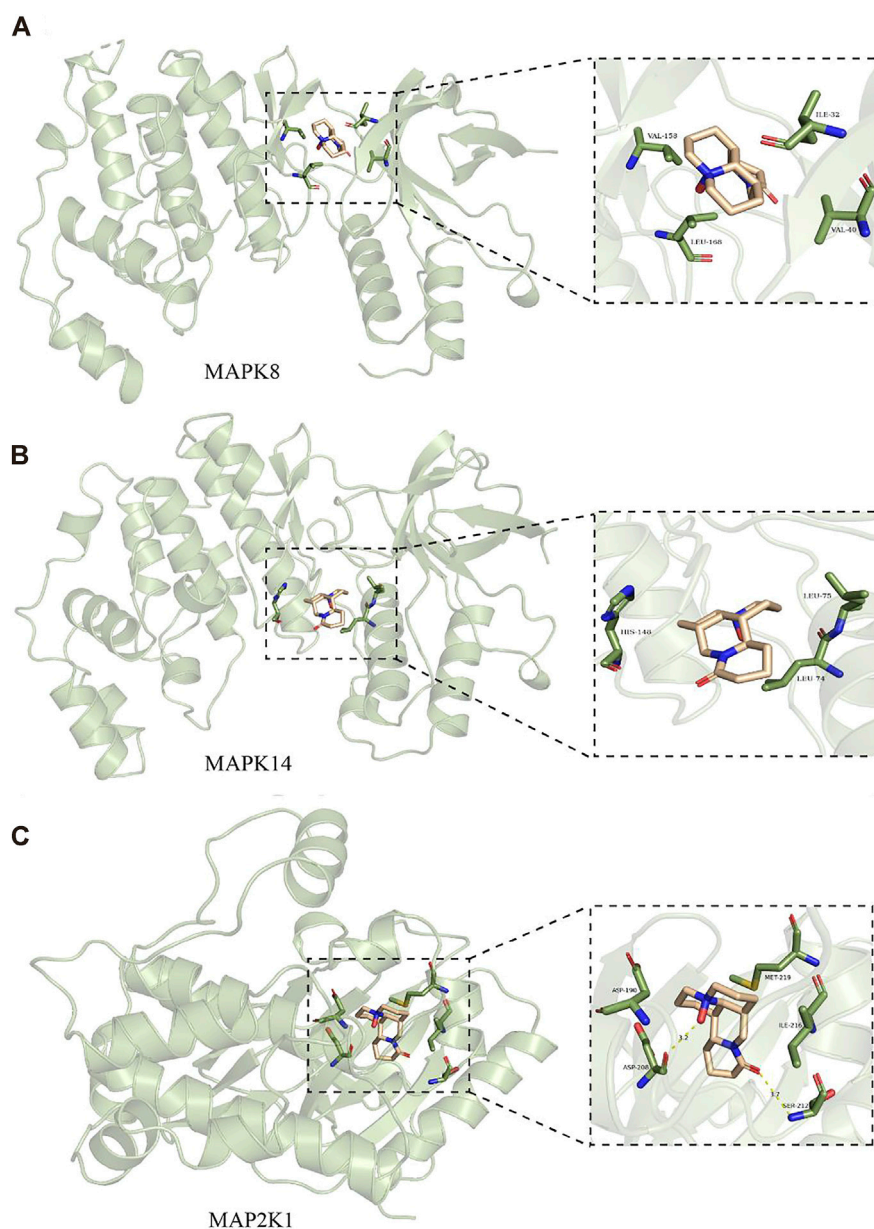
To further verify the analysis results, we conducted the following experiments. MAPK14 (p38) is a major MAPK signaling pathway target gene and in the LPS-induced RAW264.7 cell inflammation model, the effect of OMT on the mRNA, protein, and phosphorylation levels of the p38 gene was investigated. As shown in Figure 12, the RAW264.7 cells exerted no significant difference in the relative expression of p38 mRNA

when compared to LPS 1 µg/ml for 24 h, while the 25, 50, and 100 µM OMT groups significantly decreased the relative expression of p38. Subsequently, the protein levels of p38 and p-p38 were determined. The results indicated that after 24 h of LPS 1 µg/ml treatment, the protein levels of p38 and p-p38 in RAW264.7 cells were facilitated compared to the blank control group. The expression of p38 protein of the group did not differ substantially from that of the blank control and the LPS group, however, the p-p38 protein level was considerably lower than that of the LPS group and the ratio of p38/p-p38 represented the amount of phosphorylation of p38. The phosphorylation level of p38 in RAW264.7 cells was significantly increased after 24 h of exposure to 1 µg/ml LPS, whereas 100 µM OMT pre-protection significantly reduced the level of p38. These results suggested that OMT may have an anti-inflammatory effect by inhibiting p38 phosphorylation.

Discussion

Resource identification initiative

Many skin disorders such as atopic dermatitis, psoriasis, dry skin diseases, liver diseases, kidney diseases, and metabolic diseases are characterized by significant itching sensations. These disease types are mostly non-histamine-dependent

**FIGURE 6**

Molecular docking models of MAPK8, MAPK14, and MAP2K1. **(A)** are OBIT and MAPK8 docking mode and the interaction plane diagram. **(B)** are ONIT and MAPK14 docking model and the interaction plane diagram. **(C)** were OMT and MAP2K1 docking model and the interaction plane diagram.

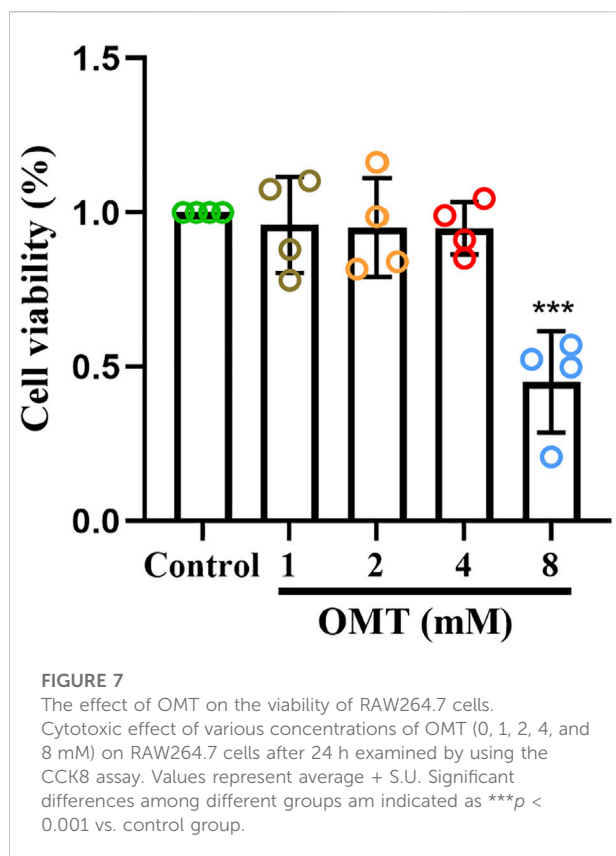
pruritus (Cevikbas and Lerner, 2020). Pruritus can be classified as histamine-dependent or histamine-independent based on the involvement of histamine in the development of the itch. It can help with the symptoms of histamine-dependent itching, but it won't help with refractory itching (Paus et al., 2006; Johaneke et al., 2007).

Macrophages of innate immune cells play an important role in the development of chronic pruritus. Which contribute to histamine-independent pruritus through chronic inflammation and are one of

the main reasons for maintaining chronic inflammation and neural sensitization. Although corticosteroids can be used for therapy, they are easy to abuse and long-term usage can result in major side effects such as skin thickening, substance metabolism issues, rebound after medication withdrawal, and even skin itching (Elmariah and Lerner, 2011).

OMT is one of the main active ingredients of *Sophora flavescens* and is commonly used for analgesia, anti-inflammatory, and anti-itching in the acute phase of the disease. According to previous

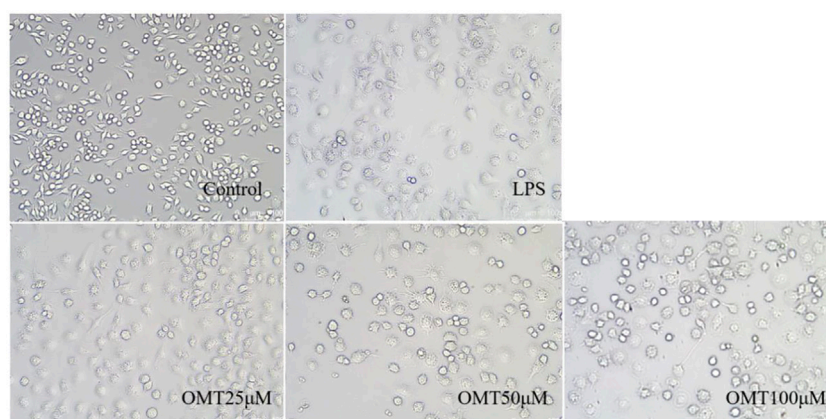




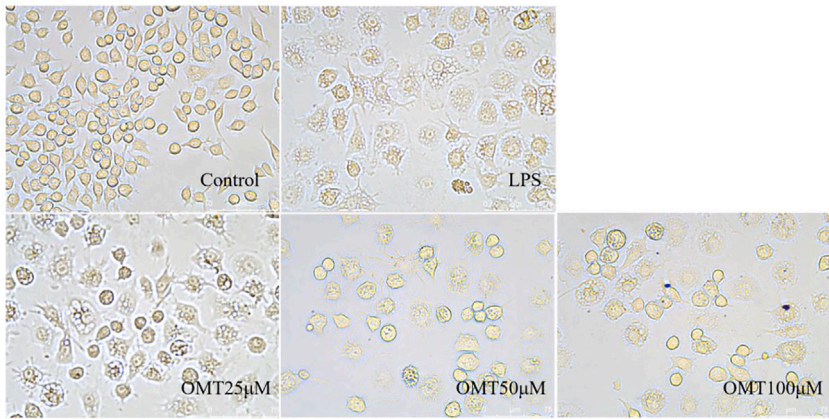
research (Xu et al., 2018), OMT exerts antipruritic and anti-inflammatory actions in ACD mice by modulating inflammatory mediators and restoring Th1/Th2 and Th17/Treg immunological balance. However, the impact on innate immune cells and the mechanism of action in neutrophils and macrophages are unclear, prompting more research.

Therefore, in our study, we analyzed the common targets of OMT by utilizing network pharmacology. The results of PPI analysis and GO analysis showed that OMT, regulates inflammatory response and related signal transduction, including MAPK signaling pathway, the PI3K-AKT signaling pathway, and others heavily represented in the KEGG pathway. To study the OMT targets with a more holistic approach, we used the GEO database to screen differentially expressed genes in Atopic dermatitis cases and conduct a WGCNA analysis. Atopic dermatitis is a chronic, inflammatory skin disease characterized by pruritus and recurrent eczematous lesions (Otsuka et al., 2017). To treat the illness, a variety of therapeutic options are available, including topical treatments, systemic medications, and biologics. Despite this, due to the chronic nature of many patients' illnesses and their repeated episodes, care can be difficult (Folster-Holst et al., 2022).

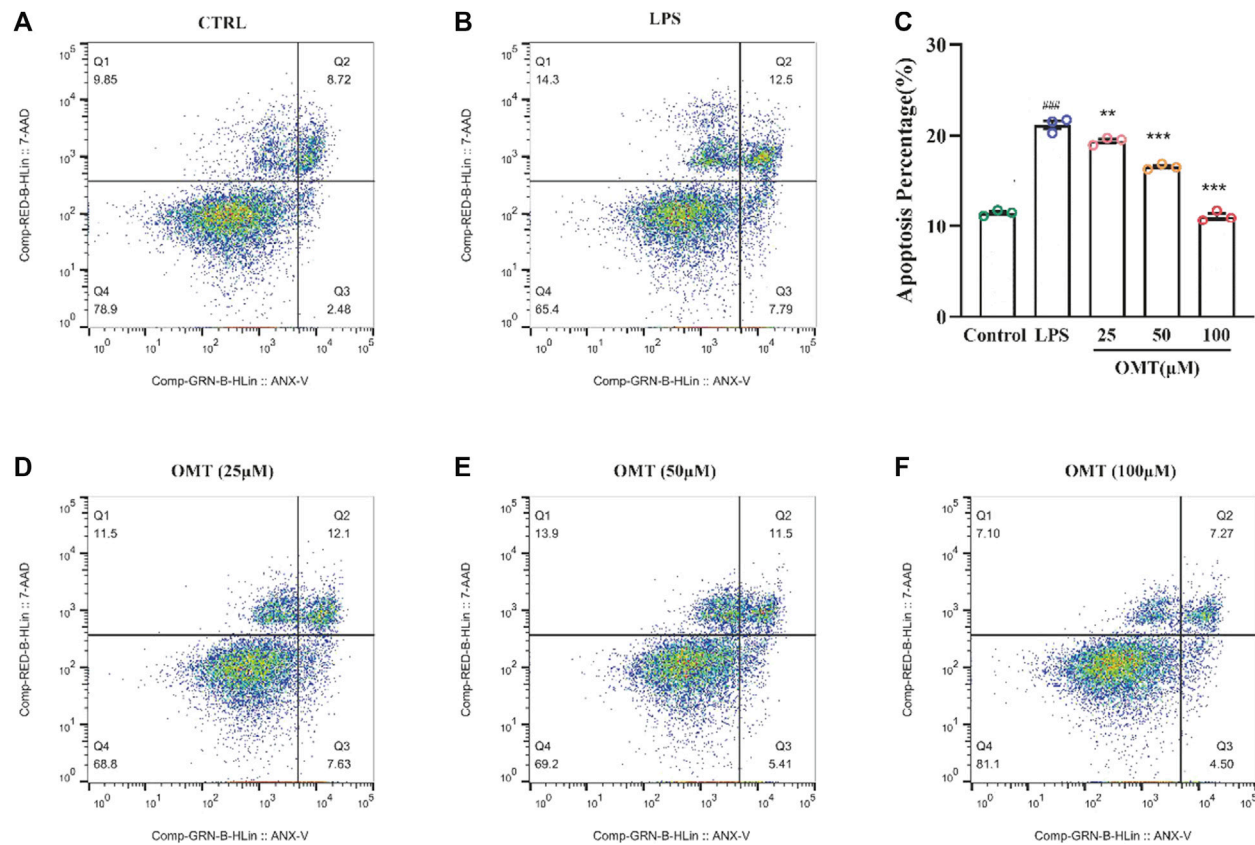
The results showed that 2127 differential genes were separated into 8 modules, and three gene groups closely connected to the occurrence and development of atopic dermatitis were mined in this study using the WGCNA approach coupled with network pharmacology to design a scale-free network. Furthermore, we further verified that the selected MAPK signaling pathway such as MAPK8, MAPK14, MAPK2K1, and MAPKAP-K2 was associated with OMT binding through molecular docking technology combined with network pharmacology analysis and WGCNA analysis. LCK, AMD1, and MAPKAPK2 might be possible oxymatrine targets in the treatment of pruritus. The results of molecular docking demonstrate that OMT is compatible with the structure of protein receptors, including MAPK8 and other MAPK signaling pathway targets. MAPK14 and MAP2K1 had binding energies of  $-7.8$ ,  $-7.9$ , and  $-8.4$ , respectively, indicating a good binding impact. These findings suggest that OMT is a multi-signaling system that inhibits inflammation,



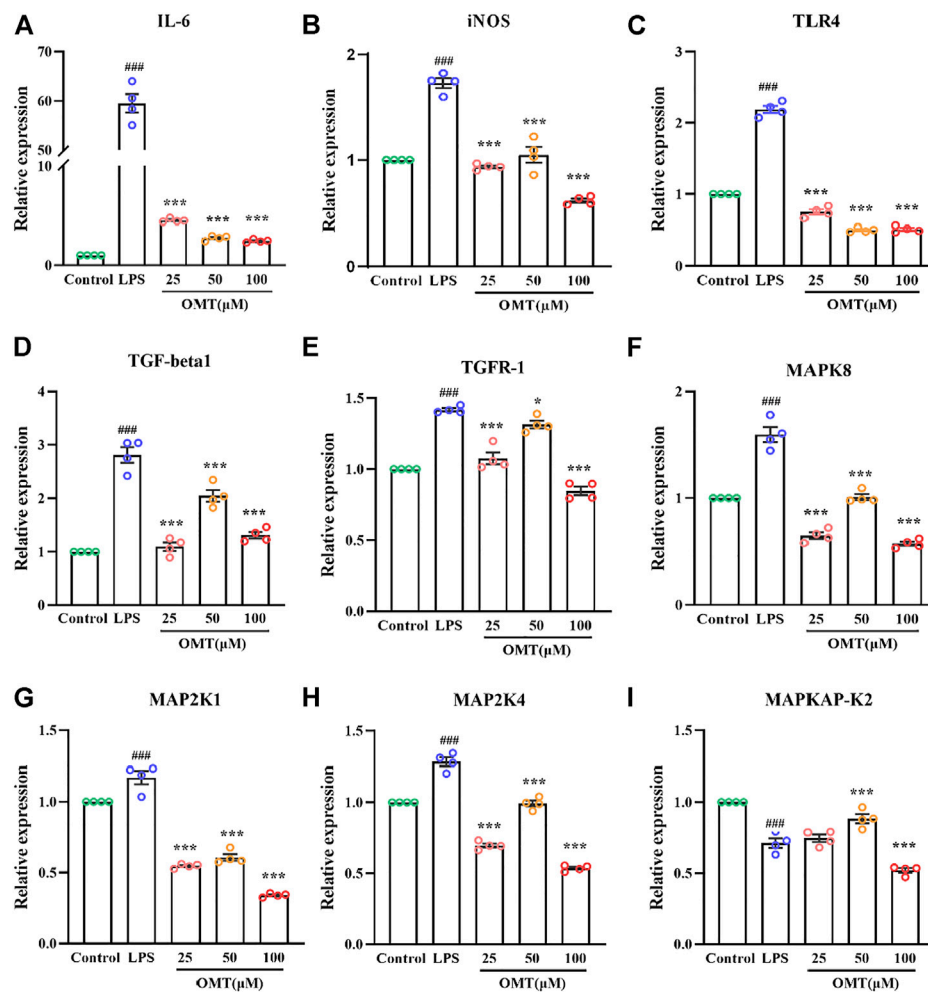
**FIGURE 8**  
The effect of OMT on the cell morphology of LPS-induced RAW264.7 cell inflammation model. Each group was visualized by an ordinary light microscope ( $\times 200$  magnification).



**FIGURE 9**  
The effect of OMT on the cell mormology of LPS-induced RAW264.7 cell inflammation model. Each group was visualized by an ordinary light microscope (x 400 magnification).



**FIGURE 10**  
Effects of OMT on the apoptosis of LPS-induced RAW264.7 cell inflammation model detected by flow cytometry and the histogram of apoptosis rate of cells. **(A)** Raw264.7 cells (control): live cells: 78.9%, necrotic: 9.85%, early apoptosis: 2.48%, late apoptosis: 8.72% **(B)** RAW264.7 cell+ LPS: live cells: 65.4%, necrotic: 14.3%, early apoptosis: 7.79%, late apoptosis: 12.5% **(C)** RAW264.7 cells + OMT (25 iM): live cells: 68.8%, necrotic: 11.5%, early apoptosis: 7.63%, late apoptosis: 12.1% **(D)** RAW264.7 cells+ OMT (50 iM): live cells: 69.2%, necrotic: 13.9%, early apoptosis: 5.41%, late apoptosis: 4.50% **(E)** RAW264.7 cells + OMT (100 iM): live cells: 81.1%, necrotic: 7.10%, early apoptosis: 4.50%, late apoptosis: 7.27%. Values represent average  $\pm$  S.D. Significant differences among different groups are indicated as ### $p < 0.001$  vs. control; \* $p < 0.05$ , \*\* $p < 0.01$ , \*\*\* $p < 0.001$ vs. LPS group.

**FIGURE 11**

Effects of OMT on the mRNA expression of LPS-induced RAW264.7 cell inflammation model. (A–E) The mRNA expression of inflammatory factors (IL-6, iNOS), and receptors (TLR4, TOF-R-1, TGF-β1). (F–I) The mRNA expression of MARK signaling pathway targets (MAPK8, MAP2K1, MAP2K4, MAPKAP-K2). Values represent average  $\pm$  S.D. Significant differences among different groups are indicated as ### $p < 0.001$  vs. control; \* $p < 0.05$ , \*\* $p < 0.01$  vs. LPS group. \*\*\* $p < 0.001$  vs. LPS group.

oxidative stress, and other processes while also acting as an antipruritic.

This suggested that OMT affected the inflammatory response of macrophages *via* regulating the MAPK signaling pathway. In the development of chronic pruritus, various factors lead to the activation of the MAPK pathway of inflammatory cells to cause pruritus and neural sensitization. How does activation of the TLR4/MAPK pathway lead to the development of chronic pruritus and neural sensitization? The MAPKs are a family of serine/threonine protein kinases that can be triggered by a variety of external stimuli (such as cytokines, neurotransmitters, etc.). MAPK kinase kinases, MAPKs kinases, and MAPKs are the fundamental components of the MAPK signaling pathway, which is largely conserved from yeast to humans. These three

kinases can all be active at the same time to control cell development, differentiation, stress response, inflammatory response, and other important biological processes. Extracellular signal-regulated protein kinase (ERK), c-Jun N-terminal kinase (JNK), p38 mitogen-activated protein kinase (p38 MAPK), and extracellular signal Regulatory Kinase 5 (ERK5) are the four main branches of the MAPK pathway (Sun et al., 2015). JNK and p38 MAPK signaling pathways, for example, have comparable activities and are involved in stress responses including inflammation and apoptosis (Yeung et al., 2018; Hammouda et al., 2020). Moreover, LPS constantly activates a crucial axis formed by reciprocal crosstalk between the p38 (MAPK) pathway and signal transducer and activator of transcription (STAT) 3-mediated signal transduction. The production and

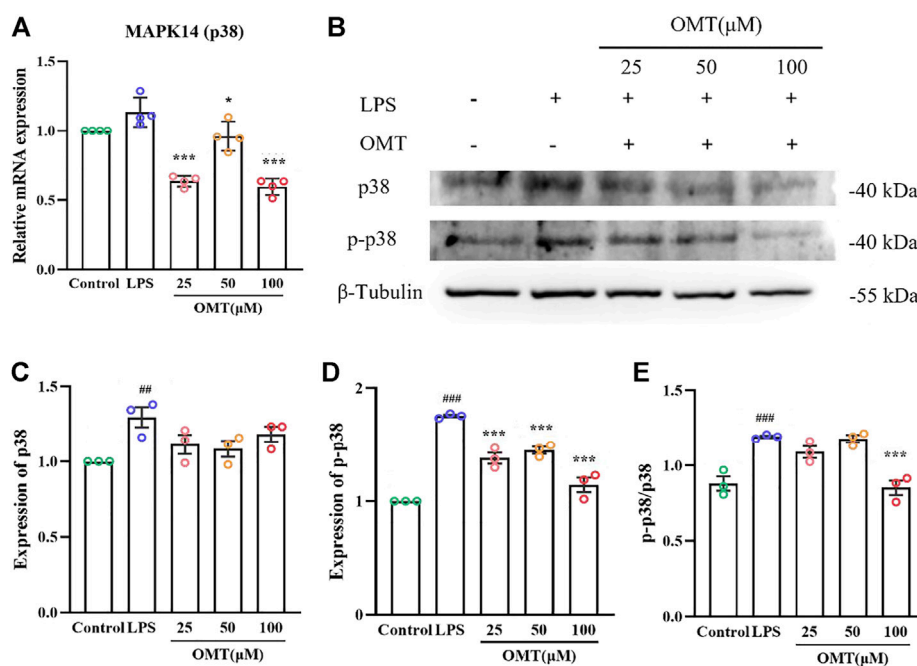


FIGURE 12

Effects of OM on the mRNA expression and protein phosphorylation expression of LPS-induced RAW264.7 cell inflammation model. (A) The mRNA expression of p38 mRNA, (B–E) protein level and phosphorylation level of p38. Values represent average  $\pm$  S.D. Significant differences among different groups are indicated as ## $p$  < 0.01, ### $p$  < 0.001 vs. control; \* $p$  < 0.05, \*\* $p$  < 0.01, \*\*\* $p$  < 0.001 vs. LPS group.

proliferation of inflammatory macrophages dependent on homeostatic activation of this axis (Bode et al., 2012).

In our study, after different doses of OMT pre-protected the LPS-induced inflammatory model of mouse macrophages (RAW264.7 cells), the cell morphology improved to various degrees, and the morphological alterations of LPS-induced RAW264.7 cells were blocked, according to flow cytometry data. The fraction of apoptotic RAW264.7 cells dropped to varying degrees, and the LD content induced by LPS was greatly reduced. These results demonstrated that OMT exerted a protective effect on LPS-induced inflammatory apoptosis. In addition, OMT can inhibit the release of inflammatory factors and the expression of inflammatory factor receptors in LPS-induced RAW264.7 cells. The mitogen-activated protein kinase (MAPK) family includes p38 MAPK. P38 MAPK residues Thr180 and Tyr182 are phosphorylated by p38-specific MKK3 and MKK6 in the p38 MAPK signaling cascade. When p38 MAPK is phosphorylated, it undergoes a conformational shift, allowing the substrate to access the catalytic residue. The functions of the p38 MAPK signaling pathway have been mediated by more than 60 downstream substrates so far (Trempele et al., 2013). P38 MAPK is divided into four isoforms, each of which is encoded by a separate gene (Jiang et al., 1997). In monocytes and macrophages, pharmacological investigations have demonstrated that several drugs that

selectively inhibit isoforms have anti-inflammatory effects. Since p38 is highly expressed in these cells, it is thought that p38 is primarily involved in the inflammatory response. P38 MAPK, which can be activated by upstream pro-inflammatory cytokine receptors and produce downstream signaling molecules to regulate macrophages, has multiple roles in the inflammatory response. The inflammatory response is influenced by several biological mechanisms involving cells and other immune cells. A recent study has shown the potential of the p38 MAPK-MK2 signaling axis as a target for therapeutic intervention in many neurological diseases (Beamer and Correa, 2021).

RT-qPCR was also utilized to assess inflammatory factor levels, and the pre-protective impact of different doses of OMT considerably prevented the rise in the mRNA expression of inflammatory factor IL-6, INOS, and the inflammation relative receptor TLR4, TGF-beta1, TGFR-1 induced by LPS. Moreover, OMT also suppresses downstream of the MAPK signaling pathway-associated genes' relative mRNA expression levels. The findings revealed that, in addition to the MAPKAPK-2 gene, OMT significantly reduced abnormally high mRNA expression of genes produced by LPS, such as TGF-beta1, TGFR-1, and MAPK8, MAP2K1, and MAP2K4.

Finally, the activity of phosphorylation sites in the MAPK pathway was examined and the facilitation of phosphorylation of P-38 protein induced by LPS was inhibited, indicating that OMT



takes functional regulation of macrophages *via* the MAPK signaling pathway.

## Conclusion

OMT interacts with a multitude of targets and possesses anti-inflammatory and antipruritic properties that are multi-channel, multi-link, multi-target, and overall synergistic. In addition, the MAPK signaling network was mostly enriched when WGNCA, molecular docking, and KEGG pathway enrichment analysis were combined with *in vitro* experimental results, suggesting that OMT may exert anti-inflammatory and antipruritic effects by affecting the MAPK signaling pathway, providing a reference for future mechanism research.

## Data availability statement

The datasets presented in this study can be found in online repositories. The names of the repository/repositories and accession number(s) can be found in the article/Supplementary Material.

## Author contributions

Conceptualization, ZL; Funding acquisition, AV and HN; Investigation, ZZ, WL, and TZ; Methodology LL and TZ; Formal

analysis ZL and TZ; Supervision, AV, NL, SL, and HN; Writing—original draft, ZL; Writing—review and editing, ZL, MY, TW and HN. All authors have read and agreed to the published version of the manuscript.

## Funding

This study was supported by grants from the National Natural Science Foundation of China (No. 8181101216) and the Undergraduate Entrepreneurship Project Fund (CX21233).

## Conflict of interest

The authors declare that the research was conducted in the absence of any commercial or financial relationships that could be construed as a potential conflict of interest.

## Publisher's note

All claims expressed in this article are solely those of the authors and do not necessarily represent those of their affiliated organizations, or those of the publisher, the editors and the reviewers. Any product that may be evaluated in this article, or claim that may be made by its manufacturer, is not guaranteed or endorsed by the publisher.

## References

- Beamer, E., and Correa, S. A. L. (2021). The p38(MAPK)-MK2 signaling Axis as a critical link between inflammation and synaptic transmission. *Front. Cell Dev. Biol.* 9, 635636. doi:10.3389/fcell.2021.635636
- Bernhard, J. D. (2005). Itch and pruritus: What are they, and how should itches be classified? *Dermatol. Ther.* 18 (4), 288–291. doi:10.1111/j.1529-8019.2005.00040.x
- Bode, J. G., Ehrling, C., and Haussinger, D. (2012). The macrophage response towards LPS and its control through the p38(MAPK)-STAT3 axis. *Cell. Signal.* 24 (6), 1185–1194. doi:10.1016/j.cellsig.2012.01.018
- Cevikbas, F., and Lerner, E. A. (2020). Physiology and pathophysiology of itch. *Physiol. Rev.* 100 (3), 945–982. doi:10.1152/physrev.00017.2019
- Doncheva, N. T., Morris, J. H., Gorodkin, J., and Jensen, L. J. (2019). Cytoscape StringApp: Network analysis and visualization of proteomics data. *J. Proteome Res.* 18 (2), 623–632. doi:10.1021/acs.jproteome.8b00702
- Elmariash, S. B., and Lerner, E. A. (2011). Topical therapies for pruritus. *Semin. Cutan. Med. Surg.* 30 (2), 118–126. doi:10.1016/j.sder.2011.04.008
- Folster-Holst, R., Torrello, A., Das, K., Murrell, D. F., Patil, A., Rahmat Pour Rokni, G., et al. (2022). Biological medication in atopic dermatitis. *Expert Opin. Biol. Ther.* 22 (5), 643–649. doi:10.1080/14712598.2022.2026920
- Goodsell, D. S., Zardecki, C., Di Costanzo, L., Duarte, J. M., Hudson, B. P., Persikova, I., et al. (2020). RCSB Protein Data Bank: Enabling biomedical research and drug discovery. *Protein Sci.* 29 (1), 52–65. doi:10.1002/pro.3730
- Guo, C., Zhang, C., Li, L., Wang, Z., Xiao, W., and Yang, Z. (2014). Hypoglycemic and hypolipidemic effects of oxymatrine in high-fat diet and streptozotocin-induced diabetic rats. *Phytomedicine*. 21 (6), 807–814. doi:10.1016/j.phymed.2014.02.007
- Halim, C. E., Xinjing, S. L., Fan, L., Bailey Vitarbo, J., Arfuso, F., Tan, C. H., et al. (2019). Anti-cancer effects of oxymatrine are mediated through multiple molecular mechanism(s) in tumor models. *Pharmacol. Res.* 147, 104327. doi:10.1016/j.phrs.2019.104327
- Hammouda, M. B., Ford, A. E., Liu, Y., and Zhang, J. Y. (2020). The JNK signaling pathway in inflammatory skin disorders and cancer. *Cells* 9 (4), 857. doi:10.3390/cells9040857
- He, X., Fang, J., Huang, L., Wang, J., and Huang, X. (2015). *Sophora flavescens* Ait.: Traditional usage, phytochemistry and pharmacology of an important traditional Chinese medicine. *J. Ethnopharmacol.* 172, 10–29. doi:10.1016/j.jep.2015.06.010
- Jiang, Y., Gram, H., Zhao, M., New, L., Gu, J., Feng, L., et al. (1997). Characterization of the structure and function of the fourth member of p38 group mitogen-activated protein kinases, p38delta. *J. Biol. Chem.* 272 (48), 30122–30128. doi:10.1074/jbc.272.48.30122
- Jiang, Y., Zhu, Y., Mu, Q., Luo, H., Zhi, Y., and Shen, X. (2017). Oxymatrine provides protection against Coxsackievirus B3-induced myocarditis in BALB/c mice. *Antivir. Res.* 141, 133–139. doi:10.1016/j.antiviral.2017.01.013
- Johanek, L. M., Meyer, R. A., Hartke, T., Hobelmann, J. G., Maine, D. N., LaMotte, R. H., et al. (2007). Psychophysical and physiological evidence for parallel afferent pathways mediating the sensation of itch. *J. Neurosci.* 27 (28), 7490–7497. doi:10.1523/JNEUROSCI.1249-07.2007
- Kiebert, G., Sorensen, S. V., Revicki, D., Fagan, S. C., Doyle, J. J., Cohen, J., et al. (2002). Atopic dermatitis is associated with a decrement in health-related quality of life. *Int. J. Dermatol.* 41 (3), 151–158. doi:10.1046/j.1365-4362.2002.01436.x
- Kim, S., Chen, J., Cheng, T., Gindulyte, A., He, J., He, S., et al. (2019). PubChem 2019 update: Improved access to chemical data. *Nucleic Acids Res.* 47 (D1), D1102–D1109. doi:10.1093/nar/gky1033
- Langfelder, P., and Horvath, S. (2008). Wgcna: an R package for weighted correlation network analysis. *BMC Bioinforma.* 9, 559. doi:10.1186/1471-2105-9-559
- Li, J. J., Zhang, X., Shen, X. C., Long, Q. D., Xu, C. Y., Tan, C. J., et al. (2020). Phytochemistry and biological properties of isoprenoid flavonoids from *Sophora flavescens* Ait. *Fitoterapia* 143, 104556. doi:10.1016/j.fitote.2020.104556

- Liu, X., Ouyang, S., Yu, B., Liu, Y., Huang, K., Gong, J., et al. (2010). PharmMapper server: A web server for potential drug target identification using pharmacophore mapping approach. *Nucleic Acids Res.* 38, W609–W614. doi:10.1093/nar/gkq300
- Liu, H. Y., Li, Y. X., Hao, Y. J., Wang, H. Y., Dai, X. Y., Sun, T., et al. (2012). Effects of oxymatrine on the neuropathic pain induced by chronic constriction injury in mice. *CNS Neurosci. Ther.* 18 (12), 1030–1032. doi:10.1111/cns.12026
- Liu, X., Wang, D., Yang, W., and Wu, X. (2020). Oxymatrine exerts anti-fibrotic effects in a rat model of hepatic fibrosis by suppressing endoplasmic reticulum stress. *J. Int. Med. Res.* 48(10), 300060520961681. doi:10.1177/0300060520961681
- Luo, Z., Zeng, A., Chen, Y., He, S., He, S., Jin, X., et al. (2021). Ligustilide inhibited Angiotensin II induced A7r5 cell autophagy via Akt/mTOR signaling pathway. *Eur. J. Pharmacol.* 905, 174184. doi:10.1016/j.ejphar.2021.174184
- Matterner, U., Apfelbacher, C. J., Vogelgsang, L., Loerbroks, A., and Weisshaar, E. (2013). Incidence and determinants of chronic pruritus: A population-based cohort study. *Acta Derm. Venereol.* 93 (5), 532–537. doi:10.2340/00015555-1572
- Nutten, S. (2015). Atopic dermatitis: Global epidemiology and risk factors. *Ann. Nutr. Metab.* 66, 8–16. doi:10.1159/000370220
- Otsuka, A., Nomura, T., Rerknimitr, P., Seidel, J. A., Honda, T., and Kabashima, K. (2017). The interplay between genetic and environmental factors in the pathogenesis of atopic dermatitis. *Immunol. Rev.* 278 (1), 246–262. doi:10.1111/imr.12545
- Paus, R., Schmelz, M., Biro, T., and Steinhoff, M. (2006). Frontiers in pruritus research: Scratching the brain for more effective itch therapy. *J. Clin. Invest.* 116 (5), 1174–1186. doi:10.1172/JCI28553
- Pereira, M. P., and Stander, S. (2019). How to define chronic prurigo? *Exp. Dermatol.* 28 (12), 1455–1460. doi:10.1111/exd.13972
- Reich, A., Medrek, K., and Szepletowski, J. C. (2016). Interplay of itch and psyche in psoriasis: An update. *Acta Derm. Venereol.* 96 (217), 55–57. doi:10.2340/00015555-2374
- Rishe, E., Azarm, A., and Bergasa, N. V. (2008). Itch in primary biliary cirrhosis: A patients' perspective. *Acta Derm. Venereol.* 88 (1), 34–37. doi:10.2340/00015555-0350
- Safran, M., Dalah, I., Alexander, J., Rosen, N., Iny Stein, T., Shmoish, M., et al. (2010). GeneCards version 3: The human gene integrator. *Database.* 2010, baq020. doi:10.1093/database/baq020
- Standar, S., Weisshaar, E., Mettang, T., Szepletowski, J. C., Carstens, E., Ikoma, A., et al. (2007). Clinical classification of itch: A position paper of the international forum for the study of itch. *Acta Derm. Venereol.* 87 (4), 291–294. doi:10.2340/00015555-0305
- Sun, Y., Liu, W. Z., Liu, T., Feng, X., Yang, N., and Zhou, H. F. (2015). Signaling pathway of MAPK/ERK in cell proliferation, differentiation, migration, senescence and apoptosis. *J. Recept. Signal Transduct. Res.* 35 (6), 600–604. doi:10.3109/10799893.2015.1030412
- Tremple, N., Dave-Coll, N., and Nebreda, A. R. (2013). SnapShot: p38 MAPK signaling. *Cell* 152 (3), 656–656.e1. e651. doi:10.1016/j.cell.2013.01.029
- Trott, O., and Olson, A. J. (2010). AutoDock vina: Improving the speed and accuracy of docking with a new scoring function, efficient optimization, and multithreading. *J. Comput. Chem.* 31 (2), 455–461. doi:10.1002/jcc.21334
- UniProt, C. (2021). UniProt: The universal protein knowledgebase in 2021. *Nucleic Acids Res.* 49 (D1), D480–D489. doi:10.1093/nar/gkaa1100
- Wang, W. J., Ma, Y. M., He, M. T., Zhang, D. H., Wang, R., Jing, L., et al. (2022). Oxymatrine alleviates hyperglycemic cerebral ischemia/reperfusion injury via protecting microvessel. *Neurochem. Res.* 47 (5), 1369–1382. doi:10.1007/s11064-022-03535-x
- Xiang, X., Tu, C., Li, Q., Wang, W., Huang, X., Zhao, Z., et al. (2020). Oxymatrine ameliorates imiquimod-induced psoriasis pruritus and inflammation through inhibiting heat shock protein 90 and heat shock protein 60 expression in keratinocytes. *Toxicol. Appl. Pharmacol.* 405, 115209. doi:10.1016/j.taap.2020.115209
- Xu, X., Xiao, W., Zhang, Z., Pan, J., Yan, Y., Zhu, T., et al. (2018). Anti-pruritic and anti-inflammatory effects of oxymatrine in a mouse model of allergic contact dermatitis. *J. Dermatol. Sci.* S0923-1811 (18), 134–141. doi:10.1016/j.jdermsci.2018.04.009
- Yeung, Y. T., Aziz, F., Guerrero-Castilla, A., and Argüelles, S. (2018). Signaling pathways in inflammation and anti-inflammatory therapies. *Curr. Pharm. Des.* 24 (14), 1449–1484. doi:10.2174/1381612824666180327165604
- You, L., Yang, C., Du, Y., Wang, W., Sun, M., Liu, J., et al. (2020). A systematic review of the pharmacology, toxicology and pharmacokinetics of matrine. *Front. Pharmacol.* 11, 01067. doi:10.3389/fphar.2020.01067
- Zhang, B., and Horvath, S. (2005). A general framework for weighted gene co-expression network analysis. *Stat. Appl. Genet. Mol. Biol.* 4, Article. 17. doi:10.2202/1544-6115.1128
- Zhang, Y., Yan, R., and Hu, Y. (2015). Oxymatrine inhibits lipopolysaccharide-induced inflammation by down-regulating Toll-like receptor 4/nuclear factor-kappa B in macrophages. *Can. J. Physiol. Pharmacol.* 93 (4), 253–260. doi:10.1139/cjpp-2014-0362
- Zhou, H., Shi, H. J., Yang, J., Chen, W. G., Xia, L., Song, H. B., et al. (2017). Efficacy of oxymatrine for treatment and relapse suppression of severe plaque psoriasis: Results from a single-blinded randomized controlled clinical trial. *Br. J. Dermatol.* 176 (6), 1446–1455. doi:10.1111/bjd.15316
- Zhu, T., Zhou, D., Zhang, Z., Long, L., Liu, Y., Fan, Q., et al. (2020). Analgesic and antipruritic effects of oxymatrine sustained-release microgel cream in a mouse model of inflammatory itch and pain. *Eur. J. Pharm. Sci.* 141, 105110. doi:10.1016/j.ejps.2019.105110



## OPEN ACCESS

## EDITED BY

Ren-You Gan,  
Agency for Science, Technology and  
Research, Singapore

## REVIEWED BY

Ming Niu,  
Fifth Medical Center of the PLA General  
Hospital, China  
Hengjing Cui,  
University of Eastern Finland, Finland  
Jiangtao Niu,  
Qinghai University, China

## \*CORRESPONDENCE

Yi-ying Wu,  
wuyiying@cmc.edu.cn  
Qiong Man,  
manqiong@cmc.edu.cn  
Sha Liu,  
102015005@cmc.edu.cn

<sup>†</sup>These authors have contributed equally  
to this work and share first authorship

## SPECIALTY SECTION

This article was submitted to  
Ethnopharmacology,  
a section of the journal  
Frontiers in Pharmacology

RECEIVED 08 August 2022

ACCEPTED 20 September 2022

PUBLISHED 06 October 2022

## CITATION

Liao Y-f, Luo F-l, Tang S-s, Huang J-w,  
Yang Y, Wang S, Jiang T-y, Man Q, Liu S  
and Wu Y-y (2022), Network analysis  
and experimental pharmacology study  
explore the protective effects of  
Isoliquiritigenin on 5-fluorouracil-  
Induced intestinal mucositis.  
*Front. Pharmacol.* 13:1014160.  
doi: 10.3389/fphar.2022.1014160

## COPYRIGHT

© 2022 Liao, Luo, Tang, Huang, Yang,  
Wang, Jiang, Man, Liu and Wu. This is an  
open-access article distributed under  
the terms of the [Creative Commons  
Attribution License \(CC BY\)](#). The use,  
distribution or reproduction in other  
forums is permitted, provided the  
original author(s) and the copyright  
owner(s) are credited and that the  
original publication in this journal is  
cited, in accordance with accepted  
academic practice. No use, distribution  
or reproduction is permitted which does  
not comply with these terms.

# Network analysis and experimental pharmacology study explore the protective effects of Isoliquiritigenin on 5-fluorouracil-Induced intestinal mucositis

Yi-fan Liao<sup>1,2†</sup>, Feng-lin Luo<sup>1,2†</sup>, Shan-shan Tang<sup>1,2†</sup>,  
Jing-wei Huang<sup>3</sup>, Ying Yang<sup>1,2</sup>, Shuang Wang<sup>1,2</sup>,  
Tang-yu Jiang<sup>1,2</sup>, Qiong Man<sup>1,2\*</sup>, Sha Liu<sup>1,2\*</sup> and Yi-ying Wu<sup>1,2\*</sup>

<sup>1</sup>Department of Pharmacology, School of Pharmacy, Chengdu Medical College, Chengdu, Sichuan, China, <sup>2</sup>Department of Pharmacy, Study on the Structure-Specific Small Molecule Drug in Sichuan Province College Key Laboratory, Chengdu Medical College, Chengdu, Sichuan, China, <sup>3</sup>Key Laboratory of Coarse Cereal Processing, Ministry of Agriculture and Rural Affairs, Sichuan Engineering & Technology Research Center of Coarse Cereal Industrialization, Chengdu University, Chengdu, Sichuan, China

5-fluorouracil (5-FU) is one of the most widely used chemotherapy drugs for malignant tumors. However, intestinal mucositis caused by 5-FU is a severe dose-limiting toxic effect and even leads to treatment interruption. Isoliquiritigenin (ISL) is one of the main active compounds of licorice, which is a traditional Chinese herbal medicine commonly used in inflammation and gastrointestinal diseases. It is speculated that ISL have protective effects on intestinal mucositis. However, no such studies have been reported. Therefore, to investigate the impact of ISL on 5-FU-induced intestinal mucositis, a strategy based on network prediction and pharmacological experimental validation was proposed in this study. Firstly, the targets and mechanism of ISL in alleviating 5-FU-induced gastrointestinal toxicity were predicted by network analysis. And the results were further confirmed by molecular docking. Then, a mouse model of intestinal mucositis was established by intraperitoneal injection of 5-FU (384 μmol/kg) to verify the prediction of network analysis. The network analysis results suggested that PTGS2 (Prostaglandin G/H synthase 2) and NOS2 (Nitric oxide synthase, inducible) might be the critical targets of ISL for reducing the intestinal toxicity of 5-FU. In addition, KEGG and GO enrichment analysis revealed that the HIF-1, TNF, MAPK, IL-17, PI3K-Akt, Ras, NF-kappa B signaling pathway, and biological processes of the inflammatory response, apoptosis regulation, NO production and NF-kappa B transcription factor activity might be involved in the mechanism of ISL against intestinal mucositis. Subsequent animal experiments showed that ISL could reduce the weight loss, leukopenia and mucosal damage caused by 5-FU. Compared with the intestinal mucositis model, the protein expressions of PTGS2, NOS2, TNFα (Tumor necrosis factor-alpha) and NF-κB p65 (nuclear factor kappa-B P65) were decreased after ISL treatment. In conclusion, this

study is the first time to find that ISL can attenuate 5-FU-induced intestinal mucositis in mice. Its anti-mucositis effect may be through regulating TNF/NF- $\kappa$ B pathway and inhibiting inflammatory mediators PTGS2 and NOS2. It will provide a potential candidate for the prevention and treatment of chemotherapy-induced intestinal mucositis.

#### KEYWORDS

5-fluorouracil, intestinal mucositis, Isoliquiritigenin, inflammatory mediator, network analysis

## 1 Introduction

5-fluorouracil (5-FU) is an analogue of uracil (McQuade et al., 2016). It can be activated into fluorouracil deoxynucleotide (FdUMP) in cells, which disrupts DNA synthesis by suppressing thymidylate synthase (Panchenko et al., 2018). 5-FU has been the backbone of therapy for many solid tumors, such as esophageal, breast, stomach and intestinal malignant tumors (McQuade et al., 2016; Zhang et al., 2019).

However, the non-selective cytotoxicity of 5-FU can cause serious side effects, including gastrointestinal dysfunction, mucosal inflammation, cardiotoxicity, and even myelosuppression (Atiq et al., 2019). Mucositis is the most common gastrointestinal toxicity, involving the entire gastrointestinal tract from the mouth to the anus. Especially intestinal mucositis has been regarded as one of the main obstacles to tumor chemotherapy. Intestinal mucositis usually presents with anorexia, nausea, vomiting, diarrhea and so on (Justino et al., 2020). And severe mucositis will develop into ulcers that invade the entire submucosa. This can cause severe pain and even require narcotic analgesics to relieve it (Xing et al., 2015). So that, patients have to reduce the drug dose or discontinue the medication, which may lead to efficacy reduction or treatment failure. However, the clinical treatment of intestinal mucositis is mainly symptomatic support, such as drugs to relieve pain or diarrhea. So far, chemotherapy-induced intestinal mucositis is still lack of effective drugs to target its pathogenesis. Therefore, it is necessary to explore drugs for intestinal mucositis.

Traditional Chinese medicine (TCM) has the advantages of low adverse reactions and stable efficacy. It has been widely used in tumor adjuvant therapy to enhance the efficacy of chemotherapy and reduce toxic effects. Clinical studies have shown that TCM can significantly reduce the incidence of diarrhea and other gastrointestinal symptoms during chemotherapy. Among these TCM, licorice, called Gancao in Chinese, is the most frequently used herbal medicine (Yang et al., 2017). In TCM treatment, licorice is one of the essential Chinese herbal medicines for treating gastrointestinal diseases (Yang et al., 2017).

ISL is one of the most important bioactive compounds in licorice (Tang et al., 2018). Numerous studies have demonstrated that ISL has inhibitory effects on various malignant tumors, such

as breast cancer, prostate cancer, colon cancer, lung cancer, Ovary Cancer, cervical cancer and leukemia (Wang et al., 2021). It can also be combined with chemotherapeutic agents to enhance anti-tumor efficacy (Peng et al., 2015). In addition, ISL is an effective anti-inflammatory agent, which can reduce inflammation by inhibiting IL-1 $\beta$ , IL-6, TNF $\alpha$  and other cytokines (Du et al., 2016; Liao et al., 2020). Recent studies have shown that ISL can significantly suppress the dextran sulfate sodium (DSS)-induced colitis-associated tumorigenesis in mice and maintain the integrity of the intestinal mucosal barrier (Zhao et al., 2014; Wu C. H. et al., 2016). Those findings suggest that ISL can protect intestinal mucosa and reduce inflammatory injury. It may be used as an adjunctive agent to relieve 5-FU-induced intestinal mucositis during chemotherapy. Although the antitumor and the synergistic effect of ISL have been widely reported, the protective effect of ISL on intestinal mucositis has not been investigated, which is also one of the major factors affecting cancer treatment.

Network pharmacology is a new branch of pharmacology based on system biology and computer science. By constructing the molecular network of a biological system, the overall relationship between drug-target-disease can be comprehensively analyzed, and the target and mechanism of the drug on diseases can also be predicted (Zhu et al., 2018). Nowadays, network analysis has been widely used to screen the active ingredients and explore the mechanism of TCM.

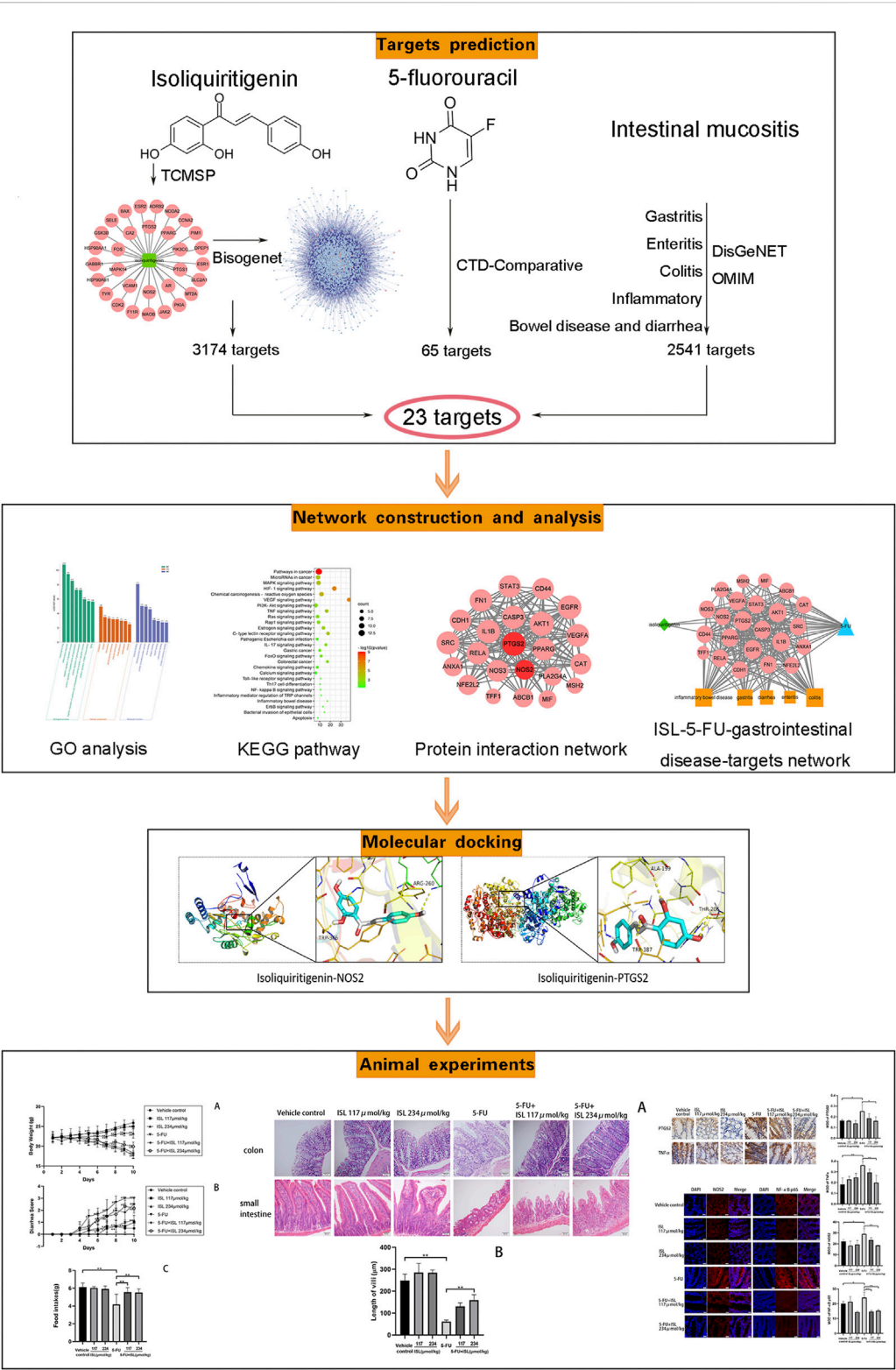
In this study, a comprehensive network analysis approach was used to predict the mechanism of ISL on 5-FU-induced gastrointestinal toxicity. And the prediction results were further verified in a mouse model of intestinal mucositis. The flow of this study was shown in Figure 1. This is the first time to explore the effect and mechanism of ISL against intestinal mucositis induced by 5-FU. It may provide reference for clinical treatment and drug development of chemotherapy-induced intestinal mucositis.

## 2 Materials and methods

### 2.1 Collection of pharmacological targets

The TCMSP database (<https://old.tcmsp-e.com/tcmsp.php>) (Fan et al., 2022) was employed to predict the pharmacological





**FIGURE 1**  
Flow chart of this study.

targets of ISL (ISL target, iT). A total of 31 iTs were collected. And the Bisogenet plug-in in Cytoscape 3.8.0 (Martin et al., 2010) was used to screen out 3,174 target proteins related to ISL targets (related target, rT), thus expanding the range of prediction targets and protein interaction network. The therapeutic targets for the gastrointestinal disease were obtained from the DisGeNET database (<http://www.disgenet.org/>) (Piñero et al., 2017) and the OMIM database (<https://omim.org/>) (Amberger et al., 2015). Five diseases associated with gastrointestinal injury were searched in those databases, such as gastritis, enteritis, colitis, inflammatory bowel disease and diarrhea. A total of 2,541 targets (duplicate value removed) associated with gastrointestinal disease (disease target, dT) were collected. Then, the CTD-Comparative database (<http://ctdbase.org/>) (Aihaiti et al., 2021) was used for the collection of 5-FU gastrointestinal toxic targets (toxic targets of 5-FU, tT). In total, 65 potential tTs were collected.

## 2.2 Network construction and analysis

23 common targets were found among iT, rT, tT and dT, and submitted to the DAVID database (<https://david.ncifcrf.gov/>) (Aihaiti et al., 2021) to use Gene ontology (GO) analysis and Kyoto Encyclopedia of Genes and Genomes (KEGG) pathway enrichment analysis. The protein interaction relationship of the common targets was obtained by the database STRING (<https://www.string-db.org/>) (Aihaiti et al., 2021). And the networks were visualized using Cytoscape software (<http://www.cytoscape.org/>) (Aihaiti et al., 2021).

## 2.3 Molecular docking

To verify the critical targets of ISL, a molecular docking of ISL with PTGS2 (Prostaglandin G/H synthase 2) and NOS2 (Nitric oxide synthase, inducible) was performed. And Known inhibitors of PTGS2 (Celecoxib) and NOS2 (N-Iminoethyl-L-lysine dihydrochloride) were used as reference (Alqahtani, 2021; Lawal et al., 2021). The 3D structures of PTGS2 and NOS2 were obtained from the Protein Data Bank (PDB, <http://www.rcsb.org/>) and then imported into PyMOL (v2.3.0) to remove water molecules. The structure of ISL, Celecoxib and N-Iminoethyl-L-lysine dihydrochloride were downloaded from the website of PubChem (<https://pubchem.ncbi.nlm.nih.gov/>) and then imported into PyMOL (v2.3.0) and AutoDockTools-1.5.6 software. The target proteins and ligands were prepared for molecular docking by Autodock Tools (ADT) program. Finally, molecular docking analysis was performed using the AutoDock Vina program (Trott and Olson, 2010). The crystal structures used for PTGS2 and NOS2 and the parameter settings for the grid box were provided in the Supplementary Material S1.

## 2.4 Pharmacological experimental validation of network analysis

### 2.4.1 Materials

ISL (HPLC  $\geq 98\%$ ) was purchased from Chengdu Pufei De Biotechnology Co., Ltd. 5-FU (HPLC  $>99\%$ ) was purchased from Dalian Meilun Biotechnology Co., Ltd. ISL was dissolved in saline containing 2% dimethylsulfoxide (DMSO). 5-FU was prepared in pyrogen-free saline.

### 2.4.2 Animals and treatment

36 male SPF BLAB/c mice (18–20 g, 6–8 weeks old) were obtained from Chengdu Dossy Experimental Animals Co., Ltd. Mice were raised under standard laboratory conditions at  $23 \pm 1^\circ\text{C}$  and  $55 \pm 5\%$  humidity with a 12 h light/dark cycle.

The mice were randomly allocated to six groups (6 mice per group): 1) Vehicle control (2% DMSO in saline); 2) ISL 117  $\mu\text{mol/kg}$ ; 3) ISL 234  $\mu\text{mol/kg}$ ; 4) Model (5-FU 384  $\mu\text{mol/kg}$ ); 5) 5-FU + ISL 117  $\mu\text{mol/kg}$ ; 6) 5-FU + ISL 234  $\mu\text{mol/kg}$ . All drugs were injected intraperitoneally (i.p.). Except for the vehicle control and model (5-FU) group, all mice received ISL for 10 days. Mice in model and 5-FU + ISL groups were intraperitoneally injected with 5-FU (384  $\mu\text{mol/kg}$ ) every other day. The treatment schedule was shown in Figure 2. All mice were fed and water ad libitum during the entire experiment.

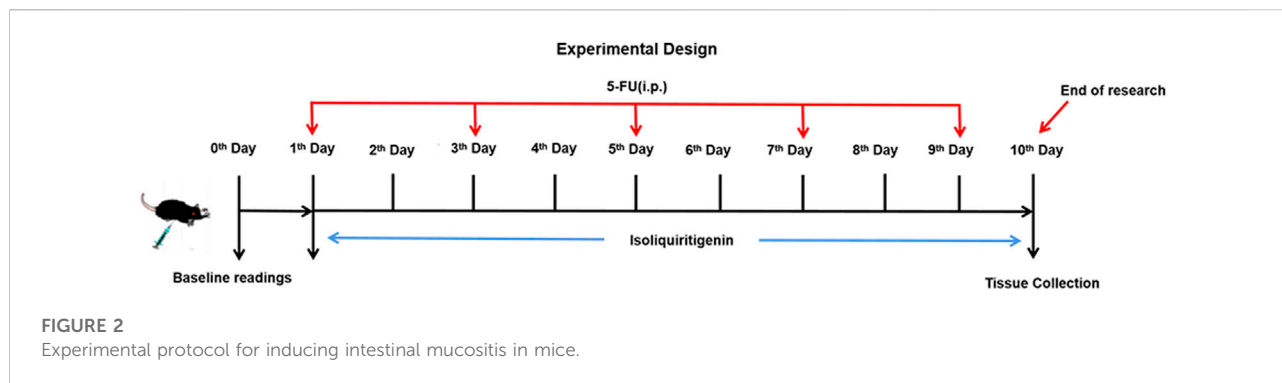
All animal experiments were approved by the Experimental Animal Ethical Committee of Chengdu Medical College, and the experimental protocols were carried out strictly in conformity with the guidance for Animal Experiments in Chengdu Medical College and the Declaration of Helsinki.

### 2.4.3 The routine observation (body weight, food intake and diarrhea) in mice

Mice were monitored daily for body weight, food intake and diarrhea. Bowen's score system was used to assess diarrhea severity, and the grade ranged from 0 to 3 based on the consistency of stool: 0, normal stool; 1, the stool is slightly wet or soft, indicating mild diarrhea; 2, the stool is moderately wet with unformed pellets, indicating moderate diarrhea; 3, the stool is watery or loose stool, indicating severe diarrhea (Yeung et al., 2015; Atiq et al., 2019).

### 2.4.4 Sample collection and preparation

24 h after the last administration, the mice were anesthetized by intraperitoneal injection of 2% pentobarbital sodium. Then, 1 ml Peripheral blood from each mouse was collected *via* orbital blood and placed into an anticoagulant tube containing EDTA. The blood was prepared for a routine blood test, which included



the analysis of white blood cell (WBC) count, neutrophil count, lymphocyte count, red blood cell (RBC) count and so on. All mice were then sacrificed immediately. And 1–2 cm of the middle segment of the small intestine and colon was dissected, washed with saline, and then fixed with paraformaldehyde for further analysis.

## 2.4.5 Histopathological analysis

The paraformaldehyde-fixed small intestine and colon tissues were embedded in paraffin and sectioned at 3  $\mu$ m thickness. The paraffin sections were baked at 60°C for 3 h. Then, sections were dewaxed with xylene, and placed in gradient ethanol (absolute ethanol twice for 3 min, 95% ethanol for 3 min, 75% ethanol for 3 min), and finally stained with hematoxylin for 12 min and eosin for 13 s. 3–5 complete longitudinal small intestinal villi were selected from each sample for measurement (3 samples per group). The villi height was measured from the top of the villus to the villus-crypt junction using ImageJ software (Atiq et al., 2019).

## 2.4.6 Immunohistochemistry and immunofluorescence experiments

After dewaxing and rehydration, paraffin sections of colon tissue were placed in sodium citrate buffer and heated by a microwave oven twice for 2–3 min to repair antigens. After washing twice with PBS for 5 min, 5% bovine serum albumin (BSA) was added to block non-special signals for 30 min at 37°C. BSA was then removed, and primary antibodies (1:200, Proteintech Group, Inc, United States) diluted with 1% BSA were added and incubated overnight at 4°C. After washing with PBS, slides were incubated with horseradish peroxidase (HRP)- or Alexa Fluor-secondary antibodies (1:1,000, Proteintech Group, Inc, United States) at room temperature in dark for 1 h. The slides were washed twice with PBS for 5 min, and incubated with diaminobenzidine (DAB) for 3–10 min to develop color, or with DAPI for 10 min to stain nuclei. Finally, the slides were sealed by neutral glue or anti-

fluorescence quencher. 3–5 fields were randomly selected for each sample (3 samples per group) and observed under an Olympus BX63 fluorescence microscope (Olympus, Tokyo, Japan) at  $\times 400$ . And ImageJ analysis software was used to assess the staining results. Protein expression was quantified as mean optical density (MOD = integrated option density/area). (Du et al., 2015; Wang et al., 2022).

## 2.4.7 Statistics

Quantitative data were represented as the means  $\pm$  standard deviations (SD). SPSS and GraphPad Prism were used for statistical analysis and graph drawing, and the differences between groups were analyzed by one-way analysis of variance (ANOVA).  $p < 0.05$  was considered statistically significant.

# 3 Results

## 3.1 Target prediction of ISL against 5-FU-induced gastrointestinal toxicity

Based on target prediction *via* TCMSP, the ISL-target network (Figure 3A) consisted of 31 nodes. To better evaluate the detoxification effect of ISL on 5-FU, rTs interacting with iTs were screened to expand the range of predicted targets, and a total of 3,174 rTs were obtained (Figure 3B). Finally, 23 common targets were obtained from the intersection of tTs, dTs and iTs or rTs. The 23 targets could be considered as potential targets (pT) for ISL to reduce the gastrointestinal toxicity of 5-FU. Among them, PPARG, PTGS2 and NOS2 were the direct targets of ISL (iT) predicted by TCMSP. Moreover, PTGS2 (also known as cyclooxygenases-2, COX-2) and NOS2 (also known as inducible nitric oxidesynthase, iNOS) have been reported to be involved in the occurrence of 5-FU-caused intestinal mucositis (Atiq et al., 2019; Yan et al., 2020; Huang et al., 2022). Therefore, PTGS2 and NOS2 could be considered as critical targets of ISL against 5-FU-induced gastrointestinal toxicity.

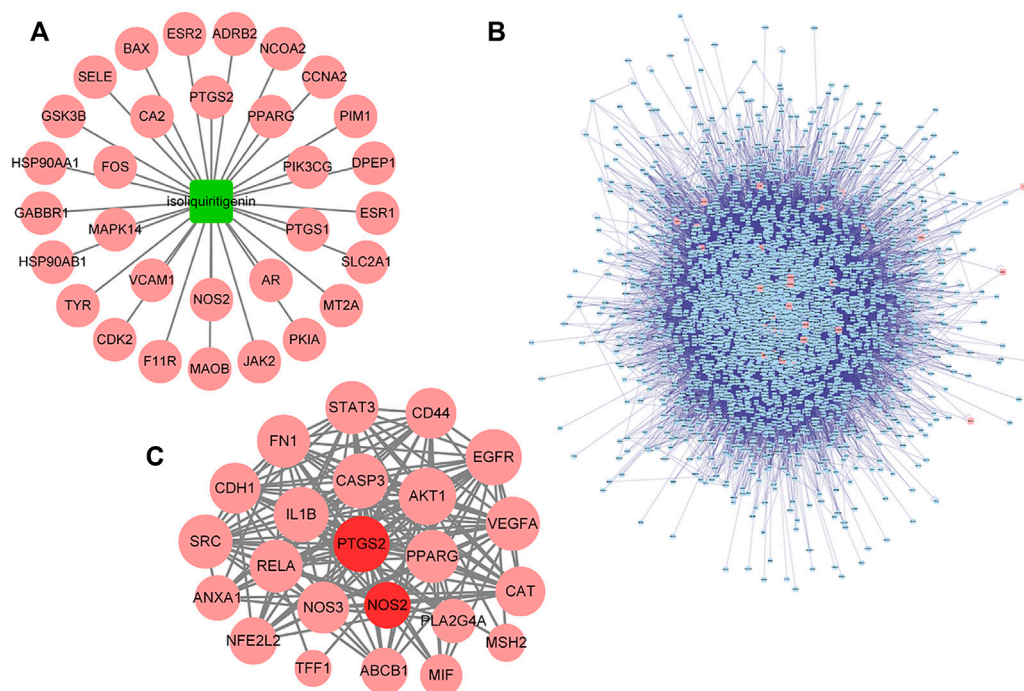


FIGURE 3

Targets of ISL against 5-FU gastrointestinal toxicity predicted by network analysis. (A) The ISL-target network. The node in green color is ISL, and the nodes in red color are candidate targets of ISL. (B) Protein interaction network of ISL target (iT) and its related target (rT). The nodes in red color are iTs, and the nodes in blue color are rTs. (C) Protein interaction network of potential targets (pT) of ISL for detoxification. The nodes in red color are pTs for ISL against the gastrointestinal toxicity of 5-FU, the nodes in dark red color are the critical targets for the detoxification of ISL.

### 3.2 Network analysis on the mechanism of ISL against 5-FU-induced gastrointestinal toxicity

As shown in Figure 4A, a network of ISL-potential targets-5-FU-gastrointestinal disease network (ISL-pT-5FU-D) was constructed to reflect the relationship between ISL (green nodes), 5-FU (blue nodes), gastrointestinal diseases (orange nodes) and their common targets (red nodes). We further investigated the correlation degree of each node and sequenced them with the node size (Shao, 2021). More information about the nodes was provided in the Supplementary Materials S2.

Next, a bioinformatics analysis of potential targets was performed. As shown in Figures 4B,C, the alleviating effect of ISL on 5-FU-induced gastrointestinal toxicity might be related to biological processes such as inflammatory response, apoptosis regulation, NO production and NF-kappa B transcription factor activity. And the molecular mechanism might involve multiple signaling pathways, such as HIF-1, VEGF, TNF, MAPK, IL-17, PI3K-Akt, Ras, NF-kappa B, Toll-like receptor pathway. Therefore, network analysis suggested that ISL might alleviate 5-FU-induced gastrointestinal toxicity through multiple targets and pathways, which were mainly involved in regulating inflammation and apoptosis.

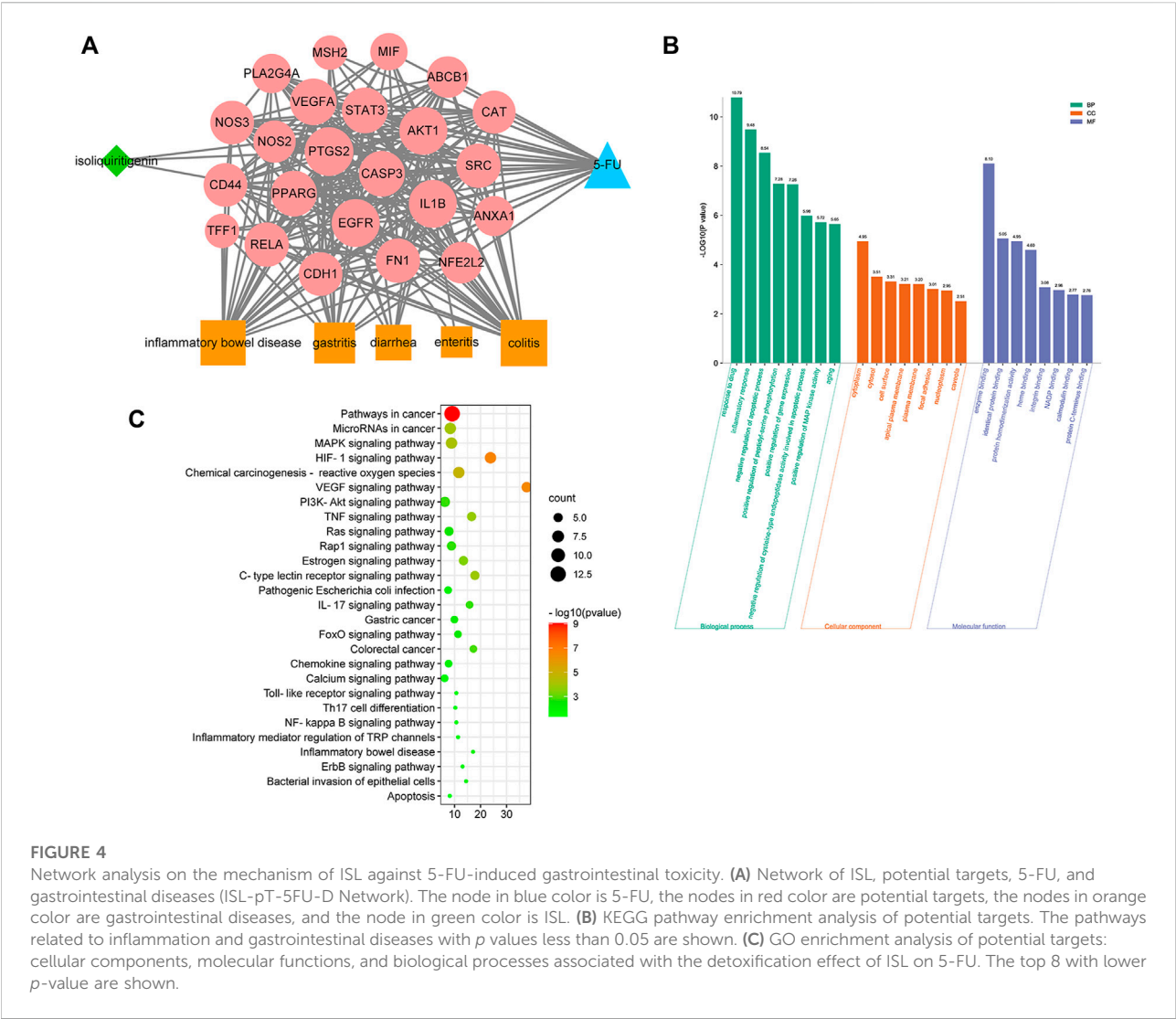
### 3.3 Molecular docking validation of the predicted critical targets

To verify the accuracy of the above predictions, a molecular docking analysis of ISL with PTGS2 and NOS2 enzyme was performed. ISL has large binding affinity for PTGS2 and NOS2 protein with binding energies of  $-9.1$  and  $-8.7$  kcal/mol, respectively. Furthermore, ISL showed a higher binding energy with PTGS2 and NOS2 than the known protein inhibitor (Table 1). This suggested that ISL might bind and inhibit PTGS2 and NOS2 protein. In addition, as shown in Figure 5, ISL can interact with NOS2 by two H-bonds with ARG260 and TRP366, and interact with PTGS2 by three H-bonds with TRP387, THR206 and ALA199. ISL was successfully docked with PTGS2 and NOS2 protein.

### 3.4 Effect of ISL on body weight, diarrhea, food intake and blood routine index in mice model

To assess the severity of gastrointestinal injury caused by 5-FU, mice were monitored daily for body weight, food intake and diarrhea. The results were shown in Figure 6. Compared





**FIGURE 4** Network analysis on the mechanism of ISL against 5-FU-induced gastrointestinal toxicity. **(A)** Network of ISL, potential targets, 5-FU, and gastrointestinal diseases (ISL-pT-5FU-D Network). The node in blue color is 5-FU, the nodes in red color are potential targets, the nodes in orange color are gastrointestinal diseases, and the node in green color is ISL. **(B)** KEGG pathway enrichment analysis of potential targets. The pathways related to inflammation and gastrointestinal diseases with *p* values less than 0.05 are shown. **(C)** GO enrichment analysis of potential targets: cellular components, molecular functions, and biological processes associated with the detoxification effect of ISL on 5-FU. The top 8 with lower *p*-value are shown.

**TABLE 1** The binding energies of ISL with NOS2 and PTGS2 protein targets.

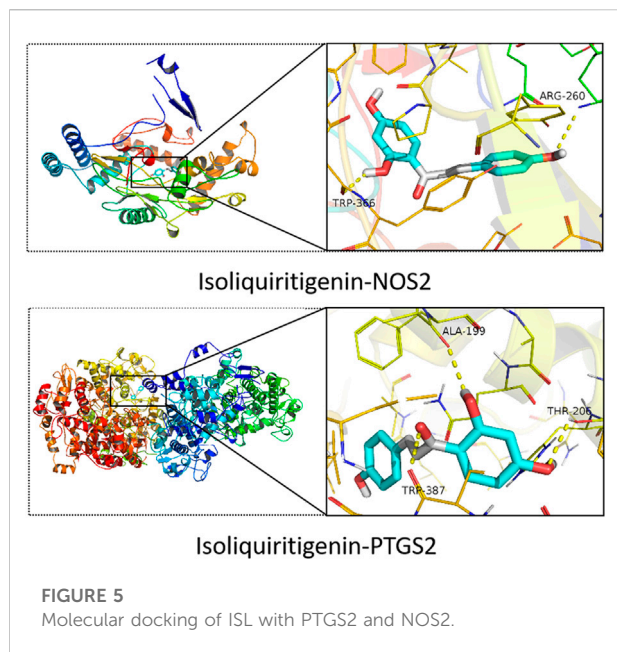
Protein	PDB ID	Binding energy (kcal/mol)	
		Inhibitor	ISL
NOS2	2BHJ	-6.1	-9.1
PTGS2	1CX2	-8.1	-8.7

NOS2 Inhibitor: N-Iminoethyl-L-lysine dihydrochloride.  
PTGS2 inhibitor: Celecoxib.

with the vehicle control, intraperitoneal injection with 5-FU significantly reduced body weight, increased diarrhea, and decreased food intake of mice ( $p < 0.05$ ). After combined

treatment with ISL, the weight loss of mice was slower, and the food intake in mice was increased compared with that of the 5-FU group ( $p < 0.05$ ). Although no significant difference was observed in diarrhea scores between the 5-FU and 5-FU + ISL groups, the diarrhea of mice in the combination groups showed a decreasing trend.

Furthermore, the blood routine indexes were detected to evaluate the effect of ISL on hematotoxicity. As shown in Table 2, the counts of WBC, lymphocytes, neutrophils and RBC were significantly decreased in the 5-FU group compared with the vehicle control group ( $p < 0.05$ ). And compared to the 5-FU group, the WBC, lymphocytes, and neutrophils indexes in the 5-FU + 234  $\mu\text{mol/kg}$  ISL combination group were significantly increased ( $p < 0.05$ ). Thus, these results suggested that ISL could alleviate gastrointestinal toxicity symptoms and leukopenia caused by 5-FU.



### 3.5 ISL alleviates mucosal damage induced by 5-FU in mice

As shown in Figure 7, no histomorphological changes were observed in the small intestine and colon of the vehicle control mice, with clear intestinal tissue structure, neatly arranged villi, normal epithelial cell morphology, and densely arranged intestinal glands. In the ISL groups, the mucosal structure of mice remained intact. The intestinal mucosa of mice in the 5-FU group was the most seriously damaged, with loose cell arrangement and obvious inflammatory cell infiltration. And the villi heights were significantly lower than that of the vehicle control ( $p < 0.01$ ). Compared with the 5-FU group, the mice in the 5-FU + ISL combination groups exhibited less mucosal damage, less inflammatory cell infiltration, and greater villi height ( $p < 0.01$ ). It indicated the protective effect of ISL on 5-FU-induced intestinal mucosal damage.

### 3.6 The effects of ISL on the expressions of PTGS2, NOS2, TNF $\alpha$ and NF- $\kappa$ B p65

To verify the molecular mechanism of ISL against 5-FU-induced intestinal mucositis, the expression of PTGS2, NOS2, TNF $\alpha$ , and NF- $\kappa$ B p65 in colon tissues were detected. As shown in Figure 8, compared with the vehicle control, 5-FU treatment significantly increased the expression of PTGS2, NOS2, TNF $\alpha$  and NF- $\kappa$ B p65 ( $p < 0.05$ ). These protein levels were obviously decreased in the colon tissues of mice in the 5-FU + ISL combination groups compared to the 5-FU group. And the decrease in the 5-FU+234  $\mu$ mol/kg ISL group was highly

significant ( $p < 0.05$ ). The results suggested that the alleviating effect of ISL on 5-FU-induced intestinal mucositis might be related to the inhibition of PTGS2, NOS2, TNF $\alpha$  and NF- $\kappa$ B p65, which was consistent with our network pharmacological predictions.

## 4 Discussion

Currently, 5-FU is a routine treatment for a variety of malignant tumors. It is also known to cause severe gastrointestinal toxicity, such as intestinal mucositis. In intestinal mucositis, 5-FU can induce cell apoptosis, force intestinal mucosa to atrophy, damage the intestinal villi, and reduce the absorption of intestinal contents and water, thus causing dyspepsia, anorexia, abdominal pain and diarrhea (Yan et al., 2020). These serious toxic effects of 5-FU will reduce patients' treatment compliance, and even lead to the interruption of chemotherapy (Kato et al., 2015; King et al., 2015). Therefore, it is necessary to explore novel drugs to prevent and treat intestinal mucositis caused by 5-FU.

Recent studies have shown that inflammatory cytokines IL-1 $\beta$ , IL-6, TNF $\alpha$ , and NF- $\kappa$ B are significantly increased in 5-FU-induced intestinal mucositis in mice (Ali et al., 2019; Atiq et al., 2019). 5-FU can induce the production of reactive oxygen species (ROS), promote DNA damage and then activate NF- $\kappa$ B (Chang et al., 2012; Oliveira et al., 2021). Next, NF- $\kappa$ B activation leads to the release of inflammatory mediators, including TNF $\alpha$ , COX-2, iNOS, IL-1 $\beta$ , and so on (Kim et al., 2009; Abdelhamid et al., 2020). TNF $\alpha$ , in turn, activates NF- $\kappa$ B. This positive feedback mechanism results in signal amplification and increased production of inflammatory mediators, which eventually destroy the intestinal mucosal barrier and lead to the formation of mucosal ulcers (Huang et al., 2022; Shi et al., 2022).

In this study, a mouse model of intestinal mucositis was established by intraperitoneal injection of 5-FU. Consistent with the previous studies, administration of 5-FU caused severe diarrhea, weight loss and anorexia in mice, which were the main symptoms of intestinal mucositis. (Soares et al., 2013; Zhang et al., 2019). And histopathological changes were also demonstrated, such as shortening of villi, inflammatory cell infiltration and loss of mucosal structure. And the expressions of NOS2, TNF $\alpha$ , NF- $\kappa$ B P65 and PTGS2 in colon tissues were significantly increased. It suggested that these inflammatory mediators and their signaling pathways might be implicated in the occurrence of intestinal mucositis.

ISL, a natural chalcone flavonoid, has been shown to exhibit good pharmacokinetic properties and a variety of biological activities (Wang et al., 2021), including anti-tumor, anti-inflammatory, immunomodulatory, gastrointestinal protection and so on (Wu M. et al., 2016; Zhao et al., 2019; Liao et al., 2020). In particular, its high antitumor efficacy has attracted extensive attention in recent years. Numerous studies have found that ISL

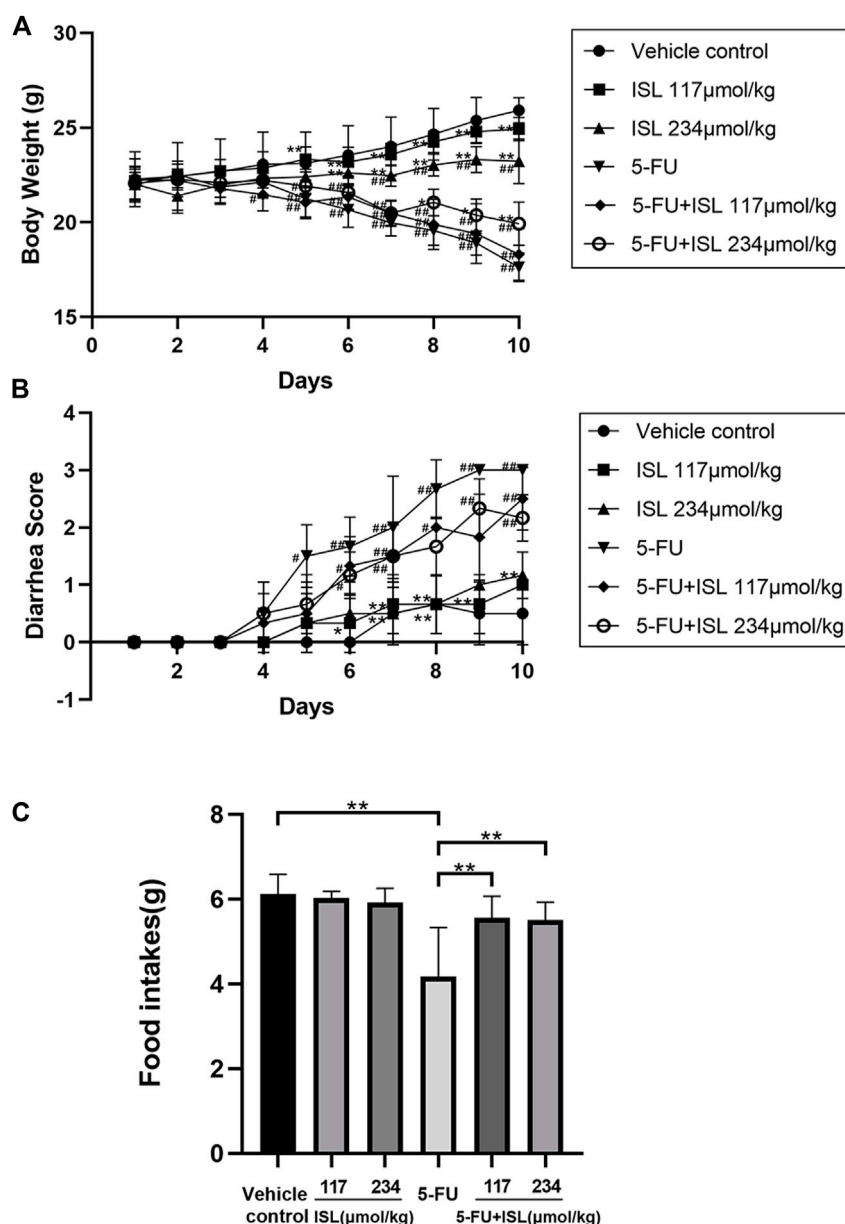


FIGURE 6

Effect of ISL on body weight, diarrhea, and daily food intake in mice with or without 5-FU intraperitoneal injection. (A) Changes in daily body weights. (B) Changes in daily diarrhea. (C) Mean daily food intake. Data are presented as mean  $\pm$  S.D. ( $n = 6$  in each group).  $\#p < 0.05$  and  $\#\#p < 0.01$  vs. control group;  $*p < 0.05$  and  $**p < 0.01$  vs. 5-FU group.

can inhibit the proliferation and induce apoptosis of various cancer cells (Peng et al., 2015; Wang et al., 2021). At the same time, its cytotoxic effect shows selectivity, which can significantly inhibit the viability of tumor cells but almost no cytotoxicity to normal cells (Wu C. H. et al., 2016). ISL also significantly suppresses the growth and metastasis of various tumors in mouse models (Peng et al., 2015; Wang et al., 2021). In addition, ISL has synergistic antitumor effect with chemotherapies. For example, Zhang et al. reported that ISL

synergistically sensitized the cytotoxic effect of gemcitabine and 5-FU on pancreatic cancer cells (Zhang et al., 2022). Consistently, Jin et al. demonstrated that ISL potentiated the apoptotic effects of 5-FU on HCT-116 cells (Jin et al., 2018). Overall, both *in vitro* and *in vivo* studies have demonstrated the potential of ISL for cancer treatment and adjuvant chemotherapy.

In addition, the anti-inflammatory effect of ISL has also been widely reported. Studies have shown that ISL can attenuate the inflammatory injury induced by LPS or carrageenan. Its anti-

TABLE 2 Changes in indexes of blood routine in mice (n = 3 in each group).

Groups	WBC( $10^9/L$ )	LY ( $10^9/L$ )	NE ( $10^9/L$ )	RBC( $10^{12}/L$ )
Control	$5.07 \pm 0.49$	$4.30 \pm 0.26$	$0.70 \pm 0.17$	$10.15 \pm 0.14$
5-FU	$1.00 \pm 0.36^{**}$	$0.67 \pm 0.25^{**}$	$0.30 \pm 0.10^*$	$9.21 \pm 0.21^*$
5-FU + ISL (117 $\mu\text{mol/kg}$ )	$0.97 \pm 0.29^{**}$	$0.70 \pm 0.20^{**}$	$0.23 \pm 0.12^{**}$	$9.62 \pm 0.69$
5-FU + ISL (234 $\mu\text{mol/kg}$ )	$2.13 \pm 0.49^{**/+}$	$1.40 \pm 0.17^{**/+}$	$0.67 \pm 0.021^*$	$9.57 \pm 0.17$

WBC, white blood cell count; LY, lymphocyte count; NE, neutrophil count; RBC, red blood cell count. Data are presented as mean  $\pm$  S.D. \* $p < 0.05$  and \*\* $p < 0.01$  vs. control group; \* $p < 0.05$  and \*\* $p < 0.01$  vs. 5-FU, group.

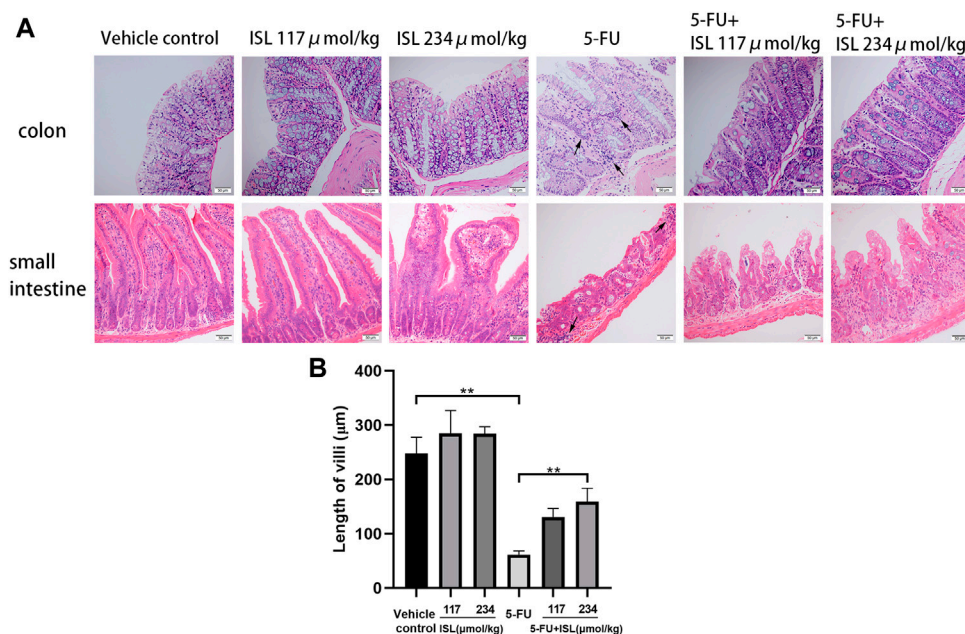


FIGURE 7

Effect of ISL on intestinal histopathological damage in mice. (A) Hematoxylin and eosin (H&E) staining of small intestine and colon. All images are displayed at  $\times 200$  magnification. Inflammatory cell infiltration (black arrows) is observed in the 5-FU group. (B) Length of small intestinal villi. Data are presented as mean  $\pm$  S.D. (n = 3 in each group). \*\* $p < 0.01$ .

inflammatory effect is through inhibiting NF- $\kappa$ B and then causing iNOS, TNF $\alpha$ , COX-2, IL-6 and other inflammatory cytokines to down-regulation (Kim et al., 2008; Kim et al., 2008; Tang et al., 2018; Liao et al., 2020). Furthermore, ISL can protect mouse gastrointestinal tracts, and suppress DSS/AOM-induced colon inflammation-related tumorigenesis by down regulating PGE2 and IL-6 (Zhao et al., 2014; Wu M. et al., 2016). These findings suggest that ISL is a promising anti-inflammatory and intestinal protective agent. However, the effect of ISL on intestinal mucositis remains unknown.

Therefore, we observed the alleviating effect of ISL on 5-FU-induced intestinal mucositis in this study. The results showed that ISL could significantly reduce intestinal mucosal damage and its symptoms caused by 5-FU in mice. In addition, leukopenia, one of the main toxic effects of 5-FU, was also observed to be attenuated by ISL. These results reveal for the

first time that ISL has good potential for alleviating 5-FU-induced gastrointestinal toxicity in adjuvant tumor therapy, and its mechanism is worthy of further investigation.

Network pharmacological analysis is a new approach to predict the potential pharmacological effects and mechanisms of TCM and its monomers. In this study, network analysis was used to predict the therapeutic targets of ISL on 5-FU-induced intestinal mucositis. And the results showed that PTGS2 and NOS2 might be the critical targets of ISL for reducing intestinal mucositis. In addition, KEGG and GO enrichment analysis indicated that the anti-intestinal mucositis mechanism of ISL was mainly related to inflammatory and apoptosis-related signaling pathways and biological processes, such as HIF-1 pathway, TNF pathway, PI3K-Akt pathway, NF- $\kappa$ B pathway, NO production, NF- $\kappa$ B transcription factor activity, etc.

As we know, TNF is the critical signaling pathway in regulating inflammatory responses (Chu, 2013). TNF family cytokines can



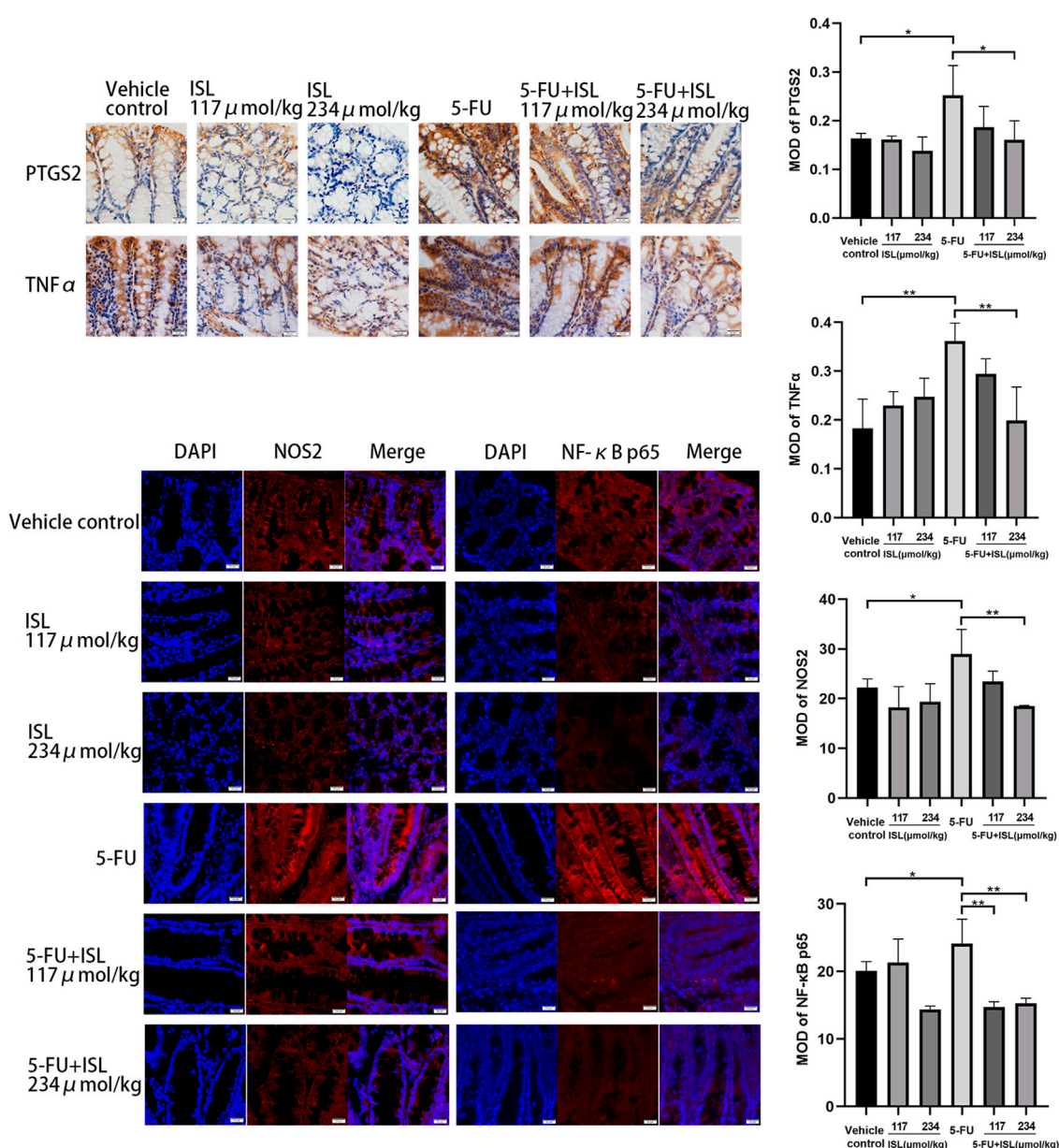


FIGURE 8

Immunohistochemistry and immunofluorescence analysis for PTGS2, NOS2, TNFα and NF-κB p65. MOD, mean optical density. All images are displayed at  $\times 400$  magnification. Data are presented as mean  $\pm$  SD. ( $n = 3$  in each group). \* $p < 0.05$  and \*\* $p < 0.01$ .

promote the expression of inflammation-related genes mainly by activating the NF-κB pathway. (Hayden and Ghosh, 2011; Gilmore and Wolenski, 2012). NF-κB plays a critical role in the transcription of multiple inflammatory mediators. It is usually inactive in the form of p50/P65 dimer binding to its inhibitor kappaB (IκB) (Oeckinghaus et al., 2011). NF-κB can be activated by a variety of intracellular and extracellular stimuli, such as viruses, oxygen free radicals, and various cytokines (Lawrence, 2009; Oeckinghaus and Ghosh, 2009). Among them, TNF family cytokines are considered to be the best-characterized inducers of NF-κB (Ciuffa et al., 2017). Upon

stimulation, IκB kinase is activated, resulting in the degradation of IκB protein and the release of NF-κB dimers. NF-κB dimers are then transferred into the nucleus to facilitate transcription of the target genes, such as iNOS, TNFα, COX-2 and IL-1β (Surh et al., 2001; Kim et al., 2009; Abdelhamid et al., 2020; Yu et al., 2020). Some of these inflammatory factors can bind to cell membrane receptors and reactivate NF-κB signaling (Figure 9).

Previous studies have suggested that TNF/NF-κB pathway and its downstream inflammatory mediators may be effective targets for alleviating chemotherapy-induced mucositis. For example, Yuan et al.



## 5 Conclusion

## Data availability statement

## Ethics statement

## Author contributions

YW and SL contributed to conception and design of the study. QM designed and directed the network pharmacology research strategy. Y-FL, F-LL, S-ST, YY, SW, and T-YJ implemented the methods of the study. YW supervised and directed the execution of the research. Y-FL, F-LL, S-ST completed the collation and statistical analysis of the experimental data and wrote the first draft of the manuscript. YW, SL, and J-WH wrote the final manuscript. All authors contributed to manuscript revision, read, and approved the submitted version.

## Funding

This study was supported by the Natural Science Foundation of Science and Technology Department of Sichuan Province (2022NSFSC1440, 2021JDR0156), the National College Students' innovation and entrepreneurship training program (201813705028), Sichuan Province College Students' Innovation and Entrepreneurship Training Program (S201913705090, 202113705021).

## Conflict of interest

The authors declare that the research was conducted in the absence of any commercial or financial relationships that could be construed as a potential conflict of interest.

## References

- Abdelhamid, A. M., Elsheekh, A. R., Abdelaziz, R. R., and Suddek, G. M. (2020). Empagliflozin ameliorates ethanol-induced liver injury by modulating NF- $\kappa$ B/Nrf-2/PPAR- $\gamma$  interplay in mice. *Life Sci.* 256, 117908. doi:10.1016/j.lfs.2020.117908
- Aihaiti, Y., Song Cai, Y., Tuerhong, X., Ni Yang, Y., Ma, Y., Shi Zheng, H., et al. (2021). Therapeutic effects of naringin in rheumatoid arthritis: Network pharmacology and experimental validation. *Front. Pharmacol.* 12, 672054. doi:10.3389/fphar.2021.672054
- Ali, J., Khan, A. U., Shah, F. A., Ali, H., Islam, S. U., Kim, Y. S., et al. (2019). Mucoprotective effects of Saikosaponin-A in 5-fluorouracil-induced intestinal mucositis in mice model. *Life Sci.* 239, 116888. doi:10.1016/j.lfs.2019.116888
- Alqahtani, Y. S. (2021). Bioactive stigmastadienone from isodon rugosus as potential anticholinesterase,  $\alpha$ -glucosidase and COX/LOX inhibitor: *In-vitro* and molecular docking studies. *Steroids* 172, 108857. doi:10.1016/j.steroids.2021.108857
- Amberger, J. S., Bocchini, C. A., Schiettecatte, F., Scott, A. F., and Hamosh, A. (2015). OMIM.org: Online Mendelian Inheritance in Man (OMIM®), an online catalog of human genes and genetic disorders. *Nucleic Acids Res.* 43, D789–D798. doi:10.1093/nar/gku1205
- Atiq, A., Shal, B., Naveed, M., Khan, A., Ali, J., Zeeshan, S., et al. (2019). Diadzein ameliorates 5-fluorouracil-induced intestinal mucositis by suppressing oxidative stress and inflammatory mediators in rodents. *Eur. J. Pharmacol.* 843, 292–306. doi:10.1016/j.ejphar.2018.12.014
- Barbosa, S., Pereira, V., Wong, D., Santana, A., Lucetti, L. T., Carvalho, L. L., et al. (2019). Amifostine reduces inflammation and protects against 5-fluorouracil-induced oral mucositis and hyposalivation. *Braz. J. Med. Biol. Res. = Revista brasileira de pesquisas medicas e Biol.* 52 (3), e8251. doi:10.1590/1414-431X20188251
- Chang, C. T., Ho, T. Y., Lin, H., Liang, J. A., Huang, H. C., Li, C. C., et al. (2012). 5-Fluorouracil induced intestinal mucositis via nuclear factor- $\kappa$ B activation by transcriptomic analysis and *in vivo* bioluminescence imaging. *PLoS one* 7 (3), e31808. doi:10.1371/journal.pone.0031808
- Chu, W. M. (2013). Tumor necrosis factor. *Cancer Lett.* 328 (2), 222–225. doi:10.1016/j.canlet.2012.10.014
- Ciuffa, R., Caron, E., Leitner, A., Uliana, F., Gstaiger, M., and Aebersold, R. (2017). Contribution of mass spectrometry-based proteomics to the understanding of TNF- $\alpha$  signaling. *J. Proteome Res.* 16 (1), 14–33. doi:10.1021/acs.jproteome.6b00728
- Du, F., Gesang, Q., Cao, J., Qian, M., Ma, L., Wu, D., et al. (2016). Isoliquiritigenin attenuates atherogenesis in apolipoprotein E-deficient mice. *Int. J. Mol. Sci.* 17 (11), 1932. doi:10.3390/ijms17111932
- Du, H., Shi, H., Chen, D., Zhou, Y., and Che, G. (2015). Cross-talk between endothelial and tumor cells via basic fibroblast growth factor and vascular endothelial growth factor signaling promotes lung cancer growth and angiogenesis. *Oncol. Lett.* 9 (3), 1089–1094. doi:10.3892/ol.2015.2881
- Fan, Z., Chen, J., Yang, Q., and He, J. (2022). Network pharmacology and experimental validation to reveal the pharmacological mechanisms of chongcaoyishen decoction against chronic kidney disease. *Front. Mol. Biosci.* 9, 847812. doi:10.3389/fmolb.2022.847812
- Gilmore, T. D., and Wolenski, F. S. (2012). NF- $\kappa$ B: Where did it come from and why? *Immunol. Rev.* 246 (1), 14–35. doi:10.1111/j.1600-065X.2012.01096.x
- Hayden, M. S., and Ghosh, S. (2011). NF- $\kappa$ B in immunobiology. *Cell Res.* 21 (2), 223–244. doi:10.1038/cr.2011.13
- Huang, R., Ai, G., Zhong, L., Mai, L., Chen, J. N., Liu, Y., et al. (2022). Protective effects of oxyberberine in 5-fluorouracil-induced intestinal mucositis in the mice model. *Evid. Based. Complement. Altern. Med.* 2022, 1238358. doi:10.1155/2022/1238358
- Jin, H., Seo, G. S., and Lee, S. H. (2018). Isoliquiritigenin-mediated p62/SQSTM1 induction regulates apoptotic potential through attenuation of caspase-8 activation in colorectal cancer cells. *Eur. J. Pharmacol.* 841, 90–97. doi:10.1016/j.ejphar.2018.10.015
- Justino, P., Franco, A. X., Pontier-Bres, R., Monteiro, C., Barbosa, A., Souza, M., et al. (2020). Modulation of 5-fluorouracil activation of toll-like/MyD88/NF- $\kappa$ B/MAPK pathway by *Saccharomyces boulardii* CNCM I-745 probiotic. *Cytokine* 125, 154791. doi:10.1016/j.cyto.2019.154791
- Kato, S., Hayashi, S., Kitahara, Y., Nagasawa, K., Aono, H., Shibata, J., et al. (2015). Saireito (TJ-114), a Japanese traditional herbal medicine, reduces 5-fluorouracil-induced intestinal mucositis in mice by inhibiting cytokine-mediated apoptosis in intestinal crypt cells. *PLoS one* 10 (1), e0116213. doi:10.1371/journal.pone.0116213
- Kim, J. Y., Park, S. J., Yun, K. J., Cho, Y. W., Park, H. J., and Lee, K. T. (2008). Isoliquiritigenin isolated from the roots of *Glycyrrhiza uralensis* inhibits LPS-induced iNOS and COX-2 expression via the attenuation of NF- $\kappa$ B in RAW 264.7 macrophages. *Eur. J. Pharmacol.* 584 (1), 175–184. doi:10.1016/j.ejphar.2008.01.032
- Kim, Y. H., Kim, D. H., Lim, H., Baek, D. Y., Shin, H. K., and Kim, J. K. (2009). The anti-inflammatory effects of methylsulfonylmethane on lipopolysaccharide-induced inflammatory responses in murine macrophages. *Biol. Pharm. Bull.* 32 (4), 651–656. doi:10.1248/bpb.32.651
- Lawal, B., Lee, C. Y., Mokgautsi, N., Sumitra, M. R., Khedkar, H., Wu, A., et al. (2021). mTOR/EGFR/iNOS/MAP2K1/FGFR/TGFB1 are druggable candidates for N-(2, 4-difluorophenyl)-2', 4'-difluoro-4-hydroxybiphenyl-3-carboxamide (NSC765598), with consequent anticancer implications. *Front. Oncol.* 11, 656738. doi:10.3389/fonc.2021.656738
- Lawrence, T. (2009). The nuclear factor NF- $\kappa$ B pathway in inflammation. *Cold Spring Harb. Perspect. Biol.* 1 (6), a001651. doi:10.1101/cshperspect.a001651
- Liao, Y., Tan, R. Z., Li, J. C., Liu, T. T., Zhong, X., Yan, Y., et al. (2020). Isoliquiritigenin attenuates UUO-induced renal inflammation and fibrosis by inhibiting mTOR/syk/NF- $\kappa$ B signaling pathway. *Drug Des. devel. Ther.* 14, 1455–1468. doi:10.2147/DDDT.S243420
- Martin, A., Ochagavia, M. E., Rabasa, L. C., Miranda, J., Fernandez-de-Cossio, J., and Bringas, R. (2010). BisoGenet: A new tool for gene network building, visualization and analysis. *BMC Bioinforma.* 11, 91. doi:10.1186/1471-2105-11-91
- McQuade, R. M., Stojanovska, V., Donald, E., Abalo, R., Bornstein, J. C., and Nurgali, K. (2016). Gastrointestinal dysfunction and enteric neurotoxicity following treatment with anticancer chemotherapeutic agent 5-fluorouracil. *Neurogastroenterol. Motil.* 28 (12), 1861–1875. doi:10.1111/nmo.12890

## Publisher's note

All claims expressed in this article are solely those of the authors and do not necessarily represent those of their affiliated organizations, or those of the publisher, the editors and the reviewers. Any product that may be evaluated in this article, or claim that may be made by its manufacturer, is not guaranteed or endorsed by the publisher.

## Supplementary material

The Supplementary Material for this article can be found online at: <https://www.frontiersin.org/articles/10.3389/fphar.2022.1014160/full#supplementary-material>

- Oeckinghaus, A., and Ghosh, S. (2009). The NF-kappaB family of transcription factors and its regulation. *Cold Spring Harb. Perspect. Biol.* 1 (4), a000034. doi:10.1101/cshperspect.a000034
- Oeckinghaus, A., Hayden, M. S., and Ghosh, S. (2011). Crosstalk in NF- $\kappa$ B signaling pathways. *Nat. Immunol.* 12 (8), 695–708. doi:10.1038/ni.2065
- Oliveira, M., de Araújo, A. A., Ribeiro, S. B., de Sales Mota, P., Marques, V. B., da Silva Martins Rebouças, C., et al. (2021). Losartan improves intestinal mucositis induced by 5-fluorouracil in mice. *Sci. Rep.* 11 (1), 23241. doi:10.1038/s41598-021-01969-x
- Panchenko, A. V., Fedoros, E. I., Pigarev, S. E., Maydin, M. A., Gubareva, E. A., Yurova, M. N., et al. (2018). Effect of the polyphenol composition BP-C3 on haematological and intestinal indicators of 5-fluorouracil toxicity in mice. *Exp. Ther. Med.* 15 (3), 3124–3132. doi:10.3892/etm.2018.5782
- Peng, F., Du, Q., Peng, C., Wang, N., Tang, H., Xie, X., et al. (2015). A review: The pharmacology of Isoliquiritigenin. *Phytother. Res.* 29 (7), 969–977. doi:10.1002/ptr.5348
- Piñero, J., Bravo, A., Queralt-Rosinach, N., Gutiérrez-Sacristán, A., Deu-Pons, J., Centeno, E., et al. (2017). DisGeNET: A comprehensive platform integrating information on human disease-associated genes and variants. *Nucleic Acids Res.* 45 (D1), D833–D839. doi:10.1093/nar/gkw943
- Ribeiro, S. B., de Araújo, A. A., Araújo Júnior, R. F., Brito, G., Leitão, R. C., Barbosa, M. M., et al. (2017). Protective effect of dexamethasone on 5-FU-induced oral mucositis in hamsters. *PloS one* 12 (10), e0186511. doi:10.1371/journal.pone.0186511
- Shao, L. (2021). Network pharmacology evaluation method guidance-draft. *World J. Tradit. Chin. Med.* 7 (01), 148–166+146154. doi:10.4103/wjtcn.wjtcn\_11\_21
- Shi, P., Zhao, T., Wang, W., Peng, F., Wang, T., Jia, Y., et al. (2022). Protective effect of homogeneous polysaccharides of Wuguchong (HPW) on intestinal mucositis induced by 5-fluorouracil in mice. *Nutr. Metab.* 19 (1), 36. doi:10.1186/s12986-022-00669-1
- Soares, P. M., Mota, J. M., Souza, E. P., Justino, P. F., Franco, A. X., Cunha, F. Q., et al. (2013). Inflammatory intestinal damage induced by 5-fluorouracil requires IL-4. *Cytokine* 61 (1), 46–49. doi:10.1016/j.cyto.2012.10.003
- Surh, Y. J., Chun, K. S., Cha, H. H., Han, S. S., Keum, Y. S., Park, K. K., et al. (2001). Molecular mechanisms underlying chemopreventive activities of anti-inflammatory phytochemicals: Down-regulation of COX-2 and iNOS through suppression of NF-kappa B activation. *Mutat. Res.* 480–481, 243–268. doi:10.1016/s0027-5107(01)00183-x
- Tang, Y., Wang, C., Wang, Y., Zhang, J., Wang, F., Li, L., et al. (2018). Isoliquiritigenin attenuates LPS-induced AKI by suppression of inflammation involving NF- $\kappa$ B pathway. *Am. J. Transl. Res.* 10 (12), 4141–4151.
- Trott, O., and Olson, A. J. (2010). AutoDock Vina: Improving the speed and accuracy of docking with a new scoring function, efficient optimization, and multithreading. *J. Comput. Chem.* 31 (2), 455–461. doi:10.1002/jcc.21334
- Wang, K. L., Yu, Y. C., and Hsia, S. M. (2021). Perspectives on the role of Isoliquiritigenin in cancer. *Cancers* 13 (1), 115. doi:10.3390/cancers13010115
- Wang, R. X., Wu, L., Chen, S. F., Li, Z. Y., Zhao, M. H., and Chen, M. (2022). Renal expression of annexin A1 is associated with the severity of renal injury in antineutrophil cytoplasmic autoantibody-associated vasculitis. *Front. Med.* 9, 769813. doi:10.3389/fmed.2022.769813
- Wu, C. H., Chen, H. Y., Wang, C. W., Shieh, T. M., Huang, T. C., Lin, L. C., et al. (2016a). Isoliquiritigenin induces apoptosis and autophagy and inhibits endometrial cancer growth in mice. *Oncotarget* 7 (45), 73432–73447. doi:10.18632/oncotarget.12369
- Wu, M., Wu, Y., Deng, B., Li, J., Cao, H., Qu, Y., et al. (2016b). Isoliquiritigenin decreases the incidence of colitis-associated colorectal cancer by modulating the intestinal microbiota. *Oncotarget* 7 (51), 85318–85331. doi:10.18632/oncotarget.13347
- Xing, F., Chen, C., Wang, C., and Lou, J. (2015). Explore the function of gancao xiexin decoction in the prevention and treatment of 5-fu related mucositis. *J. Liaoning Univ. Traditional Chin. Med.* 17 (09), 125–127. doi:10.13194/j.issn.1673-842x.2015.09.043
- Yan, X. X., Li, H. L., Zhang, Y. T., Wu, S. Y., Lu, H. L., Yu, X. L., et al. (2020). A new recombinant MS-superoxide dismutase alleviates 5-fluorouracil-induced intestinal mucositis in mice. *Acta Pharmacol. Sin.* 41 (3), 348–357. doi:10.1038/s41401-019-0295-8
- Yang, R., Yuan, B. C., Ma, Y. S., Zhou, S., and Liu, Y. (2017). The anti-inflammatory activity of licorice, a widely used Chinese herb. *Pharm. Biol.* 55 (1), 5–18. doi:10.1080/13880209.2016.1225775
- Yeung, C. Y., Chan, W. T., Jiang, C. B., Cheng, M. L., Liu, C. Y., Chang, S. W., et al. (2015). Amelioration of chemotherapy-induced intestinal mucositis by orally administered probiotics in a mouse model. *PloS one* 10 (9), e0138746. doi:10.1371/journal.pone.0138746
- Yu, H., Lin, L., Zhang, Z., Zhang, H., and Hu, H. (2020). Targeting NF- $\kappa$ B pathway for the therapy of diseases: Mechanism and clinical study. *Signal Transduct. Target. Ther.* 5 (1), 209. doi:10.1038/s41392-020-00312-6
- Yuan, K. T., Yu, H. L., Feng, W. D., Chong, P., Yang, T., Xue, C. L., et al. (2015). Bifidobacterium infantis has a beneficial effect on 5-fluorouracil-induced intestinal mucositis in rats. *Benef. Microbes* 6 (1), 113–118. doi:10.3920/BM2013.0095
- Zhang, L., Jin, Y., Peng, J., Chen, W., Lisha, L., and Lin, J. (2019). Qingjie Fuzheng Granule attenuates 5-fluorouracil-induced intestinal mucosal damage. *Biomed. Pharmacother. = Biomedicine Pharmacother.* 118, 109223. doi:10.1016/j.biopha.2019.109223
- Zhang, Z., Chen, W. Q., Zhang, S. Q., Bai, J. X., Liu, B., Yung, K. K., et al. (2022). Isoliquiritigenin inhibits pancreatic cancer progression through blockade of p38 MAPK-regulated autophagy. *Phytomedicine*. 106, 154406. Advance online publication. doi:10.1016/j.phymed.2022.154406
- Zhao, H., Zhang, X., Chen, X., Li, Y., Ke, Z., Tang, T., et al. (2014). Isoliquiritigenin, a flavonoid from licorice, blocks M2 macrophage polarization in colitis-associated tumorigenesis through downregulating PGE2 and IL-6. *Toxicol. Appl. Pharmacol.* 279 (3), 311–321. doi:10.1016/j.taap.2014.07.001
- Zhao, T. T., Xu, Y. Q., Hu, H. M., Gong, H. B., and Zhu, H. L. (2019). Isoliquiritigenin (ISL) and its formulations: Potential antitumor agents. *Curr. Med. Chem.* 26 (37), 6786–6796. doi:10.2174/092986732566618112091700
- Zhu, B., Zhang, W., Lu, Y., Hu, S., Gao, R., Sun, Z., et al. (2018). Network pharmacology-based identification of protective mechanism of Panax Notoginseng Saponins on aspirin induced gastrointestinal injury. *Biomed. Pharmacother. = Biomedicine Pharmacother.* 105, 159–166. doi:10.1016/j.biopha.2018.04.054





## OPEN ACCESS

EDITED BY  
Ren-You Gan,  
Technology and Research, Singapore

REVIEWED BY  
Giovanna Baron,  
University of Milan, Italy  
Mingquan Guo,  
Wuhan Botanical Garden (CAS), China

\*CORRESPONDENCE  
Jun Han,  
729229056@qq.com

SPECIALTY SECTION  
This article was submitted to  
Ethnopharmacology,  
a section of the journal  
Frontiers in Pharmacology

RECEIVED 09 August 2022  
ACCEPTED 21 November 2022  
PUBLISHED 01 December 2022

CITATION  
Xiahou Z and Han J (2022), Effects of  
dehydroabiatic acid on nontarget  
lipidomics and proteomics of HepG2.  
*Front. Pharmacol.* 13:1015240.  
doi: 10.3389/fphar.2022.1015240

COPYRIGHT  
© 2022 Xiahou and Han. This is an  
open-access article distributed under  
the terms of the [Creative Commons  
Attribution License \(CC BY\)](#). The use,  
distribution or reproduction in other  
forums is permitted, provided the  
original author(s) and the copyright  
owner(s) are credited and that the  
original publication in this journal is  
cited, in accordance with accepted  
academic practice. No use, distribution  
or reproduction is permitted which does  
not comply with these terms.

# Effects of dehydroabiatic acid on nontarget lipidomics and proteomics of HepG2

Zhikai Xiahou<sup>1</sup> and Jun Han<sup>2,3\*</sup>

<sup>1</sup>China Institute of Sport and Health Science, Beijing Sport University, Beijing, China, <sup>2</sup>Beijing Tcmages Pharmaceutical Co.Ltd., Beijing, China, <sup>3</sup>Beijing Kangrentang Pharmaceutical Co.,Ltd., Beijing, China

**Objective:** Studies of the effects of dehydroabiatic acid on the multiomics of HepG2 hepatoma carcinoma cells are currently lacking. In this study, the molecular mechanism of the influence of dehydroabiatic acid on HepG2 cells was disclosed by studying lipidomics and proteomics. Correlations among multiomics conjoint analysis results were verified.

**Methods:** First, proteomics analysis of HepG2 cells was carried out using dehydroabiatic acid. Differentially expressed proteins were screened and analyzed. Pathway enrichment analyses of differential proteins were compared, and the molecular mechanism was disclosed. Second, lipidomics analysis of HepG2 cells was conducted using dehydroabiatic acid. The influence of dehydroabiatic acid on HepG2 cells was determined on the lipid molecular level. Finally, a conjoint analysis of data related to differentially expressed proteins of ferroptosis and differentially changing lipid molecules was implemented.

**Results:** A total of 260 upregulated and 961 downregulated proteins were screened in the proteomics analysis. The top five significantly enriched pathways included ferroptosis, oxidative phosphorylation, and protein processing in the endoplasmic reticulum. In the lipidomics analysis, 30 significantly differential metabolites with upregulated and downregulated expression were identified, and differentially expressed lipids were mainly related to the metabolism of glyceryl phosphatide. According to the comprehensive multiomics analysis results, real-time quantitative PCR and the enzyme-linked immunosorbent assay (ELISA), ACSL3 participated in cardiolipin metabolism.

**Conclusion:** Dehydroabiatic acid influences HepG2 cells through the above biological pathways.

## KEYWORDS

dehydroabiatic acid, liver cancer, proteomics, lipidomics, ACSL3

## 1 Highlights

- 1) Proteomics analysis of HepG2 cells after administration of dehydroabiatic acid
- 2) Lipidomics analysis of HepG2 cells after administration of dehydroabiatic acid
- 3) ACSL3 participates in cardiolipin metabolism

## 2 Introduction

Liver cancer is one of the most common cancers worldwide. In recent years, the incidence of liver cancer has shown an increasing tendency each year, becoming a malignant tumor disease with high mortality (Shi et al., 2021). Treatment of liver cancer is limited, and the main effective treatment method is surgical resection supplemented by chemotherapy and radiotherapy. Postoperative tumor recurrence continues to seriously affect the survival of patients (Orcutt and Anaya, 2018; Sun et al., 2021). Therefore, the identification of effective anti-liver cancer drugs has important clinical value and social significance. Dehydroabietic acid is the main compound of rosin, derived from conifers such as spruce, larch and fir (Zhu et al., 2014). Dehydroabietic acid has anti-inflammatory biological activities. For instance, through the dual activation of PPAR- $\gamma$  and PPAR- $\alpha$ , dehydroabietic acid reduces insulin resistance and hepatic steatosis induced by a high-fat diet (Xie et al., 2020); it reduces iron death in nonalcoholic fatty liver disease by activating the Keap1/Nrf2-ARE signaling pathway (Gao et al., 2021). In the laboratory, we found that dehydroabietic acid can inhibit the growth of liver cancer cells, and we successfully screened out the genes that affect the treatment of dehydroabietic acid in the treatment of liver cancer and the genes related to cell anxiety death, based on which we established a survival line map (Han and Zhang, 2021). The potential objective and pathway of dehydroabietic acid in hepatic carcinoma have rarely been studied, and the potential molecular mechanisms remain unknown. Since the *in vivo* action of dehydroabietic acid is extremely complicated, traditional analytical methods have experienced difficulty disclosing its effective mechanism. With the rapid development of bioinformatics and systematic biology, proteomics is used as a new powerful method to disclose the complicated mechanism of drugs involving biochemical processes of disease progression. It can provide guidance for the early diagnosis, treatment and prognosis of diseases (Monti et al., 2019). Additionally, overall treatment has been one of the most critical clinical strategies, and proteomics can provide multitarget predictions (KhalKhal et al., 2019). Hence, new network science using proteomics can reveal the mechanism of action of dehydroabietic acid in inhibiting hepatic carcinoma. In addition, lipid metabolomics is a technology used to study all intermediate and final products of lipid metabolism in organic bodies and combines bioinformatics analysis. It is characterized by high throughput, high accuracy, high sensitivity, and low cost (Liu and Xu, 2018). Recently, lipid metabolomics has been used to explore effective metabolites after disease treatment by many drugs to describe the molecular process in the mechanism of drug action. It is a special effective method and can screen key metabolic pathways effectively from drugs. In this study, key targets and pathways by which dehydroabietic acid inhibits the proliferation of hepatic carcinoma cells were screened and verified by combining proteomics, lipid metabolomics and

bioinformatics analyses. The molecular mechanism of action of dehydroabietic acid in hepatic carcinoma was disclosed. The results provide scientific references to develop dehydroabietic acid as a new drug for hepatic carcinoma.

## 3 Materials

### 3.1 Experimental materials

Dehydroabietic acid standard (batch number: PCS-210816) was purchased from Chengdu Plant Standard Pure Biotechnology Co., Ltd. Methyl alcohol, acetonitrile, methyl tertiary butyl ether, ammonium formate and dichloromethane for LC-MS were purchased from CNW Technologies, and isopropanol was purchased from Fisher Chemical. Urea, dithiothreitol (DTT), Tris, iodoacetamide (IAA), formic acid and ammonium hydroxide were purchased from Sigma. Trypsin was purchased from Promega. Acetonitrile and water for LC-MS were purchased from Thermo. A BCA protein concentration assay kit and protease inhibitor were purchased from Beyotime Biotechnology. The ultrafiltration centrifugation column (10 kD) was purchased from PALL (United States). Other reagents were analytically pure and made in China. Fetal calf serum, streptomycin/penicillin and pancreatin were purchased from Gibco. The Lipofectamine™ 3000 transfection reagent was purchased from Thermo Fisher (Article No.: L3000015). The human cardiolipin ELISA kit was purchased from EK Bioscience (Article No.: EK-H11830). The reverse transcription reagents were purchased from Nanjing Novizan Co. LTD (Article No.: R323-01). The real-time quantitative PCR reagent was purchased from Nanjing Novizan Co., Ltd. (Article No.: Q311-03). The internal standard substance was 15:0–18:1-d7-PE is the internal standard substances.

HepG2 cells were purchased from the cell bank of Chinese Academy of Sciences, and dehydroabietic acid (batch No.: 210816) was purchased from Chengdu Purechem-standard Co., Ltd. TFRC antibody (Article No.: ab214039), ACACA antibody (Article No.: Ab45174) and CRLS1 antibody (Article No.: A12388, abclonal) were purchased from Abcam Company.  $\beta$ -actin (A5441) was purchased from Sigma. TRIzol was purchased from ThermoFisher Scientific Co., Ltd. HiScript Q Select RT SuperMix for qPCR and qPCR SYBR Green Master Mix were purchased from Nanjing Vazyme Biotech Co., Ltd.

### 3.2 Experimental apparatus

Vanquish ultrahigh-performance liquid chromatography, Q Exactive HFX high-resolution mass spectrometry and a Heraeus Fresco17 centrifugal machine were purchased from Thermo Fisher Scientific. The BSA124S-CW balance was purchased from Sartorius. The JXFSTPRP-24 grinding mill was

purchased from Shanghai Jingxin Technology Co., Ltd. The YM-080S ultrasonic apparatus was purchased from Shenzhen Fangao Microelectronics Co., Ltd. Other experimental apparatuses included the EASY-nLC 1000 liquid chromatogram (Thermo, United States), Thermo Orbitrap Fusion Tribrid mass spectrometer (Thermo, United States), Eppendorf refrigerated centrifuge (Eppendorf, Germany), vacuum freeze drier (Thermo, United States), ultrasonic cell disruptor VCX130 (Sonics, United States), ELISA (MK3 Thermo), and real-time fluorescence quantification PCR instrument (CFX96 Bio-Rad).

The protein electrophoresis system (V140992 Bio-Rad), ECL chemiluminescence detection system (Las-4000 GE), real-time fluorescence quantitative PCR (qPCR) instrument (CFX96 Bio-Rad), and Nanodrop (Nanodrop2000 Thermo) were used.

## 4 Materials and methods

### 4.1 Proteomic and lipidomic cell collection methods

HepG2 cells were divided into 2 groups: the control group and the experimental group (24-h pretreatment with 25 µg/ml dehydroabietic acid), with 3 replicates per group. For the proteome, the suspension cell collection method was adopted; the cells in the logarithmic growth stage were collected into a 15-ml centrifuge tube centrifuged at 1000 g, 4°C, for 5–10 min, and the supernatant was discarded. The cells were washed 3 times with 10 ml PBS. Finally, the cells with 1 ml PBS were resuspended and transferred to a new 1.5-ml centrifuge tube and centrifuged again to remove as much supernatant as possible. Liquid nitrogen was snap-frozen and stored at −80°C for a short period. A previously published report was followed for the lipidomics sample collection method (Sellick et al., 2011).

### 4.2 Proteomics

#### 4.2.1 Protein extraction

Six samples were collected, to which 0.5 ml lysis buffer (8 M urea, 100 mM Tris-HCl pH 7.6, protease inhibitor) was added. After 15 min of ice-bath ultrasound and 15 min of centrifugation at 18000 g, the supernatant was collected. Quantitative analysis was carried out using the BCA method. Each sample was collected (20 µg) and mixed in a pool to build a library. Enzymolysis of six samples and pools was implemented by the FASP (filter-aided sample preparation) method.

#### 4.2.2 Enzymatic digestion of proteins

Protein samples (total protein: 100–500 µg) were collected, to which 50 mM DTT was added according to volume for 40 min at 56°C. The ultrafiltration tube was put into the collection pipe, and the previously diluted protein samples were added into the

ultrafiltration tube and centrifuged for 15 min at a rate of 12000 g. Next, 200 µl of urea buffer was added to the ultrafiltration tube and then centrifuged for 15 min at 12000 g. Later, 100 µl urea buffer containing 50 mM IAA was added to the ultrafiltration tube and incubated for 20 min in the dark. The mixture was centrifuged for 10 min at 12000 g. Next, 100 µl urea buffer was added and centrifuged for 10 min at 12000 g. This process was repeated twice. Later, 100 µl of 50 mM ABC was added to the ultrafiltration tube and centrifuged for 10 min at 12000 g. Then, 80 µl of ABC with 50 mM pancreatin was added (pancreatin:protein = 1:50–1:100). The mixture was oscillated for 1 min, and the ultrafiltration tube was placed into a water bath at 37°C for 16–18 h. The ultrafiltration tube was transferred to a new collection tube and centrifuged for 10 min at 12000 g. Next, 50 µl of ABC was added to the ultrafiltration tube and centrifuged for 10 min at 12000 g. The protein concentration was tested directly by using the nanodrop protein concentration test mode.

### 4.2.3 Library construction of data dependence acquisition

One-dimensional high-pH reversed-phase separation of pooled samples was conducted. The merged peptide fragments were dissolved in 100 µl A-phase solution and centrifuged. The supernatant was collected using an injection syringe and injected into the loading ring. The mixture was separated and collected according to a chromatography gradient: the chromatographic column: Gemini-NX 5µ C18 110A 250 × 4.6 mm (Phenomenex, Guangzhou, China); chromatographic apparatus: Shimadzu LC-20AB HPLC Pump system; A phase: 2% CAN, pH 10; B phase: 98% CAN, pH 10; ultraviolet detection wavelength: 214 nm flow rate: 1000 µl/min; chromatography gradient: 0.1–20 min, 5%→30% B; 20–22 min, 30%→80% B; 22–24 min, 80% B; 24–24.1 min, 80%→5% B. Six components were collected and merged according to peak type and time, followed by vacuum centrifugation concentration (rotation vacuum Christ RVC 2–25, Christ, Germany). In the reversed-phase liquid mass coupling RPLC–MS and DDA analysis, six component samples were collected for LC–MS/MS testing. Polypeptide samples were dissolved into 25 µl A solution (water containing 0.1% formic acid, with iRT standard peptides). A 5-µl sample solution was loaded into the EASY-nano-LC chromatographic system and onto the precolumn at a flow rate of 4.5 µl/min. Next, the mixture was separated on the analytical column at a flow rate of 300 nL/min. The chromatographic separation gradients were as follows: 0–3 min, B solution (acetonitrile containing 0.1% formic acid) increased linearly from 3% to 7%; 3 min–83 min, B solution increased linearly from 7% to 20%; 83–107 min, B solution increased linearly from 20% to 32% and then increased to 90% over 1 min with holding until 120 min. Mass spectrometric data were acquired using an Orbitrap Fusion mass spectrometer (Thermo Scientific). Specific parameters were set as follows: the spray voltage of the ion source was set to 2.1 kV, the cycling time was set to 4 s, and the level-1 scanning

scope was 350–1500  $m/z$ , with a resolution of 60 K (at  $m/z$  200), an AGC target of  $4e5$ , and a maximum IT of 50 ms. The level-2 resolution was 30 K (at  $m/z$  200), with an isolation window of 1.6 Th, AGC target of  $5e4$ , and maximum IT of 120 ms. The MS2 activation was HCD (collision energy: 35).

#### 4.2.4 DIA analysis

Samples of 2  $\mu$ g peptides each were collected. Appropriate amounts of iRT standard peptides were mixed into each sample, and each sample was subjected to DIA mass spectrometry once for 2 h.

#### 4.2.5 Peptide data statistics

DDA original data collected by mass spectrometry were input into Spectronaut Pulsar X (Biognosys Company) for library search analysis. The human protein dataset downloaded from UniProt was used. Parameters for building the library used the default optimal parameters “GBS factory setting”, including a tolerance of MS1 = 10 ppm, tolerance of level-2 pieces = 0.02 Da, and maximum allowable missing number = 2. Cysteine carbamidomethyl was a fixed modification, while oxidation of methionine and N-terminal acetylation of protein were variable modifications. The false-positive rate of the peptide and protein levels was FDR < 0.01, and the independent peptide was at least 1. Next, the DIA original data were input into Spectronaut Pulsar X for qualitative and quantitative protein analysis. Parameters for building the library were introduced as follows: Peptides FDR PSMs FDR Proteins FDR = 1%. At least three peptides were chosen for each type, and at most 6 optimal subions were chosen to produce the library spectra: iRT Calibration Rsquare > 0.8. Quantitative parameter: The iTR standard curve used local (nonlinear) regression. Protein identification utilized a precursor  $Q_{\text{value}}$  cutoff = 0.01 and protein  $Q_{\text{value}}$  cutoff = 0.01. A kernel density estimator was applied for  $p$ -value calibration. Protein quantification used the subion peak area, and the average strength quantification of at least 3 subions was chosen.

#### 4.2.6 Differential protein expression

Statistical analysis of protein expression data is needed after completing protein expression quantification. Significantly differentially expressed proteins under different states were screened. The fold changes in protein in different comparison groups were calculated, and significance was examined by the Welch's  $t$  test. Therefore, significantly expressed proteins ( $FC \geq 1.5$  and  $p \leq 0.05$ ) were screened. Finally, enrichment analysis of different proteins was performed.

### 4.3 Nontarget lipidomics experiment

#### 4.3.1 Extraction of metabolites

Water (400  $\mu$ l) was added to the samples and mixed uniformly in a vortex for 30 s. The mixture was placed in a liquid nitrogen tank and frozen for 1 min. Later, the mixture was

removed and thawed. These procedures were repeated 2–3 times, followed by 10 min of ice water bath ultrasound. Next, 960  $\mu$ l extraction solution (MTBE: MeOH = 5:1, containing IS) was added to the mixture and then mixed uniformly in a vortex for 30 s, followed by 10 min of ice water bath ultrasound. The mixture was kept static for 1 h at  $-40^{\circ}\text{C}$ . Samples were centrifuged for 15 min at  $4^{\circ}\text{C}$  at a rate of 3000 rpm (centrifugal force of 900  $\times g$ ). The supernatant (600  $\mu$ l) was collected and placed in an EP tube, dried under vacuum, and added to 200  $\mu$ l of solution (DCM:MeOH = 1:1) for redissolving. The mixture was mixed by vortexing for 30 s, followed by 10 min of ice water bath ultrasound. Samples were centrifuged for 15 min at  $4^{\circ}\text{C}$  at a rate of 13000 rpm (centrifugal force 16200  $\times g$ ). A total of 75  $\mu$ l supernatant was collected into a loading bottle for testing.

#### 4.3.2 LC–MS/MS analysis

In this study, the chromatograph of target compounds was implemented by using a Vanquish (Thermo Fisher Scientific) ultrahigh-performance liquid chromatograph and Waters ACQUITY UPLC HSST3 (2.1  $\times$  100 mm, 1.8  $\mu$ m) liquid chromatograph. The liquid chromatogram A-phase consisted of a solution containing 40% water and 60% acetonitrile, which also contained 10 mmol/L ammonium formate. The B-phase consisted of a solution containing 10% acetonitrile and 90% isopropanol. A total of 50 ml of a 10 mmol/L ammonium formate aqueous solution was added to the B-phase every 1000 ml. Gradient elution was applied: 0–1.0 min, 40% B; 1.0–12.0 min, 40%–100% B; 12.0–13.5 min, 100% B; 13.5–13.7 min, 100%–40% B; 13.7–18.0 min, 40% B. The flow rate of the moving phase was 0.3 ml/min, the column temperature was  $55^{\circ}\text{C}$ , the sample plate temperature was  $4^{\circ}\text{C}$ , and the sampling volume was 2  $\mu$ L for positive ions and 2  $\mu$ l for negative ions.

Thermo Q Exactive HFX mass spectrometry could achieve level-1 and level-2 mass spectrometric data acquisition under the management of the controlling software (Xcalibur, Version 4.0.27, Thermo). Detailed parameters were introduced as follows: sheath gas flow rate of 30 Arb, aux gas flow rate of 10 Arb, capillary temperature of  $350^{\circ}\text{C}$ , full MS resolution of 120000, MS/MS resolution of 7500, collision energy of 10/30/60 in NCE mode, and spray voltage of 4 kV (positive) or  $-3.8$  kV (negative).

#### 4.3.3 Data processing

The original format of mass spectra was transformed into the mzXML format using ProteoWizard. Next, XCMS was applied for retention time correction, peak recognition, peak extraction, peak integral and peak alignment. Minfrac and cutoff were set to 0.5 and 0.3, respectively. In this experiment, lipids were identified by using XCMS software, the self-writing R program package and the lipidblast database. SIMCA-P 14.1 software was applied for bioinformatics and statistical analyses.



## 4.4 Omics data conjoint analysis

Differentially expressed genes of ferroptosis and differentially changing lipid molecules were screened by using HepG2 cells under the administration of dehydroabietic acid. Conjoint analysis of relevant data was carried out, and ggPlot 2 using R packets with the Spearman statistical method was applied.

## 4.5 ACSL3 participates in cardiolipin metabolism

### 4.5.1 Cell culture

HepG2 cells were cultured in high-glucose DMEM containing 10% FBS, 100 U/mL penicillin and 100 µg/ml streptomycin. The conditions of the incubator were 37°C and 5% CO<sub>2</sub>.

### 4.5.2 Construction of ACSL3 knockdown cell lines

HepG2 cells were inoculated into 6-well plates at a density of  $4 \times 10^4$  cells/mL and then cultured overnight until they adhered to the walls. On the second day, siNC and siACSL3 were transfected into cells using Lipofectamine™ 3000 transfection reagent. Specific experimental steps and dosages referred to the specification. After transfection for 6 h, the medium was changed to fresh complete culture media to culture cells continuously. After transfection for 24 h, cell samples were collected and tested. The siRNA sequences were as follows:

siACSL3-1-FP: 5'-GCCUCAGAUUUGCAGUAAU-3',  
 siACSL3-1-RP: 5'-AUUACUGCAAUAUCUGAGGGC-3';  
 siACSL3-2-FP: 5'-GCGGACAUGAGCGAAUGUAU-3',  
 siACSL3-2-RP: 5'-AUACAUCGCUCAAUGUCCGC-3';  
 siACSL3-3-FP: 5'-CCUGGAUGUGAUACUUUAGAU-3',  
 siACSL3-3-RP: 5'-AUCUAAAGUAUCACAUCAGG-3'.

### 4.5.3 Real-time quantitative PCR experiment

After RNA extraction, a reverse transcription experiment was carried out according to the manufacturer's instructions. The RNA volume for reverse transcription was 1 µg. The reverse transcription cDNA was added to an appropriate volume of ddH<sub>2</sub>O and then diluted twice. Real-time fluorescence quantitative PCR of reverse transcription cDNA was carried out with reference to the specifications of reagents from Nanjing Novizan Co., Ltd. The primer sequences were as follows:

ACSL3-F: TCCTGTTGGTCAGGGATACG;  
 ACSL3-R: ATCCACCTTCCTCCCAGTTT.  
 GAPDH-F: GGACTCATGACCACAGTCCA;  
 GAPDH-R: TCAGCTCAGGGATGACCTTG.

### 4.5.4 Enzyme-linked immunosorbent assay

Cell supernatants and broken cell lysis buffer of the siNC group and siACSL3 group were collected. The cardiolipin

content in these cells was tested using a Human Cardiolipin ELISA kit with reference to the specifications.

## 4.6 CCK8 cell proliferation test

Dehydroabietic acid was fully weighed and dissolved in DMSO to prepare a 10 mg/ml stock solution. Dehydroabietic acid was diluted to final concentrations (0, 3.125, 6.25, 12.5, 25, 50, 100, 200, 400, and 800 µg/ml) with complete medium. DMSO was used as the control group.

Cells in the logarithmic phase were inoculated into a 96-well plate, with 5000 cells per hole. The 96-well plate was cultivated in an incubator overnight, and then the culture medium was removed. Media with different concentrations of drugs were added to each experimental group and cultivated for 24 h continuously. Three parallel wells were created for each group. DMSO of the corresponding volume was added to the media and used as the blank control group. After treatment, 10% CCK8 solution (10 µl CCK8/100 µl media) was added to each well. Cells were cultivated in an incubator at 37°C for 1 h, and the absorbance at 450 nm was determined by ELISA.

## 4.7 Bioinformatics analysis of ferroptosis-related genes

### 4.7.1 Protein–protein interaction network analysis

Differential proteins were input into the STRING (<https://string-db.org/>) database for protein–protein interaction (PPI) analysis. The confidence interval was chosen as 0.4, and visual analysis was carried out using Cytoscape software. The top 6 genes were recognized by the Degree algorithm of the CytoHubba plug-in in Cytoscape, and they were defined as the Hub genes in the present study.

### 4.7.2 Differential expression analysis of hub genes in hepatic carcinoma and normal tissues

The hepatic carcinoma (HCC) RNA-Seq dataset was downloaded from the TCGA database. Later, the differential expression of hub genes at the transcriptional level in normal tissues and hepatic carcinoma tissues was analyzed by two-sample t-tests.

### 4.7.3 Hub gene expression and clinicopathologic data analysis

Clinical data of patients with HCC were downloaded from the TCGA database. The inclusion criteria were as follows: 1) patients with primary HCC (recurrent HCC excluded); 2) complete clinicopathologic features; 3) available RNA-seq data; and 4) OS set as the major endpoint. The exclusion

criteria were as follows: 1) patients who had HCC recurrence according to pathological diagnosis; 2) patients with tumors other than HCC; and 3) missing survival information and clinical pathological parameters. First, patients were divided into a high-expression group and a low-expression group according to the medians of Hub gene expression and assessed by the Kaplan–Meier survival map. Additionally, the relationships of Hub gene expression with the survival and prognosis of patients with HCC were analyzed by the 95% confidence interval of the hazard ratio (HR) and based on the *p*-value of the log-rank test (log-rank *P*). Furthermore, the differential expression of hub genes in different pathological stages was analyzed.

#### 4.7.4 Single-gene GSEA

The hallmark gene set in the MSigDB on the GSEA (<https://www.gsea-msigdb.org/gsea/index.jsp>) website was used as the reference gene set. The potential effect pathways of Hub genes in HCC development were analyzed by the default weighted enrichment statistical method. RNA-seq data samples of patients with HCC were divided into high-expression and low-expression groups according to medians of Hub gene expression. The pathways with an adjusted *p*-value < 0.05, FDR < 0.25 and NES absolute ≥ 1 were considered significantly enriched.

### 4.8 Molecular docking of dehydroabietic acid with CRLS1, ACACA and TFRC

CRLS1 is one of the key enzymes in the synthesis of cardiolipin, and it can accelerate the energy consumption of adipocytes (Sustarsic et al., 2018). Acetyl-CoA carboxylase (ACC) is a key enzyme in fatty acid synthesis (Chen et al., 2019). TFRC can bind with transferrin, which carries free iron and is the key protein that participates in the formation of ferroptosis (Jiang et al., 2021). The 3D structures of 3 proteins were acquired from UniProt: ACC: <https://www.uniprot.org/uniprotkb/Q13085/entry#structure> TFRC: <https://www.uniprot.org/uniprotkb/P02786/entry#structure> CRLS1: <https://www.uniprot.org/uniprotkb/Q9UJA2/entry#structure>. The 3D structure of dehydroabietic acid was acquired by chem3D. Open the protein 3D model in AutoDocktools for preprocessing, such as hydrogenation and charge calculation. The substrate molecules were built by Chemdraw and stored in SDF format. Dehydroabietic acid preprocessing was carried out in Atudodocktools. The docking grid documents were generated by AutoGrid of sitemap, and AutoDock was used for docking. A total of 10 docking results were produced. The docking results with the optimal conformation were chosen. PyMOL 1.6.5 software was chosen for analysis, and diagrams were plotted.

TABLE 1 RT–PCR system.

Reagent	Volume (μL)
SYBR Green I (2*)	10
primer F (10 μM)	1
primer R (10 μM)	1
Addition of ddH <sub>2</sub> O	20

TABLE 2 Primer sequences for real-time qPCR.

Primer names	Primer sequence (5'–3')
CRLS1-homo-qF	CCGAACCTCTTCCAACACCAC
CRLS1-homo-qR	CAAAGAAGCTGCCACCAAGA
ACACA-homo-qF	ATAAGGATCTGGCGGAGTGG
ACACA-homo-qR	TCCATGGCAACCTCTGGATT
GAPDH-homo-qF	GGACTCATGACCACAGTCCA
GAPDH-homo-qR	TCAGCTCAGGGATGACCTTG

### 4.9 Protein expression analysis of CRLS1, ACACA and TFRC

In this experiment, immunohistochemical images of ACACA and TFRC in normal tissues and HCC tissues were downloaded from the human protein atlas HPA database (<http://www.proteinatlas.org>), which publicly available. These images were used to compare the expression differences of ACACA and TFRC in HCC and normal liver tissues at the translational level. No expression differences in CRLS1 at the translation level between HCC and normal tissues were found.

### 4.10 Reverse transcription and real-time qPCR

Reverse transcription reactions were carried out according to the kit supplied by Nanjing Vazyme Biotech Co., Ltd. The reverse transcription RNA quantity was 1 μg. Real-time qPCR was implemented with reference to the kit supplied by Nanjing Vazyme Biotech Co., LTD. The reaction solution was prepared according to Table 1.

After the reaction liquid was prepared, the liquid was successively added into the 96-well plate followed by the cDNA. Next, reactions were carried out on the real-time qPCR instrument according to the instructions. Each gene was tested 3 times using specific primers. The expression level of genes was determined with GAPDH as the internal reference. The relative quantitative expression of genes was provided by the  $2^{-\Delta\Delta C_t}$  method. The primer sequences are shown in Table 2.

## 4.11 Western blot assay

Equivalent amounts of protein were loaded into SDS–PAGE gel pores for 2 h of electrophoresis at 100 V. Membrane transformation was performed for 1 h after the completion of electrophoresis under a constant current of 200 mA. Later, the membrane was closed with 5% closed solution for 1 h at room temperature and then incubated in 5% closed solution at room temperature for 2 h using the first antibody at an appropriate dilution ratio. Next, the membrane was washed 3 times with TBST for 5 min each. Later, the membrane was incubated in TBST with 5% closed buffer solution for 1 h at room temperature using the marked second antibody with a dilution ratio of HRP, followed by 3 washes with TBST for 5 min each. Finally, hypersensitivity ECL chemiluminescent reagent was added to the PVDF membrane for exposure imaging and photography.  $\beta$ -actin was used as the internal reference, and the relative protein expression level of the bands was analyzed using Quantity One software.

## 5 Results

### 5.1 Proteomics analysis of HepG2 cells after administration of dehydroabietic acid

#### 5.1.1 Quantitative analysis of proteins

In this experiment, preset test groups were tested and calculated using Welch's *t* test. According to the analysis, 1221 differentially expressed proteins ( $FC \geq 1.5$  and  $p \leq 0.05$ ) were screened from the test groups and the control group, including 260 upregulated and 961 downregulated proteins.

#### 5.1.2 Gene ontology enrichment analysis

The main function of the GO database is to provide annotation of protein functions. It has three major branches: cellular component (CC), molecular function (MF) and biological process (BP). The terms in CC were used to describe the positions of protein products inside and outside of cells. Terms in MF were used to define functions on the molecular layers of protein products. Terms in BP were used to describe biological paths or mechanisms in which protein products participate. CC, MF, and BP were mainly enriched in endoplasmic reticulum membrane (Figure 1A), transporter activity (Figure 1B) and transmembrane transport (Figure 1C), respectively.

#### 5.1.3 Pathway enrichment analysis

Biological pathways in which the differentially expressed proteins were located were analyzed. The results showed that metabolic pathways with significant enrichment of differential proteins ( $p < 0.05$ ) mainly participated in ferroptosis, N-glycan

biosynthesis, and oxidative phosphorylation, among others (Figure 1D). A network diagram of the top five pathways in terms of enrichment significance was built based on the common enriched proteins, which was conducive to discovering the relationship between proteins and pathways. Ferroptosis-enriched proteins included ACSL3, TFRC, and FTH1 (Figure 1E).

### 5.2 Lipidomics analysis of HepG2 cells after administration of dehydroabietic acid

#### 5.2.1 PCA of samples

The overall distribution of all samples was observed by PCA to recognize discrete points. PCA of the test and control groups was carried out using SIMCA-P software. Two PCA models with two principal components were constructed. The PCA scores are shown in Figure 2A. Figure 2A shows that in the positive ion and negative ion modes, there was obvious separation between samples of the test and control groups. PCA model parameters were obtained through 6 cyclic interaction verifications. The interpretation rates of the positive and negative ion models were  $R^2X = 0.822$  and  $R^2X = 0.816$ , respectively. Hence, it can be concluded that the PCA model could effectively interpret metabolic differences between samples of the test and control groups.

#### 5.2.2 Metabolite classification statistics

Classification statistics of identified metabolites were conducted according to chemical classification information. The proportions of different types of metabolites are shown in Figure 2B.

#### 5.2.3 OPLS-DA of samples

OPLS-DA of the test and control groups was carried out using SIMCA-P software. An OPLS-DA model was built (Figure 2C). Samples of the test group and control group were two-sided, indicating significant differences between the two groups. The model evaluation parameters gained from 6 cyclic interaction verifications were  $R^2X$ ,  $R^2Y$ , and  $Q^2$ . The positive ion mode was  $R^2X = 0.768$ ,  $R^2Y = 1$ , and  $Q^2 = 0.987$ . The negative ion mode was  $R^2X = 0.763$ ,  $R^2Y = 1$ , and  $Q^2 = 0.985$ . These findings indicated that the model was stable and reliable. Moreover, the replacement test of OPLS-DA mode was performed based on the data from the positive and negative ion modes. It could be concluded that no fitting had occurred in the OPLS-DA model, which was built based on data from positive and negative ion models.

#### 5.2.4 Significant differential metabolites

Differential metabolites among groups ( $VIP > 1$ ) were screened according to the variable weight value (VIP).

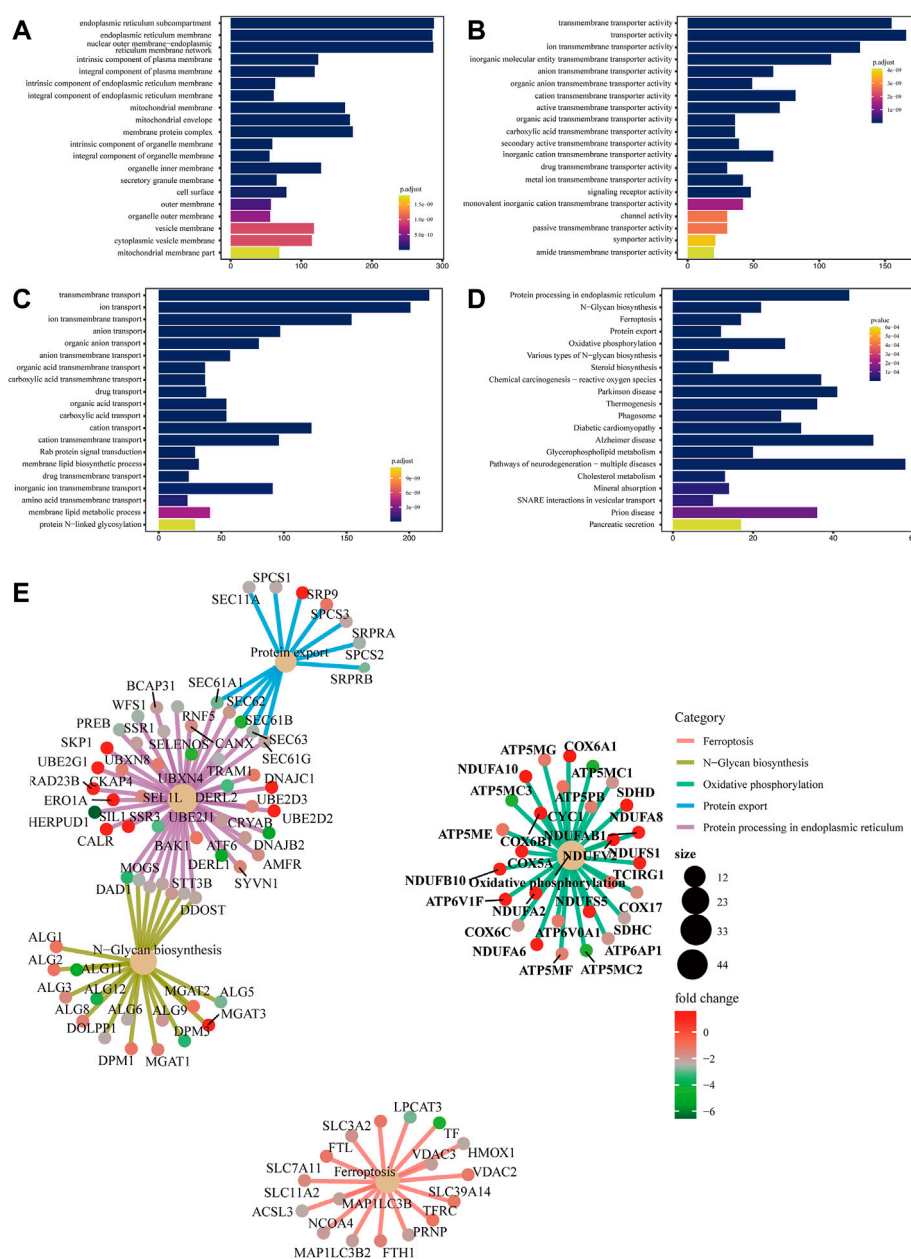


FIGURE 1

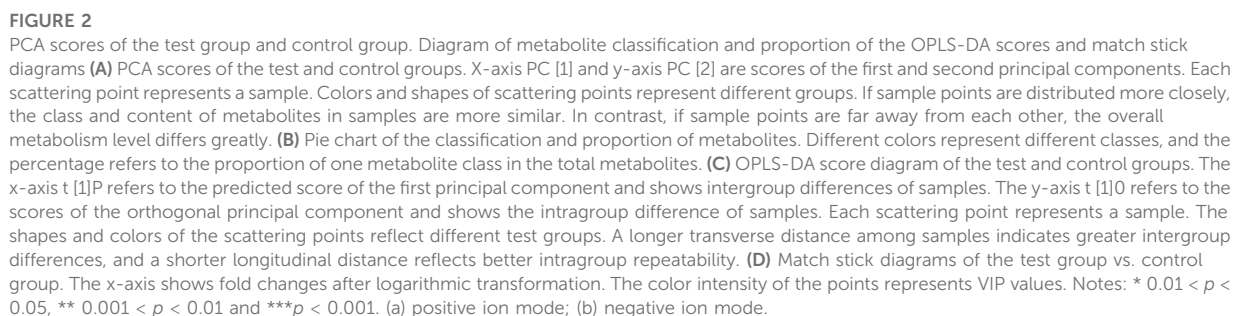
Bar chart of GO enrichment analysis and bar chart and network diagram of pathway enrichment analysis. (A) Bar chart of CC enrichment analysis. (B) Bar chart of MF enrichment analysis. (C) Bar chart of BP enrichment analysis. The x-axis shows the protein quantity, and the y-axis shows the GO term. Colors correspond to statistical significance and show the top 20 GO terms in terms of enrichment significance. (D) Bar chart of pathway enrichment analysis. The x-axis shows the protein quantity, and the y-axis indicates the pathway. Colors correspond to statistical significance and show the top 20 pathways in terms of enrichment significance. (E) Network diagram of pathway enrichment analysis. The shallow yellow circles are pathways, and the small dots are proteins. Representative proteins of the pathway are shown. The y-axis indicates the pathway. The circle size denotes the number of enriched proteins, and colors correspond to statistical significance.

Significant differential metabolites were screened by using single-variable statistical analysis ( $VIP > 1$  and  $p < 0.05$ ). A total of 30 significant differential metabolites were screened and identified through statistical analysis (Figure 2D).

## 5.2.5 Hierarchical cluster analysis of differential metabolites

The screened differential metabolites had similar/complementary biological results and functions or were subordinate to positive/negative regulation by the same metabolic pathway. They showed





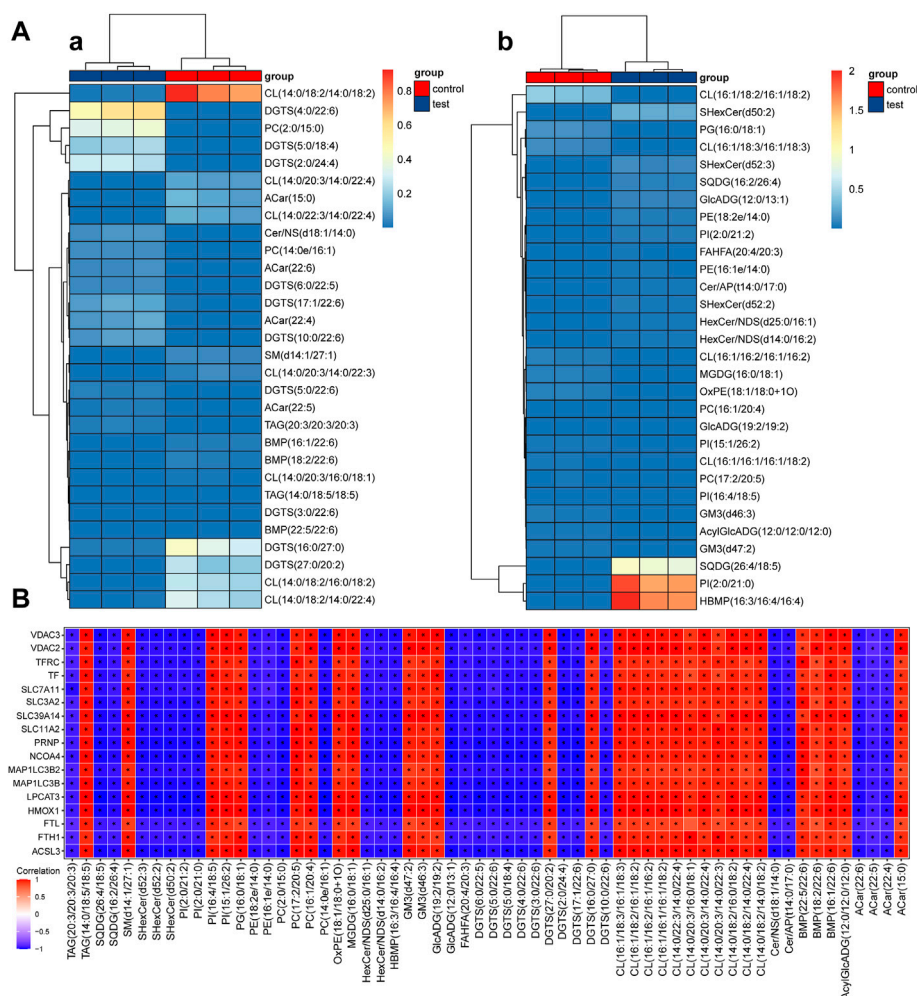


FIGURE 3

Thermodynamic diagram of the hierarchical clustering analysis of significantly differential metabolites and thermodynamic diagram of correlation between ferroptosis differential proteins and metabolites (A) Thermodynamic diagram of hierarchical clustering analysis of significantly differential metabolites between test groups and the control group (a): positive ion mode; (b): negative ion mode. The x-axis represents different test groups, and the y-axis represents differential metabolites of the group. Blocks at different positions represent the relative expression of metabolites at corresponding positions. (B) Thermodynamic diagram of the correlation between ferroptosis differential proteins and metabolites. Red (corr = 1), blue (corr = -1) and white (corr = 0). Data with  $p < 0.05$  are marked by "\*" in the diagram. The x-axis shows the differentially abundant proteins identified by proteomics, and the y-axis shows the differentially abundant metabolites identified by metabolomics.

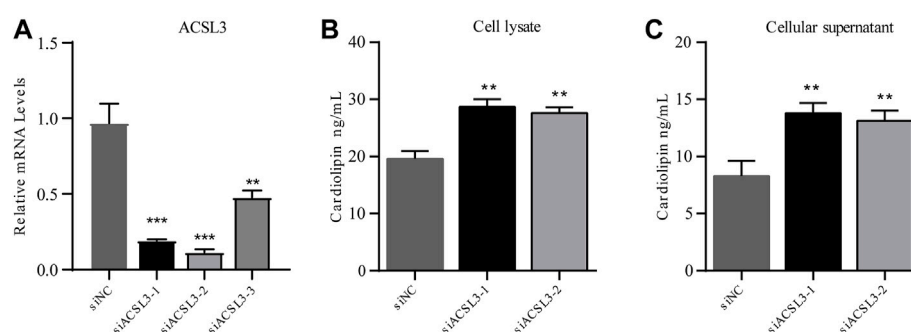
similar or opposite expression features among different test groups. Hierarchical cluster analysis of these features was conducive to classifying metabolites with the same features together and recognizing variation features of metabolites among test groups.

Hierarchical cluster analysis results of differential metabolites under positive and negative ion modes are shown in Figure 3A. The test group clearly showed significantly downregulated metabolism capacity of CL (14:0/18:2/14:0/18:2), DGTS (16:0/27:0), DGTS (27:0/20:2), CL (14:0/18:2/16:0/18:2), and CL (14:0/18:2/14:0/22:4) compared with the control group. Among them, CL (14:0/18:2/14:0/18:2) was the most significant. Additionally, the metabolic capacity of DGTS (4:0/22:6), PC(2:0/15:0), DGTS (5:0/18:4) and DGTS (2:0/24:4) in the

test group was obviously upregulated compared with that in the control group. According to the clustering heatmap, significantly differential metabolites were mainly divided into two classes. The metabolic capacities of SQDG (26:4/18:5), PI(2:0/21:0), and HBMP(16:3/16:4/16:4) in the test group were obviously upregulated compared with those in the control group.

### 5.3 Correlation analysis of ferroptosis differential proteins and metabolites

Correlation coefficients between ferroptosis differential proteins and metabolites were calculated by the Pearson



**FIGURE 4**

ACSL3 level in ACSL3 knockdown cells and ACSL3 level in cell lysis buffer and supernatant (A) The ACSL3 level in ACSL3 knockdown cells. Real-time quantitative PCR analysis of ACSL3 mRNA levels in HepG2 cells after siRNA transfection. \*\* represents  $p < 0.01$ . \*\*\* indicates  $p < 0.001$ . (B) ACSL3 levels in cell lysis buffer. ELISA results for the cardiolipin content in cell lysis buffer of siNC and siACSL3 HepG2 cells. \*\* indicates  $p < 0.01$ . (C) ACSL3 levels in the cell supernatant. ELISA analysis of cardiolipin content in siNC and siACSL3 HepG2 cells. \*\* represents  $p < 0.01$ .

method. The results are shown in a thermodynamic diagram. A good correlation between ACSL3 protein and cardiolipin was found. The results are shown in Figure 3B.

## 5.4 ACSL3 participates in cardiolipin metabolism

### 5.4.1 Successful establishment of ACSL3 knockdown cell lines

After HepG2 cells were transfected with siRNA for 24 h, cell samples were collected, and RNA was extracted. The mRNA level of ACSL3 was tested by real-time quantitative PCR. The results demonstrated that all three siRNAs significantly inhibited the mRNA levels of ACSL3. In siACSL3-1 and siACSL3-2, the mRNA level of ACSL3 decreased by approximately 80%, while the knockdown effect of siACSL3-3 was approximately 60% (Figure 4A). Therefore, siACSL3-1 and siACSL3-2 were applied in the follow-up experiment.

### 5.4.2 ACSL3 knockdown facilitates accumulation of cardiolipin in cell supernatant and lysis buffer

To investigate the regulatory effect of ACSL3 on cardiolipin, the cell lysis buffer and supernatant of the siNC group and siACSL3 group were collected, and the cardiolipin level was tested using an ELISA kit. The results showed that cardiolipin levels in cell lysis buffer and cell supernatant after ACSL3 knockdown increased significantly compared with the control group (Figures 4B,C). Altogether, these results implied that ACSL3 participated in the regulation of cardiolipin metabolism.

## 5.5 Lipidomics and proteomics analysis of molecular models of the effects of dehydroabietic acid on HepG2 hepatocellular cancer cells

To establish a molecular model under the influence of dehydroabietic acid on HepG2 hepatocellular carcinoma cells, we analyzed lipidomics and proteomics and selected metabolic and protein pathways as carriers to map differentially expressed proteins and metabolites. The results showed that the pathways involved in these differentially expressed proteins and metabolites mainly involved iron death and lipid metabolism, indicating that the differentially expressed proteins and metabolites were directly related to the effect of dehydroabietic acid on HepG2 in hepatocellular carcinoma cells.

Metabolic mapping of lipid metabolism pathways indicated that dehydroabietic acid was quite active in the performance of metabolites affected by HepG2 in hepatocellular carcinoma cells. As shown in Figure 5A, dehydroabietic acid had a significant effect on multiple metabolites in glycerol and phospholipid metabolism, including cardiolipin (CL), phosphatidylcholine (PC) downregulation, sphingomyelin (SM) upregulation, sulfoquinovosyl diacylglycerol (SQDG) upregulation, and phosphatidylinositol (PI) upregulation, among others. Phosphatidylethanolamine (PE), triacylglycerol (TAG) and phosphatidylglycerol (PG) had no significant effects. Notably, dehydroabietic acid significantly upregulated CL (14:0/18:2/14:0/18:2) but had inhibitory effects on CL (14:0/18:2/16:0/18:2) and CL (14:0/18:2/14:0/22:4). In addition, dehydroabietic acid was able to “upregulate” SQDG, an intermediate product of the glyceride metabolic pathway.

Pathway mapping of iron death pathways showed that dehydroabietic acid was quite active in protein performance under the influence of HepG2 in hepatocellular carcinoma cells. As shown in Figure 5B, AA (arachidonic acid) entered

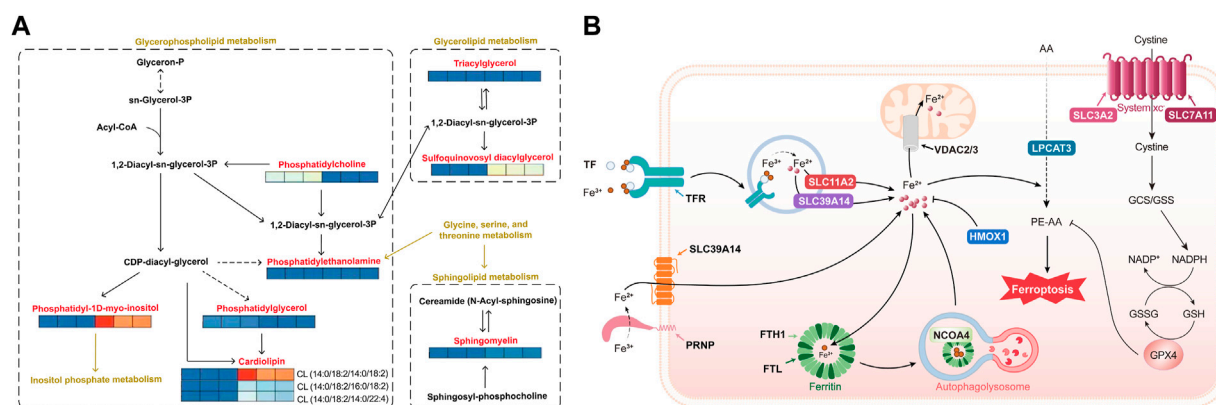


FIGURE 5

Lipidomics of molecular models of the effects of dehydroabietic acid on HepG2 hepatocellular cancer cells (A) and proteomics analysis of molecular models of the effects of dehydroabietic acid on HepG2 hepatocellular cancer cells (B).

the cell and underwent catalysis by ferrous ions and multiple enzymes (including LPCAT3) to produce the toxic substance PE-AA, resulting in iron death. The trivalent iron ions outside the cell were reduced to divalent iron ions under the action of the PRNP protein, and Fe<sup>2+</sup> traversed the SLC39A14 protein into the cell interior. In addition, extracellular Fe<sup>3+</sup> was able to bind to TF, which was recognized by TFR receptors and enters the cell in the form of vesicles. It then traversed the vesicle transmembrane proteins SLC11A2 and SLC39A14 into the cytoplasm. Part of the Fe<sup>2+</sup> in the cytoplasm entered the mitochondria through the mitochondrial membrane protein VDAC2 or 3 to function, and the other part in the form of Fe<sup>3+</sup> was stored in ferritin composed of FTH1 (heavy chain) and FTL (light chain). This portion of Fe<sup>3+</sup> was self-delivered to autophagic lysosomes under the action of NCOA4, resulting in Fe<sup>2+</sup> production. SLC3A2 and SLC7A11 together formed the system xc, which transferred cystine from outside the cell to the intracellular space, thereby promoting GSH production and affecting GPX4 activity. GPX4 was effective in clearing PE-AA and inhibiting iron death. Here, we found that dehydrorosin could inhibit the protein indicated in bold text in the figure, thereby preventing iron death.

## 5.6 Dehydroabietic acid obviously inhibits the growth of hepatic carcinoma cells

In this study, different concentrations of dehydroabietic acid were applied to process HepG2 cells for 72 h. According to the CCK8 results, dehydroabietic acid obviously inhibited cell growth at concentrations from 3.125–800 µg/ml in a concentration-dependent manner (Figures 6A,B). According to further results, the IC<sub>50</sub> value of dehydroabietic acid was

23.22 ± 0.98 µg/ml. Hence, cells were treated with this concentration in the follow-up experiment.

## 5.7 Bioinformatics analysis of ferroptosis-related genes

### 5.7.1 Hub gene screening in protein–protein interaction

Differentially expressed proteins were input into the STRING database for PPI analysis, and the PPI network was plotted using Cytoscape software. Six key genes were screened with the Degree algorithm of CytoHubba, including TFRC, FTH1, FTL, SLC11A2, SLC39A14, and HMOX1 (Figure 7A).

### 5.7.2 Differential expression analysis of hub genes in the RNA-Seq dataset of hepatic carcinoma

The transcriptional level differences of Hub genes in HCC and normal tissues were analyzed through an RNA-seq dataset. The transcriptional levels of FTH1, FTL, SLC11A2 and TFRC in the HCC group were increased compared with those in the normal group, while the transcriptional levels of HMOX1 and SLC39A14 were decreased. These differences were statistically significant ( $p < 0.01$ ) (Figures 7B–G).

### 5.7.3 Hub genes and clinical pathological analysis of hepatic carcinoma

To investigate the relationships of FTH1, FTL, HMOX1, SLC11A2, SLC39A14, and TFRC expression with the survival and prognosis of patients with HCC, a Kaplan–Meier survival analysis was performed. FTH1 ( $p = 0.014$ , HR = 1.55, 95% CI (1.09–2.19)) and TFRC ( $p = 0.016$ , HR = 1.53, 95% CI (1.08–2.17)) were related to the survival of patients (Figures



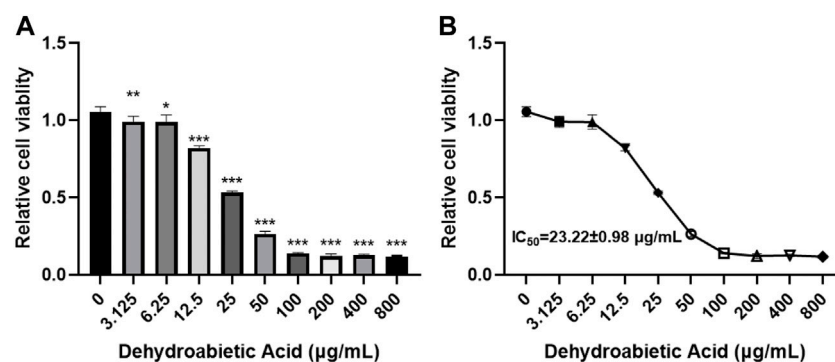


FIGURE 6

Effects of dehydroabietic acid on the growth of HCC cells (A): CCK8 analysis of the effects of dehydroabietic acid at different concentrations on cell growth. (B): IC<sub>50</sub> value of dehydroabietic acid.

7H-M). By analyzing the relationship between FTH1, FTL, HMOX1, SLC11A2, SLC39A14 and TFRC/DACH1 and the clinical pathological stages of HCC, we found that the expression of these genes increased gradually in Stage I, Stage II and Stage III. Moreover, gene expression was statistically significant in Stage I and Stage III ( $p = 0.0013$ ) (Figures 7N-S).

#### 5.7.4 GSEA

Gene enrichment analysis (GSEA) was performed on TFRC. According to the GSEA-KEGG results, TFRC was mainly enriched in cell cycle, DNA duplication, neural active ligand–receptor interaction, and axon pathways leading to mature diabetes in young individuals. Specifically, the cell cycle signal transduction pathway had the highest normalized enrichment score (NES) (NES = 1.821, adjusted  $p$ -value < 0.0002) (Figure 7T).

### 5.8 Molecular docking of dehydroabietic acid with CRLS1, ACACA and TFRC

According to the molecular docking results (Figure 8), all three proteins could bond with dehydroabietic acid and form stable interactions. The details were as follows. In ACACA, the dehydroabietic acid–protein docking score was  $-7.355$  kcal/mol. Carboxy groups of dehydroabietic acid formed hydrogen bonds with His1005 and Lys1071. In CRLS1, the dehydroabietic acid–protein docking score was  $-8.381$  kcal/mol. The carboxy groups of dehydroabietic acid formed hydrogen bonds with Thr246 and Lys174. In TFRC, the dehydroabietic acid–protein docking score was  $-7.739$  kcal/mol. The carboxy groups of dehydroabietic acid formed hydrogen bonds with Lys66 and Lys46. These data and interactions confirmed that dehydroabietic acid could bond with all 3 proteins.

### 5.9 Protein expression of ACACA and TFRC

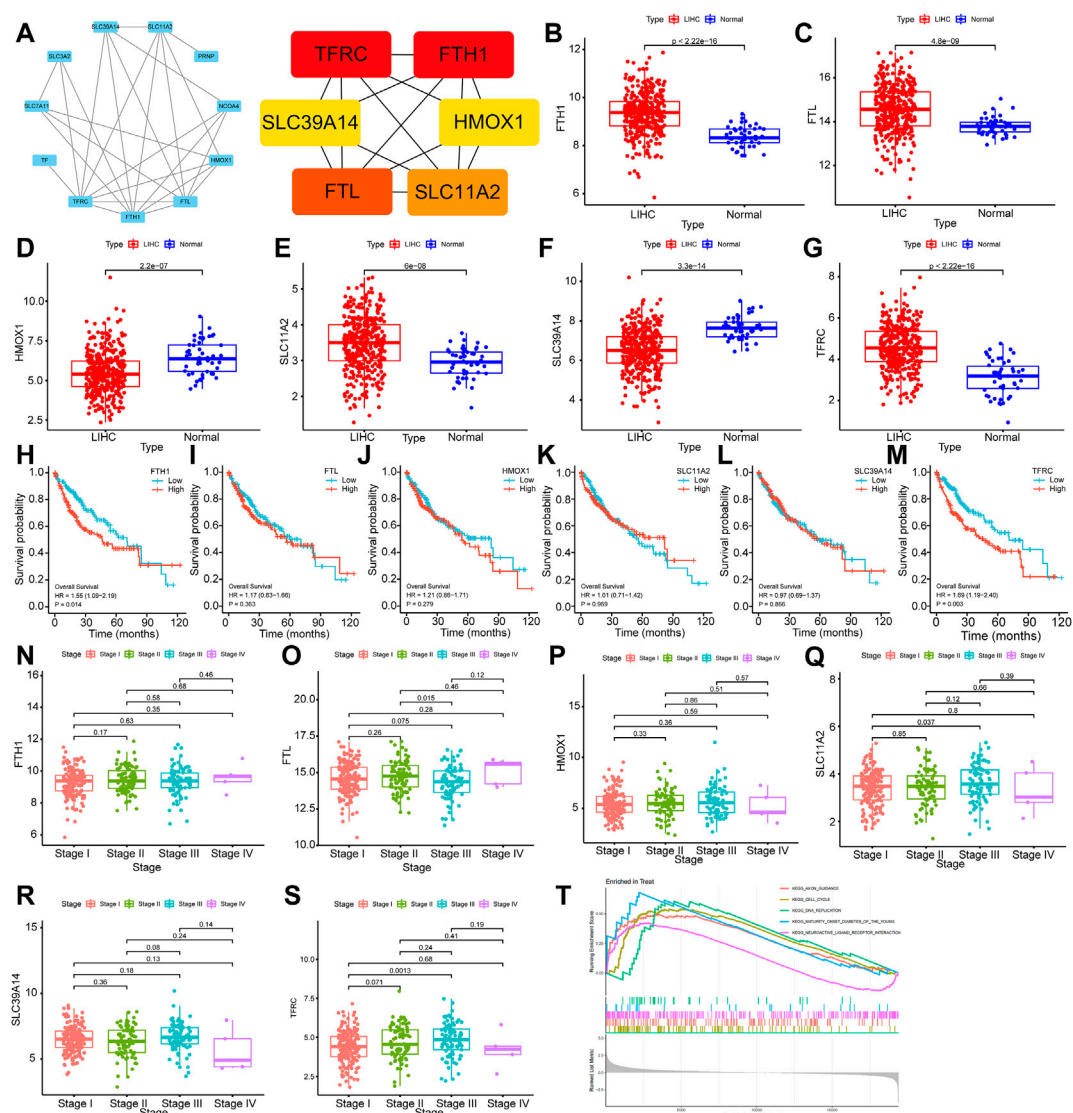
The translation levels of ACACA and TFRC in HCC and normal tissues were analyzed through the HPA dataset. The translation levels of ACACA and TFRC in HCC tissues were higher than those in normal tissues. (Figure 9).

### 5.10 Dehydroabietic acid inhibits gene expression

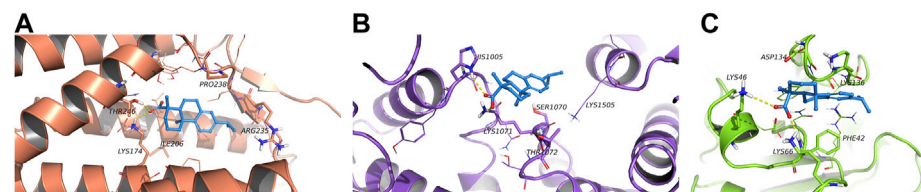
To explore the specific molecular mechanism by which dehydroabietic acid inhibits HepG2 growth, HepG2 cells were treated with  $23.22 \mu\text{g/ml}$  dehydroabietic acid for 12 h. Expression levels of CRLS1, ACACA and TFRC were detected by qPCR and WB assays. According to the qPCR results, the mRNA expression levels of CRLS1 and ACACA in HepG2 cells preprocessed by dehydroabietic acid decreased (Figure 10A). According to the WB results, the protein expression levels of CRLS1, ACACA and TFRC in HepG2 cells pretreated with dehydroabietic acid decreased (Figure 10B).

## 6 Discussion

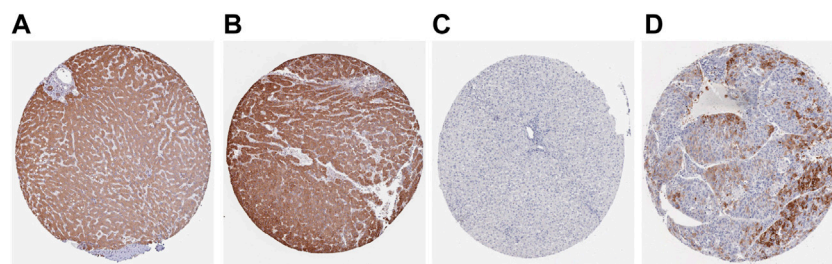
In the early period, the absolute bioavailability of dehydroabietic acid in the rat body was also studied. Dehydroabietic acid was administered orally (10 mg/kg) and *via* tail vein injection (1 mg/kg). The dehydroabietic acid concentration in plasma was tested by liquid chromatography–mass spectrometry (LC–MS). The pharmacokinetic parameters and absolute bioavailability using the two administration modes were calculated. After oral administration and tail intravenous injection of dehydroabietic acid, the major pharmacokinetic parameter peak concentrations



**FIGURE 7**  
Bioinformatics analysis of ferroptosis-related genes (A): Hub gene screening in the PPI network. (B–G): Differential expression analysis of FTH1, FTL, HMOX1, SLC11A2, SLC39A14 and TFRC. (H–M): Relationship analysis of FTH1, FTL, HMOX1, SLC11A2, SLC39A14 and TFRC and survival of HCC. (N–S): Relationship analysis of FTH1, FTL, HMOX1, SLC11A2, SLC39A14 and TFRC and clinical stages of HCC. (T): GSEA results of TFRC.

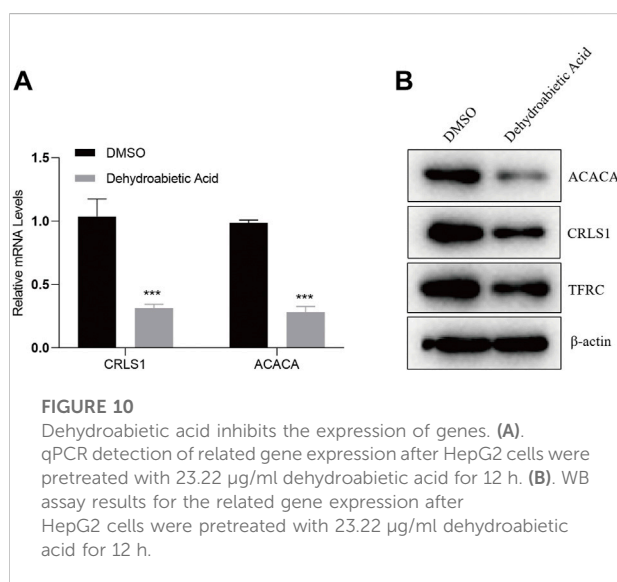


**FIGURE 8**  
Molecular docking of dehydroabietic acid with CRLS1 (A), ACACA (B) and TFRC (C).



**FIGURE 9**

The expression levels of ACACA and TFRC were verified at the translation level based on the Human Protein Atlas database. (A). ACACA protein level in normal tissues (staining: moderate; intensity: moderate; antibody No.: HPA063018). (B). ACACA protein level in HCC tissues (staining: high; intensity: strong; antibody No.: HPA063018). (C). TFRC protein level in normal tissues (staining: high; intensity: strong; antibody No.: CAB000153). (D). TFRC protein level in HCC tissues (staining: N/A; intensity: negative; antibody No.: CAB000153).



**FIGURE 10**

Dehydroabietic acid inhibits the expression of genes. (A). qPCR detection of related gene expression after HepG2 cells were pretreated with 23.22 µg/ml dehydroabietic acid for 12 h. (B). WB assay results for the related gene expression after HepG2 cells were pretreated with 23.22 µg/ml dehydroabietic acid for 12 h.

( $C_{max}$ ) in rats were  $4993.4 \pm 958.1$  and  $5928.0 \pm 803.2$  ng mL<sup>-1</sup>, respectively. The half-life periods ( $t_{1/2}$ ) were  $1.1 \pm 0.0$  and  $1.0 \pm 0.0$  h, respectively. The areas below the drug concentration in the blood-time curve ( $AUC_{0-t}$ ) were  $7419.5 \pm 976.0$  and  $4444.5 \pm 455.3$  ng h mL<sup>-1</sup>, respectively. The absolute bioavailability after oral administration and tail intravenous injection of dehydroabietic acid was 16.5%. Dehydroabietic acid could also inhibit the growth of hepatoma carcinoma cells. It inhibited cell growth clearly at concentrations from 3.125–800 µg/ml in a concentration-dependent manner.

In this study, proteomics identified 260 upregulated and 961 downregulated proteins, of which SLC11A2, SLC39A14 and GPX4 were significantly downregulated. The top five significantly enriched pathways were iron death, oxidative phosphorylation, and protein processing in the endoplasmic reticulum. According to published studies, the

SLC11A2 polymorphism is directly related to the risk of endometrial cancer, indicating that SLC11A2 might participate in the progression of tumors (Michalczyk et al., 2022). In renal carcinoma, circ\_001842 strengthens the proliferation, migration and invasion of cancer cells by inhibiting miR-502-5p and increasing the expression of SLC39A14 (Zeng et al., 2020). Glutathione peroxidase 4 (GPX4) is a major inhibitor of ferroptosis. Some studies have demonstrated that ketamine can inhibit GPX4 expression through the target lncRNA PVT1/miR-214-3p axis, thus inhibiting HCC cells (He et al., 2021). Therefore, the proteomics results showed that dehydroabietic acid could inhibit the development of liver cancer by influencing the death of cellular iron. Lipidomics screening identified 30 significantly differentially expressed metabolites; differential expression of lipids was mainly related to glycerol and phospholipid metabolism; differential metabolite level clustering results showed that it was mainly clustered into two categories and compared with the control group, the test group SQDG (26:4/18:5), PI (2:0/21:0), HBMP (16:3/16:4/16:4), and SM (SMD 14:1/27:1) metabolic capacity was significantly upregulated while PC(14:0e/16:1) metabolic level was significantly reduced. Studies have shown that SQDG is able to inhibit angiogenesis in tumor tissue and tumor cell proliferation (Maeda et al., 2008). The presence of metabolic abnormalities of PI, SM and PC in liver cancer tissues suggests that these metabolic abnormalities may be involved in the development of liver cancer (Assi et al., 2018). European metabolic data showed that high SM metabolic levels and low PC metabolic levels reflect metabolic characteristics of healthy living, which are inversely associated with the risk of liver cancer development (Li et al., 2017). Therefore, the change in the level of major metabolites in this study indicated that dehydroabietic acid could inhibit the development of hepatocellular carcinoma cells.

Cardiolipin is a type of phospholipid with specific mitochondria. It mainly exists in the mitochondrial inner membrane and is an important component in maintaining the mitochondrial structure (Chicco and Sparagna, 2007). Cardiolipin has a dimer structure, in which two groups of phosphatidic acids are connected by a central glycerol

molecule (Schlame et al., 2000). Cardiolipin mainly exists in the mitochondrial inner membrane and accounts for approximately 25% of the total phospholipid content. Approximately 65% of cardiolipin on the mitochondrial inner membrane is located in the endite, and the rest is located in the exite. There is approximately 4% cardiolipin on the mitochondrial outer membrane, especially in contact positions close to the inner and outer membranes. At inner-outer membrane interfaces, cardiolipin can reach the mitochondrial outer membrane and surface of mitochondria close to the cytoplasm (Paradies et al., 2014). According to Chinese and foreign-associated studies, cardiolipin has a unique aliphatic acyl side chain structure, which is very important in the development of the biological functions of cardiolipin (Sparagna et al., 2007). When the pathological state causes oxidative stress, high molecular weights of polyunsaturated fatty acid acyl side chains, such as arachidonic acid and docosahexaenoic acid, might replace cardiolipin. These replaced side chains further cause oxidation of cardiolipin and thereby induce pathological changes. As a result, electron transport complex I in mitochondria and its activity are damaged, thus leading to mitochondrial dysfunction (Razak and Anand, 2004). Acyl coenzyme A synthesizes long chain acyl-CoA synthetases (ACSLs), which are indispensable enzymes in organisms. ACSLs have five family members: ACSL1, ACSL3, ACSL4, ACSL5 and ACSL6. Among them, ACSL3 is the member with the highest expression and complex functions (Mashek et al., 2004). ACSL3 can activate unsaturated fatty acids with a carbon chain length of 16–20 as well as –5,8,11,14-eicosatetraenoic acids and produce lecithin and lipid droplets. Lecithin exists on the surface of very-low-density lipoprotein and is an important component. Lipid droplets are major organelles for storing neural lipids in cells, and they mainly maintain the dynamic balance of lipids (Kageyama et al., 2013). Some studies have demonstrated that when ACSL3 participates in the synthesis and autophagy of lipid droplets, ACSL3 can regulate the steady state of lipids in cells (Lv et al., 2019). According to comprehensive multiomics analysis results, real-time quantitative PCR and ELISA, ACSL3 participates in cardiolipin metabolism.

According to previous studies, CRLS1 can also be used as a tumor suppressor to decrease thrombogenesis in tumors. The long-chain noncoding RNA LINC01272 inhibits the proliferation of lung cancer cells and promotes apoptosis by modulating the miR-7-5p/CRLS1 signaling axis (Ma et al., 2021). ACC is an essential rate-limiting enzyme in fatty acid metabolism and has become an attractive target of various metabolic diseases due to its critical regulatory role in fatty acid synthesis and oxidative pathways (Chen et al., 2019). In addition, ACC also participates in the progression of tumors. Some studies have pointed out that in breast cancer, TGF $\beta$ -activated kinase (TAK) catalyzes the phosphorylation of ACC and thereby activates the transcription of Smad2, ultimately influencing the metastasis of breast cancer. Mice with ACC1 deficiency easily suffer recurrent tumors after the first tumor excision (Rios et al., 2017). TFRC can combine with transferrin, which carries free iron to transfer iron out of and into cells, thus increasing the iron level in cells (Jiang et al., 2021).

Upregulated TFRC expression has been found in various tumors, including HCC, indicating that TFRC-related pathways play an important role in the progression of tumors (Kindrat et al., 2016). The key protein TFRC was screened through a deep proteomics analysis of HCC cells treated with dehydroabiatic acid. It found that TFRC was significantly different in different clinical stages of patients with HCC. Moreover, through molecular docking, this study demonstrated that dehydroabiatic acid could bind with CRLS1, ACACA and TFRC, indicating that dehydroabiatic acid could kill HCC cells effectively by regulating ferroptosis and lipidosomes, especially cardiolipin metabolism.

## 7 Conclusion

Changes in the protein and lipid levels in HepG2 cells after administration of dehydroabiatic acid, especially those that changed significantly, were analyzed through proteomics and lipidomics studies. Moreover, the specific regulatory functions of proteins and lipids were analyzed. Conjoint analysis of ferroptosis-related proteins and significantly changed lipids was performed. According to experimental verification, ACSL3 knockdown facilitated the accumulation of cardiolipin in the cell supernatant and lysate.

## Data availability statement

The datasets presented in this study can be found in online repositories. The names of the repository/repositories and accession number(s) can be found below: ProteomeXchange, PXD036015.

## Author contributions

ZX: Methodology, writing an original manuscript. JH: Conception, design, and supervision of the research project. Design and critical revisions of the manuscript.

## Acknowledgments

We thank “SHANGHAI BIOTREE BIOTECH CO., LTD.” for assistance with the laboratory testing and analysis.

## Conflict of interest

Author JH was employed by the company Beijing Tcmages Pharmaceutical Co.Ltd. JH Beijing Kangrentang Pharmaceutical Co.,Ltd.



The remaining author declares that the research was conducted in the absence of any commercial or financial relationships that could be construed as a potential conflict of interest.

## Publisher's note

All claims expressed in this article are solely those of the authors and do not necessarily represent those of their affiliated organizations, or those of the publisher, the editors and the

reviewers. Any product that may be evaluated in this article, or claim that may be made by its manufacturer, is not guaranteed or endorsed by the publisher.

## Supplementary material

The Supplementary Material for this article can be found online at: <https://www.frontiersin.org/articles/10.3389/fphar.2022.1015240/full#supplementary-material>

## References

- Assi, N., Gunter, M. J., Thomas, D. C., Leitzmann, M., Stepien, M., Chajes, V., et al. (2018). Metabolic signature of healthy lifestyle and its relation with risk of hepatocellular carcinoma in a large European cohort. *Am. J. Clin. Nutr.* 108, 117–126. doi:10.1093/ajcn/nqy074
- Chen, L., Duan, Y., Wei, H., Ning, H., Bi, C., Zhao, Y., et al. (2019). Acetyl-CoA carboxylase (ACC) as a therapeutic target for metabolic syndrome and recent developments in ACC1/2 inhibitors. *Expert Opin. Investig. Drugs* 28 (10), 917–930. doi:10.1080/13543784.2019.1657825
- Chicco, A. J., and Sparagna, G. C. (2007). Role of cardiolipin alterations in mitochondrial dysfunction and disease. *Am. J. Physiol. Cell. Physiol.* 292, C33–C44. doi:10.1152/ajpcell.00243.2006
- Gao, G., Xie, Z., Li, E. W., Yuan, Y., Fu, Y., Wang, P., et al. (2021). Dehydroabietic acid improves nonalcoholic fatty liver disease through activating the Keap1/Nrf2-ARE signaling pathway to reduce ferroptosis. *J. Nat. Med.* 75, 540–552. doi:10.1007/s11418-021-01491-4
- Han, J., and Zhang, Z. X. (2021). Screening of pyroptosis-related genes influencing the therapeutic effect of dehydroabietic acid in liver cancer and construction of a survival nomogram. *Biochem. Biophysical Res. Commun.* 585, 103–110. doi:10.1016/j.bbrc.2021.11.027
- He, G., Bao, N. R., Wang, S., Xi, M., Zhang, T. H., and Chen, F. S. (2021). Ketamine induces ferroptosis of liver cancer cells by targeting lncRNA PVT1/miR-214-3p/GPX4. *Drug Des. devel. Ther.* 15, 3965–3978. doi:10.2147/DDDT.S332847
- Jiang, L., Wang, J., Wang, K., Wang, H., Wu, Q., Yang, C., et al. (2021). RNF217 regulates iron homeostasis through its E3 ubiquitin ligase activity by modulating ferroportin degradation. *Blood* 138, 689–705. doi:10.1182/blood.202008986
- Kageyama, A., Matsui, H., Ohta, M., Sambuichi, K., Kawano, H., Notsu, T., et al. (2013). Palmitic acid induces osteoblastic differentiation in vascular smooth muscle cells through ACSL3 and NF- $\kappa$ B, novel targets of eicosapentaenoic acid. *PLoS One* 8, e68197. doi:10.1371/journal.pone.0068197
- KhalKhal, E., Rezaei-Tavirani, M., and Rostamii-Nejad, M. (2019). Pharmaceutical advances and proteomics researches. *Iran. J. Pharm. Res.* 18, 51–67. doi:10.22037/ijpr.2020.112440.13758
- Kindrat, I., Tryndyak, V., Conti, A., Shpyleva, S., Mudalige, T. K., Kobets, T., et al. (2016). MicroRNA-152-mediated dysregulation of hepatic transferrin receptor 1 in liver carcinogenesis. *Oncotarget* 7, 1276–1287. doi:10.18632/oncotarget.6004
- Li, Z., Guan, M., Lin, Y., Cui, X., Zhang, Y., Zhao, Z., et al. (2017). Aberrant lipid metabolism in hepatocellular carcinoma revealed by liver lipidomics. *Int. J. Mol. Sci.* 18, 2550. doi:10.3390/ijms18122550
- Liu, X., and Xu, G. (2018). Recent advances in using mass spectrometry for mitochondrial metabolomics and lipidomics - a review. *Anal. Chim. Acta* 1037, 3–12. doi:10.1016/j.aca.2017.11.080
- Lv, Y., Cao, Y., Gao, Y., Yun, J., Yu, Y., Zhang, L., et al. (2019). Effect of ACSL3 expression levels on preadipocyte differentiation in Chinese red steppe cattle. *DNA Cell. Biol.* 38, 945–954. doi:10.1089/dna.2018.4443
- Ma, X., Liu, Y., Tian, H., Zhang, B., Wang, M., and Gao, X. (2021). LINC01272 suppressed cell multiplication and induced apoptosis via regulating MiR-7-5p/CRLS1 Axis in lung cancer. *J. Microbiol. Biotechnol.* 31 (2021), 921–932. doi:10.4014/jmb.2102.02010
- Maeda, N., Kokai, Y., Ohtani, S., Sahara, H., Kumamoto-Yonezawa, Y., Kuriyama, I., et al. (2008). Anti-tumor effect of orally administered spinach glycolipid fraction on implanted cancer cells, colon-26, in mice. *Lipids* 43, 741–748. doi:10.1007/s11745-008-3202-5
- Mashek, D. G., Bornfeldt, K. E., Coleman, R. A., Berger, J., Bernlohr, D. A., Black, P., et al. (2004). Revised nomenclature for the mammalian long-chain acyl-CoA synthetase gene family. *J. Lipid Res.* 45, 1958–1961. doi:10.1194/jlr.E400002-JLR200
- Michalczyk, K., Kapczuk, P., Witzak, G., Bosiacki, M., Kurzawski, M., Chlubek, D., et al. (2022). The associations between metalloestrogens, GSTP1, and SLC11A2 polymorphism and the risk of endometrial cancer. *Nutrients* 14, 3079. doi:10.3390/nu14153079
- Monti, C., Zilocchi, M., Colugnat, I., and Alberio, T. (2019). Proteomics turns functional. *J. Proteomics* 198, 36–44. doi:10.1016/j.jpro.2018.12.012
- Orcutt, S. T., and Anaya, D. A. (2018). Liver resection and surgical strategies for management of primary liver cancer. *Cancer* 25, 1073274817744621. doi:10.1177/1073274817744621
- Paradies, G., Paradies, V., De Benedictis, V., Ruggiero, F. M., and Petrosillo, G. (2014). Functional role of cardiolipin in mitochondrial bioenergetics. *Biochim. Biophys. Acta* 1837, 408–417. doi:10.1016/j.bbabo.2013.10.006
- Razak, F., and Anand, S. S. (2004). Impaired mitochondrial activity in the insulin-resistant offspring of patients with type 2 diabetes. Petersen KF, Dufour S, Befroy D, Garcia R, Shulman GI. *N Engl J Med* 2004; 350: 664–71. *Vasc. Med.* 9, 223–224. doi:10.1191/1358863x04vm568xx
- Rios, G. M., Steinbauer, B., Srivastava, K., Singhal, M., Mattijssen, F., Maida, A., et al. (2017). Acetyl-CoA carboxylase 1-dependent protein acetylation controls breast cancer metastasis and recurrence. *Cell. Metab.* 26, 842–855. doi:10.1016/j.cmet.2017.09.018
- Schlame, M., Rua, D., and Greenberg, M. L. (2000). The biosynthesis and functional role of cardiolipin. *Prog. Lipid Res.* 39, 257–288. doi:10.1016/s0163-7827(00)00005-9
- Sellick, C. A., Hansen, R., Stephens, G. M., Goodacre, R., and Dickson, A. J. (2011). Metabolite extraction from suspension-cultured mammalian cells for global metabolite profiling. *Nat. Protoc.* 6, 1241–1249. doi:10.1038/nprot.2011.366
- Shi, J. F., Cao, M., Wang, Y., Bai, F. Z., Lei, L., Peng, J., et al. (2021). Is it possible to halve the incidence of liver cancer in China by 2050? [J]. *Int. J. Cancer* 148, 1051–1065. doi:10.1002/ijc.33313
- Sparagna, G. C., Chicco, A. J., Murphy, R. C., Bristow, M. R., Johnson, C. A., Rees, M. L., et al. (2007). Loss of cardiac tetralinoleoyl cardiolipin in human and experimental heart failure. *J. Lipid Res.* 48, 1559–1570. doi:10.1194/jlr.M600551-JLR200
- Sun, Y., Wu, L., Zhong, Y., Zhou, K., Hou, Y., Wang, Z., et al. (2021). Single-cell landscape of the ecosystem in early-relapse hepatocellular carcinoma. *Cell.* 184, 404–421. doi:10.1016/j.cell.2020.11.041
- Sustarsic, E. G., Ma, T., Lynes, M. D., Larsen, M., Karavaeva, I., Havelund, J. F., et al. (2018). Cardiolipin synthesis in Brown and beige fat mitochondria is essential for systemic energy homeostasis. *Cell. Metab.* 28, 159–174. doi:10.1016/j.cmet.2018.05.003
- Xie, Z., Gao, G., Wang, H., Li, E., Yuan, Y., Xu, J., et al. (2020). Dehydroabietic acid alleviates high fat diet-induced insulin resistance and hepatic steatosis through dual activation of PPAR- $\gamma$  and PPAR- $\alpha$ . *Biomed. Pharmacother.* 127, 110155. doi:10.1016/j.biopha.2020.110155
- Zeng, J. W., Feng, Q., Wang, Y. D., Xie, G., Li, Y., Yang, Y., et al. (2020). Circular RNA circ\_001842 plays an oncogenic role in renal cell carcinoma by disrupting microRNA-502-5p-mediated inhibition of SLC39A14. *J. Cell. Mol. Med.* 24, 9712–9725. doi:10.1111/jcmm.15529
- Zhu, Y., Zhang, S., Geng, Z., Wang, D., Liu, F., Zhang, M., et al. (2014). Analysis of abietic acid and dehydroabietic acid residues in raw ducks and cooked ducks. *Poult. Sci.* 93, 2663–2667. doi:10.3382/ps.2014-04045



## OPEN ACCESS

## EDITED BY

Yibin Feng,  
The University of Hong Kong, Hong  
Kong SAR, China

## REVIEWED BY

Gao Zhu Ye,  
China Academy of Chinese Medical  
Sciences, China  
Weicheng Hu,  
Huaiyin Normal University, China

## \*CORRESPONDENCE

Guobin Liu,  
✉ 15800885533@163.com

<sup>†</sup>These authors have contributed equally  
to this work and share first authorship

## SPECIALTY SECTION

This article was submitted to  
Ethnopharmacology,  
a section of the journal  
Frontiers in Pharmacology

RECEIVED 25 August 2022

ACCEPTED 25 November 2022

PUBLISHED 13 December 2022

## CITATION

Wang J, Wang Y, Huang R, Li W, Fan W,  
Hu X, Yang X, Han Q, Wang H and Liu G  
(2022), Uncovering the  
pharmacological mechanisms of Zizhu  
ointment against diabetic ulcer by  
integrating network analysis and  
experimental evaluation *in vivo*  
and *in vitro*.  
*Front. Pharmacol.* 13:1027677.  
doi: 10.3389/fphar.2022.1027677

## COPYRIGHT

© 2022 Wang, Wang, Huang, Li, Fan, Hu,  
Yang, Han, Wang and Liu. This is an  
open-access article distributed under  
the terms of the [Creative Commons  
Attribution License \(CC BY\)](#). The use,  
distribution or reproduction in other  
forums is permitted, provided the  
original author(s) and the copyright  
owner(s) are credited and that the  
original publication in this journal is  
cited, in accordance with accepted  
academic practice. No use, distribution  
or reproduction is permitted which does  
not comply with these terms.

# Uncovering the pharmacological mechanisms of Zizhu ointment against diabetic ulcer by integrating network analysis and experimental evaluation *in vivo* and *in vitro*

Jie Wang<sup>1†</sup>, Yu Wang<sup>2†</sup>, Renyan Huang<sup>1†</sup>, Wenhui Li<sup>3†</sup>,  
Weijing Fan<sup>1</sup>, Xiaoming Hu<sup>1</sup>, Xiao Yang<sup>1</sup>, Qiang Han<sup>1,4</sup>,  
Hongfei Wang<sup>1</sup> and Guobin Liu<sup>1\*</sup>

<sup>1</sup>Department of Peripheral Vascular Surgery, Shuguang Hospital Affiliated to Shanghai University of Traditional Chinese Medicine, Shanghai, China, <sup>2</sup>Academy of Integrative Medicine, Shanghai University of Traditional Chinese Medicine, Shanghai, China, <sup>3</sup>Collaborative Innovation Center, Shanghai University of Medicine and Health Sciences, Shanghai, China, <sup>4</sup>Beicai Community Health Service Center, Shanghai, China

Diabetic ulcer (DU) has been recognized as one of the most prevalent and serious complications of diabetes. However, the clinical efficacy of standard treatments for DU remains poor. Traditional Chinese medicine (TCM) shows a positive therapeutic effect on DU. Specifically, Zizhu ointment (ZZO) has been widely used to treat DU in long-term clinical practice, but the exact mechanism by which it promotes DU wound healing remains unknown. In this study, network analysis and high-performance liquid chromatography–high resolution mass spectrometry (UPLC–HRMS) were conducted to identify the active compounds of ZZO. We detected isovalerylshikonin (ISO), mandenol, daidzein, kaempferol, and formononetin in both network analysis and UPLC–HRMS. Moreover, ZZO could ameliorate DU by regulating the phosphatidylinositol-3-kinase (PI3K)/protein kinase B (AKT) and inflammation signaling pathways, according to the results of KEGG analysis. We established a DU mouse model with a high-fat diet and streptozotocin injection *in vivo* to evaluate the network analysis result. The experimental results showed that ZZO could inhibit inflammation, remodel fibrous tissue, and promote angiogenesis in the DU area, facilitating wound healing in DU mice. Moreover, the PI3K/AKT signaling pathway was indeed activated by ZZO treatment, promoting macrophage M2 polarization. In addition, we used molecular docking technology to evaluate the binding sites between ZZO and the PI3K/AKT pathway. The results showed that ISO has a good binding interaction with AKT. Moreover, ISO promoted M2 polarization in macrophages in a dose-dependent manner *in vitro*. Our study found that ZZO could promote DU wound healing by inhibiting inflammation, which was achieved by macrophage M2 polarization through activating the PI3K/AKT pathway. Further studies have demonstrated that ISO plays major role in the above process. These findings

provide a theoretical basis for further preclinical evaluation and lay a foundation for nano-gel compound treatment with ZZO.

#### KEYWORDS

Zizhu ointment, diabetic ulcer, PI3K-AKT signaling pathway, macrophage, network analysis, UPLC-HRMS

## Introduction

Diabetic ulcer (DU) is regarded as one of the most prevalent complications of diabetes, with a global prevalence of 6.3% (Gupta et al., 2017), leading to high mortality and disability in diabetes patients (Zhao et al., 2020). About 19–34% of diabetes patients may develop a DU during their lifetime (Armstrong et al., 2017). Moreover, the recurrence rates of DU remain high, at approximately 40% within one year and 65% within five years (Armstrong et al., 2017). Clinically, the current treatment of DU includes debridement, antibiotics, and revascularization, but its efficacy is poor (da Silva et al., 2010; Shang et al., 2019). Thus, it is urgent to find an effective additional therapy to promote the wound healing of DU when combined with standard treatment.

Traditional Chinese medicine (TCM) has become popular in the treatment of DU at multiple levels and in multiple pathways (Zhou et al., 2022). In a systematic review of 49 randomized controlled trials of TCM anti-DU, Wang et al. found that healing rates with TCM therapy were 42–60.4%, or twice times as high as healing rates with standard therapy (Wang et al., 2019). Our research group has been engaged in clinical studies of TCM in anti-DU for a long time. We have found that Zizhu ointment (ZZO)—which consists of cinnabaris (Zhusha, ZS), *Astragalus mongholicus* Bunge (Fabaceae; Huangqi, HQ), *Arnebia guttata* Bunge (Boraginaceae; Zicao, ZC), *Asini corii colla* (Ejiao, EJ), *Borneolum* (Bingpian, BP), and *Calamus draco* Willd. (Arecaceae; Xuejie, XJ)—is helpful in clinical practice (Huang et al., 2022). We recruited 76 DU patients to compare wound healing rates with ZZO treatment and basic fibroblast growth factor (bFGF) spray treatment. The results showed that ZZO is more effective in DU recovery, with a response rate of up to 50% compared with 28% in the control group (Han and Liu, 2021). Recently, the preparation process, parameters, and clinical efficacy of ZZO have been awarded a national invention patent (ZL201010186284.X).

Based on the accepted anti-DU clinical efficacy of ZZO, we aimed to further investigate its mechanisms and active compounds. Our previous study found that ZZO accelerates the wound healing process *via* inhibiting Notch4 signaling and promoting the M2 polarization of macrophages (Huang et al., 2022). Nevertheless, the anti-DU active ingredients of ZZO have not been clearly elucidated and warrant further exploration. In this study, we adopted a network analysis approach, employing the framework of “one drug, one target, one disease” (Gocho et al., 2021) to understand the mechanisms underlying ZZO against DU. We also used high-performance

liquid chromatography-high resolution mass spectrometry (UPLC-HRMS) to compare the compounds screened from the network analysis. Furthermore, the mechanisms of ZZO predicted by network analysis were evaluated *in vivo* and *in vitro*. An overview flowchart of the study design is shown in Figure 1.

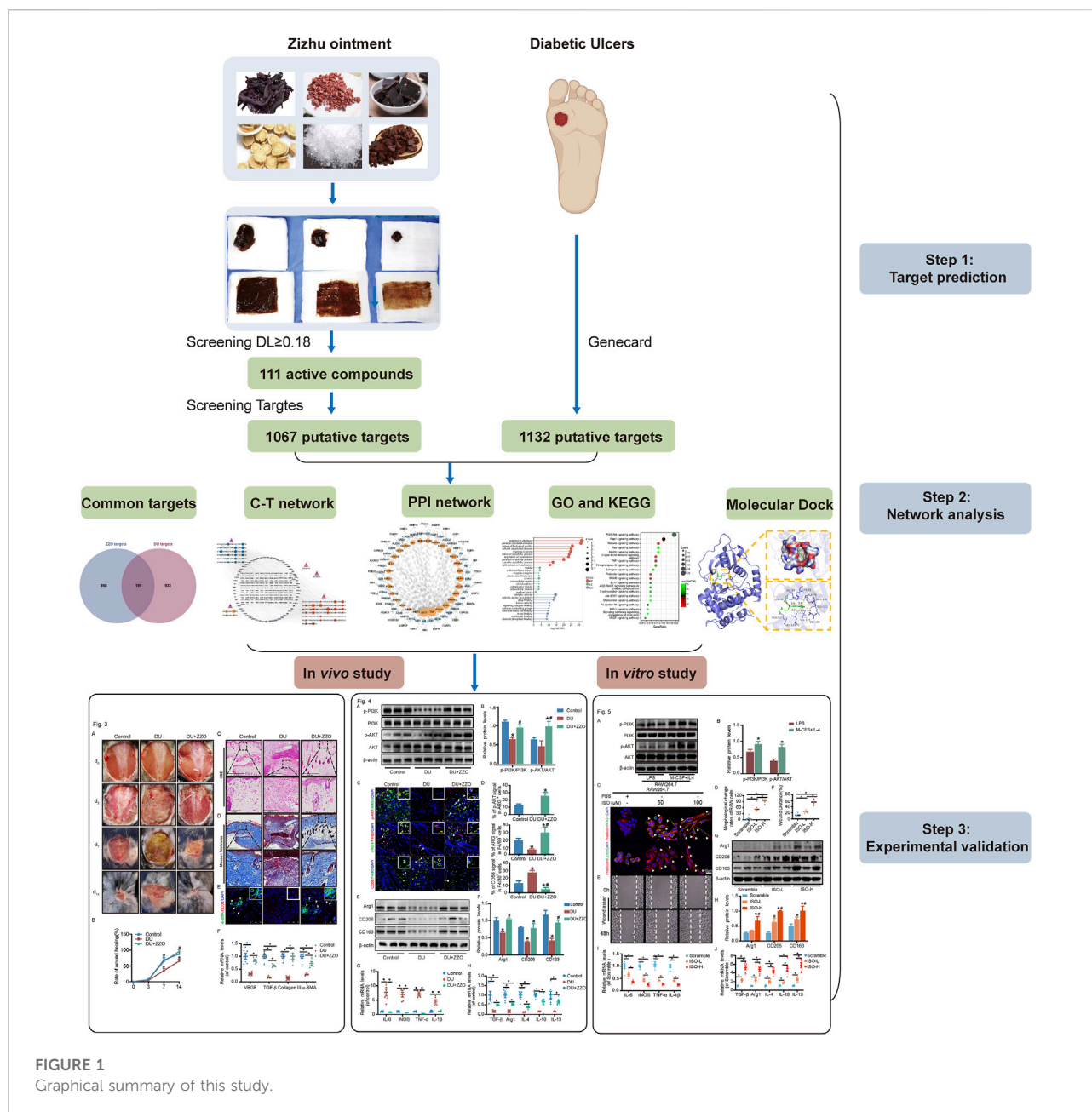
## Materials and methods

### Composition and preparation of ZZO and chemical component profiling

The crude ingredients of ZZO were purchased from Shanghai Kangqiao Chinese Medicine Tablet Co., Ltd. and processed by the Wuhan Ma Yinglong workshop, with all ingredients corresponding to quality control standards. The ratios of the main medicines (by weight) of ZS, ZC, XJ, HQ, EJ, and BP were 7: 3: 3: 6: 5: 1, and the ratio of the components of ZZO to the base materials was 1: 8 (Huang et al., 2022). The ZZO preparation was also composed of excipients including poloxamer, propylene, water, glycerol, polyethylene glycol (PEG), PEG 1500, PEG 4000, and ethyl p-hydroxybenzoate, for which the ratios were 34: 24: 70: 2.6: 9:9: 3:0.06.

### UPLC-MS analysis

UPLC-MS analysis was accomplished by Shanghai Applied Protein Technology. Purified ZZO samples of 0.02 g were weighed and placed in 1.5 ml centrifuge tubes. The samples were dissolved in 1 ml of 70% methanol, then vortexed for 30 min and centrifuged (16,000 g/15 min, 4°C, Eppendorf Centrifuge 5430 R). The supernatant was collected and vacuum freeze-dried. The residue after lyophilization was again dissolved in 2 ml of 40% methanol. The samples were vortex mixed, rotated, and centrifuged (16,000 g/15 min, 4°C), and the supernatant was collected. The ZZO extracts were analyzed using a UPLC-HRMS system (UPLC, ACQUITY Waters UPLC HSST3; MS, Q Exactive, Thermo Scientific). UPLC separation was conducted on an ACQUITY UPLC HSS T3 column (2.1 × 100 mm, 1.8μm, Thermo Scientific) at a flow rate of 0.3 ml/min. HPLC-grade solvents and additives were from ThermoFisher Scientific (United States). The gradient program using 0.1% formic acid in water (phase A) and 0.1% formic acid acetonitrile (phase B) was adopted as follows: 95% A at 0 min to



2% A at 17 min, 95% A at 17.2 min, lasting for 2.8 min, then back to original condition. The column temperature was 35°C and the injection volume of ZZO solution was 2  $\mu$ L. MS analysis was conducted using the positive ion mode. The instrument was calibrated using external standards before analysis to ensure a mass accuracy of better than 3 ppm throughout the experiment. The source parameters were as follows: spray voltage of 3.8 kV, capillary temperature of 320°C, sheath gas flow rate of 45 arb. units, Aux gas flow rate of 20 arb. units, spare gas flow rate of 0 arb. units, and probe heater temperature of 370°C. A full MS scan (m/z 90–1300) with a resolution of dd-MS2 was used.

## Analysis of ZZO by network analysis

### Prediction of the active compounds in ZZO

The candidate compounds of ZZO were collected from the Traditional Chinese Medicine Systems Pharmacology Database and Analysis Platform (TCMSP) (<http://tcmsp-e.com.tcmsp.php>), the largest database to include data for TCM pharmacology (Ru et al., 2014), and the Herbal Ingredients' Targets Database (HIT) database (<http://lifecenter.biosino.org/>)



hit; Xiao et al., 2019). As ZZO is not absorbed orally, drug-like quality (DL), an established concept used in drug design to evaluate the solubility and chemical stability of a potential compound, was adopted as a parameter for the initial screening of the active compounds (Jia et al., 2020). Herein, we adopted a DL value  $\geq 0.18$  as the criterion for identifying prospective active compounds (Li et al., 2020).

## Potential common targets of ZZO against DU

Multiple ingredients of ZZO exerted interactive synergistic therapeutic effects with multiple targets. We used the Swiss Target Prediction (<http://www.swisstargetprediction.ch>; Gfeller et al., 2014) and PharmMapper databases (<http://lilab-ecust.cn/pharmmapper/>; Gu et al., 2020) and the STITCH system (<http://stitch.embl.de/cgi/input.pl>; Aihaiti et al., 2021) to screen potential targets of these compounds. Meanwhile, known DU-related targets were screened by the DrugBank database (<https://www.drugbank.ca/>; Wishart et al., 2018), the online Mendelian Inheritance in Man (OMIM) database (<https://omim.org/search/advanced/geneMap>), and the GeneCards database (<https://www.genecards.org/>) using the keywords “diabetic foot ulcer” and “diabetic ulcer” (Sayers et al., 2021) in the OMIM and GeneCards databases (choosing the target of relevance score  $> 5$ ). (Tao et al., 2020). All potential targets were converted to official names by importing them into the UniProt knowledge base (<https://www.uniprot.org/>; UniProt Consortium, 2021). The targets common to ZZO and DU were identified as potential therapeutic targets.

## Constructing the common target predicted protein–protein interaction network

To detect the systemic effect of the common target proteins, these targets were imported into the online STRING database (<https://string-db.org/>; Szklarczyk et al., 2021), which contains confirmed PPI, and the confidence level score was set to  $\geq 0.4$ . Moreover, Cytoscape software (version 3.9.1) was used to visualize the PPI network (Kohl et al., 2011) and to evaluate the statistical properties of nodes in the network. We included targets with top-100-degree values for further pathway analyses.

## Gene Ontology (GO) and Kyoto Encyclopedia of Genes and Genomes pathway enrichment analyses

The top-100 degree targets were evaluated by GO enrichment and KEGG pathway analysis using the Sangerbox database

(<https://www.sangerbox.com/>), and only items with  $p$ -values  $< 0.05$  were selected (Shen et al., 2022). Furthermore, human disease pathways were excluded, and the gene ratio  $> 10$  pathways in KEGG analysis were included.

## Molecular docking

The structures of the compounds were downloaded from the PubChem database (<https://pubchem.ncbi.nlm.nih.gov/>; Kim et al., 2016). Next, the protein structures were imported into the Chem3D software (Meng et al., 2004), and the 3D crystal structures of compounds were obtained. Meanwhile, the structures of targets were obtained from the Research Collaboratory for Structural Bioinformatics database (<https://www.rcsb.org/structure/2ZUT>; Segura et al., 2020), including the removal of ligands and water molecules, addition of polar hydrogen, and combination of non-polar hydrogen. Then, the compounds and targets were imported into Schrödinger Maestro software (Friesner et al., 2004). The compounds were shortlisted based on their docking scores in the Standard Precision method.

## Experimental evaluation

### Establishment of a DU mouse model and treatment

Adult male C57BL/6 mice (21–25 g, 8–10 weeks) were purchased from Shanghai Model Organisms Center, Inc. The mice were housed in the Experimental Animal Center of Shanghai University of TCM in a specific pathogen-free environment under a 12 h light/dark cycle with freely available water and food. Mice were randomly assigned to each group ( $n = 4$ ), including the non-diabetic group (phosphate-buffered saline, PBS) and the DU group without or with ZZO treatment. DU groups were fed a high-fat diet comprised of 60% calories (FB-D12451, Wuxi Fan Bo Biotechnology Co., Ltd.) for three weeks and subjected to STZ (40 mg/kg/day, ip. Cat. No. 2196GR001, BioFRox) for one week (Cheng et al., 2021). It was considered type 2 diabetes until the level of fasting blood glucose exceeded 11.1 mmol/L (Gupta et al., 2016). Subsequently, full-thickness skin wounds (1\*1 cm, with depth to the fascial layer) were surgically created on the back of mice by lifting the skin with forceps (Qiu et al., 2020). The wound was bandaged with 1 cm<sup>2</sup> gauze with excipients or ZZO (50 mg/cm<sup>2</sup>). The dressing was changed daily. All animal experiments were approved by the Animal Ethics Committee of Shanghai University of Traditional Chinese Medicine (Approval No. PZSHUTCM220711028) and correspond to the National Institutes of Health guide for the care and use of Laboratory animals (NIH Publications No. 8023, revised 1978).

TABLE 1 Prime sequences.

Primer	Forward (5'–3')	Reverse (5'–3')
<i>mGapdh</i>	TGGATTTGGACGCATTGGTC	TTTGCACTGGTACGTGTTGAT
<i>mArg1</i>	TGTGGGAAAAGCCAATGAAC	GGTGTGACGCGAGTGTTG
<i>mIl-4</i>	CGTGATGTACCTCCGTGCTT	GTGAGTTCAGACCGCTGACA
<i>mIl-13</i>	CCTGGCTCTTGCTTGCCTT	GGTCTTGTGTGATGTTGCTCA
<i>mIl-10</i>	TTGAACCACCCGGCATCTAC	CCAAGGAGTTGCTCCCGTTA
<i>mIl-6</i>	GCTACAGCACAAAGCACCTG	GACTTCAGATTGGCGAGGAG
<i>miNos</i>	GATAAAGGGACAGCGTCAGC	CCTTCGGGCCAAAGATCCTG
<i>mTnf-α</i>	TACTGAACTTCGGGGTGATTGGTCC	CAGCCTTGTCCTTGAAGAGAACC
<i>mIl-1β</i>	ATCTCGCAGCAGCACATCAAC	TGTTTCATCTCGGAGCCTGTAGT
<i>ma-SMA</i>	GTCCAGACATCAGGGAGTAA	TCGGATACTTCAGCGTCAGGA
<i>m-CollalIII</i>	CTGTAACATGGAACTGGGGAAA	CCATAGCTGAACTGAAAACCACC
<i>m-Vegf</i>	GAGGTCAAGGCTTTTGAAGGC	CTGTCCTGGTATTGAGGGTGG
<i>m-Tgfb</i>	ATGTCACGGTTAGGGGCTC	GGCTTGCATACTGTGCTGTATAG

## Wound closure analysis

To assess the condition of wound healing in mouse backs, the wound was photographed by a digital camera (Nikon, Tyoto) on days 0, 3, 7, and 14 (Huang et al., 2020). The wound closure rate was quantified by ImageJ software (Bethesda, MD) and calculated as follows:  $t-t_0/t_0 \times 100\%$  ( $t$ : the wound healing was assessed,  $t_0$ : initial wounding).

## Hematoxylin and Eosin and Masson staining

The wound tissues were fixed with 4% paraformaldehyde (PFA, Cat. No. P0099, Beyotime) for 48 h. Following standard paraffin embedding and sectioning, the wound tissues were subjected to hematoxylin and eosin (H&E, Cat. No. C01105M, Beyotime, China) and Masson staining (Cat. No. G1340, Solarbio Life Sciences, China). Stained tissues were analyzed using a digital slide scanning system (Precipoint M8).

## Immunofluorescence staining

To detect the co-localization of macrophages, a double IF was performed. After routine deparaffinization, rehydration, and antigen repair, the sections were incubated with 3% bovine serum albumin (BSA; Cat. No.3610 ES76, Yeasen Biotech Co., Ltd.). Then a rabbit anti-F4/80 antibody (Cat. No. 30325, CST; 1:200) mixed with a mouse anti-arginase 1 (ARG1; Cat. No.SC-271430, Santa Cruz; 1:200) or a mouse anti-CD68 (Cat. No.

YM3050, Immunoway; 1:200), and a mouse anti-ARG1 (Cat. No.SC-271430, Santa Cruz; 1:200) mixed with a rabbit anti-p-AKT (Cat. No.9271S, CST; 1:200) were incubated overnight at 4°C. Tissue sections were washed with PBS three times and cultured in the dark with donkey anti-mouse Alexa Fluor 488 (Cat. No. A21202, Life Technologies; 1:500) or donkey anti-rabbit Alexa Fluor 488 (Cat. No. A21206, Life Technologies; 1:500) and donkey anti-rabbit Alexa Fluor 555 (Cat. No. A31572, Life Technologies; 1:500) or goat anti-mouse Alexa Fluor 555 (Cat. No. A31570, Invitrogen; 1:500) for 2 h at room temperature at the next day and then washed three times with PBS. Nuclei were counterstained with DAPI (Cat. No.C1006, Beyotime) for 10 min and then washed with PBS; antifade mountant (Cat. No. P0126, Beyotime) was added to each coverslip, and the coverslips were placed on the slides. Positive signals were captured using a confocal microscope (Leica SP-8, Leica Corporation, German) and further analyzed with the Adobe Photoshop CS software program. Analysis of fibrosis and angiogenesis was performed by dual IF with mouse anti-α-SMA (Cat. No. MA5-15871, Invitrogen; 1:200) and rabbit anti-CD31 antibodies (Cat. No. PA5-32321, Invitrogen; 1:200). The methods were as described previously.

## RNA extraction and quantitative real-time PCR array

Trizol (Cat. No. R0016, Beyotime, China) was used to extract RNA according to the manufacturer's instructions. NanoDrop ND-1000 was used to determine the concentration of RNA, and the extracted RNA was stored in a refrigerator at −80°C. Using

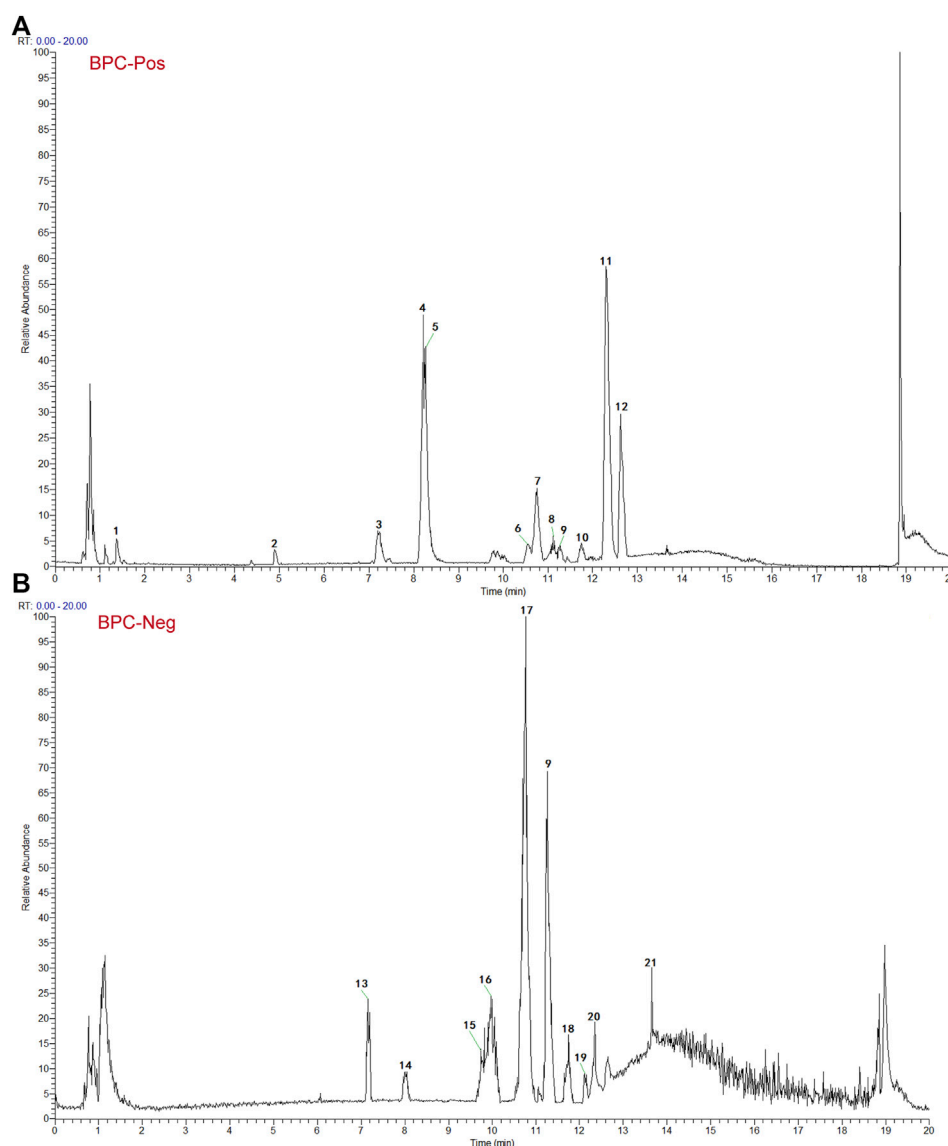


FIGURE 2

Identification results of the main chemical components of ZZO by UPLC-Q-HRMS. (A) Total ion flow diagram of ZZO in negative mode. (B) Total ion flow diagram of ZZO in positive ion mode.

500 ng total RNA as a template, cDNA was synthesized with the cDNA Synthesis Kit (Cat. No. R312, Vazyme, China). Samples were stored at  $-20^{\circ}\text{C}$  and subjected to qPCR using a StepOnePlus Real-Time PCR System (Applied Biosystems). Each qPCR sample was performed in a  $10\ \mu\text{L}$  reaction containing 2xSYBR Green qPCR Master Mix (Cat. No. R711-02, Vazyme, China), 10 nM forward and reverse primers, and  $2\ \mu\text{L}$  cDNA in triplicate. The qPCR protocol was executed for 45 cycles, with each cycle consisting of denaturation at  $95^{\circ}\text{C}$  for 15 s, annealing at  $60^{\circ}\text{C}$  for 1 min, and extension at  $72^{\circ}\text{C}$  for 1 min. Using *GAPDH* as an internal control, quantitative PCR analysis was performed to quantify the relative mRNA expression of targeted genes. The

result of qPCR from the threshold cycle ( $C_t$ ) and use the  $2^{-\Delta\Delta C_t}$  method was defined to calculate the relative expression level. The primer pairs specific for various genes used in our experiments are listed in Table 1.

## Western blot analysis

Wound tissues and cells were lysed in a RIPA lysis buffer (Cat. No. P0013C, Beyotime, China) containing proteinase and phosphatase inhibitor cocktails (Cat. No. P1005, Beyotime, China; Cat. No. P1045, Beyotime, China). An equal amount

TABLE 2 The top 21 compounds of ZZO by UPLC-HRMS analysis.

PeakNo	m/z	RT min	ppm	Compound name	Score	PubCHEM	Molecular formula
						CID	
1	155.0818	1.40	0.4	Pyrrolloperazine-2,5-dione	0.997	Cid_193540	C <sub>7</sub> H <sub>10</sub> N <sub>2</sub> O <sub>2</sub>
2	188.1432	4.92	0.6	N-[1-(2-Phenylethyl)-4-piperidinyl]-2-naphthamide	0.9995	Cid_35296170	C <sub>24</sub> H <sub>26</sub> N <sub>2</sub> O
3	253.0857	7.23	0.2	4'-Methoxyflavone	0.9975	Cid_77793	C <sub>16</sub> H <sub>12</sub> O <sub>3</sub>
4	267.1019	8.22	0.2	3,4'-Dimethoxy-2-hydroxychalcone	0.9938	Cid_5976425	C <sub>17</sub> H <sub>16</sub> O <sub>4</sub>
5	298.2163	8.25	11.4	C11:db-UHQ aka 2-undecenyl-quinoloin-4(1H)-one position of double bond unknown	0.9637	Cid_129846253	C <sub>20</sub> H <sub>27</sub> NO
6	167.0703	10.56	0.9	3,5-Dimethoxycinnamic acid	0.8941	Cid_5324677	C <sub>11</sub> H <sub>12</sub> O <sub>4</sub>
7	285.1122	10.74	0.1	1,2-Propanediol, 1,2-dibenzoate	0.9944	Cid_517637	C <sub>17</sub> H <sub>16</sub> O <sub>4</sub>
8	137.1326	11.13	0.3	Eucalyptol	0.9981	Cid_2758	C <sub>10</sub> H <sub>18</sub> O
9	257.0810	11.28	1.9	Pinocembrin	0.9871	Cid_68071	C <sub>15</sub> H <sub>12</sub> O <sub>4</sub>
10	137.1326	11.77	0.8	Decalin-2-carboxylic acid	0.9977	Cid_656885	C <sub>11</sub> H <sub>18</sub> O <sub>2</sub>
11	372.1167	12.31	17.1	Isovalerylshikonin	0.9895	Cid_479497	C <sub>21</sub> H <sub>24</sub> O <sub>6</sub>
12	271.1329	12.63	21.4	Difenpiramide	0.7295	Cid_100472	C <sub>19</sub> H <sub>16</sub> N <sub>2</sub> O
13	303.2169	7.17	0.3	Aleuritic acid	0.9985	Cid_222178	C <sub>16</sub> H <sub>32</sub> O <sub>5</sub>
14	181.0502	8.02	3.4	Gallacetophenone-4'-methyl ether	0.9889	Cid_12820	C <sub>9</sub> H <sub>10</sub> O <sub>4</sub>
15	269.0814	9.76	0.1	Echinatin	0.915	Cid_6442675	C <sub>16</sub> H <sub>14</sub> O <sub>4</sub>
16	245.3384	9.98	5.3	Mandenol	0.988	Cid_5282184	C <sub>20</sub> H <sub>36</sub> O <sub>2</sub>
17	283.0976	10.74	21.6	Curculigoside	0.8576	Cid_158845	C <sub>22</sub> H <sub>26</sub> O <sub>11</sub>
18	398.3437	11.74	6.81	Daidzein	0.993	Cid_5281708	C <sub>15</sub> H <sub>10</sub> O <sub>4</sub>
19	269.0820	12.13	0.3	Cryptostrobin	0.9949	Cid_6453244	C <sub>16</sub> H <sub>14</sub> O <sub>4</sub>
20	243.1959	12.35	1	14-Hydroxymyristic acid	0.997	Cid_3084276	C <sub>14</sub> H <sub>28</sub> O <sub>3</sub>
21	271.2274	13.68	0.1	3-Hydroxypalmitic acid	0.9972	Cid_301590	C <sub>16</sub> H <sub>32</sub> O <sub>3</sub>

of protein sample (20 µg) from each group was loaded on a 7.5% or 10% SDS-PAGE gel (Cat. No. PG111, PG112, EpiZyme, China) along with standard molecular weight markers (Cat. No.26619, 26,625, Thermo Fisher, United States), followed by transfer onto a polyvinylidene difluoride (PVDF) membrane (Cat. No. IPVH00010, Millipore), which was then blocked with 5% BSA for 2 h. Membranes were incubated overnight at 4°C with a rabbit anti-p-AKT antibody (Cat. No. T40067, Abmart; 1:3000), a rabbit anti-p-PI3K antibody (Cat. No. T40064, Abmart; 1:3000), a mouse anti-PI3K antibody (Cat. No. 13666S, CST; 1:2000), a rabbit anti-AKT antibody (Cat. No. 4691S, CST; 1:1000), a rabbit anti-Arg1 antibody (Cat. No. 93668T, CST; 1:2000), a rabbit anti-CD206 antibody (Cat. No. 24595S, CST; 1:2000), a rabbit anti-CD163 antibody (Cat. No. 93498S, CST; 1:2000), and a rabbit anti-β-actin antibody (Cat. No. AF7018, Affinity; 1:5000) in 5% BSA. After rigorously washing with TBS containing 0.1% Tween-20 (Cat. No. T8220, Solarbio, China), membranes were incubated at room

temperature for 1 h with a goat anti-rabbit HRP-conjugated IgG antibody (Cat. No. A0208, Beyotime; 1:10,000) or a goat anti-mouse HRP-conjugated IgG antibody (Cat. No. A0216, Beyotime; 1:10,000). Subsequently, membranes were washed three times with TBST. Target proteins were visualized using a super-sensitive electrochemiluminescence (ECL) reagent (Cat. No. MA0186, Meilunbio, China) with a Molecular Imager ChemiDoc XRS System (Tanon).

## Cell culture

RAW264.7 (mouse macrophage line) cells were purchased from American Type Culture Collection and cultured in Dulbecco's Modified Eagle Medium (DMEM) supplemented with 10% heat-inactivated fetal bovine serum (FBS), 100 U/ml penicillin, and 100 µg/ml streptomycin under 37°C, 5% CO<sub>2</sub> conditions. M1 macrophages were induced by



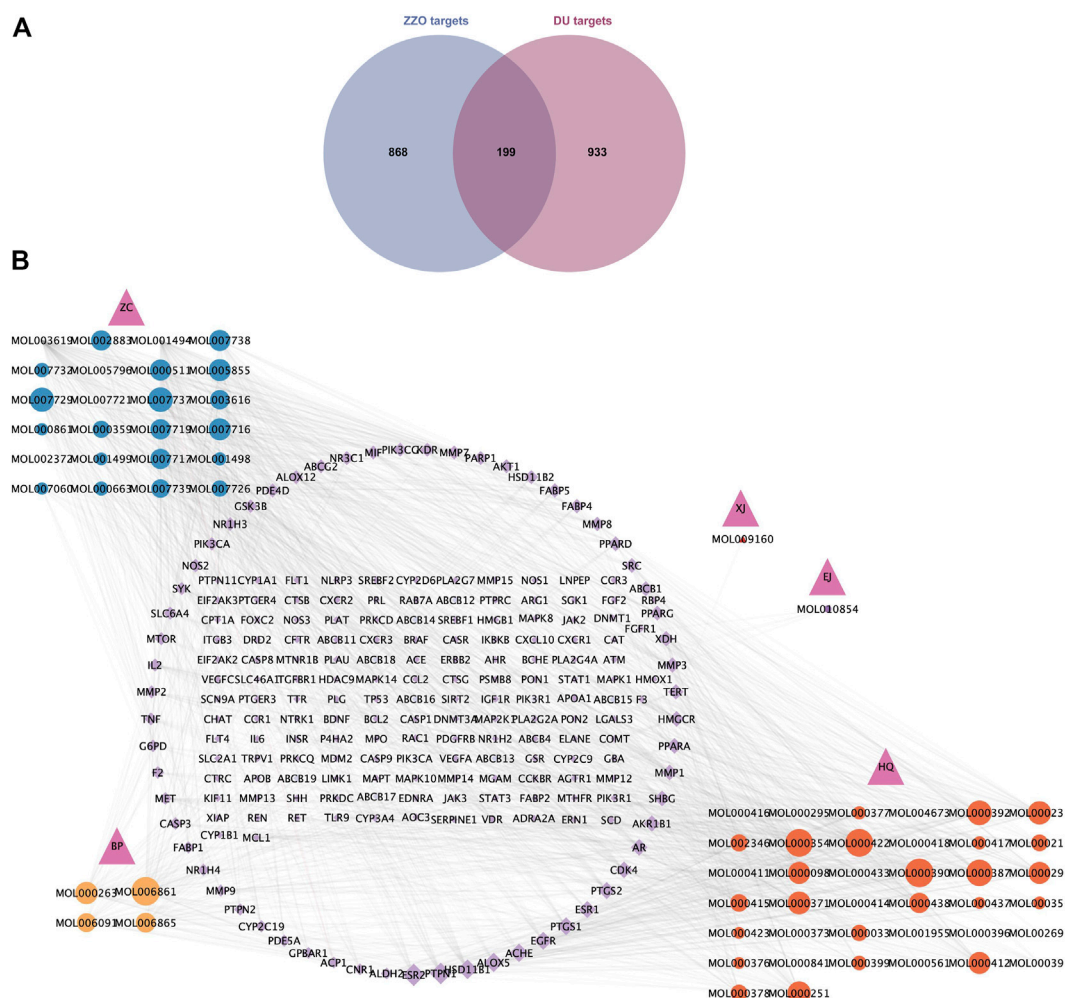


FIGURE 3

Common targets and C-T network of anti-DU ZZO. (A) Targets common to ZZO and DU. There are 199 common targets between ZZO and DU. (B) C-T network of ZZO anti-DU. Pink triangles represent herbal medicines, circles represent compounds, and diamonds represent targets. Node size reflects node degree: bigger size means a larger degree value.

lipopolysaccharide (LPS; 100 ng/ml, Cat. No. L2630, Sigma-Aldrich, United States; Lv et al., 2021), whereas M2 macrophages were induced by IL-4 (20 ng/ml, Cat. No. 214-14, Peprotech, United States) and M-CSF (25 ng/ml, Cat. No. 315-02, Peprotech, United States) (Moore et al., 2015).

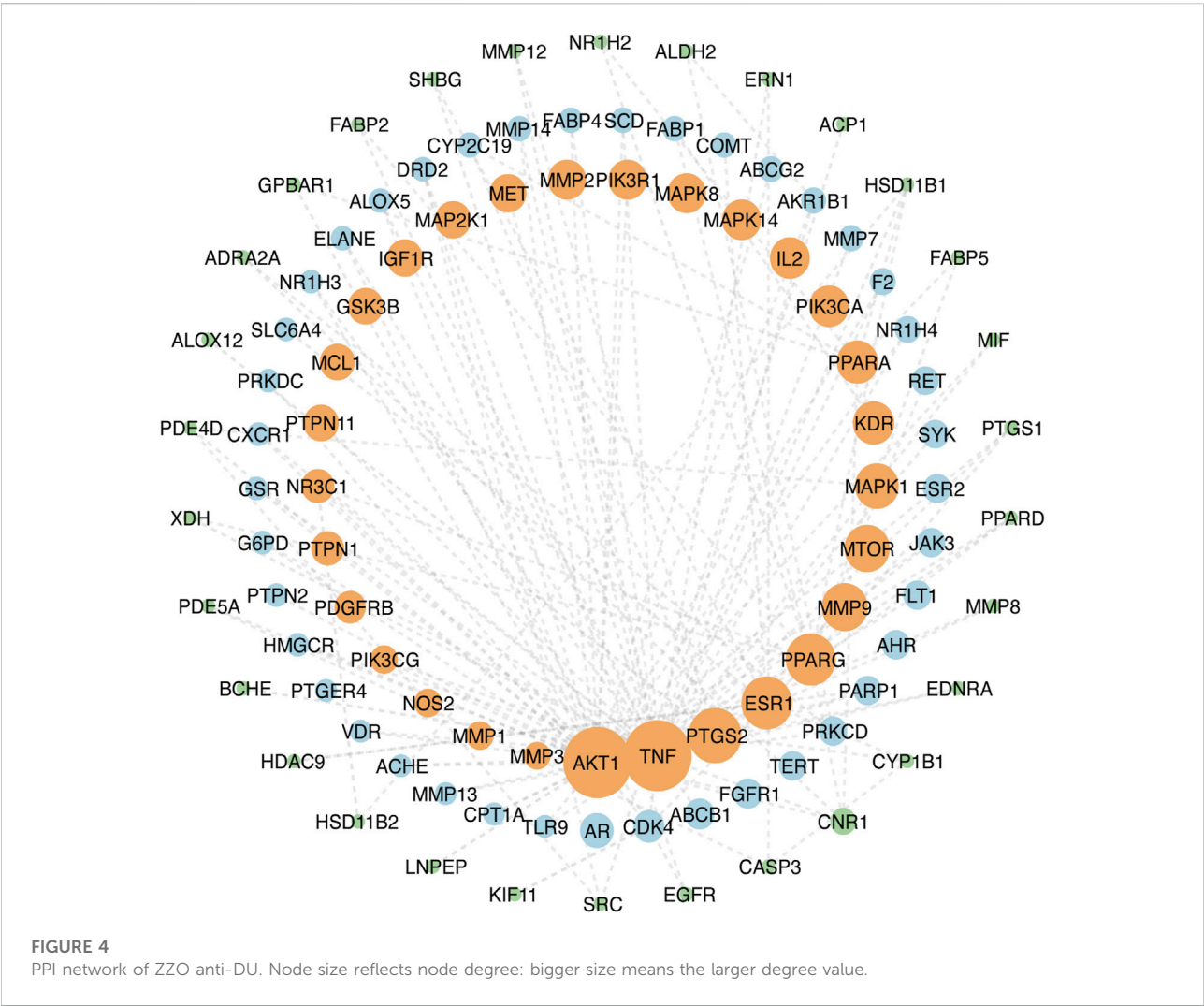
## Cell morphological assay

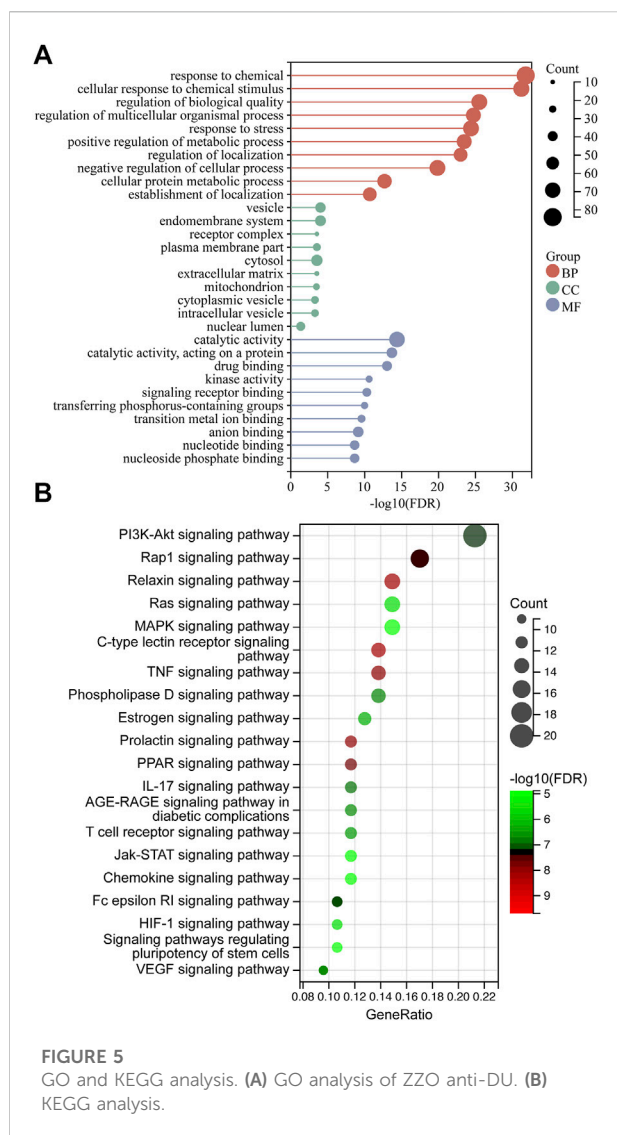
RAW264.7 cells treated with ISO-L (50  $\mu$ M, Cat. No. HY-N3012, MCE) or ISO-H (100  $\mu$ M) were grown on coverslips in 24-well plates to about 30% confluency. After 24 h of incubation, cells were fixed with 4% PFA for 30 min. After washing with PBS three times, cells were stained with a mouse

anti-CD68 antibody (Cat. No. YM3050, Immunoway; 1:200) and a mouse anti-ARG1 antibody (Cat. No. SC-271430, Santa Cruz; 1:200) overnight at 4°C. Next, cells were gently rinsed three times with PBS and incubated in the dark with donkey anti-mouse Alexa Fluor 488 (Cat. No. A21202, Life Technologies; 1:500) for 2 h at room temperature. After rigorous rinsing, cells were stained with Alexa Fluor 555-phalloidin (Cat. No. A34055, Invitrogen; 1:200) for 30 min at 37°C. Subsequently, nuclei were counterstained with 4',6-diamidino-2-phenylindole (DAPI; Cat. No. C1006, Beyotime, China) and mounted with an antifade mounting medium (Cat. No. P0126, Beyotime, China). Photographs were taken using a confocal microscope (Leica SP-8, Leica Corporation, German).

TABLE 3 Information on top 10-degree compounds of ZZO.

No.	Compound	MOL ID	Molecular formula	Herb medicine	DL
1	Isovalerylshikonin	MOL003619	C <sub>12</sub> H <sub>24</sub> O <sub>6</sub>	Zicao	0.35
2	Mandenol	MOL001494	C <sub>20</sub> H <sub>36</sub> O <sub>2</sub>	Zicao	0.19
3	Daidzein	MOL000390	C <sub>15</sub> H <sub>10</sub> O <sub>4</sub>	Huangqi	0.19
4	Asiatic acid	MOL006861	C <sub>30</sub> H <sub>48</sub> O <sub>5</sub>	Bingpian	0.71
5	Isorhamnetin	MOL000354	C <sub>12</sub> H <sub>12</sub> O <sub>7</sub>	Huangqi	0.31
6	Kaempferol	MOL000422	C <sub>15</sub> H <sub>10</sub> O <sub>6</sub>	Huangqi	0.24
7	Bifendate	MOL000387	C <sub>20</sub> H <sub>18</sub> O <sub>10</sub>	Huangqi	0.67
8	α-Methyl-n-butylshikonin	MOL007737	C <sub>21</sub> H <sub>28</sub> O <sub>5</sub>	Zicao	0.35
9	Formononetin	MOL000392	C <sub>16</sub> H <sub>12</sub> O <sub>4</sub>	Huangqi	0.21
10	Shikonofuran C	MOL007729	C <sub>21</sub> H <sub>26</sub> O <sub>5</sub>	Zicao	0.3





and pairwise comparisons within groups were analyzed by the Student's *t*-test. *p*-values <0.05 were considered to indicate statistical significance.

## Results

### Identification of active components of ZZO

Based on the TCMSP and HIT, 111 compounds from ZS, HQ, ZC, EJ, BP, and XJ were obtained. A total of four duplicate compounds were included, including oleanolic acid, rhamnocitrin, daidzein, and formomonetin. Moreover, there were found to be 38 compounds in ZC, 61 compounds in HQ, 5 compounds in BP, 5 compounds in ZS, 4 compounds in EJ, and 2 compounds in XJ. The overall compounds in ZZO are summarized in [Supplementary Table S1](#). Moreover, ZZO was further analyzed by UPLC-HRMS and yielded 392 identified compounds ([Supplementary Table S2](#)); the top 21 compounds of ZZO are shown in ([Figure 2](#); [Table 2](#)).

### Compound–target network construction

Among the six active herb medicines, 1067 targets were retrieved from target prediction databases. A total of 1132 candidate targets for DU were obtained from the Genecard, Drugbank, and OMIM databases. Eventually, 199 common targets ([Figure 3A](#)) were considered potential targets of ZZO against DU. Then, the compound–target (C-T) network was constructed ([Figure 3B](#)). Among these bioactive components, isovalerylshikonin (ZC, degree = 97) exhibited the highest correlation with DU targets, and the other top four based on degree value were mandenol (ZC, degree = 65), daidzein (HQ, degree = 48), Asiatic acid (BP, degree = 48), and isorhamnetin (HQ, degree = 46). The details of the top ten compounds are summarized in [Table 3](#).

### PPI network analysis

The top 100 common target genes were imported into the STRING database, and medium confidence of PPI was input to Cytoscape 3.9.1 for analyzing and constructing the PPI network ([Figure 4](#)). In the PPI network, targets with higher degrees played central roles in multi-protein interactions. The top 15 genes, ranked by degree value, were identified as the hub targets: *AKT1* (degree = 72), tumor necrosis factor (*TNF*; degree = 72), SRC proto-oncogene (*SRC*; degree = 57), epidermal growth factor receptor (*EGFR*; degree = 55), caspase 3 (*CASP3*; degree = 51), prostaglandin-endoperoxide synthase 2 (*PTGS2*; degree = 50), estrogen

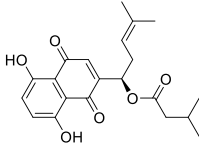

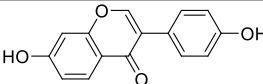
## Wound healing assay

RAW264.7 cells were seeded into a 6-well plate and then treated with ISO-L or ISO-H. After the cells grew to a 100% confluent layer, 2 ml of serum-free DMEM medium was added. A 10  $\mu$ L pipette tip was used to make a straight scratch on the upper surface. Then, cell debris was removed with PBS, and images were taken at 0 and 48 h using an inverted microscope.

## Statistical analysis

Statistical analyses were conducted using GraphPad Prism (GraphPad, United States). One-way ANOVA and two-way ANOVA were used for comparisons between multiple groups,

TABLE 4 Docking results for AKT with compounds.

Target ID	Compounds	Structure	Docking score (kcal/mol)	Combination type
AKT	Isovalerylshikonin		-7.09	Hydrogen bond Hydrophobic interactive
	Mandenol		-3.26	Hydrophobic interactive
	Daidzein		-7.81	Hydrogen bond Hydrophobic interactive

receptor (*ESR1*; degree = 47), peroxisome proliferator-activated receptor gamma (*PPARG*; degree = 46), matrix metalloproteinase 9 (*MMP9*; degree = 41), mechanistic target of rapamycin kinase (*MTOR*; degree = 40), mitogen-activated protein kinase 1 (*MAPK1*; degree = 38), kinase insert domain receptor (*KDR*; degree = 35), peroxisome proliferator-activated receptor alpha (*PPARA*; degree = 35), interleukin-2 (*IL-2*; degree = 33), and phosphatidylinositol-4,5-bisphosphate 3-kinase catalytic subunit alpha (*PIK3CA*; degree = 33).

### Pathway enrichment analysis of the candidate ZZO targets

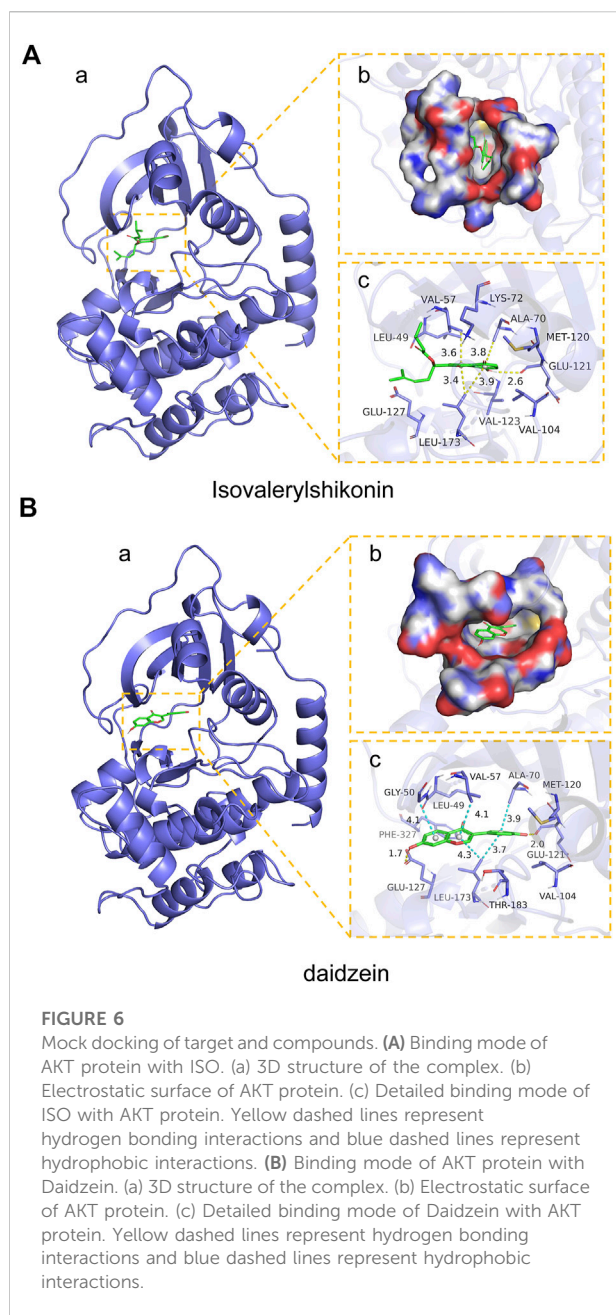
The 100-core putative ZZO targets were subjected to GO and KEGG analysis. The results revealed that 3380 biological process (BP), 251 cellular component (CC), and 3288 molecular function (MF) terms, and 136 pathways, were enriched among the targets ( $p < 0.05$ ). The overall results of the GO analysis are summarized in [Supplementary Table S3](#). The 10 significantly enriched BP, CC, and MF terms are visualized in [Figure 5A](#). The GO analysis revealed that these targets are involved in response to chemicals, drugs, and cellular metabolic processes. After excluding human disease pathways, pathways with gene ratios >10 were visualized ([Figure 5B](#)); KEGG pathways are summarized in [Supplementary Table S4](#). Various signaling pathways were linked to DU, especially the PI3K/AKT signaling pathway. This finding, in combination with a central protein analysis of the 100 core targets, indicates that AKT1 is the most important protein but that other

proteins associated with the PI3K/AKT pathway are important as well, including EGFR, PIK3CG, KDR, PIK3CA, GSK3B, MTOR, IL-2, MET, MCL1, MAPK1, IGF1R, PDGFRB, MAPK8, MAPK1, PTGS2, and MMP9. Other important pathways are the TNF, MAPK, IL-17, chemokine, HIF, and VEGF signaling pathways, suggesting that ZZO anti-DU is highly correlated with anti-inflammation and pro-angiogenesis.

### Molecular docking of targets and compounds

We next analyzed the docking level of the top three-degree compounds (ISO, mandenol, and daidzein) with the AKT target. The results from the molecular docking software are shown in [Table 4](#). Molecular docking results show that the conformation of ISO and daidzein with AKT showed good binding interactions, with binding energy of -7.09 kcal/mol and -7.81 kcal/mol, respectively. Then, using the Pymol2.1 software to visualize the binding process ([Figure 6](#)), ISO was shown to form a hydrogen bond with the hydroxyl group of (GLU-121) at the base of the AKT pocket and hydrophobic interaction with ALA-70, LEU-173, VAL-5 ([Figure 6A](#)). ISO could form stable complexes with AKT by these bindings. The hydrophobic groups of daidzein interact with the hydrophobic amino acids (ALA-70, LEU-173, VAL-57, GLY-50) at the base of the AKT pocket and play a role in stabilizing the compound-target network. Daidzein also combined with GLU-121 and GLU-127 by forming hydrogen bonding interactions with them ([Figure 6B](#)).





## ZZO promotes wound healing of DU

According to our results, ZZO significantly promoted wound healing of DU on days 7 and 14 (Figure 7A). The rate of wound healing was faster in the ZZO treatment group than in the DU group (Figure 7B). Additionally, H&E staining of the wound tissue revealed decreased inflammatory cells (i.e., polymorphonuclear leukocytes and plasma cells) and more integral epithelium in the ZZO group (Figure 7C). We also evaluated collagen deposition and angiogenesis in different groups. More collagen was formed, and the newly formed

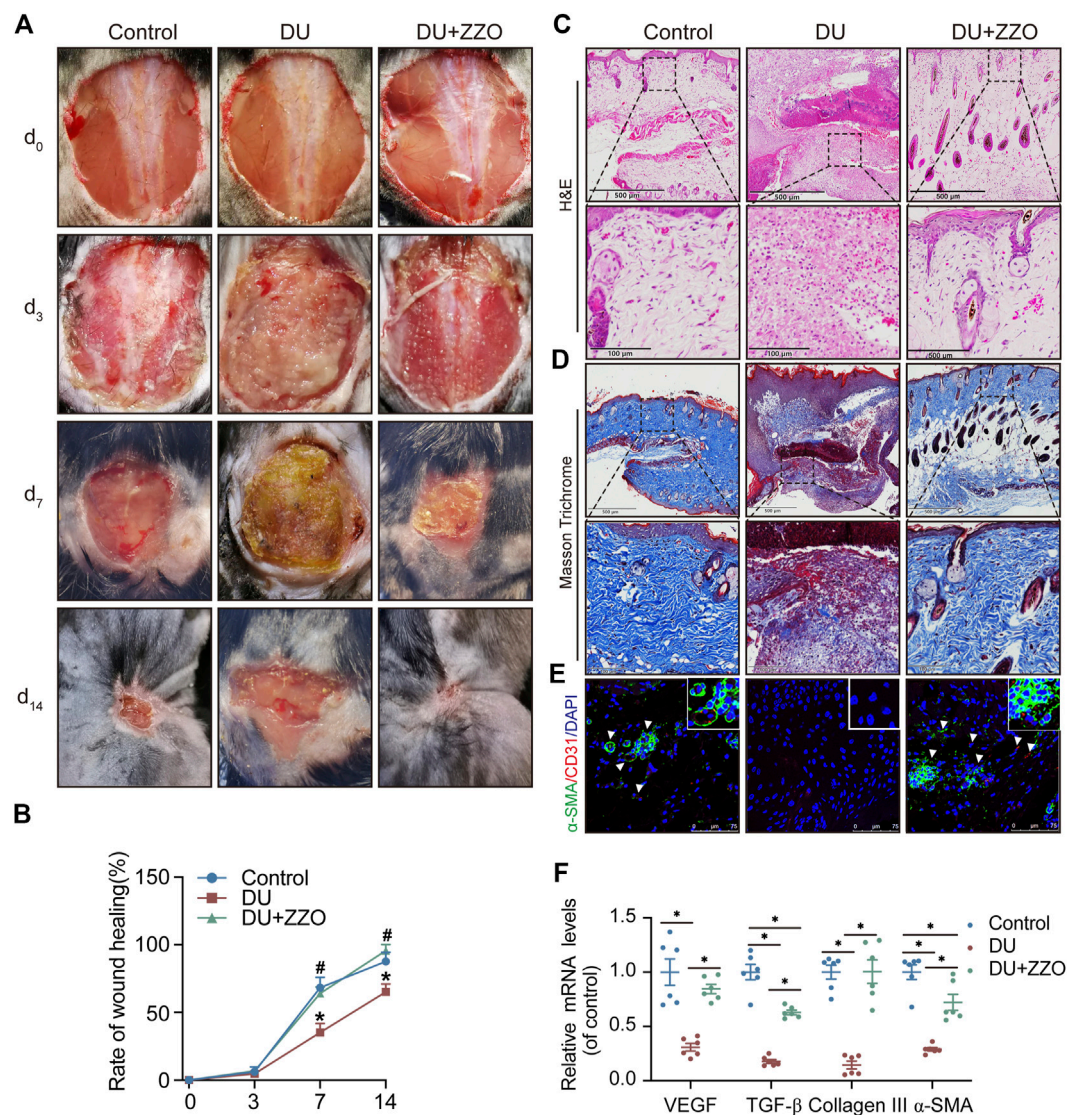
collagen fibers were remarkably thicker in the ZZO-treated group (Figure 7D). Colocation of  $\alpha$ -SMA and CD31 revealed that the amount of newly formed blood vessels and collagen fibers were remarkably higher in the ZZO group compared with the DU group (Figure 7E). Meanwhile, the mRNA expression of  $\alpha$ -SMA, Collagen I, Collagen III, and VEGF was higher in ZZO treatment group as well (Figure 7F). These results indicate that the treatment of ZZO promotes wound healing by anti-inflammation, pro-angiogenesis, and pro-fibrosis of the wound area in DU mice.

## ZZO promotes macrophage M2 polarization by activating PI3K/AKT signaling pathway in wound tissue of DU mice

The results of network analysis reveal that the PI3K/AKT signaling pathway is the most important pathway in ZZO anti-DU. Meanwhile, anti-inflammation pathways such as the TNF, IL-17, and chemokine signaling pathways play central roles as well. Therefore, we investigated the PI3K/AKT pathway and phenotypes of macrophages in wound tissues. The WB results showed that p-PI3K and p-AKT expression significantly decreased in diabetic mice, whereas those proteins were activated through ZZO treatment (Figures 8A,B). Furthermore, ZZO reversed diabetic-induced M1 macrophage infiltration and promoted M2 polarization of macrophages (Figures 8C–F). We also explored the co-expression of p-AKT and Arg1 in wound tissues, finding that the expression levels of p-AKT and Arg1 were positively correlated, which demonstrates that the M2 macrophage polarization in the ZZO group may be related to activation of the PI3K/AKT pathway (Figure 8C). We further induced M1 polarization by LPS and M2 polarization by M-CSF and IL4 in RAW264.7 cells. Indeed, M2 macrophages showed strong activation of the PI3K/AKT pathway (Figure 9A). These results indicate that diabetic mice show an inflammatory microenvironment in wound tissues but that ZZO could alleviate this environment by recruiting M2 macrophages to activate the PI3K/AKT pathway.

## ISO treatment promotes M2 macrophage polarization *in vitro*

The results of network analysis show that ISO, mandenol, and daidzein are the most important active anti-DU compounds of ZZO. We further conducted molecular docking studies to find a suitable tight ligand binding compound. ISO forms a strong tight ligand with AKT (Figure 6A). Therefore, we constructed a series of ISO-stimulated *in vitro* experiments in RAW264.7 cells. ISO changed the morphology of RAW264.7 cells, which

**FIGURE 7**

Efficacy of ZZO anti-DU *in vivo*. (A,B) Optical pictures and related quantification of the wound closure rate in the Control group, DU group, and DU + ZZO group at days 0, 3, 7, and 14 after the skin operation ( $n = 3$ ,  $*p < 0.05$ , compared with the control group at the same time point,  $^{\#}p < 0.05$ , compared with the DU group at the same time point). (C) H&E staining images of wound tissues in the Control group, DU group, and DU + ZZO group at day 14 ( $n = 3$  scale bar = 500  $\mu\text{m}$  for 10 $\times$  and 100  $\mu\text{m}$  for 40 $\times$ ). (D) Masson's trichrome staining at day 14 post-operation ( $n = 3$ , scale bar = 500  $\mu\text{m}$  for 10 $\times$  and 100  $\mu\text{m}$  for 40 $\times$ ). (E) IF expression of  $\alpha$ -SMA and CD31 in wound healing areas ( $n = 3$ , Scale bar = 75  $\mu\text{m}$ ). (F) Relative gene expression of the collagen synthesis-related genes  $\alpha$ -SMA, *Collagen I*, and *Collagen III* in the Control group, DU group, and DU + ZZO group; relative gene expression of angiogenesis-related gene *VEGF* in the Control group, DU group, and DU + ZZO group ( $n = 6$ ,  $*p < 0.05$ ).

transitioned from the M1 to the M2 phenotype (Figures 9C,D). Moreover, ISO prompted the invasion of RAW264.7, indicating an M2 phenotype (Figures 9E,F). The protein expression of ARG1, CD206, and CD163 all increased after ZZO treatment (Figures 9G,H). Furthermore, we detected the levels of proinflammatory (*i*NOS, *TNF- $\alpha$* , *IL-6*, and *IL-1 $\beta$* ), as well as anti-inflammatory factors (*IL-4*, *IL-13*, *IL-10*, *TGF- $\beta$* , and *ARG1*) by RT-PCR, and the results fully correspond with the *in vivo* findings (Figures 9I,J).

## Discussion

DU is a primary complication of diabetes and has always been a health issue in long-term clinical practice. Wound healing in DU is a prolonged process with various stages, including hemostasis, inflammation, proliferation, and remodeling (Zarei et al., 2018). Diverse cells, with different chemokine activities, take part in the process of wound healing at different stages of DU (Zhao et al., 2016). During the inflammation stage, wound



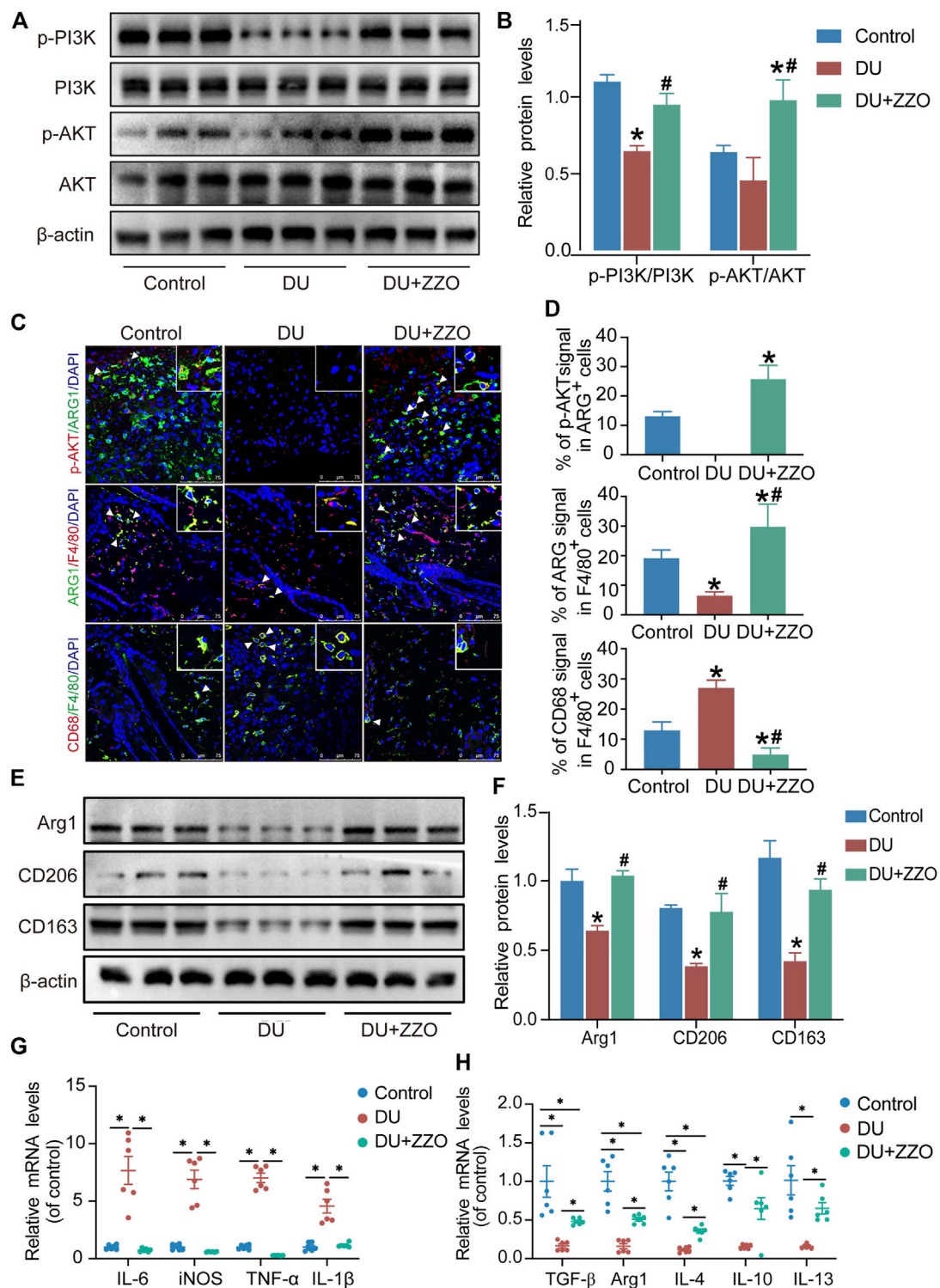


FIGURE 8

ZZO suppressed M1 macrophage-induced inflammation by activating the PI3K-AKT signaling pathway. (A,B) Expressions of PI3K, p-PI3K, AKT, and p-AKT proteins were tested in wound tissues ( $n = 3$ ,  $*p < 0.05$ , compared with the control group,  $^{\#}p < 0.05$ , compared with the DU group). (C,D) Co-localization of p-AKT/ARG1, ARG1/F4/80, and CD68/F4/80 ( $n = 3$ ,  $*p < 0.05$ , compared with the control group,  $^{\#}p < 0.05$ , compared with the DU group, Scale bar = 75  $\mu$ m). (E,F) Expressions of ARG1, CD206, and CD163 proteins were tested in wound tissues ( $n = 3$ ,  $*p < 0.05$ , compared with the control group,  $^{\#}p < 0.05$ , compared with the DU group). (G) mRNA expression of M1 macrophage markers ( $n = 6$ ,  $*p < 0.05$ ). (H) mRNA expression of M2 macrophage markers ( $n = 6$ ,  $*p < 0.05$ ).

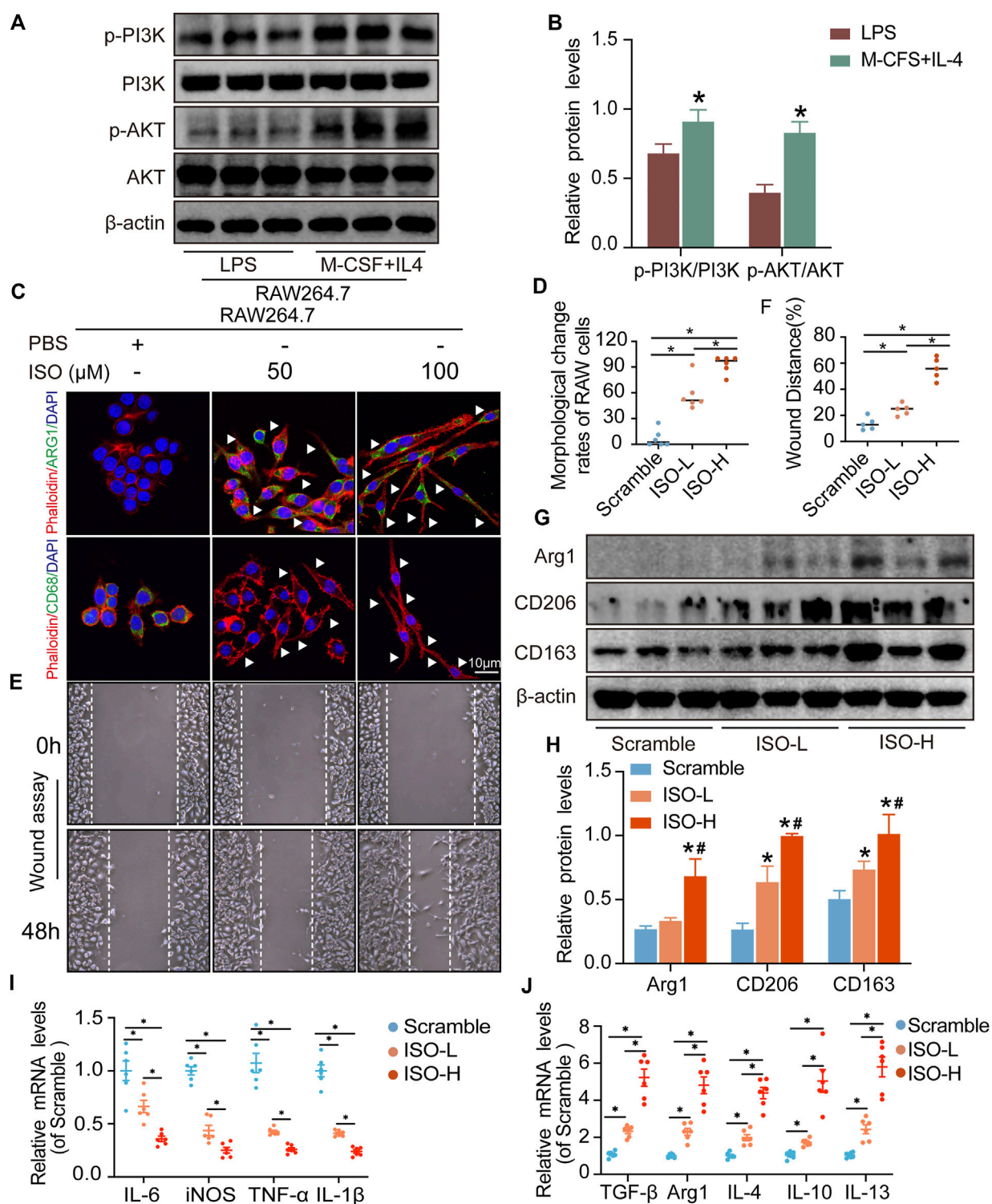
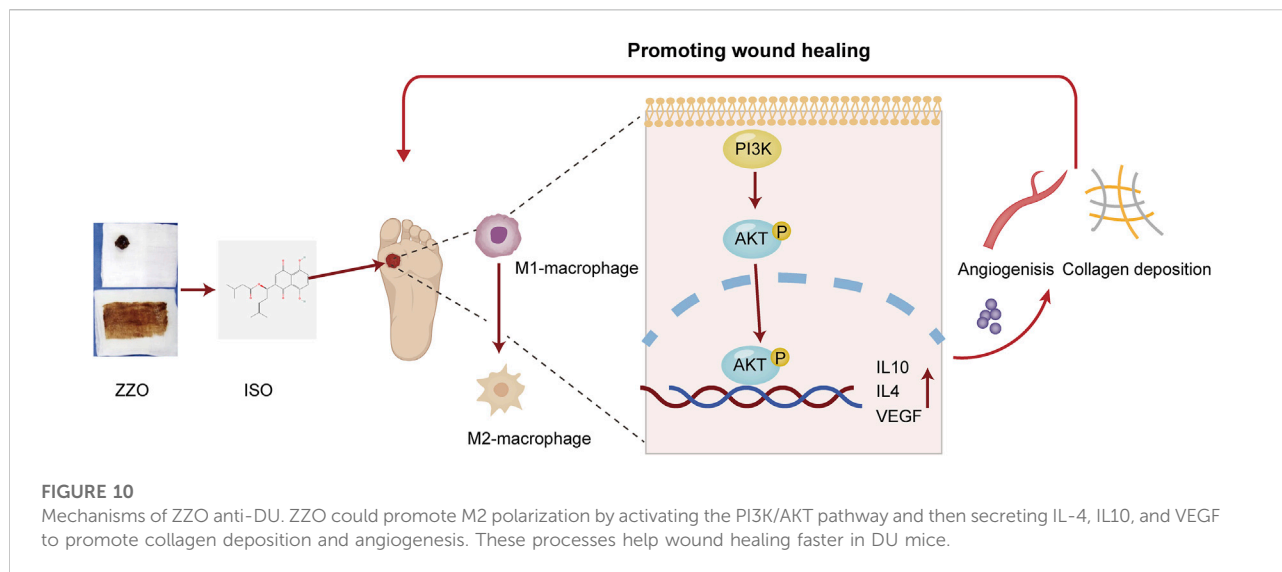


FIGURE 9

ISO promoted M2 polarization of macrophages *in vitro*. (A,B) Expressions of PI3K, p-PI3K, AKT, and p-AKT proteins were tested in RAW264.7 cells ( $n = 3$ ,  $*p < 0.05$ , compared with the LPS group). (C,D) Visualization and quantitative analysis of co-location of phalloidin and CD68 or Arg1 of RAW264.7 cells in different groups ( $n = 6$ ,  $*p < 0.05$ ). (E,F) Visualization and quantitative analysis of wound assay of RAW264.7 cells in different groups ( $n = 6$ ,  $*p < 0.05$ ). (G,H) Expressions of ARG1, CD206, and CD163 proteins were tested on RAW264.7 cells in different groups. (I) mRNA expression of M1 macrophage markers ( $n = 3$ ,  $*p < 0.05$ ). (J) mRNA expression of M2 macrophage markers ( $n = 6$ ,  $*p < 0.05$ ).





tissue harbors predominantly macrophages, which both promote and inhibit inflammation (Louiselle et al., 2021). In routine wound healing, M2 macrophages occupy the wound healing area with fewer M1 macrophages existing after three days, whereas M1 macrophages continue to be present in the wound area, with little or even no M2 macrophages present in the DU site (Louiselle et al., 2021). During the proliferative stage, wound healing features granulation tissue formation, collagen synthesis, and angiogenesis, while diabetes promotes the production of advanced glycation end products, which inhibit the proliferation and migration of fibroblasts (Li et al., 2017). Due to these various cell types, cell-cell interactions, chemokines, and complex mechanisms, it is difficult to achieve the desired therapeutic effect of DU.

The multicomponent-multitarget methods of TCM offer various therapeutic activities for DU. As discussed in the introduction, our previous studies have verified that ZZO can promote wound healing in DU though the specific compounds and potential mechanisms have remained unclear. Thus, we adopted network analysis to determine the active compounds and anti-DU mechanisms of ZZO. The results show that ZC and HQ play key roles in anti-DU ZZO. After excavating related targets, the PI3K/AKT pathway was identified for further study. PI3K is activated under physiological stimuli and binds to receptor tyrosine kinase provided with a ligand binding domain. A central component in the PI3K pathway is the serine/threonine-specific protein kinase AKT, with multiple downstream target proteins (Madhunapantula et al., 2011). The PI3K/AKT cascade especially contributes to macrophage polarization (Tan et al., 2018), and PI3K knockout (KO) mice induce NF- $\kappa$ B activation and IL-1 $\beta$  release, which is characteristic of the M1 phenotype (Solinas and Becattini, 2017). Our results also show activation of PI3K/AKT in

M2 macrophages. Thus, we constructed a DU mouse model and evaluated the condition of the PI3K/AKT signaling pathway. In DU mice, the PI3K/AKT pathway was inhibited and prone to greater M1 macrophage infiltration in wound tissues. Surprisingly, the PI3K/AKT pathway was activated with M2 macrophage infiltration after ZZO treatment.

Moreover, M2 macrophages can recruit fibroblasts directly or by the secretion of chemokines, such as TGF- $\beta$ , which promote collagen deposition and damage repair (Jie et al., 2018). Meanwhile, during the angiogenesis stage, macrophages induce blood vessel maturation through the secretion of VEGF and IGF-1 (Gurevich et al., 2018). Altogether, M2 macrophages promote fibroblast cell proliferation, ECM reconstruction, and angiogenesis. Thus, we found that treatment of ZZO facilitates the secretion of IL-4, IL-10, and VEGF in macrophages, thereby inducing fibrosis and angiogenesis during wound healing. Furthermore, the autodocking results show that ISO is the highest-binding compound for AKT. Thus, we treated RAW264.7 cells with ISO to observe their phenotype *in vitro*. Similarly, ISO promotes the transition of RAW264.7 cells into the M2 phenotype in a dose-dependent manner.

In conclusion, we conducted an integrative network analysis and experimental evaluation of ZZO against DU. We evaluated the activation of the PI3K/AKT pathway under ZZO treatment. We found that ZZO can promote M2 polarization by activating the PI3K/AKT pathway and then secreting IL-4, IL10, and VEGF to promote collagen deposition and angiogenesis (Figure 10). However, the network analysis has its own limitations. The data is derived from public databases, which are constantly updated; therefore, some other bioactive compounds may have been excluded. Moreover, targets and pathways that come from network analysis may lead to bias in the study. Considering

this, PI3K/AKT inhibitors and activators may be required to further verify this mechanism. Moreover, the complex components and mechanisms of ZZO may affect the promotion of its clinical application in the future. In the future, we will focus more on the nano-gel formulation of single compounds, such as ISO, and anticipate promoting their clinical efficacy in DU.

## Data availability statement

The datasets presented in this study can be found in online repositories. The names of the repository/repositories and accession number(s) can be found in the article/Supplementary Material.

## Ethics statement

The animal study was reviewed and approved by the Animal Ethics Committee of the Shanghai University of Traditional Chinese Medicine (Approval No. PZSHUTCM220711028).

## Author contributions

GL and JW designed and performed the study; JW and YW wrote the manuscript and performed the study; RH and WL performed the study; XH, QH, and XY analyzed the data; WF contributed to language polishing; HW made critical comments during the whole process of this study. All authors have reviewed and approved the final version of the manuscript.

## References

- Aihaiti, Y., Song Cai, Y., Tuerhong, X., Ni Yang, Y., Ma, Y., Shi Zheng, H., et al. (2021). Therapeutic effects of naringin in rheumatoid arthritis: Network pharmacology and experimental validation. *Front. Pharmacol.* 12, 672054. doi:10.3389/fphar.2021.672054
- Armstrong, D. G., Boulton, A. J. M., and Bus, S. A. (2017). Diabetic foot ulcers and their recurrence. *N. Engl. J. Med.* 376 (24), 2367–2375. doi:10.1056/NEJMra1615439
- Cheng, Y., Peng, L., Deng, X., Li, T., Guo, H., Xu, C., et al. (2021). Prostaglandin F2 $\alpha$  protects against pericyte apoptosis by inhibiting the PI3K/Akt/GSK3 $\beta$ /catenin signaling pathway. *Ann. Transl. Med.* 9 (12), 1021. doi:10.21037/atm-21-2717
- da Silva, L., Carvalho, E., and Cruz, M. T. (2010). Role of neuropeptides in skin inflammation and its involvement in diabetic wound healing. *Expert Opin. Biol. Ther.* 10 (10), 1427–1439. doi:10.1517/14712598.2010.515207
- Friesner, R. A., Banks, J. L., Murphy, R. B., Halgren, T. A., Klicic, J. J., Mainz, D. T., et al. (2004). Glide: A new approach for rapid, accurate docking and scoring. 1. Method and assessment of docking accuracy. *J. Med. Chem.* 47 (7), 1739–1749. doi:10.1021/jm0306430
- Gfeller, D., Grosdidier, A., Wirth, M., Daina, A., Michielin, O., and Zoete, V. (2014). SwissTargetPrediction: A web server for target prediction of bioactive small molecules. *Nucleic Acids Res.* 42, W32–W38. doi:10.1093/nar/gku293
- Gocho, Y., Liu, J., Hu, J., Yang, W., Dharia, N. V., Zhang, J., et al. (2021). Network-based systems pharmacology reveals heterogeneity in LCK and BCL2 signaling and therapeutic sensitivity of T-cell acute lymphoblastic leukemia. *Nat. Cancer* 2 (3), 284–299. doi:10.1038/s43018-020-00167-4
- Gu, S., Xue, Y., Gao, Y., Shen, S., Zhang, Y., Chen, K., et al. (2020). Mechanisms of indigo naturalis on treating ulcerative colitis explored by GEO gene chips combined with network pharmacology and molecular docking. *Sci. Rep.* 10 (1), 15204. doi:10.1038/s41598-020-71030-w
- Gupta, N. K., Srivastva, N., Bubber, P., and Puri, S. (2016). The antioxidant potential of *Azadirachta indica* ameliorates cardioprotection following diabetic mellitus-induced microangiopathy. *Pharmacogn. Mag.* 12 (3), S371–S378. doi:10.4103/0973-1296.185772
- Gupta, S., Andersen, C., Black, J., de Leon, J., Fife, C., Lantis Ii, J. C., et al. (2017). Management of chronic wounds: Diagnosis, preparation, treatment, and follow-up. *Wounds* 29 (9), S19–S36.
- Gurevich, D. B., Severn, C. E., Twomey, C., Greenhough, A., Cash, J., Toye, A. M., et al. (2018). Live imaging of wound angiogenesis reveals macrophage orchestrated vessel sprouting and regression. *Embo J.* 37 (13), e97786. doi:10.15252/emboj.201797786
- Han, G., and Liu, G. B. (2021). Curative observation of using Zizhu ointment for external application in the treatment of non-ischemic diabetic foot ulcer. *J. Sichuan Traditional Chin. Med.* 39 (3), 112–117.
- Huang, R., Hu, X., Li, W., Wang, L., Fan, W., Han, Q., et al. (2022). Zizhu ointment accelerates wound-healing of diabetic ulcers through promoting

## Funding

This work was supported by research grants from the Pudong New Area Health Committee Health and Family Planning Research Project (PW2020E-4), the Project of Shanghai Traditional Chinese Medicine Standardization Technical Committee (ZYYBZH-202101), and the Siming Youth Foundation of Shuguang Hospital (SGKJ-202119).

## Conflict of interest

The authors declare that the research was conducted in the absence of any commercial or financial relationships that could be construed as a potential conflict of interest.

## Publisher's note

All claims expressed in this article are solely those of the authors and do not necessarily represent those of their affiliated organizations, or those of the publisher, the editors and the reviewers. Any product that may be evaluated in this article, or claim that may be made by its manufacturer, is not guaranteed or endorsed by the publisher.

## Supplementary material

The Supplementary Material for this article can be found online at: <https://www.frontiersin.org/articles/10.3389/fphar.2022.1027677/full#supplementary-material>

- M2 macrophage polarization via downregulating the Notch4 signaling pathway. *Comput. Intell. Neurosci.* 2022, 5173836. doi:10.1155/2022/5173836
- Huang, S., Hu, Z., Wang, P., Zhang, Y., Cao, X., Dong, Y., et al. (2020). Rat epidermal stem cells promote the angiogenesis of full-thickness wounds. *Stem Cell Res. Ther.* 11 (1), 344. doi:10.1186/s13287-020-01844-y
- Jia, C. Y., Li, J. Y., Hao, G. F., and Yang, G. F. (2020). A drug-likeness toolbox facilitates ADMET study in drug discovery. *Drug Discov. Today* 25 (1), 248–258. doi:10.1016/j.drudis.2019.10.014
- Jie, J., Yang, J., He, H., Zheng, J., Wang, W., Zhang, L., et al. (2018). Tissue remodeling after ocular surface reconstruction with denuded amniotic membrane. *Sci. Rep.* 8 (1), 6400. doi:10.1038/s41598-018-24694-4
- Kim, S., Thiessen, P. A., Bolton, E. E., Chen, J., Fu, G., Gindulyte, A., et al. (2016). PubChem substance and compound databases. *Nucleic Acids Res.* 44 (1), D1202–D1213. doi:10.1093/nar/gkv951
- Kohl, M., Wiese, S., and Warscheid, B. (2011). Cytoscape: Software for visualization and analysis of biological networks. *Methods Mol. Biol.* 696, 291–303. doi:10.1007/978-1-60761-987-1\_18
- Li, L., Yang, D., Li, J., Niu, L., Chen, Y., Zhao, X., et al. (2020). Investigation of cardiovascular protective effect of Shenmai injection by network pharmacology and pharmacological evaluation. *BMC Complement. Med. Ther.* 20 (1), 112. doi:10.1186/s12906-020-02905-8
- Li, M., Zhao, Y., Hao, H., Dong, L., Liu, J., Han, W., et al. (2017). Umbilical cord-derived mesenchymal stromal cell-conditioned medium exerts *in vitro* antiaging effects in human fibroblasts. *Cytotherapy* 19 (3), 371–383. doi:10.1016/j.jcyt.2016.12.001
- Louiselle, A. E., Niemiec, S. M., Zgheib, C., and Liechty, K. W. (2021). Macrophage polarization and diabetic wound healing. *Transl. Res.* 236, 109–116. doi:10.1016/j.trsl.2021.05.006
- Lv, Z., Xu, X., Sun, Z., Yang, Y. X., Guo, H., Li, J., et al. (2021). TRPV1 alleviates osteoarthritis by inhibiting M1 macrophage polarization via Ca(2+)/CaMKII/Nrf2 signaling pathway. *Cell Death Dis.* 12 (6), 504. doi:10.1038/s41419-021-03792-8
- Madhunapantula, S. V., Mosca, P. J., and Robertson, G. P. (2011). The akt signaling pathway: An emerging therapeutic target in malignant melanoma. *Cancer Biol. Ther.* 12 (12), 1032–1049. doi:10.4161/cbt.12.12.18442
- Meng, Z., Yamazaki, T., and Sode, K. (2004). A molecularly imprinted catalyst designed by a computational approach in catalysing a transesterification process. *Biosens. Bioelectron.* 20 (6), 1068–1075. doi:10.1016/j.bios.2004.02.032
- Moore, C. S., Ase, A. R., Kinsara, A., Rao, V. T., Michell-Robinson, M., Leong, S. Y., et al. (2015). P2Y12 expression and function in alternatively activated human microglia. *Neurol. Neuroimmunol. Neuroinflamm.* 2 (2), e80. doi:10.1212/wnxi.0000000000000080
- Qiu, Y., Wang, Q., Chen, Y., Xia, S., Huang, W., and Wei, Q. (2020). A novel multilayer composite membrane for wound healing in mice skin defect model. *Polym. (Basel)* 12 (3), 573. doi:10.3390/polym12030573
- Ru, J., Li, P., Wang, J., Zhou, W., Li, B., Huang, C., et al. (2014). Tcmsp: A database of systems pharmacology for drug discovery from herbal medicines. *J. Cheminform.* 6, 13. doi:10.1186/1758-2946-6-13
- Sayers, E. W., Beck, J., Bolton, E. E., Bourexis, D., Brister, J. R., Canese, K., et al. (2021). Database resources of the national center for Biotechnology information. *Nucleic Acids Res.* 49 (1), D10–d17. doi:10.1093/nar/gkaa892
- Segura, J., Rose, Y., Westbrook, J., Burley, S. K., and Duarte, J. M. (2020). RCSB protein data bank 1D tools and services. *Bioinformatics* 36 (22–23), 5526–5527. doi:10.1093/bioinformatics/btaa1012
- Shang, W., Chen, G., Li, Y., Zhuo, Y., Wang, Y., Fang, Z., et al. (2019). Static magnetic field accelerates diabetic wound healing by facilitating resolution of inflammation. *J. Diabetes Res.* 2019, 5641271. doi:10.1155/2019/5641271
- Shen, W., Song, Z., Zhong, X., Huang, M., Shen, D., Gao, P., et al. (2022). Sangerbox: A comprehensive, interaction-friendly clinical bioinformatics analysis platform. *iMeta* 1, e36. doi:10.1002/imt.2.36
- Solinas, G., and Becattini, B. (2017). The role of PI3Kγ in metabolism and macrophage activation. *Oncotarget* 8 (63), 106145–106146. doi:10.18632/oncotarget.22068
- Szklarczyk, D., Gable, A. L., Nastou, K. C., Lyon, D., Kirsch, R., Pyysalo, S., et al. (2021). The STRING database in 2021: Customizable protein-protein networks, and functional characterization of user-uploaded gene/measurement sets. *Nucleic Acids Res.* 49 (D1), D605–d612. doi:10.1093/nar/gkaa1074
- Tan, J. L., Lau, S. N., Leaw, B., Nguyen, H. P. T., Salamonsen, L. A., Saad, M. I., et al. (2018). Amnion epithelial cell-derived exosomes restrict lung injury and enhance endogenous lung repair. *Stem Cells Transl. Med.* 7 (2), 180–196. doi:10.1002/sctm.17-0185
- Tao, Q., Du, J., Li, X., Zeng, J., Tan, B., Xu, J., et al. (2020). Network pharmacology and molecular docking analysis on molecular targets and mechanisms of Huashi Baidu formula in the treatment of COVID-19. *Drug Dev. Ind. Pharm.* 46 (8), 1345–1353. doi:10.1080/03639045.2020.1788070
- UniProt Consortium (2021). UniProt: The universal protein knowledgebase in 2021. *Nucleic Acids Res.* 49 (1), D480–d489. doi:10.1093/nar/gkaa1100
- Wang, Y., Cao, H. J., Wang, L. Q., Lu, C. L., Yan, Y. Q., Lu, H., et al. (2019). The effects of Chinese herbal medicines for treating diabetic foot ulcers: A systematic review of 49 randomized controlled trials. *Complement. Ther. Med.* 44, 32–43. doi:10.1016/j.ctim.2019.03.007
- Wishart, D. S., Feunang, Y. D., Guo, A. C., Lo, E. J., Marcu, A., Grant, J. R., et al. (2018). DrugBank 5.0: A major update to the DrugBank database for 2018. *Nucleic Acids Res.* 46 (1), D1074–D1082. doi:10.1093/nar/gkx1037
- Xiao, H., Qin, X., Wan, J., and Li, R. (2019). Pharmacological targets and the biological mechanisms of formononetin for alzheimer's disease: A network analysis. *Med. Sci. Monit.* 25, 4273–4277. doi:10.12659/msm.916662
- Zarei, F., Negahdari, B., and Eatemadi, A. (2018). Diabetic ulcer regeneration: Stem cells, biomaterials, growth factors. *Artif. Cells Nanomed. Biotechnol.* 46 (1), 26–32. doi:10.1080/21691401.2017.1304407
- Zhao, L., Guo, Z., Chen, K., Yang, W., Wan, X., Zeng, P., et al. (2020). Combined transplantation of mesenchymal stem cells and endothelial colony-forming cells accelerates refractory diabetic foot ulcer healing. *Stem Cells Int.* 2020, 8863649. doi:10.1155/2020/8863649
- Zhao, R., Liang, H., Clarke, E., Jackson, C., and Xue, M. (2016). Inflammation in chronic wounds. *Int. J. Mol. Sci.* 17 (12), 2085. doi:10.3390/ijms17122085
- Zhou, X., Guo, Y., Yang, K., Liu, P., and Wang, J. (2022). The signaling pathways of traditional Chinese medicine in promoting diabetic wound healing. *J. Ethnopharmacol.* 282, 114662. doi:10.1016/j.jep.2021.114662



## OPEN ACCESS

## EDITED BY

Yibin Feng,  
The University of Hong Kong, Hong Kong  
SAR, China

## REVIEWED BY

Shuying Han,  
North China University of Science and  
Technology, China  
Jingjing Wan,  
Second Military Medical University, China

## \*CORRESPONDENCE

Xue Bai,  
✉ bx\_1226@163.com

<sup>†</sup>These authors have contributed equally  
to this work and share first authorship

## SPECIALTY SECTION

This article was submitted to  
Ethnopharmacology,  
a section of the journal  
Frontiers in Pharmacology

RECEIVED 07 June 2022

ACCEPTED 03 January 2023

PUBLISHED 23 January 2023

## CITATION

Zhang T, Xu H, Zhen D, Fu D, Zhao M, Wei C  
and Bai X (2023), Comparative clinical-  
related outcomes of Chinese patent  
medicines for cardiac hypertrophy: A  
systematic review and network meta-  
analysis of randomized clinical trials.  
*Front. Pharmacol.* 14:963099.  
doi: 10.3389/fphar.2023.963099

## COPYRIGHT

© 2023 Zhang, Xu, Zhen, Fu, Zhao, Wei and  
Bai. This is an open-access article  
distributed under the terms of the [Creative  
Commons Attribution License \(CC BY\)](#).  
The use, distribution or reproduction in  
other forums is permitted, provided the  
original author(s) and the copyright  
owner(s) are credited and that the original  
publication in this journal is cited, in  
accordance with accepted academic  
practice. No use, distribution or  
reproduction is permitted which does not  
comply with these terms.

# Comparative clinical-related outcomes of Chinese patent medicines for cardiac hypertrophy: A systematic review and network meta-analysis of randomized clinical trials

Tianqi Zhang<sup>1,2†</sup>, Haoyang Xu<sup>3†</sup>, Dong Zhen<sup>2</sup>, Danni Fu<sup>2</sup>, Ming Zhao<sup>3</sup>,  
Chengxi Wei<sup>2</sup> and Xue Bai<sup>1,2\*</sup>

<sup>1</sup>Medical College of Inner Mongolia Minzu University, Tongliao, China, <sup>2</sup>Inner Mongolia Key Laboratory of Mongolian Medicine Pharmacology for Cardio-Cerebral Vascular System, Inner Mongolia Minzu University, Tongliao, China, <sup>3</sup>Affiliated Hospital of Inner Mongolia Minzu University, Tongliao, China

**Background:** Persistent pathological cardiac hypertrophy has been associated with increased risk of heart failure and even sudden death. Multiple Chinese patent medicines (CPMs) have gained attention as alternative and complementary remedies due to their high efficiency and few side effects. However, the effects of CPM-related treatment regimens for cardiac hypertrophy had not been systematically evaluated.

**Aim:** The objective of this study was to estimate and compare the effectiveness of different mechanisms of CPMs to improve clinical outcomes, including clinical efficacy and echocardiographic indices, in the treatment of cardiac hypertrophy patents.

**Methods:** A network meta-analysis was conducted on CPM-related randomized controlled trials (RCTs) published between 2012 and 2022 involving cardiac hypertrophy patients from four foreign and four Chinese databases. The outcomes concerned efficacy and related indicators, including echocardiographic indices, cardiac biomarkers, and functional exercise capacity, which were evaluated as odds ratios, mean differences, and 95% credible intervals. Network plots, league tables, surface-under-the-cumulative ranking (SUCRA), and funnel plots were created for each outcome, and all analyses were conducted using Stata 16.0 software.

**Results:** A total of 25 RCTs were evaluated; these involved 2395 patients in a network meta-analysis (NMA). The results from existing evidence indicate that blood-activating and stasis-removing Chinese patent medicine (BASR-CPM) + Western medicine (WM) showed a good improvement in clinical efficacy (OR = 8.27; 95%CI = 0.97, 70.73). A combined treatment regimen of CPM with a function of qi-replenishing, blood-activating and stasis-removing, and Western medicine was an effective treatment regimen for echocardiographic indices such as decreasing left ventricular end-systolic dimension (LVESD) (SMD = -2.35; 95%CI = -3.09, -1.62) and left ventricular mass index (LVMI) (SMD = -1.73; 95%CI = -2.92, -0.54). Furthermore, KWYR-CPM + WM and BASR-CPM also showed good improvement for echocardiographic indices of LVEDD (SMD = -1.84; 95%CI = -3.46, -0.22) and left ventricular ejection fraction (SMD = 1.90; 95%CI = -0.46, -3.35), respectively.



**Conclusion:** The study showed that BASR-CPM + WM may be the potentially superior treatment regimen for improving clinical efficacy among cardiac hypertrophy patients. QR&BASR-CPM + WM might be the optimal treatment for decreasing LVESD and LVMI. However, due to potential risks from bias and limited RCTs, further studies with larger samples and high-quality RCTs are needed to support these findings.

**Systematic Review Registration:** [[https://www.crd.york.ac.uk/prospero/display\\_record.php?RecordID=329589](https://www.crd.york.ac.uk/prospero/display_record.php?RecordID=329589)], identifier [CRD42022329589].

#### KEYWORDS

cardiac hypertrophy, Qi-replenishing, blood-activating and stasis-removing, Chinese patent medicines, network meta-analysis

## Introduction

Heart failure (HF) is a complex disease that seriously threatens human health, mainly manifesting in cardiac structural or functional dysfunction, and impaired ventricular filling or blood ejection (Beldhuis et al., 2022). In recent years, there have been more than 40 million HF patients worldwide, nearly half of whom died within 5 years of diagnosis. To some extent, the mortality rate of HF exceeds that of many cancers (Murphy et al., 2020).

HF is closely related to cardiac hypertrophy, which is the initial adaptive response of the heart to maintain cardiac function under physiological and pathological overload. Cardiac hypertrophy is characterized by an increased volume and mass of cardiomyocytes: the total amount of cardiomyocytes increases and their contractility is enhanced so that the heart can maintain normal contractility. This comprehensive and in-depth investigation of the mechanism of cardiac hypertrophy will contribute to preventing and controlling the occurrence and development of cardiac hypertrophy in its early stage and will have important practical significance for the prevention and treatment of heart failure. Cardiac hypertrophy is divided into physiological and pathological cardiac hypertrophy; persistent pathological myocardial hypertrophy is associated with an increased risk of heart failure and even sudden death.

At present, Western medicine (WM) and traditional Chinese medicine (TCM) are widely applied in inhibiting cardiac hypertrophy (Yokota et al., 2014). According to treatment guidelines, the main drugs in WM for the clinical treatment of HF are angiotensin receptor blockers (ARBs), angiotensin-converting enzyme inhibitors (ACEIs), statins, and mineralocorticoid receptor antagonists (MRAs) (Kuno et al., 2020; Chen et al., 2022). Previous studies have shown that ACEI/ARBs can inhibit cardiac hypertrophy by inhibiting the activity of matrix metalloproteinase (MMP) in plasma, while statin therapy can reduce cardiac hypertrophy by recovering the coronary endothelial function through endogenous nitric oxide for improving long-term clinical efficiency and related clinical outcomes (Yokota et al., 2010; Ishida et al., 2012). However, some studies have shown that a large dose of ARBs could cause AngII accumulation to directly activate AT2R in the body, which could increase the risk of cardiovascular events (Solomon et al., 2011). In addition, ACEIs can induce an irritating dry cough and even nausea and vomiting among patients (Ren et al., 2010). At present, there is increasing *in vitro* and *in vivo* research into the treatment of cardiac hypertrophy with Chinese patent medicine (CPM) (Zhang et al., 2021). Studies have shown that CPM can effectively target cardiac hypertrophy by the regulatory mechanism of TGF- $\beta$ 1 and CTGF to relieve the cardiac fibrosis process (Li et al., 2021; Lv et al., 2021). Hence, the evidence for the combination therapy of TCM and WM

indicates that it not only directly acts on the lesion but balances the whole body to improve clinical efficacy and achieve simultaneous treatment at the root. Combined TCM and WM could improve clinical efficacy by as much as 125% compared to just WM in aspects of echocardiographic indices (Zhang et al., 2021). This further indicates that the effectiveness of TCM-related combined treatment can have better long-term and multiple superior effects than conventional WM, especially for improving LVEF and E/A, and reducing SV and serum levels of BNP and CRP (Zhang et al., 2021). However, there is no systematic evaluation of CPM with different mechanisms to treat different clinical outcomes among patients with cardiac hypertrophy, which significantly limits their reliability and popularization in clinical practice (Zhang et al., 2021).

Meta-analysis could get close to real statistical analyses from random controlled trials which have been widely used (Mbuagbaw and Aves, 2022). Conventional meta-analysis on the treatment effects of drugs is conducted on the effect size based on pairwise head-to-head direct comparison but is limited by fewer direct comparisons. Therefore, the need for both direct and indirect comparisons of various drugs of the same efficacy used in clinical practice has received increased attention. Accordingly, network meta-analysis (NMA) is an approach that could directly and indirectly compare any comparative evidence based on logical inference (Shim et al., 2017). Therefore, with the development of research, traditional meta-analysis is being replaced by NMA (Watt and Del Giovane, 2022). In order to more accurately estimate the effects of CPM, we explore the consistency of research evidence and the differing efficacy of all the outcome indicators between CPM which has been limited in the previous literature. In our study, a systematic review and NMA of randomized clinical trials was made to compare clinical outcomes, including efficacy and echocardiographic indices, of CPM related to cardiac hypertrophy. Based on this, better designed trials and more detailed clinical outcomes like safety and efficacy are required to further validate their potential effectiveness from the point of TCM in clinical application to treat cardiomyopathies. Our findings should provide targeted and valuable references for clinical settings.

## Methods

### Protocol and study registration

This NMA study was performed following the Preferred Reporting Items for Systematic Reviews and Meta-Analysis (PRISMA) guidelines Supplementary Material Appendix 1 [Registration ID: CRD42022329589].

## Literature search

The literature search was performed using electronic network databases, including PubMed, EMBASE, Web of Science, the Cochrane Library, China National Knowledge Infrastructure (CNKI), China Biology Medicine disc (CBM), the Information Resource Integration Service Platform (VIP), and the Wanfang Data Knowledge Service Platform (Wanfang Data). All the researched articles were published from 2012 to 2022. The retrieval terms were MeSH subject words and free words such as “cardiac hypertrophy,” “Chinese patent medicine,” and “Randomized Controlled Trials (RCTs)” (for full details, see [Supplementary Appendix S2](#)).

## Inclusion and exclusion criteria

The inclusion criteria used for selection studies were

- 1) patients included in the study were diagnosed with cardiomyopathies, including hypertrophic, familial or hypertrophy, left ventricular hypertrophy, cardiomegaly, or cardiomyopathy. The age of selected patients was over 18 years old;
- 2) treatment regimens in the intervention group (IG) were assigned with either a combination of CPM with WM, or TCM, CPM and WM, or CPM alone;
- 3) control group (CG) was treated only with WM;
- 4) all studies with clinical efficacy as the primary outcome indicator were included;
- 5) all collected studies were limited to RCTs.

The exclusion criteria were

- 1) research that includes non-RCTs or duplicated papers;
- 2) research such as systematic reviews, commentaries, case reports, or animal tests;
- 3) trials with inconsistent study samples or inappropriate study designs;
- 4) trials which did not provide complete data or information, or where authors failed to reply upon being contacted.

## Outcome indicators

In this study, the primary outcome was clinical efficacy. Secondary outcomes included echocardiographic indices, cardiac biomarkers, and functional exercise capacity. Echocardiographic indices included left ventricular ejection fraction (LVEF), left ventricular end-diastolic dimension (LVEDD), and left ventricular end-systolic dimension (LVESD). Cardiac biomarkers comprised C-reactive protein (CRP) and N-terminal pro-B-type natriuretic peptide (NT-proBNP). Functional exercise capacity was measured by the six-minute walk test (6-MWT), which is a good index for evaluating the exercise endurance for chronic heart failure. In this test, a patient is required to walk as fast as possible in a straight corridor and measure the walking distance for 6 minutes. If they walk less than 150 m, it indicates severe cardiac insufficiency; if they walk 150–450 m, it indicates moderate cardiac insufficiency; if they walk more than 450 m, it is considered mild cardiac insufficiency.

## Data extraction and screening

The selected papers were extracted and imported into Note Express for electronic and manual checks. Two researchers (TQZ and HXY) independently searched, read, and screened the papers according to the aforementioned criteria. Any controversial results were cross-checked and discussed with a third evaluator (MZ) until consistent conclusions and a consensus were reached. The following information was extracted from the final eligible articles and recorded in Microsoft Excel: name of first author, publication year, basic patient characteristic, sample size in each group, type of intervention and control, duration of follow-up time, and before and after treatment outcome data. All outcome parameters were presented as mean  $\pm$  standard deviation (SD) and median  $\pm$  quartile range based on the data provided.

## Quality assessment of extract studies

Two authors (TQZ and HXY) independently evaluated researcher bias using Cochrane Collaboration bias risk tools, which included random sequence generation, allocation concealment, double blinding, triple blinding, incomplete data, and selective reporting. Each of these evaluation domains were then categorized as three levels: high, low, or unclear.

## Data analysis

The categorical variables were expressed by the odds ratio (OR) between the groups before and after treatment. The continuity variables were expressed by the standardized mean deviation (SMD) and 95% confidence interval (CI). Network maps were first constructed and analyzed for direct and indirect comparison of each treatment outcome. Next, we performed a standard pairwise meta-analysis as a direct comparison by forest map and league table (for forest maps, see [Supplementary Figure S2](#)) to illustrate the differences between each treatment regimen. Finally, the hierarchy of treatment probability was estimated according to the value of surface under the cumulative ranking curves (SUCRA) in which a larger value was regarded as more probably a superior treatment regimen. The closer to 100 in SUCRA, the more useful the treatment regimen is. All analyses were conducted in Stata 16.0. All *p*-values were two-tailed with statistical significance specified at 0.05 and CI computed at the 95% level.

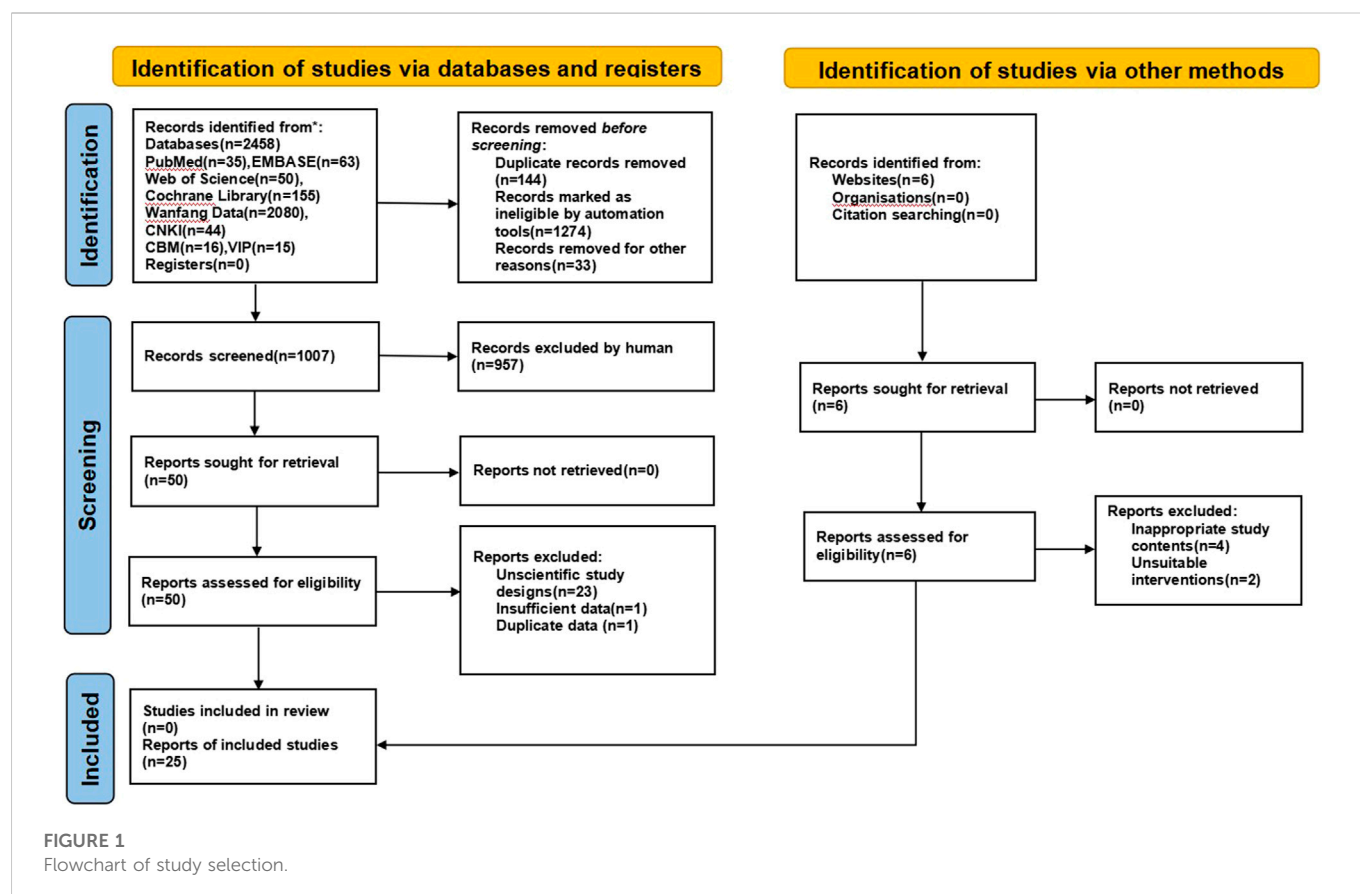
## Publication bias

Funnel plots were used to test publication bias in this study. There was publication bias, which was hard to control when positive data were more likely to be published in journals with similar research papers with statistical significance.

## Results

### Study selection

The initial search of eight databases yielded 2458 articles, 1451 of which were excluded due to duplicates ( $n = 144$ ),



animal tests ( $n = 1274$ ), review articles, and meta-analyses ( $n = 33$ ). After reading the title and abstract, 957 articles were screened out, including inappropriate study contents ( $n = 803$ ) and unsuitable interventions ( $n = 154$ ). Based on our inclusion and exclusion criteria, after reading the full texts manually, 25 articles were excluded for reasons of unscientific study interventions and study design ( $n = 23$ ) or insufficient ( $n = 1$ ) or duplicate data ( $n = 1$ ). Eventually, 25 studies were included in this NMA (Yang et al., 2012; Zheng, 2013; Liu, 2014; Han and Shen, 2015; Cui et al., 2016; Xun, 2016; Zhang et al., 2016; Fan, 2017; Li, 2017; Zhang et al., 2017; Zhou et al., 2018; Wang et al., 2019; Wu and Hu, 2019; Xie et al., 2019; Xu et al., 2019; Zheng et al., 2019; Zou, 2019; Fan et al., 2020; Peng et al., 2020; Yang and Liu, 2020; Hu, 2021; Ji et al., 2021; Meng et al., 2021; Wu et al., 2021; Zhang and Gou, 2021). These were all two-arm studies. The selection process is illustrated in Figure 1.

## Characteristics of included studies

A total of 2,395 patients with cardiac hypertrophy were included in the NMA, with the duration of follow-up ranging from 2 weeks to 1 year. Among them, 1,199 patients were allocated to the intervention group (IG) with CPM-related treatment regimens (261 cases used CPM alone, 902 employed a combination of CPM and WM, and 36 received a combination of CPM, TCM, and WM). A further 1,196 cases were located in the WM-only control group (CG). Detail information for each RCT is

shown in Table 1; Table 2 summarizes detailed information about the CPMs in the research articles.

According to the efficacy noted in the original text of the included studies, the CPMs in this study were categorized as *qi*-replenishing Chinese patent medicine (QR-CPM); blood-activating and stasis-removing CPM (BASR-CPM); heat-clearing CPM (HC-CPM); kidney-warming and *yang*-restoring CPM (KWYR-CPM); and *qi*-replenishing, blood-activating, and stasis-removing CPM (QR&BASR-CPM).

## Summary of quality assessment

The detailed risk of bias is shown in Figure 2 according to assessment with the Cochrane Collaboration tool. A random sequence was generated in all the studies, suggesting the risk of bias in randomization was low. Among them, 14 were rated as a low risk of bias and 11 had unclear information about the methods used to conceal the allocation; therefore, we considered that the risk of bias was unclear for the domain of allocation concealment. Regarding the blinding of participants and personnel, high risk was observed in 11 RCTs; a large proportion of studies had an unclear risk of detection bias. As for incomplete outcomes, there was a low risk of bias because most studies ( $n = 20$ ) reported complete data. Only two had unclear risks regarding selective reporting bias, and seven had unclear risks of other bias. Overall, 25 trials were deemed as unclear bias risk, which showed that the certainty of their evidence was moderate. For a summary of quality assessment, see Figure 3.

TABLE 1 Characteristics of each RCTs in included studies.

No.	Study	Year	Country	Number of participants	Mean age	Male/ female		Treatment regimen	Chinese patent medicine of IG and dose	Duration of the follow-up (week)
				(IG/CG)	Mean age of participants	IG	CG	(IG vs. CG)		
					(All or IG/CG)					
1	Zhou et al.	2018	China	66/66	46.06 ± 7.12/ 45.37 ± 6.81	35/ 31	38/ 28	QR-CPM + WM vs. WM	Yiqi Fumai injection, 250–500 ml qd iv	2
2	Wang et al.	2019	China	80/80	48.5 ± 2.4	58/42		QR&BASR-CPM + WM vs. WM	Yixinshu capsule, 3 goals/ time tid po	4
3	Xun	2016	China	50/50	49.6 ± 2.3	58/42		QR&BASR-CPM + WM vs. WM	Yixinshu capsule, 3 goals/ time tid po	NA
4	Cui et al.	2016	China	50/50	58.1 ± 3.1	55/45		BASR-CPM + WM vs. WM	Xinkeshu capsule, 4 goals/ time tid po	24
5	Zheng et al.	2019	China	25/25	57.64 ± 3.97/ 57.72 ± 4.03	12/ 13	12/ 13	QR&BASR-CPM + WM vs. WM	Heart-protecting musk pill, 2 goals/time tid po	12
6	Han and Sen	2015	China	40/40	65.5 ± 2.4/ 66.0 ± 2.6	22/ 18	21/ 19	QR-CPM + WM vs. WM	Qiliqiangxin capsule, 4 goals/time tid po	24
7	Zhang et al.	2016	China	40/40	65.3 ± 2.5/ 63.0 ± 0.4	21/ 19	24/ 16	QR&BASR-CPM + WM vs. WM	Yiqihuayu capsule, 4 goals/ time tid po	6
8	Fan et al.	2020	China	64/64	63.8 ± 4.3/ 63.6 ± 4.5	34/ 30	33/ 31	BASR-CPM vs. WM	Ginkgo ester drop pills, 4 goals/time tid po	8
9	Li	2014	China	46/44	68.6 ± 8.4/ 69.3 ± 3.6	29/ 17	27/ 17	QR&BASR-CPM vs. WM	Yiqihuayu capsule, 4 goals/ time tid po	6
10	Yang et al.	2012	China	30/29	64.0 ± 11.0/ 66.0 ± 12.0	17/ 13	11/ 18	QR&BASR-CPM + WM vs. WM	Tongxinluo capsule, 3 goals/ time tid po	12
11	Wu and Hu	2019	China	86/86	63.9 ± 6.7/ 65.1 ± 7.5	45/ 41	49/ 37	QR&BASR-CPM vs. WM	Musk tongxin dropping pills, 2 goals/time tid po	24
12	Wu et al.	2021	China	65/66	66.52 ± 6.71/ 66.47 ± 6.53	40/ 30	43/ 27	QR&BASR-CPM vs. WM	Musk tongxin dropping pills, 2 goals/time tid po	24
13	Zou	2019	China	71/71	63.24 ± 5.73/ 63.17 ± 5.49	38/ 33	37/ 34	QR&BASR-CPM + WM vs. WM	Heart-protecting musk pill, 2 goals/time tid po	12
14	Yang and Liu	2020	China	43/43	60.14 ± 6.35/ 61.26 ± 6.27	23/ 20	19/ 24	HC-CPM vs. WM	Sanwei sandalwood capsule, 3 goals/time bid po	4
15	Xu et al.	2019	China	40/40	56.85 ± 6.71/ 55.92 ± 6.64	22/ 18	24/ 16	BASR-CPM + WM vs. WM	Compound Danshen dripping pills, 10 goals/time tid po	24
16	Fan	2017	China	40/40	54.2 ± 2.4/ 53.6 ± 2.7	23/ 17	25/ 15	QR-CPM + WM vs. WM	Qiliqiangxin granules, 4 goals/time tid po	12
17	Zhang et al.	2017	China	30/30	64.70 ± 7.82/NA	12/ 18	14/ 16	QR-CPM + WM vs. WM	Qiliqiangxin granules, 4 goals/time tid po	4
18	Zheng	2013	China	31/30	73.7 ± 10.6/ 73.4 ± 9.4	13/ 18	13/ 17	QR-CPM + WM vs. WM	Fumai granule, 1 bag/time tid po	4
19	Peng et al.	2020	China	30/30	59.17 ± 9.21/ 58.22 ± 9.31	17/ 13	15/ 15	QR-CPM + WM vs. WM	Jianxin Pinglv pills, 6 g/time tid po	8
20	Hu	2021	China	36/36	61.29 ± 5.22/ 62.88 ± 5.27	21/ 15	23/ 13	KWYR-CPM + THSWT + WM vs. WM	Kidney-qi-tonifying pill, 10 goals/time tid po	12
21	Meng et al.	2021	China	34/34	68.85 ± 4.43/ 68.48 ± 4.37	17/ 17	18/ 16	BASR-CPM + WM vs. WM	Compound Danshen dripping pills, after 20 goals/ time tid po, x3D, 10 goals/ time tid po	12

(Continued on following page)



TABLE 1 (Continued) Characteristics of each RCTs in included studies.

No.	Study	Year	Country	Number of participants	Mean age	Male/ female		Treatment regimen	Chinese patent medicine of IG and dose	Duration of the follow-up (week)
				(IG/CG)	Mean age of participants	IG	CG	(IG vs. CG)		
					(All or IG/CG)					
22	Ji et al.	2021	China	63/63	75.51 ± 5.22/ 75.55 ± 5.23	34/ 29	33/ 30	QR-CPM + WM vs. WM	Buxinqi oral solution, 10 ml/time tid po	12
23	Liu	2014	China	50/50	50.2 ± 4.1/ 51.1 ± 4.1	27/ 23	28/ 22	QR&BASR-CPM + WM vs. WM	Wenxin granule, 2g/time tid po	4
24	Xie et al.	2019	China	40/40	57.8 ± 8.5/ 59.6 ± 9.1	10/ 30	12/ 28	QR-CPM + WM vs. WM	Qishen Yiqi droplet, 0.5 g/ time tid po	48

Notes: ① Clinical efficacy; ② LVEF, left ventricular ejection fraction; ③ LVEDD, left ventricular end-diastolic dimension; ④ LVESD, left ventricular end-systolic dimension; ⑤ LVMI, left ventricular mass index; ⑥ CRP, C-reactive protein; ⑦ NT-proBNP, N-terminal proBNP; ⑧ 6-MWT, six-minute walk test.

## Network meta-analysis (NMA) results

In network maps, the center of WM was compared to eight CPM-related treatment regimens in IG, among which a combined regimen was denoted with “+” signs. The thickness of the line means the number of trials, and the size of the circle indicates the number of patients included. Detailed information for each treatment regimen is presented in Table 3.

In the network map for primary outcomes, WM as a center point is compared by six CPM-related treatment regimens of IG, among which the circle of QR-CPM + WM had the largest number of included patients in IG and the connection line between QR-CPM + WM and WM has the largest quantity of included trials (Figure 4A). In the network map for secondary outcomes, the point and line results regarding LVEF and LVEDD of echocardiographic indices were the same as the primary outcome (Figures 4B, C). Other secondary outcomes including echocardiographic indices (LVESD and LVMI) are shown in Figures 4D and E, cardiac biomarkers (CRP and NT-proBNP) which show CRP in Figure 4F, NT-proBNP in Supplementary Figure S1A, and functional exercise capacity (6-MWT) in Supplementary Figure S1B. The overall network relationship was centered on WM, which had no closed ring.

## Difference in mean changes in primary clinical efficacy

Clinical efficiency was useful for planning future clinical trials on cardiac hypertrophy treatment and predicting the impact of CPM-related treatment regimens.

Azzimondi et al. (1997) Some 19 studies (Zheng, 2013; Liu, 2014; Han and Shen, 2015; Xun, 2016; Zhang et al., 2016; Fan, 2017; Li, 2017; Zhang et al., 2017; Zhou et al., 2018; Wang et al., 2019; Wu and Hu, 2019; Xu et al., 2019; Zou, 2019; Fan et al., 2020; Peng et al., 2020; Yang and Liu, 2020; Ji et al., 2021; Wu et al., 2021; Zhang and Gou, 2021) involving 1,966 patients comprised WM in CG, and six CPM-related treatment regimens including QR-CPM + WM, BASR-CPM, BASR-CPM + WM, QR&BASR-CPM, QR&BASR-CPM + WM, and HC-CPM + WM in IG were measured for clinical efficacy.

The pairwise comparison of clinical efficacy was evaluated by OR and 95% CI for each treatment regimen, which is shown in a league table (Table 4) and forest map (Supplementary Figure S2A). First, BASR-CPM + WM was more significant for improving clinical efficacy than any other treatment regimen, especially over WM (OR = 8.27; 95%CI = 0.97,70.73)—however, there was no statistical difference. Second, all CPM-related treatment regimens in IG were superior to CG in clinical efficacy, which had significant differences expect for BASR-CPM + WM. The pairwise comparisons of all treatment regimens in IG had no differences.

According to the SUCRA probability in improving clinical efficacy, BASR-CPM + WM had the highest probability of being the best treatment regimen out of the seven (Supplementary Figure S3A).

## Difference in mean changes in Echocardiographic indices

Changes in echocardiographic indices can reflect the morphological features of progressive cardiac remodeling (Cheng et al., 2010).

## Left ventricular ejection fraction (LVEF)

All data from the 21 studies (Yang et al., 2012; Zheng, 2013; Han and Shen, 2015; Cui et al., 2016; Zhang et al., 2016; Fan, 2017; Li, 2017; Zhang et al., 2017; Wu and Hu, 2019; Xie et al., 2019; Xu et al., 2019; Zheng et al., 2019; Zou, 2019; Fan et al., 2020; Peng et al., 2020; Yang and Liu, 2020; Hu, 2021; Ji et al., 2021; Meng et al., 2021; Wu et al., 2021; Zhang and Gou, 2021) were analyzed—they consisted of 1,903 patients with WM in the CG and seven CPM-related treatment regimens in the IG (QR&BASR-CPM + WM, BASR-CPM, BASR-CPM + WM, KWYR-CPM + THSWT + WM, QR-CPM + WM, HC-CPM + WM, and QR&BASR-CPM).

The pairwise comparison of each treatment regimen in IG and CG is shown in Table 5 and Supplementary Figure S2B. The results show that BASR-CPM was the most effective treatment regimen in increasing the level of LVEF in the IG. In addition, QR&BASR-CPM + WM (SMD = 1.67; 95%CI = 0.48, 2.86), BASR-CPM + WM (SMD = 1.54; 95%CI = 0.50, 2.59), and QR-CPM + WM (SMD = 0.87, 95%CI = 0.14, 1.59) also had significant improvement

TABLE 2 Summary of composition of CPMs.

Study	Formulation	Source	Species, concentration	Quality control reported? (Y/N)	Chemical analysis reported? (Y/N)	Therapeutic claims in TCM
Zhou et al. (2018)	Yiqi Fumai injection	[Tianjin Tasly Pride Pharmaceutical Co., Ltd.]	<i>Talinum paniculatum</i> (Jacq.) Gaertn. [Talinaceae; Talinum], 0.5g; <i>Schisandra chinensis</i> (Turcz.) Baill. [Schisandraceae; Schisandra], and 0.75g; <i>Ophiopogon japonicus</i> (Thunb.) Ker Gawl. [Asparagaceae; Ophiopogon], 1.5 g.	Y—Prepared according to the National Food and Drug Administration National Drug Standards	N	Replenishing <i>qi</i> and restoring pulse, nourishing <i>yin</i> , and engendering liquid
Wang et al. (2019)	Yixinshu capsule	[Guizhou Xinbang Pharmaceutical Co., Ltd.]	<i>Panax ginseng</i> C.A.Mey. [Araliaceae; Panax], 200g; <i>Ophiopogon japonicus</i> (Thunb.) Ker Gawl. [Asparagaceae; Ophiopogon], 200g; <i>Schisandra chinensis</i> (Turcz.) Baill. [Schisandraceae; Schisandra], 133g; <i>Astragalus mongholicus</i> Bunge [Fabaceae; Astragalus], 200g; <i>Salvia miltiorrhiza</i> Bunge [Lamiaceae; Salvia], 267g; <i>Conioselinum anthriscoides</i> 'Chuanxiong' [Apiaceae; Conioselinum], 133g; and <i>Crataegus pinnatifida</i> Bunge [Rosaceae; Crataegus], 200 g.	Y—Prepared according to People's Republic of China Pharmacopoeia, 2020	Y—HPLC	Replenishing <i>qi</i> and restoring pulse, activating blood, and removing stasis
Xun, (2016)	Yixinshu capsule	[Shandong Zhongtai Pharmaceutical Co. Ltd.]	<i>Panax ginseng</i> C.A.Mey. [Araliaceae; Panax], 200g; <i>Ophiopogon japonicus</i> (Thunb.) Ker Gawl. [Asparagaceae; Ophiopogon], 200g; <i>Schisandra chinensis</i> (Turcz.) Baill. [Schisandraceae; Schisandra], 133g; <i>Astragalus mongholicus</i> Bunge [Fabaceae; Astragalus], 200g; <i>Salvia miltiorrhiza</i> Bunge [Lamiaceae; Salvia], 267g; <i>Conioselinum anthriscoides</i> 'Chuanxiong' [Apiaceae; Conioselinum], 133g; and <i>Crataegus pinnatifida</i> Bunge [Rosaceae; Crataegus], 200 g.	Y—Prepared according to People's Republic of China Pharmacopoeia, 2020	Y—HPLC	Replenishing <i>qi</i> and restoring pulse, activating blood, and removing stasis
Cui et al. (2016)	Xinkeshu capsule	[Chongqing Xieran Pharmaceutical Co. Ltd.]	<i>Crataegus pinnatifida</i> Bunge [Rosaceae; Crataegus], 375g; <i>Salvia miltiorrhiza</i> Bunge [Lamiaceae; Salvia], 375g; <i>Pueraria lobata</i> (Willd.) Ohwi [Fabaceae; Pueraria], 375g; <i>Panax notoginseng</i> (Burkill) F.H.Chen [Araliaceae; Panax], 25g; and <i>Aucklandia lappa</i> (Decne.) Decne. [Asteraceae; Dolomiaea], 25 g.	Y—Prepared according to the Ministry of Health of the People's Republic of China Drug Standards	Y—HPLC	Activating blood and removing stasis, promoting <i>qi</i> , and alleviating pain
Zheng et al. (2019)	Heart-protecting musk pill	[Shanghai Hehuang Pharmaceutical Co.Ltd.]	<i>Moschus</i> [Cervidae; Moschus]; <i>Panax ginseng</i> C.A.Mey. [Araliaceae; Panax]; oriental sweetgum [Hamamelidaceae; <i>Styracis propionata</i> ]; bovis calculus [Bovine; <i>Calculus bovis</i> ]; <i>Cinnamomum cassia</i> Siebold [Lauraceae; Cinnamomum]; toad [Bufonidae; toad venom].	Y—Prepared according to People's Republic of China Pharmacopoeia, 2005	Y—HPLC	Replenishing <i>qi</i> and restoring pulse, activating blood, and removing stasis
Han and Shen, (2015)	Qiliqiangxin capsule	[Shijiazhuang Yiling Pharmaceutical Co., Ltd.]	<i>Astragalus mongholicus</i> Bunge [Fabaceae; Astragalus], 450g; <i>Panax ginseng</i> C.A.Mey. [Araliaceae; Panax], 225g; <i>Aconitum carmichaelii</i> Debeaux [Ranunculaceae; Aconitum],	Y—Prepared according to People's Republic of China Pharmacopoeia, 2020	Y—HPLC	Replenishing <i>qi</i> and restoring <i>yang</i> , restoring pulse and cardiotonic

(Continued on following page)

TABLE 2 (Continued) Summary of composition of CPMs.

Study	Formulation	Source	Species, concentration	Quality control reported? (Y/N)	Chemical analysis reported? (Y/N)	Therapeutic claims in TCM
			112.5g; <i>Salvia miltiorrhiza</i> Bunge [Lamiaceae; Salvia], 225g; <i>Lepidium apetalum</i> Willd. [Brassicaceae; Lepidium], 150g; <i>Alisma plantago-aquatica</i> L. [Alismataceae; Alisma], 225g; <i>Polygonatum odoratum</i> (Mill.) Druce [Asparagaceae; Polygonatum], 75g; <i>Cinnamomum cassia</i> Siebold [Lauraceae; Cinnamomum], 90g; <i>Carthamus tinctorius</i> L. [Asteraceae; Carthamus], 90g; <i>Periploca sepium</i> Bunge [Apocynaceae; Periploca], 180g; and <i>Citrus reticulata</i> Blanco [Rutaceae; Citrus], 75 g.			
Zhang et al. (2016)	Yiqihuayu capsule	[Haisen Pharmaceutical Company of Hebei Medical University, Ltd.]	<i>Astragalus mongholicus</i> Bunge [Fabaceae; Astragalus]; <i>Pseudostellaria</i> Pax [Caryophyllaceae; Pseudostellaria]; <i>Conioselinum anthriscoides</i> 'Chuanxiong' [Apiaceae; Conioselinum]; <i>Pheretima</i> [Siliquariidae; Pheretima]; <i>Paeonia rubra</i> Steud. [Paeoniaceae; Paeonia]; and <i>Spatholobus suberectus</i> Dunn [Fabaceae; Spatholobus].	N	N	Warming kidney and replenishing <i>qi</i> , activating blood, and removing stasis
Fan et al. (2020)	Ginkgo ester drop pills	[Zhejiang Jiuxu Pharmaceutical Co. Ltd.]	<i>Ginkgo biloba</i> L. [Ginkgoaceae; Ginkgo], 10 mg.	Y—Prepared according to the National Food and Drug Administration National Drug Standards	N	Activating blood and removing stasis, restoring pulse and alleviating pain
Li, (2017)	Yiqihuayu capsule	[Tangshan Hospital of Traditional Chinese Medicine]	<i>Astragalus mongholicus</i> Bunge [Fabaceae; Astragalus]; <i>Pseudostellaria</i> Pax [Caryophyllaceae; Pseudostellaria]; <i>Conioselinum anthriscoides</i> 'Chuanxiong' [Apiaceae; Conioselinum]; <i>Pheretima</i> [Siliquariidae; Pheretima]; <i>Paeonia rubra</i> Steud. [Paeoniaceae; Paeonia]; and <i>Spatholobus suberectus</i> Dunn [Fabaceae; Spatholobus].	N	N	Warming kidney and replenishing <i>qi</i> , activating blood, and removing stasis
Yang et al. (2012)	Tongxinluo capsule	[Shijiazhuang Yiling Pharmaceutical Co., Ltd.]	<i>Panax ginseng</i> C.A.Mey. [Araliaceae; Panax]; <i>Whitmania pigra</i> Whitman [Hirudinidae; Hirudo]; scorpion [Buthidae; Scorpio]; ground beetle; <i>Scolopendra subspinipes</i> [Scolopendridae; centipede]; <i>Cryptotympana atrata</i> Fabricius [Cicadidae; Periostracum Cicadae]; <i>Paeonia rubra</i> Steud. [Paeoniaceae; Paeonia]; <i>Dalbergia odorifera</i> T.C.Chen [Fabaceae; Dalbergia]; <i>Pistacia lentiscus</i> L. [Anacardiaceae; Pistacia]; <i>Santalum album</i> L. [Santalaceae; Santalum]; <i>Ziziphus jujuba</i> Mill. [Rhamnaceae; Ziziphus]; and <i>Dipterocarpus turbinatus</i> C.F.Gaertn. [Dipterocarpaceae; Dipterocarpus].	Y—Prepared according to People's Republic of China Pharmacopoeia, 2020	Y—HPLC	Replenishing <i>qi</i> and activating blood, removing stasis, and restoring pulse

(Continued on following page)

TABLE 2 (Continued) Summary of composition of CPMs.

Study	Formulation	Source	Species, concentration	Quality control reported? (Y/N)	Chemical analysis reported? (Y/N)	Therapeutic claims in TCM
Wu and Hu, (2019)	Musk tongxin dropping pills	[Inner Mongolia Kangenbei Pharmaceutical Co. Ltd. Shenglong Branch]	<i>Panax ginseng</i> C.A.Mey. [Araliaceae; Panax]; artificial <i>Moschus</i> ; <i>Salvia miltiorrhiza</i> Bunge [Labiatae; Salvia]; <i>Dipterocarpus turbinatus</i> C.F.Gaertn. [Dipterocarpaceae; Dipterocarpus]; toad [Bufonidae; Toad Venom]; Ursidae [Ursidae; Bear gall powder]; and artificial bezoar.	Y—Prepared according to People's Republic of China Pharmacopoeia, 2020	Y—HPLC	Inducing aromatic, replenishing <i>qi</i> and restoring pulse, activating blood, removing stasis, and alleviating pain
Wu et al. (2021)	Musk tongxin dropping pills	[Inner Mongolia Kangenbei Pharmaceutical Co. Ltd. Shenglong Branch]	<i>Panax ginseng</i> C.A.Mey. [Araliaceae; Panax]; Artificial <i>Moschus</i> ; <i>Salvia miltiorrhiza</i> Bunge [Labiatae; Salvia]; <i>Dipterocarpus turbinatus</i> C.F.Gaertn. [Dipterocarpaceae; Dipterocarpus]; toad [Bufonidae; Toad Venom]; Ursidae [Ursidae; Bear gall powder]; and artificial bezoar.	Y—Prepared according to People's Republic of China Pharmacopoeia, 2020	Y—HPLC	Inducing aromatic, replenishing <i>qi</i> and restoring pulse, activating blood, removing stasis, and alleviating pain
Zou, (2019)	Heart-protecting musk pill	[Shanghai Hehuang Pharmaceutical Co. Ltd.]	<i>Moschus</i> [Cervidae; Moschus]; <i>Panax ginseng</i> C.A.Mey. [Araliaceae; Panax]; oriental sweetgum [Hamamelidaceae; Styralyl propionate]; Bovis Calculus [Bovine; <i>Calculus bovis</i> ]; <i>Cinnamomum cassia</i> Siebold [Lauraceae; Cinnamomum]; and toad [Bufonidae; toad venom].	Y—Prepared according to People's Republic of China Pharmacopoeia, 2005	Y—HPLC	Replenishing <i>qi</i> and restoring pulse, activating blood, and removing stasis
Yang and Liu, (2020)	Sanwei sandalwood capsule	[Inner Mongolia Kemeng Pharmaceutical Co. Ltd.]	<i>Santalum album</i> L. [Santalaceae; Santalum]; <i>Choerospondias axillaris</i> (Roxb.) B.L.Burt and A.W.Hill [Anacardiaceae; Choerospondias]; and <i>Myristica fragrans</i> Houtt. [Myristicaceae; Myristica].	Y—Prepared according to the National Food and Drug Administration National Drug Standards.	N	Clearing heat
Xu et al. (2019)	Compound Danshen dripping pills	[Tianjin Tasly Pride Pharmaceutical Co., Ltd.]	<i>Salvia miltiorrhiza</i> Bunge [Labiatae; Salvia], 90g; <i>Panax notoginseng</i> (Burkill) F.H.Chen [Araliaceae; Panax], 17.6g; and <i>Dipterocarpus turbinatus</i> C.F.Gaertn. [Dipterocarpaceae; Dipterocarpus], 1 g.	Y—Prepared according to People's Republic of China Pharmacopoeia, 2020	Y—HPLC	Activating blood and removing stasis, promoting <i>qi</i> , and alleviating pain
Fan. (2017)	Qiliqiangxin granules	[Shijiazhuang Yiling Pharmaceutical Co., Ltd.]	<i>Astragalus mongholicus</i> Bunge [Fabaceae; Astragalus], 450g; <i>Panax ginseng</i> C.A.Mey. [Araliaceae; Panax], 225g; <i>Aconitum carmichaelii</i> Debeaux [Ranunculaceae; Aconitum], 112.5g; <i>Salvia miltiorrhiza</i> Bunge [Lamiaceae; Salvia], 225g; <i>Lepidium apetalum</i> Willd. [Brassicaceae; Lepidium], 150g; <i>Alisma plantago-aquatica</i> L. [Alismataceae; Alisma], 225g; <i>Polygonatum odoratum</i> (Mill.) Druce [Asparagaceae; Polygonatum], 75g; <i>Cinnamomum cassia</i> Siebold [Lauraceae; Cinnamomum], 90g; <i>Carthamus tinctorius</i> L. [Asteraceae; Carthamus], 90g; <i>Periploca sepium</i> Bunge [Apocynaceae; Periploca], 180g; and <i>Citrus reticulata</i> Blanco [Rutaceae; Citrus], 75 g.	Y—Prepared according to People's Republic of China Pharmacopoeia, 2020	Y—HPLC	Replenishing <i>qi</i> and restoring <i>yang</i> , and restoring pulse and cardiostonic

(Continued on following page)



TABLE 2 (Continued) Summary of composition of CPMs.

Study	Formulation	Source	Species, concentration	Quality control reported? (Y/N)	Chemical analysis reported? (Y/N)	Therapeutic claims in TCM
Zhang et al. (2017)	Qiliqiangxin granules	[Shijiazhuang Yiling Pharmaceutical Co., Ltd.]	<i>Astragalus mongholicus</i> Bunge [Fabaceae; Astragalus], 450g; <i>Panax ginseng</i> C.A.Mey. [Araliaceae; Panax], 225g; <i>Aconitum carmichaelii</i> Debeaux [Ranunculaceae; Aconitum], 112.5g; <i>Salvia miltiorrhiza</i> Bunge [Lamiaceae; Salvia], 225g; <i>Lepidium apetalum</i> Willd. [Brassicaceae; Lepidium], 150g; <i>Alisma plantago-aquatica</i> L. [Alismataceae; Alisma], 225g; <i>Polygonatum odoratum</i> (Mill.) Druce [Asparagaceae; Polygonatum], 75g; <i>Cinnamomum cassia</i> Siebold [Lauraceae; Cinnamomum], 90g; <i>Carthamus tinctorius</i> L. [Asteraceae; Carthamus], 90g; <i>Periploca sepium</i> Bunge [Apocynaceae; Periploca], 180g; and <i>Citrus reticulata</i> Blanco [Rutaceae; Citrus], 75 g.	Y—Prepared according to People's Republic of China Pharmacopoeia, 2020	Y—HPLC	Replenishing qi and restoring yang, and restoring pulse and cardiogenic
Zheng, (2013)	Fumai granule	Prepared by Huang C.L.	<i>Panax ginseng</i> C.A.Mey. [Araliaceae; Panax]; <i>Ophiopogon japonicus</i> (Thunb.) Ker Gawl. [Asparagaceae; Ophiopogon]; and <i>Schisandra chinensis</i> (Turcz.) Baill. [Schisandraceae; Schisandra].	N	N	Replenishing qi, nourishing yin, and restoring pulse
Peng et al. (2020)	Jianxin Pinglv pills	[Shenzhen Traditional Chinese Medicine Hospital]	<i>Astragalus mongholicus</i> Bunge [Fabaceae; Astragalus]; <i>Pseudostellaria</i> Pax [Caryophyllaceae; Pseudostellaria]; <i>Ophiopogon japonicus</i> (Thunb.) Ker Gawl. [Asparagaceae; Ophiopogon]; <i>Caulis Bambusae in Taeniam</i> [Poaceae; Phyllostachys]; <i>Pinellia ternata</i> (Thunb.) Makino [Araceae; Pinellia]; <i>Citrus reticulata</i> Blanco [Rutaceae; Citrus]; <i>Atractylodes macrocephala</i> Koidz. [Asteraceae; Atractylodes]; <i>Salvia miltiorrhiza</i> Bunge [Lamiaceae; Salvia]; <i>Panax notoginseng</i> (Burkill) F.H.Chen [Araliaceae; Panax]; and <i>Ziziphus jujuba</i> Mill. [Rhamnaceae; Ziziphus].	N	N	Replenishing qi and nourishing yin, resolving phlegm and removing stasis, calming heart, and tranquilizing mind
Hu, (2021)	Kidney-qi-tonifying pill	[Beijing Tongrentang Science and Technology Development Co., Ltd. pharmaceutical factory]	<i>Rehmannia glutinosa</i> (Gaertn.) DC. [Orobanchaceae; Rehmannia], 108g; <i>Dioscorea polystachya</i> Turcz. [Dioscoreaceae; Dioscorea], 27g; <i>Cornus officinalis</i> Siebold and Zucc. [Cornaceae; Cornus], 27g; <i>Poria cocos</i> (Schw.) Wolf [Polyporaceae; Poria], 78g; <i>Paeonia × suffruticosa</i> Andrews [Paeoniaceae; Paeonia], 27g; <i>Alisma plantago-aquatica</i> L. [Alismataceae; Alisma], 27g; <i>Cinnamomum cassia</i> Siebold [Lauraceae; Cinnamomum], 27g; <i>Aconitum carmichaelii</i> Debeaux [Ranunculaceae; Aconitum], 4.5g; <i>Achyranthes bidentata</i> Blume [Amaranthaceae; Achyranthes],	Y—Prepared according to People's Republic of China Pharmacopoeia, 1963	N	Warming kidney and restoring yang

(Continued on following page)

TABLE 2 (Continued) Summary of composition of CPMs.

Study	Formulation	Source	Species, concentration	Quality control reported? (Y/N)	Chemical analysis reported? (Y/N)	Therapeutic claims in TCM
			27g; and <i>Plantago asiatica</i> L. [Plantaginaceae; Plantago], 27 g.			
Meng et al. (2021)	Compound Danshen dripping pills	[Tianjin Tasly Pride Pharmaceutical Co., Ltd.]	<i>Salvia miltiorrhiza</i> Bunge [Labiatae; Salvia], 90g; <i>Panax notoginseng</i> (Burkill) F.H.Chen [Araliaceae; Panax], 17.6 g; and <i>Dipterocarpus turbinatus</i> C.F.Gaertn. [Dipterocarpaceae; Dipterocarpus], 1 g.	Y—Prepared according to People's Republic of China Pharmacopoeia, 2020	Y—HPLC	Activating blood and removing stasis, promoting <i>qi</i> , and alleviating pain
Ji et al. (2021)	Buxinqi oral solution	[Hubei Furen Jinshen Pharmaceutical Co. Ltd.]	<i>Astragalus mongholicus</i> Bunge [Fabaceae; Astragalus], 500g; <i>Panax ginseng</i> C.A.Mey. [Araliaceae; Panax], 100g; <i>Acorus tatarinowii</i> [Araceae; Acorus], 333g; and <i>Allium macrostemon</i> Bunge. [Amaryllidaceae; Allium], 200 g.	Y—Prepared according to People's Republic of China Pharmacopoeia, 2020	Y—HPLC	Tonifying heart, replenishing and regulating <i>qi</i> , and alleviating pain
Liu, (2014)	Wenxin granule	[Shandong Buchang Pharmaceutical Co. Ltd.]	<i>Codonopsis pilosula</i> (Franch.) Nannf. [Campanulaceae; Codonopsis], 300g; <i>Panax notoginseng</i> (Burkill) F.H.Chen [Araliaceae; Panax], 60g; <i>Nardostachys jatamansi</i> (D.Don) DC [Caprifoliaceae; Nardostachys], 200g; Ambrum, 40g; <i>Polygonatum odoratum</i> (Mill.) Druce [Asparagaceae; Polygonatum], 400 g.	Y—Prepared according to People's Republic of China Pharmacopoeia, 2020	Y—HPLC	Tonifying blood and replenishing <i>qi</i> , activating blood and removing stasis, calming heart, and tranquilizing mind
Xie et al. (2019)	Qishen Yiqi Droplet	[Tianjin Tasly Pride Pharmaceutical Co., Ltd.]	<i>Astragalus mongholicus</i> Bunge [Fabaceae; Astragalus], 1800g; <i>Salvia miltiorrhiza</i> Bunge [Labiatae; Salvia], 900; <i>Dalbergia odorifera</i> T.C.Chen [Fabaceae; Dalbergia], 12g; and <i>Panax notoginseng</i> (Burkill) F.H.Chen [Araliaceae; Panax], 180 g.	Y—Prepared according to People's Republic of China Pharmacopoeia, 2020	Y—HPLC	Replenishing <i>qi</i> and restoring pulse, activating blood, and alleviating pain
Zhang and Gou, (2021)	Qishen Yiqi Droplet	[Tianjin Tasly Pride Pharmaceutical Co., Ltd.]	<i>Astragalus mongholicus</i> Bunge [Fabaceae; Astragalus], 1800 g; <i>Salvia miltiorrhiza</i> Bunge [Labiatae; Salvia], 900; <i>Dalbergia odorifera</i> T.C.Chen [Fabaceae; Dalbergia], 12 g; and <i>Panax notoginseng</i> (Burkill) F.H.Chen [Araliaceae; Panax], 180 g.	Y—Prepared according to People's Republic of China Pharmacopoeia, 2020	Y—HPLC	Replenishing <i>qi</i> and restoring pulse, activating blood, and alleviating pain

compared to WM. All mean changes in pairwise comparison had no differences within the IG.

The SUCRA for each regimen indicated that the use of BASR-CPM (78.2%) had the highest probability of being the best option for effectively improving the level of LVEF among the eight types of treatment regimens (Supplementary Figure S3B).

## Left ventricular end-diastolic dimension (LVEDD)

Out of 25 RCTs, 14 (Yang et al., 2012; Fan, 2017; Zhang et al., 2017; Wu and Hu, 2019; Xie et al., 2019; Xu et al., 2019; Zheng et al., 2019; Zou, 2019; Peng et al., 2020; Hu, 2021; Ji et al., 2021; Meng

et al., 2021; Wu et al., 2021; Zhang and Gou, 2021) were analyzed, consisting of 1,278 patients undergoing five IG treatment regimens—QR-CPM + WM, BASR-CPM + WM, QR&BASR-CPM, QR&BASR-CPM + WM, and KWYR-CPM + THSWT + WM—and WM in the CG.

The pairwise comparison outcome of LVEDD is presented in Table 6 and Supplementary Figure S2C. Compared to WM, KWYR-CPM + THSWT + WM was superior to other treatment regimens in reducing LVEDD. Meanwhile, compared with WM, QR&BASR-CPM + WM (SMD = −1.54; 95%CI = −2.49, −0.60) and QR-CPM + WM (SMD = −0.76; 95%CI = −1.41, −0.11) were also significantly associated with a reduction in LVEDD. When the pairwise comparison was made between treatment regimens in the IG, all mean changes showed no significant differences within it.

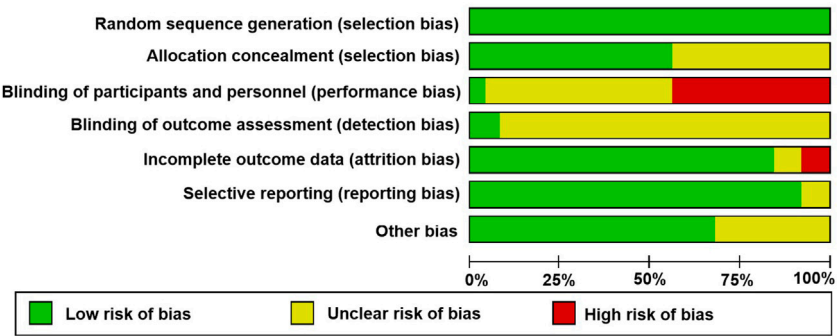


FIGURE 2  
Risk of bias.

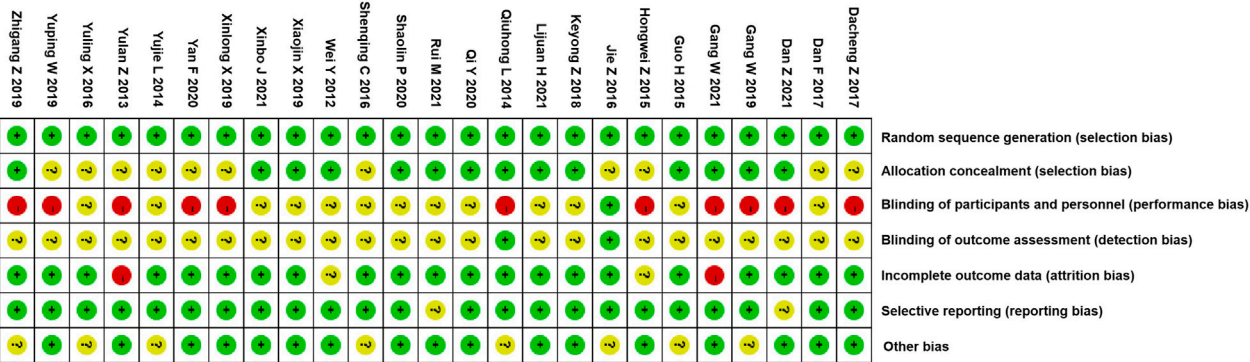


FIGURE 3  
Summary of risk of bias based on selection bias.

Meanwhile, the SUCRA result showed that KWYR-CPM + THSWT + WM (82.7%) had the highest probability of being ranked first in reducing the level of LVEDD, followed by others in the IG (Supplementary Figure S3C).

Left ventricular end-systolic dimension (LVESD)

Nine trials (Yang et al., 2012; Fan, 2017; Zhang et al., 2017; Wu and Hu, 2019; Xie et al., 2019; Xu et al., 2019; Zheng et al., 2019; Zou, 2019; Zhang and Gou, 2021) of LVESD involved 821 patients with four CPM-related treatment regimens and one WM. QR&BASR-CPM + WM (SMD = -2.35; 95%CI = -3.09,-1.62) was the most effective treatment regimen in decreasing LVESD with significant differences except for BASR-CPM (Table 7; Supplementary Figure S2D).

SUCRA indicated QR&BASR-CPM + WM to be ranked first and considered the best option for reducing the level of LVESD (Supplementary Figure S3D).

Left ventricular mass index (LVMI)

LVMI changes in patients were reported in seven studies (Liu, 2014; Cui et al., 2016; Wu and Hu, 2019; Xie et al., 2019; Hu, 2021; Meng et al., 2021; Wu et al., 2021) involving five treatment regimens in IG plus a WM in CG. QR&BASR-CPM + WM and BASR-CPM + WM were considered effective treatment regimens for reducing the level of LVM with significant differences (Table 8; Supplementary Figure S2E).

On the basis of SUCRA results, QR&BASR-CPM + WM (90.9%) is most probably the best treatment regimen for reducing LVMI (Supplementary Figure S3E).

Difference in mean changes in cardiac biomarkers

Cardiac biomarkers suggest that their measurement can be used for preclinical diagnosis of left ventricular hypertrophy (LVH) (Koycheva et al., 2016).

TABLE 3 Detailed information for each treatment regimen of all outcomes.

Treatment regimen	No. of trials	No. of patients
Clinical efficacy	19	1966
WM	19	982
BASR-CPM	1	64
QR&BASR-CPM	3	197
QR-CPM + WM	8	349
HC-CPM + WM	1	43
BASR-CPM + WM	1	40
QR&BASR-CPM + WM	5	291
<b>LVEF</b>	<b>21</b>	<b>1903</b>
WM	21	950
BASR-CPM	2	110
QR&BASR-CPM	2	151
QR-CPM + WM	8	323
HC-CPM + WM	1	43
BASR-CPM + WM	4	164
QR&BASR-CPM + WM	3	126
KWYR-CPM + THSWT + WM	1	36
<b>LVEDD</b>	<b>14</b>	<b>1278</b>
WM	14	639
QR&BASR-CPM	2	151
QR-CPM + WM	6	252
BASR-CPM + WM	2	74
QR&BASR-CPM + WM	3	126
KWYR-CPM + THSWT + WM	1	36
<b>LVEDS</b>	<b>9</b>	<b>821</b>
WM	9	410
QR&BASR-CPM	1	86
QR-CPM + WM	4	159
BASR-CPM + WM	1	40
QR&BASR-CPM + WM	3	126
<b>LVMI</b>	<b>7</b>	<b>714</b>
WM	7	362
QR-CPM + WM	1	40
QR&BASR-CPM	2	151
BASR-CPM + WM	2	84
QR&BASR-CPM + WM	1	50
KWYR-CPM + THSWT + WM	1	36
<b>CRP</b>	<b>7</b>	<b>689</b>
WM	7	338

(Continued in next column)

TABLE 3 (Continued) Detailed information for each treatment regimen of all outcomes.

Treatment regimen	No. of trials	No. of patients
BASR-CPM	2	110
BASR-CPM + WM	2	74
QR-CPM + WM	2	71
QR&BASR-CPM	1	86
<b>NT-proBNP</b>	<b>6</b>	<b>609</b>
WM	6	305
BASR-CPM	1	64
QR&BASR-CPM	1	65
QR-CPM + WM	2	70
BASR-CPM + WM	1	34
QR&BASR-CPM + WM	1	71
<b>6-MWT</b>	<b>6</b>	<b>615</b>
WM	6	308
BASR-CPM	1	64
QR&BASR-CPM	1	65
QR-CPM + WM	3	142
KWYR-CPM + THSWT + WM	1	36

Note: Specific treatment regimen information is commented upon as in Table 1. The bold values indicated outcome indicators in the study.

## C-reactive protein (CRP)

Seven trials (Zheng, 2013; Zhang et al., 2016; Fan, 2017; Li, 2017; Wu and Hu, 2019; Fan et al., 2020; Meng et al., 2021) with CRP included 679 patients with four CPM-related treatment regimens in IG and a WM in CG.

There was no significant difference in CRP between the two treatment regimens related to BASR: BASR-CPM and BASR-CPM + WM (Table 9; Supplementary Figure S2F).

By SUCRA, BASR-CPM (92.3%) had the highest probability of being ranked first in reducing CRP (Supplementary Figure S3F).

## N-terminal proBNP (NT-proBNP)

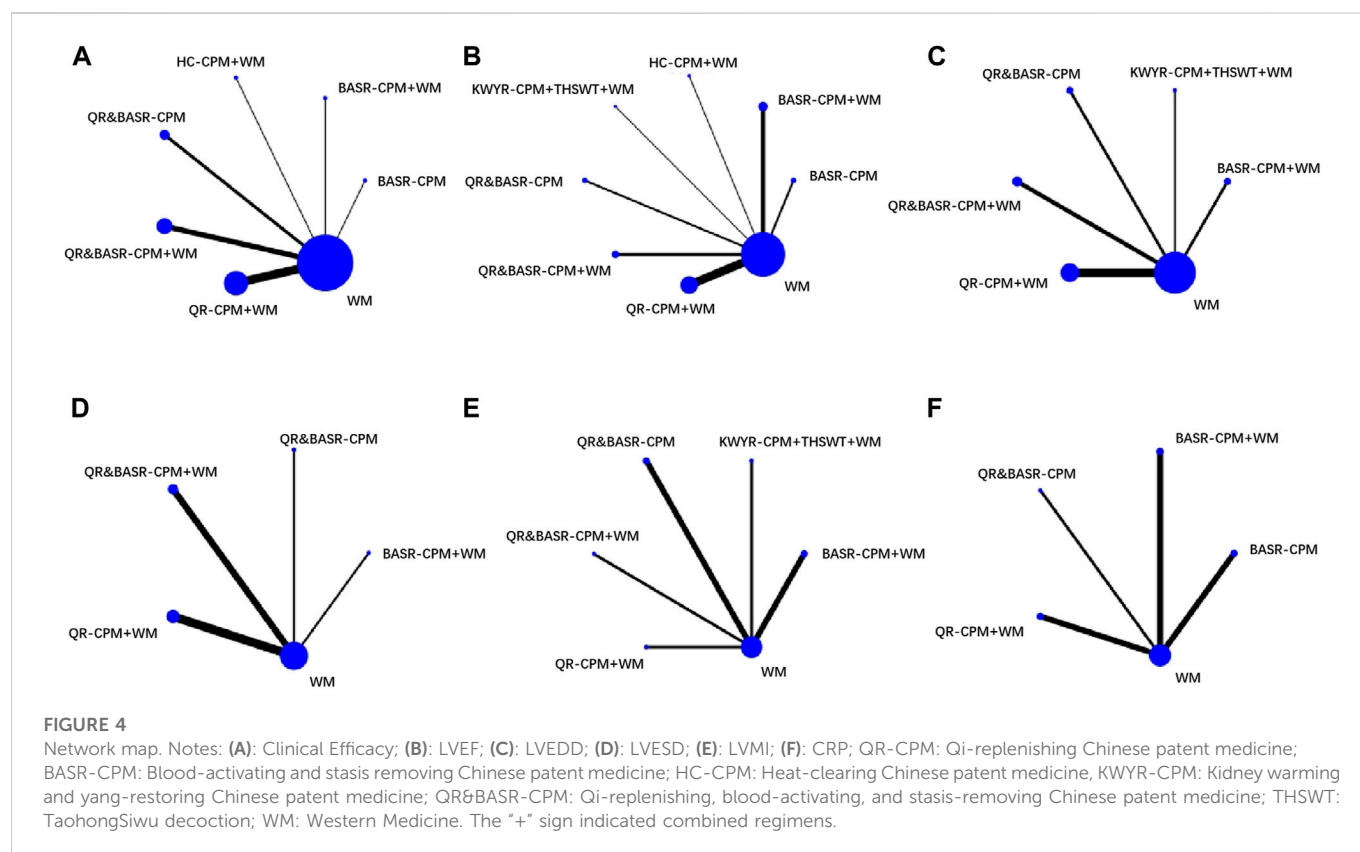
The pairwise comparison in NT-proBNP manifesting among each treatment regimen showed no differences in all included studies (Table 10; Supplementary Figure S2G). Therefore, the results for NT-proBNP do not allow clear conclusions to be drawn.

## Difference in mean changes in functional exercise capacity

### Six-minute walk test (6-MWT)

Functional capacity was measured with 6-MWT, a well-tolerated, practical, and useful tool with worldwide recommendations for the





**TABLE 4** Results of network meta-analysis for clinical efficacy.

BASR-CPM+WM						
1.33 (0.09, 19.20)	HC-CPM+WM					
1.57 (0.17, 14.76)	1.18 (0.21, 6.53)	QR&BASR-CPM+WM				
2.14 (0.23, 19.84)	1.61 (0.30, 8.74)	1.37 (0.57, 3.30)	QR&BASR-CPM			
2.35 (0.26, 20.96)	1.77 (0.34, 9.12)	1.50 (0.69, 3.27)	1.10 (0.53, 2.27)	QR-CPM+WM		
2.80 (0.26, 30.09)	2.10 (0.32, 13.84)	1.78 (0.53, 5.99)	1.31 (0.40, 4.25)	1.19 (0.39, 3.59)	BASR-CPM	
8.27 (0.97, 70.73)	6.21 (1.27, 30.34)	5.28 (2.75, 10.14)	3.86 (2.14, 6.98)	3.52 (2.30, 5.38)	2.96 (1.07, 8.21)	WM

Notes: The bold values indicated that the pairwise comparison between treatment regimens are statistical significance differences ( $p < 0.05$ ). The treatment regimens is the same as the note of Figure 4.

**TABLE 5** Results of network meta-analysis for LVEF.

BASR-CPM							
0.24 (-1.64, 2.11)	QR&BASR-CPM+WM						
0.36 (-1.41, 2.13)	0.12 (-1.45, 1.69)	BASR-CPM+WM					
0.46 (-2.05, 2.97)	0.23 (-2.14, 2.60)	0.10 (-2.19, 2.40)	KWYR-CPM+THSWT+WM				
1.13 (-1.36, 3.63)	0.90 (-1.46, 3.25)	0.77 (-1.50, 3.05)	0.67 (-2.21, 3.56)	HC-CPM+WM			
1.04 (-0.58, 2.65)	0.80 (-0.59, 2.19)	0.68 (-0.58, 1.93)	0.57 (-1.60, 2.75)	-0.10 (-2.25, 2.06)	QR-CPM+WM		
1.16 (-0.87, 3.19)	0.92 (-0.93, 2.77)	0.80 (-0.96, 2.55)	0.69 (-1.80, 3.19)	0.02 (-2.46,2.50)	0.12 (-1.48,1.71)	QR&BASR-CPM	
1.90 (0.46, 3.35)	1.67 (0.48, 2.86)	1.54 (0.52, 2.57)	1.44 (-0.61, 3.49)	0.77 (-1.26, 2.80)	0.87 (0.14, 1.59)	0.75 (-0.68, 2.17)	WM

Notes: The bold values indicated that the pairwise comparison between treatment regimens are statistical significance differences ( $p < 0.05$ ). The treatment regimens is the same as the note of Figure 4.

**TABLE 6 Results of network meta-analysis for LVEDD.**

KWYR-CPM+THSWT+WM					
-0.30 (-2.17, 1.58)	QR&BASR-CPM+WM				
-0.75 (-2.73, 1.23)	-0.45 (-1.93, 1.03)	BASR-CPM+WM			
-1.08 (-2.83, 0.67)	-0.79 (-1.93, 0.36)	-0.34 (-1.65, 0.97)	QR-CPM+WM		
-1.32 (-3.28, 0.64)	-1.02 (-2.47, 0.43)	-0.57 (-2.16, 1.01)	-0.24 (-1.52, 1.04)	QR&BASR-CPM	
-1.84 (-3.46, -0.22)	-1.54 (-2.49, -0.60)	-1.09 (-2.23, 0.04)	-0.76 (-1.41, -0.11)	-0.52 (-1.62, 0.58)	WM

Notes: The bold values indicated that the pairwise comparison between treatment regimens are statistical significance differences ( $p < 0.05$ ). The treatment regimens is the same as the note of Figure 4.

**TABLE 7 Results of network meta-analysis for LVESD.**

QR&BASR-CPM+WM					
-1.25 (-2.66, 0.15)	BASR-CPM+WM				
-1.67 (-2.62, -0.72)	-0.41 (-1.76, 0.93)	QR-CPM+WM			
-2.15 (-3.51, -0.79)	-0.90 (-2.56, 0.76)	-0.48 (-1.78, 0.81)	QR&BASR-CPM		
-2.35 (-3.09, -1.62)	-1.10 (-2.30, 0.10)	-0.69 (-1.29, -0.09)	-0.20 (-1.35, 0.94)	WM	

Notes: The bold values indicated that the pairwise comparison between treatment regimens are statistical significance differences ( $p < 0.05$ ). The treatment regimens is the same as the note of Figure 4.

**TABLE 8 Results of network meta-analysis for LVMI.**

QR&BASR-CPM+WM					
-0.59 (-2.06, 0.87)	BASR-CPM+WM				
-1.05 (-2.49, 0.39)	-0.45 (-1.63, 0.72)	QR&BASR-CPM			
-1.10 (-2.79, 0.59)	-0.50 (-1.97, 0.96)	-0.05 (-1.49, 1.40)	KWYR-CPM+THSWT+WM		
-1.35 (-3.03, 0.32)	-0.76 (-2.22, 0.70)	-0.31 (-1.74, 1.13)	-0.26 (-1.94, 1.43)	QR-CPM+WM	
-1.73 (-2.92, -0.54)	-1.14 (-1.99, -0.29)	-0.68 (-1.49, 0.13)	-0.63 (-1.83, 0.56)	-0.37 (-1.56, 0.81)	WM

Notes: The bold values indicated that the pairwise comparison between treatment regimens are statistical significance differences ( $p < 0.05$ ). The treatment regimens is the same as the note of Figure 4.

**TABLE 9 Results of network meta-analysis for CRP.**

BASR-CPM					
-0.49 (-1.51, 0.53)	BASR-CPM+WM				
-0.79 (-1.99, 0.40)	-0.30 (-1.51, 0.90)	QR&BASR-CPM			
-0.98 (-2.00, 0.03)	-0.49 (-1.52, 0.54)	-0.19 (-1.39, 1.01)	QR-CPM+WM		
-1.31 (-2.02, -0.60)	-0.82 (-1.55, -0.09)	-0.52 (-1.48, 0.44)	-0.33 (-1.05, 0.40)	WM	

Notes: The bold values indicated that the pairwise comparison between treatment regimens are statistical significance differences ( $p < 0.05$ ). The treatment regimens is the same as the note of Figure 4.

cardiorespiratory domain (Hojan et al., 2020). There is no statistical significance in the pairwise comparison among all treatment regimens (Table 11; Supplementary Figure S2H). Therefore, the results for 6-MWT do not enable clear conclusions to be drawn.

Using SUCRA, the probability rank information on all treatment regimens for each outcome is summarized in Table 12.

### Risk of publication bias

The risk of publication bias could be assessed by a funnel plot. The funnel plot about the primary outcome of

clinical efficacy is shown in Figure 5, and the secondary outcomes with LVEF and LVEDD are shown in Supplementary Figure S4A, B—funnel plots were not feasible for those including fewer than 10 studies. According to the funnel plot of the primary outcome, all trials were basically distributed on both sides of the middle, and the left and right distribution were roughly symmetrical; this indicated no strong evidence of publication bias in all the trials for the primary outcome. The results for other funnel plots also indicated no strong publication bias.

TABLE 10 Results of network meta-analysis for NT-proBNP.

BASR-CPM					
-0.28 (-4.22, 3.65)	QR-CPM+WM				
-0.31 (-4.84, 4.22)	-0.03 (-3.95, 3.90)	QR&BASR-CPM+WM			
-0.57 (-5.11, 3.98)	-0.28 (-4.23, 3.66)	-0.26 (-4.80, 4.28)	BASR-CPM+WM		
-2.04 (-5.96, 1.88)	-1.75 (-4.97, 1.46)	-1.73 (-5.65, 2.19)	-1.47 (-5.41, 2.46)	QR&BASR-CPM	
-2.13 (-5.33, 1.07)	-1.85 (-4.13, 0.44)	-1.82 (-5.02, 1.38)	-1.56 (-4.78, 1.66)	-0.09 (-2.35, 2.17)	WM

TABLE 11 Results of network meta-analysis for 6-MWT.

QR-CPM+WM				
0.43 (-3.77, 4.62)	QR&BASR-CPM			
0.57 (-3.64, 4.78)	0.14 (-5.00, 5.29)	KWYR-CPM+THSWT+WM		
0.91 (-3.29, 5.10)	0.48 (-4.65, 5.61)	0.34 (-4.81, 5.48)	BASR-CPM	
1.68 (-0.42, 3.79)	1.25 (-2.37, 4.88)	1.11 (-2.53, 4.75)	0.77 (-2.85, 4.40)	WM

TABLE 12 All treatment regimen information on each outcome.

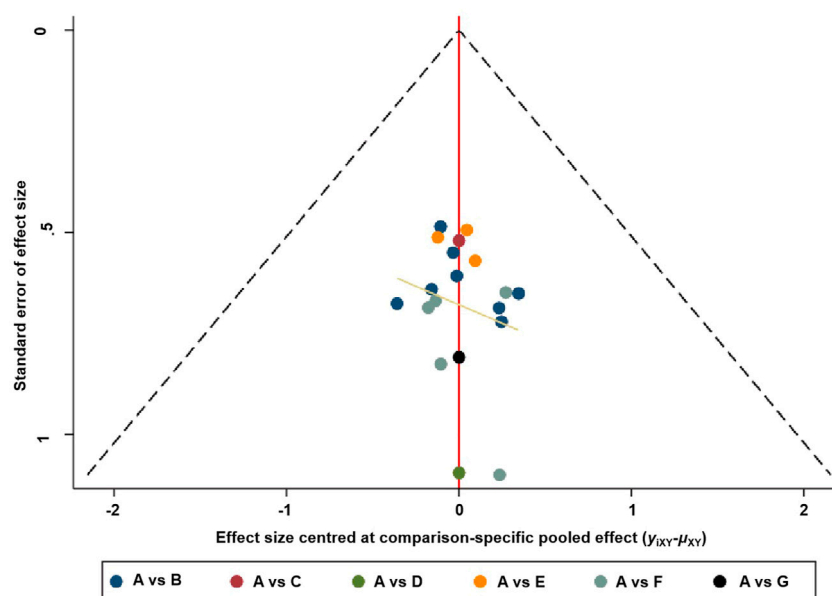
Treatment regimen outcome	Clinical efficacy	LVEF	LVEDD	LVESD	LVMI	CRP	NT-proBNP	6-MWT
WM	7	8	6	5	6	5	6	5
BASR-CPM	6	1	NA	NA	NA	1	1	4
QR&BASR-CPM	4	7	5	4	3	3	5	2
QR-CPM + WM	5	6	4	3	5	4	2	1
BASR-CPM + WM	1	3	3	2	2	2	4	NA
QR&BASR-CPM + WM	3	2	2	1	1	NA	3	NA
KWYR-CPM + THSWT + WM	NA	4	1	NA	4	NA	NA	3
HC-CPM + WM	2	5	NA	NA	NA	NA	NA	NA

Note: Specific treatment regimen information is commented upon as in Table 1.

## Discussion

With increasing clinical trials into combining traditional and Western medicines in the treatment of myocardial hypertrophy, this study conducted a NMA to compare for clinical efficacy, echocardiographic indices, cardiac biomarkers, and functional capacity for each CPM-related treatment regimen used for patients with cardiac hypertrophy. It provided scientific and meaningful evidence for precision medicine in clinical settings. The results of pairwise comparison of different treatment regimens in the present network meta-analysis showed that BASR-CPM + WM (OR = 8.27; 95%CI = 0.97, 70.73) might be the optimum selection, being ranked first for improving clinical efficacy over other treatment regimens. It is worth mentioning that QR&BASR-CPM + WM showed the highest effectiveness in echocardiographic indices such as reducing LVESD (SMD = -2.35; 95% CI = -3.09, -1.62) and LVMI (SMD = -1.73; 95%CI = -2.92, -0.54). For included studies in this meta-analysis, there were no overall obvious publication bias or small-study effects.

BASR-CPM + WM, as mainly used for treating cardiovascular diseases, had the highest clinical efficacy (OR = 8.27; 95%CI = 0.97, 70.73) in this study; the function of blood activation and stasis removal could unblock and activate blood vessels by relieving blockages, resisting myocardial ischemia and inhibiting platelet aggregation and anticoagulant and antithrombotic formation, leading to improved cardiovascular blood supply (Zhou et al., 2017; Liu et al., 2019). The components of BASR-CPM for treating cardiovascular and cerebrovascular diseases mainly included *Ligusticum chuanxiong* Hort, *Salvia miltiorrhiza*, *Radix paeoniae* Rubra, and *Panax notoginseng*, which could improve blood supply by inhibiting the activity of erythrocyte membrane adenosine triphosphatase (ATPase), inhibiting ATP consumption, and regulating the blood or fibrinolytic system (Li et al., 2015; Ma et al., 2020; Wu et al., 2020). According to the researched trials investigated, Xinkeshu capsule and Compound Danshen dropping pill all have as main ingredients *S. miltiorrhiza* and *P. notoginseng*. In addition, previous studies have indicated that  $\beta$ -blocker, angiotensin II receptor blockers and similar in WM were beneficial in protecting and improving cardiac function and inhibiting



**FIGURE 5**  
Funnel plot for clinical efficacy.

ventricular remodeling (Graudins et al., 2016). Therefore, we speculate that combined CPM and WM treatment might have better therapeutic effects and better reduce complications for greater performance in short- and long-term outcomes in previous studies (Wang et al., 2017). According to the Chinese medicine therapeutic rule “To alleviate the symptoms if the disease progresses fast and eradicate the cause if the disease develops slowly,” such a combination might have the advantage of combined therapy. In the past, it has been thought that combined CPM and WM is superior to WM alone: our review provides new evidence for this view.

Interestingly, in our study result, the combined treatment regimen of *qi*-replenishing, blood-activating, and stasis-removing and WM could significantly decrease echocardiography indices such as LVESD (SMD = -2.35; 95%CI = -3.09, -1.62) and LVMI (SMD = -1.73 95% CI = -2.92, -0.54), which were similar to previous conclusions in animal and clinical tests (Li et al., 2011; Chen et al., 2016; Chen et al., 2021). As a non-invasive technique, echocardiography could provide an effective reference and supplementary index for the clinical evaluation of cardiac function (Edyta et al., 2019). *Qi*-replenishing Chinese medicine could increase the antioxidant capacity of myocardium by regulating antioxidant-free radicals to improve heart function, thereby improving echocardiography indices (Scott et al., 2001; Xia et al., 2020). The components of *qi*-replenishing Chinese medicine for treating cardiovascular and cerebrovascular diseases mainly include *Astragalus*, *Ginseng*, and *Dangshen*, which play an important role in dilating blood vessels, breaking down cyclic adenosine, decreasing peripheral vascular resistance, inhibiting platelet aggregation, increasing the calcium inflow of cells, and activating calmodulin (Zhang and Zhang, 2017; Wang et al., 2021). In the included studies, Wenxin granule, Shexiang Tongxin dropping pill, and Yiqi Huayu capsule all contained the aforementioned *qi*-replenishing ingredients. This study, which is conducive to making clinical decisions, is the first to indicate that combined treatment regimen of CPM with the function of *qi*-

replenishing, blood-activating, and stasis-removing, and WM might be optimal for improving the echocardiography indices of patients with cardiac hypertrophy. However, the original head-to-head clinical trials were few and low quality and need more related findings to support our results.

This NMA has provided new support for the hypothesis that patients with cardiac hypertrophy may obtain better clinical efficacy and related indicators from the perspective of CPM mechanism classification over other treatment regimens. However, this research also had some limitations. First, it did not directly compare treatment regimens (all studies were intervention versus WM), indicating that the strength of inference made in an NMA between different treatments was not as robust as it could be and that consistency between direct and indirect evidence could not be assessed. In addition, the number of studied samples was relatively small, resulting in potentially exaggerated therapeutic effects of treatment and preventing stronger conclusions from being made. Therefore, it will be necessary to carry out a larger sample and include more diverse Chinese medicine clinical trials to evaluate the long-term effect and further verify the function of each CPM-related mechanism and treatment regimen for patients with cardiac hypertrophy in future research.

## Conclusion

This NMA performed a generally comprehensive evaluation of CPM-related treatments for cardiac hypertrophy on different clinical outcomes. Our results indicated that the combined treatment regimen BASR-CPM and WM may exhibit outstanding efficacy compared with other treatment regimens in improving clinical efficacy for patients with cardiac hypertrophy. The QR&BASR-CPM and WM combination may be beneficial in



decreasing LVESD and LVMI. Although the current estimated effects of most CPMs for cardiac hypertrophy are significant and clinically relevant, the design and included original trials are not high quality and have an unclear bias of risk. Thus, larger sample sizes and higher quality RCTs are needed to confirm and support this NMA.

## Data availability statement

The original contributions presented in the study are included in the article/Supplementary Material; further inquiries can be directed to the corresponding author.

## Author contributions

The study was designed and conducted by XB and CW. Literature screening, risk of bias assessment, and data extraction were performed by DZ and DF. Discrepancies were resolved by MZ. Data were analyzed by TZ and HX. The manuscript draft was written by TZ and HX. The final manuscript was approved by all authors.

## Funding

This work is supported by the National Natural Science Foundation (NO. 82160958).

## References

- Azzimondi, G., Bassein, L., Fiorani, L., Nonino, F., Montaguti, U., and Celin, D. (1997). Variables associated with hospital arrival time after stroke: Effect of delay on the clinical efficiency of early treatment. *Stroke* 28 (3), 537–542. doi:10.1161/01.str.28.3.537
- Beldhuis, I. E., Lam, C. S. P., Testani, J. M., Voors, A. A., Van Spall, H. G. C., Ter Maaten, J. M., et al. (2022). Evidence-based medical therapy in patients with heart failure with reduced ejection fraction and chronic kidney disease. *Circulation* 145 (9), 693–712. doi:10.1161/CIRCULATIONAHA.121.052792
- Chen, J. X., Xu, X., Li, Z. F., Gao, K., Zhang, F. L., Li, Z. H., et al. (2016). Qishen Yiqi Drop Pill improves cardiac function after myocardial ischemia. *Sci. Rep.* 6, 24383. doi:10.1038/srep24383
- Chen, L. H., Wang, R., Liu, H. H., Wei, S. Z., Jing, M. Y., Wang, M., et al. (2021). Clinical efficacy and safety of qishen Yiqi dropping pill combined with conventional western medicine in the treatment of chronic heart failure: A systematic review and meta-analysis. *Evid. Based Complement. Altern. Med.* 2021, 6612653. doi:10.1155/2021/6612653
- Chen, X. B., Xu, Z. J., Liu, T., Dai, T. Z., Huang, X., Zheng, F., et al. (2022). Analysis of related risk factors and prognostic factors of gastric cancer with bone metastasis: A SEER-based study. *J. Immunol. Res.* 2022, 3251051. doi:10.1155/2022/3251051
- Cheng, S. S., Xanthakis, V., Sullivan, L. M., Lieb, W., Massaro, J., Aragam, J., et al. (2010). Correlates of echocardiographic indices of cardiac remodeling over the adult life course: Longitudinal observations from the framingham heart study. *Circulation* 122 (6), 570–578. doi:10.1161/CIRCULATIONAHA.110.937821
- Cui, S. Q., Kong, L. C., Ling, X., and Huang, M. (2016). Effect of irbesartan combined with Xinkeshu capsule on blood pressure and left cardiac function in patients with hypertension merged with left ventricular hypertrophy. *J. Journal Hainan Med. Univ.* 21, 1007–1237. doi:10.13210/j.cnki.jhmu.20160814.005
- Edyta, P. G., Barbara, L., Andrzej, S., Tomasz, K., Jarosław, D. K., Olga, D. D., et al. (2019). Echocardiography in adults. *J. Ultrason.* 19 (76), 54–61. doi:10.15557/JoU.2019.0008
- Fan, D. (2017). Effects of Qiangxin granule on ventricular remodeling and diastolic function in patients with chronic heart failure. *Yiyao Qianyan* 35, 2095–1752.
- Fan, Y., Chen, R., and Chen, X. (2020). Efficacy of ginkgo ketone ester dripping pills combined with metoprolol in treatment of chronic heart failure and its effect on serum inflammatory factors and myocardial fibrosis. *J. Guangxi Med. Univ.* 09, 1005–930x. doi:10.16190/j.cnki.45-1211/r.2020.09.013
- Graudins, A., Lee, H. M., and Druda, D. (2016). Calcium channel antagonist and beta-blocker overdose: Antidotes and adjunct therapies. *Br. J. Clin. Pharmacol.* 81 (3), 453–461. doi:10.1111/bcp.12763
- Han, G., and Shen, G. X. (2015). To evaluate the efficacy of Qili Qiangxin combined with lisinopril hydrochlorothiazide in the treatment of hypertensive left ventricular hypertrophy and myocardial ischemia. *China Health Care & Nutrition*. Available at: <https://d.wanfangdata.com.cn/periodical/ChlQZXXjpb2RpY2FsQ0hjTmV3UzlwMjMwMTEyEhJ6Z2JqZXkta3AyMDE1MDgwNDgwNDgaCHRmcDEzcjVv>
- Hojan, K., Procyk, D., Horyńska-Kęstowicz, D., Leporowska, E., and Litwiniuk, M. (2020). The preventive role of regular physical training in ventricular remodeling, serum cardiac markers, and exercise performance changes in breast cancer in women undergoing trastuzumab therapy—an REH-HER study. *J. Clin. Med.* 9 (5), 1379. doi:10.3390/jcm9051379
- Hu, L. J. (2021). Efficacy of Jin gui Shen qi pill and Tao hong Si Wu decoction combined with Western medicine on heart rate variability, left ventricular remodeling and renal function in patients with chronic heart failure. *Shaan xi J. Traditional Chin. Med.*, 1576–1580. doi:10.3969/j.issn.1000-7369.2021.11.019
- Ishida, H., Kogaki, S., Ichimori, H., Narita, J., Nawa, N., Ueno, T., et al. (2012). Overexpression of endothelin-1 and endothelin receptors in the pulmonary arteries of failed Fontan patients. *Int. J. Cardiol.* 159 (1), 34–39.
- Ji, X. B., Fu, B. W., Gu, S. H., Mai, H. D., Chen, J. M., and Zeng, W. Y. (2021). Study on effect of buxinqi oral liquid combined with sacubatro valsartan sodium on cardiac function and myocardial remodeling indexes in elderly patients with chronic heart failure. *Chin. Archives Traditional Chin. Med.* 10, 1673–7717. doi:10.13193/j.issn.1673-7717.2021.10.043
- Koycheva, R. Y., Cholakov, V., Andreev, J., Penev, M., Iliev, R., Nancheva, K., et al. (2016). Cardiac biomarkers and left ventricular hypertrophy in asymptomatic hemodialysis patients. *Open Access Maced. J. Med. Sci.* 4 (1), 59–64. doi:10.3889/oamjms.2016.011
- Kuno, T., Ueyama, H., Fujisaki, T., Briasoulis, A., Takagi, H., and Briasoulis (2020). Meta-analysis evaluating the effects of renin-angiotensin-aldosterone system blockade on outcomes of heart failure with preserved ejection fraction. *Am. J. Cardiol.* 125 (8), 1187–1193. doi:10.1016/j.amjcard.2020.01.009

## Acknowledgments

The authors sincerely appreciate the support of the Key Laboratory of Mongolian Medicine Pharmacology for Cardio-Cerebral Vascular System at the Inner Mongolia Minzu University.

## Conflict of interest

The authors declare that the research was conducted in the absence of any commercial or financial relationships that could be construed as a potential conflict of interest.

## Publisher's note

All claims expressed in this article are solely those of the authors and do not necessarily represent those of their affiliated organizations, or those of the publisher, the editors, and the reviewers. Any product that may be evaluated in this article, or claim that may be made by its manufacturer, is not guaranteed or endorsed by the publisher.

## Supplementary material

The Supplementary Material for this article can be found online at: <https://www.frontiersin.org/articles/10.3389/fphar.2023.963099/full#supplementary-material>

- Li, Q. H. (2017). *Clinical study on early ventricular remodeling after acute myocardial infarction treatment of Yiqi Huayu Capsule*. Tangshan, HB: University of Hebei United. [master's thesis].
- Li, R., Zhang, Q., and Yi, Q. J. (2011). Effect of carvedilol and Radix astragali on ryanodine receptor in heart failure in mice. *Zhonghua Er Ke Za Zhi* 49 (6), 433–438.
- Li, S. J., Lin, H., Tang, Y. P., Li, W. X., Shen, J., Kai, J., et al. (2015). Comparative metabolomics analysis on invigorating blood circulation for herb pair Gui-Hong by ultra-high-performance liquid chromatography coupled to quadrupole time-of-flight mass spectrometry and pattern recognition approach. *J. Pharm. Biomed. Anal.* 107, 456–463. doi:10.1016/j.jpba.2015.01.029
- Li, X., Li, L., Lei, W., Chua, H. Z., Li, J. N., Huang, X. L., et al. (2021). Traditional Chinese medicine as a therapeutic option for cardiac fibrosis: Pharmacology and mechanisms. *Biomed. Pharmacother.* 142, 111979. doi:10.1016/j.biopha.2021.111979
- Liu, X. Y., Shao, R., Yang, X. Y., Xiao, G. X., He, S., Feng, Y. X., et al. (2019). Untargeted safety Pharmacology screen of blood-activating and stasis-removing patent Chinese herbal medicines identified nonherbal ingredients as a cause of organ damage in experimental models. *Front. Pharmacol.* 12 (10), 993. doi:10.3389/fphar.2019.00993
- Liu, Y. J. (2014). Efficacy of metoprolol combined with Wenxin granule in the treatment of hypertensive heart disease with ventricular premature beat. *Clin. Res.* 14, 2095–1752.
- Lv, S. H., Wang, Q., Wu, M. F., Li, M., Wang, X. J., Xu, L., et al. (2021). QiShenYiQi pill improves myocardial hypertrophy caused by pressure overload in rats. *Evid. Based Complement. Altern. Med.* 2021, 5536723. doi:10.1155/2021/5536723
- Ma, R., Chen, G., Li, H., Zhang, Y., Liu, Y., He, H., et al. (2020). Panax notoginseng saponins inhibits ventricular remodeling after myocardial infarction in rats through regulating ATF3/MAP2K3/p38 MAPK and NF  $\kappa$  B pathway. *Chin. J. Integr. Med.* 26 (12), 897–904. doi:10.1007/s11655-020-2856-6
- Mbuagbaw, L., and Aves, T. (2022). Meta-analysis of pragmatic and explanatory trials. *Methods Mol. Biol.* 2345, 147–158. doi:10.1007/978-1-0716-1566-9\_9
- Meng, R., Wei, Y. J., Yi, Z., and Wang, E. N. (2021). Effects of Compound danshen dripping pills combined with sarkubatrovalsartan on elderly patients with myocardial infarction after PCI. *Prog. Mod. Biomed.* 11, 1673–6273. doi:10.13241/j.cnki.pmb.2021.11.035
- Murphy, S. P., Ibrahim, N. E., and Januzzi, J. L., Jr. (2020). Heart failure with reduced ejection fraction: A review. *JAMA* 324 (5), 488–504. doi:10.1001/jama.2020.10262
- Peng, S. L., He, X. P., and Zhang, W. Y. (2020). Effect and mechanism of jianxin pinglu pill on myocardial fibrosis in patients with diabetic cardiomyopathy. *Clin. J. Traditional Chin. Med.* 11, 1672–7134. doi:10.16448/j.cjctm.2020.1151
- Ren, R. M., Kou, M., and Lan, X. X. (2010). Efficacy and safety of tamsulosin for the treatment of benign prostatic hyperplasia: A meta analysis. *Chin. Med. J. (Engl.)* 123 (2), 234–238.
- Scott, G. I., Colligan, P. B., Ren, B. H., and Ren, J. (2001). Ginsenosides Rb1 and Re decrease cardiac contraction in adult rat ventricular myocytes: Role of nitric oxide. *Br. J. Pharmacol.* 134, 1159–1165. doi:10.1038/sj.bjp.0704377
- Shim, S., Yoon, B. H., Shin, I. S., and Bae, J. M. (2017). Network meta-analysis: Application and practice using Stata. *Epidemiol. Health* 39, e2017047. doi:10.4178/epih.e2017047
- Solomon, C., Meyer, N. R., and Sørensen, B. (2011). Fibrin formation is more impaired than thrombin generation and platelets immediately following cardiac surgery. *Thromb Res.* 128 (3), 277–282.
- Wang, J. N., Kan, C. D., Lee, L. T., Huang, L., Hsiao, Y. L., Chang, H., et al. (2021). Herbal extract from codonopsis pilosula (franch.) nannf. Enhances cardiogenic differentiation and improves the function of infarcted rat hearts. *Life* 11 (5), 422. doi:10.3390/life11050422
- Wang, Y. P., Zhang, L. X., Li, H. D., and Wang, G. Z. (2019). Clinical observation on integrated traditional Chinese and western medicine in the treatment of hypertrophic cardiomyopathy. *World Chin. Med.* doi:10.3969/j.issn.1673-7202.2019.06.026
- Wang, Y., Xiao, L., Mu, W., Yu, H., Zhang, S., Tian, G., et al. (2017). A summary and evaluation of current evidence for myocardial infarction with Chinese medicine. *Chin. J. Integr. Med.* 23 (12), 948–955. doi:10.1007/s11655-017-2824-y
- Watt, J., and Del Giovane, C. (2022). Network meta-analysis. *Methods Mol. Biol.* 2345, 187–201. doi:10.1007/978-1-0716-1566-9\_12
- Wu, D. X., Huo, M. Q., Chen, X., Zhang, Y. L., and Qiao, Y. J. (2020). Mechanism of tanshinones and phenolic acids from Danshen in the treatment of coronary heart disease based on co-expression network. *BMC Complement. Med. Ther.* 20 (1), 28. doi:10.1186/s12906-019-2712-4
- Wu, G., and Hu, L. Q. (2019). Effect of trimetazidine combined with Shexiang Tongxin dropping pill on neurohormones-cytokine and left ventricular remodeling in patients with ischemic heart failure. *Liaoning J. Traditional Chin. Med.* 2019, 1000–1719. doi:10.13192/j.issn.1000-1719.2019.04.002
- Wu, G., Yu, D. L., Li, L., and Hu, L. Q. (2021). Influence mechanism of myocardial fibrosis and vascular regeneration of Shexiang Tongxin pills to syndrome of qi deficiency and blood Stasis in ischemic heart failure. *Chin. J. Exp. Traditional Med. Formulae*, 1005–9903. doi:10.13422/j.cnki.syfx.20201034
- Xia, S. J., Gao, B. Z., Chen, S. J., Lin, X. J., Zhang, P., Chai, Y. J., et al. (2020). Verification of the efficacy and safety of qi-replenishing Chinese medicine in treating prediabetes: A meta-analysis and literature review. *Evid. Based Complement. Altern. Med.* 2020, 7676281. doi:10.1155/2020/7676281
- Xie, X. L., Xu, Z. J., Xiang, Y., and Ni, G. S. (2019). The influence of qishenyiqi pills on ventricular remodeling and cardiac function of patient undergoing coronary artery bypass surgery. *Chin. J. Integr. Med. Cardio/Cerebrovascular Dis.* doi:10.12102/j.issn.1672-1349.2019.08.005
- Xu, X. J., Zhang, Y. Y., Zhang, S. J., Gong, J. X., Lou, B., Gu, M. L., et al. (2019). Effect of Compound Danshen Dripping Pills combined with Rosuvastatin on left ventricular remodeling and myocardial fibrosis in patients with acute myocardial infarction after percutaneous coronary intervention. *CHINA Med. Her.* 12, 1673–7210.
- Xun, Y. L. (2016). To analyze the clinical value of Yixinshu capsule combined with bisoprolol fumarate in the treatment of hypertrophic cardiomyopathy. *Cardiovascular Disease. J. Integr. traditional Chin. West. Med.* ISSN.2095-6681.2016.32.039.01.
- Yang, Q., and Liu, J. C. (2020). Efficacy of Sanwei sandalwood capsule combined with ticagrelor tablets in the treatment of coronary heart disease and its effect on cardiac function and serum TIMP-1 level. *Lab. Med. Clin.* 2020, 1672–9455. doi:10.3969/j.issn.1672-9455.2020.16.029
- Yang, W., Xu, X. H., Wang, S., and Zhang, C. F. (2012). Effects of Tongxinluo capsule on serum procollagen III N-terminal peptide and left ventricular remodeling in patients with acute myocardial infarction and emergency PCI. *Chin. J. Difficult Complicat. Cases*, 452–453. doi:10.3969/j.issn.1671-6450.2012.06.021
- Yokota, F., Arima, H., Hirano, M., Uchikawa, T., Inden, Y., Nagatani, T., et al. (2010). Normalisation of plasma growth hormone levels improved cardiac dysfunction due to acromegalic cardiomyopathy with severe fibrosis. *BMJ Case Rep.*, bcr1220092559. doi:10.1136/bcr.12.2009.2559
- Yokota, T., Shiraishi, R., Aida, T., Iwai, K., Liu, N. M., Yokoyama, U., et al. (2014). hromboxane A(2) receptor stimulation promotes closure of the rat ductus arteriosus through enhancing neointima formation. *PLOS One* 9 (4), e94895.
- Zhang, D. C., Zhang, C. Y., and Lu, M. X. (2017). Effects of Qiliqiangxin capsule combined with conventional Western medicines on ventricular remodeling and related immune indexes of patients with chronic congestive heart failure. *Hebei Med. J.* 2017, 1002–7386. doi:10.3969/j.issn.1002-7386.2017.21.002
- Zhang, D., and Gou, W. H. (2021). Efficacy of qishen Yiqi dropping pill combined with bisoprolol in the treatment of left ventricular ejection fraction retained heart failure and its effect on oxidative stress and ventricular remodeling. *Chin. J. Integr. Med. Cardio/Cerebrovascular Dis.*, 1844–1847. doi:10.12102/j.issn.1672-1349.2021.11.013
- Zhang, J., Ji, Z. H., and Wen, X. H. (2016). Clinical study of Yiqi Huayu capsule combined with Western medicine in the treatment of early ventricular remodeling after acute myocardial infarction. *J. NEW Chin. Med.*, 0256–7415. doi:10.13457/j.cnki.jncm.2016.09.008
- Zhang, X. X., Liang, B., Chao, C. L., and Gu, N. (2021). Traditional Chinese medicine intervenes ventricular remodeling following acute myocardial infarction: Evidence from 40 random controlled trials with 3,659 subjects. *Front. Pharmacol.* 12, 707394. doi:10.3389/fphar.2021.707394
- Zhang, X., and Zhang, H. (2017). The clinical effect of trimetazidine combined with Qishenyiqi dropping pill in the treatment of chronic heart failure and its effect on the levels of BNP, ang II and ALD in plasma. *Chin. J. Evid. Based Cardiovasc. Med.* 9 (6), 705–708. doi:10.3969/j.issn.1674-4055
- Zheng, Y. L. (2013). *Clinical observation of fumai Granule on reversion of atrial remodeling in patients with atrial fibrillation*. Guangzhou: University of Chinese Medicine. [master's thesis].
- Zheng, Z. G., Yu, M., Tang, P., and Yu, X. H. (2019). Clinical effect of Shexiang Baoxin PiUs combined with Losartan in the treatment of hypertension complicated with left Ventricular hypertrophy. *China Mod. Med.* 6, 1674–4721. (a)-0028-03.
- Zhou, H. W., Li, X. J., Tian, L. T., and Jing, Z. Q. (2018). Effect of Yiqifumai for injection (lyophilized) combined with metoprolol sustained-release tablets in the treatment of hypertrophic obstructive cardiomyopathy and its influence on the expression of serum GGT, IGF-1 and VEGF. *Mod. J. Integr. Traditional Chin. West. Med.* 26, 1008–8849. doi:10.3969/j.issn.1008-8849.2018.26.012
- Zhou, Z. Y., Huan, L. Y., Zhao, W. R., Tang, N., Jin, Y., and Tang, J. Y. (2017). Spatholobi Caulis extracts promote angiogenesis in HUVECs in vitro and in zebrafish embryos in vivo via up-regulation of VEGFRs. *J. Ethnopharmacol.* 200, 74–83. doi:10.1016/j.jep.2016.10.075
- Zou, K. Y. (2019). To observe the effect of Shexiang Baoxin pill combined with metoprolol and trimetazidine in the treatment of coronary heart disease with heart failure and its effect on myocardial remodeling. *J. Med. Theor. & Prac.* 3256–3258. doi:10.19381/j.issn.1001-7585.2019.20.015

## Glossary

**BASR-CPM** blood-activating and stasis-removing Chinese patent medicine

**CBM** China Biology Medicine disc

**CNKI** China National Knowledge Infrastructure

**CPM** Chinese patent medicine

**CI** confidence interval

**CG** control group

**CRP** C-reactive protein

**HC-CPM** heat-clearing Chinese patent medicine

**VIP** Information Resource Integration Service Platform

**IG** intervention group

**KWYR-CPM** kidney-warming and *yang*-restoring Chinese patent medicine

**LVEF** left ventricular ejection fraction

**LVEDD** left ventricular end-diastolic dimension

**LVESD** left ventricular end-systolic dimension

**LVMI** left ventricular mass index

**NMA** network meta-analysis

**NA** not available

**non-RCTs** non-randomized controlled trials

**NT-proBNP** N-terminal proBNP

**OR** odds ratio

**QR-CPM** *Qi*-replenishing Chinese patent medicine

**QR&BASR-CPM** *Qi*-replenishing, blood-activating, and stasis-removing Chinese patent medicine

**RCT** randomized controlled trial

**PRISMA** Preferred Reporting Items for Systematic Reviews and Meta-Analyses

**SD** standard deviation

**SMD** standardized mean deviation

**SUCRA** surface-under-the-cumulative-ranking curves

**THSWT** Taohong Siwu decoction

**TCM** traditional Chinese medicine

**Wanfang Data** Wanfang Data Knowledge Service Platform

**WM** Western medicine

**6-MWT** Six-minute walk test



## OPEN ACCESS

## EDITED BY

Ren-You Gan,  
Singapore Institute of Food and  
Biotechnology Innovation, Singapore

## REVIEWED BY

Ji Wei Tan,  
Monash University Malaysia, Malaysia  
Min Jiang,  
Nankai University, China  
Yaozu Xiang,  
Tongji University, China

## \*CORRESPONDENCE

Lin Li,  
✉ 13516122373@126.com  
Han Zhang,  
✉ zhanghan0023@126.com

## SPECIALTY SECTION

This article was submitted to  
Ethnopharmacology,  
a section of the journal  
Frontiers in Pharmacology

RECEIVED 07 September 2022

ACCEPTED 14 February 2023

PUBLISHED 27 February 2023

## CITATION

Han R, Han G, Yan Y, Han L, Li L and  
Zhang H (2023), Protective effects and  
mechanisms of the Erzhi formula on  
glucocorticoid induced primary cortical  
neuron injury.  
*Front. Pharmacol.* 14:1038492.  
doi: 10.3389/fphar.2023.1038492

## COPYRIGHT

© 2023 Han, Han, Yan, Han, Li and Zhang.  
This is an open-access article distributed  
under the terms of the [Creative  
Commons Attribution License \(CC BY\)](#).  
The use, distribution or reproduction in  
other forums is permitted, provided the  
original author(s) and the copyright  
owner(s) are credited and that the original  
publication in this journal is cited, in  
accordance with accepted academic  
practice. No use, distribution or  
reproduction is permitted which does not  
comply with these terms.

# Protective effects and mechanisms of the Erzhi formula on glucocorticoid induced primary cortical neuron injury

Rui Han<sup>1,2,3</sup>, Guoying Han<sup>1,2,3</sup>, Yiqi Yan<sup>1,2,3</sup>, Lifeng Han<sup>1,3</sup>, Lin Li<sup>1,2,3\*</sup> and Han Zhang<sup>1,2,3\*</sup>

<sup>1</sup>Institute of Traditional Chinese Medicine, Tianjin University of Traditional Chinese Medicine, Tianjin, China, <sup>2</sup>Key Laboratory of Pharmacology of Traditional Chinese Medical Formulae, Tianjin University of Traditional Chinese Medicine, Ministry of Education, Tianjin, China, <sup>3</sup>State Key Laboratory of Component-Based Chinese Medicine, Tianjin University of Traditional Chinese Medicine, Tianjin, China

High concentrations of glucocorticoids (GC) can cross the blood-brain barrier into the brain parenchyma, triggering a stress state that can lead to a range of physiological changes. This study investigated whether Erzhi formula has neuroprotective effects against glucocorticoid damage by establishing a dexamethasone-induced primary cortical neuron injury model *in vitro*. The results showed that Erzhi formula could reduce dexamethasone-induced apoptosis in primary cultured cortical neurons and improve synaptic damage. Further, network pharmacological analysis revealed that Erzhi formula may exert antidepressant effects by multi-component, multi-target, and multi-pathway characteristics, in which Salidroside, Biochanin-A and other ingredients are key components, HSD11B1, NR3C1, and other proteins are key targets, and steroid metabolism may be a key process in its action. Moreover, our study found that the neuroprotective effect of Erzhi formula might be related to the 11 $\beta$ -HSD1-GC/glucocorticoid receptor (GR) signaling pathway. The Erzhi formula could significantly inhibit the activity of 11 $\beta$ -hydroxysteroid dehydrogenase 1 (11 $\beta$ -HSD1) *in vitro* using homogeneous time-resolved fluorescence. In addition to providing evidence for the pharmacological effects of the Erzhi formula, the present study lays down the foundation for subsequent experiments.

## KEYWORDS

the erzhi formula, primary cortical neuron, stress, depression, glucocorticoids, apoptosis, synaptic plasticity, network analysis

## 1 Introduction

Depression is a major emerging mental mood disorder worldwide, with excessive stress being one of its primary causes. Prolonged stimulation can cause dysfunction of the sympathetic-adrenomedullary system and the hypothalamic-pituitary-adrenal (HPA AXIS), leading to neural network remodeling and neuronal damage, or even psychiatric disorders such as depression or cognitive impairment (Zhang et al., 2020). HPA AXIS dysfunction can lead to abnormal corticosterone regulation, impaired neurogenesis, synaptic dysfunction, and other problems that can further lead to depressive-like behavior.

The glucocorticoid (GC) system plays an important role in the regulation of the HPA AXIS, and endogenous cortisol is an important stress hormone. Studies have shown that elevated cortisol is beneficial to the body's response to external stimuli and stress; however,



the high concentrations of cortisol produced under prolonged uninterrupted stress not only jeopardize cardiovascular system function, but also cause dendritic atrophy of neurons, synaptic structure change, and neuronal apoptosis, which ultimately induces cognitive dysfunction (Ajala, 2017). In addition, exogenous GC may increase the risk of neurodegenerative diseases by promoting lactate dehydrogenase (LDH) release from hippocampal neurons and altering neuronal synaptic structure and function (Macpherson et al., 2005; Finsterwald et al., 2015). Sustained stress causes hyperactivity of the HPA AXIS, resulting in excessive GC secretion. After crossing the blood-brain barrier to enter the hippocampus or cortical tissues, GC levels in local tissues are regulated by the negative feedback effect of the glucocorticoid receptor (GR) (Terunuma et al., 2003). In contrast, mifepristone (RU486), a GR blocker, may improve cognitive impairment by blocking synaptic damage to hippocampal neurons induced by stressful doses of GC (Block et al., 2017). 11 $\beta$ -hydroxysteroid dehydrogenase 1 (11 $\beta$ -HSD1) is a key enzyme in the intracellular production of cortisol, is widely distributed in the liver, brain, and adipose tissues, and plays a dual role in redox and dehydrogenation, regulating the conversion between non-biologically active cortisol (human)/11-dehydrocorticosterone (mouse) and active cortisol (human)/corticosterone (CORT) (mouse) (White, 2018). Studies have shown that RU486 completely inhibits the upregulation of 11 $\beta$ -HSD1 mRNA expression induced by the stress hormone cortisol (Wyrwoll et al., 2011) and inhibition of 11 $\beta$ -HSD1-induced reduction in GC is strongly associated with improved cognitive performance (Puigoriol-Illamola et al., 2020a; Puigoriol-Illamola et al., 2020b). Currently, stress-related diseases are attracting increasing attention. Stress may trigger damage to the body, and in turn, the imbalance or dysfunction caused by the damage may further amplify stress, causing the body to enter a negative cyclic chain.

The Erzhi formula, consisting of *Ligustri lucidi fructus* and *Ecliptae herba*, is a classical traditional Chinese medicine (TCM) prescription for nourishing the liver and kidney. It is mostly used clinically for the treatment of liver and kidney yin deficiency, such as dizziness, insomnia and dreaminess, soreness and weakness of the waist and knees, spermatorrhea, and premature gray hair (Lim et al., 2018). Meanwhile, Yin deficiency of liver and kidney is one of the most common syndromes of depression, suggesting that attention should be paid to liver and kidney tonifying in the clinical treatment of depression. Pharmacological studies have shown that Erzhi Pill can improve the learning and memory ability of aging rats, scavenge free radicals, protect neural function and show anti-aging effects (Wang et al., 2017). A previous study found that the Erzhi formula significantly reduced CORT levels and downregulated CRH mRNA, adrenal CORT synthase 21 $\alpha$ -hydroxylase (CYP21A1), and steroid acute regulatory protein (STAR) mRNA in the cortex and hypothalamus of mice under a chronic mild unpredictable stimulus model. These results suggested that the Erzhi formula can inhibit restraint stress-induced hyperactivation of the HPA AXIS from both central and peripheral sources.

In our study, we established a model of dexamethasone-induced injury in primary cultured cortical neurons at stress doses and investigated the function and mechanism of the Erzhi formula in ameliorating neuronal injury using various methods and network pharmacological analysis.

## 2 Materials and methods

### 2.1 Drug and chemicals

Dexamethasone (DEX), mifepristone (RU486), and carbenoxolone disodium salt (CBX) were purchased from Sigma, United States. The Erzhi formula was provided by the Department of Pharmacy, Institute of Traditional Chinese Medicine, Tianjin University of Traditional Chinese Medicine. The Erzhi formula was prepared by mixing the alcoholic extract of *Ligustrum lucidum* Ait (Oleaceae Hoffmanns; *Ligustri lucidi fructus*) and *Eclipta prostrata* L (Asteraceae Bercht; *Ecliptae herba*) in a 1:1 ratio with raw herbs. *Ligustri lucidi fructus* and *Ecliptae herba* were purchased from the Beijing Tongrentang Group Tianjin Ping Shan Dao Pharmacy Co. Both *Ligustri lucidi fructus* and *Ecliptae herba* were extracted by heating and refluxing with 70% ethanol; the procedure was performed three times, each time for 1 h, and the amount of 70% ethanol was increased by 10 times of raw herbs for each cycle. Then the extracts were combined and concentrated in an electric heating set (98-1-C, Tianjin Taisite Instrument Co., China) at 55°C to form a concentrated solution, and the concentrated solution were lyophilized with an electric vacuum drying oven (DZG-6050, Shanghai Pein Experimental Instruments Co., China) at 45°C. Finally, 24.29 g powder was obtained from 100.00 g of *Ligustri lucidi fructus* and 20.80 g powder was obtained from 100.00 g of *Ecliptae herba*.

### 2.2 Primary cortical neuronal cultures

Cortical neurons were obtained from an embryonic 16-day Wistar rat (Beijing Weitong Lihua Laboratory Animal Technology Co., Ltd.). The cortex was separated, clipped, and digested by trypsin (Gibco, United States). Cells were plated in a 55 mm dish at a density of  $1 \times 10^6$  cells/mL or in 96-well or 24-well plates at a density of  $5 \times 10^5$  cells/mL coated with poly-d-lysine after resuspension in DMEM/F12 basal medium (Gibco, United States) containing 10% FBS (Gibco, United States) and 1% penicillin and streptomycin (Gibco, United States). The cells were maintained in DMEM/F12 basal medium supplemented with 2% B27 (Gibco, United States), 1% penicillin and streptomycin, and 0.5% glutamine (Gibco) after 4 h. In all experiments, the cells were cultured in a cell culture incubator (Thermo Fisher, United States) at 37°C and 5% CO<sub>2</sub>. After 5 days of culture, DEX, Erzhi formula, or other drugs were administered and then cultured for 72 h for subsequent experiments.

### 2.3 MTT

0.5 mg/mL solution of methyl thiazolyl tetrazolium (MTT) (Sigma, United States) was added to the cells cultured in 96-well plates and incubated for 4 h at 37°C in a 5% CO<sub>2</sub> cell incubator (protected from light). The original culture solution was replaced with dimethyl sulfoxide (DMSO) (Sigma, United States), and the crystals were dissolved by shaking for 10 min on a microtiter (Tianjin Hua Bei Experimental Instruments Co., Ltd.). The

optical density (OD) value was measured at 570 nm using an enzyme marker (Tecan, Switzerland).

## 2.4 LDH

The treated cell supernatants harvested from 96-well plates were mixed with lactate dehydrogenase (LDH) working solution (Dojindo, Japan) at a ratio of 1:1 for 30 s on a microplate shaker. After 30 min of incubation at room temperature in a light-protected environment, the stopping solution was added to the plate. The optical density (OD) value was measured at 490 nm using an enzyme marker to evaluate cell viability.

## 2.5 TUNEL

Apoptosis was detected using a TUNEL staining kit (Merck Sharp and Dohme, MSD) according to the manufacturer's instructions and a previously reported method, and then photographed with an inverted fluorescent microscope.

## 2.6 Western blot

Protein samples were harvested from cortical neurons cultured in a 55 mm dish after treatment. Total proteins were lysed using RIPA protein extraction buffer (Solarbio, Beijing, China) according to the manufacturer's instructions, and protein concentrations were determined using a BCA Kit (ThermoFisher, United States). Equal amounts of protein aliquots were used to check the expression levels of target proteins using anti-Caspase-3, anti-Cleaved Caspase-3, anti-Bcl-2, anti-Bax, anti-PSD95, anti-SYN, and anti- $\beta$ -tubulin (CST, United States) (1:1,000) through 10% SDS-PAGE gel electrophoresis. After incubation with the appropriate HRP-conjugated antibody (1:10,000) (Beijing Zhongshanjinjiao Biotechnology Co, Ltd), the proteins were visualized using the ChemiDoc™ MP Imaging System (Bio-Rad, United States).

## 2.7 Immunostaining

Cells cultured in 24-well plates were fixed in ice-cold 4% paraformaldehyde (Solarbio, China) for 5 min, washed in PBS (Solarbio, China), incubated in preblock buffer (0.3% Triton X-100 (Solarbio, China) and 5% goat serum (Solarbio, China) in PBS) for 60 min, and then incubated overnight (4°C) with primary antibodies microtubule-associated protein 2 (MAP-2) diluted (1:200) in preblock buffer. After washing with PBS, cells were incubated with secondary antibody Alexa Fluor 488-Goat anti-Rabbit IgG (ThermoFisher, United States) (1:1,000) in preblock buffer at room temperature for 2 h. Next, DAPI (4',6-diamidino-2-phenylindole) nuclear staining solution (Solarbio, China) was added and incubated for 10 min at room temperature. After washing with PBS, an anti-fluorescence quenching agent was added (Beyotime Biotechnology, China), and the views were photographed under an inverted fluorescent microscope.

## 2.8 Network analysis

### 2.8.1 Screening for active ingredients of the Erzhi formula and potential targets prediction

The components of the Erzhi formula that are absorbed into the blood were downloaded from the PubChem database (<https://pubchem.ncbi.nlm.nih.gov>) and then screened using the “Iter by Lipinski and Veber Rules” algorithm of Discovery Studio™ software (i.e., setting the selection criteria to <500 molecular weight, <5 hydrogen bond donors, <10 hydrogen bond acceptors, <5 lipid-water partition coefficients, and  $\leq 10$  rotatable bonds) to obtain the active components of the Erzhi formula. The CTD database (<https://ctdbase.com>), HERB database (<http://herb.ac.cn>), Swisstarget prediction database (<http://swisstargetprediction.ch>), and Perl software were used to identify and predict relevant targets of the active ingredients. The information obtained on the active ingredients and the related targets was then collated and the Cytoscape 3.7.1 software was used to create an “active ingredients-target” network diagram.

### 2.8.2 Target acquisition of the Erzhi formula for depression treatment

The GENECARDS database (<https://www.genecards.org>) was used to obtain targets of depression. Using R language operations, the overlapping core targets mapped from the active ingredient targets to the depression targets were identified as the potential targets of the Erzhi formula for treating depression.

### 2.8.3 PPI interaction network construction and analysis

Overlapping core targets were imported into the STRING data analysis platform (<https://cn.string-db.org/>) for protein-protein interaction (PPI) network analysis. PPIs were constructed based on the strength of the relationships between the targets using Cytoscape 3.7.1 software, and clustering analysis was performed.

### 2.8.4 GO (gene ontology) enrichment and analysis

The overlapping target names were converted into ENTREZ Gene IDs using the R language and analyzed using the DAVID database (<https://david.ncifcrf.gov>) to obtain information about GO gene function analysis. *p*-value was used as a reference value for screening, and R language and Bioinformatics (<https://www.bioinformatics.com.cn>) were used to analyze the related content of gene function enrichment analysis.

## 2.9 Homogenous time-resolved fluorescence

Glycyrrhetic acid (GA) (10  $\mu$ L) at 1  $\mu$ M and 0.1–100  $\mu$ g/mL of the Erzhi formula were placed in a 96-well transparent plate, and 10  $\mu$ L of liver microsomes at a concentration of 2 g/L were added to each well, centrifuged at 1,000 rpm for 1 min, and shaken on a microplate shaker for 5 min. Next, 30  $\mu$ L of CORT and nicotinamide adenine dinucleotide phosphate (NADPH) were added to each well, centrifuged at 1,000 rpm for 1 min, and incubated for 2 h at 37°C in an air bath shaker. Prepared cortisol standard (10  $\mu$ L) was then added to each well. After incubation, 10  $\mu$ L from the first transparent plate was pipetted into the corresponding wells of a 96-well white

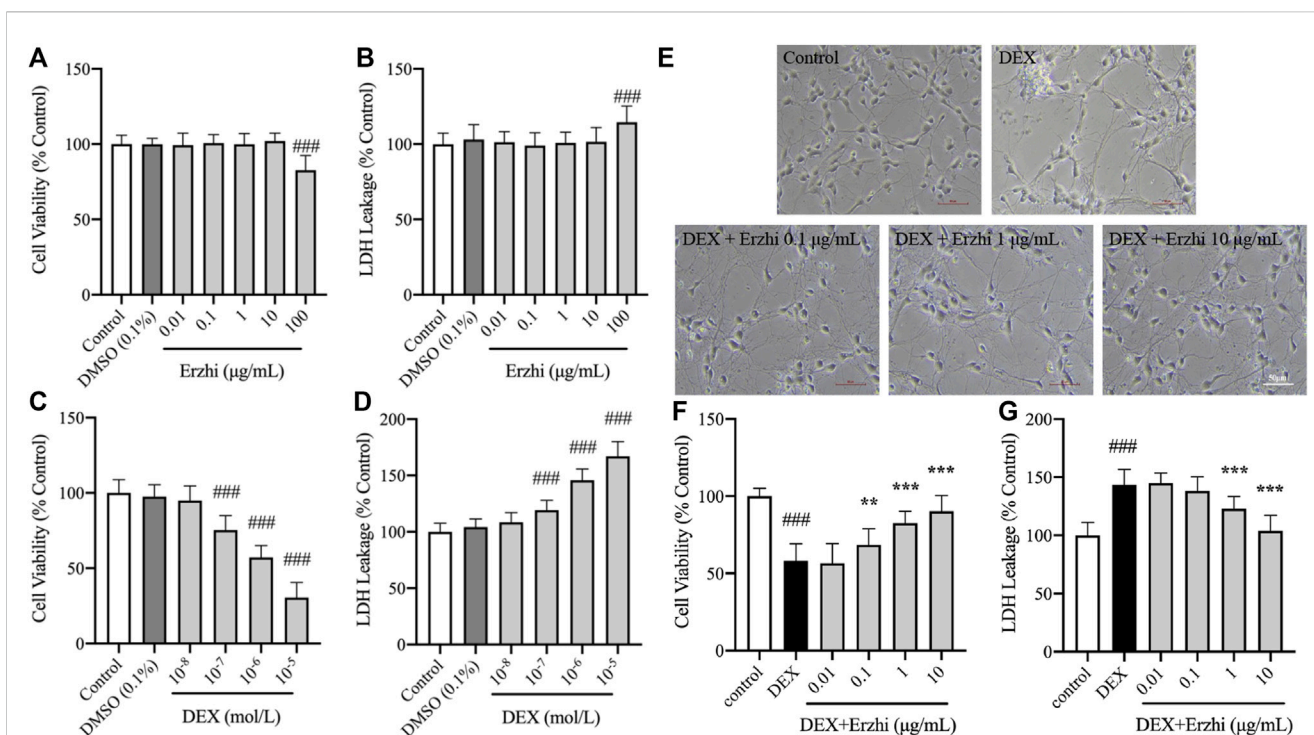


FIGURE 1

Neuroprotective effects of the Erzhi formula on primary cultured cortical neurons. (A, B) Safe dosage selection of Erzhi formula ( $n = 18$  per group). 100  $\mu\text{g/mL}$  Erzhi formula showed significant cell toxicity ( $p < 0.001$ ); (C, D) damage concentration selection of DEX ( $n = 18$  per group).  $10^{-7}$  to  $10^{-5}$  mol/L DEX showed cell toxicity; (E) growth status of primary cortical neurons with Erzhi formula treatment (bar = 50  $\mu\text{m}$ ). 0.1–10  $\mu\text{g/mL}$  Erzhi formula can reverse cell damage; (F, G) effective dosage selection of the Erzhi formula ( $n = 18$  per group). The results are expressed as mean  $\pm$  SD. ### $p < 0.001$  vs. control; \*\* $p < 0.01$ , \*\*\* $p < 0.001$  vs. DEX. DEX, dexamethasone; SD, standard deviation.

plate. Cortisol acceptor (5  $\mu\text{L}$ ) and cortisol donor (5  $\mu\text{L}$ ) were added to the wells in a white plate and incubated at room temperature for 2 h. Finally, the fluorescence signal at 665 and 620 nm was detected using an enzyme standard meter, and the fluorescence signal was calculated according to the cortisol standard curve. Cortisol concentration in each group was calculated using the standard curve.

## 2.10 Calcium phosphate-DNA coprecipitation

An appropriate amount of green fluorescent protein (GFP) plasmid was mixed with 75  $\mu\text{L}$  of autoclaved ultrapure water. Next, 87.5  $\mu\text{L}$  of HEPES buffer (280 mM NaCl, 10 mM KCl, 1.5 mM  $\text{Na}_2\text{HPO}_4$ , 12 mM D-Glucose, and 50 mM HEPES, pH 7.05) was added and mixed, and finally 10.5  $\mu\text{L}$  of  $\text{CaCl}_2$  was added and incubated for 5 min to form a calcium phosphate-DNA precipitate. After 4 days of culture, the calcium phosphate-DNA precipitate was added dropwise uniformly to the cell culture medium, and additional treatments were carried out after 48 h.

## 2.11 Statistical analyses

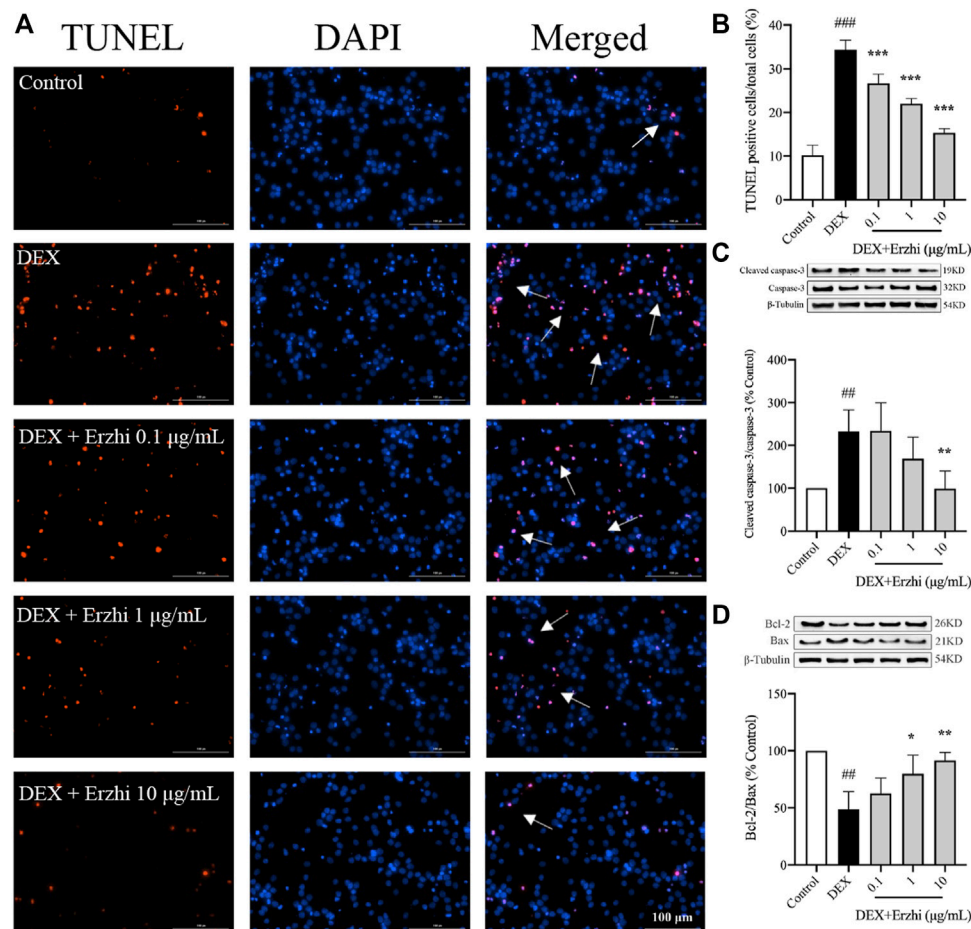
All statistical analyses were performed using the GraphPad Prism version 8. One-way ANOVA was used to test whether the

means of each experimental group were significantly different, and if the overall  $p$ -value was  $< 0.05$ , then multiple comparisons between the experimental groups were tested using Tukey's *post hoc* analysis.

## 3 Results

### 3.1 The Erzhi formula ameliorates DEX-induced primary cortical neuronal damage

Compared with the control group, 0.01–10  $\mu\text{g/mL}$  Erzhi formula had no significant toxic effect on primary cultured cortical neurons (Figures 1A, B). However, 100  $\mu\text{g/mL}$  Erzhi formula showed significant cell toxicity (Figures 1A, B), in which cell viability was reduced by approximately 17% and LDH leakage was increased by approximately 14%. Compared with the control group, there was no significant change in cell viability and LDH release in the  $10^{-8}$  mol/L DEX group ( $p > 0.05$ ). Cell viability decreased from 25% to 70% ( $p < 0.001$ ) and LDH release increased from 19% to 67% ( $p < 0.001$ ) in the  $10^{-7}$  to  $10^{-5}$  mol/L DEX groups, respectively (Figures 1C, D). The primary cortical neurons in the  $10^{-6}$  mol/L DEX group showed a decrease in cell viability of approximately 43% and an increase in LDH release of approximately 46%. The  $10^{-6}$  mol/L DEX group was selected for subsequent experiments. Primary cortical neurons cultured for 5 days were more refractive, with round,

**FIGURE 2**

Effect of the Erzhi Formula on apoptosis of primary cortical neurons. (A, B) TUNEL fluorescence staining (bar = 100  $\mu$ m) and quantitative analysis ( $n = 3$  per group). The number of apoptotic cells in the Erzhi formula group was significantly decreased compared with the DEX group ( $p < 0.001$ ); (C, D) protein expression of Cleaved caspase-3, Caspase-3, Bcl-2, and Bax ( $n = 3$  per group). The application of the Erzhi formula reversed the dexamethasone-induced increase in Cleaved caspase-3/Caspase-3 expression ( $p < 0.01$ ) and reversed the decrease in Bcl-2/Bax expression ( $p < 0.05$ ). The results are expressed as mean  $\pm$  SD. <sup>##</sup> $p < 0.01$ , <sup>###</sup> $p < 0.001$  vs. control; <sup>\*</sup> $p < 0.05$ , <sup>\*\*</sup> $p < 0.01$ , <sup>\*\*\*</sup> $p < 0.001$  vs. DEX.

oval, or irregularly shaped cytosol and two or more protrusions, which were connected to form a net-like structure. However, cells in the DEX group showed wrinkling, broken protrusions, and cell clustering, and some cells showed vacuolation. Further, protrusion breakage and vacuolation of neurons were significantly reduced in the 0.1–10  $\mu$ g/mL Erzhi formula group (Figure 1E). Compared to the control group, the cell viability of neurons significantly reduced to 55% ( $p < 0.001$ ) and LDH release significantly increased to 145% ( $p < 0.001$ ) after stimulation with  $10^{-6}$  mol/L DEX. There was a significant increase in cell viability ( $p < 0.001$ ) and decrease in LDH release ( $p < 0.001$ ) in the 1–10  $\mu$ g/mL Erzhi formula group; there was a significant increase in cell viability ( $p < 0.01$ ) and no significant change in LDH release ( $p > 0.05$ ) in the 0.1  $\mu$ g/mL Erzhi formula group; and finally, there was no significant change in cell viability and LDH release in the 0.01  $\mu$ g/mL group ( $p > 0.05$ ) (Figures 1F, G). The 10  $\mu$ g/mL Erzhi formula showed the best protective effect in this group, with cell viability of approximately 90% and LDH leakage of approximately 103%, compared with the control group.

### 3.2 The Erzhi formula ameliorates DEX-induced primary cortical neuronal apoptosis

The results of TUNEL nuclear staining showed that the number of apoptotic cells in primary cortical neurons was significantly increased in the DEX group compared with the control group ( $p < 0.001$ ), and the number of apoptotic cells in the Erzhi formula group was significantly lower than that in the DEX group ( $p < 0.001$ ), with the most significant decrease observed in the 10  $\mu$ g/mL Erzhi formula group (Figures 2A, B). Compared to the control group, the number of apoptotic cells was approximately 3.4 times higher after stimulating with  $10^{-6}$  mol/L DEX; however, after the application of the Erzhi formula, the number of apoptotic cells reduced by a factor of 1.5 times. Compared with the control group, the expression of Cleaved caspase-3/Caspase-3 was upregulated 2-fold ( $p < 0.01$ ) (Figure 2C) and the expression of Bcl-2/Bax was downregulated to half of the original in the DEX group ( $p < 0.001$ ) (Figure 2D). The expression of Cleaved caspase-3/Caspase-3 was significantly downregulated ( $p < 0.01$ ) and the



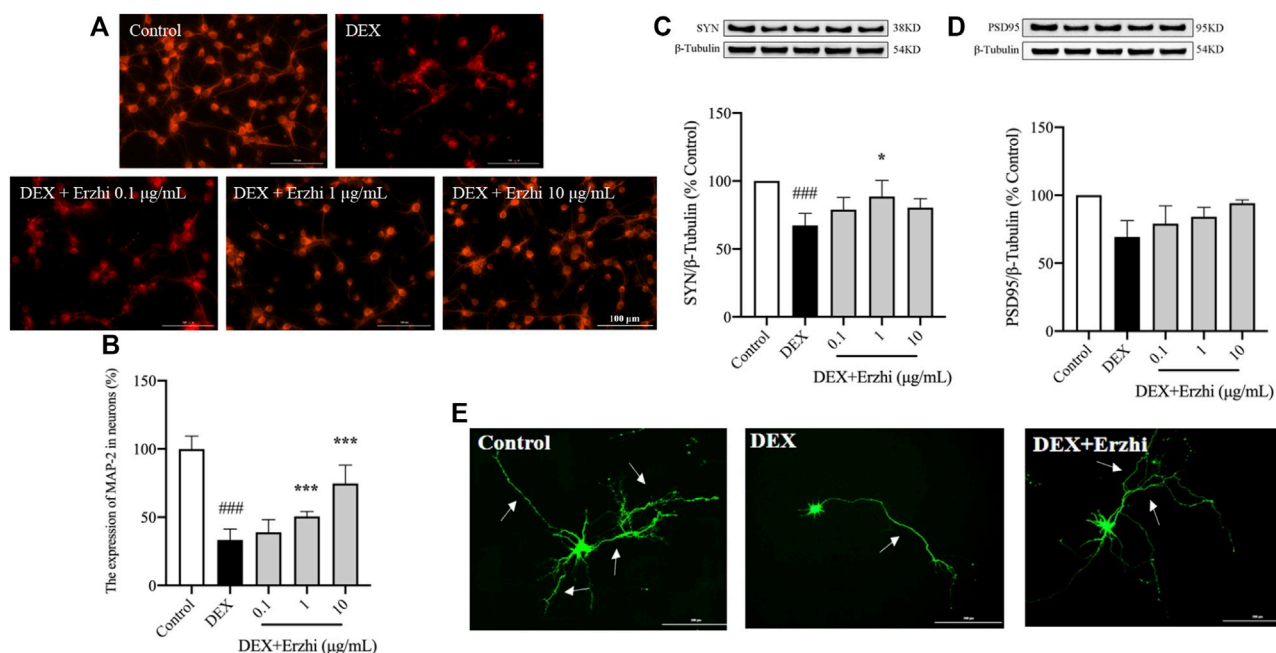


FIGURE 3

Effects of the Erzhi Formula on synapses in primary cortical neurons. (A, B) Fluorescent staining (bar = 100  $\mu$ m) and quantitative analysis of MAP-2 ( $n = 3$  per group). The application of the Erzhi formula could reverse the dexamethasone-induced attenuation of the MAP-2 red fluorescent signal ( $p < 0.001$ ); (C, D) protein expression of SYN and PSD95 ( $n = 3$  per group). The application of the Erzhi formula reversed the dexamethasone-induced decrease in SYN and PSD95 expression ( $p > 0.05$ ); (E) synaptic morphology of primary cortical neurons (bar = 200  $\mu$ m). The Erzhi formula could improve DEX-induced dendritic damage in neurons. The results are expressed as mean  $\pm$  SD. ### $p < 0.001$  vs. control; \* $p < 0.05$ , \*\*\* $p < 0.001$  vs. DEX. MAP, microtubule associated protein.

expression of Bcl-2/Bax was significantly upregulated ( $p < 0.05$ ) in the 1–10  $\mu$ g/mL Erzhi formula group compared with that in the DEX group (Figures 2C, D). In addition, the expression of Cleaved caspase-3/Caspase-3 and Bcl-2/Bax in the 10  $\mu$ g/mL Erzhi formula group was similar to that of the control group.

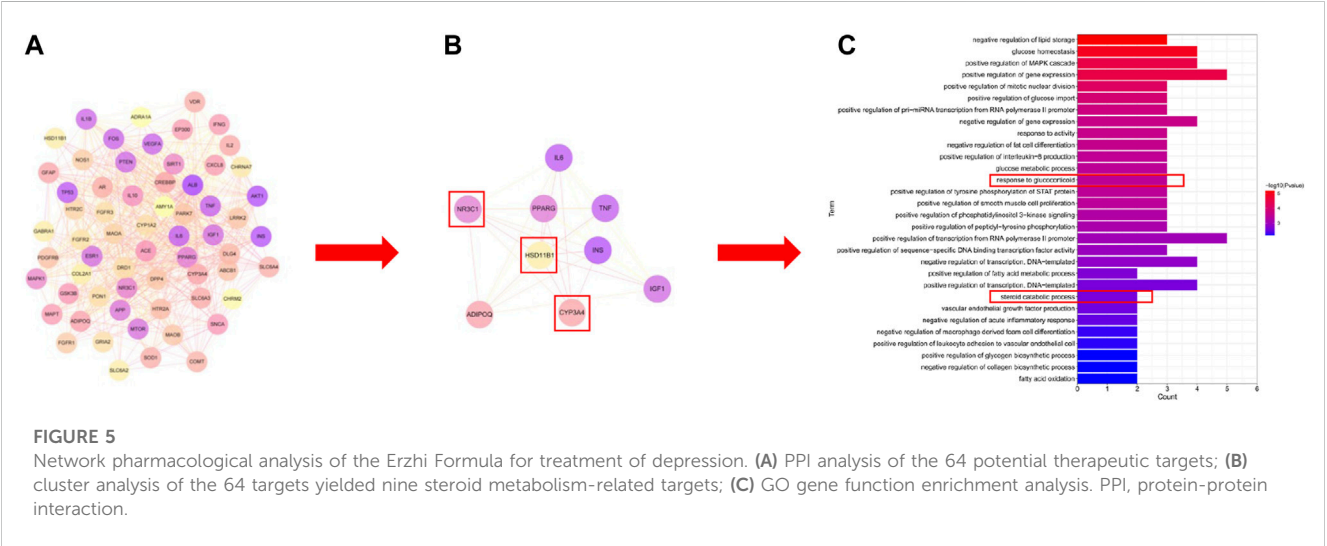
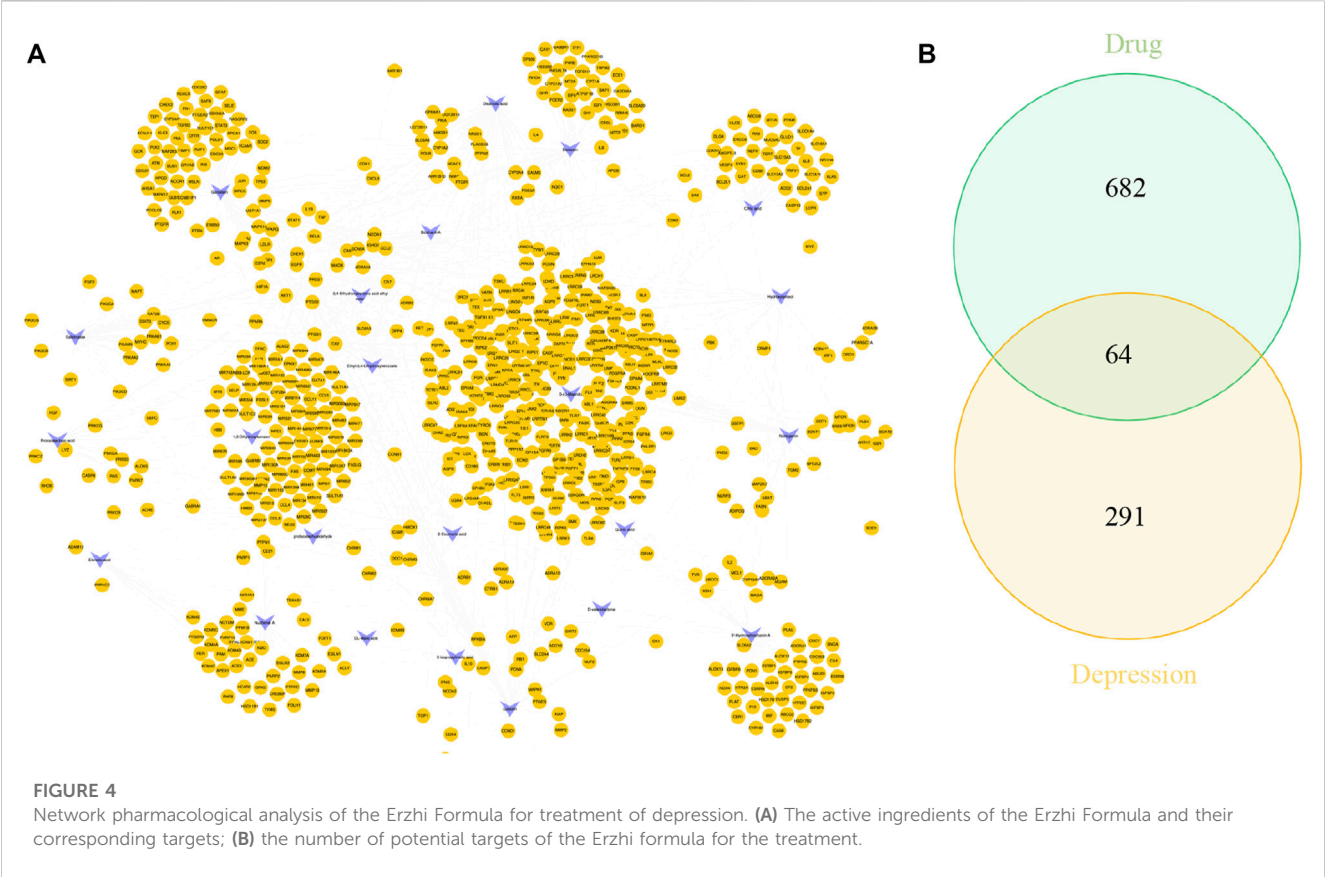
### 3.3 The Erzhi formula improves DEX-induced primary cortical neuronal synaptic damage

MAP-2 staining showed that the synapses of primary cortical neurons in the control group were interconnected into a network, with a strong red fluorescence signal in the cytoplasm and synapses (Figure 3A). Compared with the control group, the distribution of neurons in the DEX group was sparser, synaptic damage was severe and the red fluorescence signal was significantly weaker ( $p < 0.001$ ); compared with the DEX group, the red fluorescence signal in the 1–10  $\mu$ g/mL Erzhi formula group was significantly enhanced ( $p < 0.001$ ) (Figure 3B). In the statistical analysis of fluorescence intensity, the reduction of MAP-2 expression in neuronal cells induced by  $10^{-6}$  mol/L DEX was 33% compared to the control group, while the reduction of MAP-2 fluorescence intensity in neurons was reversed after the administration of the Erzhi formula, and the expression of MAP-2 was recovered to approximately 75% in the 10  $\mu$ g/mL Erzhi formula group. Compared with the control group, expression of SYN and

PSD95 was significantly downregulated in the DEX group ( $p < 0.001$ ); compared with the DEX group, 1  $\mu$ g/mL Erzhi formula significantly upregulated SYN expression ( $p < 0.01$ ), and 0.1–10  $\mu$ g/mL Erzhi formula had the potential to upregulate PSD95 expression ( $p > 0.05$ ) (Figures 3C, D). Calcium phosphate transfection revealed that the control group had a complete cellular structure and abundant protrusions. Compared with the control group, the DEX group had shriveled cellular structures and significantly reduced dendrites; the Erzhi formula could improve DEX-induced dendritic damage in neurons (Figure 3E).

### 3.4 Network analysis of the Erzhi formula

UHPLC/Q-Orbitrap MS analysis was used to analyze rat plasma samples after oral administration of the Erzhi formula extract, and a total of 64 chemical components were identified (unpublished data from the research group). The 64 chemical components in the Erzhi formula that are absorbed into blood were analyzed using the Discovery Studio™ software with the “Iter by Lipinski and Veber Rules” and 23 active ingredients were obtained (Supplementary Table S1), including 3'-Hydroxybiochanin A, Biochanin-A, and Salidroside. The CTD, HERB, and SwisstargetPrediction databases were used to search and predict the 23 active ingredients corresponding to 746 potential targets. The targets of active ingredients and potential targets were imported into Cytoscape 3.7.1 software to obtain the “active ingredient-target”



network diagram (Figure 4A). In the diagram, the light purple irregular shapes represent the 23 active ingredients, the yellow circles in the middle represent the 746 potential targets, and the lines in the middle represent the interrelationship between the active ingredients and the targets. For example, target Bcl-2 could be regulated by citric acid, genistein, naringenin, protocatechuic acid, and salidroside, target SYN1 could be regulated by citric

acid, target HSD11B1 (11 $\beta$ -HSD1) could be regulated by nuzhenal A, and NR3C1 could be regulated by oleanolic acid. By searching the GENECARDS database for depression, 3,170 depression disease targets were obtained, and 355 targets were obtained with a “relevance score >5” as the reference value. The PPI of depression was obtained (Supplementary Figure S1A) by analyzing the STRING database and Cytoscape 3.7.1 software. The

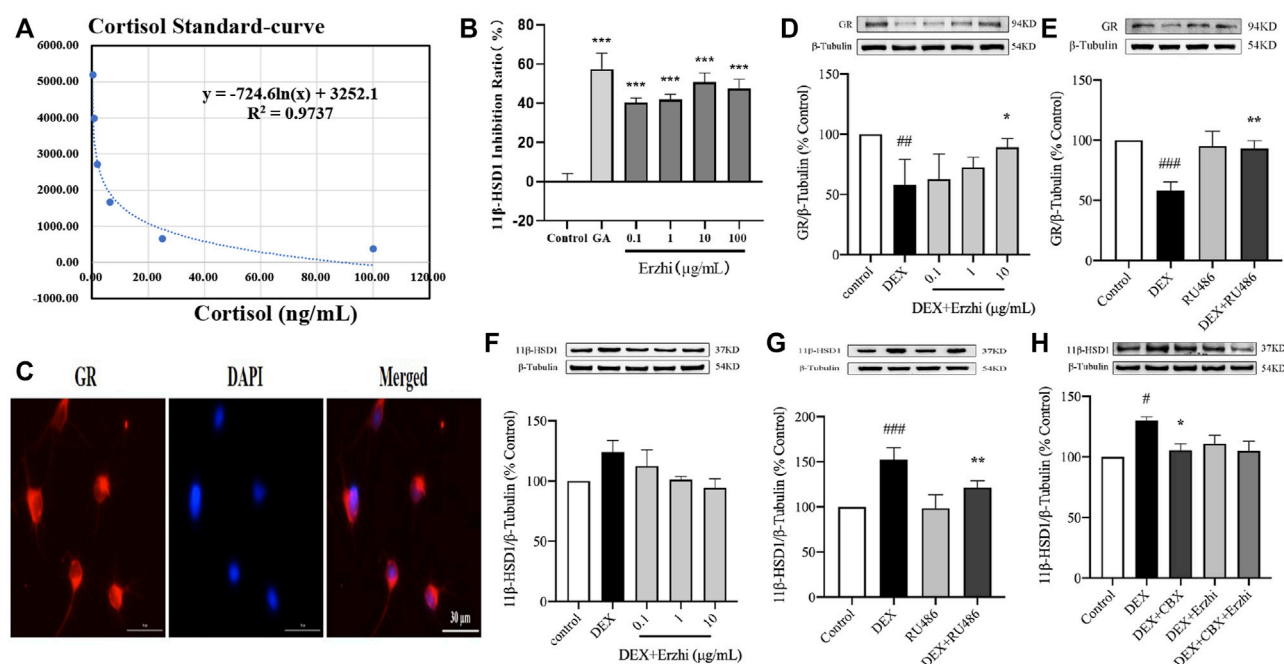


FIGURE 6

Effect of the Erzhi formula on 11β-HSD1. (A, B) Effect of the Erzhi formula on 11β-HSD1 activity by the HTRF method *in vitro* ( $n = 3$  per group). 0.1–100 μg/mL Erzhi formula could significantly inhibit hepatic microsomal 11β-HSD1 activity ( $p < 0.001$ ); (C) identification of GR in primary cortical neurons (bar = 30 μm); (D–H) protein expression of GR and 11β-HSD1 ( $n = 3$  per group). RU486, CBX, and the Erzhi formula could affect the expression of GR and 11β-HSD1. The results are expressed as mean  $\pm$  SD. ### $p < 0.001$  vs. control; \* $p < 0.05$ , \*\*\* $p < 0.001$  vs. DEX. ## $p < 0.01$ , ### $p < 0.001$  vs. control; \* $p < 0.05$ , \*\* $p < 0.01$ , \*\*\* $p < 0.001$  vs. DEX.

enrichment analysis of gene function types (Supplementary Figure S1B) revealed that the 5-Hydroxytryptamine receptor family, steroid hormone receptor, and dopamine receptor family were regulated. The 746 active ingredient potential targets were intersected with 355 depression disease targets after screening using R language software, and 64 core targets for the Erzhi formula to treat depression were obtained (Figure 4B). The 64 core targets were analyzed in the STRING database, and the PPI network was visualized using Cytoscape 3.7.1 software (Figure 5A), with the target color changes representing the relative magnitude of the degree values. Subsequent clustering analysis allowed for the extraction of nine targets related to steroid metabolism (Figure 5B). The nine core targets obtained from the clustering analysis were analyzed for GO functions, and a total of 38 functions with  $p$ -value  $< 0.01$  was obtained. The top 30 functions were selected in descending order of  $p$ -value for display (Figure 5C), where the vertical coordinates represent the function names, and the horizontal coordinates indicate the number of targets involved. The functions closely related to our study were steroid catabolic processes ( $p$ -value =  $2.49E-03$ ) and response to glucocorticoids ( $p$ -value =  $3.39E-04$ ), and the targets included HSD11B1, CYP3A4, and NR3C1, amongst others.

The Erzhi formula influences 11β-HSD1 activity *in vitro* and affects the 11β-HSD1-GC/glucocorticoid receptor (GR) signaling pathway in primary cortical neurons.

Compared to the control group, using the HTRF assay, 0.1–100 μg/mL Erzhi formula showed significant inhibition of hepatic microsomal 11β-HSD1 activity ( $p < 0.001$ ) (Figures 6A,

B), where glycyrrhetic acid (GA) had an inhibition efficiency of approximately 58% and 0.1, 1, 10, and 100 μg/mL Erzhi formula had inhibition efficiencies of 40%, 42%, 50%, and 48%, respectively. Microscopic observations showed that GR-positive cells emitted red fluorescence, indicating that GR was widely expressed in the cytoplasm of primary cortical neurons (Figure 6C). Compared with the control group, GR expression was significantly reduced by half in the DEX group ( $p < 0.01$ ). Compared with the DEX group, 10 μg/mL Erzhi formula significantly reversed GR expression ( $p < 0.05$ ) (Figure 6D). After administration of 1 μM GR blocker RU486, there was no statistical difference in the RU486 group ( $p > 0.05$ ); compared to the DEX group, RU486 significantly upregulated GR expression ( $p < 0.01$ ) (Figure 6E). Compared to the control group, DEX upregulated 11β-HSD1 expression ( $p < 0.001$ ) and 0.1–10 μg/mL Erzhi formula upregulated 11β-HSD1 expression ( $p > 0.05$ ) (Figure 6F). Compared to the DEX group, RU486 significantly downregulated 11β-HSD1 expression ( $p < 0.01$ ) (Figure 6G). After administration of the 11β-HSD1 inhibitor CBX, the expression of 11β-HSD1 was significantly downregulated ( $p < 0.05$ ) (Figure 6H).

## 4 Discussion

GC is important for maintaining the stability of the internal environment under stress, and is an immunosuppressant involved in regulating various metabolic pathways in the body and the function of the central nervous system (Moraitis et al., 2016). However, under

stressful conditions, excess GC affects not only the functioning of the cardiovascular and peripheral immune systems but also the central nervous system by inducing psychiatric disorders such as depression or cognitive impairment (Joëls, 2018). DEX is a synthetic GC with anti-inflammatory and immunosuppressive effects (Parra-Sanchez and Parada, 2013), as well as a stress hormone with receptors widely distributed in the central nervous system.

Excess GC secreted under stress binds to GR in the cytoplasm and translocates to the nucleus, initiating or modifying gene transcription, causing apoptosis and synaptic damage, and ultimately damaging the central nervous system. Apoptosis is a physiological process that occurs in the body to maintain its own stability (Xia et al., 2016), and Bcl-2 and Bax act synergistically to regulate apoptosis (Noguti et al., 2015). Bcl-2 exerts its anti-apoptotic effects mainly by inhibiting Caspase-3 activation, blocking cytochrome C release, and maintaining intracellular calcium homeostasis (Jianyu et al., 2019). Stress stimuli can lead to the cleavage and activation of Caspase-3 precursors to form cleaved Caspase-3, which can degrade structural and functional proteins in cells and thus initiate the apoptotic process (Wang et al., 2019). Our results showed that DEX-induced apoptosis in primary cortical neurons was reduced by upregulating Bcl-2/Bax and downregulating cleaved Caspase-3/Caspase-3 protein expression. However, application of the Erzhi formula can downregulate Bcl-2/Bax and upregulate cleaved Caspase-3/Caspase-3 protein expression to exert anti-apoptotic effects.

Synaptic integrity is essential for maintaining normal neuronal function. Studies have shown that high concentrations of GC induce synaptic damage in the neurons. MAP-2 is a neuron-specific cytoskeletal protein involved in dendrite formation and maintenance of neuronal function (Kim et al., 2020). SYN and PSD95 are synaptic plasticity-associated proteins and markers of neuronal synaptic damage. PSD95 is involved in regulating synaptic strength, plasticity, maturation, and the promotion of dendritic spine morphogenesis and maturation (Ma et al., 2017), while SYN is mainly located at the presynaptic terminal and is involved in the regulation of synaptic vesicle cytokinesis. SYN deficiency may lead to synaptic dysfunction (Somayaji et al., 2020; Somayaji et al., 2021). Calcium phosphate precipitation is the preferred method for the transfection of appressed cells, and GFP transfection of neurons can clearly delineate the axons and dendrites of individual neurons. Our results showed that GFP was stably expressed in primary neurons, and the Erzhi formula ameliorated DEX-induced dendritic damage in primary cortical neurons. The Erzhi formula can improve neural growth and alleviate synaptic damage by regulating synaptic-related protein expression.

To investigate the mechanism of the Erzhi formula, we conducted a network pharmacological exploration. We found that the active ingredients in the Erzhi formula included 3'-Hydroxybiochanin A, Biochanin-A, Citric acid, Daidzein, and Salidroside. Potential targets included SYN, CASP3, CASP9, IL6, IL10, and so on. To elucidate the role of the Erzhi formula in treating depression, we crossed the potential targets of the Erzhi formula with the targets of depression and identified 64 intersecting targets. Nine core targets were selected using PPI and cluster analyses. They were found to be involved in steroid metabolic function after GO gene function enrichment analysis, which is consistent with the regulation of steroid hormone receptors in PPI analysis of depression. Among steroid metabolic functions, the target

11 $\beta$ -HSD1 is particularly important. 11 $\beta$ -HSD1 is a major determinant of cortisol overload, and its inhibition alleviates metabolic abnormalities (Mohd Azmi et al., 2021). Cortisol status is an objective marker of the stress response and the end-product of the HPA AXIS in response to various stressors (Qin et al., 2016; Huang et al., 2020). Neurosteroid hormone action can alter neuronal excitability and modulate stressful emotional responses such as anxiety and depression (Mendell and MacLusky, 2018). Depression leads to abnormalities in the HPA AXIS and abnormally high levels of corticosterone, which binds to corticosteroid receptors in the brain and induces various impairments (Vincent et al., 2013).

RU486, a GR blocker, has a high affinity for GR and antagonizes the binding of GC to GR by competitive occupation (Zalachoras et al., 2013). RU486 not only reverses the reduction in hippocampal neurons induced by long-term GC application but also reduces stress-induced apoptosis of newborn neurons and improves cognitive impairment (Mayer et al., 2006; Llorens-Martín and Trejo, 2011). GR mediates the action of GC by activating genes through association with the glucocorticoid responsive elements (GRE) (Timmermans et al., 2019). Sequence analysis of the cloned 11 $\beta$ -HSD1 gene revealed the presence of a CTGAT-ACAG sequence similar to the structural sequence of GRE at base pairs 197 to 190 upstream of the transcription start site of the 11 $\beta$ -HSD1 gene. Therefore, we hypothesized that DEX might regulate the gene and protein expression of 11 $\beta$ -HSD1 through GR-induced 11 $\beta$ -HSD1 gene promoter activation. Our results showed that RU486 blocked DEX-induced 11 $\beta$ -HSD1 increase in primary cortical neurons, suggesting that 11 $\beta$ -HSD1 expression caused by GC action on primary cortical neurons is partially mediated by GR. CBX, an inhibitor of 11 $\beta$ -HSD1, inhibits the activity of 11 $\beta$ -HSD1 and protects cells from neurotoxic damage (Sharma et al., 2021). 11 $\beta$ -HSD1, an isoform of 11 $\beta$ -HSD (Kadmiel and Cidlowski, 2013), is a low-affinity NADP<sup>+</sup>-dependent enzyme that catalyzes the interconversion between hydrocortisone and cortisone (Lagos et al., 2014). It is widely distributed in GC target organs, such as the liver, brain, and adipose (Bisschop et al., 2013). 11 $\beta$ -HSD1 is an important enzyme that regulates peripheral GC metabolism. Under stress, GC promotes hepatic 11 $\beta$ -HSD1 gene and protein expression and activity, and excess cortisol accelerates the negative feedback failure of the HPA AXIS, further exacerbating stress injury (Hinkelmann et al., 2009; Sarabdjitsingh et al., 2014). In our study, we selected liver microsomes and used CORT as the substrate and GA as the positive control drug to determine the concentration of cortisol using the HTRF method and found that the Erzhi formula had a significant effect on hepatic microsomal 11 $\beta$ -HSD1 activity *in vitro*. The Erzhi formula regulates GR and 11 $\beta$ -HSD1 protein expression in primary cortical neurons.

According to the above results, the Erzhi formula may exert an anti-depression effect by reducing neural apoptosis and alleviating synaptic damage. However, only network analysis and *in vitro* experiments were performed in the present study, and further *in vivo* analyses are required to confirm these results. Notably, the network analysis revealed a correlation between the modulation of steroid metabolism by the Erzhi formula and its treatment of depression, which was confirmed by *in vitro* validation of enzyme activity and protein expression assays, providing ideas for further studies.



## 5 Conclusion

In summary, the Erzhi formula has been shown to be effective in improving DEX-induced damage to primary cortical neurons, primarily by reducing neuronal apoptosis and improving synaptic damage. This potential mechanism is partly related to the inhibition of the 11 $\beta$ -HSD1-GC/GR signaling pathway.

## Data availability statement

The datasets presented in this study can be found in online repositories. The names of the repository/repository and accession number(s) can be found in the article/[Supplementary Material](#).

## Ethics statement

The animal study was reviewed and approved by Animal Ethics Committee of Tianjin University of Chinese Medicine and the ethical review number is TCM-LAEC2022088.

## Author contributions

RH and GH contributed equally to this work and share first authorship. LL and HZ conceived the research. RH and GH collected the data. YY and LH did the Network analysis. RH drafted the manuscript. LL and HZ revised the manuscript content.

## Funding

This work was supported by National Natural Science Foundation of China (81973792). This work is supported by

Innovation Team and Talents Cultivation Program of National Administration of Traditional Chinese Medicine (No: ZYYCXTD-C-202009).

## Acknowledgments

We are grateful for the support of the 2022 Chinese Medicine Clinical Efficacy Enhancement Project of National Administration of Traditional Chinese Medicine.

## Conflict of interest

The authors declare that the research was conducted in the absence of any commercial or financial relationships that could be construed as a potential conflict of interest.

## Publisher's note

All claims expressed in this article are solely those of the authors and do not necessarily represent those of their affiliated organizations, or those of the publisher, the editors and the reviewers. Any product that may be evaluated in this article, or claim that may be made by its manufacturer, is not guaranteed or endorsed by the publisher.

## Supplementary material

The Supplementary Material for this article can be found online at: <https://www.frontiersin.org/articles/10.3389/fphar.2023.1038492/full#supplementary-material>

## References

- Ajala, T. (2017). The effects of adaptogens on the physical and psychological symptoms of chronic stress. *J. Discov. Ga. State Honors Coll. Undergrad. Res. J.* 4 (1), 2. doi:10.31922/disc4.2
- Bisschop, P. H., Dekker, M. J., Osterthun, W., Kwakkel, J., Anink, J. J., Boelen, A., et al. (2013). Expression of 11 $\beta$ -hydroxysteroid dehydrogenase type 1 in the human hypothalamus. *J. Neuroendocrinol.* 25 (5), 425–432. doi:10.1111/jne.12017
- Block, T., Petrides, G., Kushner, H., Kalin, N., Belonaff, J., and Schatzberg, A. (2017). Mifepristone plasma level and glucocorticoid receptor antagonism associated with response in patients with psychotic depression [J]. *J. Clin. Psychopharmacol.* 37, 505–511. doi:10.1097/JCP.0000000000000744
- Finsterwald, C., Steinmetz, A. B., Travaglia, A., and Alberini, C. M. (2015). From memory impairment to posttraumatic stress disorder-like phenotypes: The critical role of an unpredictable second traumatic experience. *J. Neurosci. official J. Soc. Neurosci.* 35 (48), 15903–15915. doi:10.1523/JNEUROSCI.0771-15.2015
- Hinkelmann, K., Moritz, S., Botzenhardt, J., Riedesel, K., Wiedemann, K., Kellner, M., et al. (2009). Cognitive impairment in major depression: Association with salivary cortisol. *Biol. psychiatry* 66 (9), 879–885. doi:10.1016/j.biopsych.2009.06.023
- Huang, Y., Xu, C., He, M., Huang, W., and Wu, K. (2020). Saliva cortisol, melatonin levels and circadian rhythm alterations in Chinese primary school children with dyslexia. *Med. Baltim.* 99 (6), e19098. PMID: 32028434. doi:10.1097/MD.00000000000019098
- Jianguo, F., Yushan, Z., Quan, C., and Jialing, L. (2019). Physiological function and structural basis of bcl-2 family proteins. *Zhongguo Xi Bao Sheng Wu Xue Xue Bao* 41 (8), 1477–1489. Chinese. Epub 2019 Sep 12. PMID: 34249113; PMCID: PMC8265309.
- Joëls, M. (2018). Corticosteroids and the brain. *J. Endocrinol.* 238 (3), R121–R130. Epub 2018 Jun 6. PMID: 29875162. doi:10.1530/JOE-18-0226
- Kadmiel, M., and Cidlowski, J. A. (2013). Glucocorticoid receptor signaling in health and disease. *Trends Pharmacol. Sci.* 34 (9), 518–530. doi:10.1016/j.tips.2013.07.003
- Kim, Y., Jang, Y. N., Kim, J. Y., Noh, S., and Kim, H. (2020). Microtubule-associated protein 2 mediates induction of long-term potentiation in hippocampal neurons. *EASEB J. official Publ. Fed. Am. Soc. Exp. Biol.* 34 (5), 6965–6983. doi:10.1096/fj.201902122RR
- Lagos, C. F., Vecchiola, A., Allende, F., Fuentes, C. A., Tichauer, J. E., Valdivia, C., et al. (2014). Identification of novel 11 $\beta$ -HSD1 inhibitors by combined ligand- and structure-based virtual screening. *Mol. Cell. Endocrinol.* 384 (1–2), 71–82. doi:10.1016/j.mce.2014.01.011
- Lim, L., Mi, D., Llorca, A., and Marin, O. (2018). Development and functional diversification of cortical interneurons. *Neuron* 100 (2), 294–313. doi:10.1016/j.neuron.2018.10.009
- Llorens-Martín, M., and Trejo, J. L. (2011). Mifepristone prevents stress-induced apoptosis in newborn neurons and increases AMPA receptor expression in the dentate gyrus of C57/BL6 mice. *PLoS one* 6 (11), e28376. doi:10.1371/journal.pone.0028376
- Ma, Q., Ruan, H., Peng, L., Zhang, M., Gack, M. U., and Yao, W. D. (2017). Proteasome-independent polyubiquitin linkage regulates synapse scaffolding, efficacy, and plasticity. *Proc. Natl. Acad. Sci. U. S. A.* 114 (41), E8760–E8769. doi:10.1073/pnas.1620153114
- Macpherson, A., Dinkel, K., and Sapolsky, R. (2005). Glucocorticoids worsen excitotoxin-induced expression of pro-inflammatory cytokines in hippocampal cultures. *Exp. Neurol.* 194 (2), 376–383. doi:10.1016/j.expneurol.2005.02.021

- Mayer, J. L., Klumpers, L., Maslam, S., de Kloet, E. R., Joels, M., and Lucassen, P. J. (2006). Brief treatment with the glucocorticoid receptor antagonist mifepristone normalises the corticosterone-induced reduction of adult hippocampal neurogenesis. *J. Neuroendocrinol.* 18 (8), 629–631. doi:10.1111/j.1365-2826.2006.01455.x
- Mendell, A. L., and MacLusky, N. J. (2018). Neurosteroid metabolites of gonadal steroid hormones in neuroprotection: Implications for sex differences in neurodegenerative disease. *Front. Mol. Neurosci.* 11, 359. PMID: 30344476. doi:10.3389/fnmol.2018.00359
- Mohd Azmi, N. A. S., Juliana, N., Azmani, S., Mohd Effendy, N., Abu, I. F., Fahmi Teng, M., et al. (2021). Cortisol on circadian rhythm and its effect on cardiovascular system. *Int. J. Environ. Res. Public Health* 18 (2), 676. doi:10.3390/ijerph18020676
- Moraitis, A. G., Block, T., Nguyen, D., and Belanoff, J. K. (2016). The role of glucocorticoid receptors in metabolic syndrome and psychiatric illness. *J. steroid Biochem. Mol. Biol.* 165, 114–120. doi:10.1016/j.jsbmb.2016.03.023
- Noguti, J., Alvarenga, T. A., Marchi, P., Oshima, C. T. F., Andersen, M. L., and Ribeiro, D. A. (2015). The influence of sleep restriction on expression of apoptosis regulatory proteins p53, Bcl-2 and Bax following rat tongue carcinogenesis induced by 4-nitroquinoline 1-oxide. *J. oral pathology Med. official Publ. Int. Assoc. Oral Pathologists Am. Acad. Oral Pathology* 44 (3), 222–228. doi:10.1111/jop.12225
- Parra-Sanchez, I., and Parada, K. (2013). Perioperative uses of dexamethasone. 2013.
- Puigoriol-Illamola, D., Companys-Alemany, J., and Homer, N. (2020). *RL-118 and 11β-HSD1 target engagement through TAPS assay: Behaviour and molecular analysis*. New York: Cold Spring Harbor Laboratory.
- Puigoriol-Illamola, D., Leiva, R., Vázquez-Carrera, M., Vazquez, S., Grinan-Ferre, C., and Pallas, M. (2020). 11β-HSD1 inhibition rescues SAMP8 cognitive impairment induced by metabolic stress. *Mol. Neurobiol.* 57 (1), 551–565. doi:10.1007/s12035-019-01708-4
- Qin, D. D., Rizak, J., Feng, X. L., Yang, S. C., Lü, L. B., Pan, L., et al. (2016). Prolonged secretion of cortisol as a possible mechanism underlying stress and depressive behaviour. *Sci. Rep.* 6, 30187. doi:10.1038/srep30187
- Sarabdjitsingh, R. A., Zhou, M., Yau, J. L., Webster, S. P., Walker, B. R., Seckl, J. R., et al. (2014). Inhibiting 11β-hydroxysteroid dehydrogenase type 1 prevents stress effects on hippocampal synaptic plasticity and impairs contextual fear conditioning. *Neuropharmacology* 81, 231–236. doi:10.1016/j.neuropharm.2014.01.042
- Sharma, S., Saini, A., and Nehru, B. (2021). Neuroprotective effects of carbenoxolone against amyloid-beta 1-42 oligomer-induced neuroinflammation and cognitive decline in rats. *Neurotoxicology* 83, 89–105. Epub 2021 Jan 4. PMID: 33412218. doi:10.1016/j.neuro.2020.12.015
- Somayaji, M., Cataldi, S., Choi, S. J., Edwards, R. H., Mosharov, E. V., and Sulzer, D. (2020). A dual role for α-synuclein in facilitation and depression of dopamine release from substantia nigra neurons *in vivo*. *Proc. Natl. Acad. Sci. U. S. A.* 117 (51), 32701–32710. Epub 2020 Dec 3. PMID: 33273122; PMCID: PMC7768743. doi:10.1073/pnas.2013652117
- Somayaji, M., Lanseur, Z., Choi, S. J., Sulzer, D., and Mosharov, E. V. (2021). Roles for α-synuclein in gene expression. *Genes (Basel)* 12 (8), 1166. doi:10.3390/genes12081166
- Terunuma, T., Kawauchi, S., Kajihara, M., and Takahashi, S. (2003). Effect of acoustic stress on glucocorticoid receptor mRNA in the cochlea of the Guinea pig. *Brain Res. Mol. Brain Res.* 120 (1), 65–72. doi:10.1016/j.molbrainres.2003.10.002
- Timmermans, S., Souffriau, J., and Libert, C. (2019). A general introduction to glucocorticoid biology. *Front. Immunol.* 10, 1545. PMID: 3133367. doi:10.3389/fimmu.2019.01545
- Vincent, V., Feng, J., Robison, A. J., and Nestler, E. J. (2013). Epigenetic mechanisms of depression and antidepressant action. *Annu. Rev. Pharmacol. Toxicol.* 53 (1), 59–87. doi:10.1146/annurev-pharmtox-010611-134540
- Wang, H., Zhuang, W., and Xue, X. (2017). Study on the Origin, Evolution and modern pharmacological research of traditional Chinese medicine compound Erzhi Pill [J]. *J. LIAONING Univ. TRADITIONAL Chin. Med.* 019 (012), 93–97.
- Wang, Q., Gan, X., Li, F., Chen, Y., Fu, W., Zhu, X., et al. (2019). PM<sub>2.5</sub> exposure induces more serious apoptosis of cardiomyocytes mediated by Caspase3 through JNK/P53 pathway in hyperlipidemic rats. *Int. J. Biol. Sci.* 15 (1), 24–33. doi:10.7150/ijbs.28633
- White, P. C. (2018). Alterations of cortisol metabolism in human disorders. *Horm. Res. Paediatr.* 89 (5), 320–330. Epub 2018 May 29. PMID: 29843121. doi:10.1159/000485508
- Wyrwoll, C. S., Holmes, M. C., and Seckl, J. R. (2011). 11β-hydroxysteroid dehydrogenases and the brain: From zero to hero, a decade of progress. *Front. Neuroendocrinol.* 32 (3), 265–286. doi:10.1016/j.yfrne.2010.12.001
- Xia, P., Liu, Y., and Cheng, Z. (2016). Signaling pathways in cardiac myocyte apoptosis [J]. *BioMed Res. Int.* 2016, 9583268. doi:10.1155/2016/9583268
- Zalachoras, I., Houtman, R., Atucha, E., Devos, R., Tijssen, A. M., Hu, P., et al. (2013). Differential targeting of brain stress circuits with a selective glucocorticoid receptor modulator. *Proc. Natl. Acad. Sci. U. S. A.* 110 (19), 7910–7915. Epub 2013 Apr 23. PMID: 236135. doi:10.1073/pnas.1219411110
- Zhang, Y., Dai, Z., Hu, J., Qin, S., Yu, R., and Sun, U. (2020). Stress-induced changes in modular organizations of human brain functional networks [J]. *Neurobiol. stress* 13, 100231. doi:10.1016/j.ynstr.2020.100231

# Frontiers in Pharmacology

Explores the interactions between chemicals and living beings

The most cited journal in its field, which advances access to pharmacological discoveries to prevent and treat human disease.

## Discover the latest Research Topics

[See more →](#)

### Frontiers

Avenue du Tribunal-Fédéral 34  
1005 Lausanne, Switzerland  
[frontiersin.org](https://frontiersin.org)

### Contact us

+41 (0)21 510 17 00  
[frontiersin.org/about/contact](https://frontiersin.org/about/contact)



### Frontiers in Pharmacology

